Electromagnetic Performance of Fractional Slot Interior Permanent Magnet and Synchronous Reluctance Brushless AC Machines Having Non-overlapping Concentrated Windings

Ziad Azar

A thesis submitted for the degree of Doctor of Philosophy

Department of Electronic and Electrical Engineering
The University of Sheffield
Mappin Building
Mappin Street
Sheffield
S1 3JD
UK

October 2012

Abstract

This thesis investigates the electromagnetic performance of the fractional-slot interior permanent magnet (IPM) and salient-pole synchronous reluctance (SynR) brushless AC machines having non-overlapping concentrated windings, the SynR machines being excited by bipolar AC sinusoidal currents with and without DC bias. The analyses are validated by finite element calculations and measurements.

The PM machines with modular stators are often employed to improve the electromagnetic performance and ease the manufacture process, particularly stator winding. The influence of uniform and non-uniform additional gaps between the stator teeth and back-iron segments on the electromagnetic performance of fractional-slot IPM machines having either un-skewed or step-skewed rotors and different slot openings, viz. open slot, closed slot and hybrid slot (sandwiched open and closed slots), is investigated. The influence of load conditions on cogging torque and back-emf waveforms and the effectiveness of rotor skew on the minimization of the cogging torque, thus the torque ripple, are also examined. It is found that the additional gaps have a negligible influence on the average output torque, but significantly increase the cogging torque magnitude, while their non-uniformity can cause a large increase in both the peak and periodicity of cogging torque waveform, which in turn makes the skew method ineffective. The magnetic cross-coupling level and the sensitivity of cogging torque to manufacturing limitations and tolerances strongly depend on the slot opening materials. The cogging torque magnitude is significantly increased by load, while its periodicity also changes with load which makes the rotor skew less effective unless the machine is skewed by one cogging torque period on load.

The electromagnetic performance of the SynR machines under AC sinusoidal bipolar excitation with and without DC bias is investigated and compared for three different winding connections, such as asymmetric, symmetric and hybrid. In general, the SynR brushless AC machines with DC bias excitation exhibit significantly higher torque density than those without DC bias. Comparing with the asymmetric and symmetric winding connections, their hybrid counterpart results in significantly larger mutual inductance variations. Consequently, it results in significantly larger output torque, since such torque is produced by the variation of both the self and mutual inductances. In terms of torque ripple, the symmetric winding connection leads to the best performance. On the other hand, at significantly larger current densities, the hybrid winding connection become more suitable, since it exhibits large average output torque and relatively low torque ripple.

Acknowledgments

Great thanks are due to my supervisor, Prof. Zi-Qiang Zhu, for his strong and continued support, advices and encouragements, which have been invaluable in the completion of this thesis. Thanks are also due to all members of the Electrical Machines and Drives Group at the University of Sheffield, particularly Mr John Wilkinson and Mr Lawrence Obodo for their assistances in the building of the prototype machines.

I would like also to thank the Engineering and Physics Sciences Research Council (EPSRC) for the financial support, as well as Brose Germany and IMRA UK for their help in the fabrication of the prototype machines.

Finally, I warmly thank my wife, Batool, for her support and understanding, also my children, Sarah and Mark, and my Parents for their love and encouragement.

Contents

List of Symbols

B_m	Flux Density Amplitude (T)
B_{PC}	Current Flux Density (T)
B_{PM}	PM Flux Density (T)
B_{WP}	Flux Density of Working Point (T)
C_T	Cogging Torque Goodness Factor
f_{B_m}	Flux Density Frequency (Hz)
H_{PC}	Current Field Strength (A/m)
H_{PM}	PM Field Strength (A/m)
H_{WP}	Field Strength of Working Point (A/m)
I_d	d-axis Current (A)
I_{ph}	Phase Current (A)
I_q	q-axis Current (A)
I_{rms}	RMS Phase Current (A)
K_{B_m}	Hysteresis Loss Minor Loop Coefficient
K_{sk}	Skew Factor
L_d	d-axis Inductance (H)
L_q	q-axis Inductance (H)
L_d^{SK}	Skewed d-axis Inductance (H)
L_q^{SK}	Skewed q-axis Inductance (H)
N_S	Number of Slot
p	Pole Pair Number
P_{copper}	Copper Loss (W)
P_{input}	Input Power (W)
P_{iron}	Iron Loss (W)
P_{output}	Output Power (W)

Q_{PS}	Slot/Pole number Last Common Multiple
R_{ph}	Phase Resistance (Ω)
T	Output Torque (N.m)
T_{cog}	Cogging Torque (N.m)
T_{PM}	Electromagnetic Output Torque (N.m)
V_d	d-axis Voltage (V)
V_{line}	Line Voltage (V)
V_{ph}	Phase Voltage (V)
V_q	q-axis Voltage (V)
ω	Electrical Rotating Speed (red.S^{-1})
α_p	Optimal Pole Arc to Pole Pitch Ratio
β	Current Angle (deg)
ΔL_{dq}	Variation of dq-axis Inductances Differentiation (H)
$\Delta\psi_{md}$	Variations of PM flux linkage on d-axis (Wb)
μ_r	Relative Permeability
θ	Rotor position (deg)
η	Efficiency (%)
Ψ_{cd}	Current Flux Linkage on d-axis (Wb)
Ψ_{cq}	Current Flux Linkage on q-axis (Wb)
ψ_d	Total Flux Linkage on d-axis (Wb)
ψ_{md}	PM Flux Linkage on d-axis (Wb)
ψ_{mq}	PM Flux Linkage on q-axis (Wb)
ψ_{ph}	Phase Flux linkage (Wb)
Ψ_q	Total Flux Linkage on q-axis (Wb)

Chapter 1: Introduction

1.1. General Introduction

Due to the concerns of global warming and energy crisis, the requirements of reducing the energy consumption and CO_2 emission become more significant. Therefore, there is a strong trend to replace the conventional mechanical components by more efficient electrical counterparts, e.g. more electric aircrafts [1] and hybrid electric or pure electric vehicles [2]. Meanwhile, the wind power generation, which produces the renewable energy, is being rapidly utilised [3, 4]. The key enabling technologies of the mentioned systems are electrical machines, either motors or generators. The main criteria of employing such machines include:

- High torque/power density;
- High efficiency ;
- High reliability;
- Low cost.

Furthermore, significant investigations and researches have been carried out to further increase the efficiency and power capability of conventional electrical machines and to develop new machine topologies, which exhibit an improved electromagnetic performance. The following are examples of typical electrical machines that may be used in the foregoing mentioned applications:

a). Permanent magnet (PM) machines;
b). Switched reluctance (SR) machines;
c). Induction machines.

In this thesis, the first two machine topologies are discussed, investigated and analysed:

a). PM machines, which will be further highlighted in section 1.2, will be analysed for power steering systems.
b). SR machines, which will be discussed in more details in section 1.3, will be operated and investigated as salient-pole synchronous reluctance (SynR) for hybrid electrical vehicles.

1.2. Permanent Magnet Machines

The history of PM machines can be traced back to mid of last century [5]. However, the interest and utilising of such machines dramatically increased in early 70's and 80's when the rare earth magnet materials, i.e. SmCo and NdFeB magnets, which have high energy product, e.g. remanence flux density (Br) ≈ 1.1-1.2 T, were invented. Comparing with the conventional electrical machines, the PM counterparts exhibit inherently high torque density and efficiency, since the magnets are utilised as exciters. Currently, the PM machines are widely utilised in industrial and commercial applications and for all power ranges [6-14]. The main benefits of such machines can be summarised by:

- High torque and power density;
- High efficiency;
- High reliability; low maintenance (no brushes);
- Ability to exhibit a wide speed range;
- Ability to operate in direct drive systems.

On the other hand, their main disadvantages include:

- Cogging torque;
- Torque ripple;
- Possibility of irreversible demagnetization;
- High cost of magnet materials.

In general, the PM machines are designed to have either a sinusoidal or trapezoidal back-emf waveform [15-18]. To maximise the average output torque and minimise the torque ripple, the machines having sinusoidal back-emf waveform are desirable to be driven by sinusoidal currents, e.g. the brushless AC (BLAC) drive mode as illustrated in Fig. 1.1(a). On the other hand, the rectangular phase currents should be injected when the back-emf is trapezoidal, e.g. the brushless DC (BLDC) drive mode, as shown in Fig. 1.1(b). However, in theory, any PM machine can be operated in either the BLAC or BLDC drive mode. Furthermore, the torque-speed performance of the PM machines having sinusoidal back-emf waveform can be improved by utilising a hybrid drive mode, i.e. the BLAC mode in constant-torque region and BLDC mode in the flux weakening operation region, as discussed in [16].

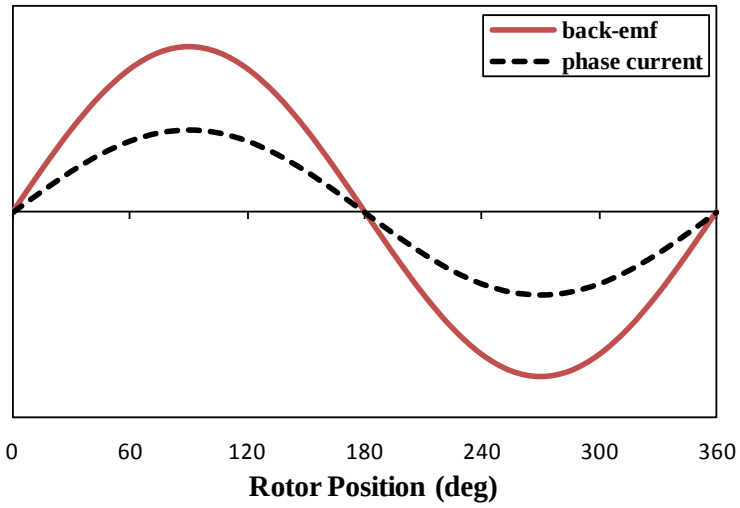

(a) BLAC drive mode.

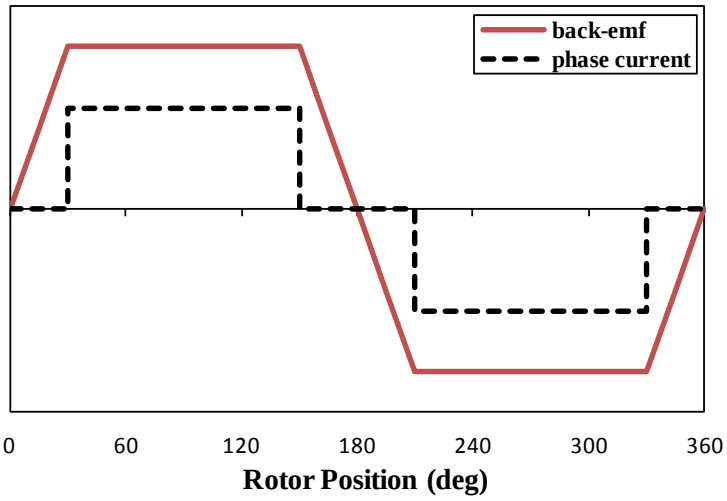

(b) BLDC drive mode.

Fig. 1.1 Ideal back-emf and phase current waveforms of PM machines having different operation modes.

1.2.1. PM Machine Topologies

In addition to more conventional surface-mounted and interior PM machines, many novel PM machine topologies have been proposed and investigated in literature, such as multi-layer interior, double salient, switched flux, and transverse-flux PM machines [19-24]. The suitability and benefits of each topology depend on the application where the machine is employed. For example, the external rotor radial field PM machine is a good choice for the direct drive wind power generator, since the blades can be fixed directly on the rotor [3]. On the other hand, the axial field PM machines are a good solution for the in wheel traction applications because they are very compact, thus can be fitted within the wheel [25]. In

general, the PM machines can be categorized in many different groups, for example according to:

- Rotating part: internal/external rotor;
- Magnetic field direction: radial/axial or
- Location of magnets: on/in rotor or stator.....etc.

In this section, two common machine topologies are highlighted. The surface mounted PM (SPM) machine topology, which is the most common topology [26], and the interior PM (IPM) machines since it is also a very common topology [6] and is the research subject of chapters 2, 3, 4 and 5.

1.2.1.1. Surface Mounted PM machines

This topology is usually classified as radial magnetic field PM machines having their magnets on the rotor surface, as illustrated in Fig. 1.2. Although the topology shown in Fig. 1.2 is internal rotor, the SPM machines with external rotor or axial field are also possible and have also been widely investigated [27, 28]. In addition to the common benefits of PM machines, such topology also has relatively low flux leakage, thus relatively larger torque density, and low rotor iron loss since the influence of armature reaction is relatively low due to the large effective air gap. For the same reason, the d-axis inductance of the SPM machines is relatively small, thus the flux weakening capability is also relatively low, which is considered as a disadvantage for this topology [29]. Furthermore, this topology does not exhibit any reluctance torque since the d- and q-axis reluctances are nearly the same, i.e. its saliency ratio is nearly one. Therefore, in order to increase this ratio thus to enlarge the generated reluctance torque, a special SPM machine topology has been introduced. In this topology, the magnets are inserted in the rotor with iron bridges between them, as shown in Fig. 1.3, [30]. However, whatever the magnets are on the surface or inserted in the rotor body, in general the SPM topology exhibits a relatively low demagnetisation withstanding because the magnets are directly exposed to the armature reaction field. This is a serious weakness point of such topology and could limit its uses, especially in the applications that have relatively large electric loading.

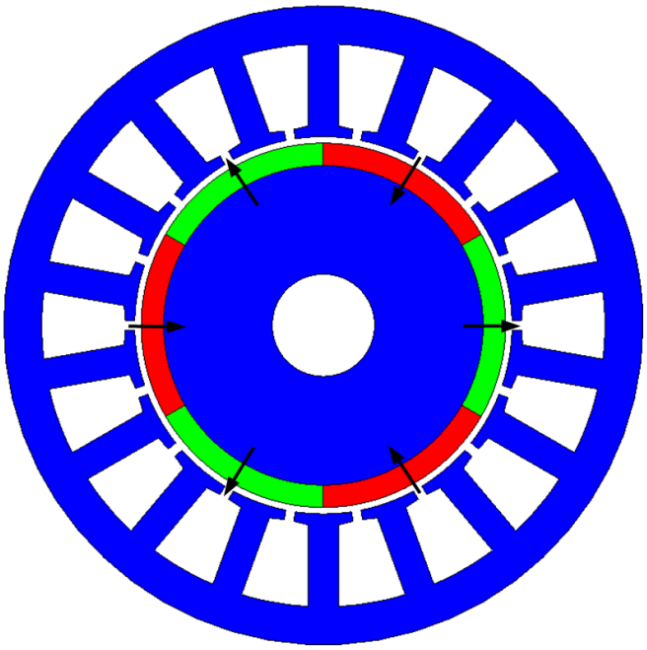

Fig. 1.2 Surface-mounted PM machines

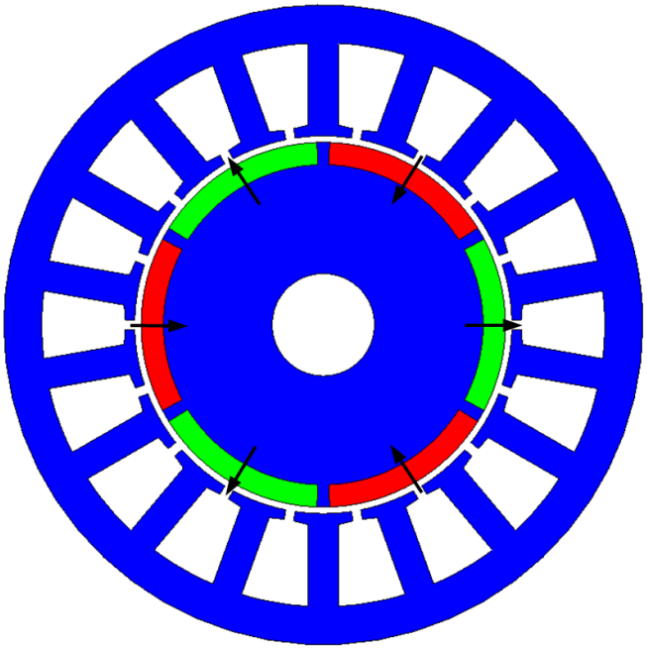

Fig. 1.3 Inset PM machines

1.2.1.2. Interior PM machines

In this topology the magnets are placed inside the rotor iron body. Therefore, according to the burial way, the IPM machines can have different categories:

- Circumferential I-shape IPM machines, Fig. 1.4(a).
- Radial I-shape IPM machines, Fig. 1.4(b).
- Flux focusing V-shaped IPM machines, Fig. 1.4(c).

Due to the geometry, the IPM machines have relatively large reluctance torque, since q-axis reluctance is lower than the d-axis reluctance, thus q-axis inductance is larger than its d-axis counterpart. In addition, comparing with the SPM machines, the IPM topology offers better demagnetisation withstanding and less magnet loss since its magnets are shielded by the rotor iron. Further, it exhibits wider flux weakening operation region since its d-axis inductance is larger. On the other hand, the IPM machine presents relatively high flux leakage and more air gap flux density harmonics. Comparing with the SPM machines, this results in relatively low PM torque and larger iron loss [31]. Moreover, the multi-layer V-shape design, e.g. usually 2 or 3 magnet layers, can be utilised to further improve the reluctance torque and flux weakening capability [20, 32]. An extreme case of the multi-layer design is the axially laminated IPM machines, where the magnet sheet layers are axially sandwiched between rotor laminations. Such design can produce a significantly wide flux weakening operation region and high reluctance torque [33, 34], but it is relatively hard and costly to manufacture.

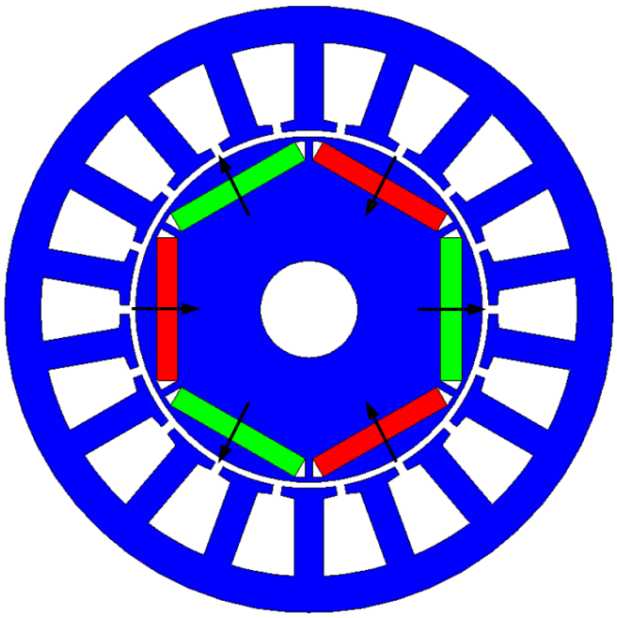

(a) Circumferential I-shape

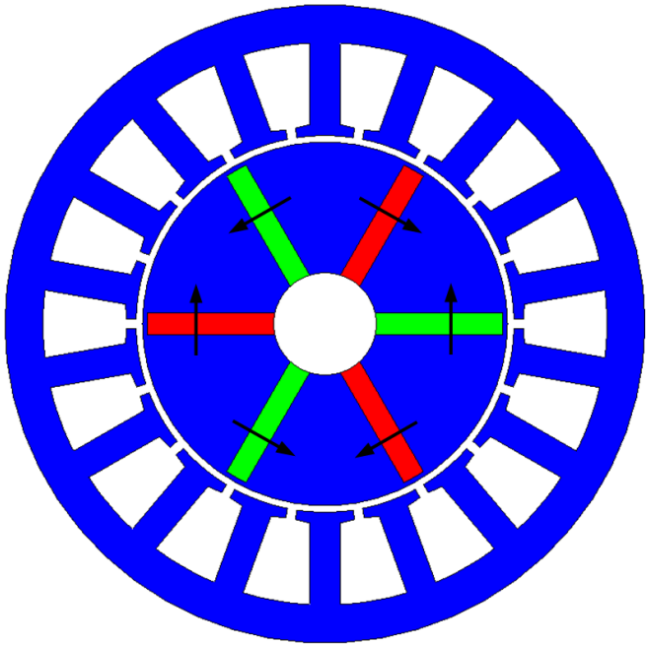

(b) Radial I-shape

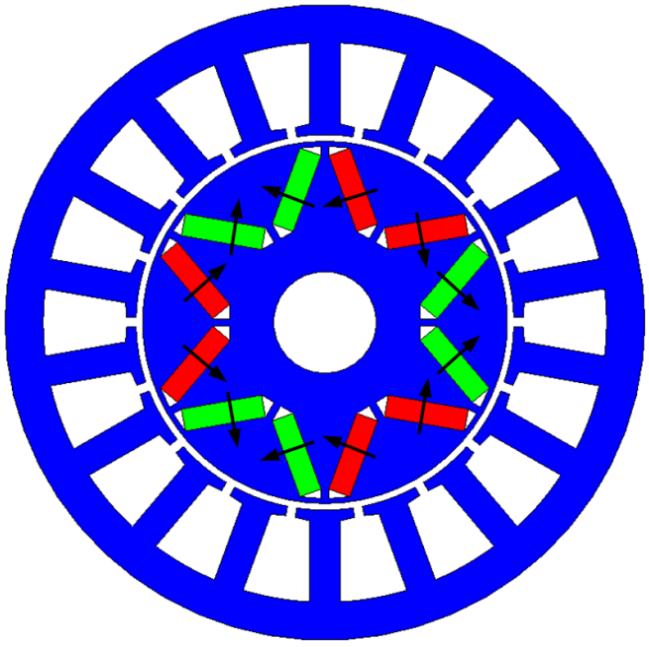

(c) Single layer V-shaped

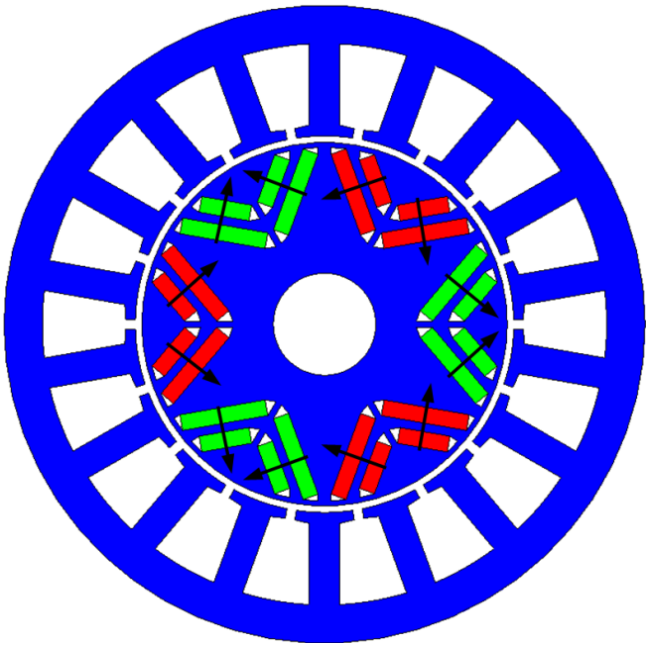

(d) Two layer V-shaped

Fig. 1.4 Interior PM machines having different topologies.

1.2.2. Electromagnetic Performance and Characteristics

The cogging torque and output torque of the PM machines as well as their flux weakening operation characteristics and dq-axis inductances are reviewed in this section since they are the major subjects for investigation in this thesis. In addition, this section also highlights the frozen permeability (FP) technique, which is utilised to segregate the influence of PMs and armature reaction field with fully accounting for the magnetic saturation.

1.2.2.1. Cogging Torque

The cogging torque, which is produced by the interaction between the permanent magnets (PMs) and stator slotting, is considered as a major disadvantage in the PM machines, especially at low load and speed. It is one of the major sources of torque ripple, which causes acoustic noise and vibration.

Many different design techniques have been proposed to minimise the cogging torque, e.g. to choose the appropriate pole-slot combination, to skew either the stator or rotor and/or to optimise the machine parameters, such as the pole arc to pole pitch ratio, magnet shaping and slot opening [35-41]. The authors in [35] have introduced the cogging torque goodness

factor, which reflects the goodness of pole-slot combination, e.g. the higher the goodness factor is the larger the cogging torque. This factor is analytically given by:

$$C_T = \frac{2pN_S}{Q_{PS}} \tag{1.1}$$

where Q_{PS} is the least common multiple between the pole number $2p$ and slot number N_S.

In addition, it is a common and effective technique to skew the machine by one cogging torque period, which is given by:

$$\text{Cogging torque period} = \frac{2\pi}{Q_{PS}} \tag{1.2}$$

Furthermore, the optimal pole arc to pole pitch ratio, can be calculated by [35]:

$$\alpha_P = \frac{\frac{Q_{PS}}{2p} - k}{\frac{Q_{PS}}{2p}} \qquad \left(k = 1,2.....\frac{Q_{PS}}{2p} - 1\right) \tag{1.3}$$

In the previous techniques, the influence of the manufacturing tolerance, errors and defects are not considered, i.e. the design is assumed to be ideal. However, in reality, such issues could have a significant influence on the cogging torque [42, 43]. For example, the stator asymmetry, which results from the manufacturing tolerances, can cause a significant increase in the cogging torque magnitude and generate low order cogging torque components [43]. Also, the assembly tolerance as well as the PMs imperfection can cause additional cogging torque components [44-46]. Furthermore, in practice, the effectiveness of cogging torque reduction techniques could be limited or diminished due to the manufacturing defects [47]. A combined analytical and numerical technique to account for the manufacturing tolerance during the machine design process has been proposed in [48]. In this thesis, the influences of the manufacturing tolerances and limitations on the cogging torque as well as the effectiveness of the skewing technique are highlighted and examined in details in chapters 3 and 4. In addition, the influence of the electric loading and magnetic saturation on such torque is also investigated and analysed in chapter 5.

1.2.2.2. Output Torque

The dq-axis machine model, thus the dq-axis parameters are often utilized to analyze, e.g. predicted torque-speed characteristics, as well as to control the PM machines [49, 50]. Based on this theory the output torque of the PM machines can be calculated by:

$$T = \frac{3}{2} p[(\psi_{md} I_q + (L_d - L_q) I_d I_q] \tag{1.4}$$

where $p, \psi_{md}, L_d, L_q, I_d$ and I_q are the pole pair number, PM flux linkage, d-axis and q-axis inductances and currents, respectively. $\psi_m I_q$ is the electromagnetic torque, which is due to the interaction between the PMs and armature current, while $(L_d - L_q) I_d I_q$ is the reluctance torque, which is due to the difference between d- and q-axis inductances. The dq-axis currents are determined by the phase current magnitude, I_{ph}, and its angle, β, as follows:

$$I_d = I_{ph} \sin(\beta) \tag{1.5}$$

$$I_q = I_{ph} \cos(\beta) \tag{1.6}$$

As mentioned before, the reluctance torque of the SPM machines is zero. Thus, the maximum torque is obtained by injecting the phase current in q-axis, i.e. at β=0, while in the IPM machines the dq-axis reluctances are different. Thus, the optimal current angle should be determined to operate the machine at its maximum output torque. Fig. 1.5 illustrates and compares the torque-current angle characteristics of both SPM and IPM machines. Furthermore, in order to guarantee the maximum performance out of the machine, the dq-axis parameters should be accurately determined [51]. Normally, the PM machines are operated under high electric loading, thus the magnetic saturation level is relatively high. Therefore, the d- and q-axis parameters could be correlated due to the magnetic cross-coupling between both axes [50-52]. This phenomenon is well recognized and has been deeply investigated in literature [53-57]. However, it is further investigated and different techniques are proposed and discussed to account for it in chapters 2 and 4.

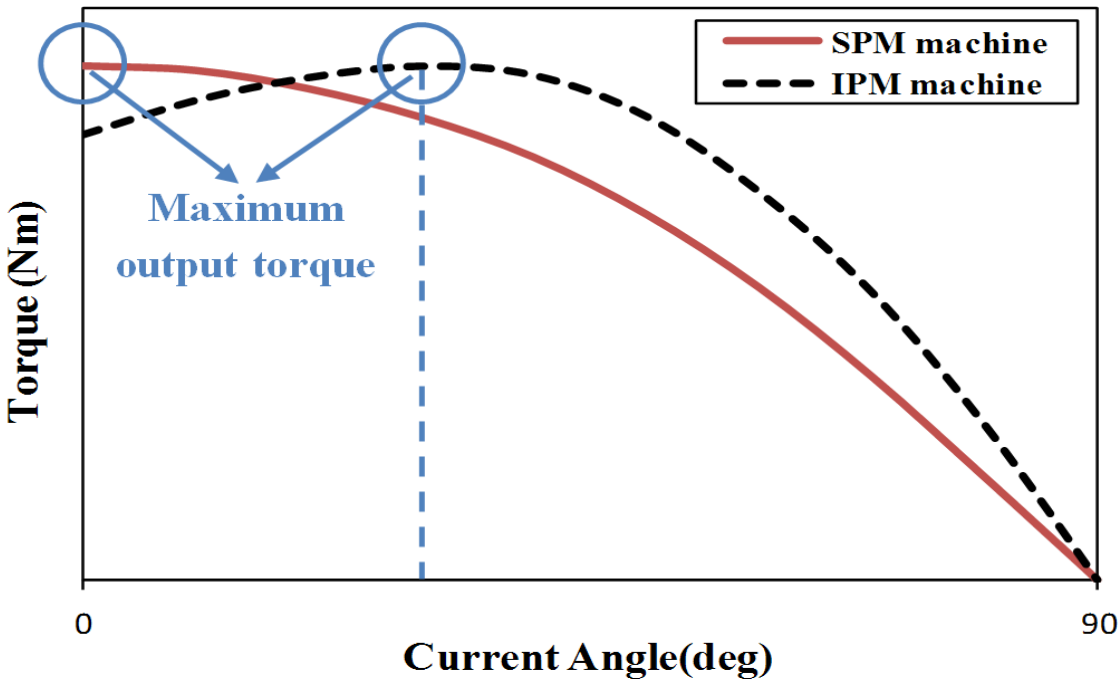

Fig. 1.5 Comparison of torque-current angle characteristics of SPM and IPM machines.

1.2.2.3. Flux Weakening Operation

In general, the operation range for any PM machine can be divided into two regions [58], as shown in Fig. 1.6:

a). **Constant-torque:** it extends between zero and the rated speed. Within this region, the machine can deliver a constant torque and the maximum torque per ampere control is often employed, while the power gradually increases from zero to reach the rated power at the rated speed.

b). **Flux weakening operation:** it is the region beyond the rated speed up to the maximum feasible speed of the machine within the rated phase current and voltage. This region could possibly contain both a constant power region at relatively medium speeds and decreased power range at relatively high speeds or it could be just one of them, as illustrated in Fig. 1.6. This strongly depends on the phase current rated value, d-axis inductance and PM flux linkage.

Theoretically, the maximum speed is infinite when:

$$\frac{\psi_{md}}{I_{ph} \cdot L_d} \leq 1 \tag{1.7}$$

Thus, the higher the d-axis inductance the wider the flux weakening operation region [13, 14]. In general, comparing with the SPM machines, their IPM counterparts have the ability to exhibit much wider flux weakening operation region because they have larger d-axis inductance, which in turn is due to the small air gap in such topology [59]. However, according to [60], at specific designs and operation parameters any PM machine, no matter whether it is SPM or IPM, could be able to exhibit an infinite flux weakening operation region.

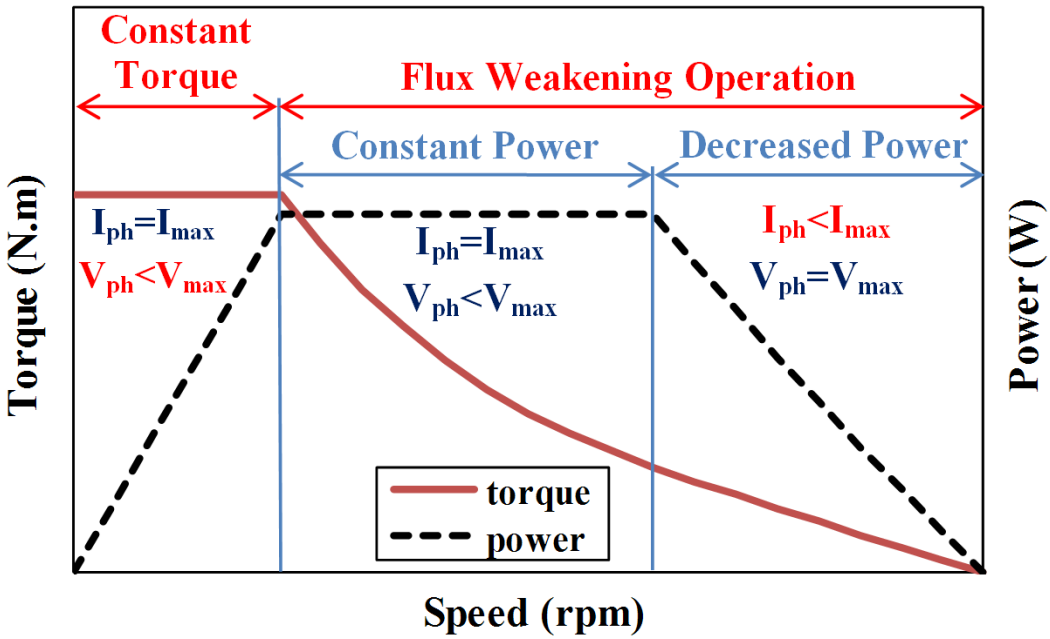

Fig. 1.6 Torque-speed characteristics of PM machines.

Moreover, since the PM excitation flux is constant, the negative d-axis current is normally utilised to weaken such flux to make the machine voltage satisfy the supply voltage limitation [61]. Therefore, at relatively high speeds the flux weakening needs to be stronger thus higher d-axis current is required. When the electric loading of the machine is significant an irreversible demagnetisation could be experienced. This illustrates the reason for better demagnetisation withstanding in the IPM machines, since the armature reaction has an alternative path to flow, i.e. the rotor iron block outside the magnet. However, in the SPM machine, the PMs are directly exposed to the armature reaction [60].

1.2.2.4. Torque- and Power-Speed Characteristics

Ideally, it is desirable to operate the machine at the maximum torque per ampere, thus the maximum capability of the machine is utilized. However, at relatively high speeds, i.e. higher than the base speed, the machine operation is restricted by the voltage limitation. Thus, part of the phase current is utilized to weaken the PM flux rather than generate output torque. Based on the dq-axis parameters, the machine phase voltage is given by:

$$V_{ph} = \sqrt{V_d^2 + V_q^2} = \sqrt{[R_{ph} I_d - \omega L_q I_q]^2 + [R_{ph} I_q + \omega (L_d I_d + \psi_{md}]^2} \tag{1.8}$$

where R_{ph} and ω are the phase resistance and electrical rotating speed.

The finite element (FE) tools have become very accurate and reliable. Therefore, in order to predict the torque- and power-speed characteristics, a FE tool can be directly used to calculate the output torque and check the machine phase voltage limitation, this is called the direct FE calculation method. It fully accounts for the magnetic cross-coupling and magnetic saturation, but it is also very time consuming, especially when both current magnitude and angle need to be adjusted [49]. Alternatively, the output torque equation (1.4) and the machine phase voltage equation (1.8) can be utilised together to analytically predict these characteristics, but the PM flux linkage and dq-axis inductances should be pre-calculated by the FE tool [49]. This is called the indirect FE calculation method, which can be much faster comparing with the direct FE counterpart. On the other hand, its accuracy is determined according to the level accounting for the magnetic cross-coupling and saturation during the calculation of the dq-axis parameters. Different computing techniques have been proposed and employed in [49, 51-55]. Furthermore, the dq-axis parameters can be also accurately calculated, i.e. with totally accounting for the magnetic cross-coupling and saturation, using the frozen permeability (FP) technique. This technique will be more highlighted and employed in section 1.2.2.6 and chapter 2. Moreover, the prediction methods of the torque-speed characteristics of the PM machine will be further illustrated, discussed, utilised and analysed in chapters 2 and 4.

1.2.2.5. Dq-axis Inductance

The dq-axis inductances significantly influence both the steady-state and dynamic performances of PM machines since, as illustrated before, they directly define the output

torque and flux weakening operation capability. Furthermore, these inductances also determine the fault tolerance ability of such machines [62]. Therefore, it is desirable to accurate determine such inductances. Due to the high magnetic saturation as well as the geometry structure of some PM machines, e.g. IPM topology [63], the magnetic cross-coupling between the d- and q-axes could be significant. This influence can be represented by the mutual dq-axis inductance, e.g. L_{dq} and l_{qd}, [54]. Alternatively, the magnetic cross-coupling can be accounted for within the self d- and q-axis inductances. In [49], the following equations have been proposed to estimate the dq-axis inductances:

$$L_d(I_d, I_q) = \frac{\psi_d(I_d, I_q) - \psi_{md}(I_q)}{I_d} \tag{1.9}$$

$$L_q(I_d, I_q) = \frac{\psi_q(I_d, I_q)}{I_q} \tag{1.10}$$

where, $\psi_d(I_d, I_q)$ and $\psi_q(I_d, I_q)$ and are the total dq-axis flux linkages as functions of both d- and q-axis currents, respectively.

It is worth mentioning that in the previous equations the influence of the d-axis current on the PM flux linkage as well as the PM flux linkage of q-axis are not accounted for, thus they are approximated values. However, according to [49], the utilisation of such inductances together with equation (1.4) results in an accurate torque-speed characteristics, which are identical to the direct FE method. On the other hand, the dq-axis inductances can be accurately calculated, i.e. with 100% account for the magnetic cross-coupling and saturation, by using:

$$L_d(I_d, I_q) = \frac{\psi_{cd}(I_d, I_q)}{I_d} \tag{1.11}$$

$$L_q(I_d, I_q) = \frac{\psi_{cq}(I_d, I_q)}{I_q} \tag{1.12}$$

where, $\psi_{cd}(I_d, I_q)$ and $\psi_{cq}(I_d, I_q)$ are the dq-axis armature flux linkages as functions of both d- and q-axis currents and PM flux linkage as function of q-axis, respectively. However,

these flux linkages should be calculated using the FP technique. Such calculations are employed and will be further discussed in the second chapter.

These flux linkages, thus the dq-axis inductances can be calculated using the 2D FE model. However, when the PM machine is skewed the 3D FE analyses are required. Such analyses are very time consuming and it could not be realistic in some designs. Therefore, the authors in [64] have alternatively proposed a simple and accurate hybrid technique, i.e. FE and analytical, to calculate the dq-axis inductances of the skewed PM machines using the 2D FE analyses. This method can be summarised as follows: the dq-axis inductances of the un-skewed machine counterpart are firstly calculated, e.g. using one set of the previous equations, then such inductances are employed together with the skew factor (k_{sk}) to predict their skewed equivalents using (1.13) and (1.14). It is worth mentioning that the obtained inductances can be then utilised to predict the torque-speed characteristics of the skewed machine using the same output torque and line voltage equations, i.e. (1.4) and (1.8), respectively.

$$L_d^{SK} = L_d + \frac{1-k_{SK}}{2}\left(L_q - L_d\right) \tag{1.13}$$

$$L_q^{SK} = L_q - \frac{1-k_{SK}}{2}\left(L_q - L_d\right) \tag{1.14}$$

$$k_{SK} = \frac{\sin(\alpha_{SK})}{\alpha_{SK}} \tag{1.15}$$

where L_d, L_q and α_{SK} are the dq-axis inductances of the un-skewed machine and skew angle, respectively.

On the other hand, the skewed machine can be also analyzed by dividing its axial length into several uniform slices, then the 2D FE modelling can be used to analyse each slice separately with due consideration of each slice's position. Consequently, the total solution is the sum of all slice results [65]. This technique is more practical and accurate when the machine is step skewed rather than fully skewed. Therefore, it will be employed to analyse the step skewed machines in this thesis.

1.2.2.6. Frozen Permeability Technique

The main purpose for employing the FP technique is to allow for a linear analysis of the PM machines with fully accounting for the magnetic saturation, thus the superposition theory becomes applicable between the two PM machine excitation sources, i.e. PMs and phase currents [66]. In this case the influence of the full saturation, e.g. with both PMs and phase currents excitations, can be taken into account when the parameters of one excitation source are analysed. For example, the influence of the magnetic saturation can be fully considered when the winding inductances, which are due to the phase currents only, or PM flux linkage, which is due to PMs only, are calculated. For further illustration, the theory of this technique is to be highlighted. Fig. 1.7 shows the BH characteristics of the machine iron core material, due to the nonlinearity of such material the flux density due to PM plus its counterpart due to phase currents are not equal to the total flux density at the working point (B_{WP}). However, if the permeability, which is the slope of the line between zero and the working point on the BH curve, is frozen then the superposition between the PMs and phase currents excitations becomes correct. In other words, the flux density due to magnet (B_{PM}) plus its counterpart due to current (B_{PC}) are equal to the total flux density at working point (B_{WP}), [20, 67].

non-linear characteristics: $$B_{WP} \neq \mu_{PM} H_{PM} + \mu_{PC} H_{PC} \tag{1.16}$$

linear characteristics (FP): $$B_{WP} = \mu_F H_{PM} + \mu_F H_{PC} = \mu_F H_{WP} \tag{1.17}$$

where $B_{WP}, H_{WP}, H_{PM}, H_{PC}, \mu_{PM}, \mu_{PC}$ and μ_F are working point flux density and field strength, PMs and phase currents field strengths, nonlinear permeability due to PMs and phase currents, frozen permeability of working point, respectively.

During the machine analysis, the utilising of such technique can be summarised as follow: the machine is firstly solved nonlinearly in the FE tool under full load conditions, then the permeability of each element is saved and used to resolve the model linearly without either the electric loading, i.e. open-circuit, or without PMs, i.e. phase currents excitation only [55]. In this case, the open-circuit and the armature field characteristics can be calculated with totally accounting for the influence of full loading conditions, i.e. the full magnetic saturation is accounted for. The FP technique has been illustrated and utilised to account for the magnetic cross-coupling saturation between the d- and q-axis parameters as well as to

segregate the PM and reluctance torque components in [20, 54, 55, 66, 67]. In this thesis, the FP technique is utilised to simplify the prediction of the torque-speed characteristics of the fractional slot PM machines having concentrated winding. It is also employed to investigate the influence of the electric loading and magnetic saturation on the open-circuit characteristics, i.e. the cogging torque and back-emf.

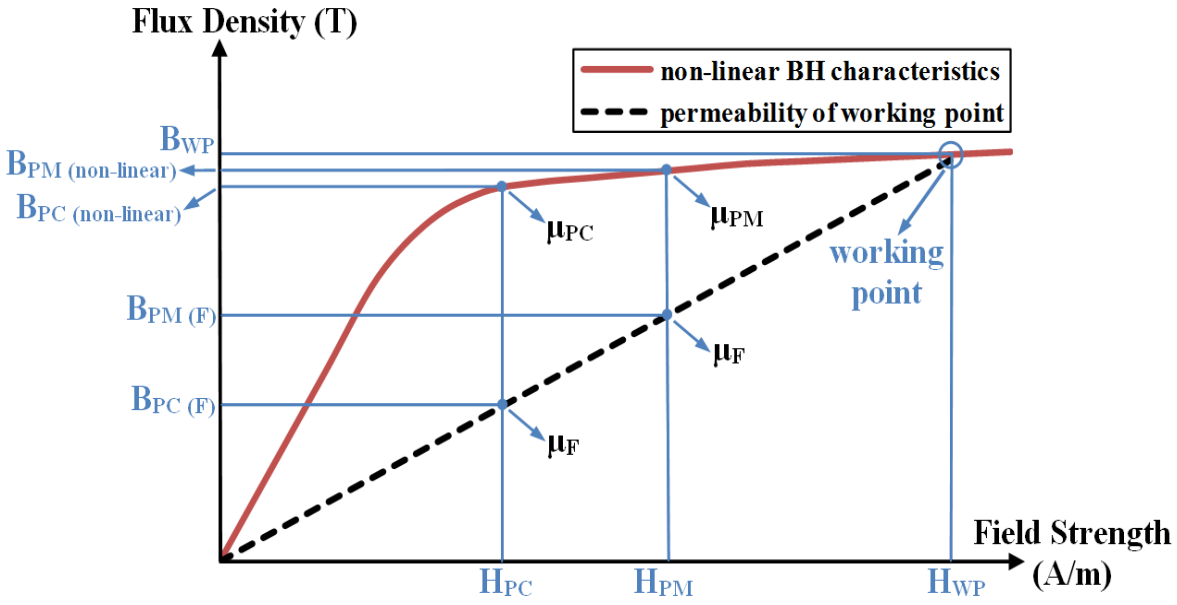

Fig. 1.7 BH characteristics of PM machines with frozen permeability technique, PM and PC refer to the PMs and phase currents excitations.

1.2.3. Pole-Slot Number Combinations

According to the number of slot per pole per phase, the PM machines can be mainly classified into two groups [68-72]:

a). **Integral-slot:** when the number of slot per phase per pole is integral, e.g. 3 phase machines having 4 poles-12 slots or 8 poles-48 slots.

b). **Fractional-slot:** when such number is fraction, for example 3 phase machines with 8-pole/12-slot or 6-pole/9-slot.

Comparing with the integral-slot, the fractional-slot combination exhibits inherently low cogging torque as well as short end-winding, less copper loss and high efficiency when the stator is equipped with concentrated windings. However, on the other hand, such

combination could result in unbalanced magnetic forces (UMFs) if the phase windings are asymmetrically located in the stator slots [73]. The maximum flux linkage per coil, thus the maximum output torque density of the fractional-slot PM machines is obtained when the pole and slot numbers are differed by one, e.g. 10-pole/9-slot or 8-pole/9-slot. In addition, such combination can exhibit significantly low cogging torque since the least common multiple between pole and slot numbers is relatively large, as shown in Fig. 1.8. However, on the other hand, these combinations generate relatively large UMFs [74], as shown in Fig. 1.9. These forces are not desirable, especially when high electrical loading is applied since they reduce the bearing life time and also result in relatively high acoustic noise and vibration. Alternatively, if a slight reduction in the flux linkage per coils is tolerated, the UMFs can be significantly eliminated when the pole number and slot number are differed by two, e.g. 10-pole/12-slot or 10-pole/8-slot:

$$N_S = 2p \mp 2 \tag{1.18}$$

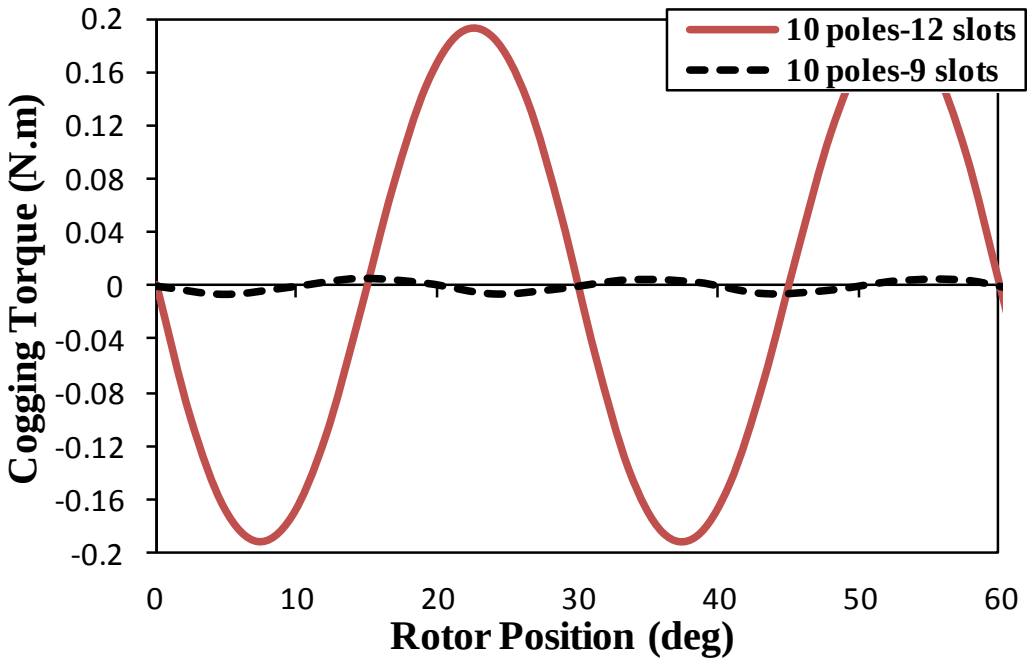

Fig. 1.8 Comparison of cogging torque of fractional-slot PM machine having same external dimensions and magnet volume, but different pole-slot number combinations.

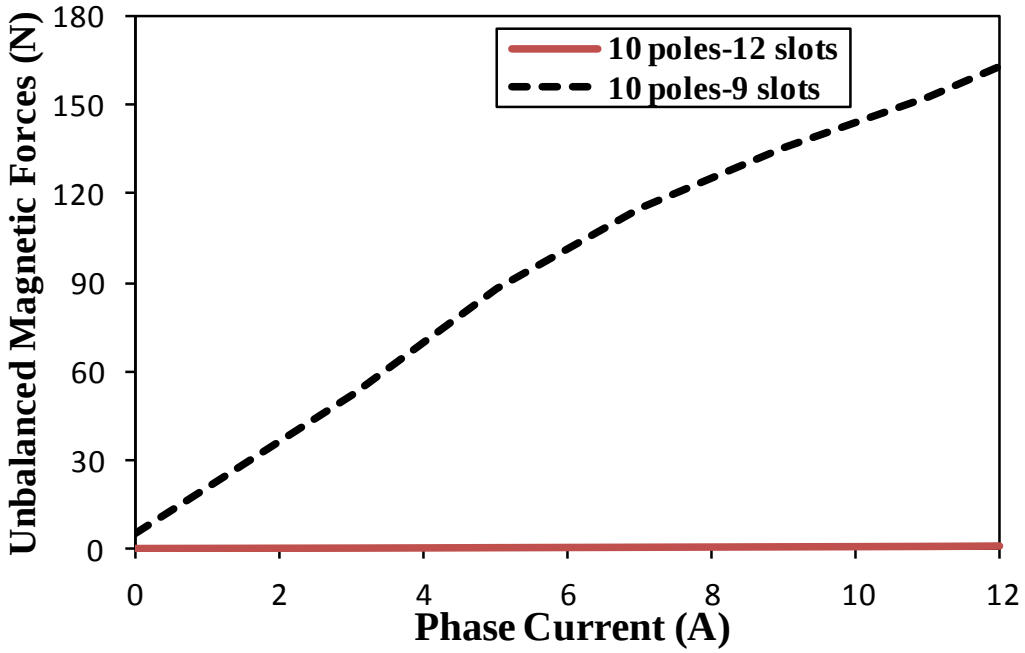

Fig. 1.9 Comparison of unbalanced magnetic forces of PM machine having same external dimensions and magnet volume, but different pole-slot number combinations.

1.2.4. Phase Winding Configurations

The phase winding configurations are normally determined according to pole-slot number combinations. Thus, the maximum flux linkage and consequently the maximum output torque are obtained. In general, such configurations in the 3 phase PM machines can be classified into [75-81]:

a). Distributed-overlapping winding: the number of slot per pole per phase is an integral number and larger than one, e.g. 8-pole/48-slot combination. This combination can be occupied by either single or double layer per slot, as illustrated in Fig. 1.10. On the other hand, such winding configuration can be also employed when the number of slot per pole per phase is fractional and larger than one, e.g. 8-pole/42-slot number combination. However only the double layer winding is possible as shown in Fig. 1.11.

b). Concentrated-overlapping winding: the number of slot per pole per phase is one, e.g. 8-poles/24-slot combination, as shown in Fig. 1.12.

c). Concentrated-non overlapping winding: the number of slot per pole per phase is fractional and less than one, e.g. 8-poles/12-slot combination. Furthermore, this winding configuration can be further divided into:

i. double layer winding: one coil is wound around each stator tooth, as illustrated in Fig. 1.13 (a).

ii. single layer winding: the coils are alternatively wound around the stator teeth, as shown in Fig. 1.13 (b).

In this thesis, the investigation is focused on the fractional-slot PM machines having concentrated winding. Thus, the advantages of such machines will be further highlighted and compared with the integral-slot counterpart machines in section 1.2.5.

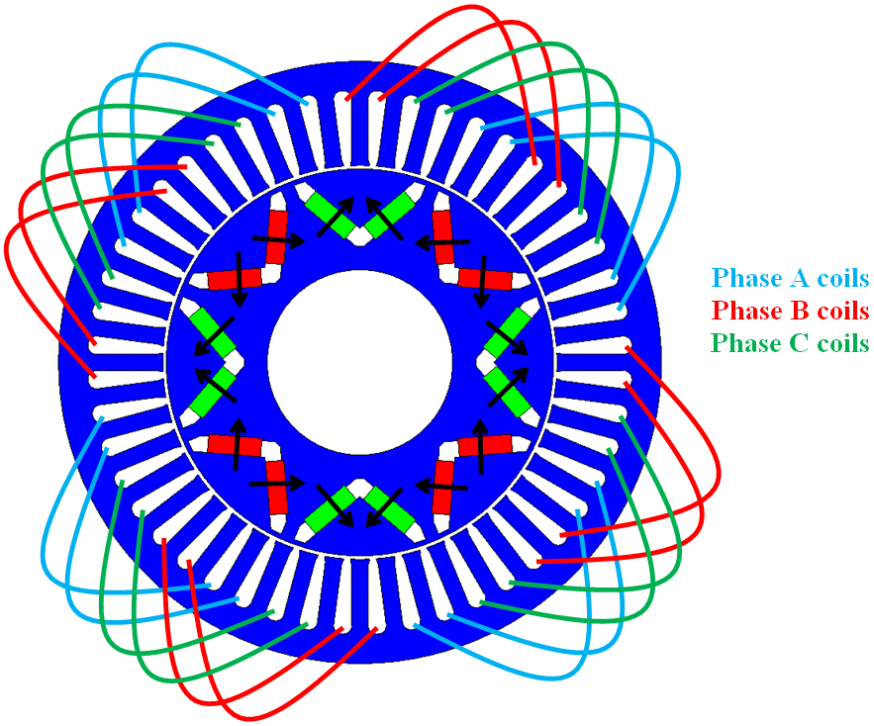

(a) Overlapping distributed winding, single layer per slot

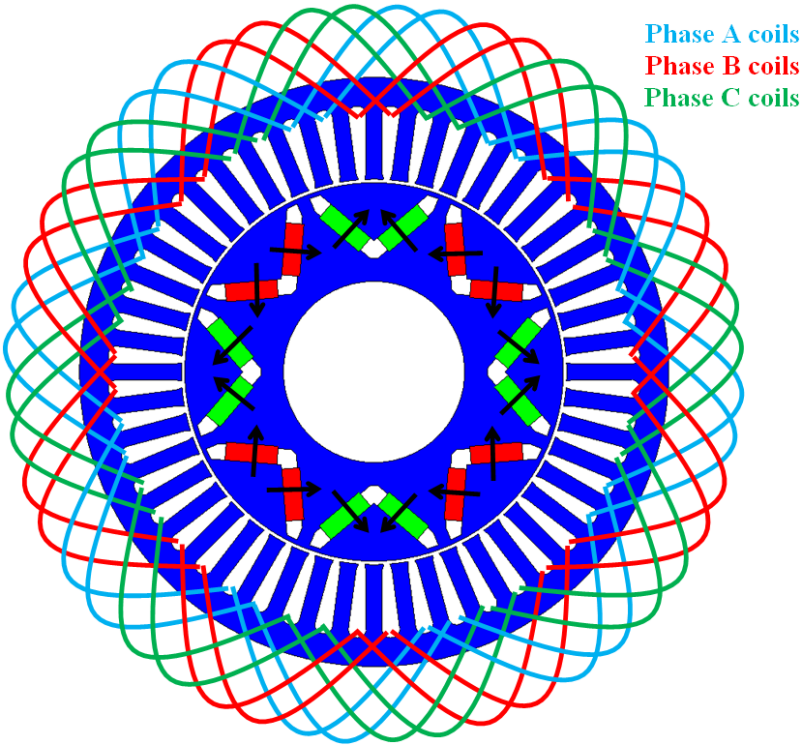

(b) Overlapping distributed winding, double coil side per one slot

Fig. 1.10 Overlapping distributed winding configuration of PM machines having integral number of slot per pole per phase and larger than one.

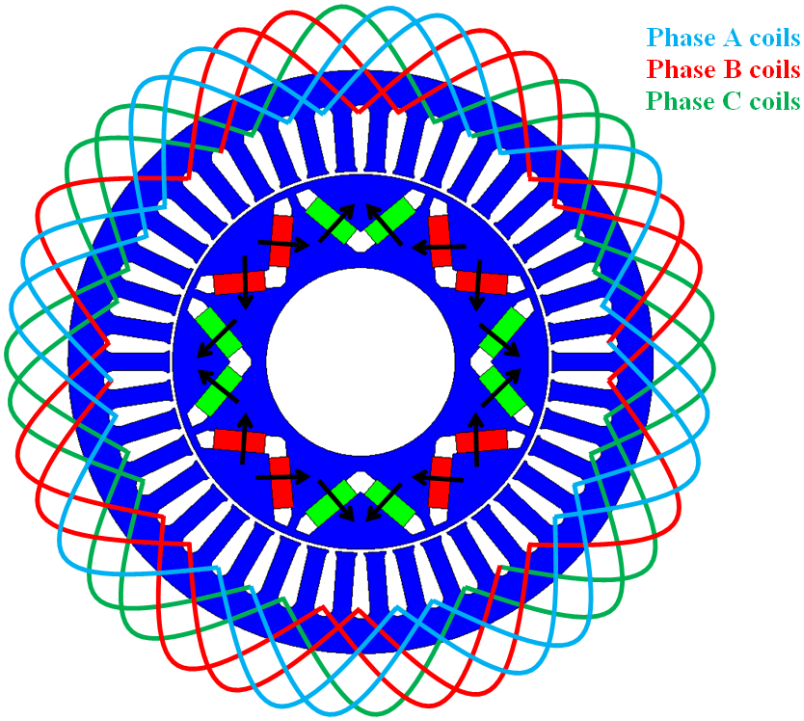

Fig. 1.11 Overlapping distributed winding configuration of PM machines having fractional number of slot per pole per phase and larger than one.

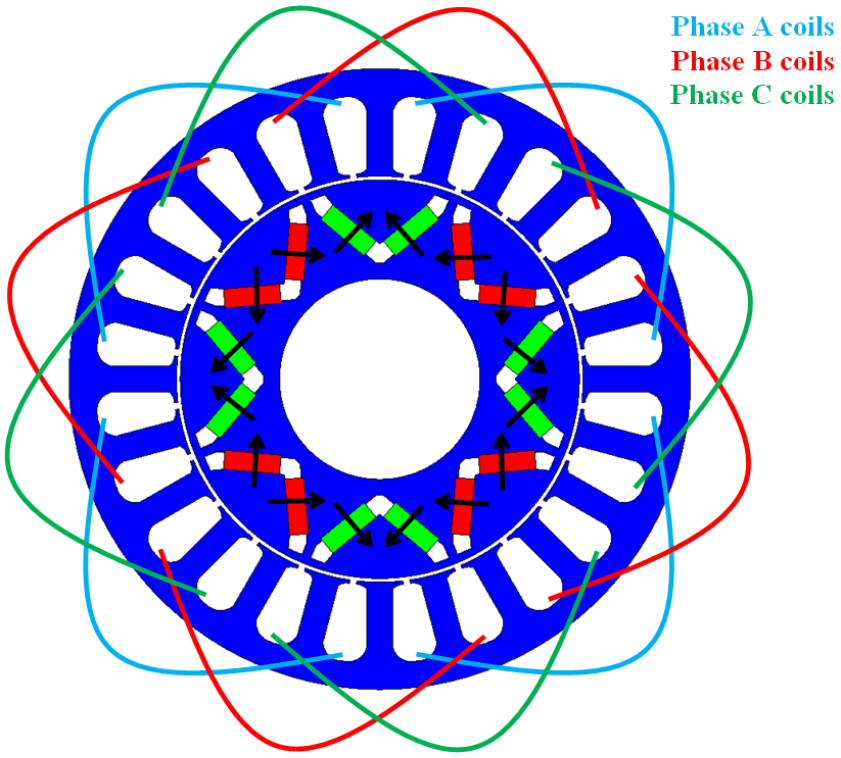

Fig. 1.12 Overlapping concentrated winding configuration of PM machines having one slot per pole per phase.

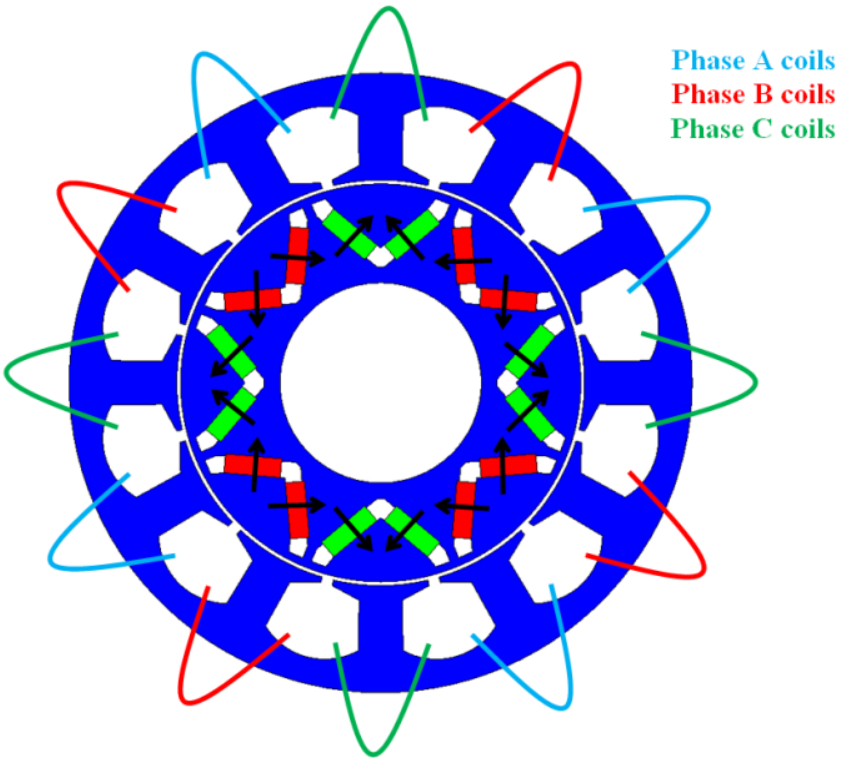

(a) Double layer winding

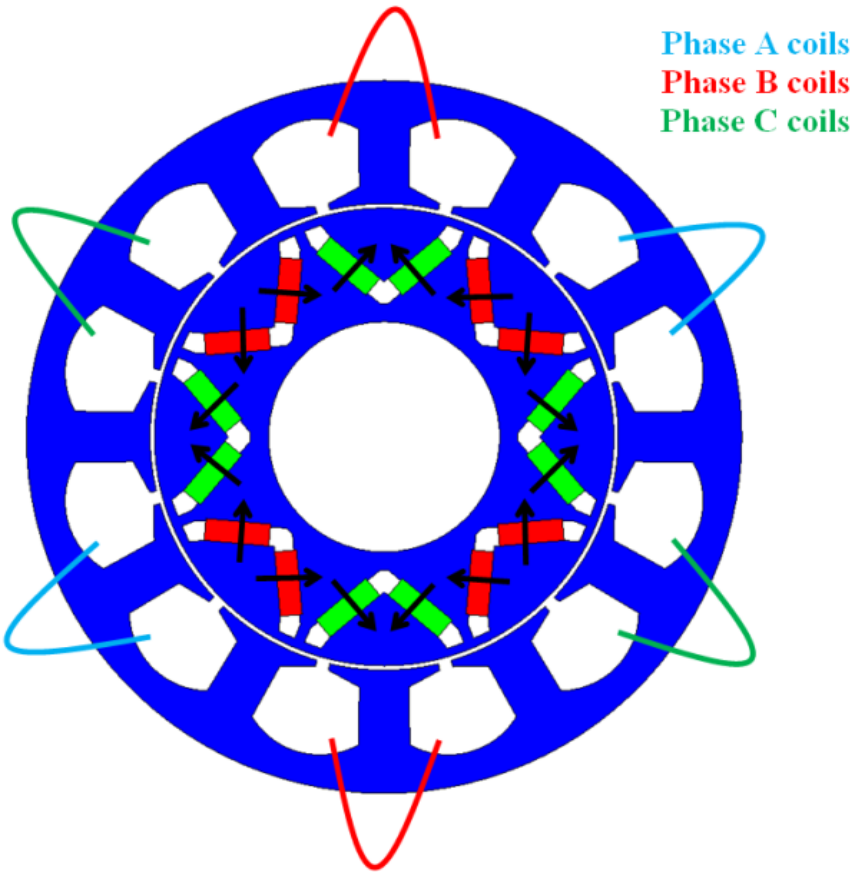

(b) Single layer winding

Fig. 1.13 Non-overlapping concentrated winding configuration of PM machines having fractional number of slot per pole per phase and smaller than one.

1.2.5. Fractional-Slot PM Machines with Concentrated Winding

Comparing with the integral-slot PM machines having distributed winding, their fractional-slot counterparts with non-overlapping concentrated winding offer the following benefits [82-89]:

- Higher torque/power density;
- Shorter end winding, thus lower copper loss;
- Shorter total axial length, smaller overall volume;
- Larger d-axis inductance, thus wider flux weakening operation region;
- Lower cogging torque, thus smoother output torque;
- Inherent fault tolerance capability;
- Potentially for low manufacturing cost, e.g. modular stator.

On the other hand, such machines have also some drawbacks and disadvantages, which can be summarized as follows:

- More flux harmonics, thus larger iron and magnet losses;
- Significantly low reluctance torque even when IPM topology is employed. However, when the number of slot per phase per pole is 0.5 the reluctance torque still exists;
- Potential high UMFs, depending on the pole slot number combination.

The fractional-slot PM machines with concentrated winding are very suitable for high torque and low to medium speed applications, where the copper loss is dominant [84, 87]. However, at high speed, when the iron loss becomes significantly large, such machines could be not desirable due to their large iron loss as well as magnet loss, which could result in irreversibly demagnetisation, [90, 91], since the output torque of the fractional-slot PM machines is produced by the interaction of the stator winding first harmonics and the p^{th} harmonic of the open-circuit air gap flux density. The low and high order air gap flux density harmonics are the reasons behind the relatively large iron and magnet losses. It is also worth mentioning that the magnet loss can be significantly decreased by either circumferential or radial magnet segmentation [83, 91, 92].

Furthermore, comparing with the fractional-slot PM machines having the double layer winding, their counterparts with the single layer winding results in larger d-axis inductance. This is due to the extra flux leakage in such configuration. Consequently, the fractional-slot PM machines exhibit a wider flux weakening operation region. In addition, a higher filling factor can be achieved, thus the copper loss can be smaller [6, 93]. Moreover, the inherent fault tolerance capability of such machine is larger, since the phase windings become magnetically and physically isolated and self inductances are relatively large [31, 81].

The electromagnet performance and characteristics of the fractional-slot IPM machines with concentrated winding will be further investigated and analysed in chapter 2, 3, 4 and 5, with particular reference to the torque-speed characteristics, output torque, torque ripple and cogging torque.

1.3. Switched Reluctance Machines

The reluctance variation, which is the operation principle of the switched reluctance (SR) machines, has been well known for a long time. However, the recent development of power electronics, thus drive systems has increased the usage ability of such machines in the practical applications [94-96]. Due to their structure advantages, e.g. no PMs and robust rotor, these machines are suitable to be operated at high speeds and in harsh environments, such as high temperature and pressure. Furthermore, due to the significant increase in the cost of the PM materials, there is a strong trend to utilise the SR machines in the electric and hybrid electric vehicles. However, the drawbacks of such machines should be first improved or even overcome to enable such application. For this purpose, the SR machines and their drives are currently very common research topics.

In general, the merits of the SR machines can be summarized by [97-99]:

- Simple and robust rotor structure;
- There are no PMs, thus can be operated at relatively high current density;
- Operated at saturation level, temperature and pressure;
- Inherent ability for fault tolerance;
- Brushless operation, thus relatively low maintenance level;
- Comparing with PM machines, the cooling is more effective in the SR machines [100];
- Although high manufacturing tolerances are required, due to relatively small air gap. However, the low manufacturing cost is still possible since the magnet materials prices and supply are not stable.

On the other hand, the most challenging drawbacks of such machines include [101-105]:

- Inherently large torque ripple;
- High acoustic noise and vibration;
- Complex phase current profiles are required to achieve smooth output torque, especially at low speeds;
- A unique drive system is required to drive such machines, i.e. asymmetric half bridge inverter;
- Large DC-link capacitor is required to filter the large voltage ripple.

1.3.1. Operation Principles

The working theory of the SR machines is simply due to the magnetic reluctance variation when the relative position between the rotor and stator changes, i.e. the rotor poles move from the aligned to unaligned position. Therefore, the feasible stator/rotor pole combinations of the SR machines are limited, for example the 6/4 and 8/6 and their multiples are the most common stator/rotor combinations. Such machines are equipped with concentrated phase windings, which should be sequentially energized or commutated to produce the output torque or power [106-108]. The cross-section and phase winding layout of 3 phase 6 stator/4 rotor poles SR machines having different rotor/stator poles align positions are illustrated in Fig. 1.14. On the other hand, the drive circuit of such machine under the conventional unipolar excitation is given in Fig. 1.15. Due to phase winding position and excitation, the magnetic coupling between the phase winding is nearly eliminated. Consequently, the produced output torque or power is mainly due to the variation of the phase self inductances. Thus, the electromagnetic torque of the SR machines can be analytically calculated by:

$$T = 0.5 i^2 \frac{\partial L}{\partial \theta} \tag{1.19}$$

where i, L and θ are phase current, self inductance and rotor relative position.

According to (1.19), it can be concluded that the operation mode of the SR machine depends on the relative phase current position according to variation of the phase self inductances. When the rotor and stator poles are fully unaligned, then the magnetic reluctance is maximum, thus the self inductance is minimum. Consequently, if the winding around the stator pole is excited, the rotor pole will tend to align with such stator pole. Thus, in motoring operation mode, a continuous rotating electromagnetic torque can be generated by powering the phase windings in sequence when the rotor poles move from unaligned to aligned position with the corresponding phase stator poles, i.e. each phase winding is energised when the corresponding inductance increases from the minimum to maximum value, as shown in Fig. 1.16. On the other hand, in generating mode the phase currents should be commutated when the rotor and stator poles are moved from the fully aligned to unaligned position, in other words when the phase self inductance decreases from the maximum to minimum value, as illustrated in Fig. 1.17.

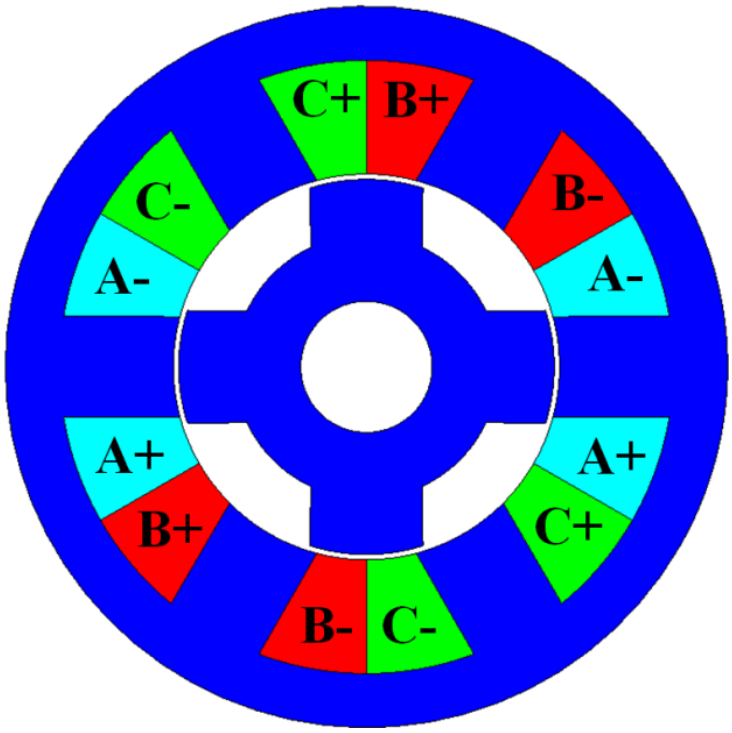

(a) Rotor is fully aligned with phase A stator poles, for motoring operation injecting current in phase B or C, or for generating operation commutate current from phase A

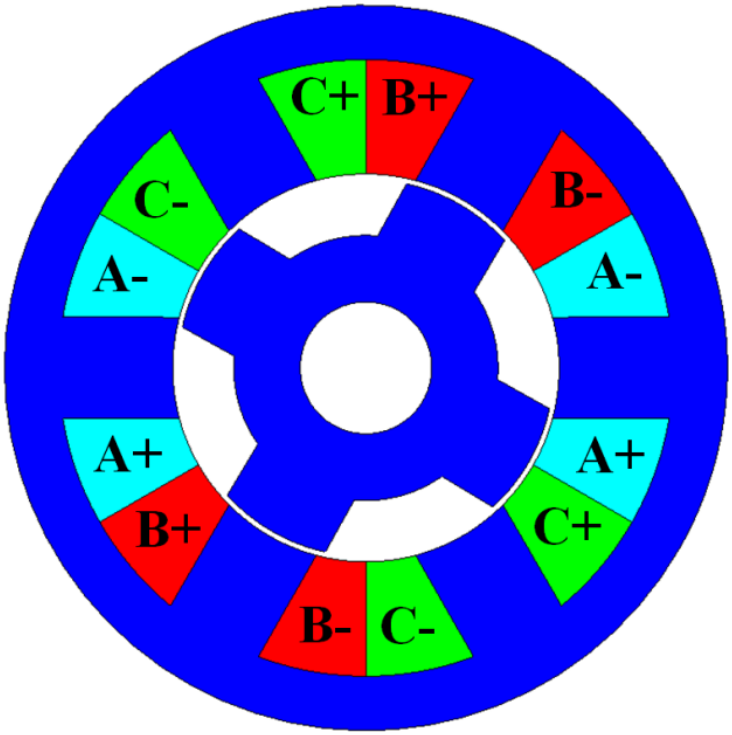

(b) Rotor is fully aligned with phase B stator poles, for motoring operation injecting current in phase A or C, or for generating operation commutate current from phase B

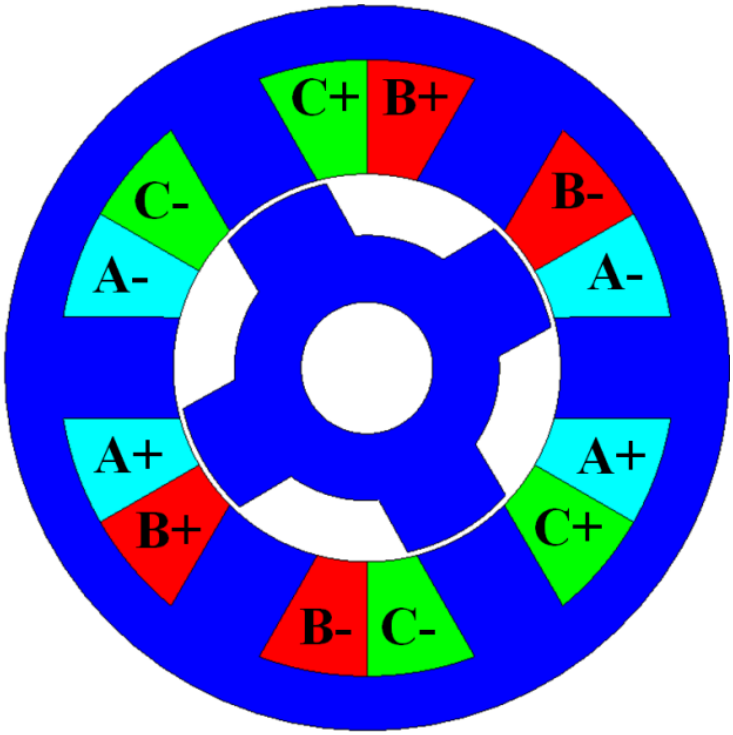

(c) Rotor is fully aligned with phase C stator poles, for motoring operation injecting current in phase A or B, or for generating operation commutate current from phase C

Fig. 1.14 Cross-section and phase winding layout of 3 phase 6 stator/4 rotor poles SR machine has symmetric winding connection and different rotor/stator poles align positions.

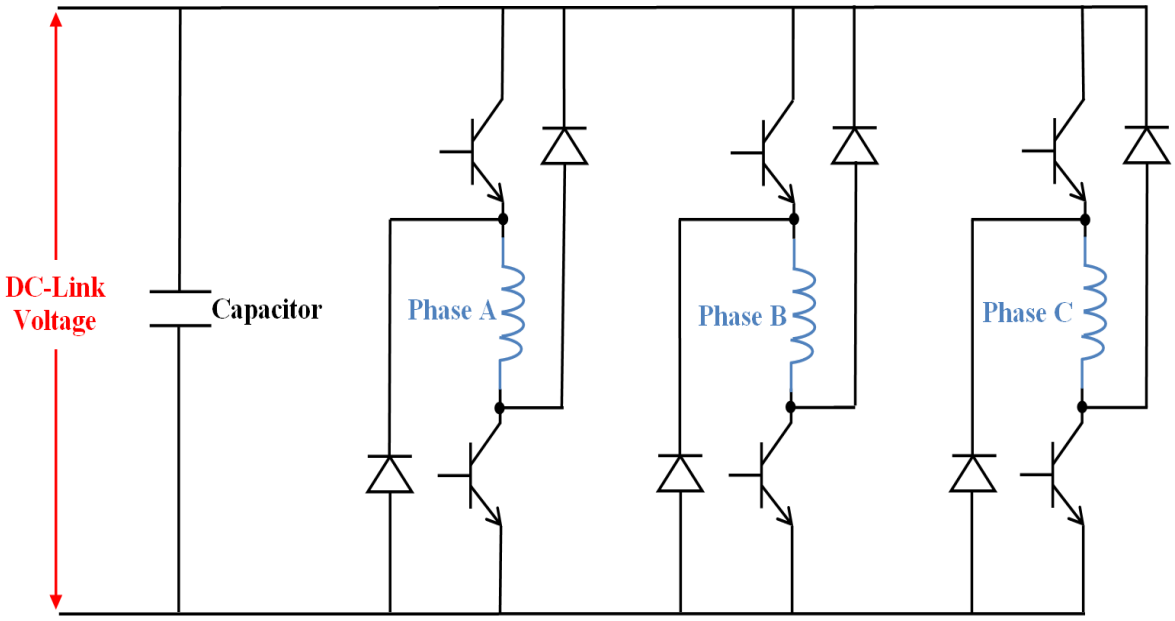

Fig. 1.15 Asymmetric unipolar driver inverter for SR machines.

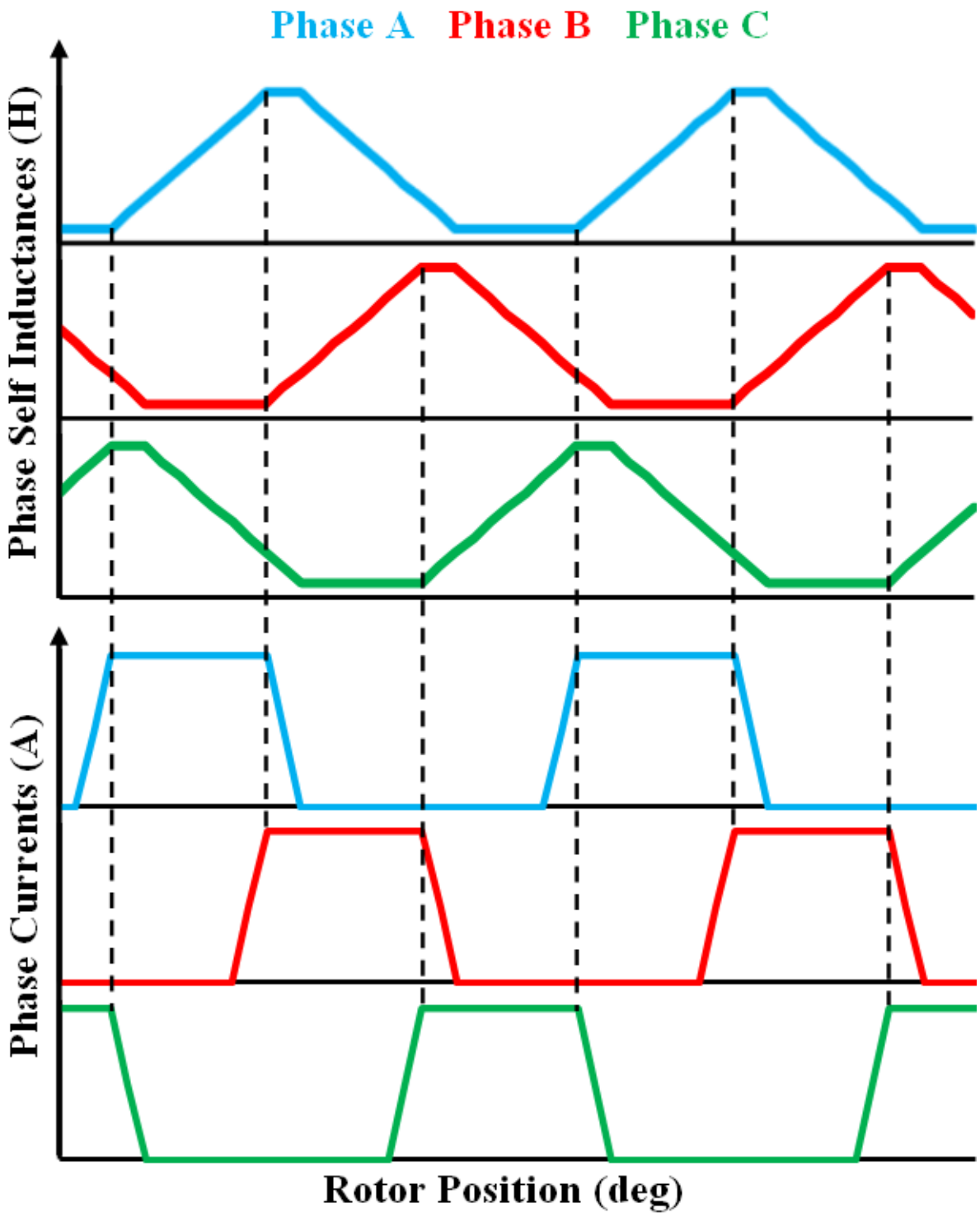

Fig. 1.16 Variation of self phase inductances and injected phase currents when SR machine is operated as a motor, under conventional unipolar excitation.

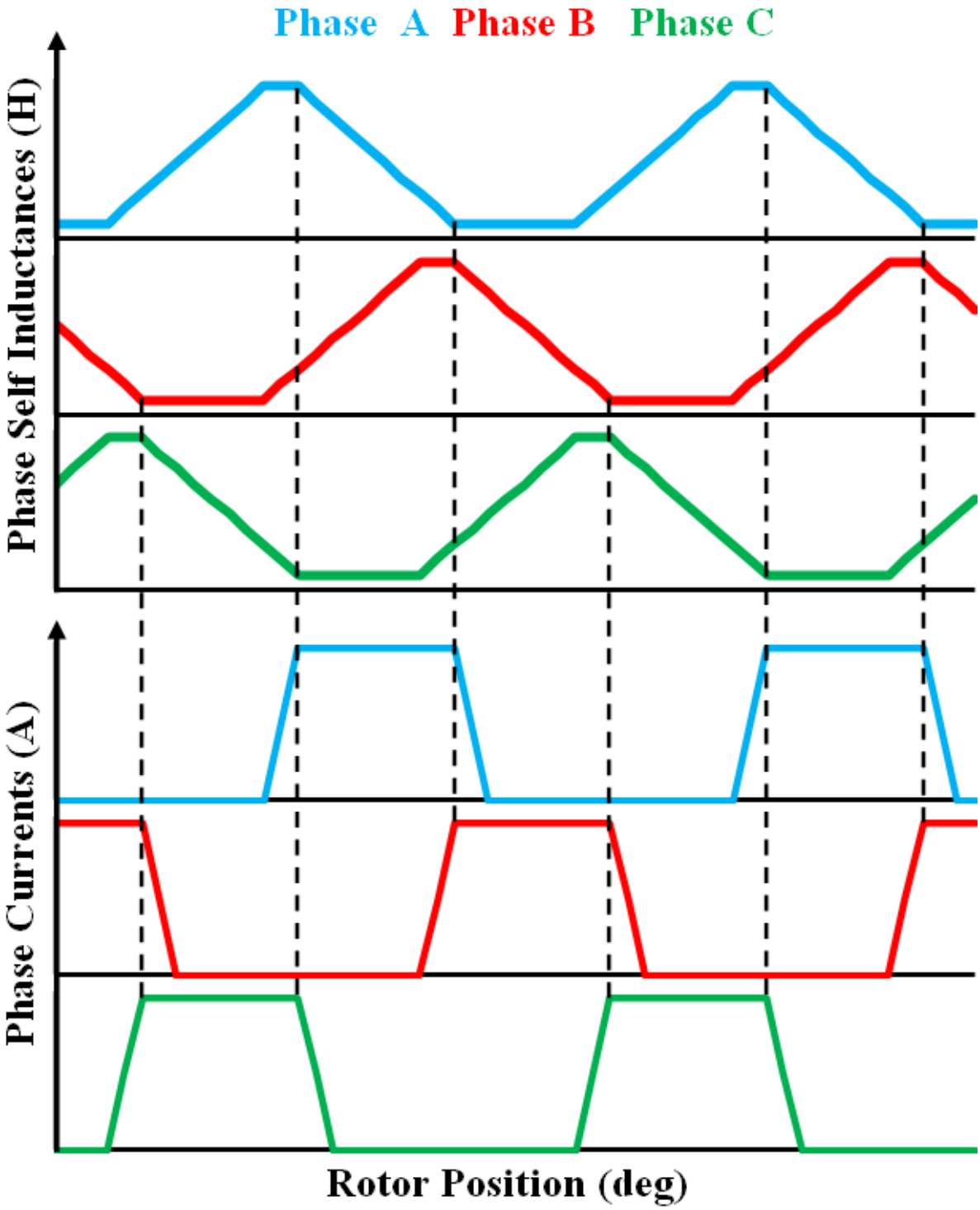

Fig. 1.17 Variation of self phase inductances and commutated phase currents when SR machine is operated as a generator, under conventional unipolar excitation.

1.3.2. Mutual Inductance Torque

As mentioned earlier, the magnetic coupling between phases is negligibly small when the phase windings of the SR machine are wound around the stator teeth. As a result, the phase mutual inductances are also neglected. Consequently, the output torque is totally produced by the variation of the phase self inductances [109]. This results in a poor electric circuit utilising, since the contribution of each phase is limited to the self inductance rising or decreasing period only, i.e. rising in motoring operation and decreasing in generating operation. This means each phase provides torque/power during only one half of its period. However, if the SR machines are occupied with full pitched coils, there will be relatively large mutual coupling between phase fluxes. Thus, the torque/power will be produced by the variation of the mutual inductances rather than the self counterparts. Fig. 1.18 shows the full pitched winding configuration of 6 stator/4 rotor poles SR machine. In order to produce torque with the full pitched winding connection, at each rotor position two phases should be excited together [110]. The conduction sequence of phase currents with the variation of the mutual phase inductances of full pitched winding configuration is clearly illustrated in Fig. 1.19. In this case, each phase contributes for more than one half of its period, thus the electric circuit can be utilised better [111]. As a result, the generated output torque/power can be larger [112]. However, as disadvantages, such winding connection results in longer end-winding and higher copper loss, in addition it reduces the fault tolerance capability comparing with the convention concentrated winding [113].

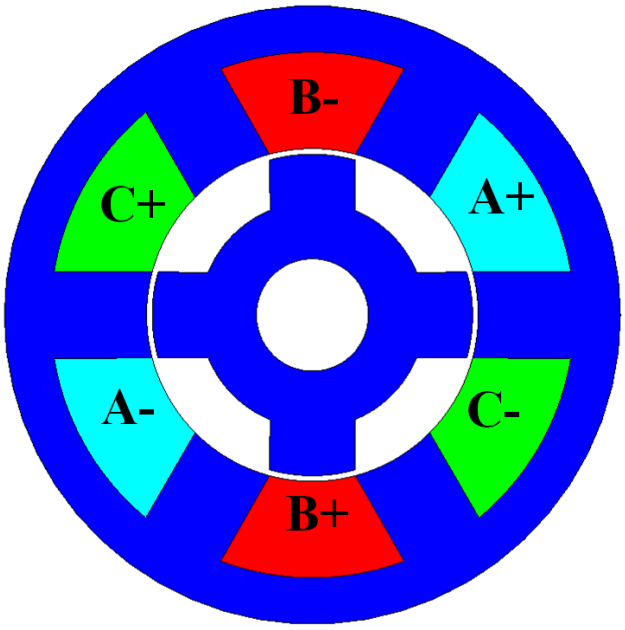

Fig. 1.18 6 stator/4 rotor poles SR machine has full pitched winding configuration.

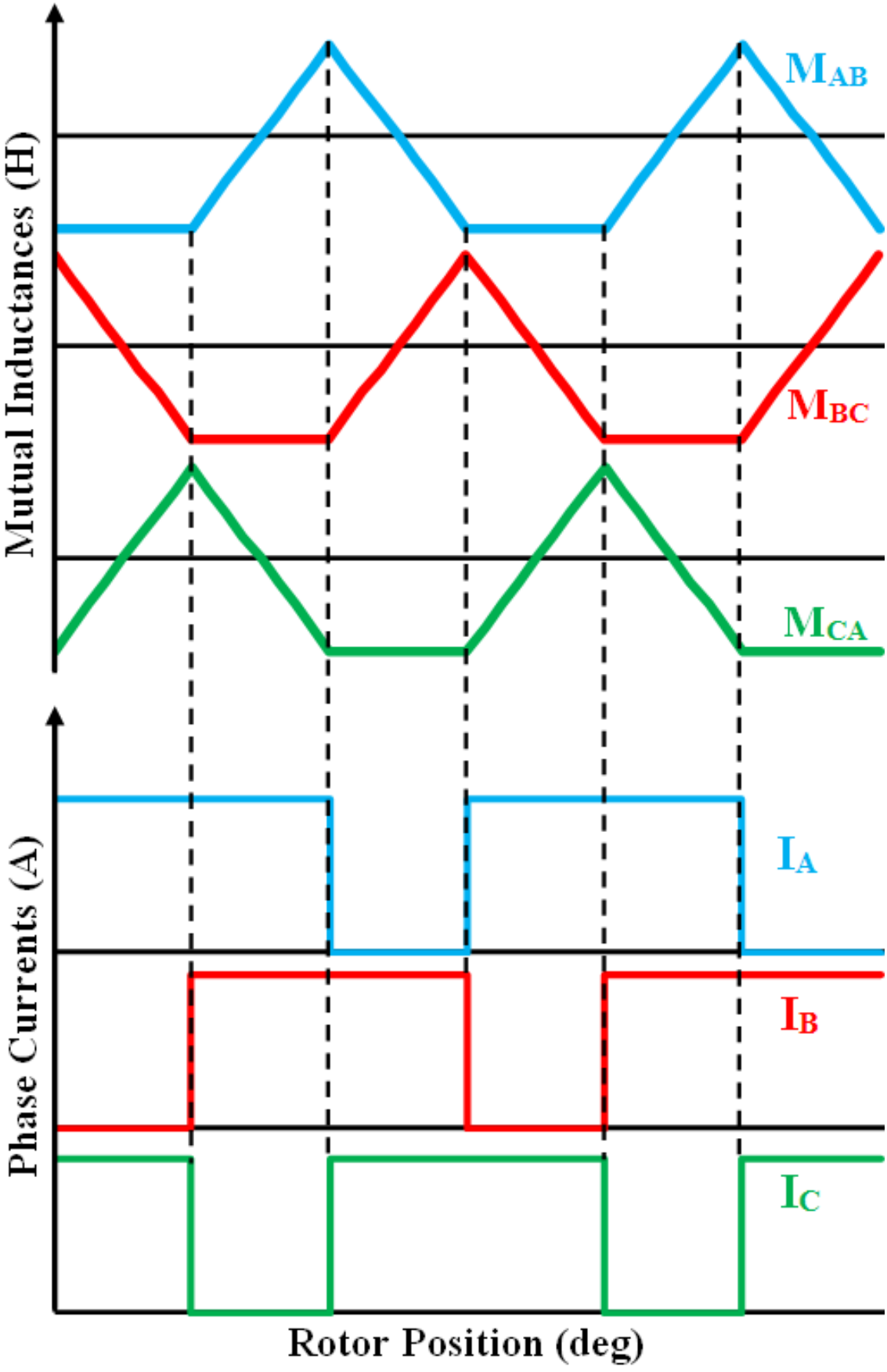

Fig. 1.19 Variation of mutual phase inductances and injected phase currents of SR machine has full pitched winding configuration.

In this thesis, the conventional concentrated winding is still utilised but with different coil polarity and under the AC sinusoidal phase current excitation, i.e. AC sinusoidal bipolar current excitation. Thus, the output torque is produced by variations of both the self and mutual phase inductances. Consequently, the benefits of the concentrated winding is kept and at the same time larger output torque can be achieved, as will be further illustrated and analysed in Chapter 6.

1.3.3. Bipolar Excitation

Under the conventional unipolar excitation, the SR machines exhibit relatively large torque ripple, which in turn causes significant acoustic noise and vibration. These are serious disadvantages, which could limit the use of the SR machines in many applications [114]. The reason behind such larger torque ripple is the rapid change of radial magnetic force, which in its turn is due to the sudden extinguishing of the phase currents during the commutation process. Many techniques and means have been proposed to reduce the torque ripple of the conventional SR machines [115-118], for example, by:

- Control strategies, e.g. produce and inject a suitable phase current profile;
- Rotor structure optimization, e.g. pole-shaping and flux barrier.

However, due to the nature of the torque production, the minimisation of torque ripple using such techniques is still limited. Alternatively, the torque ripple and thus the noise and vibration can be effectively reduced if the excitation phase currents are more overlapped. This can be satisfied by employing AC phase currents, i.e. bipolar excitation. The variation of the phase currents under both the unipolar and bipolar excitations are compared in Fig. 1.20. Moreover, comparing with the conventional unipolar excitation, the bipolar counterpart can result in the same average output torque as well as lower losses and higher efficiency, [119]. Furthermore, if the bipolar excitation is achieved by AC sinusoidal phase currents, the SR machine can be operated as a synchronous reluctance (SynR) machine with concentrated winding. Therefore, the following additional benefits can be also gained [120-123]:

- Further reduction in torque ripple comparing with the conventional bipolar excitation, since each phase current is continuously excited, i.e. there is no commutation;

- Commercial drive systems can be utilised, thus lower drive cost;
- Lower iron loss;
- Smaller DC-link capacitor, which is required to filter the voltage ripple;
- Less magnetic saturation sensitivity, since the flux paths are shorter, as will be illustrated in chapter 6.

On the other hand, the AC sinusoidal bipolar excitation leads to lower average output torque, this is the main disadvantage of such excitation [120]. However, it is still desirable since it allows the utilisation of the SR machines for many applications, such domestic and traction, where the noise and vibration are critical issues.

In this thesis, the SR machine having AC sinusoidal bipolar excitation, i.e. salient-pole synchronous reluctance (SynR) machine, is examined and discussed in details and compared for different winding connections, such as symmetric and asymmetric, and two different stator/rotor pole combinations which are the 6 stator/4 rotor poles, i.e. non-overlapping concentrated winding connection, and 12 stator/4 rotor poles, i.e. overlapping concentrated winding connection that is illustrated in Fig. 1.21. Furthermore, the hybrid bipolar excitation, i.e. AC sinusoidal phase current with DC bias, is proposed, investigated and analysed. Finally, the electromagnetic performance of the SynR machine is compared for these two excitations as well as the SR conventional unipolar counterpart.

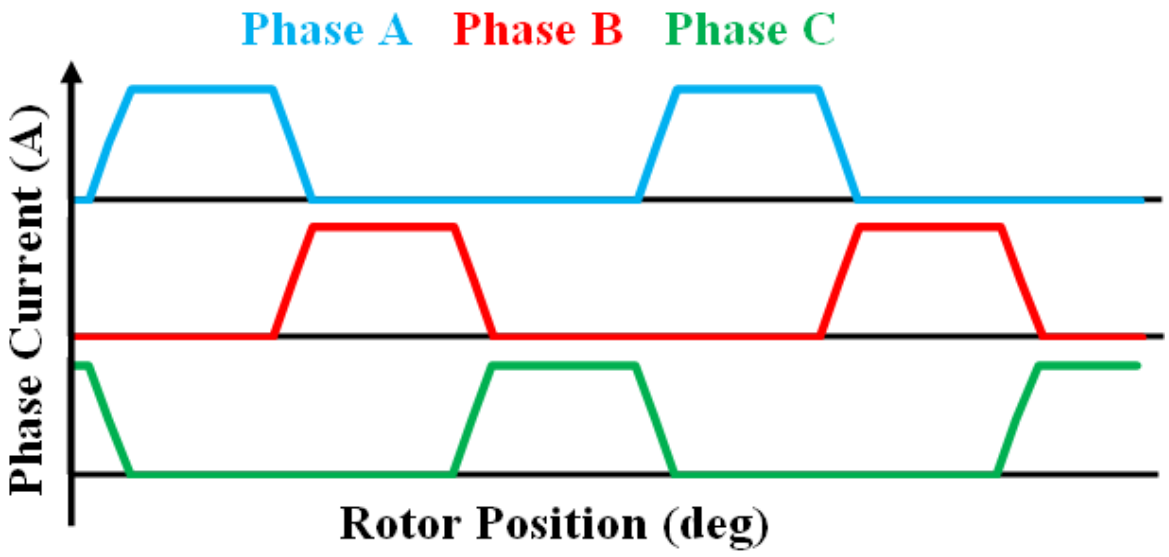

(a) Conventional excitation, i.e. unipolar excitation

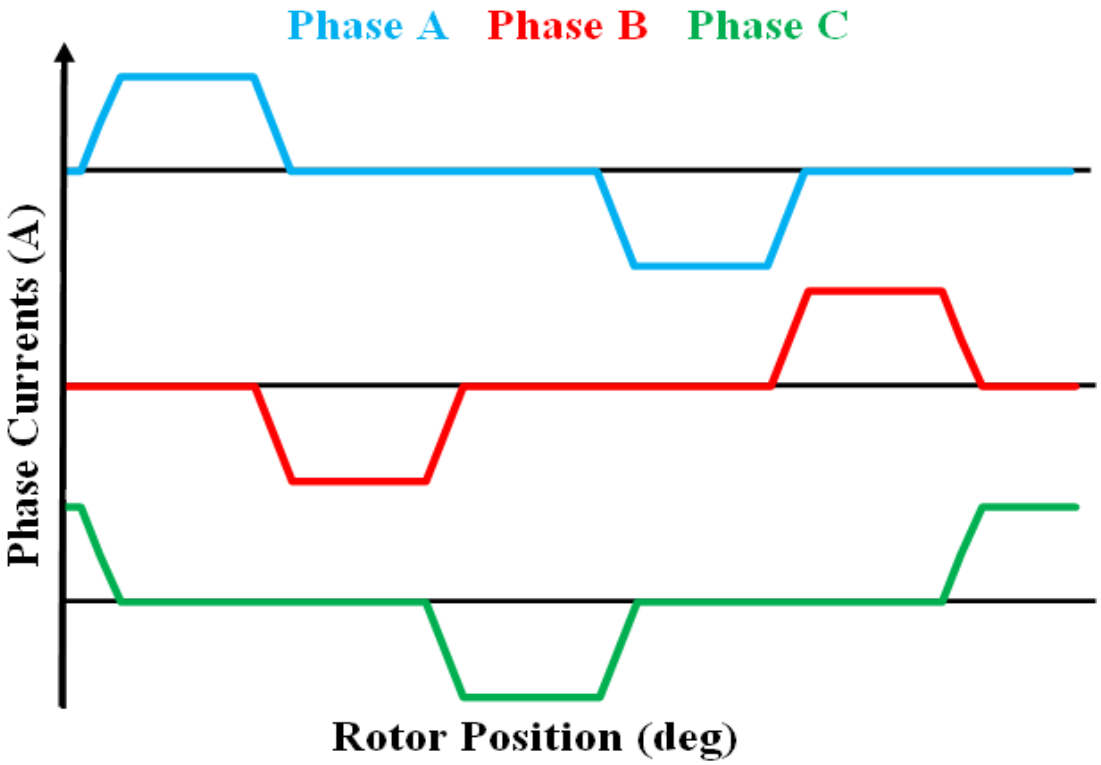

(b) Bipolar excitation

Fig. 1.20 Comparison of phase current variations of both unipolar and bipolar excitations of the SR machine.

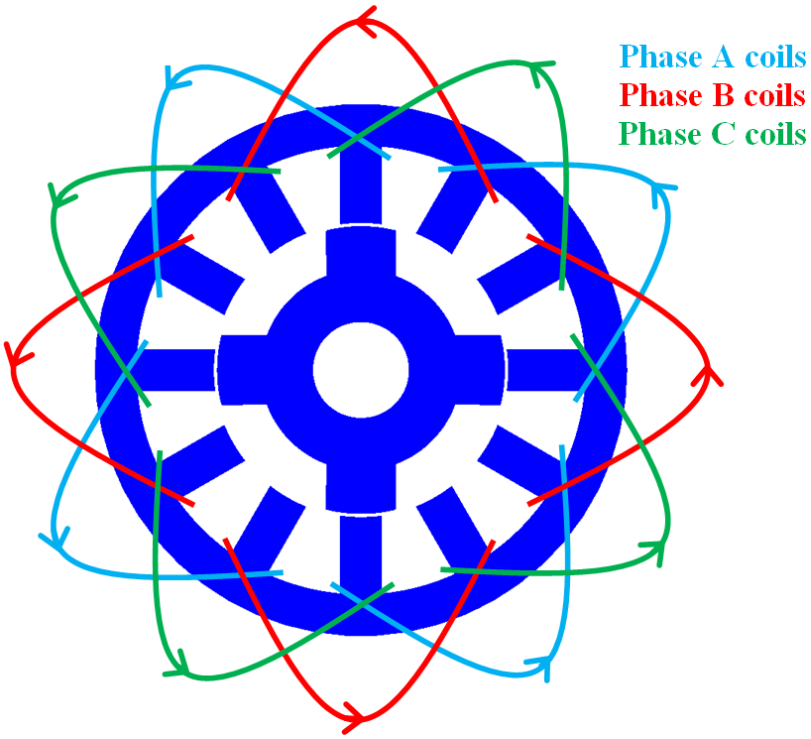

Fig. 1.21 Cross-section lamination and winding layout of 12 stator/4 rotor poles SynR machine.

1.3.4. Winding Configurations under AC Bipolar Excitation

Under the AC bipolar excitation and according to the connection technique of phase coils, the winding connection in the SynR machines, which employ concentrated wound coils, can be categorized into [113, 124]:

a). Asymmetric winding connection has uneven coil polarity in the stator slots, thus asymmetric flux directions, as shown in Fig. 1.22(a);

b). Symmetric winding connection has symmetric flux directions since its phase coil polarities are the same in each stator slot, as illustrated in Fig. 1.22(b). In these two connections, the output torque is mainly produced by the variations of phase self inductances, since the mutual inductances are negligibly small;

c). Hybrid winding connection has the same coil polarity and flux direction for all coils, as shown in Fig. 1.22(c). It is worth mentioning that in this connection the winding polarity is similar to the full pitch wounded. The reason behind this name, i.e. hybrid winding connection, is the nature of the generated output torque, which is due to the variations of both the self and mutual inductances. Further illustrations, discussions and analyses will be presented in chapter 6.

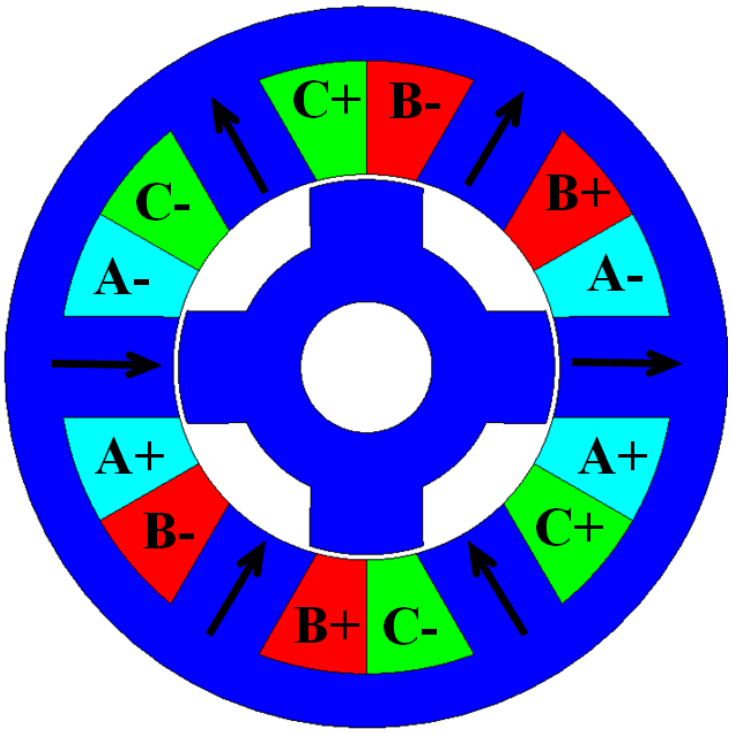

(a) Asymmetric winding connection

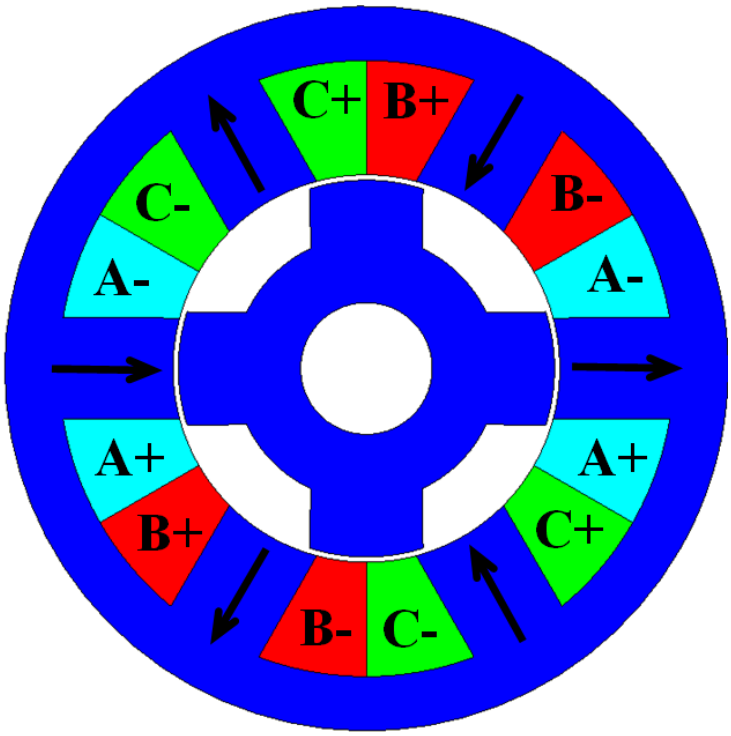

(b) Symmetric winding connection

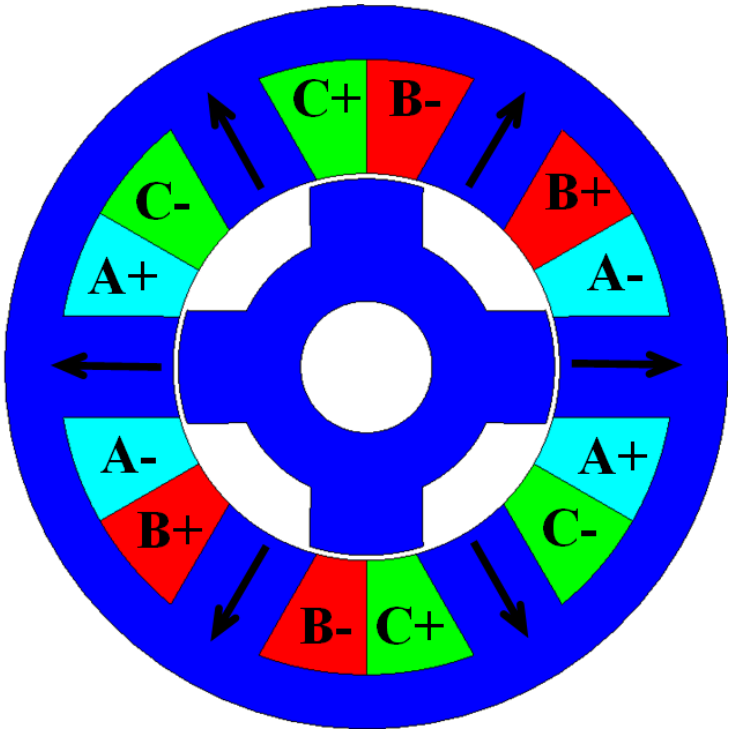

(c) Hybrid winding connection

Fig. 1.22 Comparison of three different winding connections of 6 stator/4 rotor poles SynR machine.

1.4. Scope and Contributions of Research

1.4.1. Scope of Research

The topologies and operation characteristics of the PM machines have been reviewed. A particular attention has been paid to the fractional-slot machines, which have concentrated winding. In this thesis, the techniques accounting for the influence of the magnetic cross-coupling and manufacturing tolerances on the electromagnetic performance of such machines are systematically investigated. In addition, the operation principles of the SR machines under different excitation techniques, i.e. unipolar and bipolar, have been also highlighted. The electromagnetic performance of the SR machine under the AC bipolar excitation, i.e. salient-pole SynR machine, is extensively investigated considering different winding connections. Furthermore, the AC bipolar with DC bias excitation is proposed, investigated and analysed. Finally, the SR machine electromagnetic performance is compared for three different excitation techniques. The subsequent chapters in the thesis are summarized below:

Chapter 2

In this chapter, the frozen permeability (FP), which is an accurate method to account for the magnetic cross-coupling influence, is employed to separately examine such influence on the dq-axis parameters of the fractional-slot PM machines having concentrated winding. The idea behind such investigation is to determine the level of the magnetic cross-coupling effect on each parameter and to find the simple yet accurate model to predict the torque-speed characteristics of fractional-slot PM machines having concentrated windings.

Chapter 3

In order to improve the electromagnetic performance and ease the manufacture process, particularly the stator winding, it is often preferable to employ a modular stator, e.g. individual stator tooth/back-iron segments, or separate stator tooth segments and back-iron segments. However, due to manufacture limits, there are always additional air gaps between the stator teeth and back-iron segments. In practice, such gaps are likely to be non-uniform due to manufacture tolerances. This chapter investigates the influence of uniform and non-uniform additional gaps on the electromagnetic performance of PM machines, with particular emphasis on the cogging torque.

Chapter 4

This chapter presents a comparative study of torque-speed characteristics and cogging torque of the fractional-slot interior PM (IPM) machines having different slot openings, viz. open slot, closed slot and hybrid slot (sandwiched open and closed slots), and un-skewed and step skewed rotors. The influence of such alternate slot openings on the magnetic cross-coupling and cogging torque are particularly emphasized. Furthermore, the repercussion of the manufacturing limitations and tolerances on the cogging torque of machines having these alternate slot openings is also investigated.

Chapter 5

In this chapter, the frozen permeability technique is utilised to investigate the influence of the electric loading and magnetic saturation on the cogging torque, magnitude and period, and back-emf waveforms of PM machines having un-skewed and step skewed rotors. Furthermore, the effectiveness or limitation of the rotor step skew on the minimization of the cogging torque, thus the torque ripple, is also examined.

Chapter 6

This chapter presents a comparative study for the electromagnetic performance of three 6 stator/4 rotor poles SynR machines having non-overlapping concentrated winding with different connections, i.e. asymmetric, symmetric and hybrid, and excited by AC sinusoidal currents, i.e. salient-pole SynR machines. In general, the output torque of SynR machine is generated due to the variation of the self and mutual inductances. Therefore, such inductances are particular highlighted. In addition, the machine line voltage, torque- and power-speed characteristics and efficiency are also considered. In order to further extend the investigation of this chapter, the electromagnetic performance of 12 stator/4 rotor poles SynR machine, which has overlapping and full pitched winding, is also analyzed and compared with its counterpart of the 6 stator/4 rotor poles machines.

Chapter 7

The operation principle, capability and electromagnetic performance of the 6 stator/4 rotor poles SR machines under the AC sinusoidal bipolar, i.e. salient-pole SynR, with DC bias excitation are examined and analyzed in this chapter. Both the asymmetric and symmetric winding connections are taken into account during the investigations. In addition, the

electromagnetic performance of this machine under such excitation is compared with its counterparts under the conventional unipolar and AC sinusoidal bipolar excitations

Chapter 8

This chapter contains the general conclusions of this thesis as well as the potential future work.

1.4.1. Contributions of Research

The contributions of this thesis can be summarized as follows:

- Study of influence of the manufacturing limits and tolerances on the cogging torque and skew technique effectiveness in the PM machines having modular stators.
- Analysis of influence of alternate slot openings, i.e. open slot, closed slot and hybrid slot, on the torque-speed characteristics and cogging torque of the fractional-slot IPM machines.
- Systematic investigation of the influence of the magnetic saturation on the cogging torque, back-emf waveforms of the PM machines on load.
- Development of the AC sinusoidal bipolar with DC bias excitation technique to drive the SR machines.
- Comparative study of the electromagnetic performance of SR machines under different excitations, i.e. conventional unipolar and AC sinusoidal bipolar without/with DC bias.

Chapter 2: Torque-Speed Performance Analysis of Fractional Slot PM Machines Having Concentrated Windings Using Alternate Methods

2.1 Introduction

Fractional-slot PM machines having concentrated windings have the synergies of inherent low cogging torque and copper loss, which in turn can further improve their efficiency [84, 89]. Furthermore, although the fractional-slot IPM machines with concentrated winding generate significantly small reluctance torque [125], they are still desirable to be employed, since they exhibit a wide flux weakening operation capability and strong demagnetization withstand capability, as well as a good mechanical retaining of the magnets [6]. In general, the PM machine operation is categorized into two regions, i.e. constant-torque and flux weakening operation. The dq-axis theory is often utilized to predict such characteristics and also to drive the PM machines [61]. When the electric loading is relatively high, thus a significant magnetic cross-coupling is most likely to exist between the d- and q-axis parameters. It becomes even more significant in the IPM machines [50]. Thus, the accurate analysis and control of the PM machines, especially the IPM topology, require well accounting for the influence of the magnetic cross-coupling [126]. This influence has been well recognized, examined and taken into account during machine design, analysis and drive in [49, 51, 57, 127, 128].

In this chapter, the frozen permeability (FP), which is an accurate method to account for the magnetic cross-coupling influence [20, 54, 55, 66, 67], is employed to separately examine such influence on the dq-axis parameters of the fractional-slot IPM machines having concentrated winding. The idea behind such investigation is to determine the level of the magnetic cross-coupling effect on each parameter and to find the simple yet accurate model to predict the torque-speed characteristics of fractional-slot PM machines having concentrated windings. The investigation shows that the partial cross-coupling model, which considers the PM flux as a function of the q-axis current and the d- and q-axis inductances as functions of the d- and q- axis currents, respectively, is a simple and accurate technique for predicting the torque-speed characteristics of such PM machines. This technique is compared with the direct finite element (FE) and dq-axis flux linkages prediction methods, which fully account for the magnetic cross-coupling, and are verified by the experimental results. The

analyses are carried out on a 10 poles-12 slots, i.e. fractional-slot, IPM machines having shaped and either un-skewed or step skewed rotors. These techniques are applied to minimize the output torque ripple of the prototype machine, which will be utilized in a power steering system. The lamination cross-section and winding layout of the prototype machine are shown in Fig. 2.1, while its main design parameters are given in Table 2.1.

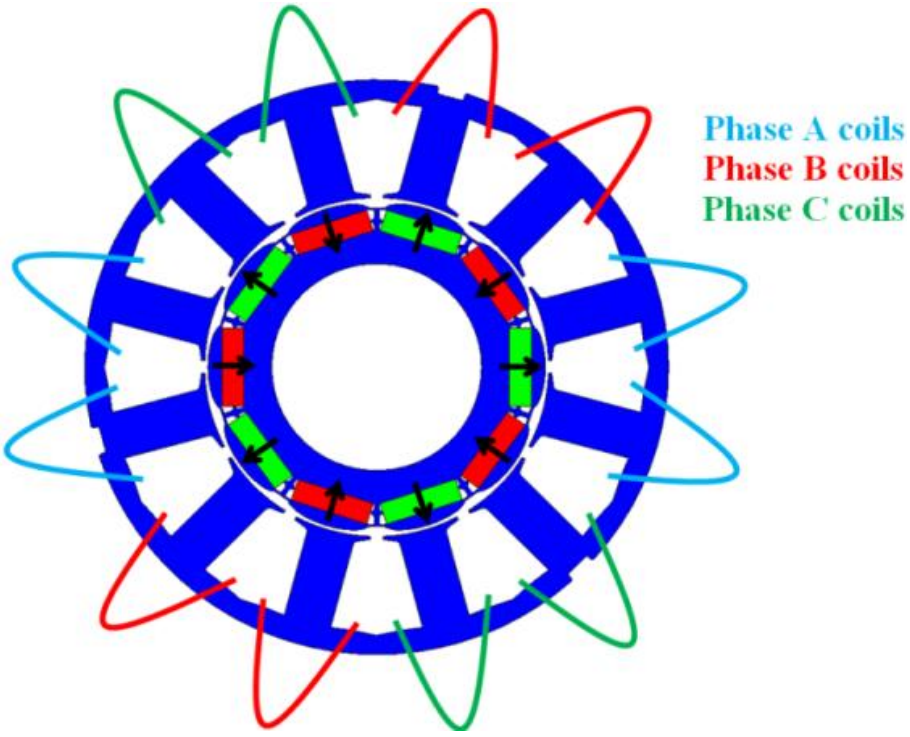

Fig. 2.1 Lamination cross section and phase winding layout of 10-pole/12-slot prototype machine.

Table 2.1 Main design parameters of prototype machine.

Parameter	***Dimension***	***Parameter***	***Dimension***
Stator outer diameter	90 mm	Stator inner diameter	53 mm
Rotor maximum diameter	52 mm	Rotor minimum diameter	50 mm
Minimum air gap length	0.5 mm	Maximum air gap length	1.5 mm
Stator yoke width	3 mm	Tooth width	7.4 mm
Magnet thickness	3.4 mm	Magnet width	12.2 mm
Shaft diameter	36 mm	Slot opening	2 mm
Rib width	0.7 mm	Tooth tip edge	0.5 mm
Rotor step skew angle	4×1.5 mech.deg	Magnet remanence	1.2 T
DC-link Voltage	6 V	Rated Current	150 A_{peak}

2.2. Frozen Permeability Method

The main purpose for freezing the permeability in the PM machines is to allow for a linear analysis with full accounting for the magnetic saturation. This means that the superposition theory for two excitation sources, i.e. PMs and phase current, becomes applicable [20]. The B-H curve of the lamination material is shown in Fig. 2.2. Because of the nonlinear property of such material, the flux density due to the PMs only plus that due to the stator winding currents only is not equal to the total flux density at the working point (B_{WP}). However, if the permeability at full load conditions is frozen, the superposition of the two excitation sources becomes applicable. In other words, the flux density due to the PMs only (B_{PM}) plus that due to the winding currents only (B_{PC}) is then equal to the total flux density (B_{WP}), [67, 126]. During the machine analyses, the utilizing of such method can be summarized as follows: the machine is firstly solved nonlinearly in the FE tool under full load conditions; the permeability of each element is fixed and used to resolve the model linearly with either the electric loading or PMs only [54]. In this case, the open-circuit and phase current characteristics can be calculated separately with exactly accounting for the influence of the saturation level under full loading conditions.

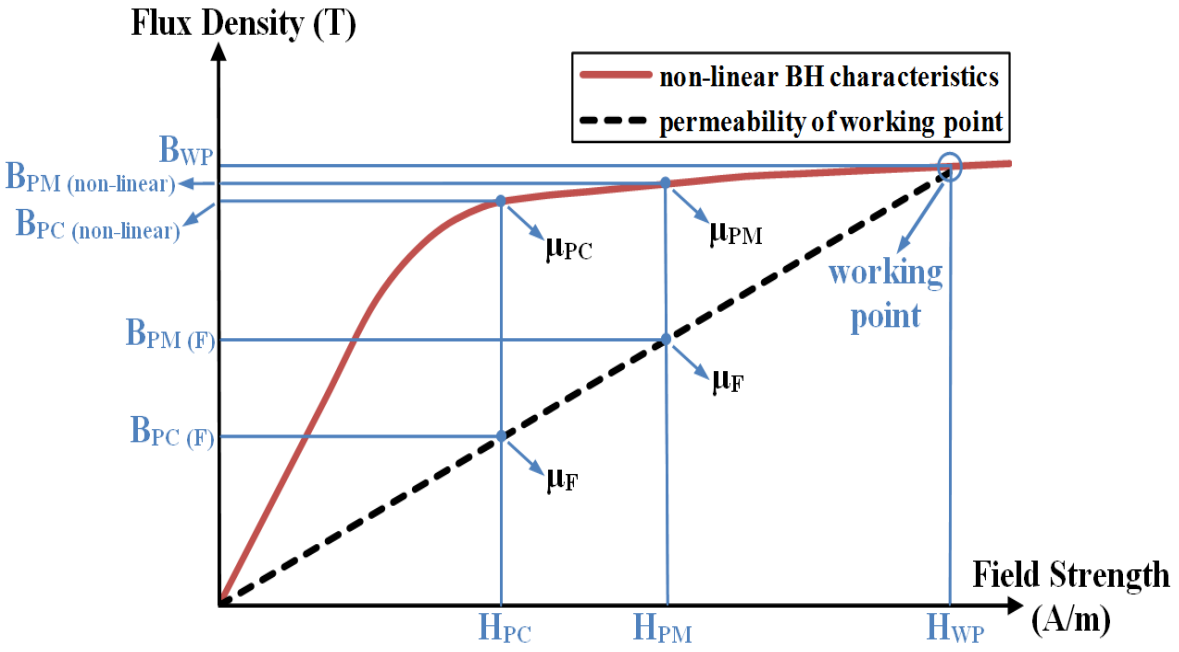

Fig. 2.2 B-H curve of lamination with frozen permeability method, PM and PC refer to the PMs and phase current excitations (the same as Fig. 1.7, duplicated here to ease discussion).

2.3. Electromagnetic Performance

This section presents the electromagnetic performance analyses of the 10 poles-12 slots prototype machines without and with rotor step skew. It is worth mentioning that the skew is accounted for in the 2D FE tool as follows: the machine axial length is divided into four equal parts, since the machine rotor is step skewed by 4 steps; each part is analysed independently; then the solutions are added together to obtain the total results. The accuracy of this technique is validated by the measurement results, which are presented in section 2.5. As mentioned earlier, the studied machine has a shaped rotor, thus its magnetic field flux lines are very concentrated over the PMs, as illustrated in Fig. 2.3. This results in a relatively sinusoidal open-circuit air gap flux density waveform, as shown in Fig. 2.4. It should be mentioned that the spikes in such waveform are caused by the slot opening. As a result of the rotor shaping, the open-circuit flux linkage, thus the back-emf waveforms of the prototype machine are very sinusoidal, as respectively shown in Fig. 2.5 and Fig. 2.6. Therefore, the torque ripple due to the back-emf harmonics should be significantly small. In addition, Fig. 2.6 also shows that the influence of the step skew on the back-emf magnitude is negligibly small. Consequently, the average output torque will not be significantly affected by the skew, as will be shown later. However, the skew further improves the sinusoidal shape of the back-emf waveform, Fig. 2.6, thus even lower torque ripple is expected. Furthermore, the cogging torque of the prototype machine is relatively small, as shown in Fig. 2.7, since it is a fractional-slot machine and has a shaped rotor. Theoretically, the cogging torque is totally diminished when the machine is step skewed, as illustrated in Fig. 2.7. It should be mentioned that the influence of the manufacturing limits and defects, electric loading and magnetic saturation on the cogging torque and effectiveness of the skew technique are tolerated, but they are further investigated in next chapters. As a conclusion of the sinusoidal back-emf and the significantly small cogging torque, the output toque waveform of the prototype machine is relatively smooth, as shown in Fig. 2.8. It also confirms that the skew, which effectively eliminates the cogging torque, Fig. 2.7, and nearly halved the output torque ripple, as shown in Fig. 2.9, exhibits an ignorable influence on the output torque. In other words, the average output torque is almost not influenced by the skew technique, as can be also noticed in Fig. 2.10.

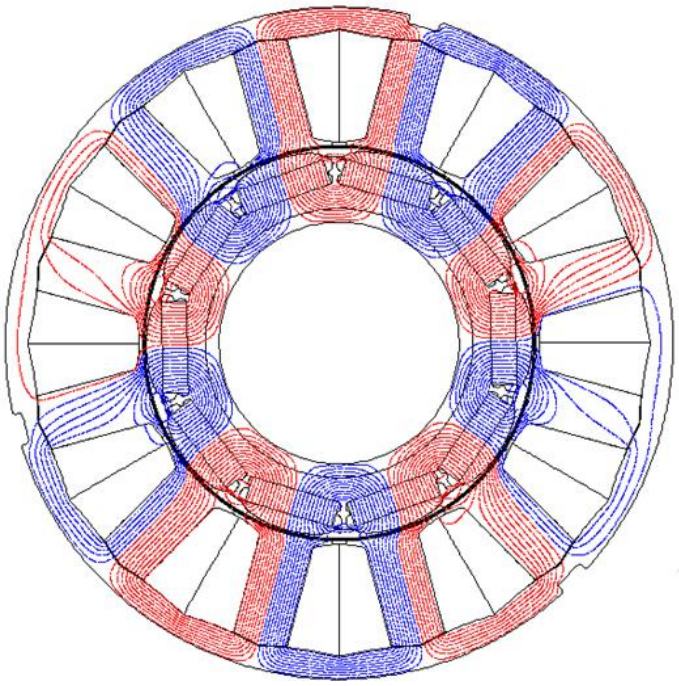

(a) Open-circuit

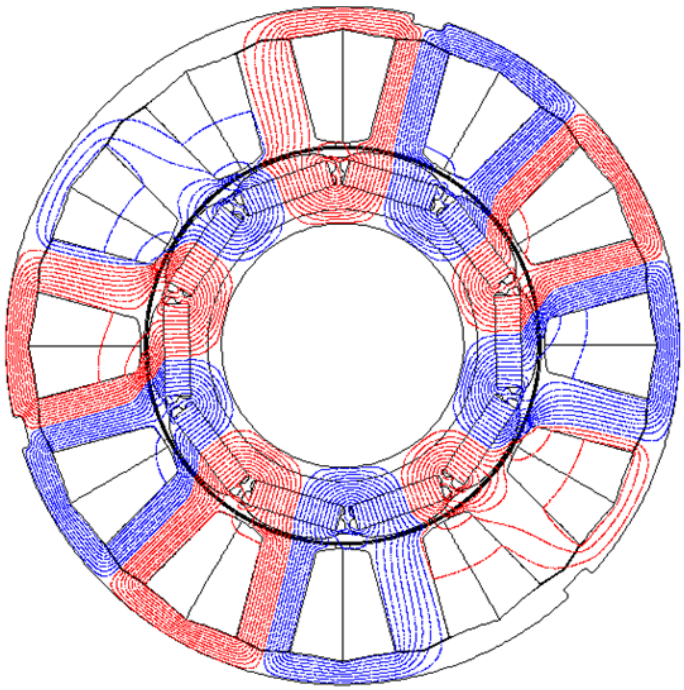

(b) Load, at 150A_{peak} phase current

Fig. 2.3 Open-circuit and load equal potential distributions of 10-poles/12-slot prototype machine.

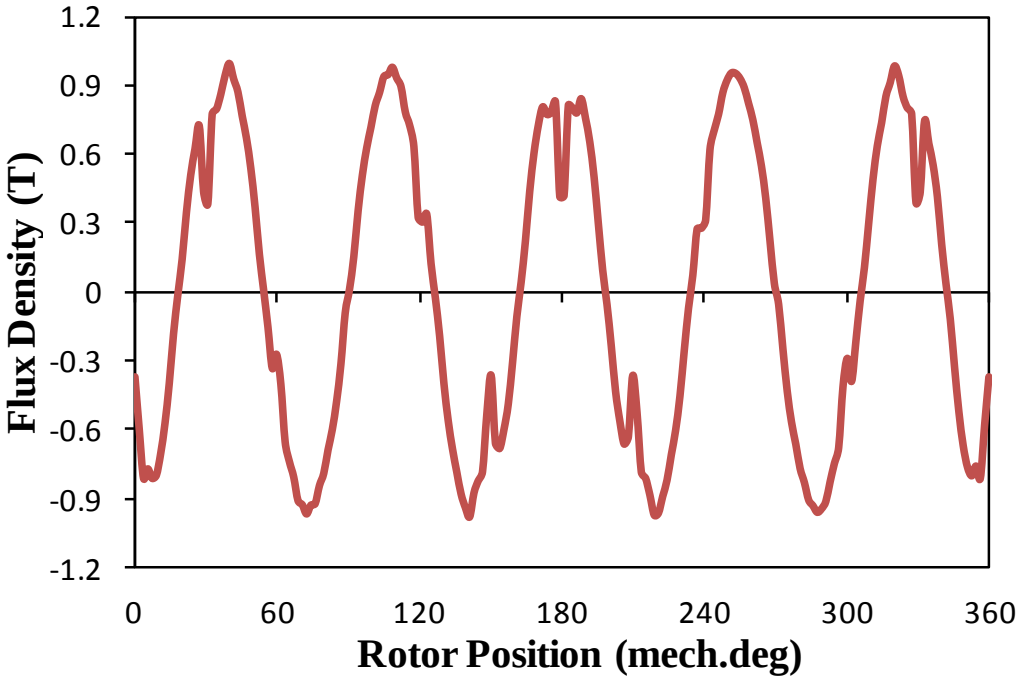

Fig. 2.4 Variation of open-circuit air gap flux density waveform of 10-pole/12-slot prototype machine when d-axis aligned with Phase A-axis.

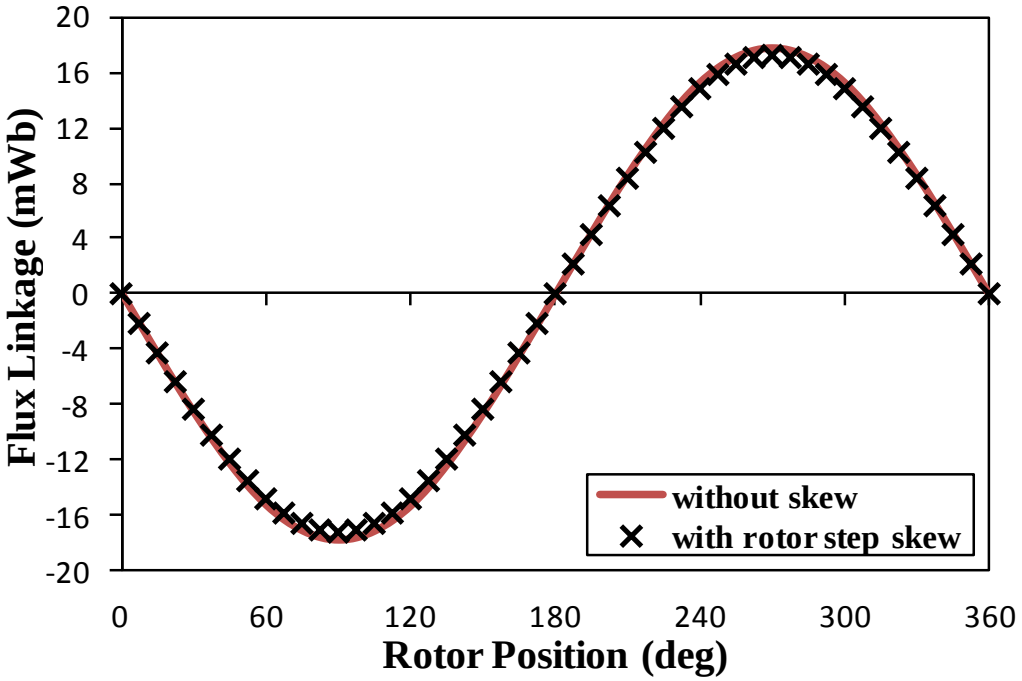

Fig. 2.5 Comparison of open-circuit flux linkage waveforms of of 10-pole/12-slot prototype machines having un-skewed and step skewed rotors.

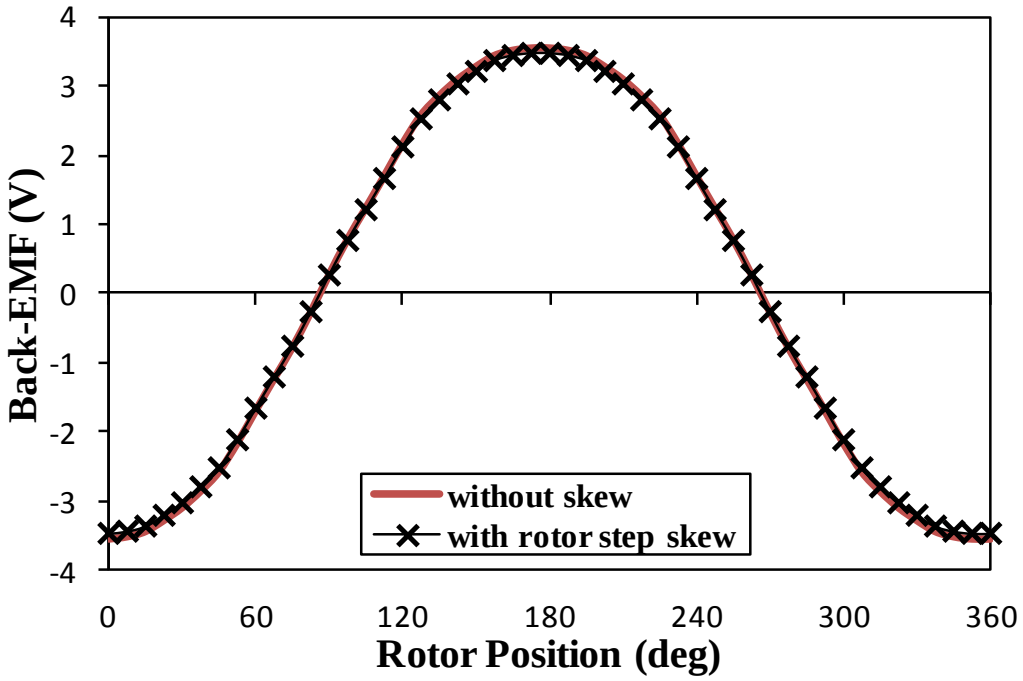

(a) Waveforms

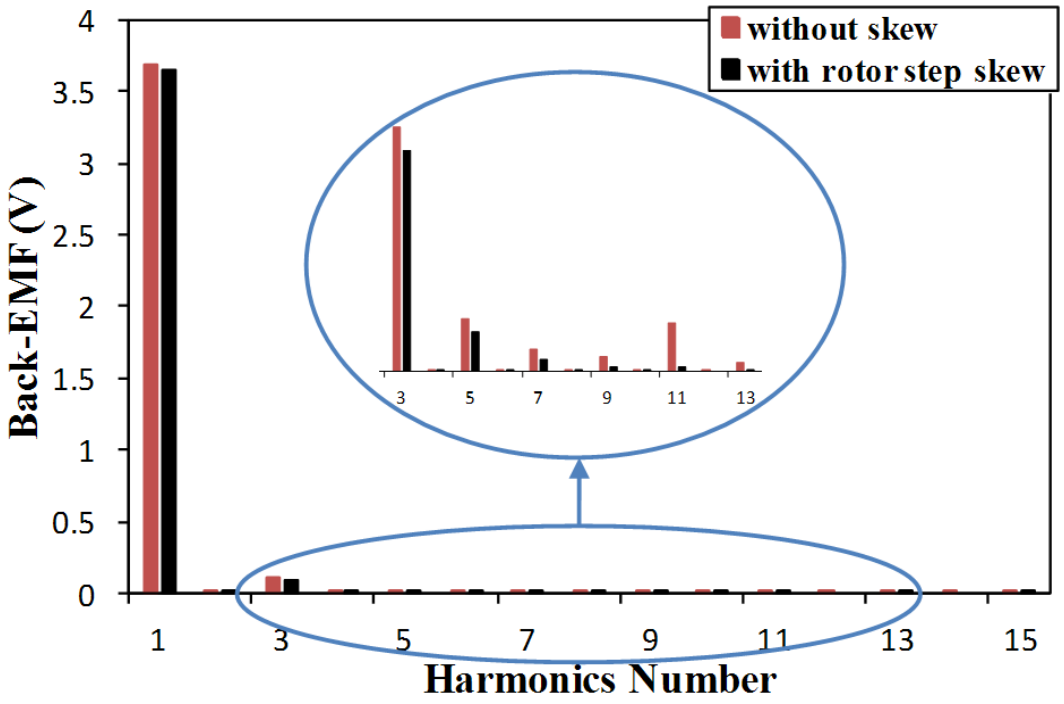

(b) Harmonics

Fig. 2.6 Comparison of back-emf waveforms and harmonics of of 10-pole/12-slot prototype machines having un-skewed and step skewed rotors, at 400 rpm rotating speed.

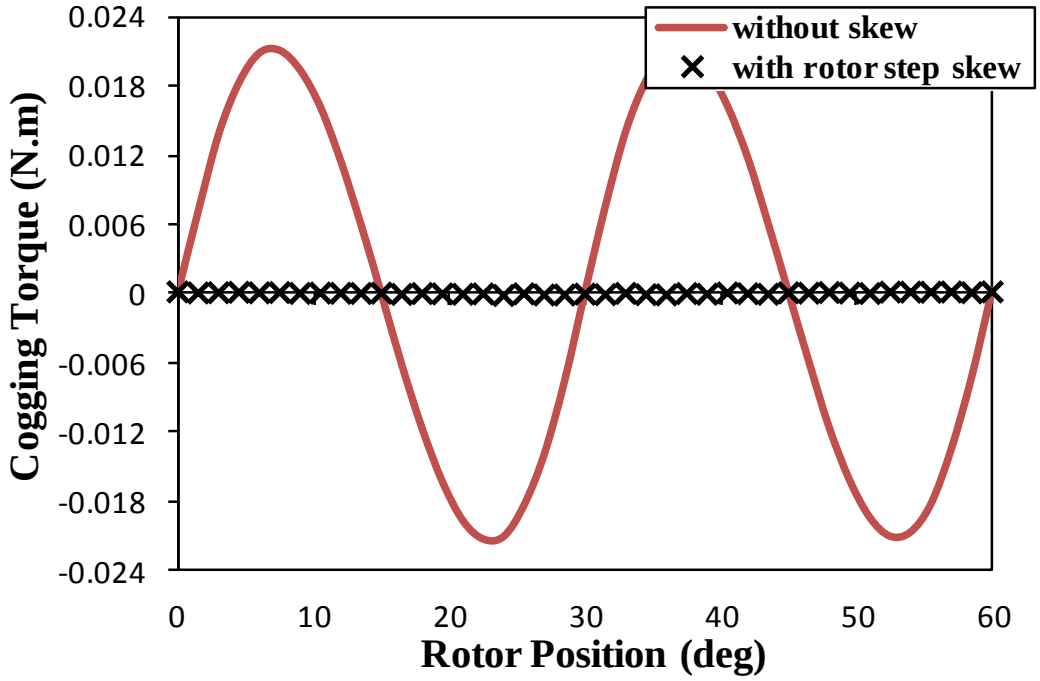

Fig. 2.7 Comparison of cogging torque waveforms of of 10-pole/12-slot prototype machines having un-skewed and step skewed rotors.

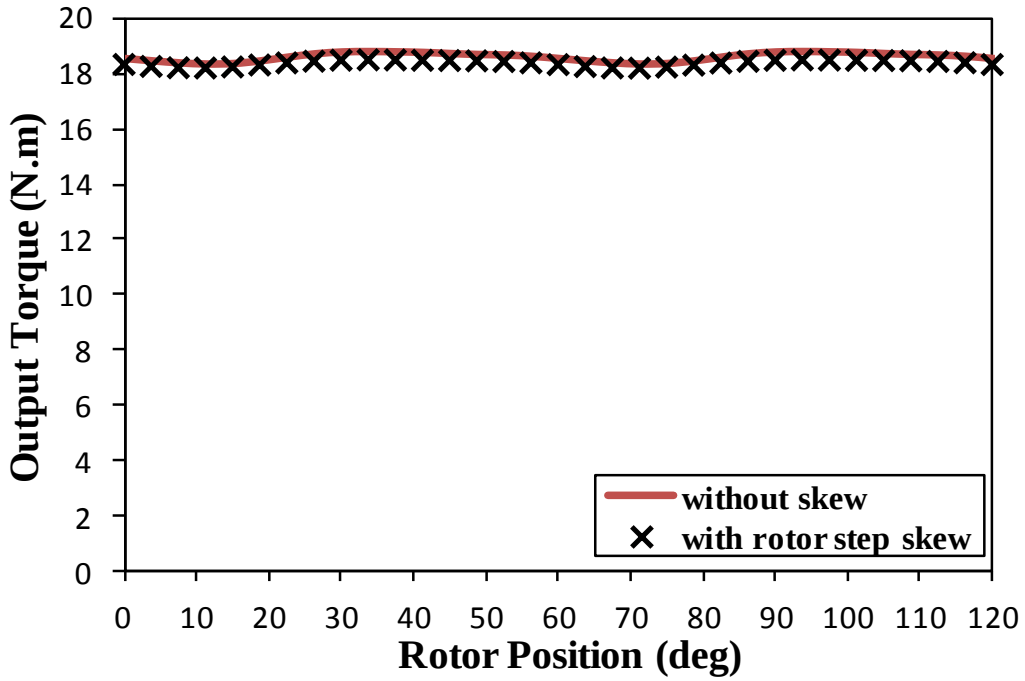

Fig. 2.8 Comparison of output torque waveforms of 10-pole/12-slot prototype machines having un-skewed and step skewed rotors, at I_q=150A, I_d=0A.

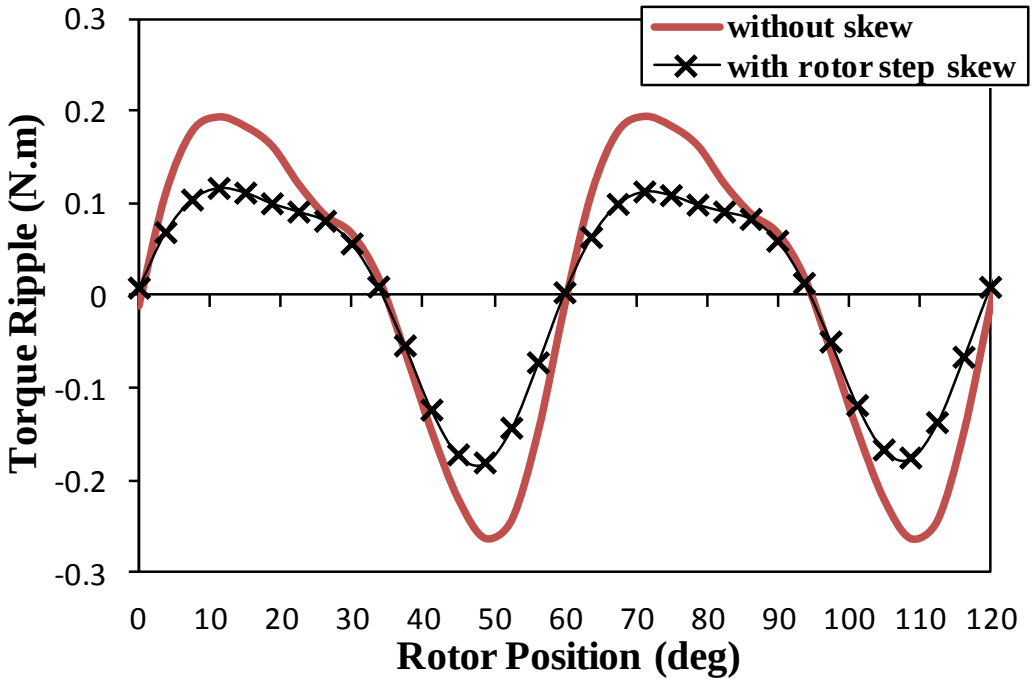

Fig. 2.9 Comparison of torque ripple waveforms of 10-pole/12-slot prototype machines having un-skewed and step skewed rotors.

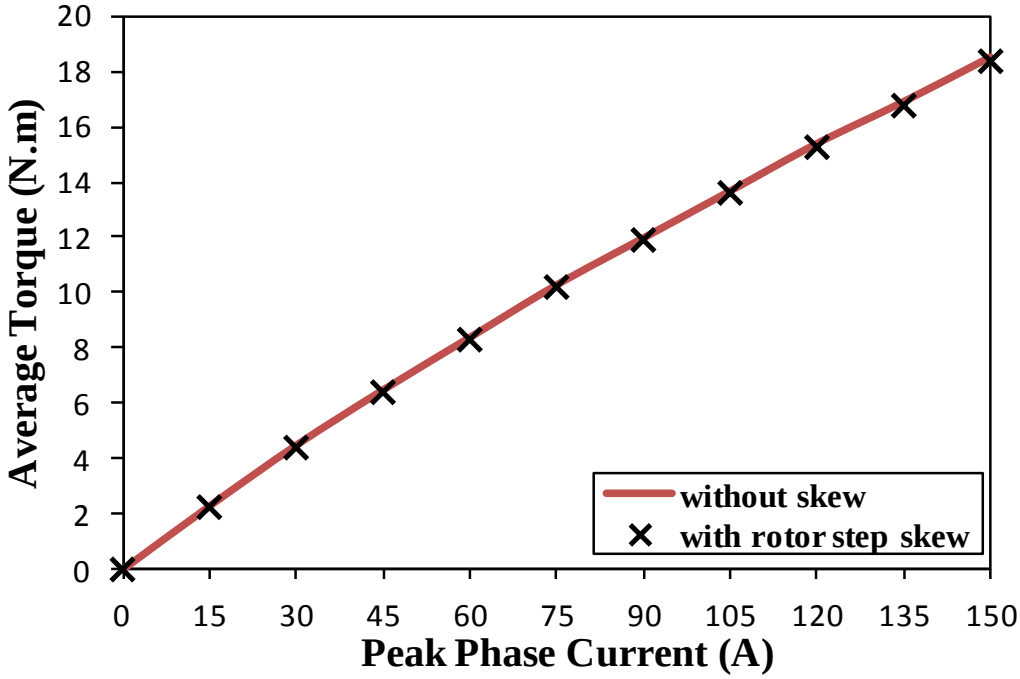

Fig. 2.10 Comparison of average output torque against peak phase current of 10-pole/12-slot prototype machines having un-skewed and step skewed rotors, at I_q=150A, I_d=0A.

2.4. Analysis Methods of Torque-Speed Characteristics

In this section, three different techniques to predict the torque-speed characteristics of fractional-slot PM machines, i.e. the partial cross-coupling, direct FE and dq-axis flux linkages, are presented and compared from the accuracy, simplicity and time consumption points of views. The FP method is utilized to simplify the full cross-coupling model with a negligible influence on the accuracy. Although the obtained simplified model only partially considers the cross-coupling effect, it still shows a high accuracy for the fractional-slot PM machines having concentrated windings.

2.4.1. Proposed Technique

The output torque of PM machines can be calculated by:

$$T = 1.5p[\psi_d I_q - \psi_q I_d] \tag{2. 1}$$

where p, ψ_d, ψ_q, I_d and I_q are the pole pair number, the dq-axis flux linkages and currents, respectively.

Each flux linkage is formed by two components: one is due to the PMs and the other is due to the phase currents. Therefore, the output torque with fully accounting for the magnetic cross-coupling and saturation can be expressed as:

$$T = 1.5p\{[\psi_{md}(I_d, I_q) + \psi_{cd}(I_d, I_q)]I_q - [\psi_{mq}(I_d, I_q) + \psi_{cq}(I_d, I_q)]I_d\} \tag{2. 2}$$

where $\psi_{md}(I_d, I_q)$ and $\psi_{mq}(I_d, I_q)$ are dq-axis flux linkages due to the PM, respectively, and $\psi_{cd}(I_d, I_q)$ and $\psi_{cq}(I_d, I_q)$ are the dq-axis flux linkages due to winding currents, respectively. They are all functions of both d- and q-axis currents.

The dq-axis flux linkages due to the winding currents can be given by their corresponding inductances and currents as follows:

$$L_d(I_d, I_q) = \frac{\psi_{cd}(I_d, I_q)}{I_d} \tag{2. 3}$$

$$L_q(I_d, I_q) = \frac{\psi_{cq}(I_d, I_q)}{I_q} \tag{2. 4}$$

By substituting (2. 3) and (2. 4) in (2. 2), the expression of the output torque becomes:

$$T = 1.5p\{[\psi_{md}(I_d, I_q)I_q + \psi_{mq}(I_d, I_q)I_d] + [L_d(I_d, I_q) - L_q(I_d, I_q)]I_d I_q\} \quad (2.\ 5)$$

The first part of the right side of (2. 5) is the electromagnetic torque, i.e. the torque due to interaction between the PMs and current, while the second part is the reluctance torque, i.e. the torque results from the difference between the dq-axis magnetic reluctances, i.e. dq-axis inductances. This equation can be analytically utilized together with the phase voltage equation (2. 6) to predict the torque-speed characteristics of any PM machine with full accounting for the magnetic cross-coupling and saturation. But the dq-axis PM flux linkages and inductances as functions of the dq-axis currents should be predicted in advance using the FP method. However, such calculations can be very complicated and time consuming. Therefore, the influence of the saturation due to the PMs and winding currents on the dq-axis parameters is analysed in depth by the FP method in order to further simplify the calculations of the torque-speed characteristics of the fractional-slot PM machines with concentrated winding equation, without the compromise of the accuracy.

$$V_{ph} = \sqrt{V_d^2 + V_q^2} \quad (2.\ 6)$$

$$V_d = I_d R_{ph} - \omega[L_q(I_d, I_q)I_q + \psi_{mq}(I_d, I_q)] \quad (2.\ 7)$$

$$V_q = I_q R_{ph} + \omega[L_d(I_d, I_q)I_d + \psi_{md}(I_d, I_q)] \quad (2.\ 8)$$

where R_{ph} and ω are the phase winding resistance and electrical rotating speed, respectively.

The variations of the dq-axis PM flux linkages against the dq-axis currents are calculated using the FP method, and given in Fig. 2.11. Due to the magnetic cross-coupling and saturation, the d-axis PM flux linkage decreases with the q-axis current. However, it slightly increases with the increasing of the negative d-axis current since the saturation level becomes lower, as illustrated in Fig. 2.11 (a). Since the influence of the d-axis current on the d-axis PM flux linkage is negligible, it can be neglected in the torque expression (2. 5) while the influence of the q-axis current on the d-axis PM flux linkage needs be maintained. As

shown in Fig. 2.11(b), the magnitude of the q-axis PM flux linkage increases with the q-axis current, but it is decreased by the negative d-axis current. However, most importantly, the q-axis PM flux linkage is significantly small. Hence, the output torque expression can be further simplified by completely neglecting the q-axis PM flux linkage. Thus, the electromagnetic torque due to the interaction between PM and current can be calculated by:

$$T_{PM} = 1.5p[\psi_{md}(I_q)I_q] \tag{2. 9}$$

where $\psi_{md}(I_q)$ is the d-axis PM flux linkage as function of q-axis current while the d-axis current is zero.

In order to illustrate the influence of the undertaken simplifications on the calculation accuracy, the electromagnetic torque due to the interaction between PM and current of the prototype machine is calculated according to the first part of the right side of (2. 5). The results are shown in Fig. 2.12(a). The influence of the d-axis current on this part of torque is small. In addition, the electromagnetic torque due to the interaction between PM and current is also calculated by (2. 9). In order to ease the comparison, each set of torque values of different d-axis currents but the same q-axis current shown in Fig. 2.12 (a) is averaged. The average torque is compared with the prediction by (2. 9) in Fig. 2.12 (b). Good agreement is achieved. This confirms that the electromagnetic torque due to interaction between PM and current can be accurately calculated by considering the influence of the q-axis current on d-axis PM flux linkage only, (2. 9). It is worth mentioning that the influence of the q-axis current on the d-axis PM flux linkage cannot be neglected, because it is significantly large, as can be noticed in Fig. 2.12(b).

Furthermore, the FP method is also employed to calculate the variations of dq-axis inductances against the dq-axis currents, as given in Fig. 2.13. It shows that the dq-axis inductances are nearly the same, since the machine employs the fractional-slot concentrated windings [125]. Hence, the reluctance torque of the analyzed machine is relatively small. Consequently, the influence of the magnetic cross-coupling between d- and q-axis inductances on the total output torque is significantly small. Thus, this magnetic cross-coupling can be neglected, i.e. each inductance can be calculated as a function of its corresponding current only, during the prediction of the reluctance torque.

Hence, the output torque of fractional-slot PM machines can be further simplified to be as follows:

$$T = 1.5p\{\psi_{md}(I_q)I_q + [L_d(I_d) - L_q(I_q)]I_d I_q\} \quad (2.\ 10)$$

where $L_d = \frac{\psi_d(I_d)}{I_d}$ and $L_q = \frac{\psi_q(I_q)}{I_q}$ are the dq-axis inductances, each of them is a function of its corresponding current only.

In the same way, the dq-axis voltages can be calculated by:

$$V_d = I_d R_{ph} - \omega L_q(I_q)I_q \quad (2.\ 11)$$

$$V_q = I_q R_{ph} + \omega[L_d(I_d)I_d + \psi_{md}(I_q)] \quad (2.\ 12)$$

Consequently, the torque-speed characteristics of the fractional-slot PM machines having concentrated winding can be analytically predicted using the simplified torque and voltage equations, i.e. (2. 10), (2. 11) and (2. 12), respectively. This requires the pre-calculating of the d-axis PM flux linkage as function of q-axis current, Fig. 2.14, and dq-axis inductances against their corresponding current only, i.e. L_d when I_q=0 in Fig. 2.13 (a) and L_q when I_d=0 in Fig. 2.13 (b). The calculation of these parameters is significantly easier and faster than that of the parameters in (2. 5), i.e. dq-axis PM flux linkages and inductances as functions of both the dq-axis currents. The electromagnetic and reluctance torque equations at different levels of cross-coupling accounting for are given in Table 2.2 for

In order to examine the influence of simplifications, the torque-speed characteristics are predicted and compared using both the full and partial magnetic cross-coupling techniques. Both techniques results in nearly the same results, as shown in Fig. 2.15. This confirms the accuracy of the simplified technique for the prototype machine, which significantly reduces the computational time and complexity.

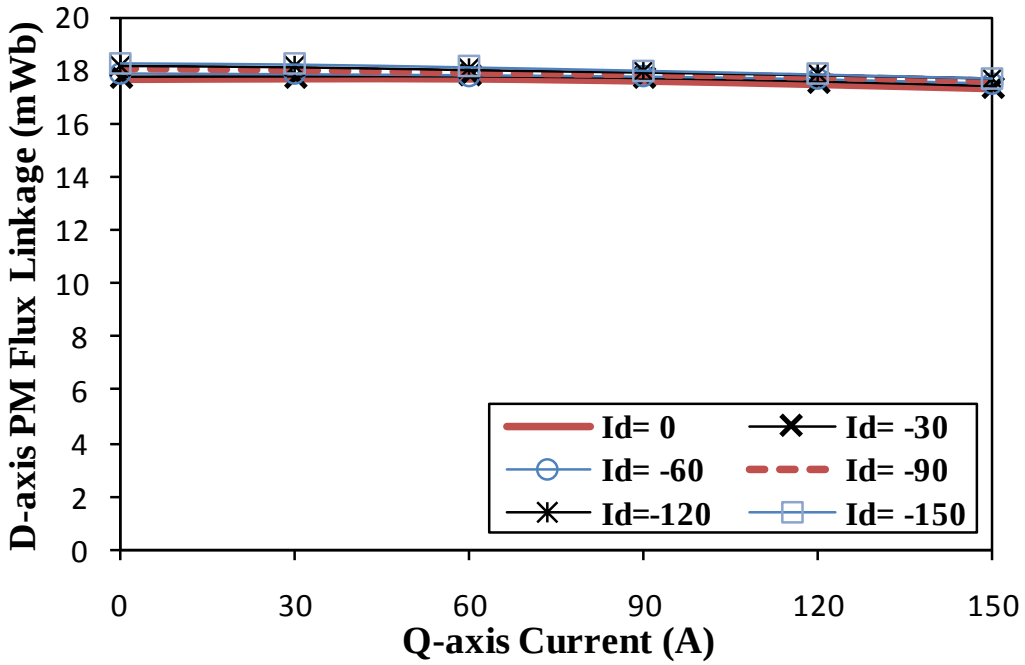

(a) D-axis PM flux linkage

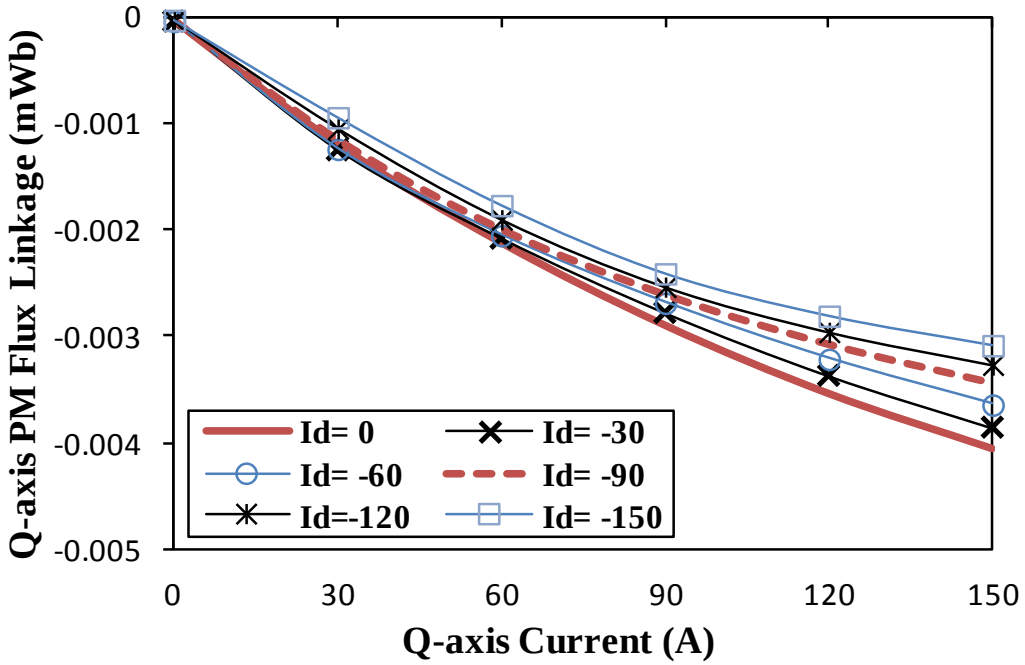

(b) Q-axis PM flux linkage

Fig. 2.11 Variations of dq-axis PM flux linkages against dq-axis currents of 10-pole/12-slot prototype machine.

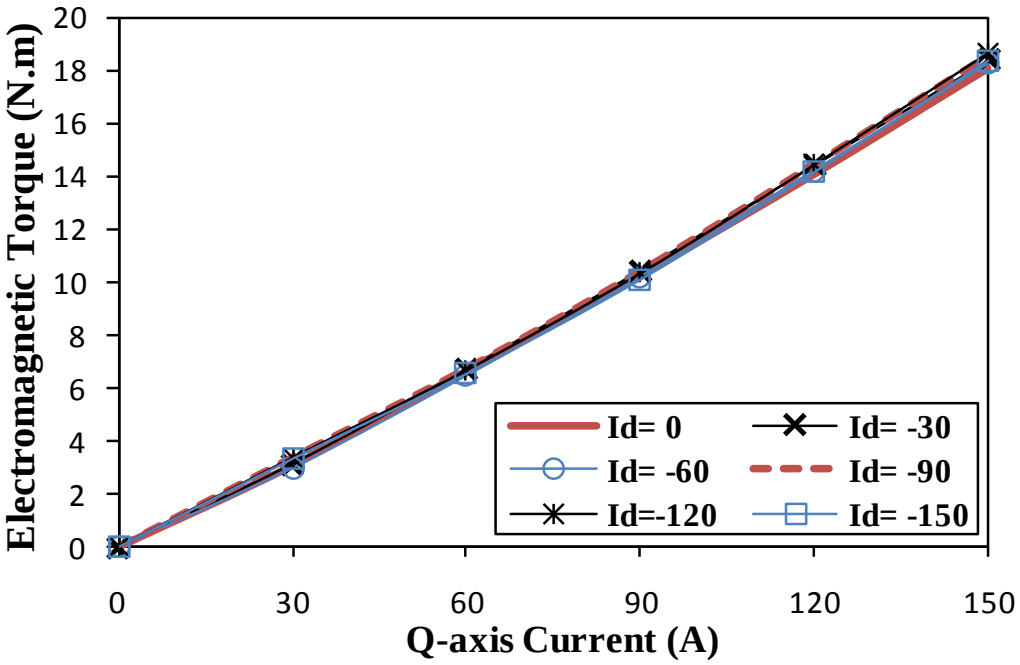

(a) Electromagnet torque against dq-axis current

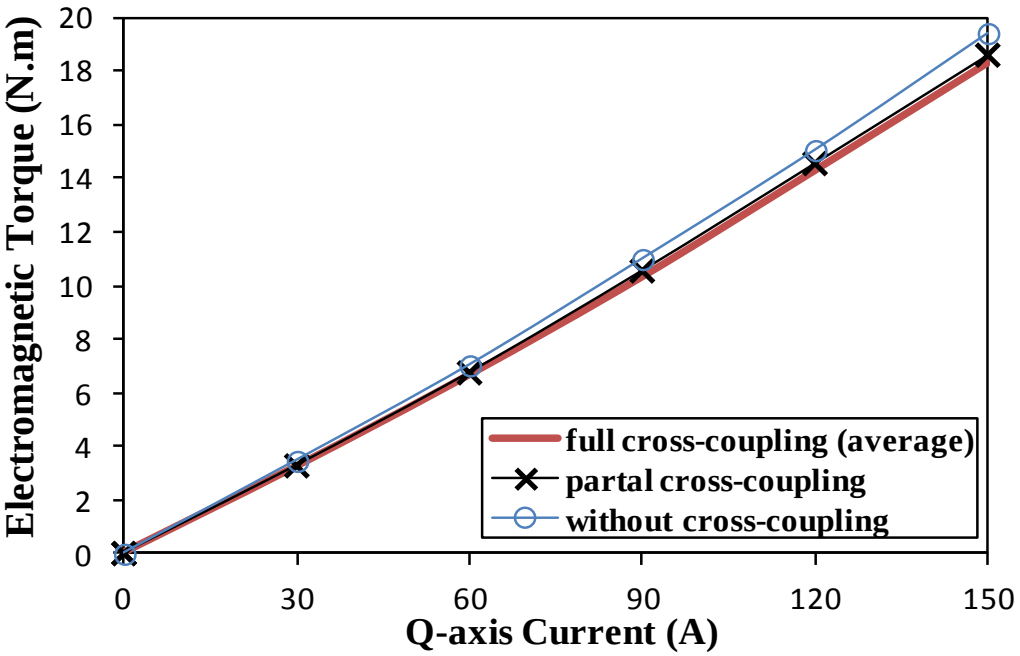

(b) Electromagnetic torque against q-axis current

Fig. 2.12 Variations of electromagnet torque of 10-pole/12-slot prototype machine due to interaction betwen PM and current against dq-axis currents.

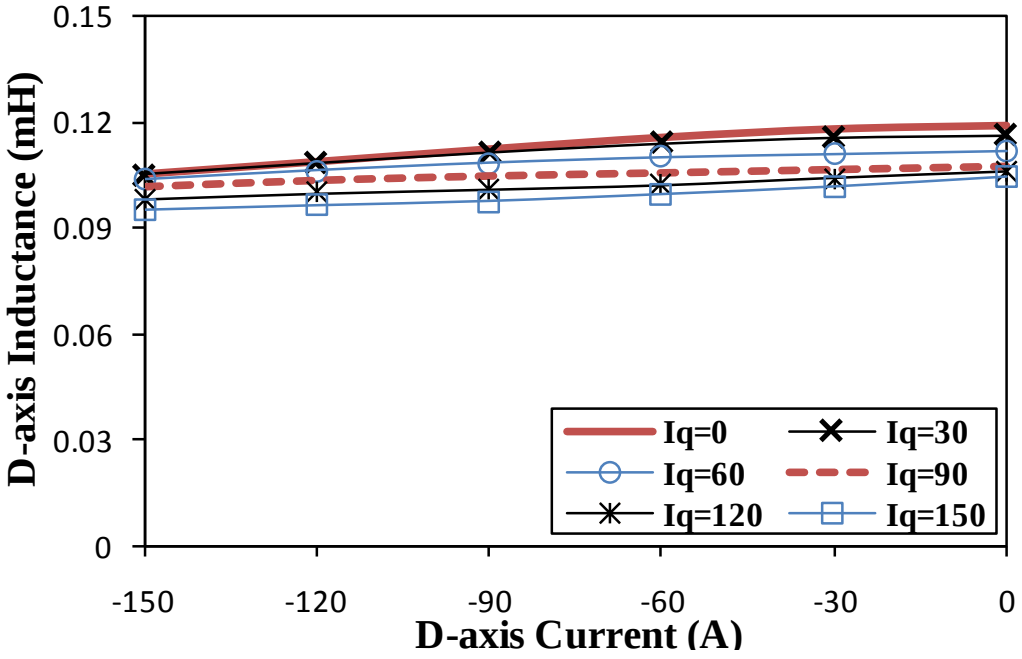

(a) D-axis inductance

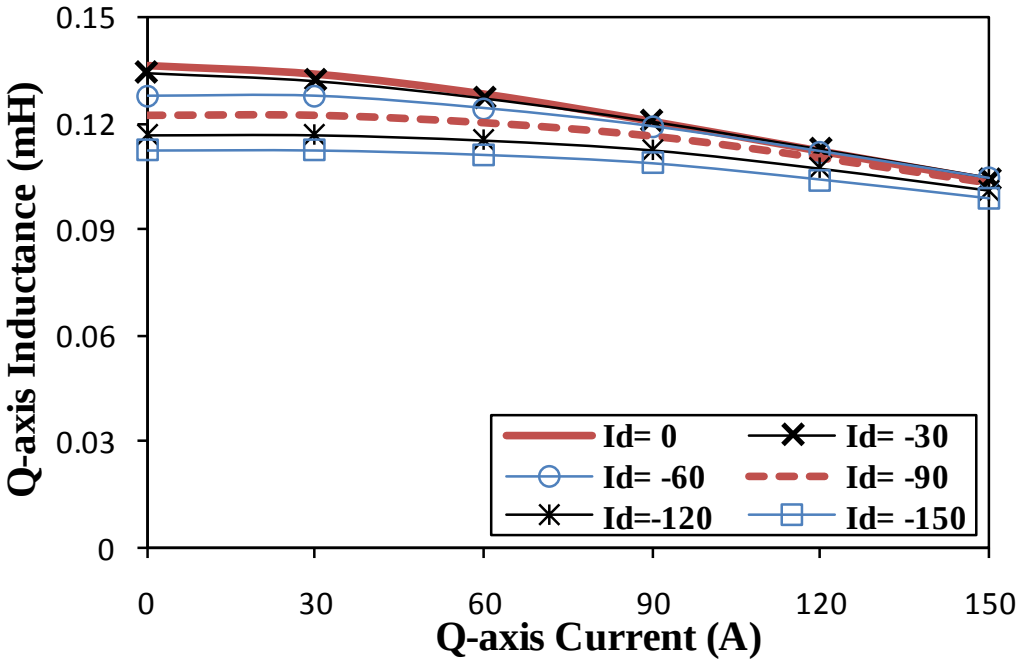

(b) Q-axis inductance

Fig. 2.13 Variations of dq-axis inductances aganist dq-axis currents of 10-pole/12-slot prototype machine.

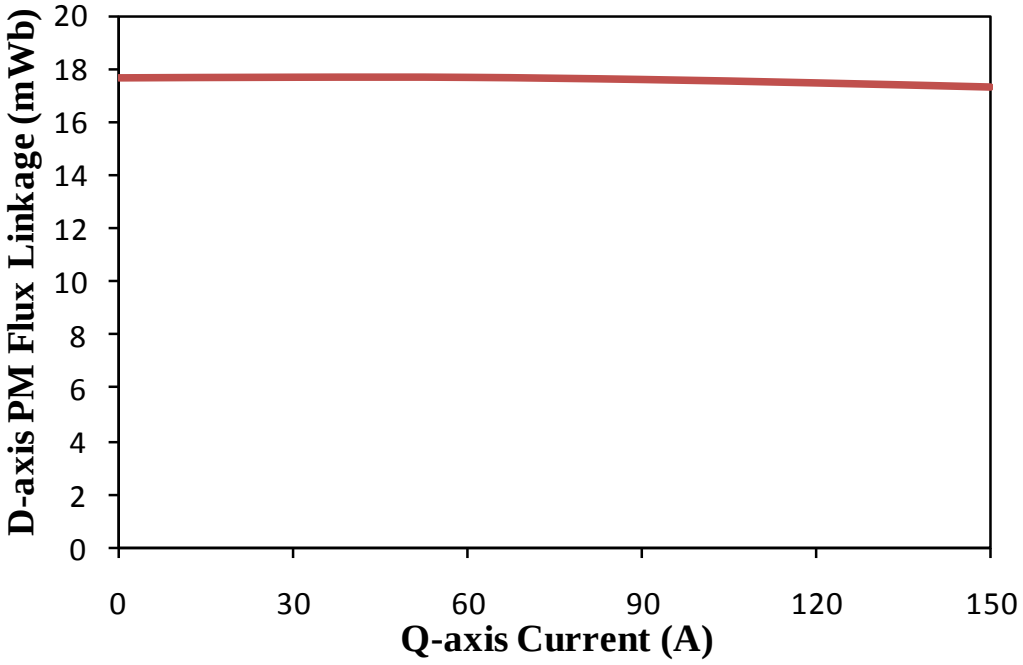

Fig. 2.14 Variations of d-axis PM flux linkage against q-axis current of 10-pole/12-slot prototype machine.

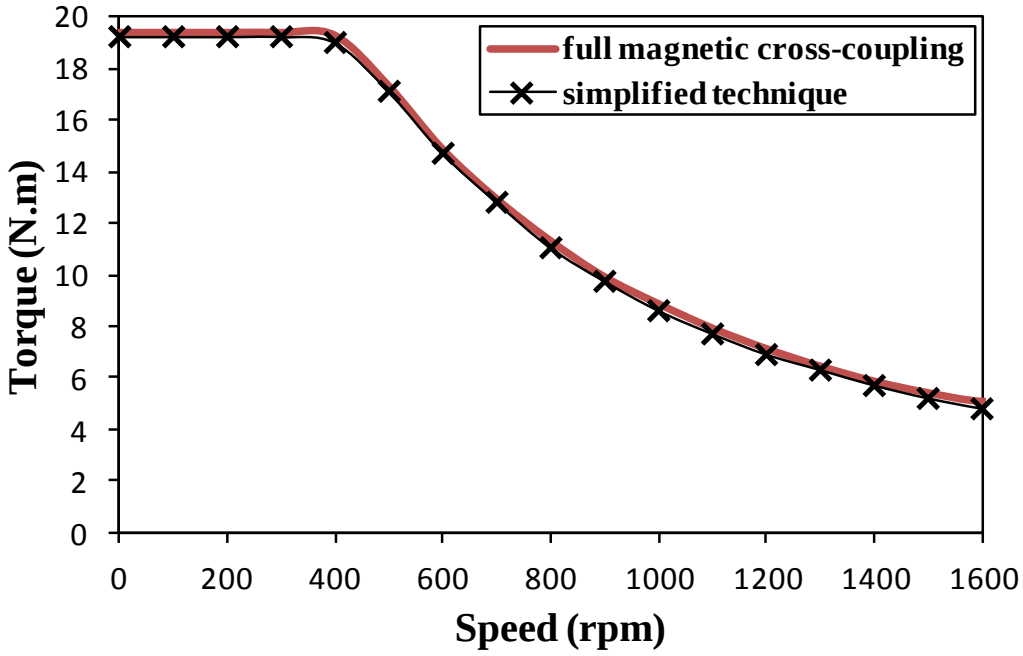

Fig. 2.15 Comparison of torque-speed characterstics of 10-pole/12-slot prototype machine predicted by full and partial cross-coupling models.

Table. 2.2 Calculation equations of electromagnetic and reluctance torque at different corss-coupling accounting for level

Level of Cross-Coupling	**Electromagnetic Torque**	**Reluctance Torque**
Full	$1.5p[\psi_{md}(I_d, I_q)I_q + \psi_{mq}(I_d, I_q)I_d]$	$1.5p[L_d(I_d, I_q) - L_q(I_d, I_q)]I_d I_q$
Partial	$1.5p\psi_{md}(I_q)I_q$	$1.5p[L_d(I_d) - L_q(I_q)]I_d I_q$
Without	$1.5p\psi_{md}I_q$	$1.5p[L_d - L_q]I_d I_q$

2.4.2. Direct Finite Element Technique

In this technique, the machine phase voltage against current angle for different speeds, as given in Fig. 2.16, and output torque-current angle characteristics, as shown in Fig. 2.17, are directly calculated from the FE tool. These results are together utilized to predict the torque-speed characteristics as follows: at each speed the output torque is determined by the current angle that satisfies the phase voltage limitation. When the machine phase voltage is lower than the voltage limitation, the machine is operated at the optimal current angle, which leads to the maximum possible output torque. However, at high speeds when the machine phase voltage is larger than the limitation, the current angle is adjusted to operate the machine at its maximum output torque within the voltage limitation. In order to clearly illustrate the prediction procedure, the output torque is determined in details at 800 rpm. At this speed the voltage limitation is satisfied when the current angle is 58 deg, as shown in Fig. 2.16. According to Fig. 2.17, the corresponding output torque of this angle is 11.4 Nm, which is considered as the maximum possible torque at 800 rpm, as illustrated in Fig. 2.18. By repeating such process for all speeds, the whole torque-speed characteristics, which are shown in Fig. 2.18, are obtained. These characteristics are for a specific electric loading value, i.e. current phase is 150 A_{peak}. However, the whole calculation process should be repeated if such characteristics are required at different electric loadings. In conclusion, this method is very accurate and fully accounts for the magnetic cross-coupling and saturation. However, on the other hand, it is significantly time consuming, especially if both the current angle and magnitude need to be varied together to satisfy the maximum output torque within the voltage limitation, as discussed in [129].

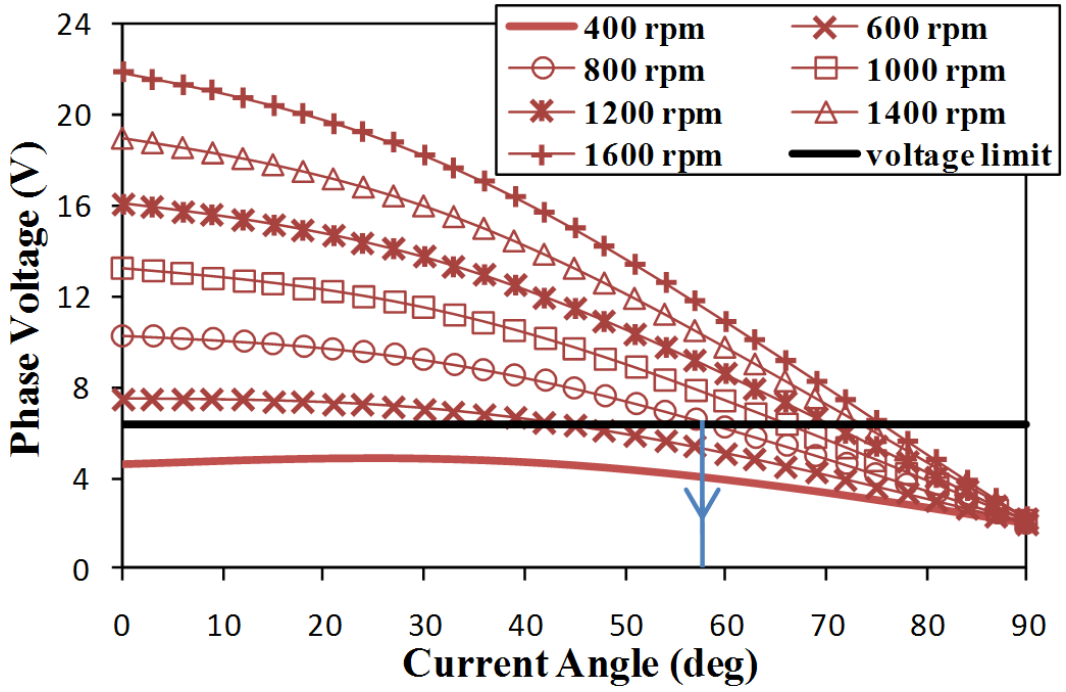

Fig. 2.16 Variations of phase voltage against current angle of 10-pole/12-slot prototype machine for different rotating speeds, at 150 A_{peak} phase current.

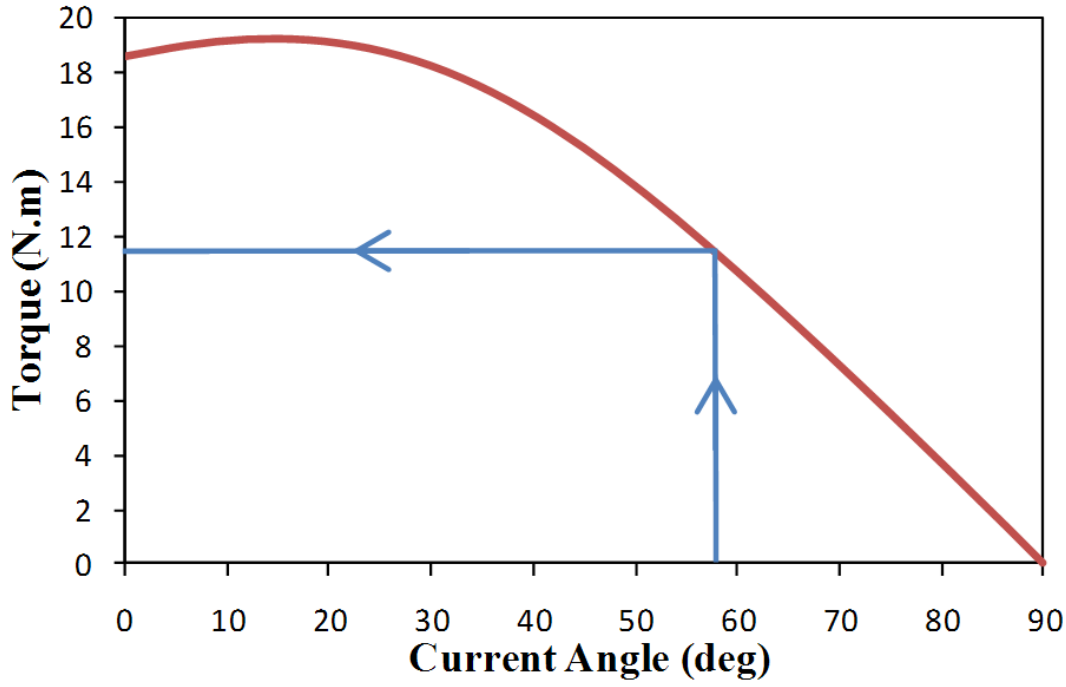

Fig. 2.17 Variations of prototype machine output torque against current angle, at 150 A_{peak} phase current.

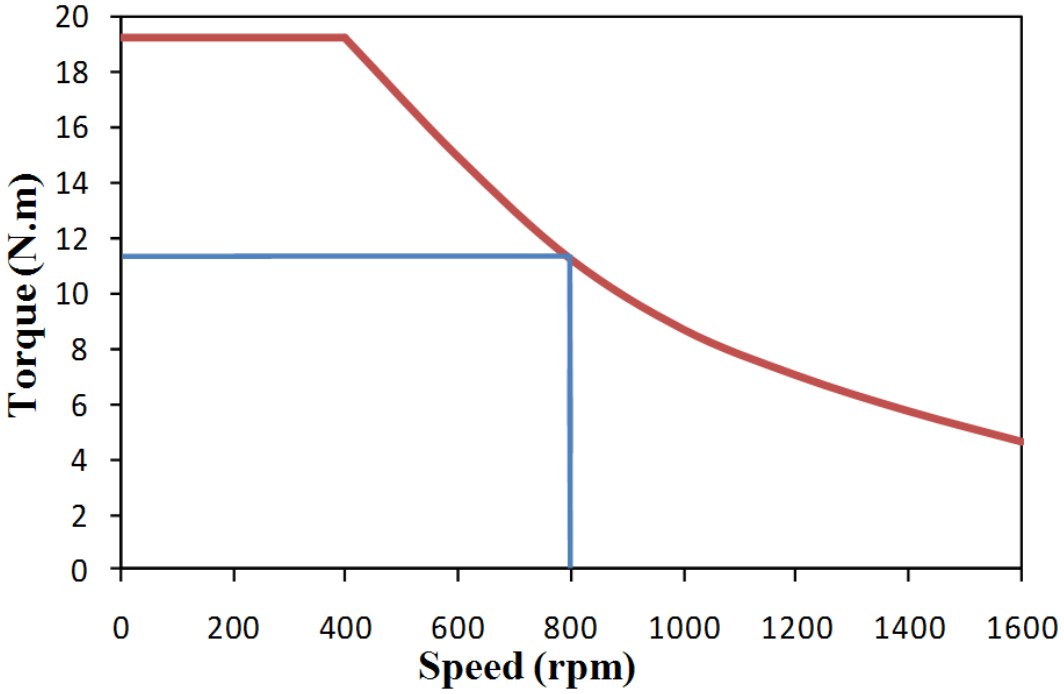

Fig. 2.18 Variatins of torque-speed characteristics of 10-pole/12-slot prototype machine using the direct FE technique, at 150 A_{peak} phase current.

2.4.3. Dq-axis Flux Linkage Technique

This is a hybrid technique. The dq-axis flux linkages are calculated by the FE tool, then they are analytically utilized to predict the torque-speed characteristics using (2. 1) and the following phase voltage equation:

$$V_{ph} = \sqrt{(I_d R_{ph} - \omega\psi_q)^2 + (I_q R_{ph} + \omega\psi_d)^2} \qquad (2.\ 13)$$

However, in order to account for the magnetic cross-coupling and saturation, the dq-axis flux linkages should be calculated as functions of both dq-axis currents, as illustrated in Fig. 2.19. This technique has the same accuracy as the direct FE method. However, in term of calculation time, it is relatively faster.

Fig. 2.20 compares the torque- and power-speed characteristics of the prototype machine predicted by three different prediction techniques, i.e. direct FE, partial cross-coupling and dq-axis flux linkages. All techniques exhibit almost the same accuracy even when the prototype machine rotor is step skewed. However, the partial cross-coupling technique is much faster and less complicated.

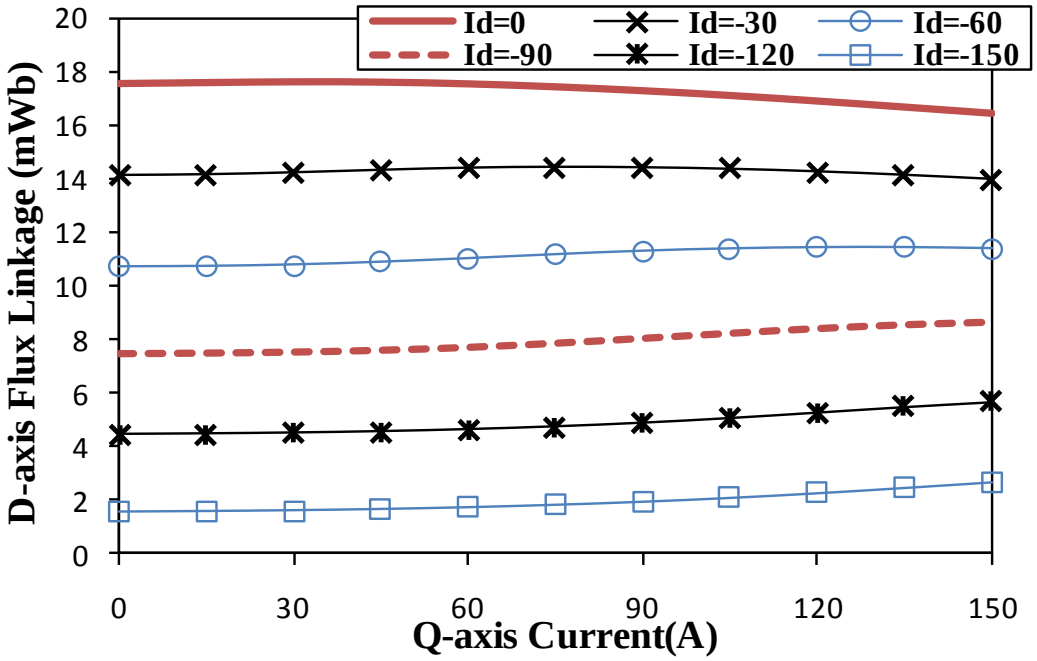

(a) D-axis flux linkage

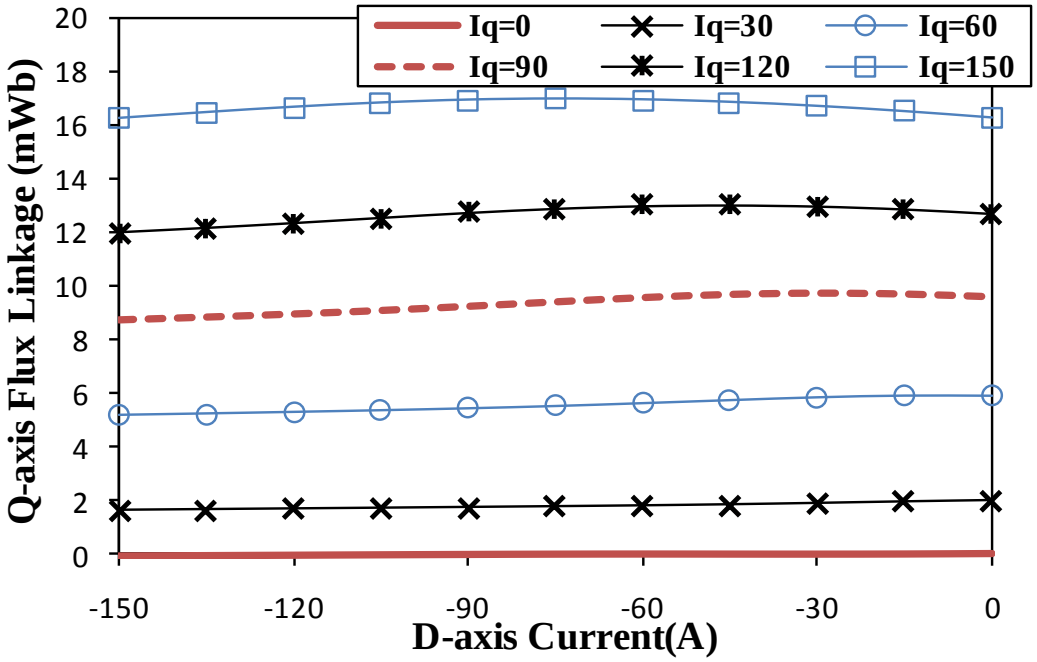

(b) Q-axis flux linkage

Fig. 2.19 Variations of dq-axis flux linkages against d- and q-axis currents of 10-pole/12-slot prototype machine.

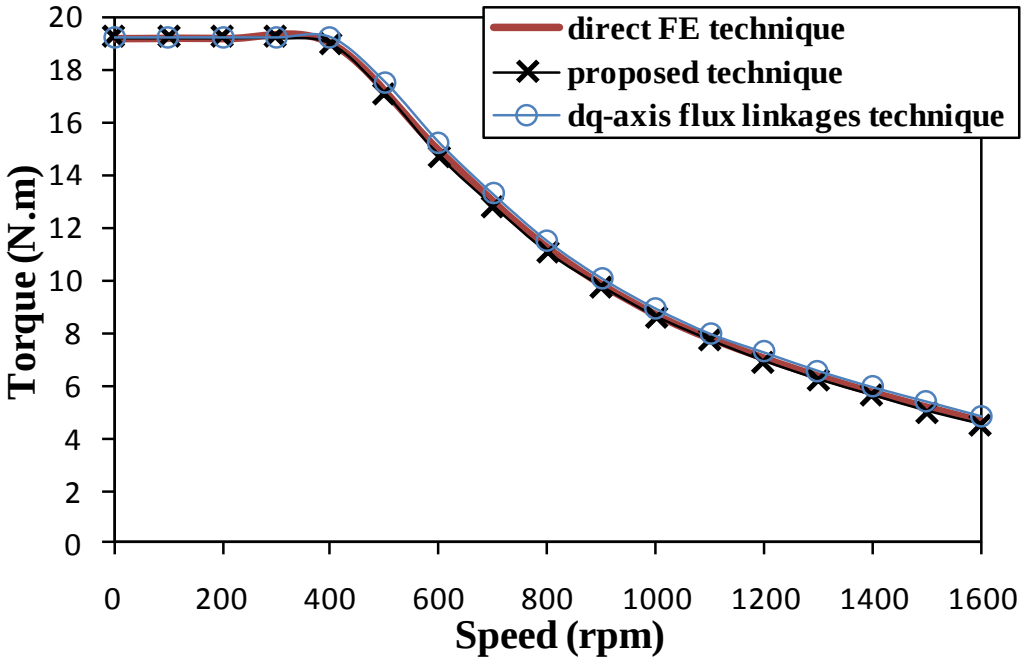

(a) Torque-speed characterstics, un-skewed rotor

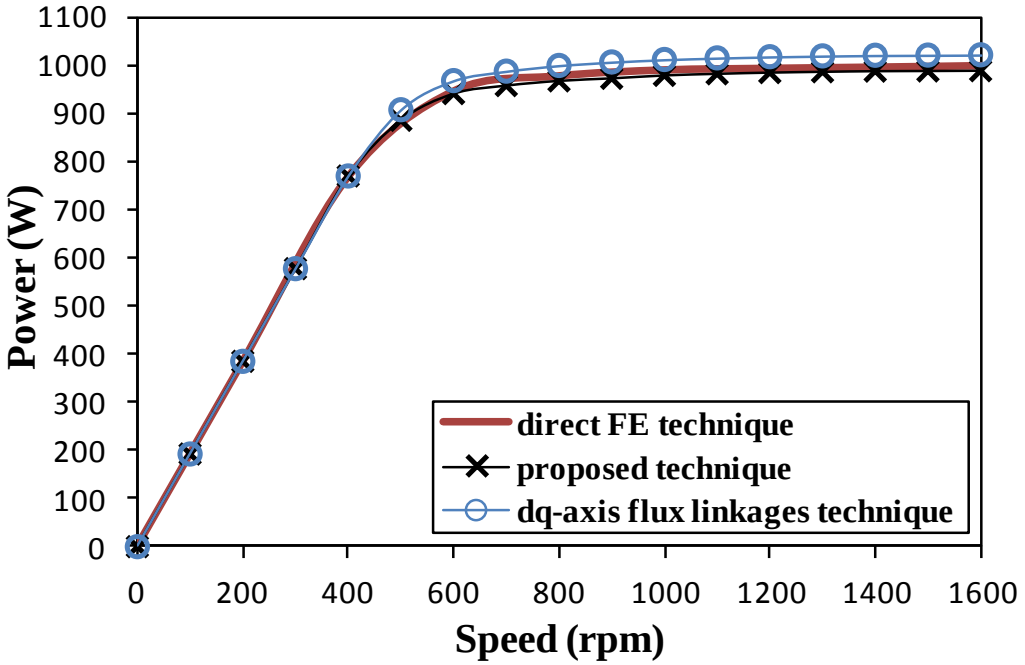

(b) Power-speed characterstics, un-skewed rotor

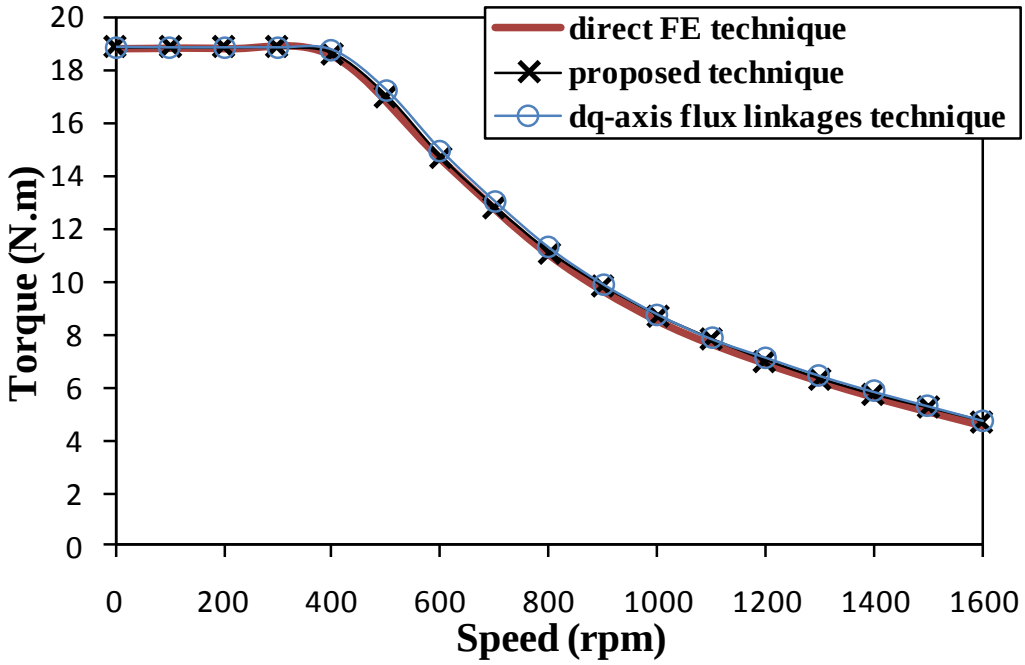

(c) Torque-speed characterstics, step skewed rotor

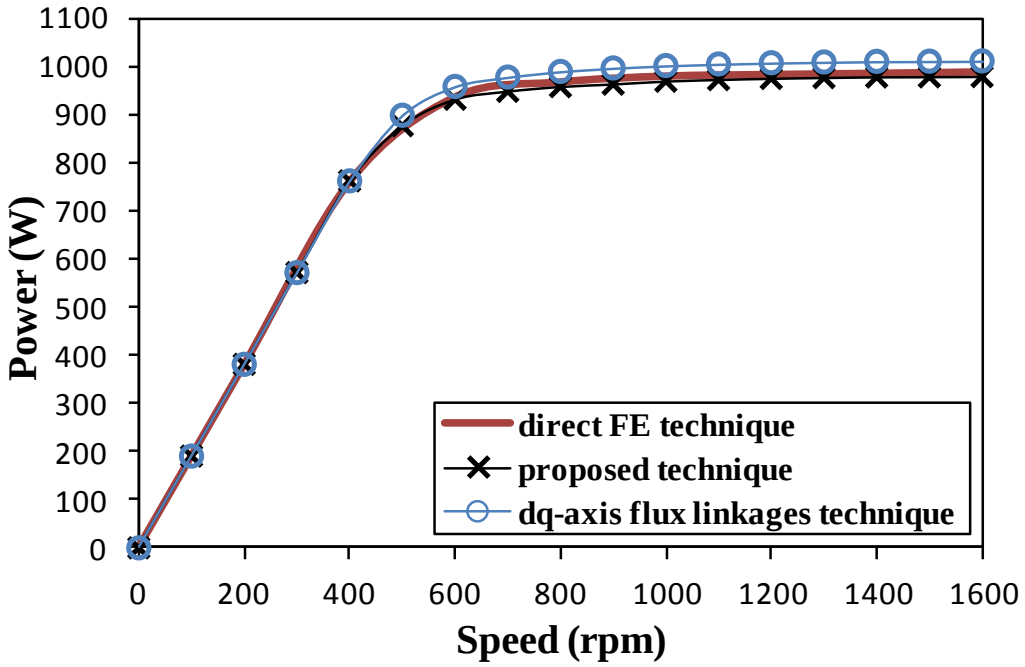

(d) Power-speed characterstics, step skewed rotor

Fig. 2.20 Comparison of torque- and power-speed characterstics of 10-pole/12-slot prototype machine having unskewed and step skewed rotor predicted by three different techniques.

2.5. Experimental Validation

For the purpose of validating the FE analyses and obtained conclusions, the analysed 10-pole/12-slots prototype machine with step skew rotor is built and tested, the test rigs are shown in Fig. 2.21 and the measuring procedures have been utilised and clearly explained in [130]. An excellent matching is shown between the measured and calculated back-emf waveforms and variations of the torque against the peak phase current and current angle, as illustrated in Fig. 2.22, Fig. 2.23 and Fig. 2.24, respectively. This proves the correctness of the utilised method to account for the skewing using the 2D FE tool.

Fig. 2.25 compares the measured torque-speed characteristics of the constructed prototype machine with their predicted counterparts, which are calculated according to the partial cross-coupling technique. The good agreement between the measured and predicted characteristics strongly confirms the accuracy of the simplified technique.

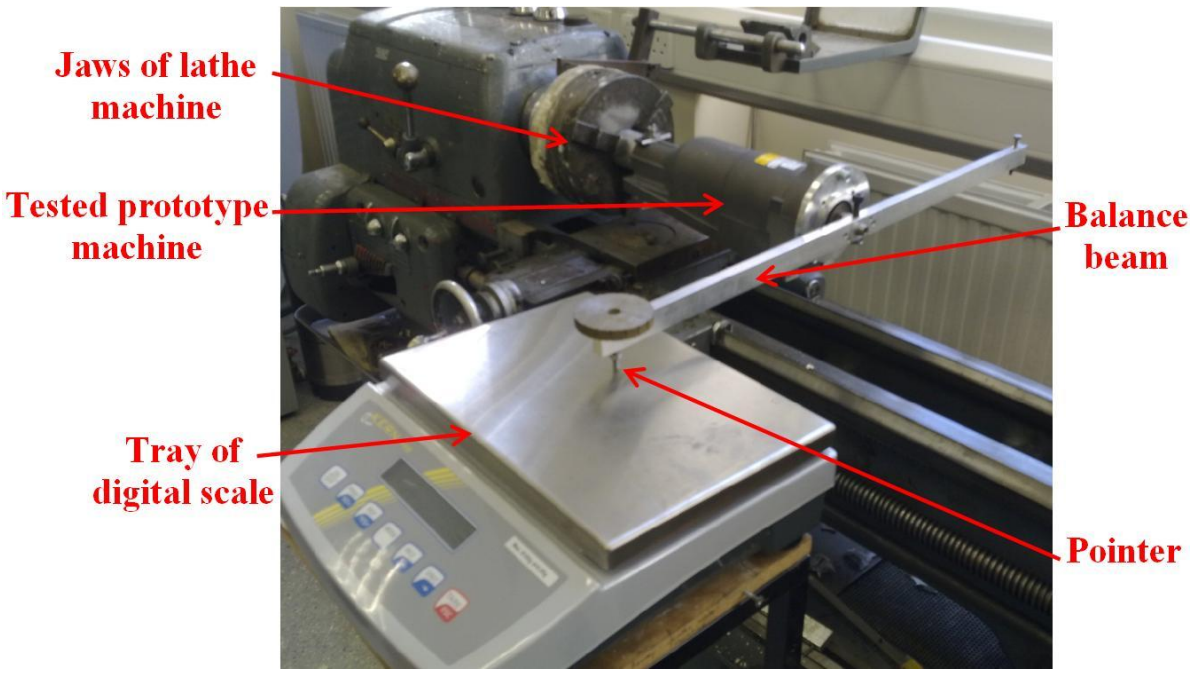

(a) Torque-current magnitude and torque-current angle characteristics

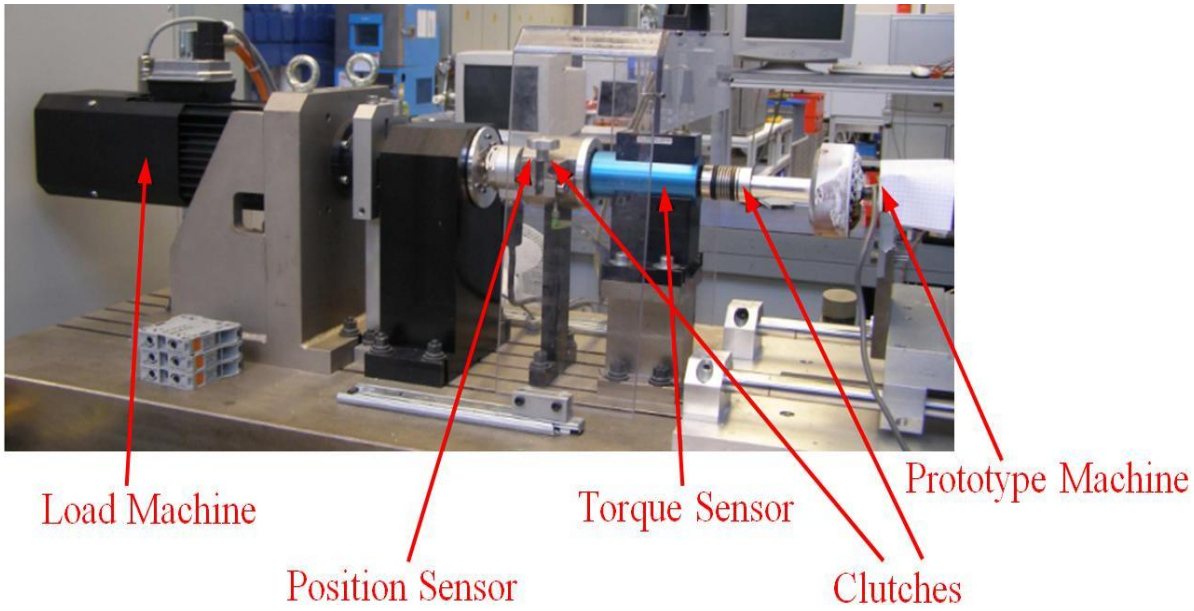

(b) Torque-speed characteristics

Fig. 2.21 Test rig measuring of torque-current magnitude, torque-current angle and torque-speed characteristics.

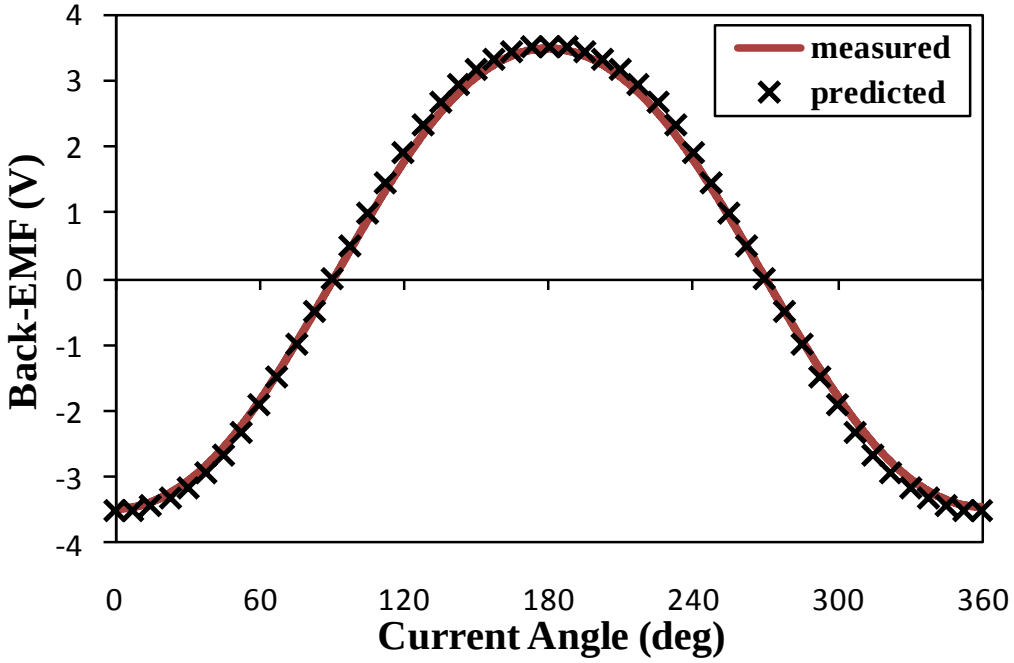

Fig. 2.22 Comparsion of measured and predicted back-emf waveform of 10-pole/12-slot prototype machine, at 400 rpm.

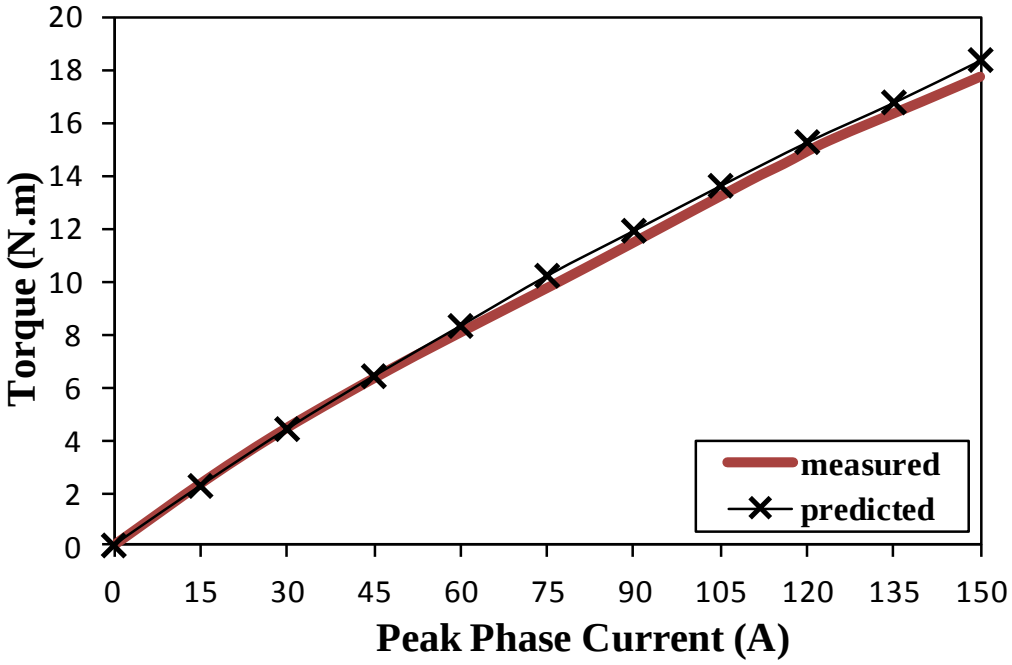

Fig. 2.23 Comparison of measured and predicted average torque against phase current of 10-pole/12-slot prototype machine, at 0 degree current angle.

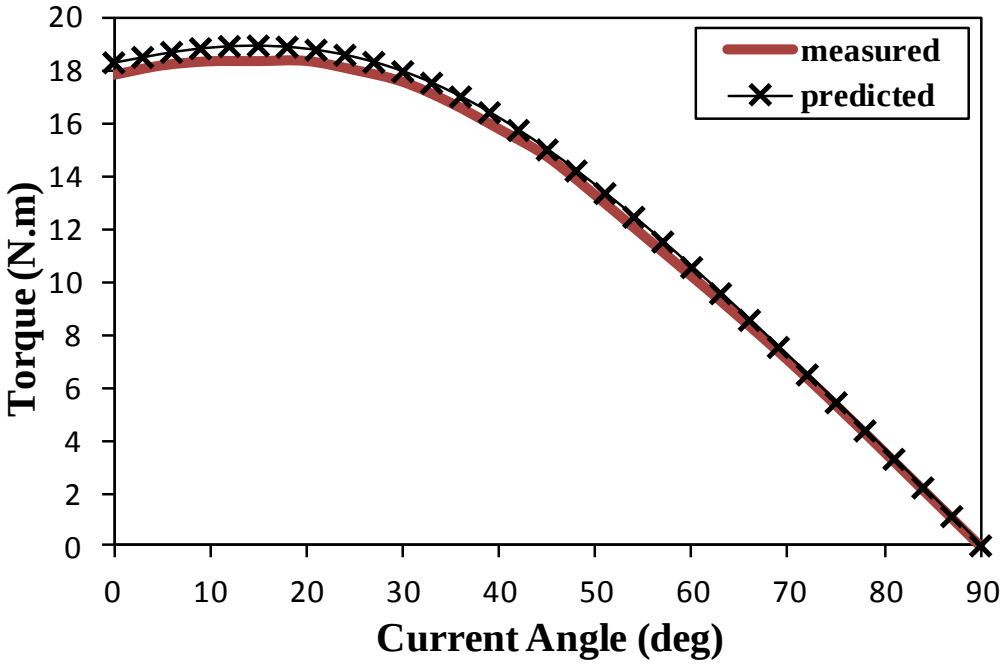

Fig. 2.24 Comparison of measured and predicted torque against current angle of 10-pole/12-slot prototype machine, at 150A_{peak}.

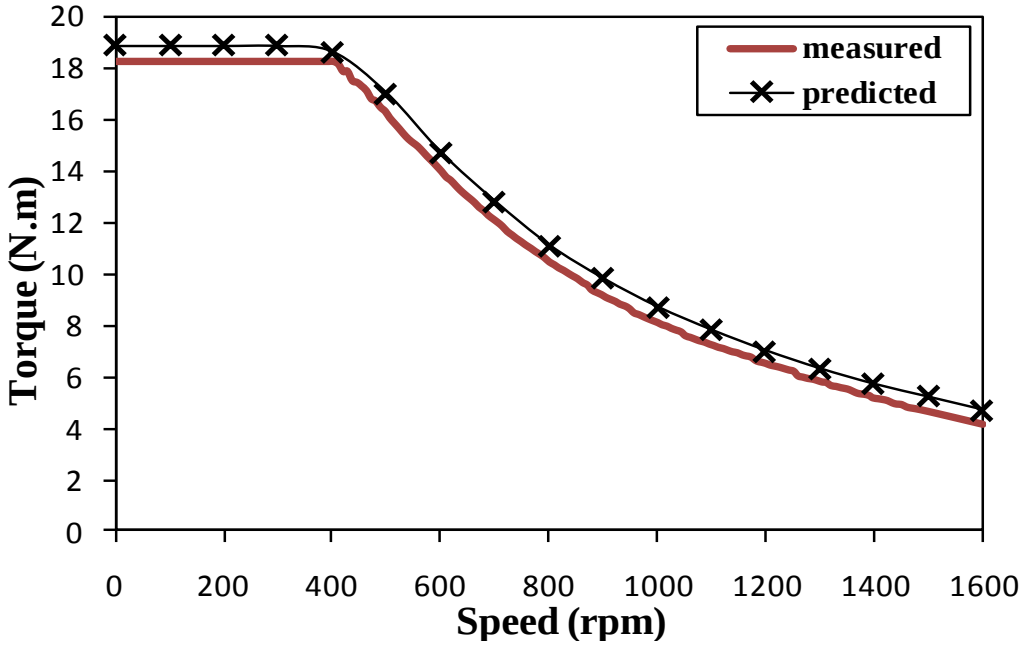

Fig. 2.25 Comparison of measured and predicted torque-speed characterstics of 10-pole/12-slot prototype machine.

2.6. Conclusions

The frozen permeability method has been used to analyse the influence of magnetic saturation due to the PMs and d- and q-axis currents on the machine main parameters, such as the PM flux linkage and dq-axis inductances, of fractional-slot PM machines having concentrated windings. The analyses show that the q-axis PM flux linkage, the influence of d-axis current on the d-axis PM flux linkage, and the cross-coupling effect on the dq-axis inductances can be neglected in the calculation of the torque-speed characteristics of such machines. The partial cross-coupling model is compared with the direct FE and dq-axis flux linkage methods. A good agreement has been achieved. The analysis has also been verified by the experimental results. Comparing with the full cross-coupling technique, the partial cross-coupling model is much faster and less complicated, while it also exhibits high accuracy for this kind of machines.

Chapter 3: Influence of Additional Air Gaps between Stator Segments on Cogging Torque of Permanent Magnet Machines Having Modular Stators

3.1. Introduction

Highly efficient electrical machines are desirable in many industrial and commercial applications. Permanent magnet (PM) machines are the most suitable candidates, since they inherently exhibit high efficiency as well as high power density [131]. They have been intensively investigated to further improve their performance and overcome their disadvantages. For example, many effective techniques, i.e. rotor and magnet shaping and skewing, have been investigated and proposed to minimise the cogging torque, which is one of the main sources of torque ripple in the PM machines [35, 37, 38, 40, 41, 132, 133]. On the other hand, from the cost point of view, it is required to simplify the manufacturing process, especially in mass production. The modular stator, e.g. individual stator tooth/back-iron segments, Fig. 3.1(a), or separated stator tooth and back-iron segments, Fig. 3.1(b), is a key solution to easing the manufacturing process, particularly stator winding process. However, due to the manufacture limitations and tolerances, additional air gaps exist between the stator teeth and yoke, Fig. 3.1. Moreover, such gaps could be non-uniform.

In general, the influence of the manufacturing tolerances, errors and defects on the electromagnetic performance can be negligible, but it is more significant on the cogging torque [42, 43]. For example, the stator asymmetry, which results from the manufacturing tolerances, can cause a significant increase in the cogging torque magnitude and generate low order cogging torque components [43]. Also, the assembly tolerance as well as the PM imperfections can cause additional cogging torque components [44-46, 134, 135]. Furthermore, in practice, the effectiveness of cogging torque reduction techniques could be limited or diminished by the manufacturing defects [47]. A combined analytical and numerical technique to account for the manufacturing tolerance during the machine design process has been proposed in [48]. However, the influence of the described additional stator gaps in the machine that has a modular stator, Fig. 3.1, has never been examined. Therefore, a detailed theoretical and experimental study is carried out in this chapter to investigate the influence of such gaps and their non-uniformity on the cogging torque and effectiveness of

the rotor step skew in a PM machine, which has a modular stator with separated stator teeth and back-iron segments, together with the back-emf waveform and output torque.

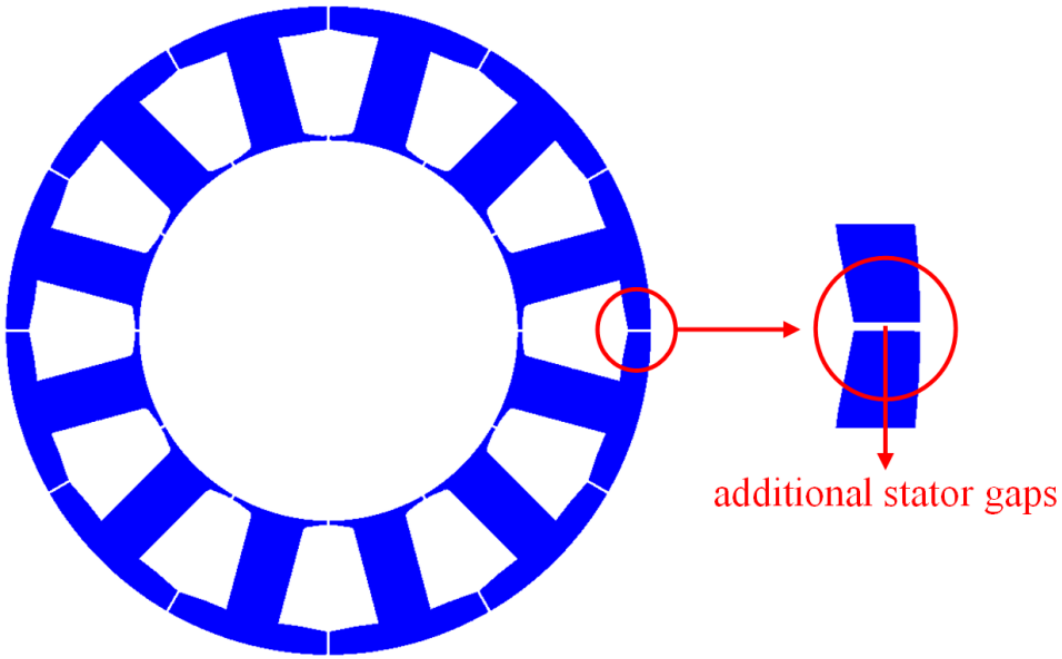

(a) Individual stator tooth/back-iron

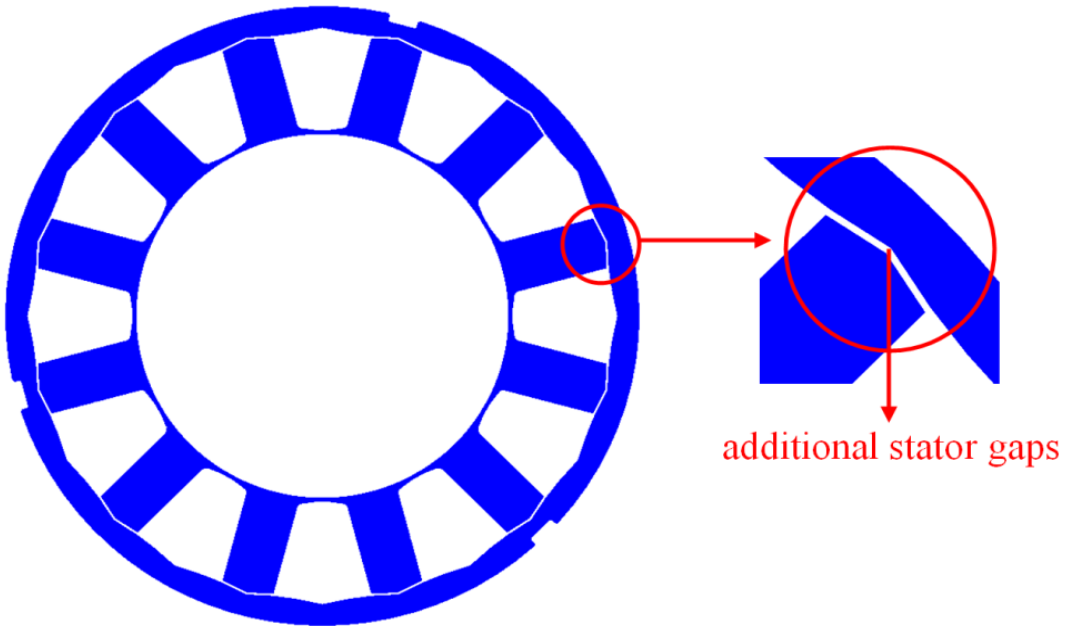

(b) Separated stator tooth and back-iron (prototype machine)

Fig. 3.1 Alternate modular stator lamination structures.

3.2. Prototype Machine

The analysed prototype machine, which is shown in Fig. 3.2 and Table 3.1, is similar to the fractional-slot 10-pole/12-slot IPM machine that has been investigated in chapter 2. However, in order to ease the winding process, since this machine will be produced in mass, the machine, which is analysed in this chapter, is designed with a modular stator. For mechanical purposes and also to further decrease the cogging torque, the closed slot design is employed, as shown in Fig. 3.1(b), although such design results in a small reduction in the electromagnetic performance of the machine, as will be shown in next chapters.

As mentioned in chapter 2, this prototype machine will be operated in a smooth electric power steering system. Therefore, in order to satisfy the output torque requirements for such application, the step-skewed rotor with shaped pole face are maintained. As mentioned before due to the manufacturing limits, there are additional stator gaps between stator teeth and yoke. During the manufacturing, a considerable effort was made to significantly reduce the length of such gaps to practically possible minimal value. Furthermore, an inter-locking technique is employed axially between the laminations in the stator teeth and yoke to improve the mechanical strength and integrity of stator laminations, thus to minimize the possibility of mechanical deformation and tolerance. Theoretically, the cogging torque of this machine should be well suppressed by using the mentioned techniques. However, an unexpected large cogging torque still exists in the prototype machine, which is one of the mass produced machines. In fact, this has motivated the investigations of this chapter.

Many manufacturing defects and errors could be behind such unexpected measured cogging torque, [42-47, 134, 135], for example it can be due to:

a). Stator and/or rotor asymmetry;

b). Mechanical deformation during manufacturing or assembly;

c). PM imperfection, e.g. placement, magnetisation and/or strength.

In addition, the large cogging torque could be also due to the presence of the additional stator gaps or their non-uniformity, which has a large probability to occur due to the manufacturing tolerances. Therefore, the influence of such possible defect on the cogging torque of the prototype machine is investigated. Consequently, the reason for the unexpected measured cogging torque is clearly explained. In addition, the back-emf waveform and output torque of the machine will be also examined. For this propose, the finite element (FE)

analyses are utilised and validated by the experimental measurements. It is worth mentioning that the addition stator gaps of the prototype machine are approximately 0.05 mm. However, different lengths will be investigated in this chapter.

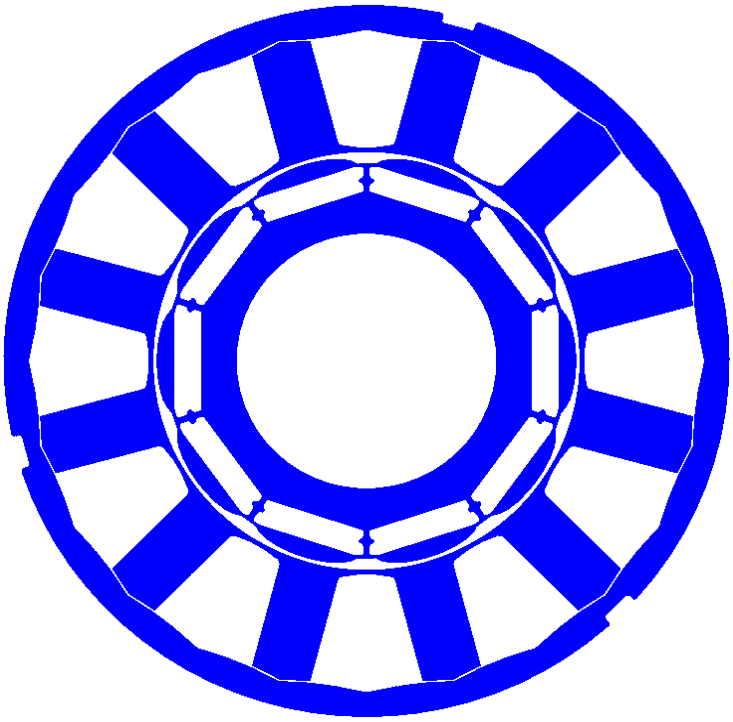

(a) Lamination cross-section

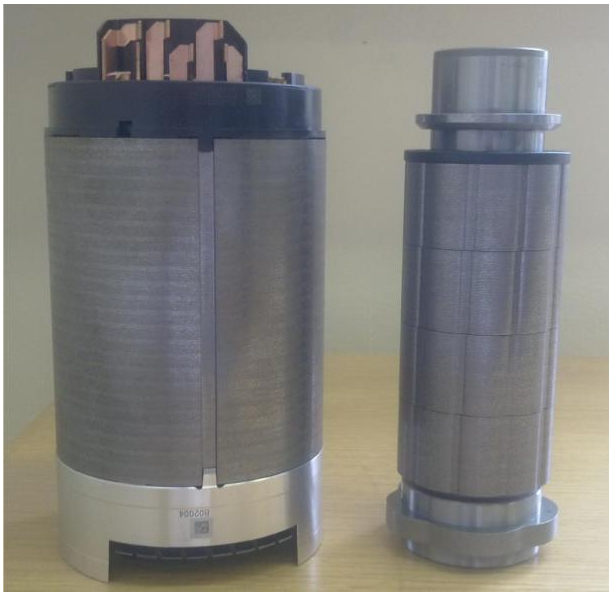

(b) Stator and rotor

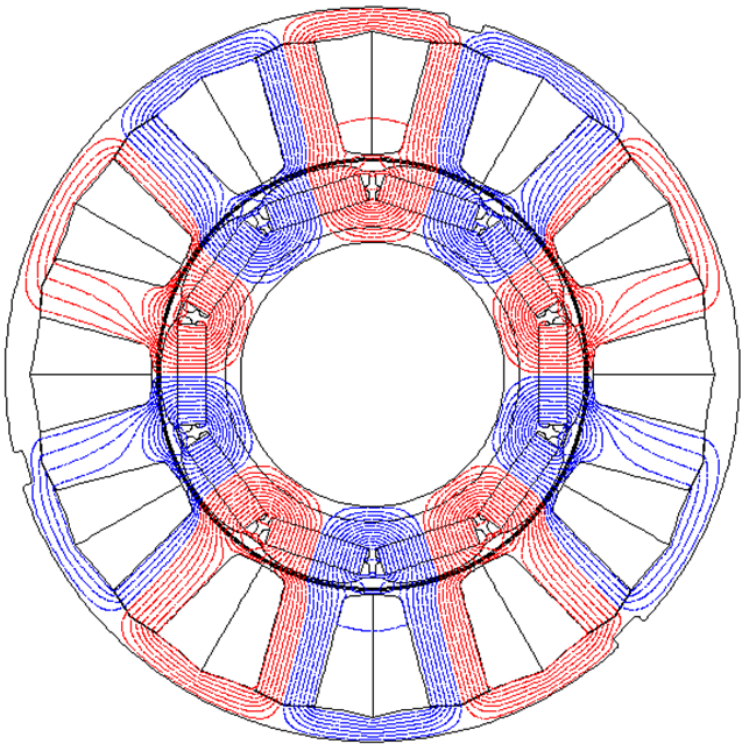

(c) Open-circuit equal potential distributions

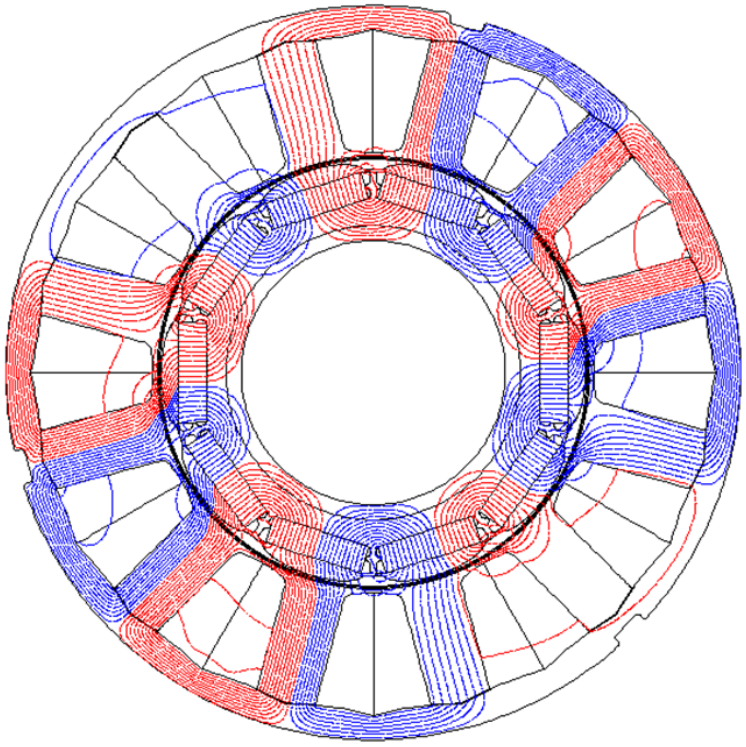

(d) Load equal potential distributions, at $150A_{peak}$ phase current

Fig. 3.2 Lamination cross-section, stator and rotor and equal potential distributions of prototype machine.

3.3. Influence of Closed Slot and Rotor Step Skew

In order to highlight the influence of the closed slot and rotor step skew on the electromagnetic performance, particularly the cogging torque, of the analysed machine. The predicted cogging torque, back-emf and output torque waveforms of the machines having un-skewed rotor/open slot stator, un-skewed rotor/closed-slot stator and step-skewed rotor/closed-slot stator are compared in Fig. 3.3. It should be mentioned that the influence of the additional stator gaps has not been accounted for yet in these calculations, i.e. such gaps are assumed to be zero. Fig. 3.3(a) shows that the machine without skew and with open slot has a relatively small cogging torque, since it has shaped rotor and a relatively large least common multiple between the pole and slot numbers [35]. However, the cogging torque can be further reduced by 66% by designing the stator with closed-slot. Theoretically, step skewing the rotor by 4 steps of 1.5 mechanical degrees for every step can totally eliminate the cogging torque. However, it will be shown later that the additional gaps between stator teeth and yoke segments can cause a significant difference. On the other hand, the closed slot design reduces the electromagnetic performance of the machine, i.e. it is about 4% down in the output torque, as shown in Fig. 3.3(c). This is due to the air gap flux density reduction, which in its turn is due to the extra flux leakage through the slot opening iron bridges. This effect is further discussed and illustrated in the next section. Furthermore, as mentioned before, the influence of the rotor step skew on such performance is negligibly small.

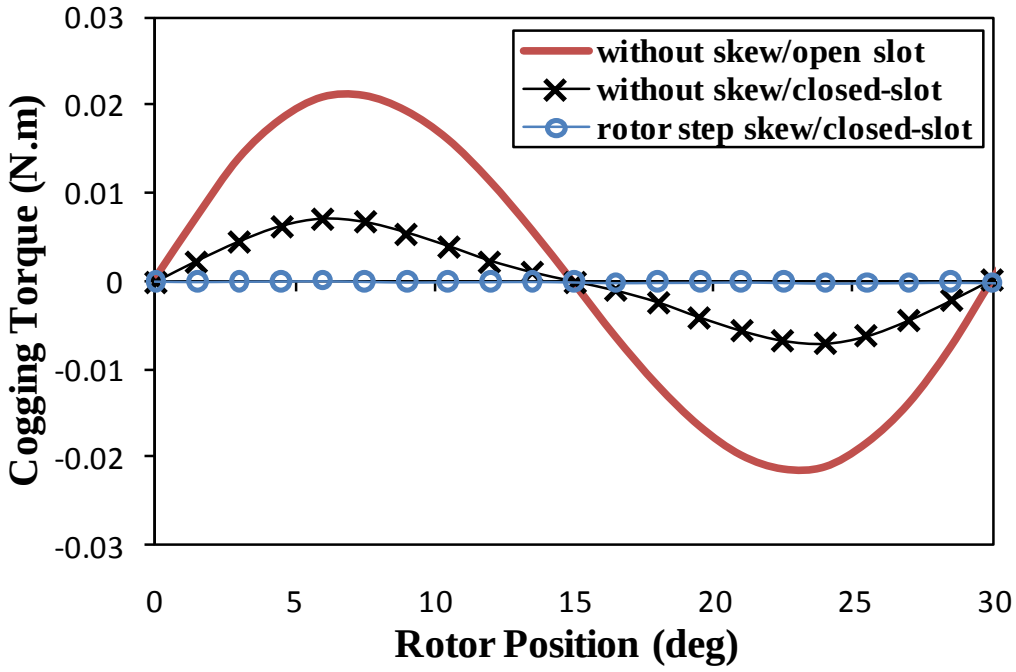

(a) Cogging torque waveform

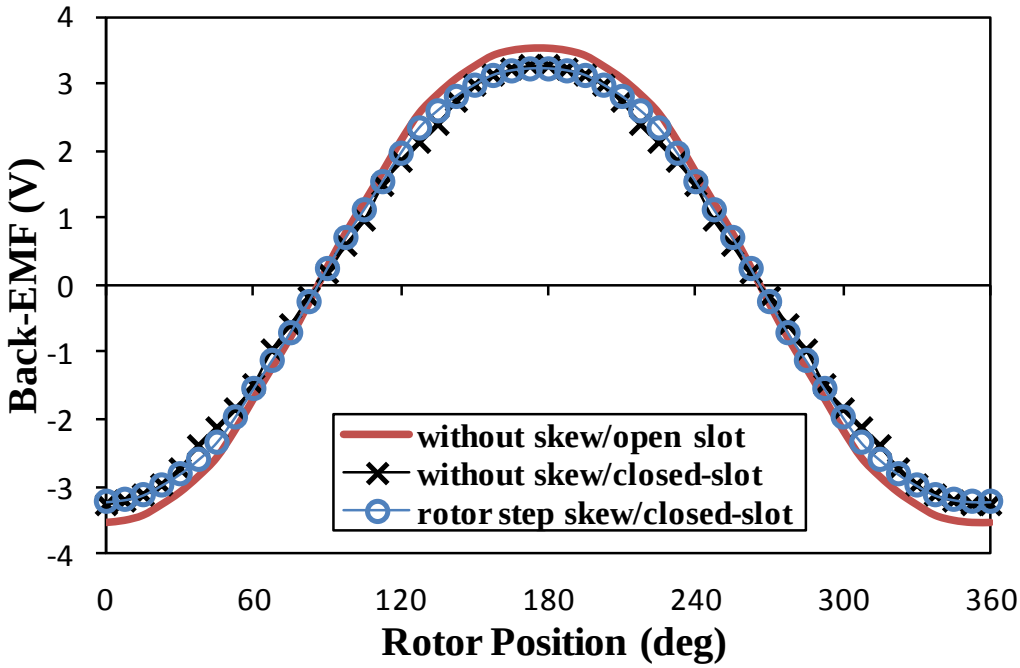

(b) Back-emf waveform, at 400 rpm

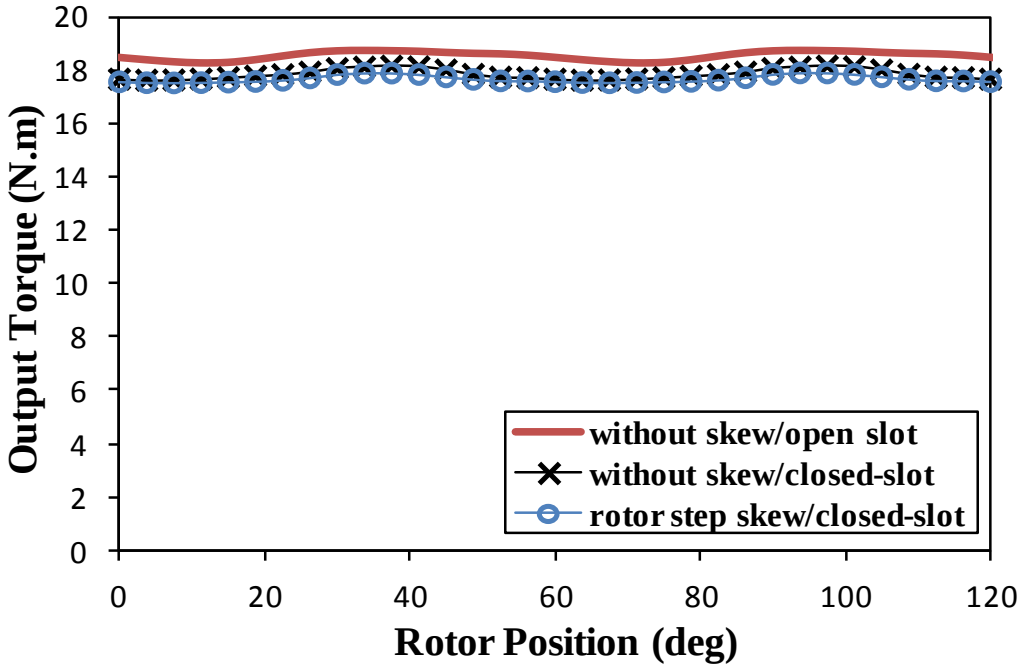

(c) Output torque waveform, at I_q=150A, I_d=0A

Fig. 3.3 Comparison of cogging torque, back-emf and output torque waveforms of analysed machines with un-skewed rotor/open slot stator, un-skewed rotor/closed-slot stator and step-skewed rotor/closed-slot stator.

Table 3.1 Major Parameters of Prototype Machine

Parameter	***Dimension***	***Parameter***	***Dimension***
Stator outer diameter	90 mm	Stator inner diameter	53 mm
Rotor maximum diameter	52 mm	Rotor minimum diameter	50 mm
Minimum air gap length	0.5 mm	Maximum air gap length	1.5 mm
Stator yoke width	3 mm	Tooth width	7.4 mm
Magnet thickness	3.4 mm	Magnet length	12.2 mm
Magnet remanence	1.2 T	Magnet relative permeability	1.05
Shaft diameter	36 mm	Rotor step skew angle	4×1.5 mech.deg

3.4. Influence of Uniform Additional Stator Gaps

The cogging torque of the un-skewed machine has been predicted for different additional uniform stator gap lengths and compared in Fig. 3.4. For relatively small additional stator gaps, i.e. 0.05 mm, the cogging torque slightly decreases due to increased effective air gap and thus reduced air gap flux density. However, when the additional stator gaps are larger, more flux leakage will go through the tooth tips and slot opening iron bridges. Such bridges gradually become saturated. Therefore, the cogging torque becomes larger for relatively large gaps, i.e. 0.1 mm or larger.

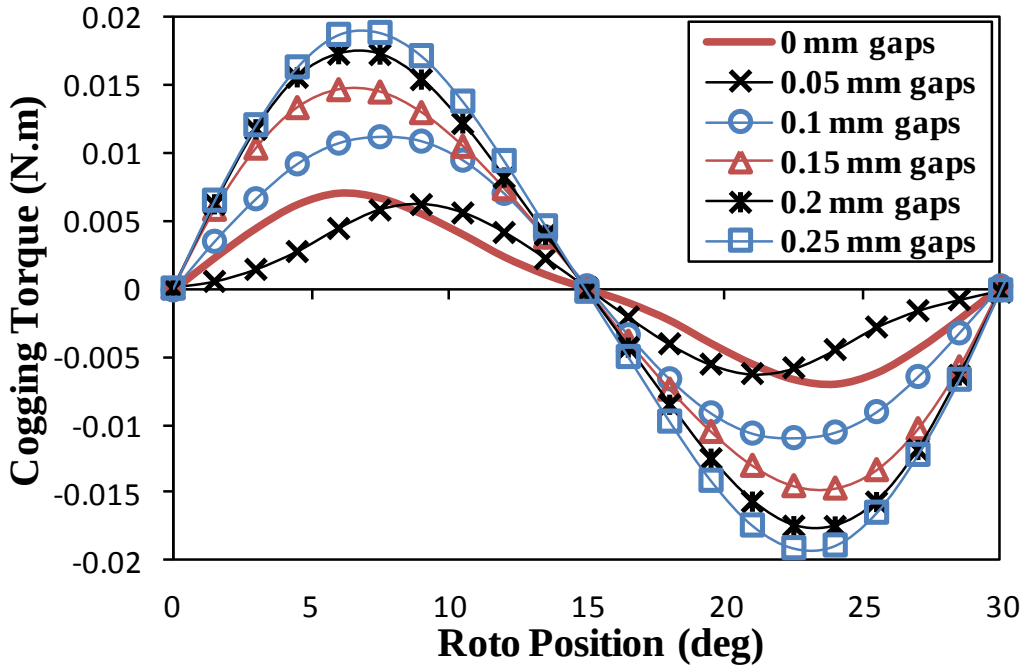

Fig. 3.4 Variation of predicted cogging torque waveforms of analysed machines having different uniform additional stator gaps.

In order to clearly illustrate this phenomenon, both the normal and tangential open-circuit air gap flux density waveforms and their harmonics when machines are ideal (no additional stator gaps) or having 0.1mm uniform additional stator gaps are shown in Figs. 3.5-8. The presence of the additional stator gaps leads to a slight reduction in the normal air gap flux density, Fig. 3.5 and Fig. 3.6, since the total effective air gap length including both real air gap and additional stator air gap is increased. On the other hand, the tangential air gap flux density is larger in the machine with additional stator gaps, Fig. 3.7 and Fig. 3.8. This is because the presence of the additional stator gaps increases the magnetic reluctance through stator teeth and yokes, which causes extra flux leakage across the slot opening, in turn this increases the cogging torque. As a percentage, the relative reduction of the normal flux density due to the additional stator gap is smaller than the relative increase of the tangential flux density due to the same reason. In other words, the product of the normal and tangential harmonics having the same order is larger when additional stator gaps exist, as illustrated in Fig. 3.9. This explains the reason behind the larger cogging torque in the machine with additional stator gaps, since the cogging torque is strongly related to the product of the normal and tangential air gap flux density components [136]. For the same reason, the larger the stator gaps the larger the cogging torque, as shown in Fig. 3.4.

It should be mentioned that the rotor step skewing can still effectively eliminate the cogging torque, no matter whatever the length of the additional stator gaps, as confirmed in Fig. 3.10, which compares the predicted cogging torque waveforms of machines having 0.1 mm additional stator gaps and un-skewed and step skewed rotors, because the uniform additional stator gaps have no effect on the period of cogging torque. However, on the other hand, the additional stator gaps cause reduction in the back-emf, thus in the output torque, as shown in Fig. 3.11. This is due to lower normal air gap flux density, Fig. 3.5, which in turn is due to the relatively larger effective air gap. However, as shown in Fig. 3.11(b), the influence on the output torque is reasonably small when such gaps are relatively small, e.g. the same as the prototype machine, 0.05 mm.

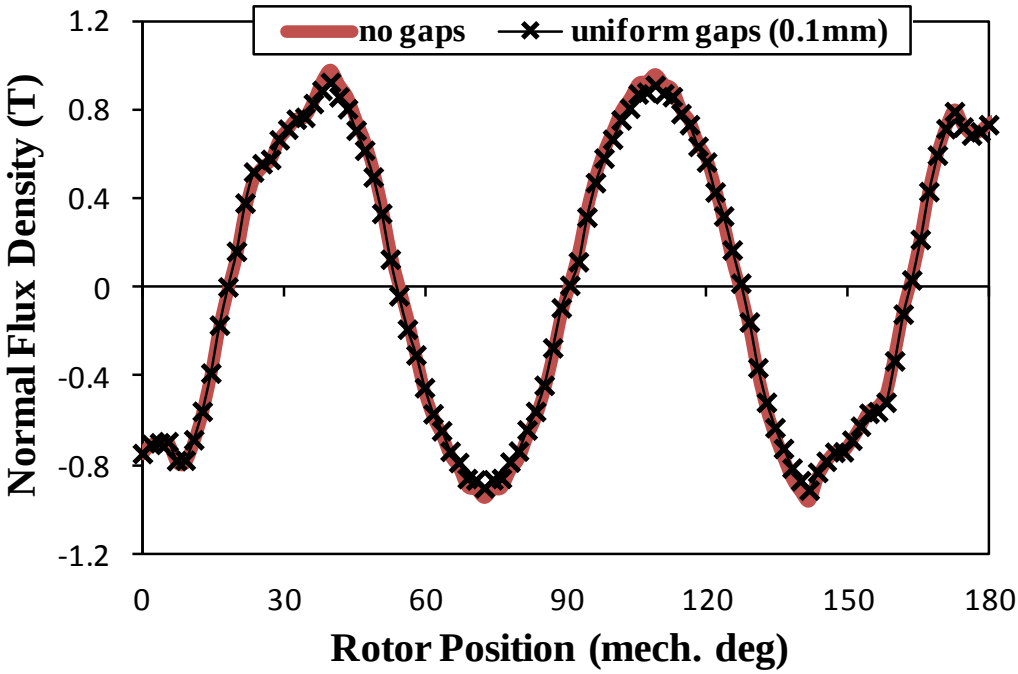

Fig. 3.5 Radial open-circuit air gap flux density waveforms of machines, with and without 0.1mm additional stator gaps.

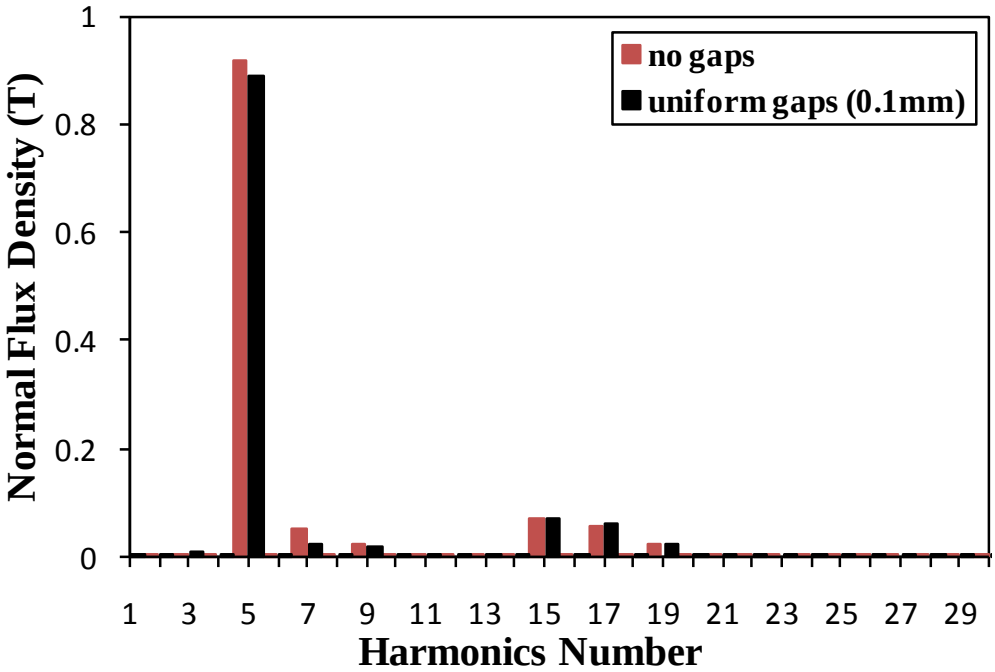

Fig. 3.6 Radial open-circuit air gap flux density harmonics of machines, with and without 0.1mm additional stator gaps.

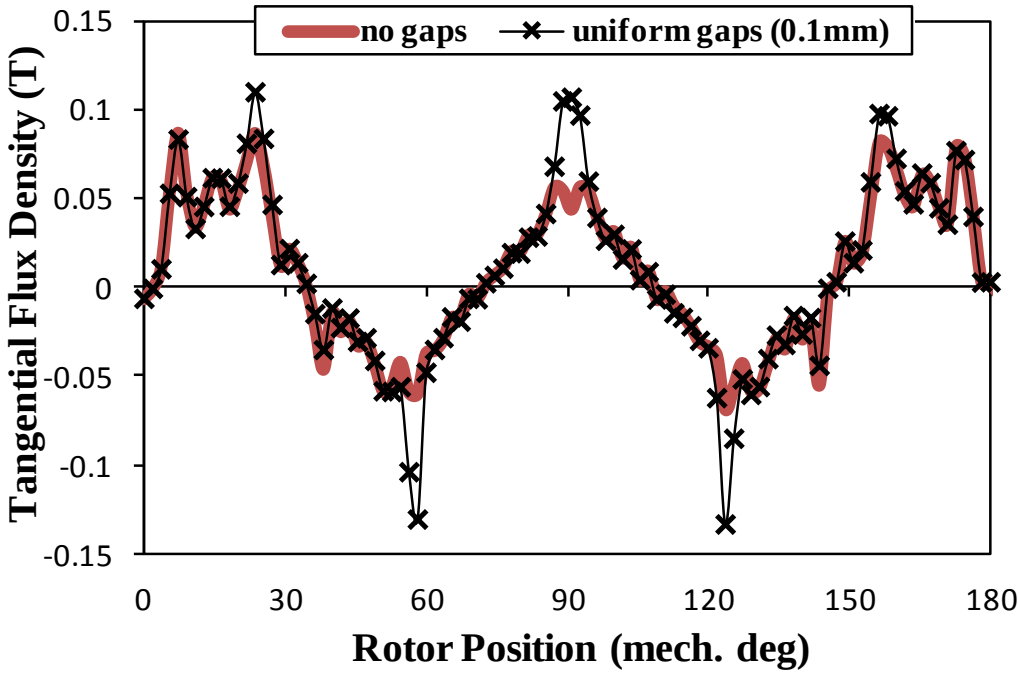

Fig. 3.7 Tangential open-circuit air gap flux density waveforms of machines, with and without 0.1mm additional stator gaps.

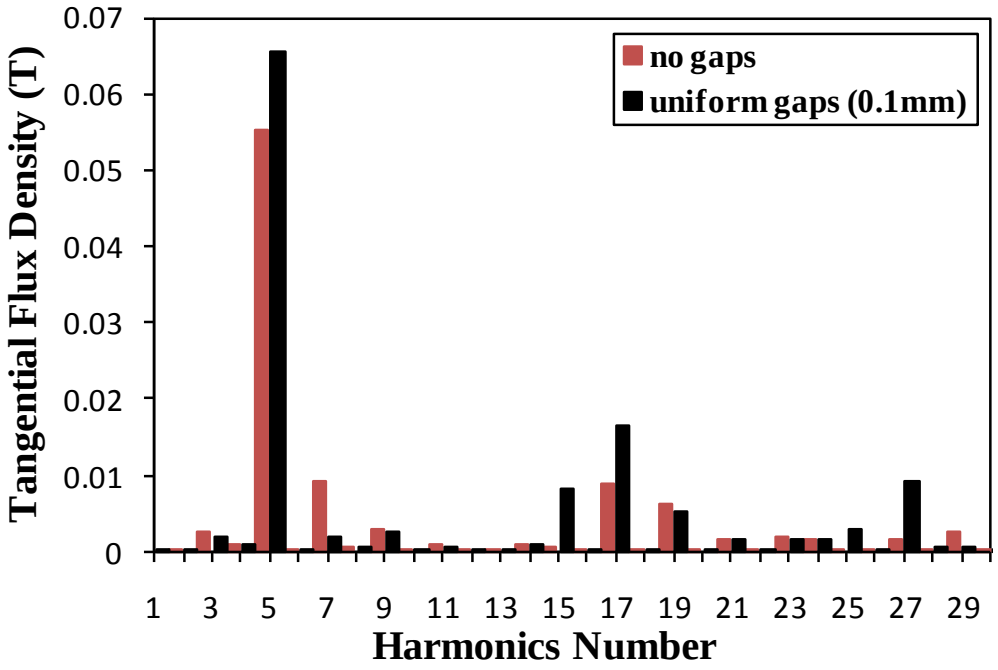

Fig. 3.8 Tangential open-circuit air gap flux density harmonics of machines, with and without 0.1mm additional stator gaps.

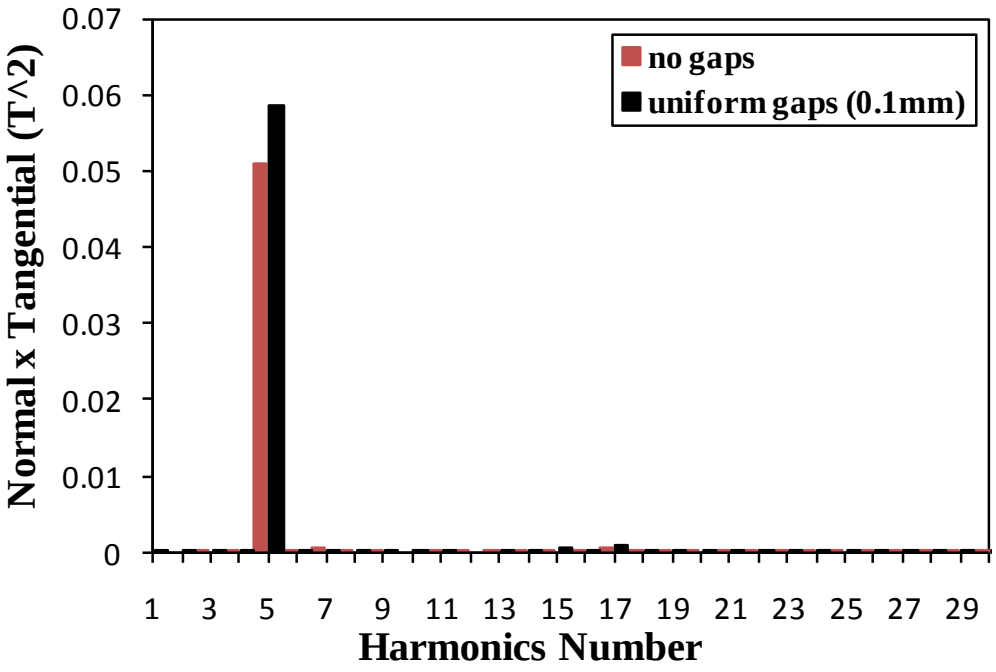

Fig. 3.9 Multiplication of radial and tangential harmonics of open-circuit air gap flux density of machines, with and without 0.1mm additional stator gaps.

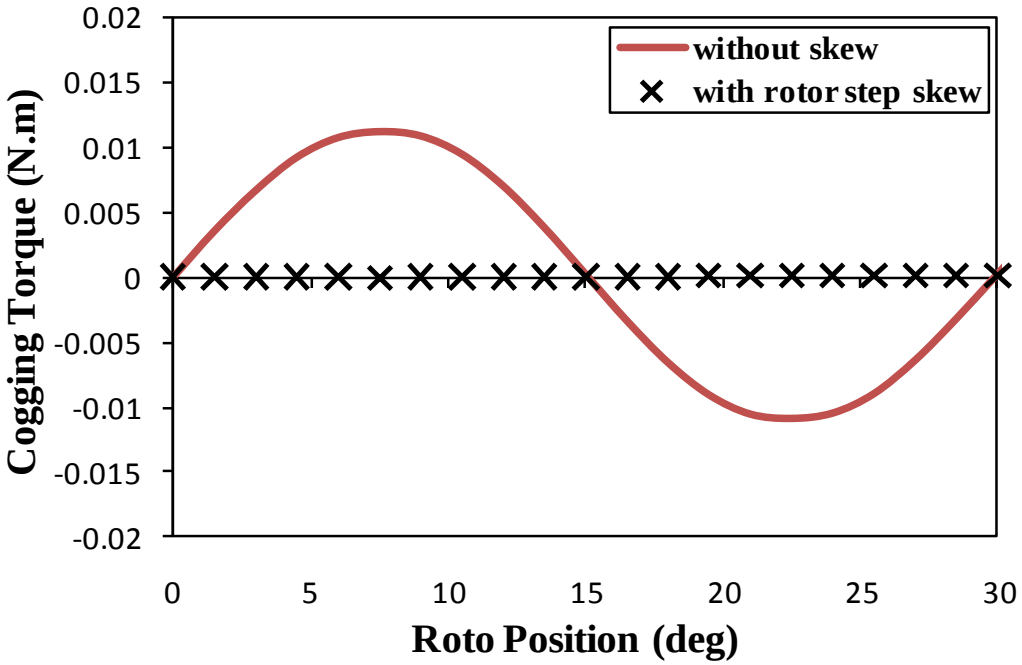

Fig. 3.10 Comparison of cogging torques of un-skewed and rotor-step skewed machines having uniform stator gaps of 0.1mm.

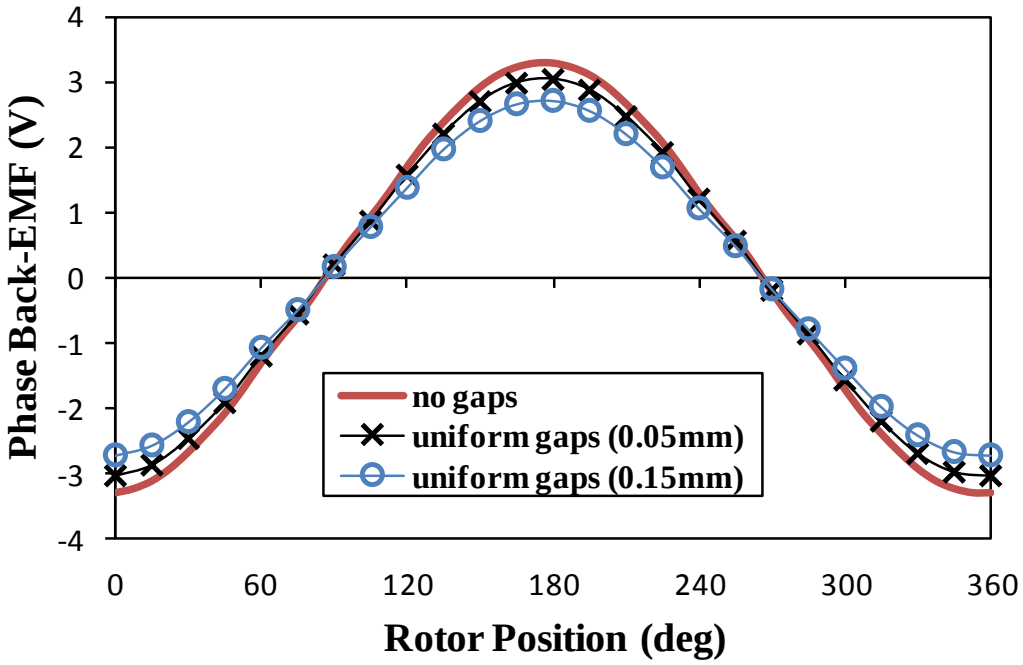

(a) Back-emf waveform, at 400 rpm

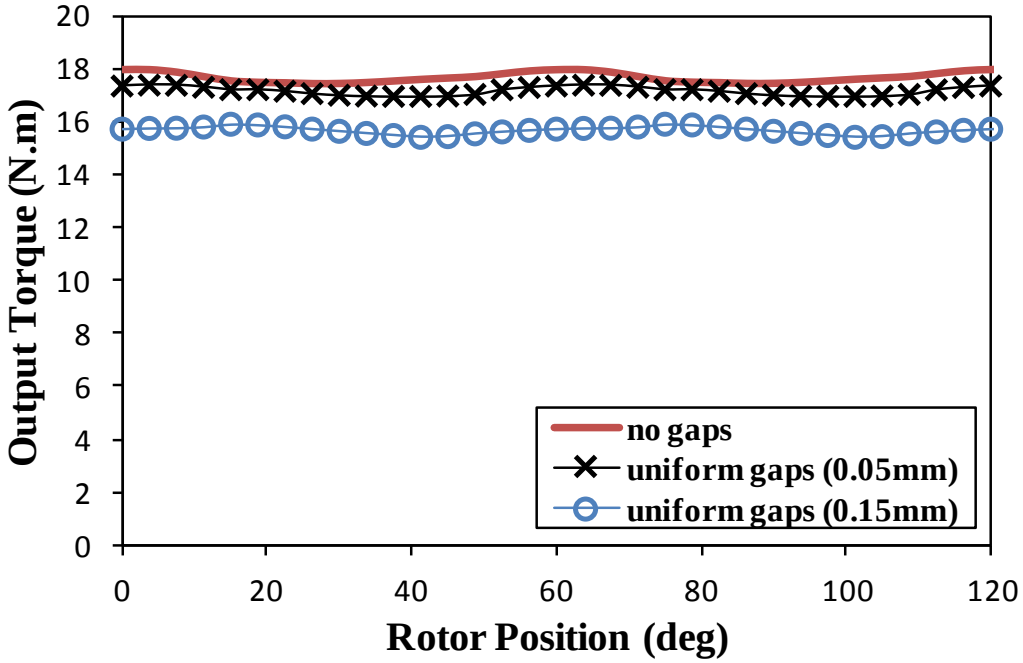

(b) Output torque waveform, at I_q=150A, I_d=0A

Fig. 3.11 Comparison of phase back-emf and output torque waveforms of machines, without, with 0.05mm and with 0.15mm additional stator gaps.

3.5. Influence of Non-uniform Additional Stator Gaps

In the foregoing analysis, the additional stator gaps are assumed to be all uniform. However, due to the manufacturing tolerances such gaps are most likely to be non-uniform in practice. The possible scenarios of non-uniformity are unlimited. One outstanding gap of different lengths, viz. 20%, 50%, 100% or 200% larger than other additional gaps of 0.05mm length, has been studied first.

Fig. 3.12 compares the cogging torque of un-skewed machines having uniform additional stator gaps of 0.05mm and non-uniform additional stator gaps, e.g. non-uniform gaps (0.06/0.05mm) means that one gap is 0.06mm and the rest are 0.05mm. Comparing with the ideal case (all gaps are 0.05mm), the cogging torque magnitude of non-uniform case is significantly larger. In addition, its periodicity is also increased. For large tolerances, the cogging torque increase becomes even more significant, as illustrated in Fig. 3.13.

The cogging torque period is equal to $360p/Q_{PS}$ electrical degree [35], where p and Q_{PS} are the pole pair number and the least common multiple between pole and slot numbers, respectively. For the 10 pole-12 slot combination, the least common multiple is 60, thus the cogging torque period is 30 electrical degrees. The presence of uniform stator gaps has no effect on the cogging torque periodicity as shown in Fig. 3.4, since the cogging toque is still produced by the interaction between 10 poles and 12 stator slots. However, when the stator has one outstanding stator gap, the stator lamination loses its original geometrical symmetry, i.e. the stator lamination geometrically repeats once over the whole circumference, which can be deemed as one slot. This slot interacts with the pole number and results in a least common multiple of 10 instead of 60. Thus, the cogging torque period changes from 30 to 180 electrical degrees. The increase of cogging torque magnitude due to the non-uniform additional gaps can be also explained from the change of the air gap flux density point of view. For this purpose, the normal and tangential components of open-circuit air gap flux density for both the uniform additional stator gaps (0.05mm) and non-uniform additional stator gaps (0.06mm/0.05mm) have been calculated and compared in Fig. 3.14. The normal open-circuit air gap flux densities for both cases are nearly the same. However, the tangential open-circuit air gap flux density of the machine with non-uniform additional stator gaps is much larger. Thus, the product of the normal and tangential air gap flux density harmonics of the machine with non-uniform additional stator gaps is larger, Fig. 3.15, in turn this leads to a larger cogging torque.

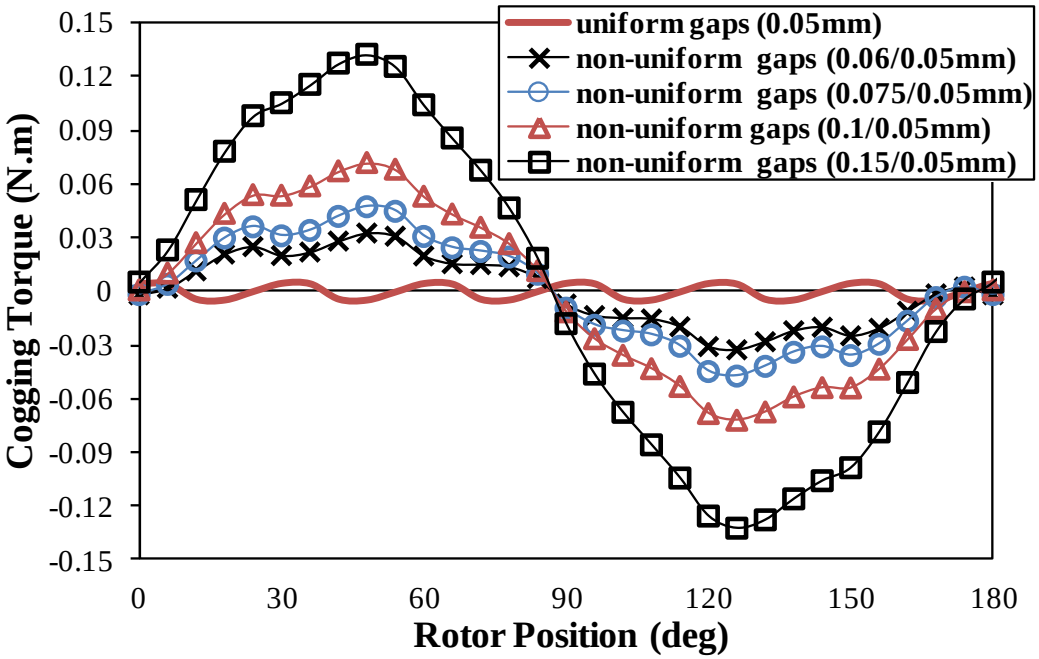

Fig. 3.12 Comparison of cogging torque waveforms of un-skewed machines having uniform and non-uniform additional stator gaps, one gap is larger/the rest are uniform.

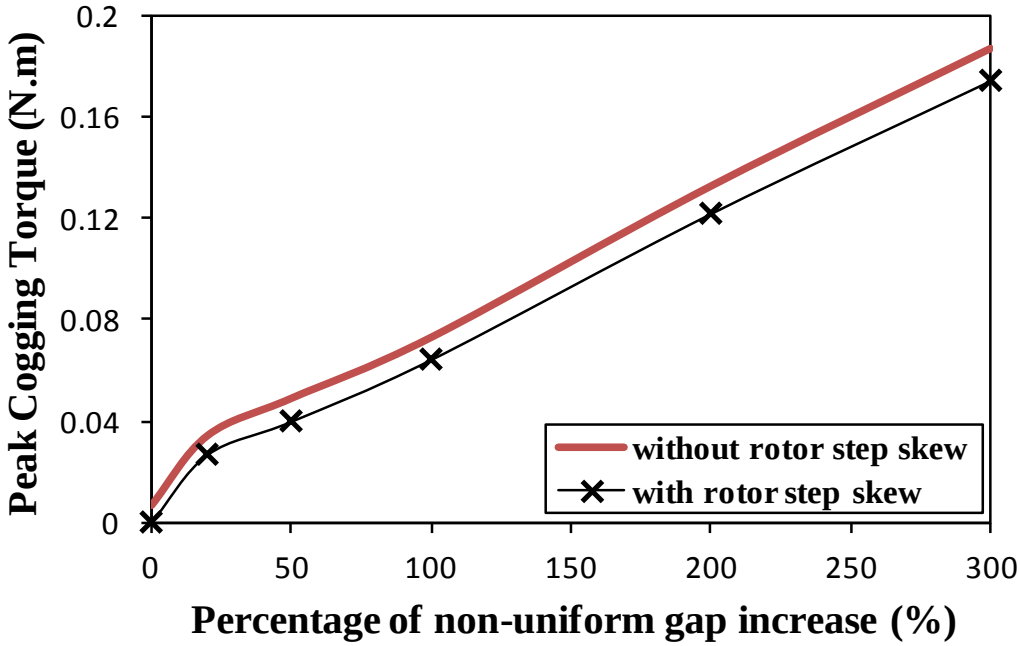

Fig. 3.13 Variation of peak cogging torque with the length of one outstanding additional stator gap.

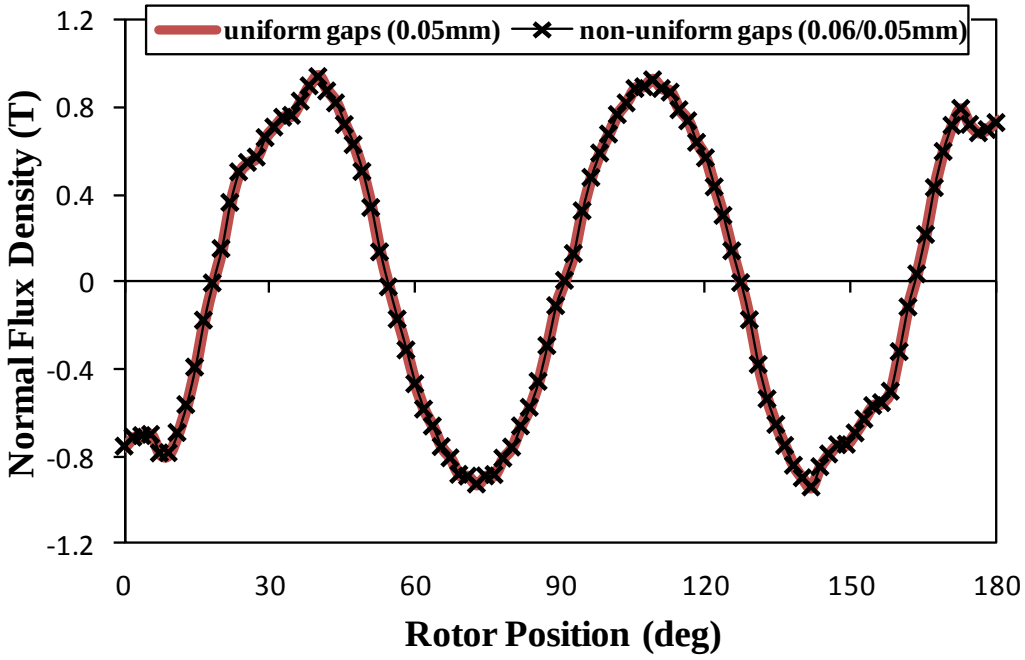

(a) Radial component waveform

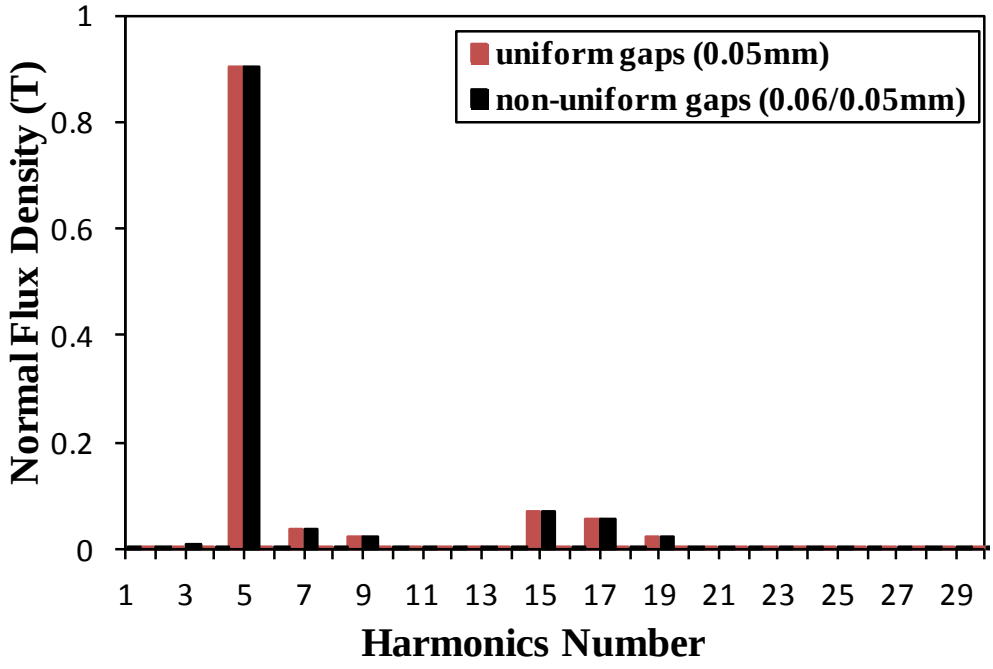

(b) Radial component harmonics

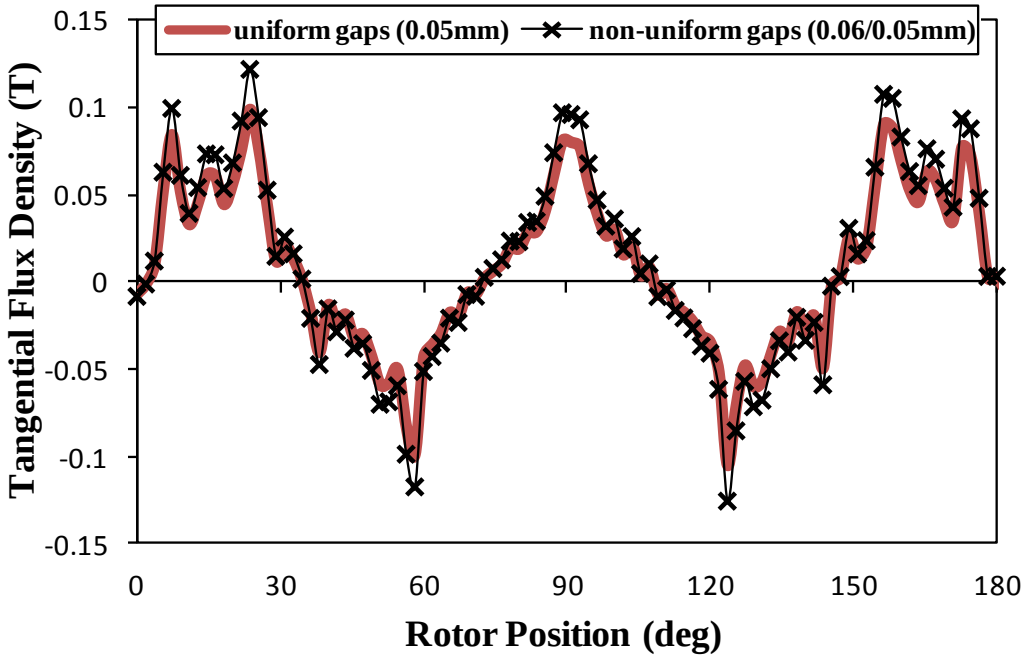

(c) Tangential component waveform

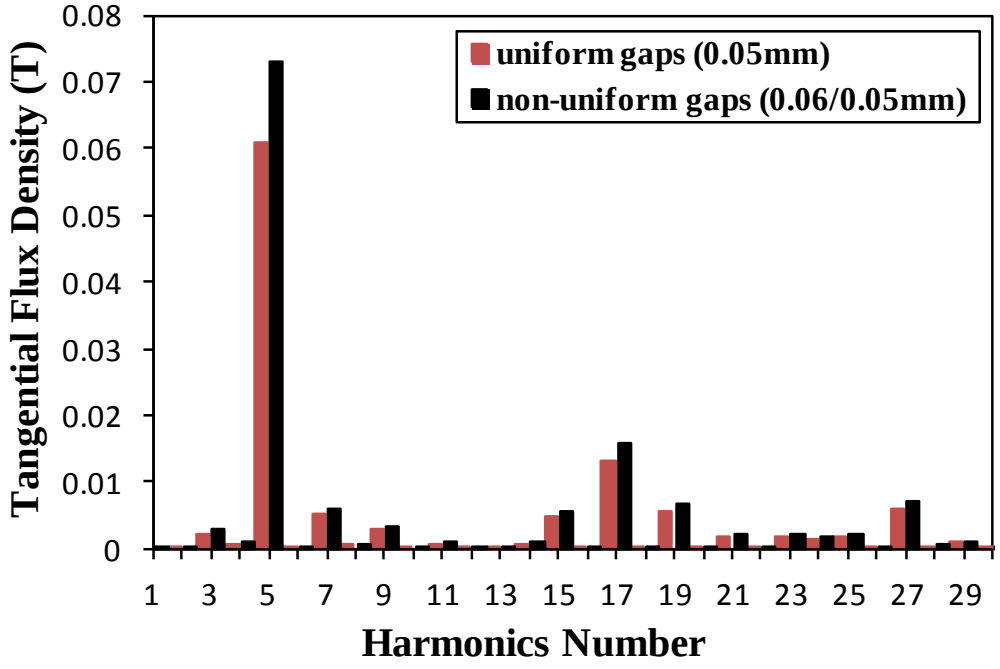

(d) Tangential component harmonics

Fig. 3.14 Comparison of open-circuit air gap flux density waveforms and harmonics of machines having uniform stator gaps of 0.05 mm and non-uniform stator gaps (one gap is 0.06mm/the rest are 0.05 mm).

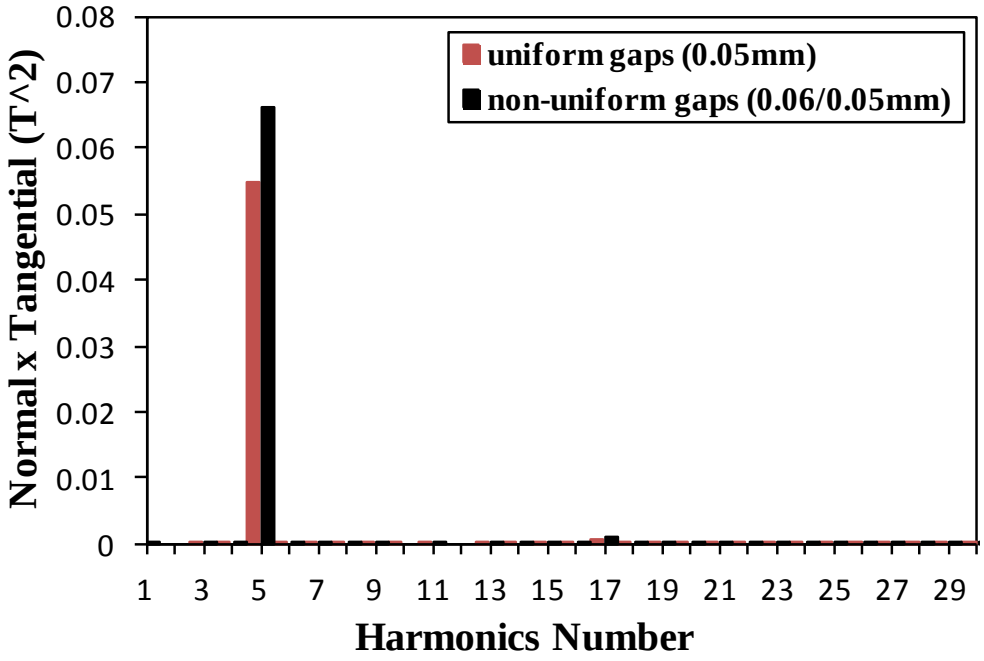

Fig. 3.15 Multiplication of radial and tangential harmonics of open-circuit air gap flux density of machines having uniform stator gaps of 0.05 mm and non-uniform stator gaps (one gap is 0.06mm/the rest are 0.05 mm).

The most detrimental effect of the non-uniform additional stator gaps on the cogging torque is the increase of cogging torque periodicity. It makes the well-known skewing method loses its expected strong capability of cogging torque reduction. By comparing Fig. 3.16 and Fig. 3.12, it can be seen that the skewing technique only suppresses the high order cogging torque harmonics but has negligible effect on the dominant component, the lower order cogging torque resulting from the non-uniform stator gaps, while this skewing technique shows significant reduction effect for the machines with uniform stator gaps as shown in Fig. 3.10. Therefore, the cogging torque of machine has non-uniform additional stator gaps is nearly the same no matter whether the rotor is skewed or not, as confirmed in Fig. 3.13. In addition, the presence of the non-uniform additional stator gaps has a negligible influence on the back-emf waveform and thus on the average output torque, as shown in Fig. 3.17(a) and (b), respectively. This is because the influence of such gaps on the normal air gap flux density is also negligible, as illustrated in Fig. 3.14(a). However, on the other hand, the non-uniformity of such gaps results in larger torque ripple, i.e. the larger the non-uniform additional gaps are the larger the peak to peak torque ripple, as shown in Fig. 3.17(c). The torque ripple increase is mainly due to the larger cogging torque, Fig. 3.16 and Fig. 3.12, since the influence of such non-uniformity on back-emf waveform is significantly small, as shown in Fig. 3.17(a).

Furthermore, it is worth mentioning that in addition to larger peak to peak torque ripple, the non-uniformity causes also change in the torque ripple period, i.e. it becomes 180 electrical degrees, as shown in Fig. 3.18. This is again because the stator lamination will lose its original geometrical symmetry when the additional stator gaps are non-uniform.

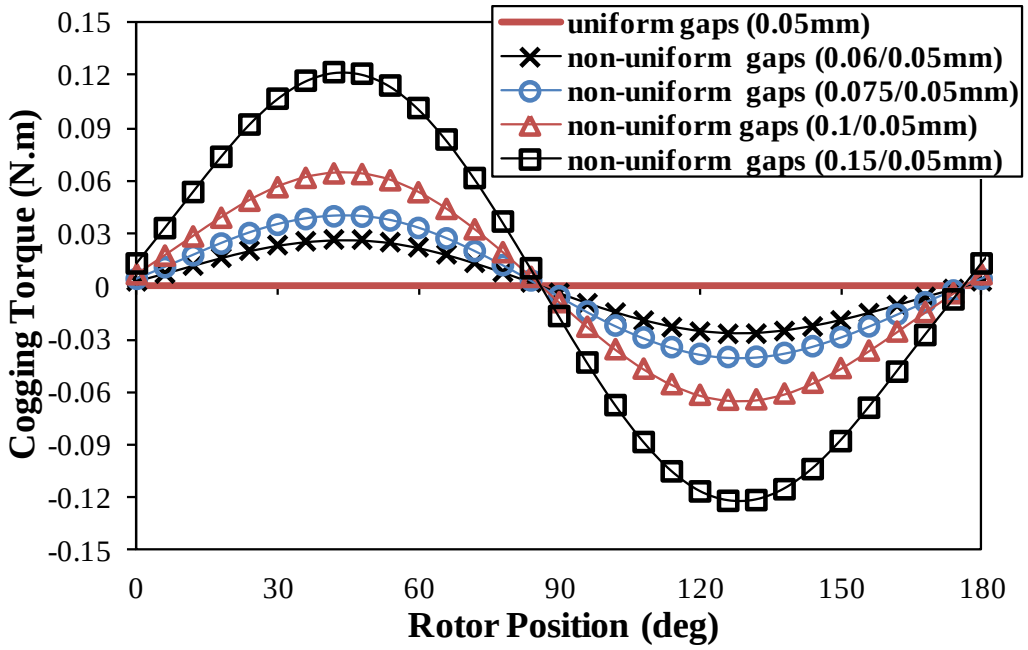

Fig. 3.16 Comparison of cogging torque waveforms of step-skewed rotor machines having uniform and non-uniform additional stator gaps, one gap is larger/the rest are uniform.

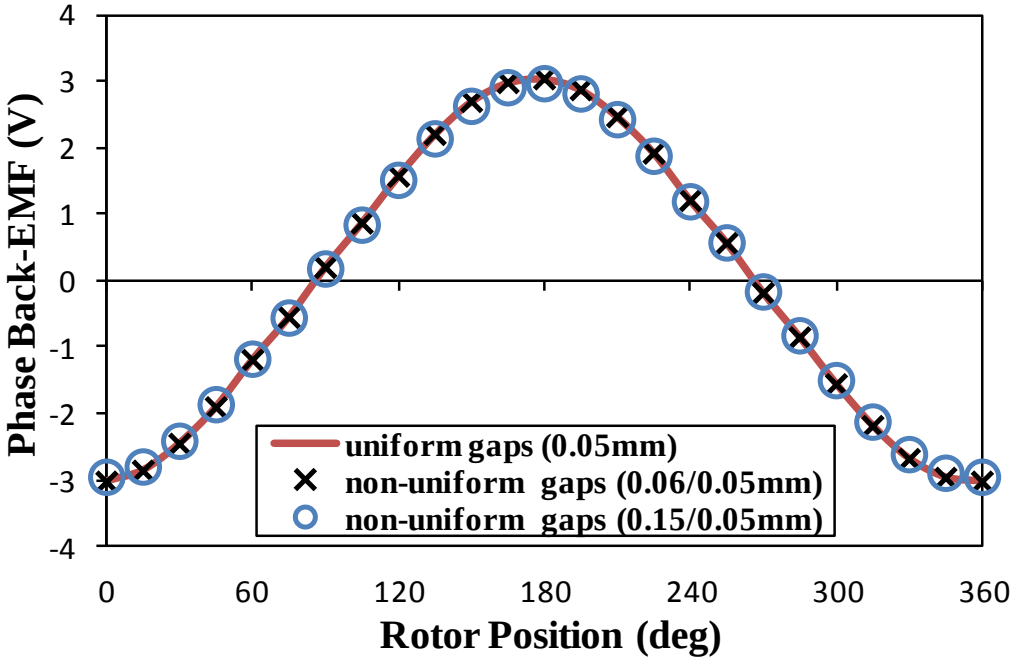

(a) Back-emf waveforms, at 400 rpm

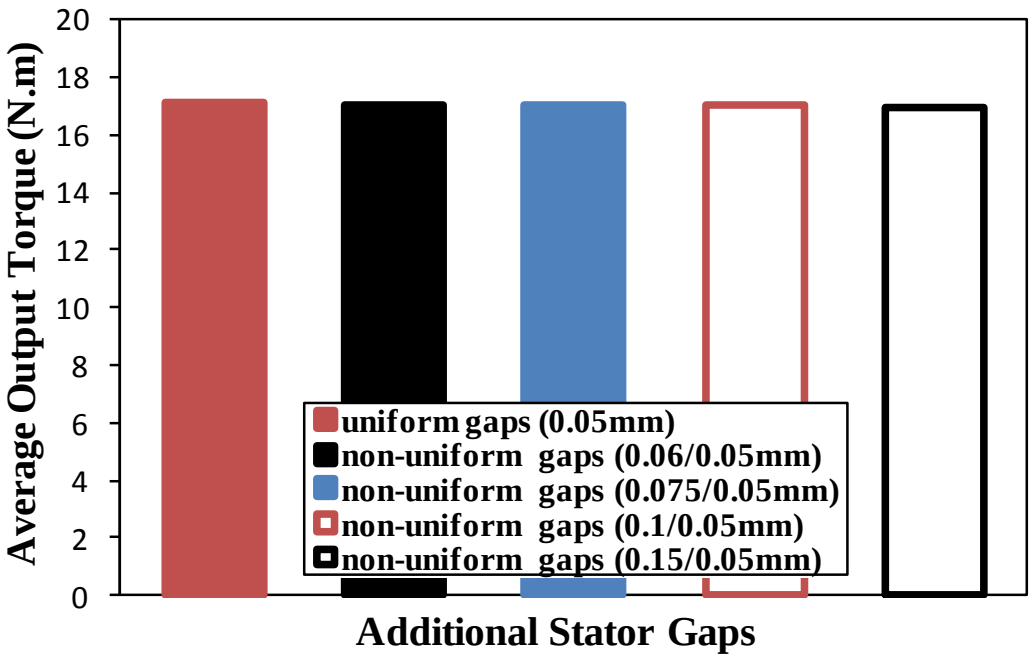

(b) Average output torque, at I_q=150A, I_d=0A

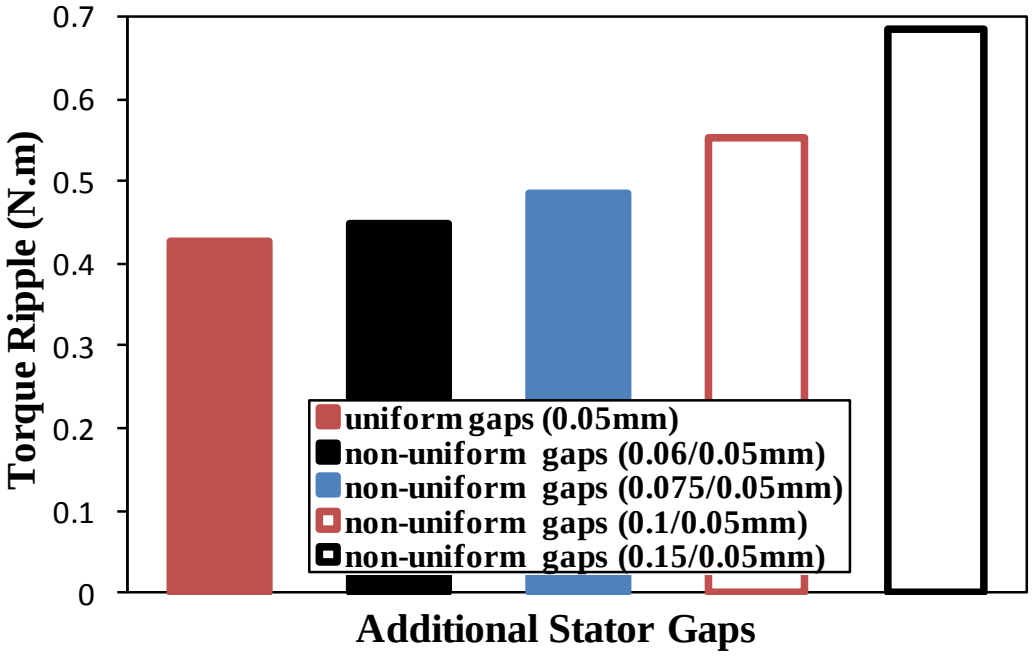

(c) Peak to peak torque ripple, at I_q=150A, I_d=0A

Fig. 3.17 Comparison of back-emf, average output torque and torque ripple of machines having uniform and non-uniform additional stator gaps, one gap is larger/the rest are uniform.

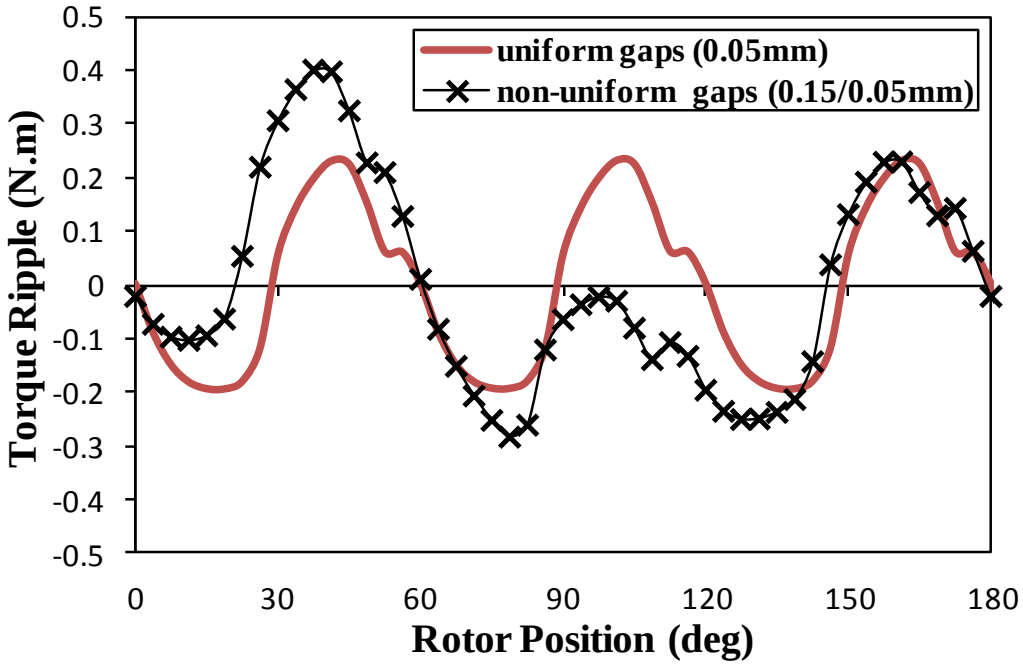

Fig. 3.18 Comparison of torque ripple waveform of machines having uniform stator gaps of 0.05 mm and non-uniform stator gaps (one gap is 0.15mm/the rest are 0.05 mm).

In order to further study the influence of the non-uniformity of such gaps on the cogging torque, more non-uniform scenarios will be investigated. The variation of cogging torque peak against the number of outstanding additional stator gaps, which have the same length of 0.1mm and are positioned in neighbouring teeth, is calculated and presented in Fig. 3.19. The machine exhibits the maximum cogging torque magnitude when there are three outstanding non-uniform additional stator gaps. Another possible scenario is that two additional gaps are non-uniform and are not neighbours. To investigate such case, the cogging torque magnitude against the location of two outstanding additional stator air gaps, which have 0.1mm length while the rest are 0.05 mm, is calculated and illustrated in Fig. 3.20. The largest cogging torque is produced when the two outstanding gaps are in the opposite position, e.g. 1st and 7^{th}, because in this position the maximum extra flux leakage through the tooth tips of the 1st and 7th outstanding gaps occurs simultaneously, as can be clearly noticed in Fig. 3.21. When the outstanding gaps are the 1st/6th, 1st/8th or neighbouring the cogging torque magnitude is the same and slightly lower than its counterpart when the outstanding gaps are opposite each other, since the maximum extra flux leakage of two outstanding gaps is slightly shifted, Fig. 3.21. On the other hand, the lowest cogging torque is generated when the two outstanding gaps are 1st/4th or 1st/10th,

since the maximum extra flux leakage of one outstanding gap takes place simultaneously with its minimum counterpart of the other outstanding gap, Fig. 3.21. Furthermore, in order to investigate the influence of a more random non-uniform scenario, the cogging torque is calculated when the machine has 12 outstanding additional stator gaps, i.e. 0.05, 0.06, 0.07, 0.08, 0.9 and 0.1 mm and each two neighbour gaps have the same length. Due to more flux leakage through the tooth tips and since the original geometrical symmetry of the stator lamination is lost. The cogging torque due to such non-uniformity is significantly larger and its period also becomes 180 electrical degrees, thus the effectiveness of skew diminishes, as illustrated in Fig. 3.22.

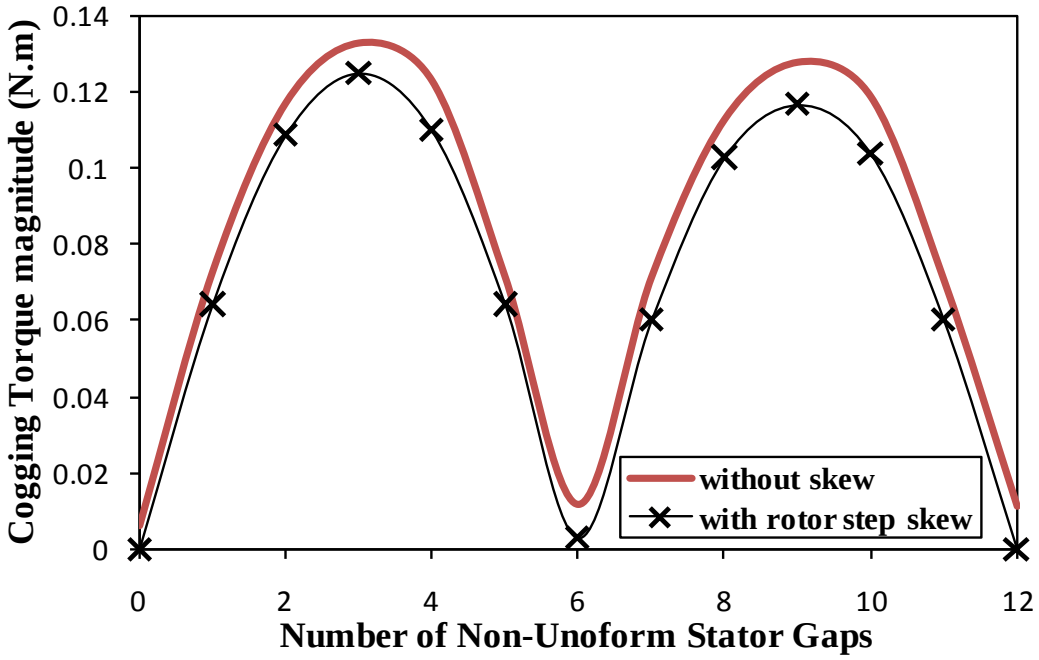

Fig. 3.19 Variation of cogging torque magnitude against number of neighbouring outstanding additional stator gaps, outstanding gap length is 0.1mm, others are 0.05mm change the non-uniform in figure (uniform).

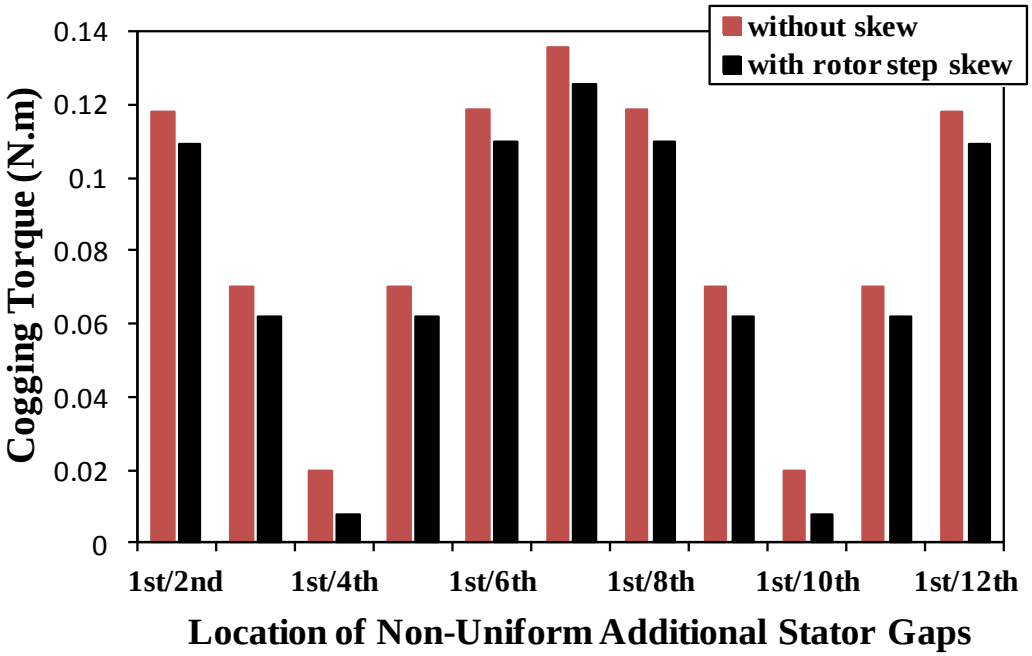

Fig. 3.20 Cogging torque magnitude against location of two outstanding additional stator gaps, outstanding gap length is 0.1mm, others are 0.05mm.

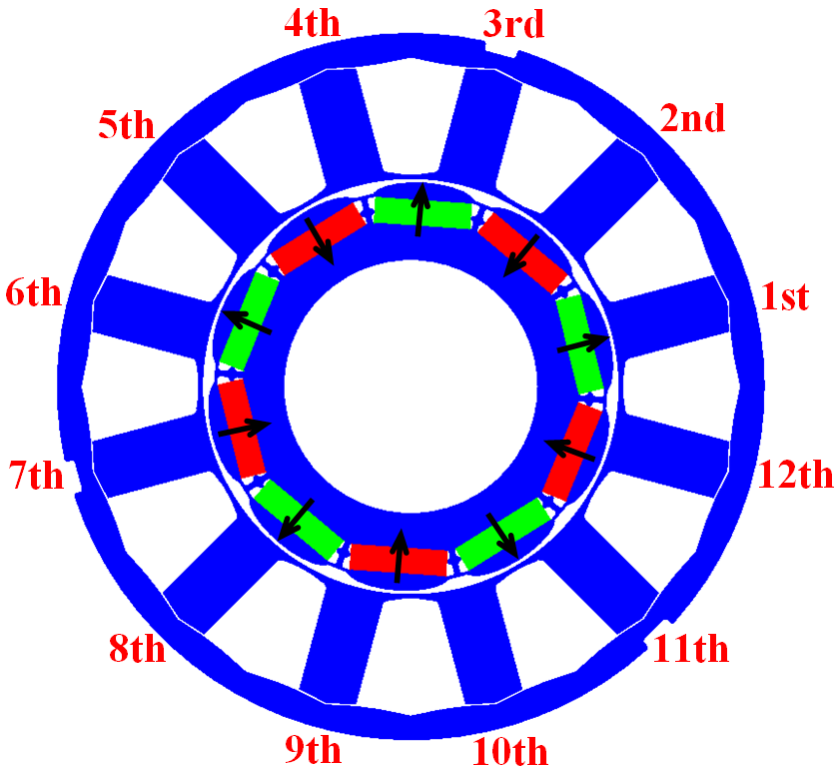

Fig. 3.21 Cross-section of prototype machine with location of additional stator gaps.

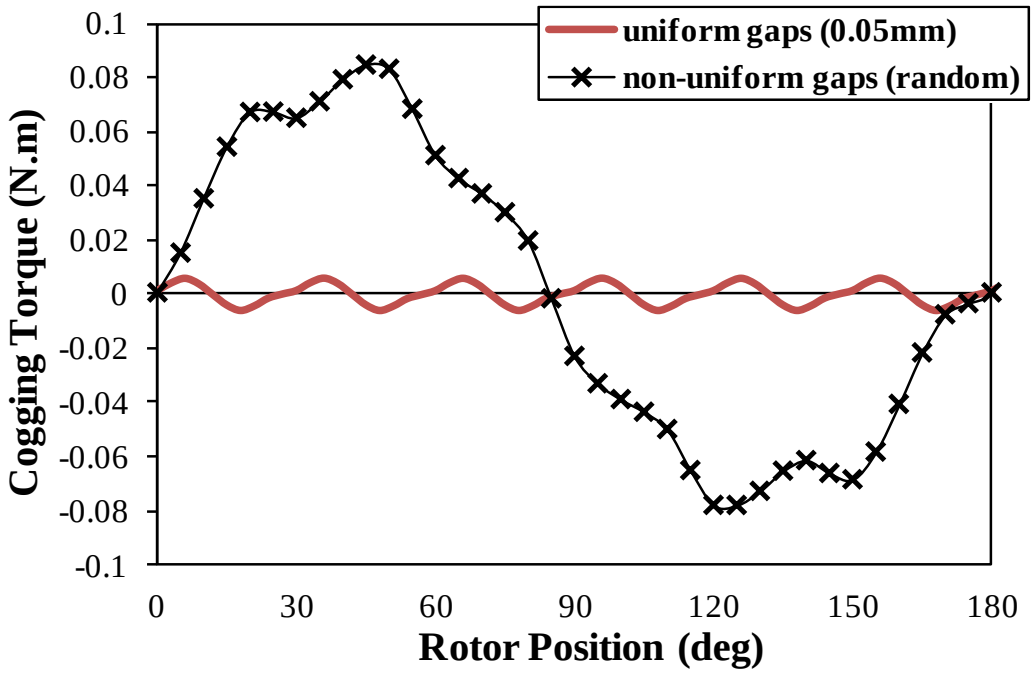

(a) Without skew

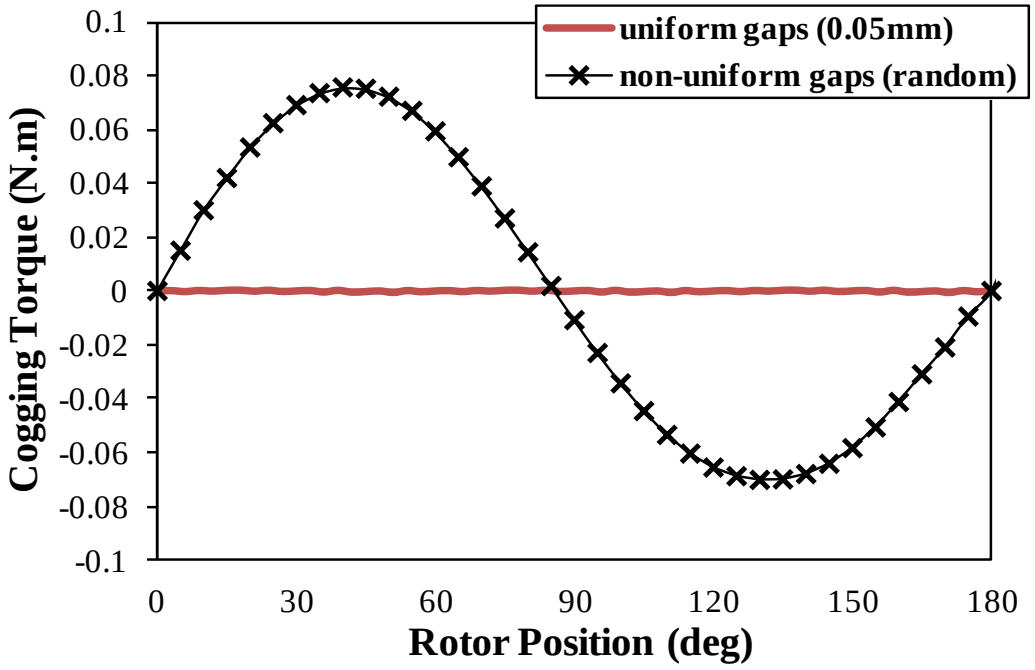

(b) With rotor step skew

Fig. 3.22 Comparison of cogging torque waveforms of machines having 0.05 mm uniform and non-uniform additional stator gaps, non-uniform gaps are: 0.05, 0.06, 0.07, 0.08, 0.9 and 0.1 mm and each two neighbour gaps have the same length.

3.6. Experimental Validation

In order to measure the cogging torque waveform, the test rig, which is shown in Fig. 3.23 and described in details in [137], is utilised. The jaws of the lathe machine hold the stator of the motor, while the rotor is connected to the beam which is rested on the digital scale with a pre-load to ensure that the torque to be measured is uni-directional. By rotating the stator, the torque acting on the rotor is measured at different relative positions between the stator and the rotor. The prototype machine, which is picked up from the mass production line, has a step-skewed rotor and a nominal additional stator gap length of 0.05mm. Theoretically, its cogging torque should be eliminated by the skewing technique if all additional stator gaps are exactly 0.05mm in length, Fig. 3.24(a). However, the measured cogging torque is significantly larger than the predicted one. The period of the measured cogging torque is 180 electrical degrees, which seems resulting from the interaction between 1 slot and 10 poles. A good agreement between the measured and the predicted cogging torque of the machine having one additional stator gap of 0.06mm length and 11 additional stator gaps of 0.05mm length is achieved in both the magnitude and periodicity. It indicates that the relative large measured cogging torque is most likely due to the non-uniform additional stator gaps, although the non-uniformity can be much more complicated in practice. It is worth mentioning that the presented analysis method can be further extended to investigate any possible non-uniform case of such additional gaps. On the other hand, the presence of the non-uniform additional stator gaps has negligible effect on the electromagnetic performance, i.e. the back-emf waveform and average output torque, as confirmed by both the prediction and measurement, Fig. 3.24(b).

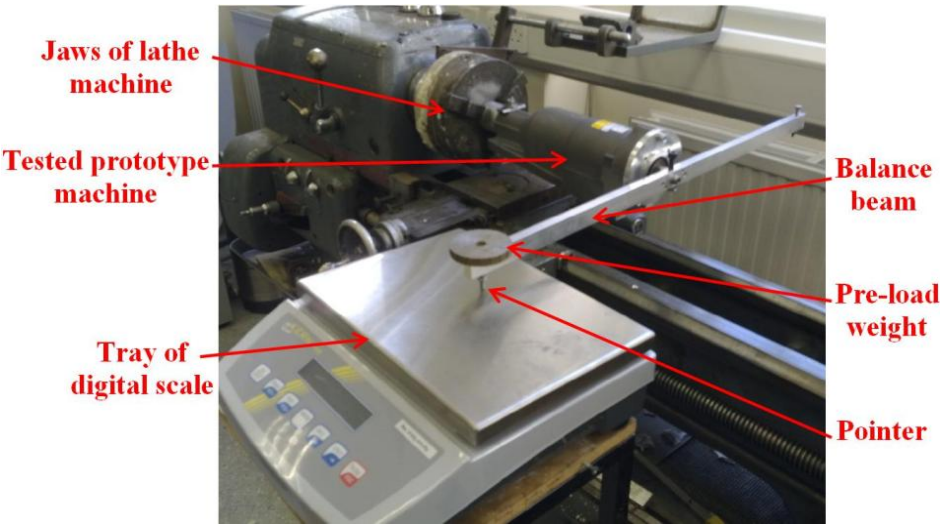

Fig. 3.23 Test rig of measuring cogging torque (the same as Fig. 2.21(a), duplicated here to ease discussion).

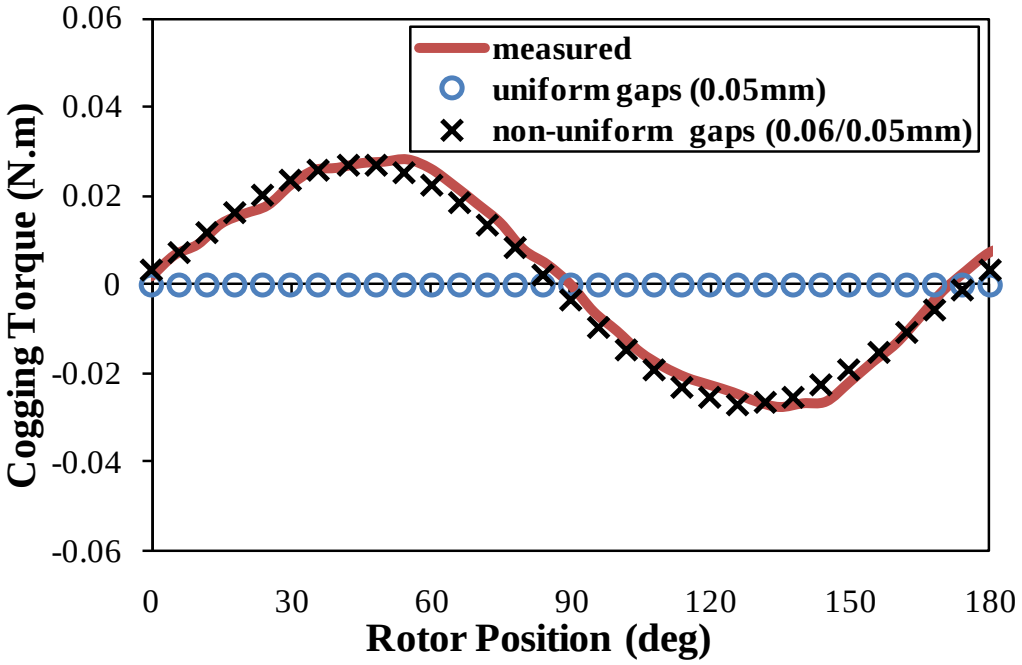

(a) Cogging torque waveforms

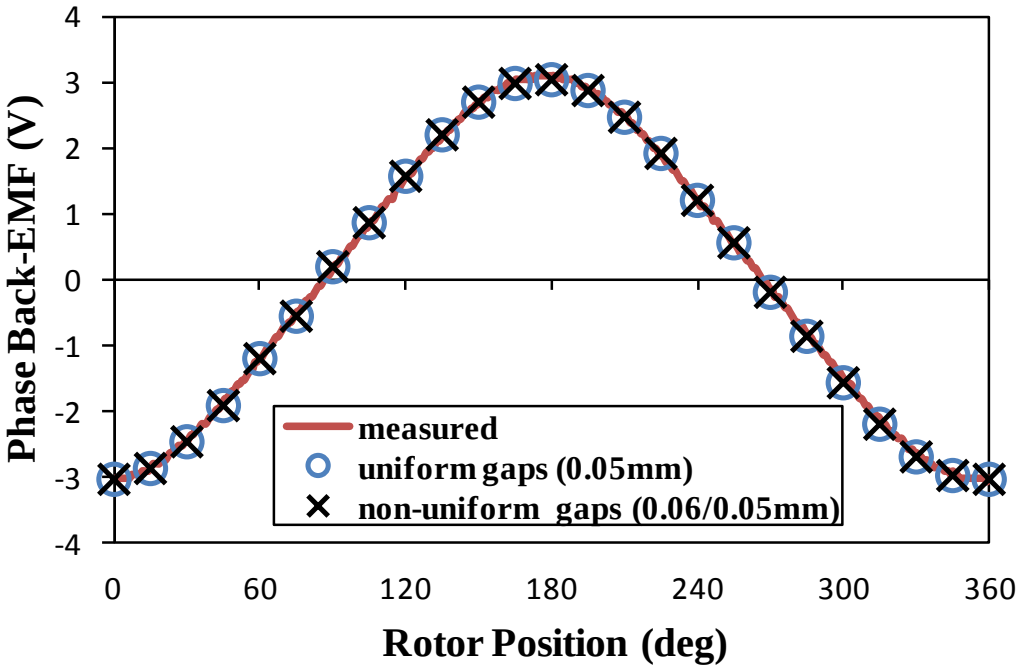

(b) Back-emf waveforms, at 400 rpm

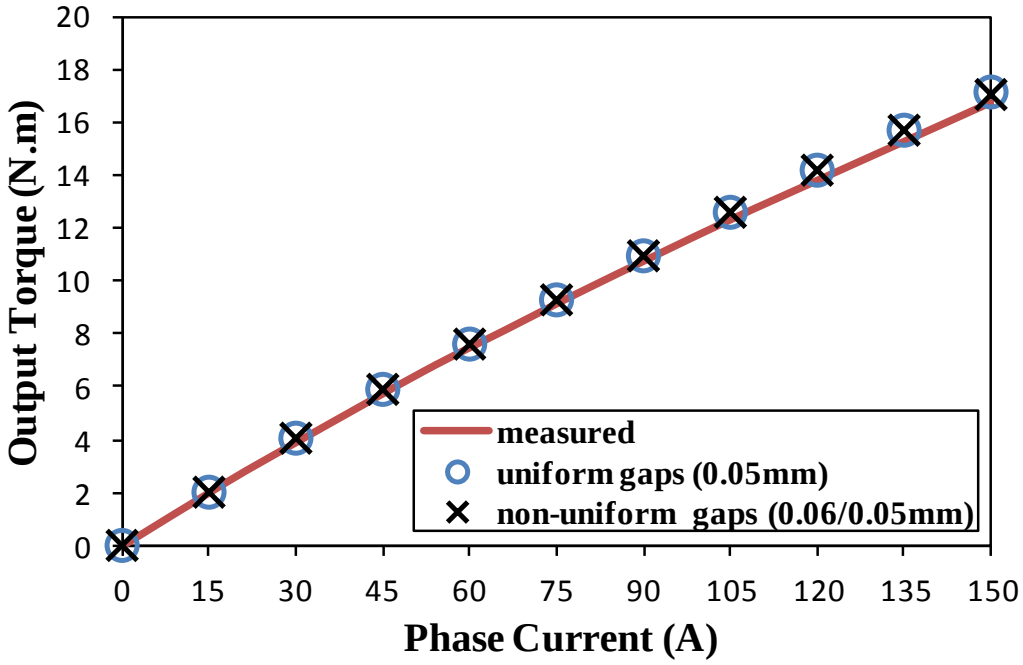

(c) Average output against phase current, at 0 degree current angle

Fig. 3.24 Comparison of measured and predicted cogging torque and back-emf waveforms and average output against phase current of machines having step-skewed rotor and uniform stator gaps of 0.05mm and non-uniform stator gaps (one gap length is 0.06 mm/the rest are 0.05 mm).

3.7. Conclusions

The influence of the additional stator gaps between segmented stator teeth and yoke, which exist due to manufacturing limits, on the electromagnetic performance, particularly the cogging torque, of PM machines having modular stators has been analysed. Both uniform and non-uniform additional stator gaps are studied. However, in practice, the latter is the most likely to occur due to the manufacture tolerances. It has been found that the uniform additional stator gaps increase the cogging torque amplitude but has no effect on its periodicity, while the non-uniform stator gaps significantly increase both the amplitude and periodicity of the cogging torque. Therefore, the skewing technique, which is a very effective cogging torque reduction method, becomes ineffective when the non-uniform additional stator gaps exist. On the other hand, the non-uniform additional stator gaps have a negligible influence on the normal air gap flux density, thus on the average output torque of the machine.

In the next chapter, the hybrid slot design, i.e. sandwiched open and closed slots, will be employed and investigated to further improve the electromagnetic performance of the analysed machine, which will be compared for three different slot opening designs, i.e. open, closed and hybrid slots.

Chapter 4: Investigation of Torque-Speed Characteristics and Cogging Torque of Fractional Slot IPM Brushless AC Machines Having Alternate Slot Openings

4.1. Introduction

Due to their attractive inherent merits, such as high torque density and efficiency, the permanent magnet (PM) machines are strong candidates for applications where the space, weight and fuel consumption are critical criteria, e.g. automobile and aerospace. The fractional-slot PM machines, which employ concentrated winding, additionally exhibit inherently low cogging torque and copper loss [6, 84]. Moreover, as mentioned earlier, the IPM machines can offer relative wide flux weakening capability and strong demagnetization withstanding [8, 14, 32, 34, 61]. Therefore, the PM machines have been widely investigated and analyzed in literature, [6, 8, 14, 20, 32, 34, 35, 38, 40, 42, 43, 47, 49-52, 54-57, 61, 64, 65, 84, 125, 132, 138-140]. However, such machines are still under intensive investigation, since some issues can be further improved and some phenomena require more understanding in depth, such as the torque-speed characteristics, magnetic cross-coupling and cogging torque, which are the research topics of this chapter.

The dq-axis machine models, thus the dq-axis parameters, are often utilized to predict the torque-speed characteristics, also to control the PM machines [49, 50]. Therefore, in order to guarantee the maximum performance out of the machine, the dq-axis parameters should be accurately determined [51]. Normally, the PM machines are operated under high electric loading, thus the magnetic saturation level is high. Therefore, the dq-axis parameters could be correlated due to the magnetic cross-coupling between both axes [50-52]. This phenomenon has been deeply investigated in literature. In addition, different techniques to calculate the dq-axis parameters with due accounting for the cross-coupling have been presented and utilised, [20, 54-57, 139].

On the other hand, some techniques, such as the total or partial closed slot opening designs as well as the rotor step skewing, can significantly decrease the cogging torque, as shown in chapter 3 and according to [35, 38, 40]. However, the effectiveness of such techniques may be limited or even diminished due to the manufacturing tolerances, [47, 132]. Furthermore,

the manufacturing errors could significantly increase the cogging torque [42]. For example, the stator asymmetry, which may be resulted by the manufacturing process, could cause high local saturation, which in turn enlarges the cogging torque and generates additional low order cogging torque components [43].

The skew can be accounted for by the 3D analysis. However, this method is very time consuming and could be not practical for some machines. Therefore, alternatively, the skewed machine can be analyzed by dividing its axial length into several uniform slices, then the 2D FE modeling can be used to analyse each slice separately. Consequently, the total solution is the sum of all slice results by taking into account of the slice positions [65]. This technique is more practical and accurate, particularly when the machine is step skewed rather than fully skewed. Furthermore, the skew can also be accounted for by using a hybrid technique, i.e. 2D FE and analytical, as proposed in [64], or by introducing a skewing factor as suggested in [140].

This chapter investigates the influence of alternate slot openings, viz. open slot, Fig. 4.1(a), closed slot, Fig. 4.1(b), and hybrid slot (sandwiched open and closed slots), on the torque-speed characteristics and cogging torque of 10 pole-12 slot IPM machines having un-skewed and step skewed rotors. The cross-coupling magnetic saturation effect and sensitivity of cogging torque to the slot openings and manufacturing tolerances are particularly highlighted. Furthermore, a 2D FE modeling technique is proposed to analyse the performance of the machine with hybrid slot.

Table 4.1 Prototype Machine Parameters

Parameter	***Dimension***	***Parameter***	***Dimension***
Stator Outer Diameter	90 mm	Tooth Width	7.4 mm
Stator Inner Diameter	53 mm	Stator Yoke Width	3 mm
Rotor Maximum Diameter	52 mm	Minimum Air Gap Length	0.5 mm
Rotor Minimum Diameter	50 mm	Maximum Air Gap Length	1.5 mm
Shaft Diameter	36 mm	Slot Opening	2 mm
Magnet Thickness	3.4 mm	Magnet Width	12.2 mm
Magnet Rib Width [Fig. 4.1(b)]	0.7 mm	Slot Opening Bridge Thickness	0.5 mm
Active Axial Length	108 mm	Phase Current	$150A_{peak}$
Number of Turns per Phase	36 turn	Phase Resistance	0.013 Ω

4.2. Analysed Machines and Modeling Techniques

4.2.1. Analysed Machines

The analyses will be carried out on the same 10 pole-12 slot IPM machines, which have been analysed in the second chapter. However, three different slot openings, viz. open slot, closed slot and hybrid slot (sandwiched open and closed slots, as will be described later), are taken into account during the investigation. In addition, the rotor step skewed (4 steps axially) is also considered. The major parameters of the prototypes are given in Table 4.1. As mentioned before, in order to ease winding, the stator teeth and the stator yoke are separated. In this case, the stator teeth are stacked together, the coils are pre-wound then placed on the teeth stack, which is finally assembled together with the stator yoke, Fig. 4.1(c). An inter-locking technique is employed axially between the laminations for the stator teeth and yoke to improve the mechanical strength and integrity of stator laminations, thus to minimize the possibility of mechanical deformation and tolerance. Again, due to the manufacturing limits, there may be additional air gaps between the stator teeth and yoke, as illustrated in Fig. 4.1. For the prototype machines under investigation, these gaps are approximately 0.05 mm and their influence on the machine performance is investigated.

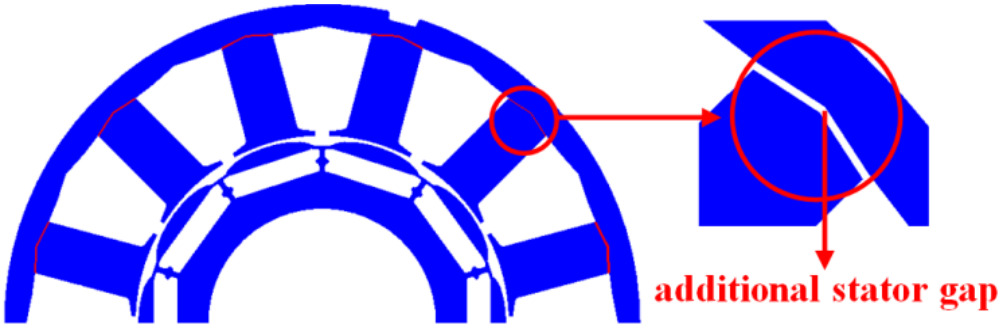

(a) Open slot

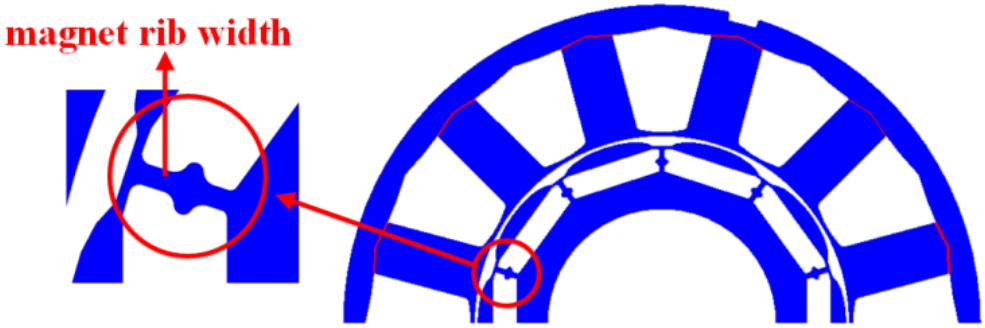

(b) Closed slot

(c) Prototype rotor and stator, together with wound stator teeth stack before insert into stator yoke

Fig. 4.1 Stator and rotor laminations of prototype machine with different slot openings and approximately 0.05 mm additional stator gaps.

4.2.2. Modeling of Hybrid Slot

In order to accurately predict the performance of the machine with hybrid slot, the 3D FE model should be employed. However, the 3D analysis is very time consuming and unrealistic for such machine. Therefore, an alternative 2D FE approximation technique is proposed to analyse such machine. In the machine under investigation every two laminations having open slot are followed by one closed slot lamination, i.e. over the slot opening the ratio of the overall iron axial length to the whole axial length is only 1/3. A 2D approximation model can be used to analyse such machine by employing a different equivalent material B-H characteristic in the slot opening area. This material should have the same field strength (H) as the stator iron but the flux density (B) should be reduced by three times compared to the original stator iron flux density, as illustrated in (4. 1) and (4. 2) and shown in Fig. 4.2.

$$H_{hyb} = H_{ste} \tag{4. 1}$$

$$B_{hyb} = \frac{B_{ste}}{3} \tag{4. 2}$$

where H_{hyb} and H_{ste} are the field strength of the hybrid material and lamination steel, B_{hyb} and B_{ste} are the flux density of the hybrid material and lamination steel.

Using this method, the back-emf waveform and torque-current angle characteristics of the machine with hybrid slot are predicated and compared with their measured counterparts in Fig. 4.3. A very good agreement is obtained. Therefore, such method will be utilised in the following analyses and investigations.

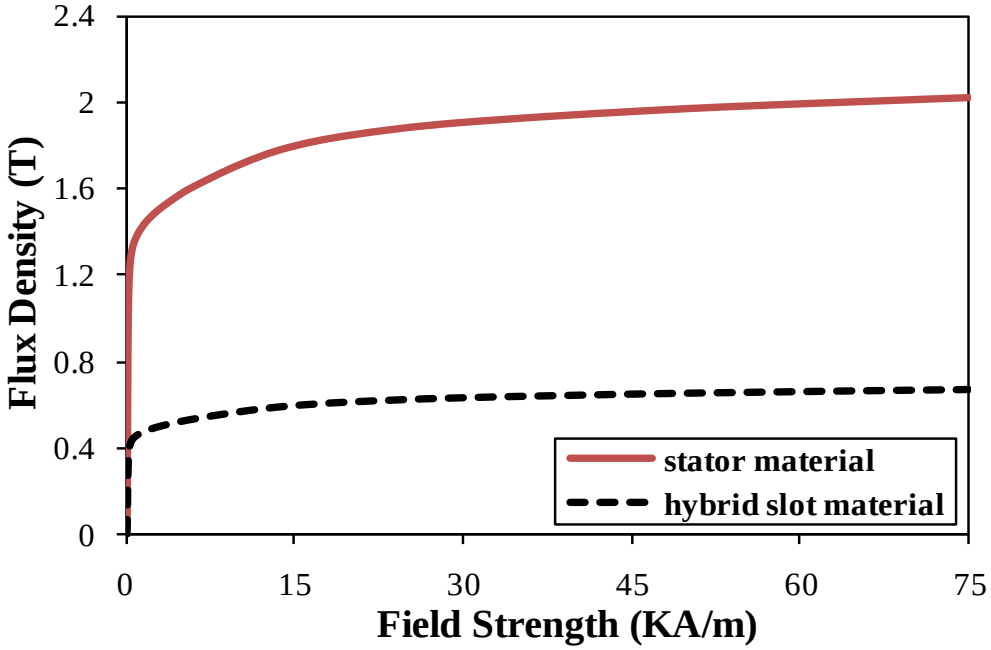

Fig. 4.2 B-H curves of stator and equivalent slot opening material of the machine with hybrid slot.

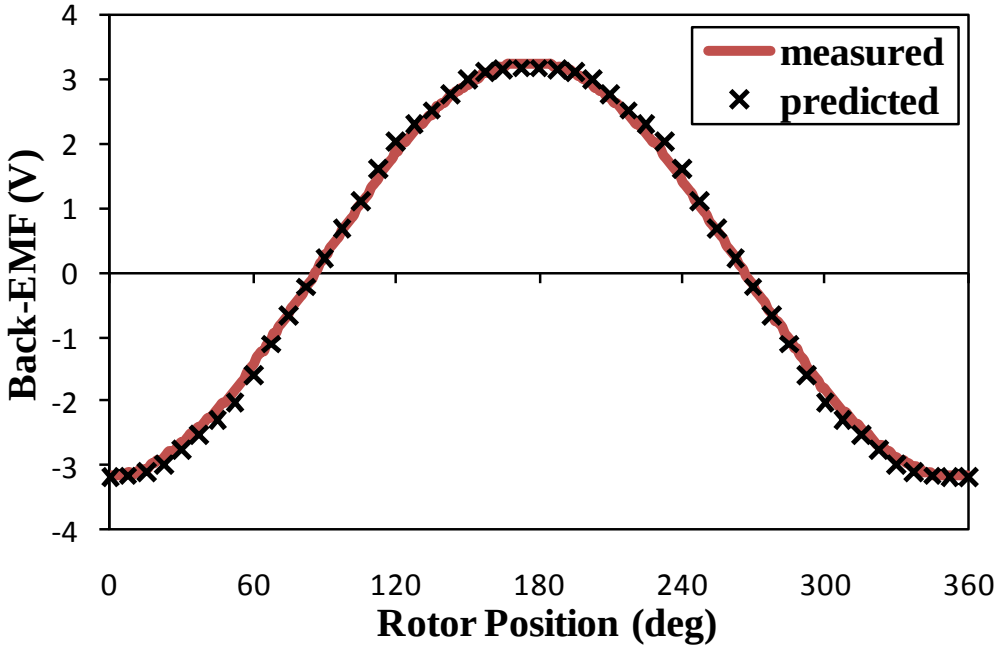

(a) Back-emf waveform at 400rpm

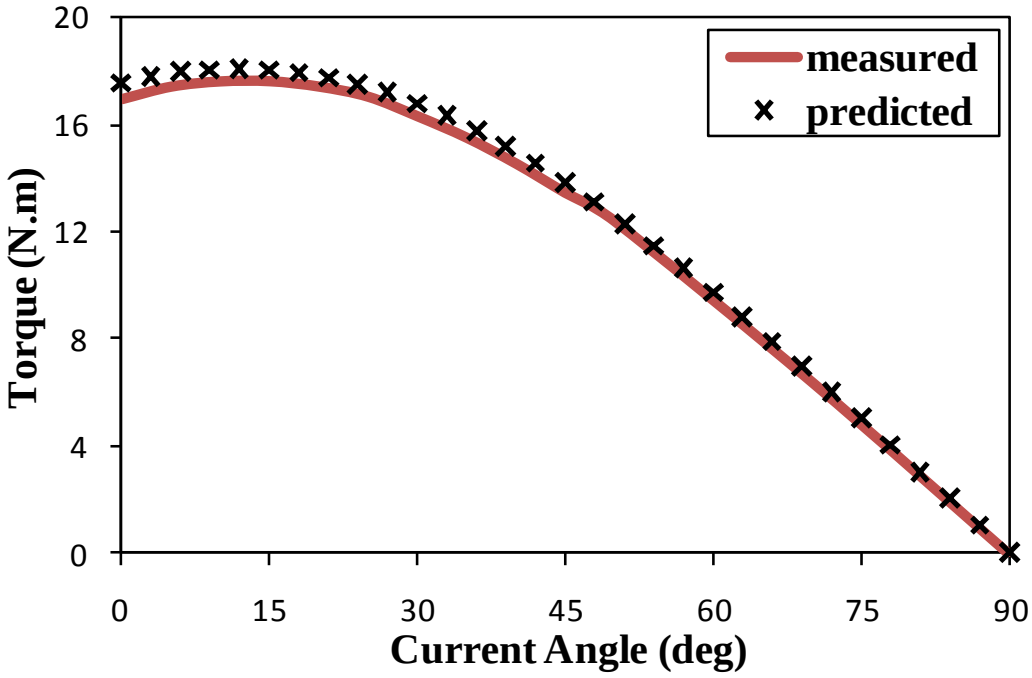

(b) Torque current angle characteistic

Fig. 4.3 Comparison of 2D FE predicted and measured back-emf waveforme and torque-current angle characteristic of machine having hybrid slot.

4.2.3. Modeling of Rotor Skew

Similar to that described in chapter 3, the skewed machines are analyzed by dividing the active length into four equal parts, since the prototype machine rotors have 4 steps of skew, each part is analysed independently, then the predicted results are combined for all parts together. In order to examine this technique, the back-emf and torque-current angle characteristics of machine having closed slot and step skewed rotor are calculated and compared with their measured counterparts in Fig. 4.4. It shows that high prediction accuracy can be obtained by employing such technique. Therefore, it is utilized in the analyses of the skewed machine in this paper.

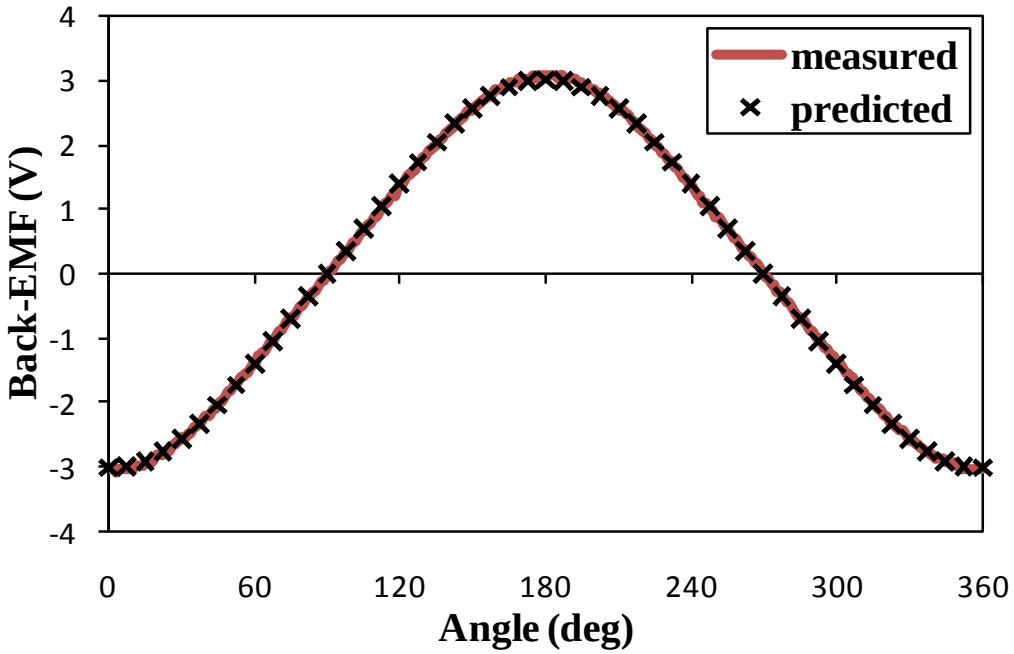

(a) Back-emf waveform, at 400 rpm

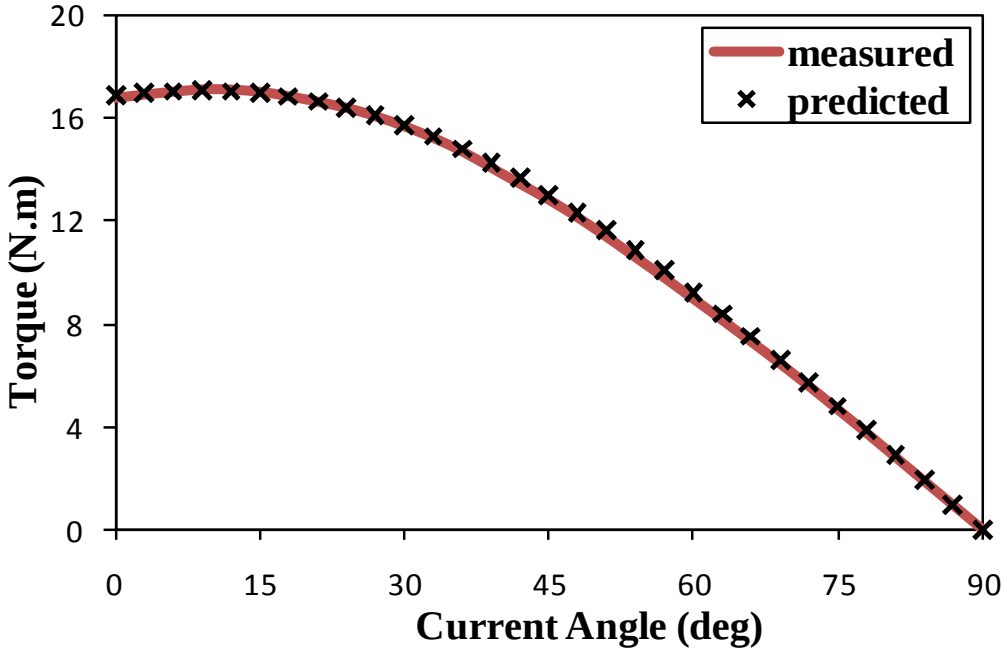

(b) Torque-current angle characteristics

Fig. 4.4 Comparison of 2D FE predicted and measured back-emf waveforme and torque-current angle characteristic of machine having closed slot and step skewed rotor.

4.2.4. Calculating of Torque Speed Characteristics

As shown before, using the dq-axis parameters, the output torque of PM machines can be calculated by:

$$T = 1.5p[\psi_{md} I_q + (L_d - L_q) I_d I_q] \tag{4. 3}$$

where I_d, I_q, ψ_{md}, L_d, L_q and p are dq-axis currents, PM flux linkage, dq-axis inductances and pole pair numbers, respectively.

The cross-coupling level in the torque calculation depends on the estimation method of the dq-axis inductances and PM flux linkage. If the dq-axis inductances are predicted as function of its corresponding current, (4. 4) and (4. 5), and the PM flux linkage as a constant value at zero currents, (4. 6), the cross coupling is not considered, i.e. no cross-coupling.

$$L_d = \frac{\psi_d(I_d) - \psi_{md}(0)}{I_d} \tag{4. 4}$$

$$L_q = \frac{\psi_q(I_q)}{I_q} \tag{4.5}$$

$$\psi_{md} = \psi_{md}(0) \tag{4. 6}$$

where $\psi_d(I_d)$, $\psi_q(I_q)$ and $\psi_{md}(0)$ are the dq-axis flux linkages each as function of its corresponding current only and PM flux linkage at zero dq-axis currents, respectively.

To fully account for the magnetic cross-coupling, i.e. full cross-coupling, the dq-axis inductances should be calculated as function of both dq-axis currents, (4. 7) and (4. 8), while the influence of the q-axis current on the PM flux linkage should be accounted for, (4. 9).

$$L_d = \frac{\psi_d(I_d, I_q) - \psi_{md}(I_q)}{I_d} \tag{4. 7}$$

$$L_q = \frac{\psi_q(I_d, I_q)}{I_q} \tag{4. 8}$$

$$\psi_{md} = \psi_{md}(I_q) \tag{4.9}$$

$$V_{ph} = \sqrt{(I_d R_{ph} - \omega L_q I_q)^2 + [I_q R_{ph} + \omega(L_d I_d + \psi_{md})]^2} \tag{4. 10}$$

where $\psi_d(I_d, I_q)$, $\psi_q(I_d, I_q)$, $\psi_{md}(I_q)$, ω, and R_{ph} are the dq-axis flux linkages each as function of both d- and q-axis currents, PM flux linkage as function of q-axis current while the d-axis current is zero, rotating speed and phase winding resistance, respectively.

The predicted inductances and PM flux linkage together with the torque equation, (4. 3) and with the restriction of the voltage equation, (4. 10), can then be used to analytically calculate the torque-speed characteristics, the method is described in details in [49]. In order to examine the accuracy of such method together with the hybrid slot and step skewed rotor analysis techniques, the dq-axis inductances, Fig. 4.5, and PM flux linkage, Fig. 4.6, of the machine with hybrid slot and step skewed rotor have been predicted and used to analytically calculate the torque-speed characteristics, which are compared with their measured counterparts in Fig. 4.7. It shows a good agreement. Therefore, these method and techniques are utilized to predict the torque-speed characteristics and cogging torque of the three prototype machines with additional stator gaps of 0.05mm, with/without considering the cross-coupling and rotor step skew. It is worth mentioning that the machine is operated at its maximum torque per ampere up to 400 rpm, i.e. the constant torque region, then the dq-axis currents are adjusted to satisfy the voltage limitation, i.e. the flux weakening operation region. The variations of the corresponding dq-axis currents are illustrated in Fig. 4.8.

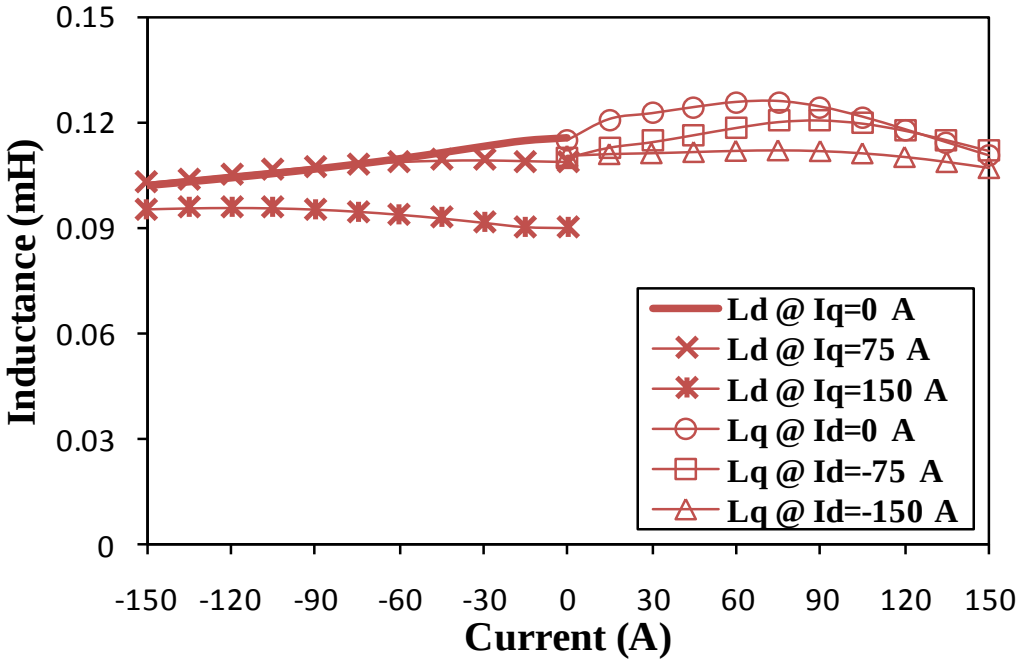

Fig. 4.5 Variation of dq-axis inductances against dq-axis currents of machine having hybrid slot and step skewed rotor.

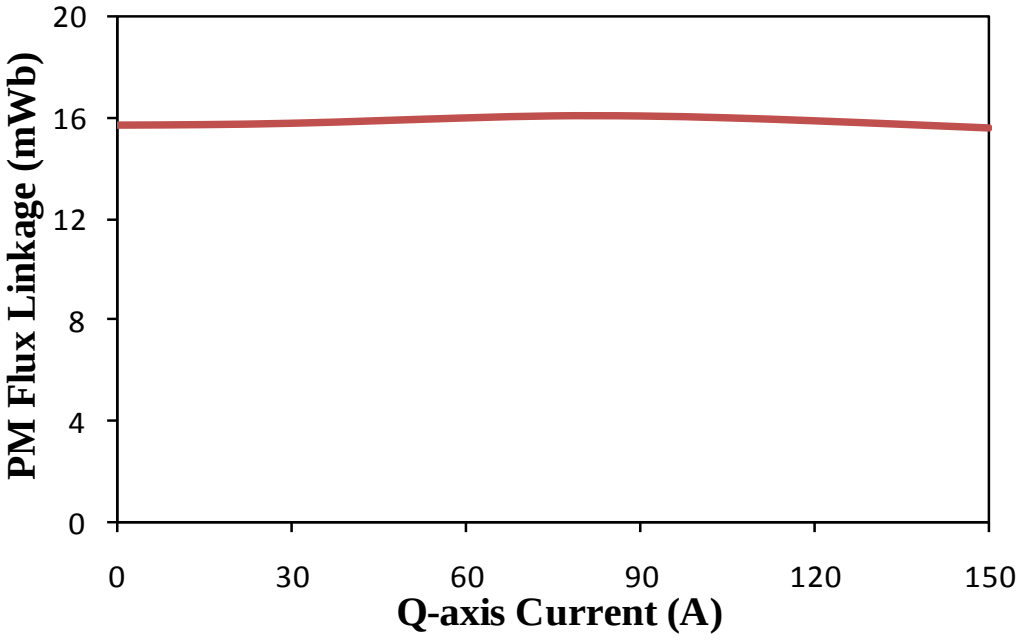

Fig. 4.6 Variation of PM flux linkage against q-axis current of machine having hybrid slot and step skewed rotor.

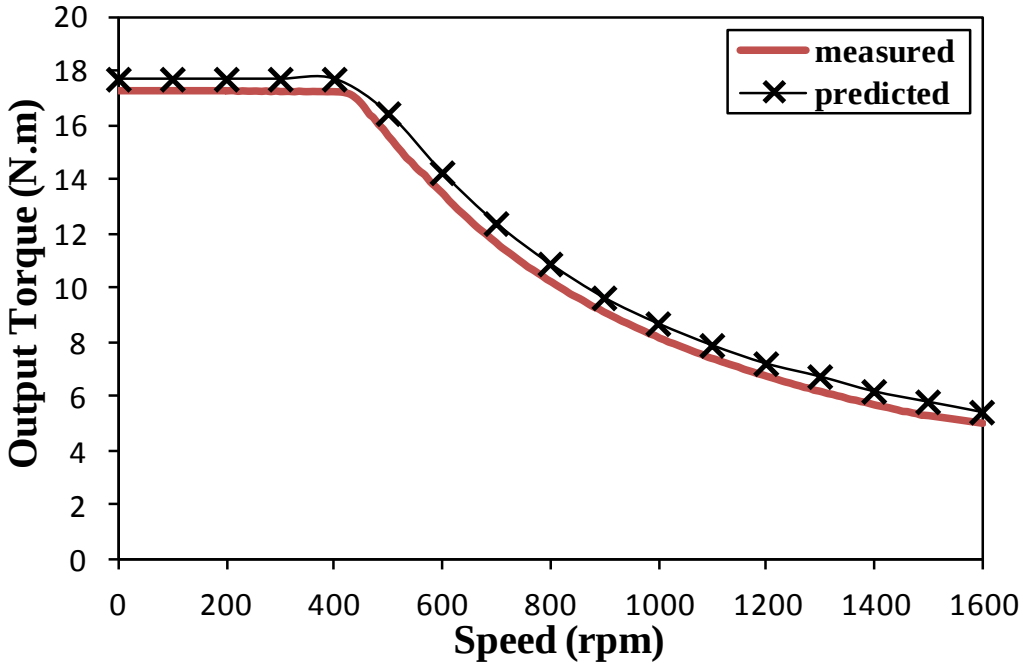

Fig. 4.7 Comparison of measured and predicted torque-speed characteristics of machines having hybrid slot and step skewed rotor.

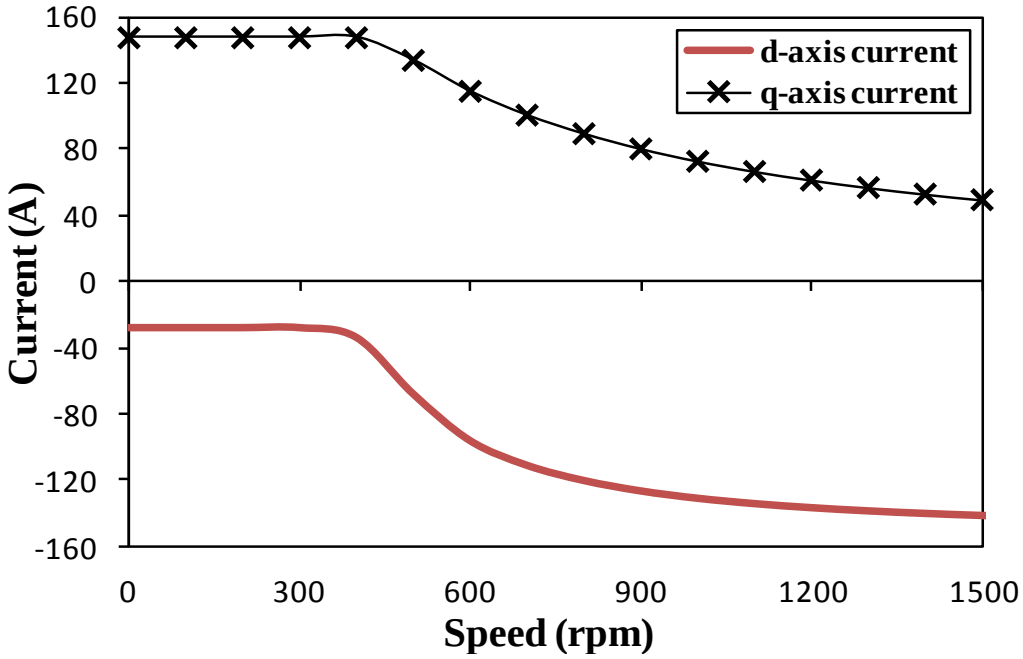

Fig. 4.8 Variation of dq-axis currents during torque-speed characteristics prediction of machine having hybrid slot and step skewed rotor.

4.3. Influence of Slot Opening

4.3.1. Electromagnetic Performance

The closed slot design is normally utilized to minimize the cogging torque, since this torque is mainly caused by the interaction between the PMs and the stator slotting [35]. However, such design also causes a relatively large reduction in the PM flux linkage, as shown in Table 4.2. This is due to the extra flux leakage through the slot iron bridges, as has been illustrated in last chapter. Consequently, the closed slot design results in lower electromagnetic performance, as confirmed in Fig. 4.9(a). Alternatively, the machine can be designed with axially hybrid slot openings (air + iron). This leads to a relatively small PM flux linkage reduction, as shown in Table 4.2, since the alternate slot iron bridges become highly saturated. Thus, the machine with hybrid slot exhibits nearly the same electromagnetic torque as the machine with open slot (the original machine), as shown in Fig. 4.9(a), while its cogging torque reduction is very similar to the totally closed-slot opening (closed slot) design, as confirmed in Fig. 4.9(b).

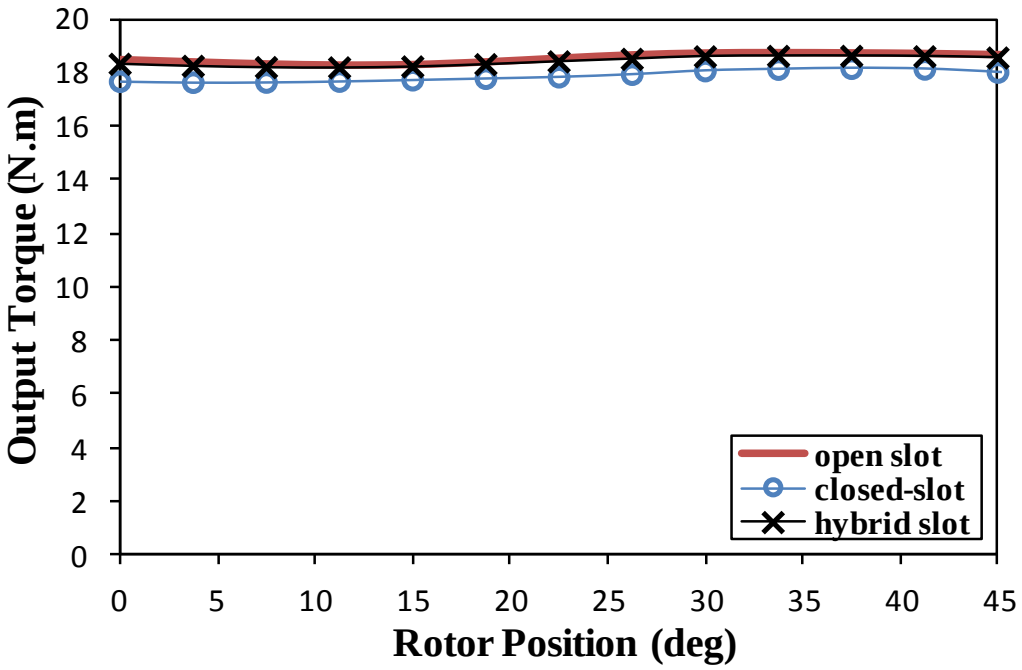

(a) Electromagnetic torque

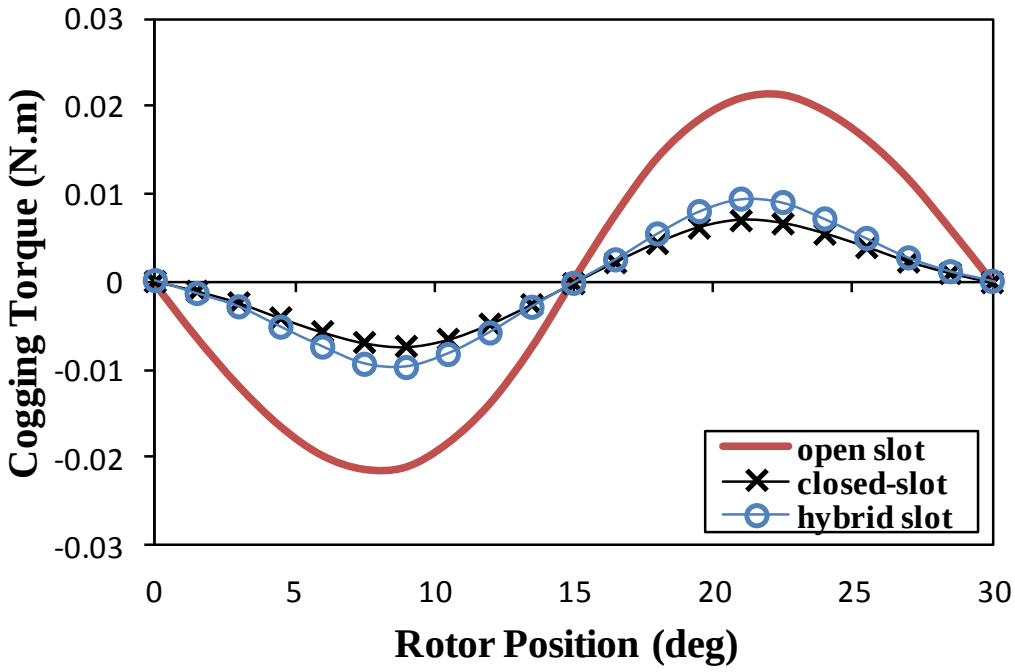

(b) Cogging torque

Fig. 4.9 Comparison of predicted electromagnetic torque and cogging torque of machines having three alternate slot openings.

Table 4.2 PM Flux Linkage at I_d=0, I_q=150 A_{peak}

Type of Slot Opening	***PM Flux Linkage***	
	(mWb)	*(%)*
Open Slot	15.9	100
Closed Slot	15.17	95.4
Hybrid Slot	15.73	98.9

4.3.2. Torque-Speed Characteristics

The reluctance torque of the studied machines is significantly small, since they are fractional-slot having concentrated winding [125]. This means their output torque is mainly due to the PM flux linkage. Fig. 4.10 compares the torque-speed characteristics with full magnetic cross-coupling consideration of three machines having different slot openings and un-skewed and step skewed rotors. The machine with closed slot exhibits the lowest characteristics. This is due to the relatively large PM flux linkage reduction, as illustrated in Table 4.2, as a result of extra flux leakage through the slot iron bridges. On the other hand, the machine with hybrid slot exhibits nearly the same characteristics as the machine with

open slot, since the PM flux linkage reduction is relatively negligible, as shown in Table 4.2. The rotor step skewing causes a negligible reduction in the characteristics for all machines, and the behaviour is still exactly the same as the un-skewed machines.

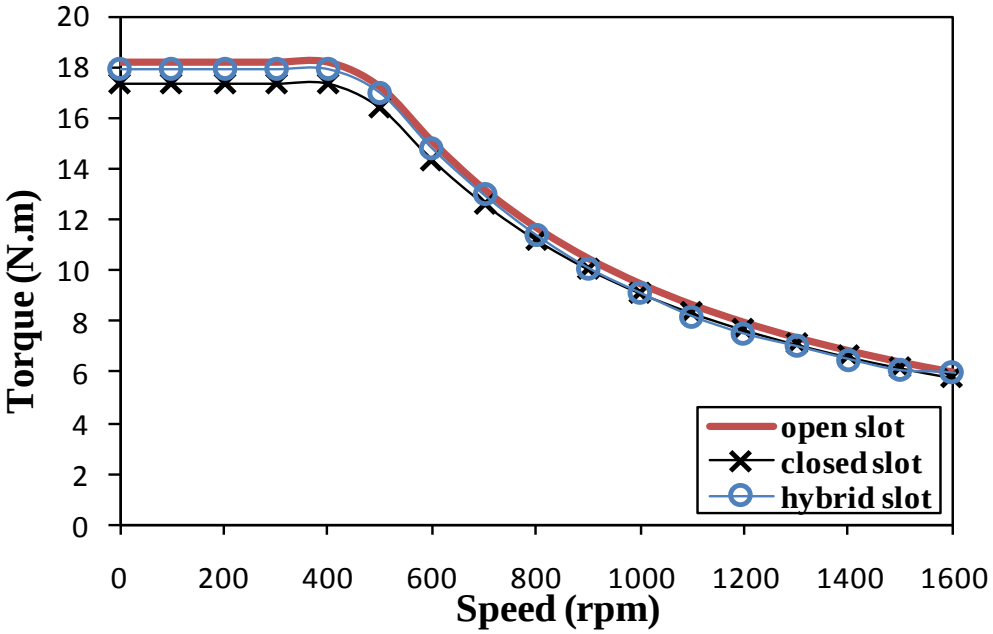

(a) Torque-speed characterstics, without skew

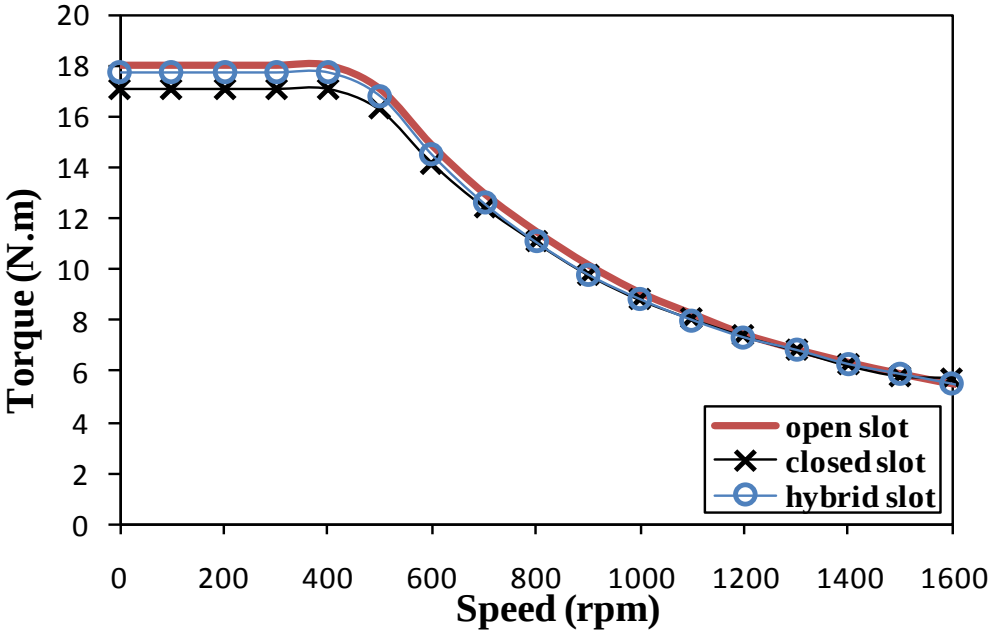

(b) Torque-speed characteristics, with rotor step skew

Fig. 4.10 Comparison of torque-speed characteristics of analysed machine under alternate slot openings, without/with rotor step skew.

4.3.3. Magnetic Cross Coupling

In order to investigate the influence of different slot openings on the magnetic cross-coupling level, the torque-speed characteristics of machines having different slot openings have been predicted with and without cross-coupling consideration, as illustrated in Fig. 4.11. The machine with closed slot exhibits a significant cross-coupling level in the constant-torque region, while in the flux weakening region the cross-coupling influence gradually diminishes, Fig. 4.11(b). On the other hand, in the machine with hybrid slot the influence of the cross-coupling is negligible all over the operation range, as shown in Fig. 4.11(c). The same behaviour is found in the machine with open slot, Fig. 4.11(a). This is due to different PM flux linkage variations in the slot openings, as shown in Fig. 4.12. For machines having open slot and hybrid slot, the influence of the q-axis current on the PM flux linkage is relatively small since there is no extra flux leakage in the open slot design and it is relatively small in the hybrid slot design as the alternate slot iron bridges become saturated, especially at high q-axis current. On the other hand, the PM flux linkage varies significantly with q-axis current in the closed slot design, it is relatively low when the q-axis current is small since the flux leakage is relatively larger. However, the slot iron bridges become gradually saturated when the current increases. This leads to less flux leakage, thus larger PM flux linkage, as can be clearly noticed in Fig. 4.12. Furthermore, although the influence of the cross-coupling on dq-axis inductances depends on the slot opening type, as illustrated in Fig. 4.13, the contribution of such inductances to the output torque is negligibly small, i.e. ~3%. Therefore, it can be concluded that in the fractional-slot PM machines the consideration of the cross-coupling on the PM flux linkage is the most important. Moreover, as mentioned before the additional stator gaps in the prototype machines are ~0.05mm. However, in order to highlight the influence of larger gaps, the variations of PM flux linkage against the additional stator gap length of machines having different slot openings is shown in Fig. 4.14. As expected, for all machines larger additional gaps result in larger PM flux linkage reduction, since the effective air gap becomes larger. But such decrease varies according to the slot opening material, which in turn determines the saturation level in the slot opening bridges and tooth tips.

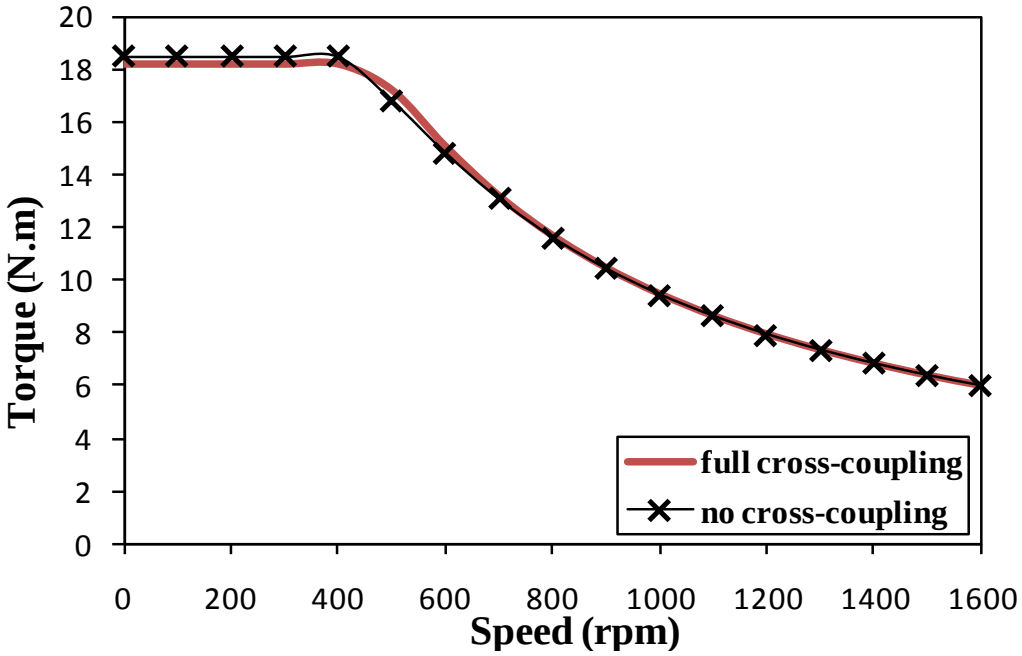

(a) Open slot

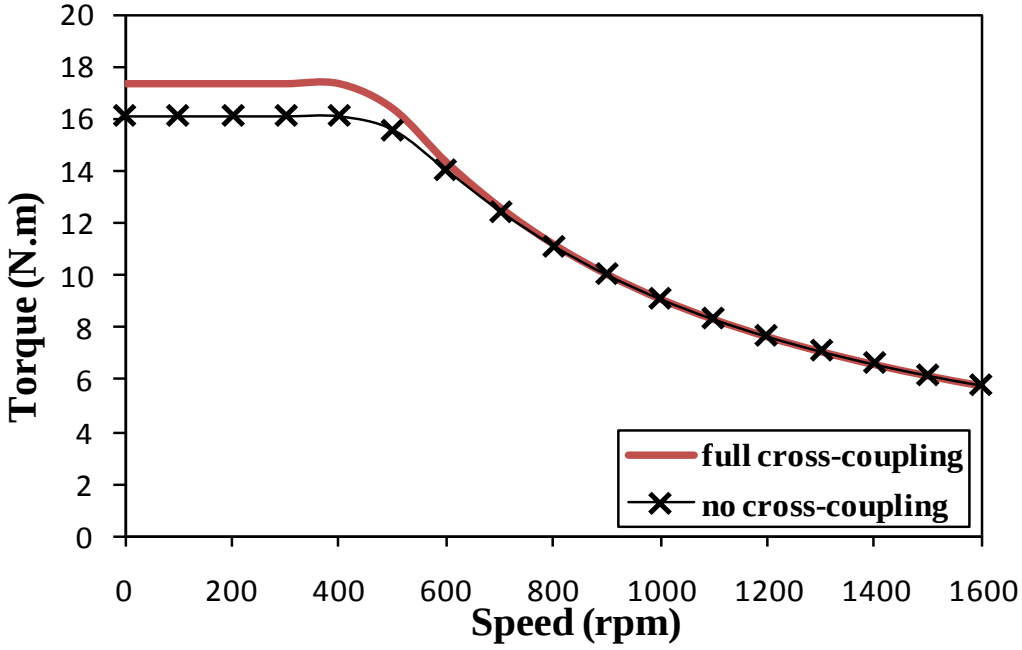

(b) Closed slot

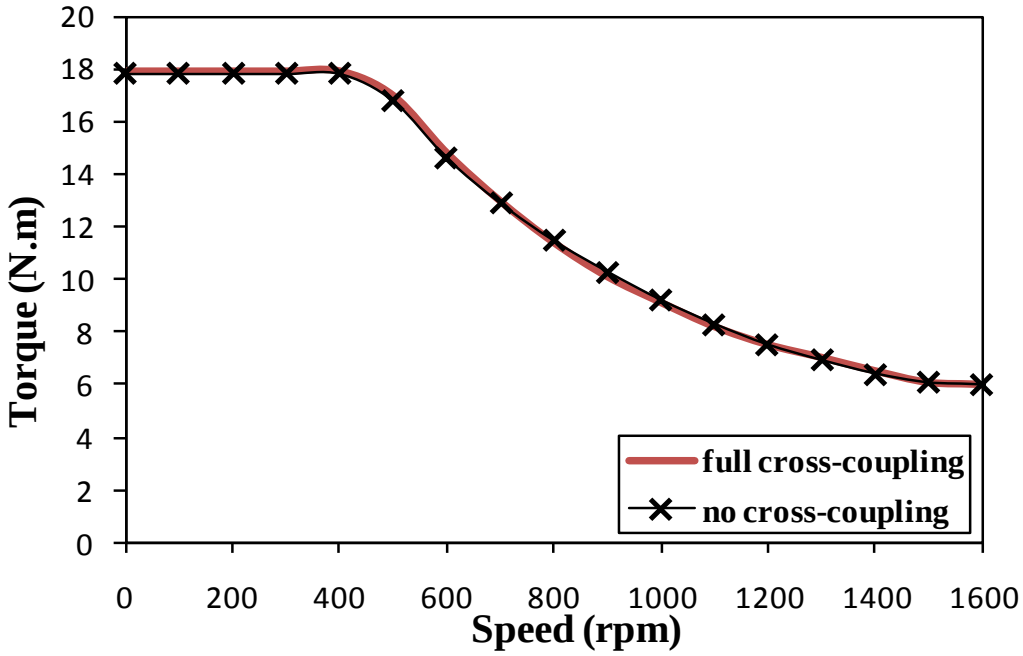

(c) Hybrid slot

Fig. 4.11 Comparison of predicted torque speed characteristics of machines having aternate slot openings.

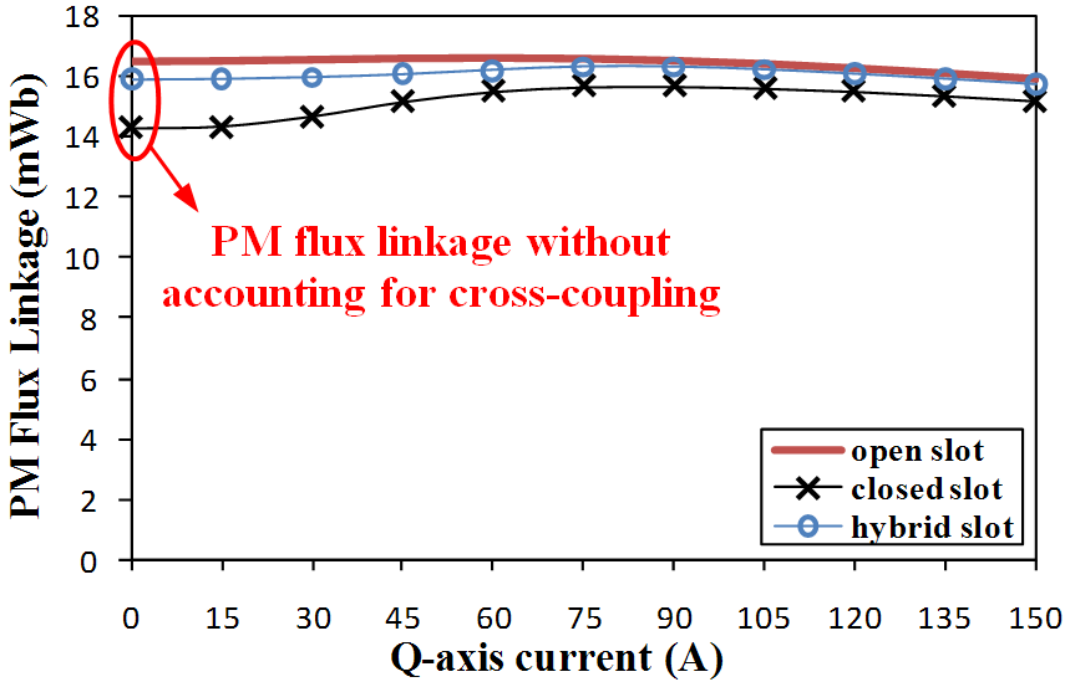

Fig. 4.12 Variation of PM flux linkage against q-axis current (cross-coupling effect) of machines having alternate slot openings.

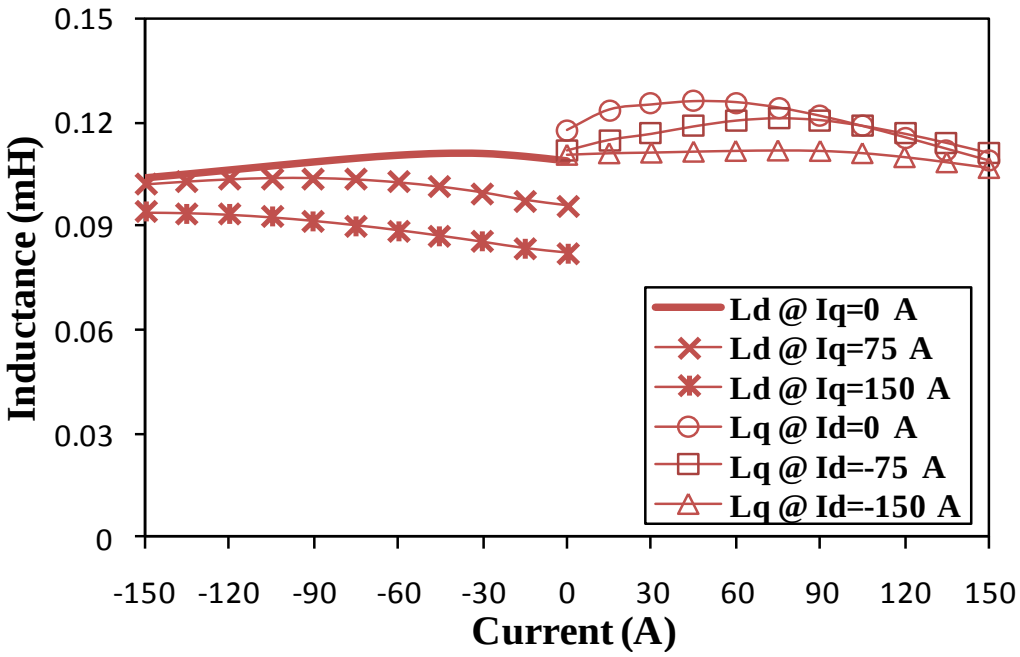

(a) Open slot

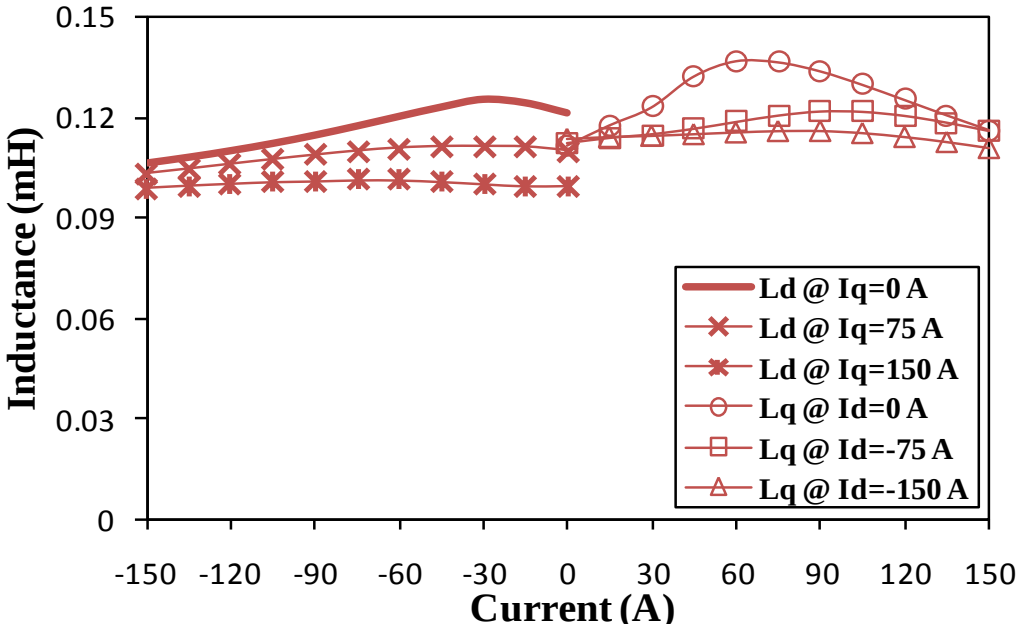

(b) Closed slot

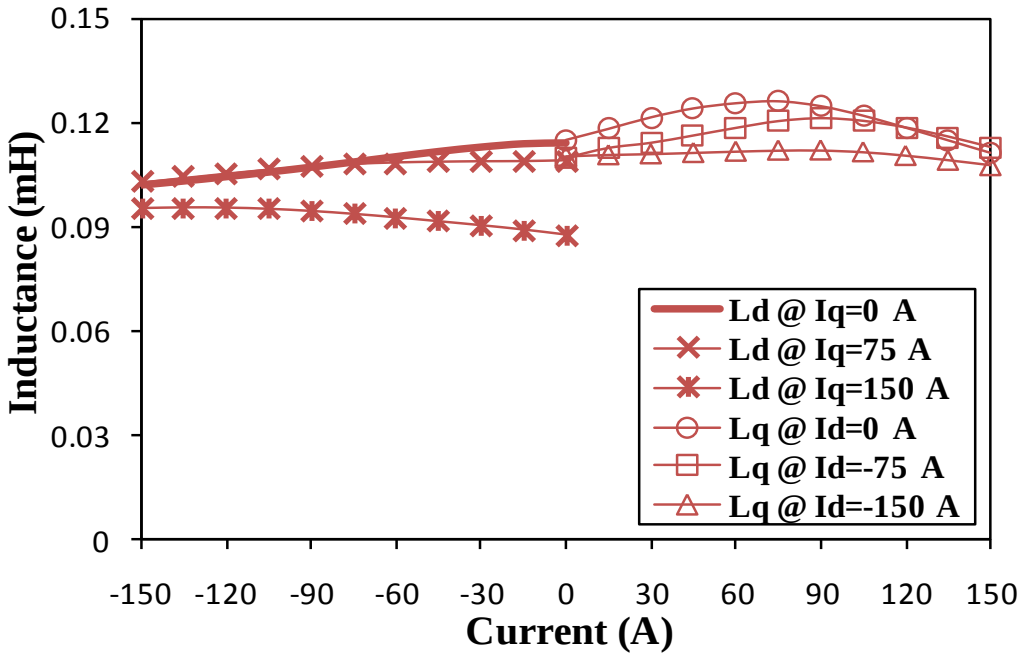

(c) Hybrid slot

Fig. 4.13 Variation of dq-axis inductances of machines having alternate slot openings.

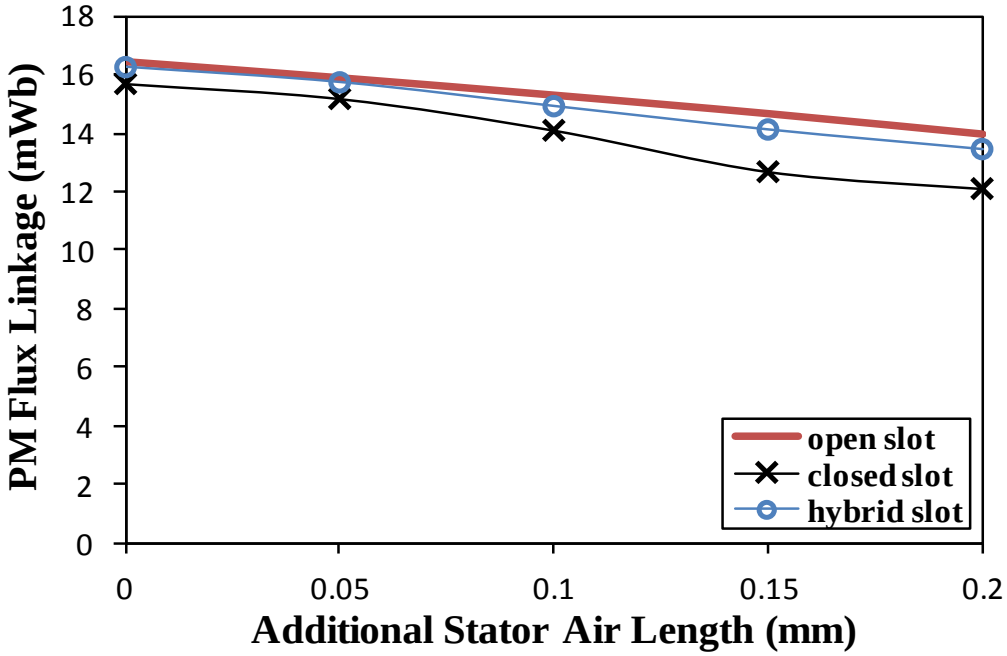

Fig. 4.14 Variation of PM flux linkage of machines having alternate slot openings and different uniform additional stator gaps at I_q=150A_{peak}.

4.3.4. Cogging Torque

As mentioned earlier, due to the manufacturing tolerances and limits there are additional stator gaps between the stator teeth and yoke. Therefore, the influence of such gaps on the cogging torque of machines having different slot openings is investigated in this section. As shown in Fig. 4.15, the sensitivity of the cogging torque against the additional gaps depends very much on the slot opening type. This is due to the different saturation levels in the tooth tips and different slot opening bridges, i.e. air, iron or hybrid (air + iron). In the machine with open slot, the cogging torque significantly increases for small additional stator gaps since larger additional gaps enlarge the effective air gap length, this results in extra flux leakage at the tooth tips. However, when the additional stator gaps are relatively large, e.g. 0.15 mm or larger, the increase in cogging torque becomes less significant, Fig. 4.15(a). This is because the tooth tips become gradually saturated, leading to a relatively lower extra flux leakage through these tips. This behaviour is different in the machine with closed slot, the cogging torque at 0.05 mm additional stator gaps is lower than its counterpart without gaps. However, it gradually increases for larger additional gaps, as shown in Fig. 4.15(b). Because the small increase in the effective air gap length causes more flux leakage through the slot iron bridges, this reduces the cogging torque. However, when the additional gaps are larger such bridges gradually become saturated, leading to more flux leakage through the tooth tips and thus larger cogging torque. The machine with hybrid slot combines the behaviours of the two foregoing machines, the cogging torque remains nearly the same when the additional stator gaps are increased to 0.05 mm, because the alternate slot iron bridges start to saturate. On the other hand, the cogging torque gradually increases when the additional gaps are larger, Fig. 4.15(c), since these bridges become saturated.

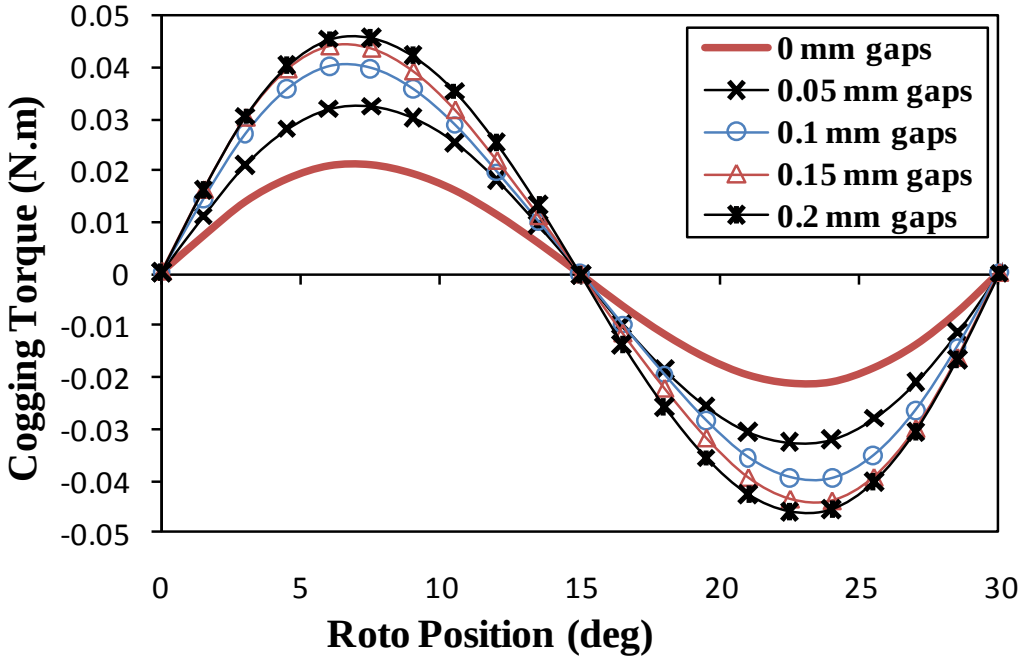

(a) Open slot

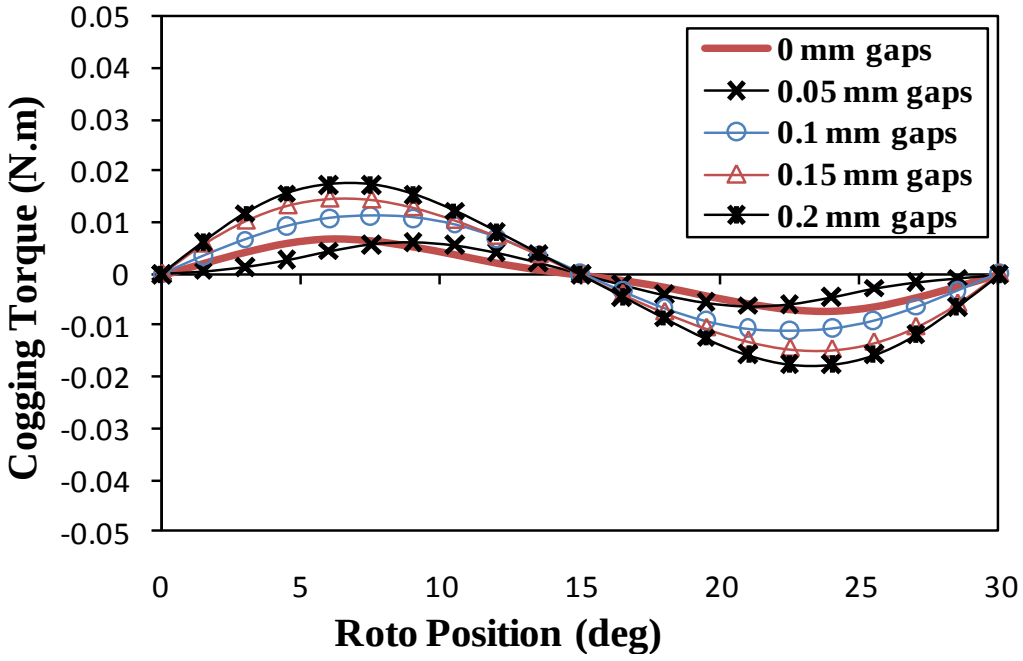

(b) Closed slot

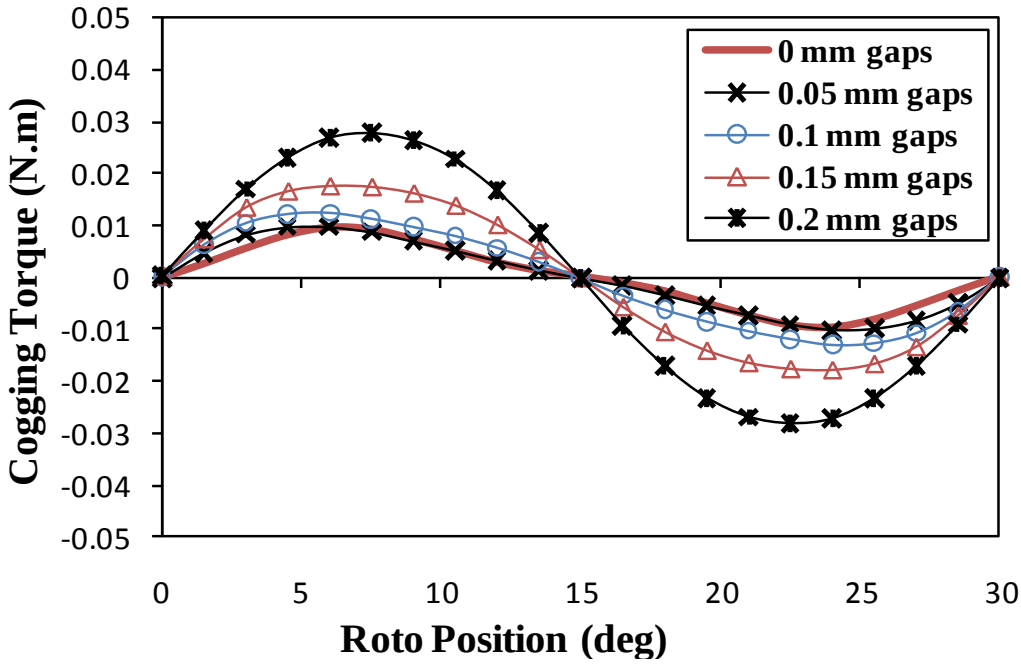

(c) Hybrid slot

Fig. 4.15 Variation of cogging torque of machines having alternate slot openings and different uniform additional stator gaps.

Furthermore, due to the manufacturing tolerance the additional stator gaps may be uneven. Indeed, in such construction, the dominant mechanical imperfections may include (a) “eccentricity" between the stator yoke and the teeth-assembly, and (b) oval stator yoke and/or teeth-assembly. Having one stator gap larger than the rest is a rapid way to simulate an eccentricity. Thus, the cogging torque is predicted for machines having different slot openings and non-uniform additional stator gaps, i.e. one gap is 0.1 mm while the rest are 0.05 mm, and compared with their counterparts of machines having uniform additional stator gaps, i.e. all gap are 0.05 mm, the comparison is given in Fig. 4.16. It shows that the presence of the uneven additional stator gaps causes a significant increase in the cogging torque magnitude even when the machines are skewed. In addition, the cogging torque periodicity has become 180 deg instead of 30 deg. This is because the non-uniform gaps result in more flux leakage through the tooth tips, and they also change the stator original geometrical symmetry, as deeply discussed and illustrated in Chapter 3. Furthermore, the influence of non-uniform additional stator gaps is different according to the slot opening materials, i.e. air, iron or hybrid. However, it is relatively more significant in the closed slot and hybrid slot designs. Again, this is due to the different saturation levels in the slot iron bridges and/or tooth tips.

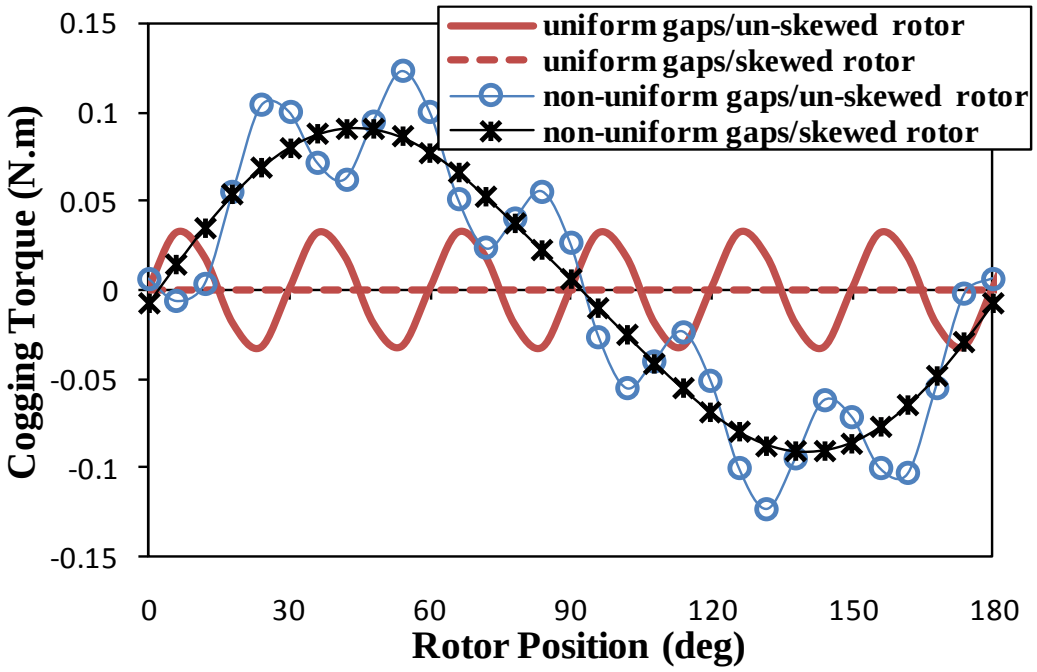

(a) Open slot

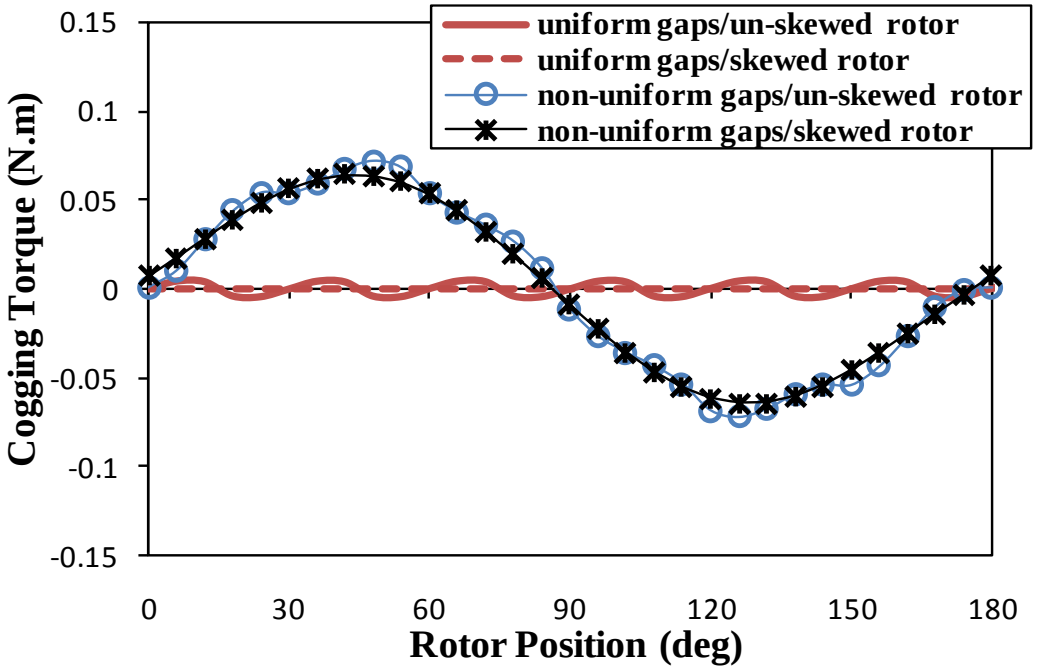

(b) Closed slot

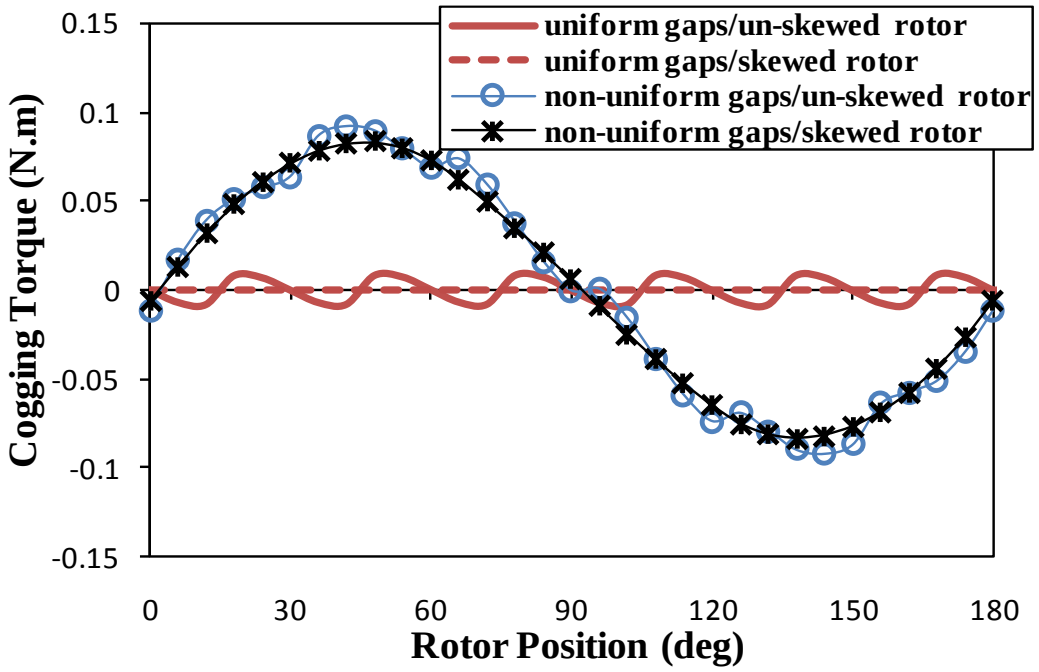

(c) Hybrid slot

Fig. 4.16 Comparison of predicted cogging torque of machines having uniform stator gaps of 0.05 mm, and non-uniform stator gaps (one gap is 0.1mm/the rest are 0.05 mm).

4.4. Experimental Validation

4.4.1. Torque-Speed Characteristics

The torque-speed characteristics of three prototypes, i.e. machine with closed slot and step skewed rotor, machine with hybrid slot and without skew and machine with hybrid slot and step skewed rotor, are measured and compared with the predicted counterparts with and without cross-coupling consideration in Fig. 4.17. It further confirms that the influence of cross-coupling largely depends on the slot opening type and it is more significant in the machine with closed slot. Furthermore, it also shows that the closed slot design results in a relatively large performance reduction. In addition, the influence of the rotor step skewing on the torque-speed characteristics is negligible.

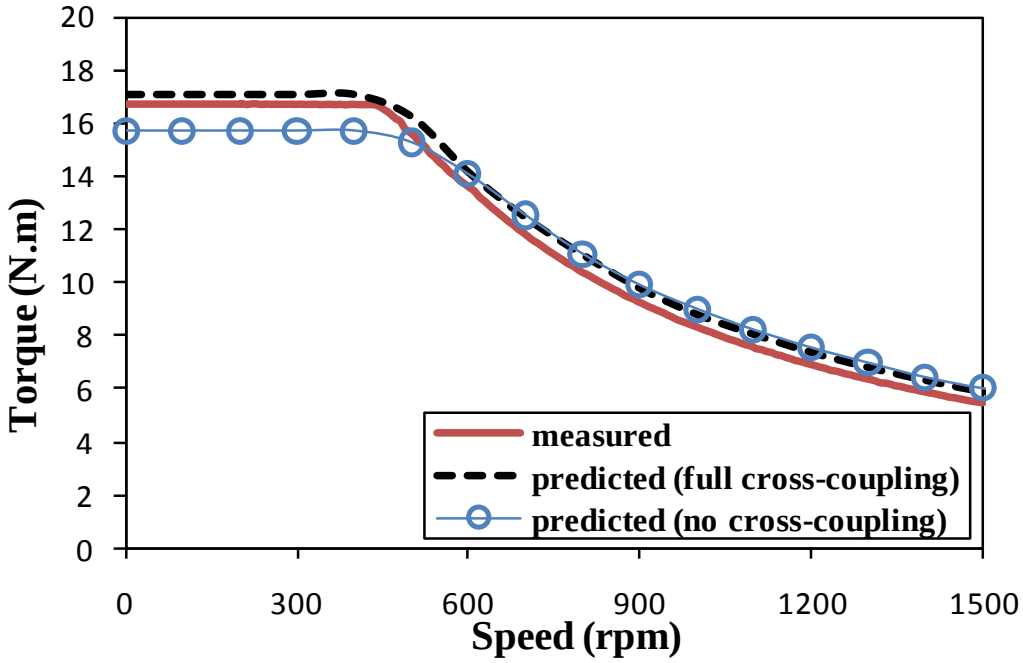

(a) Closed slot with step skewed rotor

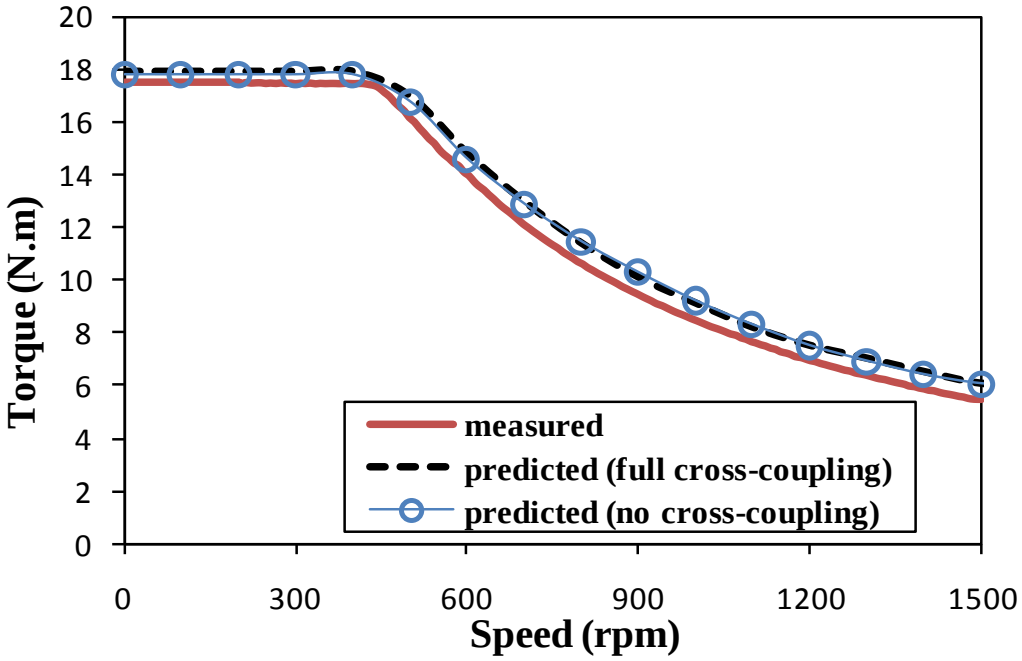

(b) Hybrid slot without skew

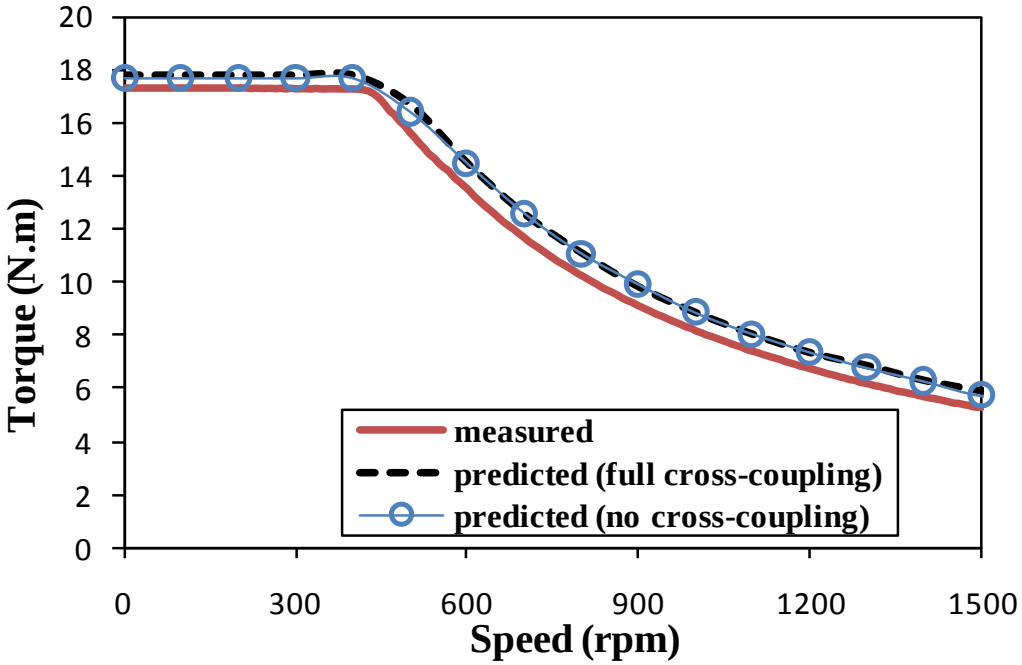

(c) Hybrid slot with step skewed rotor

Fig. 4.17 Comparison of measured and predicted torque-speed characteristics of machines having alternate slot openings.

4.4.2. Cogging Torque

The cogging torque of the prototype machines has been measured and compared with the predicted cogging torque when the additional stator gaps are uniform, i.e. all gaps are 0.05 mm, in Fig. 4.18. For all prototype machines the measured cogging torque is significantly larger and also its periodicity has become 180 deg rather than 30 deg. This phenomenon is the same as the machine with non-uniform additional stator gaps, Fig. 4.16. Therefore, the large measured cogging torque is most likely due to the presence of non-uniform additional stator gaps. For further illustrations, the cogging torque of the prototype machines with non-uniform additional stator gaps, i.e. one gap is 0.06 mm and the rest are 0.05 mm, have been predicted and also plotted in Fig. 4.18. For all prototype machines, there is a good agreement between the measured cogging torque and its predicted counterpart when the additional stator gaps are non-uniform. Thus, the significantly large measured cogging torque is most likely due to the additional stator gaps non-uniformity, which in turn is due to the manufacturing tolerance, although the non-uniformity can be much more complicated in practice. However, this non-uniformity has no noticeable influence on the torque-speed characteristics, as confirmed in Fig. 4.17.

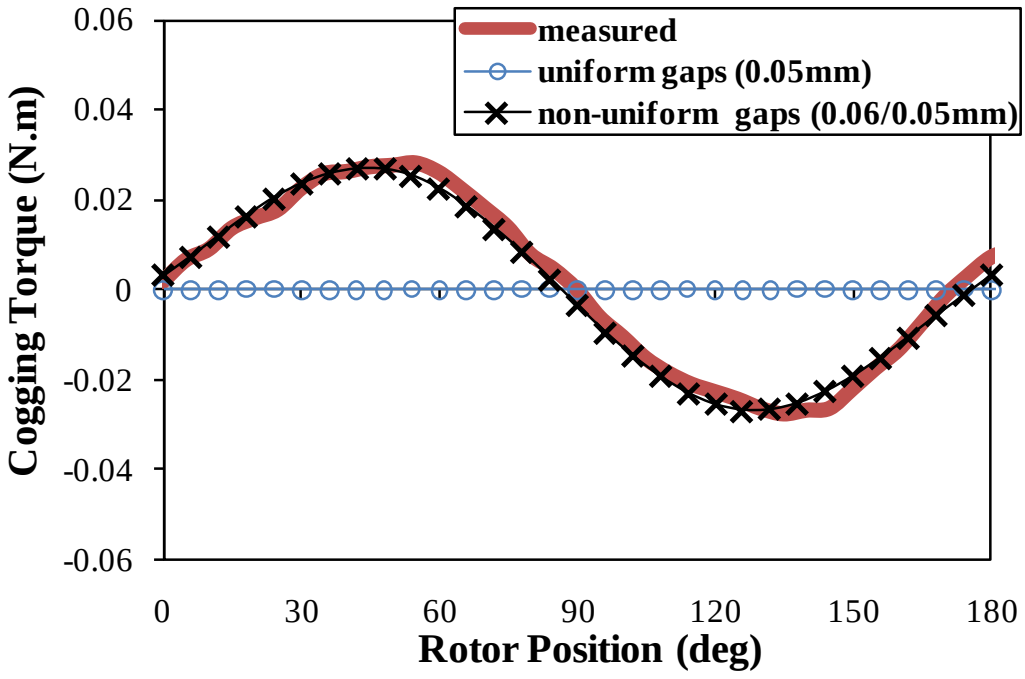

(a) Closed slot with rotor step skew

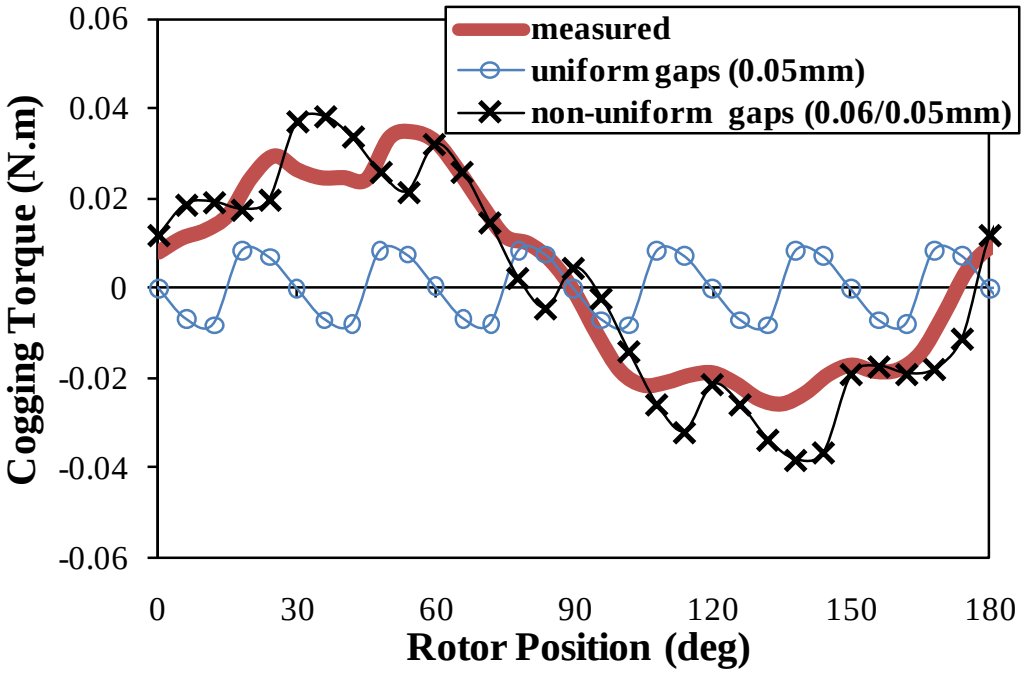

(b) Hybrid slot without skew

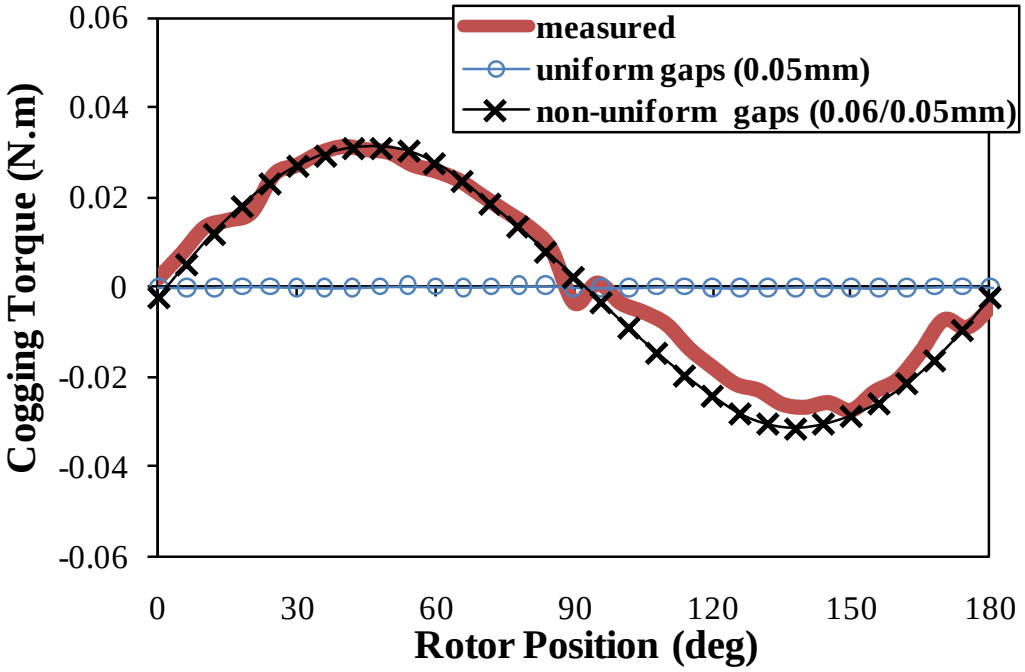

(c) Hybrid slot with rotor step skew

Fig. 4.18 Comparison of measured and predicted cogging torque of machines having uniform stator gaps of 0.05 mm, and non-uniform stator gaps (one gap is 0.06 mm/the rest are 0.05 mm).

4.5. Conclusions

This paper has investigated the influence of alternate slot openings, i.e. open, closed and hybrid slot, on the torque-speed characteristics and cogging torque of the fractional-slot IPM machines. The investigations have accounted for the influence of such slot openings on the cross-coupling level and manufacturing limitations and tolerance. In addition, a 2D FE technique to analyse the machine with hybrid slot has been proposed and examined. The machine with closed slot, which exhibits the lowest electromagnetic performance due to the relatively larger flux leakage through the slot iron bridges, exhibits also a significantly large magnetic cross-coupling level comparing with the other two machines. However, for all machines the consideration of the magnetic cross-coupling influence is more important on the PM flux linkage rather than the dq-axis inductances. The machine with hybrid slot generates nearly the same torque as the machine with open slot, while its cogging torque is very similar to the machine with closed slot. On the other hand, the cogging torque sensitivity against the additional stator gaps strongly depends on the slot opening materials. Furthermore, for all machines, the non-uniformity of such gaps causes a significant increase in the cogging torque and also diminishes the effectiveness of rotor skewing. However, this influence is comparatively more significant in the closed slot and hybrid slot designs.

Chapter 5: Influence of Electric Loading and Magnetic Saturation on Cogging Torque, Back-EMF and Torque Ripple of PM Machines

5.1. Introduction

As mentioned before, due to high torque density and efficiency, the permanent magnet (PM) machines are increasingly used in industrial and commercial applications for all power ranges. However, PM machines also exhibit some drawbacks, such as cogging torque and torque ripple, which have been extensively analyzed and investigated in literature, while many techniques either via machine design or drive control have been proposed to suppress them [35, 38, 40, 41, 132, 141-149]. This reflects that the output torque smoothness is an important criterion for some applications, such as power steering systems. Assuming the drive current waveform is pure sinusoidal and the machine is perfectly manufactured, i.e. no rotor or stator eccentricity and no manufacturing defects, the output torque ripple of PM machines is due to:

a) cogging torque;
b) electromagnetic ripple due to back-emf waveform harmonics;
c) reluctance ripple due to inductance variations.

Furthermore, it has been stated that the magnetic saturation is also a source of torque ripple [141, 142]. In fact, the torque ripple is larger when the magnet circuit is saturated, as the magnetic saturation enlarges the original sources of torque ripple, as will be further proved in this chapter.

The rotor or stator skew is a common technique and widely utilised to minimise the cogging torque and also to reduce the back-emf waveform harmonics, thus to decrease the torque ripple [35, 143-145]. Theoretically, due to the repetition and nature of the cogging torque waveform, it can be completely eliminated if the machine is skewed by one cogging torque period [41]. This rule is still effective even when the magnetic saturation influence is fully considered, i.e. including the influence of electric loading. However, the optimal skew angle should be the cogging torque period under the load conditions (rather than one slot pitch), as will be also further illustrated in this chapter.

In the previous researches, the cogging torque, back-emf harmonics and the effectiveness of skew technique have been analyzed and studied under open-circuit conditions. However, although both the cogging torque and back-emf waveform are usually considered as open-circuit characteristics, the associated torque ripples are affected by the electric load. Therefore, this will be the research subject of this chapter, which contains the calculations and analyses of the cogging torque and back-emf waveforms and harmonics as well as the torque ripple of PM machines having un-skewed and step skewed rotors accounting for the load conditions. In order to carry out such calculations, the FP technique is employed. As mentioned in the first and second chapters, this technique has been illustrated and utilised to account for the magnetic cross-coupling saturation between d- and q-axis parameters as well as to segregate the PM and reluctance torque components in [20, 54, 55, 66, 67]. It can be summarised as follows, the machine is firstly solved for the FE model under load conditions, and then the permeability of each element is fixed and used to resolve the model linearly without electric loading, similar to the conventional open-circuit. In this case, the "open-circuit" characteristics can be calculated accounting for the influence of electric loading, i.e. magnetic saturation on load. The analysis method and obtained results are confirmed and validated by the experimental results of the prototype machine, which is illustrated in Fig. 5.1 and Table 2.1.

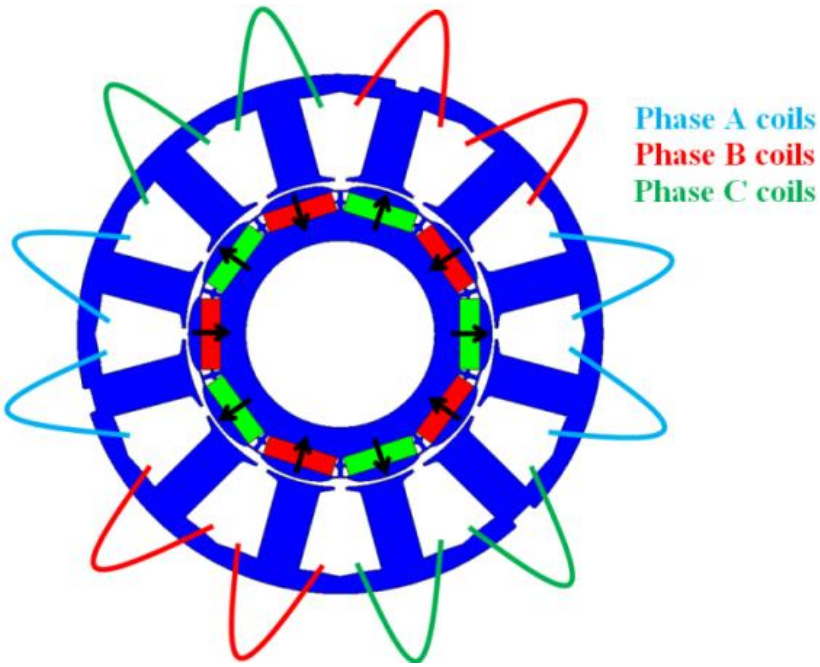

Fig. 5.1 Lamination cross section and phase winding layout of 10-pole/12 slot prototype machine (this is the same as Fig. 2.1).

5.2. Cogging Torque

5.2.1. Open-Circuit

The analyzed prototype machine, which is designed to be used in a power steering system, has relatively small cogging torque, Fig. 2, because it has a 10-pole/12-slot combination (fractional-slot), optimal pole-arc to pole-pitch ratio and a shaped rotor, [35, 38, 41, 132, 143-147, 150]. However, its rotor is still step skewed by 4 steps of 7.5 electrical degrees, i.e. one slot pitch, to guarantee that the output torque smoothness requirements are still satisfied even with the influence of manufacturing tolerances. Theoretically, the cogging torque of the step skewed machine is completely eliminated, as shown in Fig. 5.2.

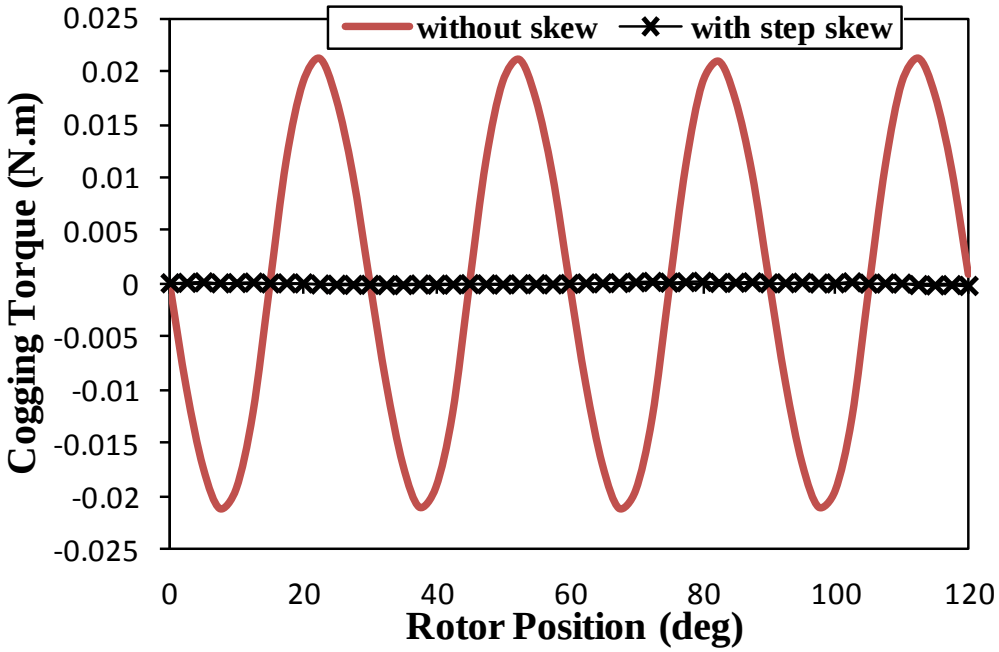

Fig. 5.2 Cogging torque waveforms of analysed 10-pole/12-slot machine without and with rotor step skew.

5.2.2. Influence of Load and Magnetic Saturation

Conventionally, the cogging torque is considered to be electric loading independent. However, if the machine iron is saturated, then the cogging torque is most likely to be influenced. In order to account for this condition, the machine model is solved by a FP FE model under load conditions, and then the permeability of each element is stored and used to resolve the model linearly without electric loading, i.e. PMs only. In this case the obtained cogging torque includes the influence of the magnetic saturation due to electric loading

(which is designated as full magnetic saturation in this paper). Fig. 5.3 compares the cogging torque of 10 pole-12 slot machines having un-skewed rotors without/with electric loading influence. It shows that the actual cogging torque magnitude, i.e. with electric loading influence, is significantly larger than the open-circuit cogging torque, i.e. without electric loading influence. In the prototype machine, the electric loading increases the magnetic saturation level in the stator teeth, which results in more flux leakage through the tooth tips, which in turn leads to larger cogging torque. In addition, when the magnetic saturation influence is fully considered the cogging torque periodicity becomes 60 electrical degrees, i.e. the same as the total load torque ripple. In order to further demonstrate such behaviour, the normal and tangential open-circuit air gap flux density components are investigated. Due to the electric loading, the machine magnetic circuit becomes more saturated, thus the machine magnetic reluctance becomes larger. This results in less flux linkage through stator tooth bodies and more flux leakage through stator tooth tips. Consequently, the actual radial component of open-circuit air gap flux density becomes slightly lower and more distorted, Fig. 5.4 (a) and Fig. 5.4 (b). For the same reason, the actual tangential component of open-circuit air gap flux density increases and also becomes more distorted, Fig. 5.4 (c) and Fig. 5.4 (d). As a percentage, the increasing of the actual tangential component of air gap flux density is larger than the decreasing of the actual radial component of air gap flux density. Thus, the multiplication of the radial and tangential open-circuit air gap flux density harmonics when the magnetic saturation is fully taken into account is larger than its counterpart when the electric loading influence is neglected, Fig. 5.5. This illustrates the reason for larger actual cogging torque, which is directly proportional to the radial and tangential harmonics multiplication [136]. Furthermore, the increase of actual cogging torque magnitude depends on the magnetic saturation level, which in turn is determined by the electric loading value, Fig. 5.6 (a). However, the actual cogging torque periodicity becomes 60 electrical degrees no matter whatever the electric loading value. The prototype machine is skewed by 30 electrical degrees, which is the optimal skew angle since it is the open-circuit cogging torque period [41]. However, the periodicity variation reduces the effectiveness of skew technique on the actual cogging torque, Fig. 5.6 (b). On the other hand, if the skew angle is adjusted to be the same as the actual cogging torque period, i.e. 60 electrical degrees, the effectiveness of skew technique is maintained, as illustrated in Fig. 5.6 (c). It can be concluded that the optimal skew angle should be one period of the actual cogging torque with the influence of electric loading (load) rather than the open-circuit counterpart.

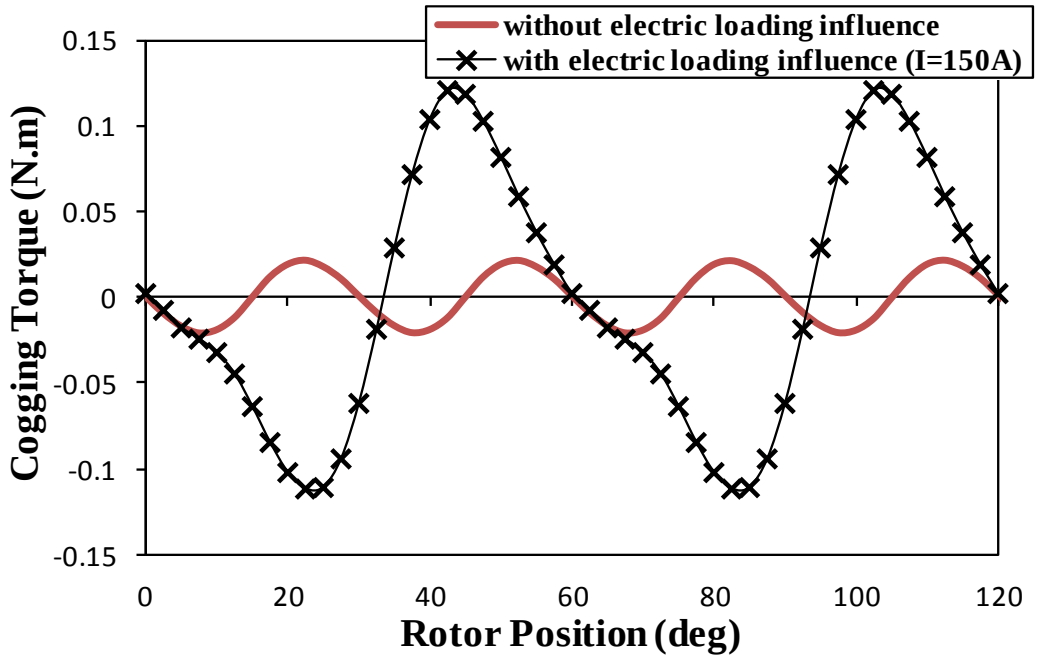

(a) Waveforms

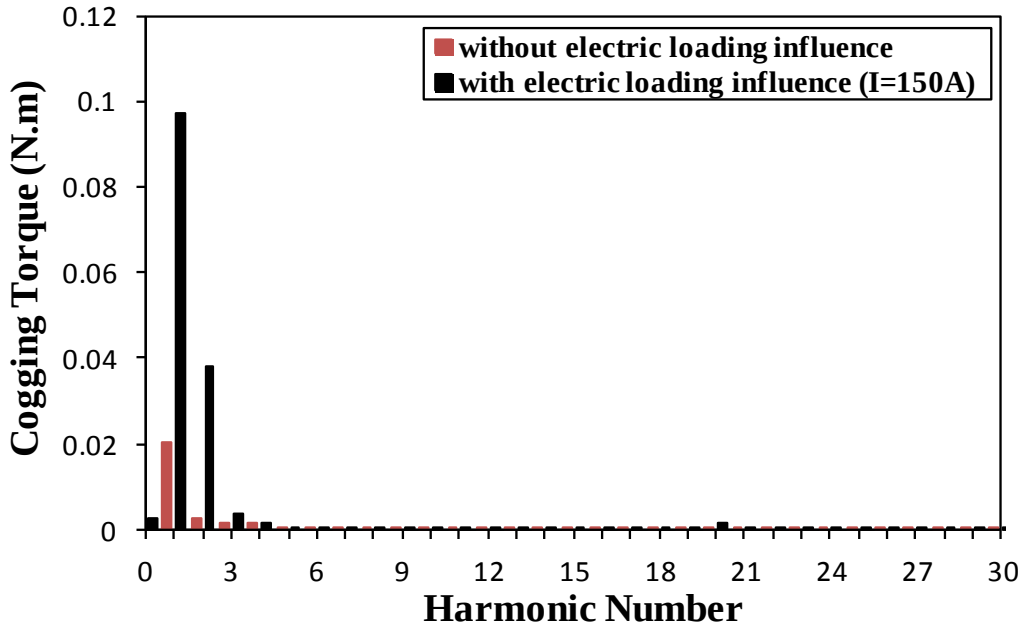

(b) Harmonics

Fig. 5.3 Comparison of cogging torque wavforms and harmonics without/ with accounting for electric loading influence, at 150 A_{peak} phase current.

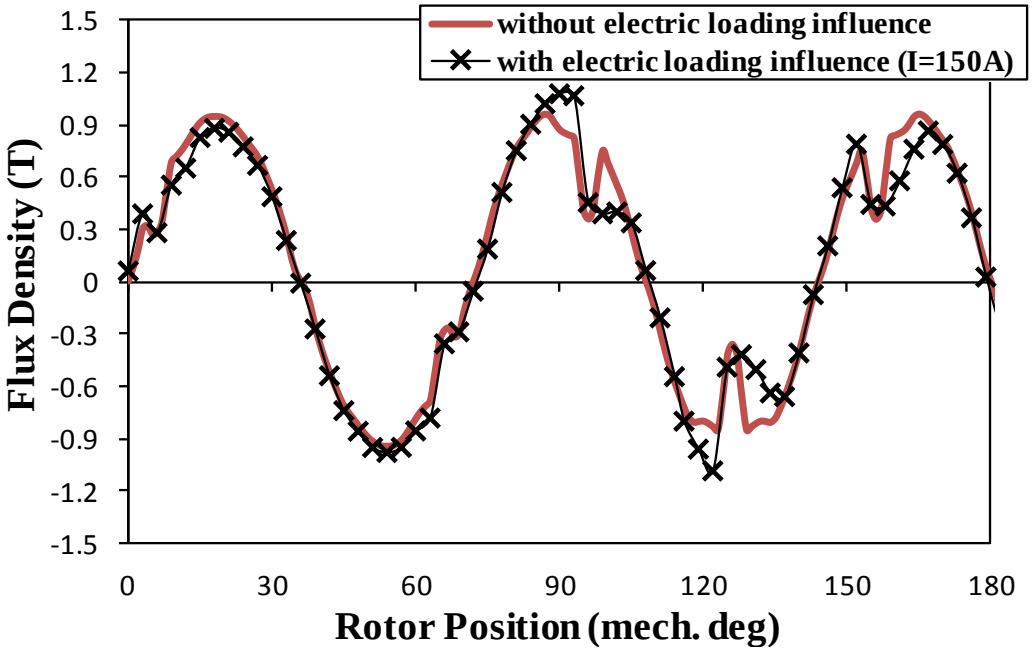

(a) Radial flux density waveforms

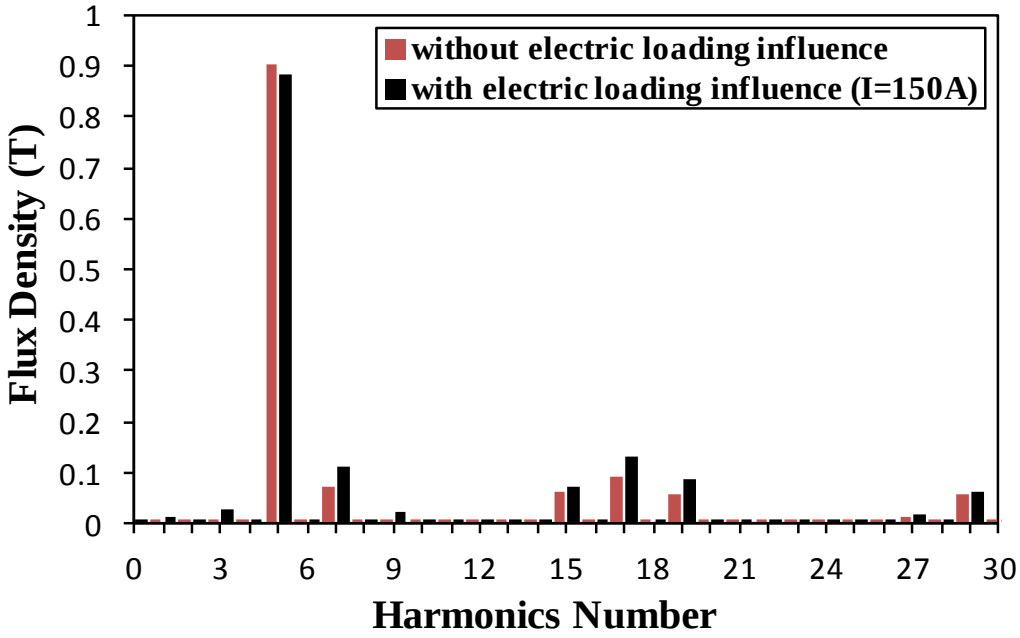

(b) Radial flux density harmonics

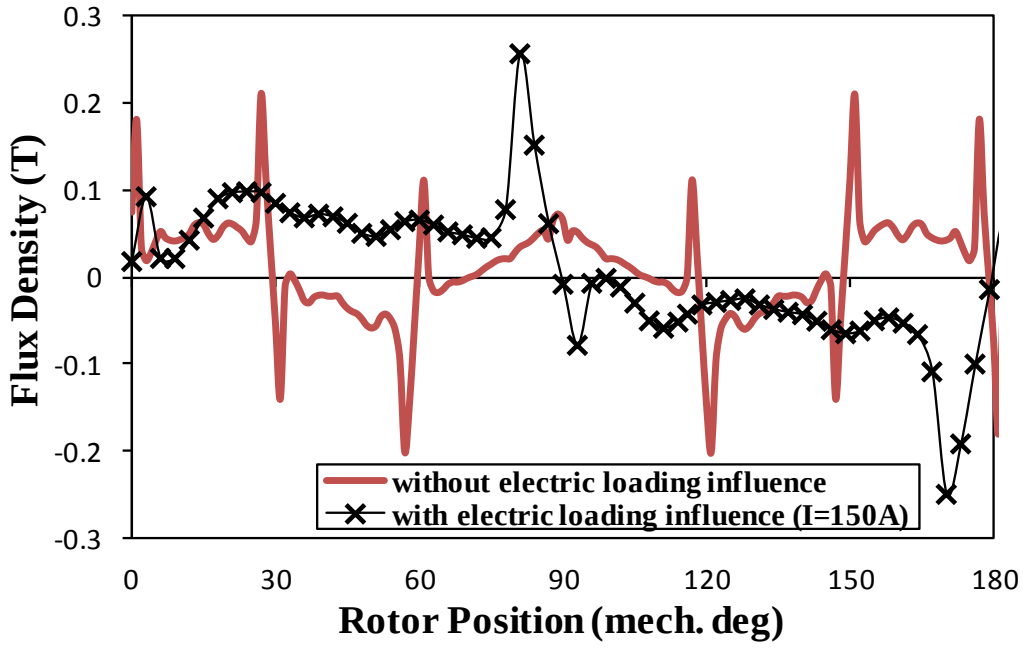

(c) Tangential flux density waveforms

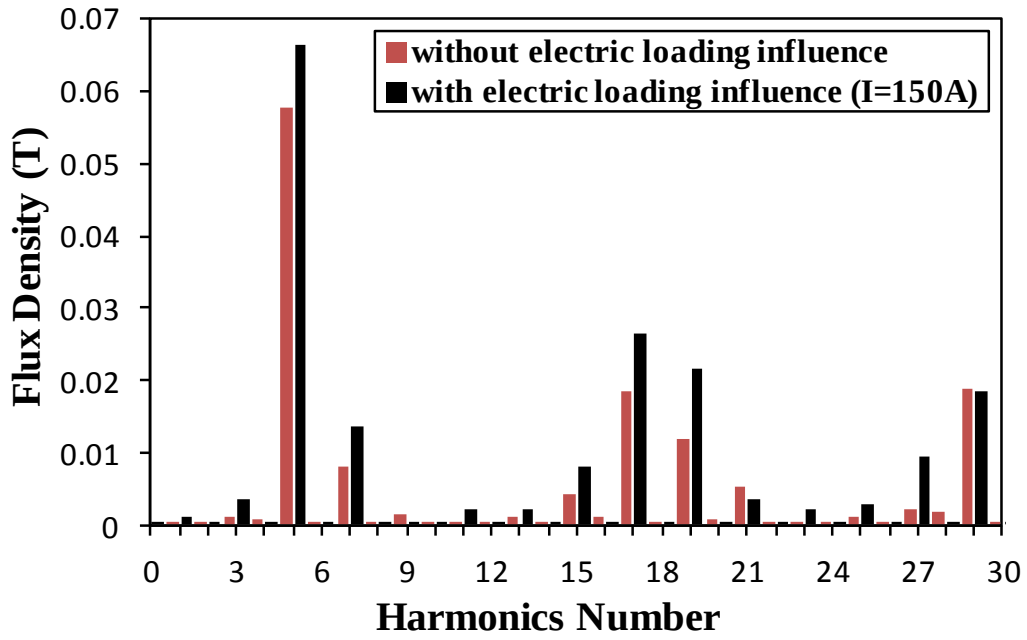

(d) Tangential flux density harmonics

Fig. 5.4 Comparison of radial and tangential open-circuit air gap flux density waveforms and harmonics without/with electric loading influence, at 150 A_{peak} phase current.

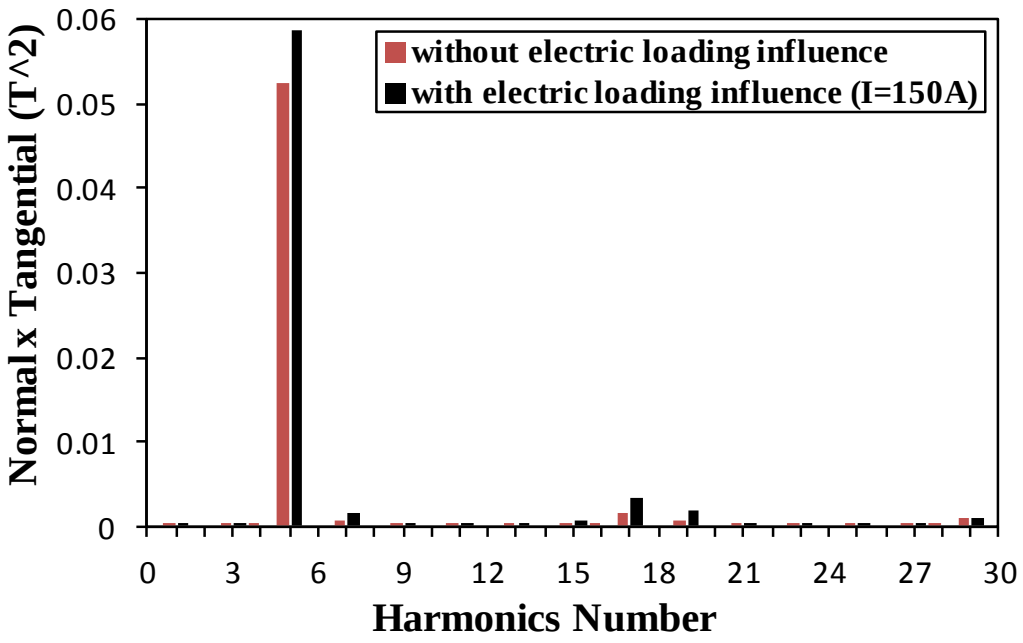

Fig. 5.5 Multiplication of radial and tangential harmonics of open-circuit air gap flux density without/with electric loading influence, at 150 A_{peak} phase current.

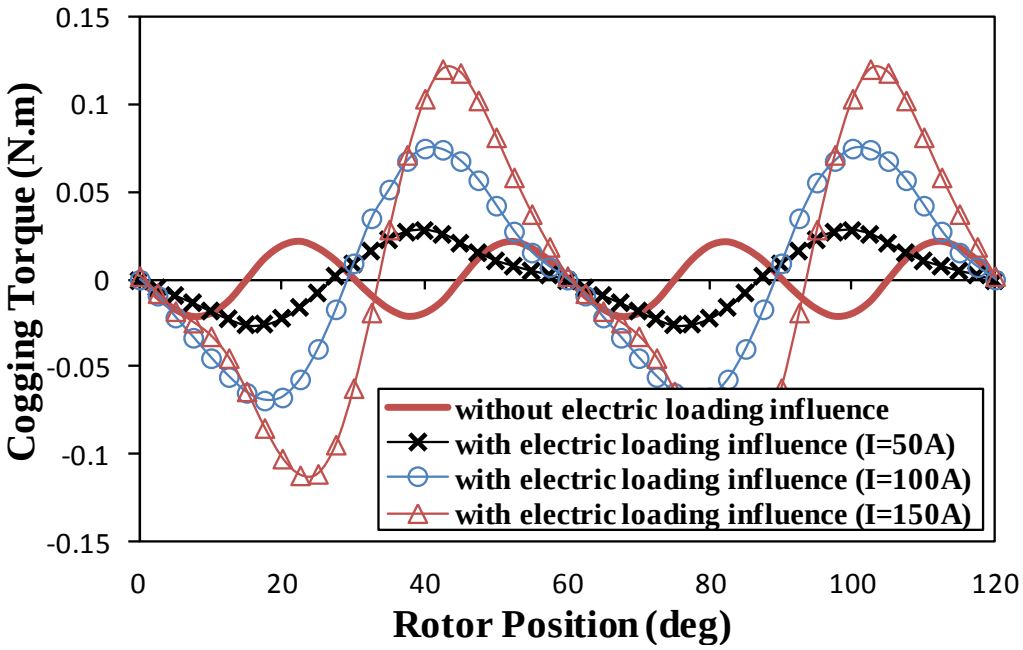

(a) Without rotor step skew

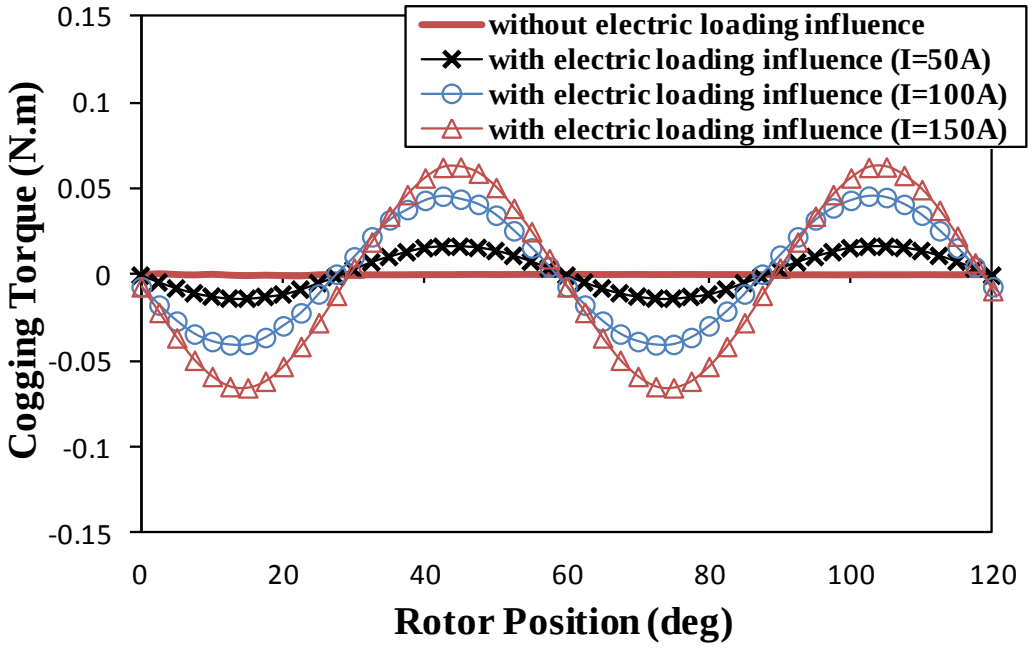

(b) With 30 electrical degree rotor step skew angle

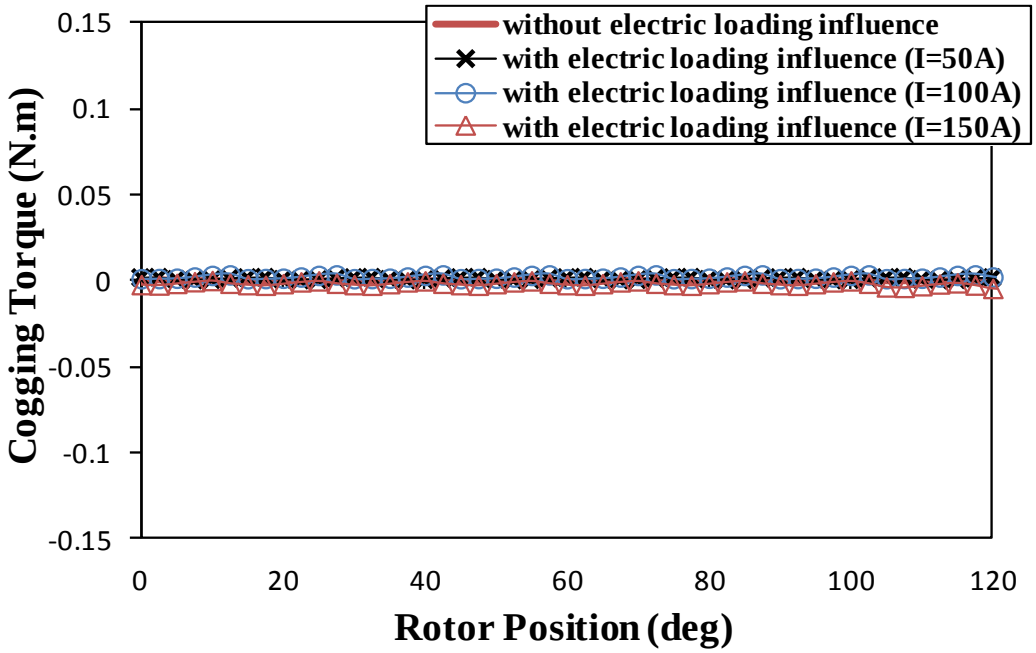

(c) With 60 electrical degree rotor step skew angle

Fig. 5.6 Cogging torque wavforms of machines having unskewed and step skewed rotors without/with accounting for electric loading influence, at different phase currents.

5.3. Back-EMF Waveform

The open-circuit back-emf waveform of the un-skewed machine is almost sinusoidal, Fig. 5.7 (a), thus it contains very small harmonics, Fig. 5.8 (a). Therefore, the electromagnetic torque ripple, which is due to the multiplication of sinusoidal current waveform with the back-emf harmonics, is relatively small, as shown in Fig. 5.9 (a). However, due to the influence of the electric loading on the "open-circuit" air gap flux density, Fig. 5.4 (a), the actual back-emf waveform becomes more distorted comparing with its open-circuit counterpart. Such extra distortion results in more back-emf harmonics, thus larger electromagnetic torque ripple. In order to illustrate this and also to investigate the influence of different rotor step skew angles on back-emf distortions. The back-emf waveforms, harmonics and electromagnetic torque ripple have been calculated for different machines having un-skewed and 30 and 60 electrical degree step skewed rotors without/with electric loading influence. As expected, when the magnetic saturation is fully considered, the back-emf waveform contains more harmonics, Fig. 5.7 (a), and Fig. 5.8 (a), thus larger electromagnetic torque ripple is produced, Fig. 9(a). The 30 degree skew angle, which is the same as the open-circuit cogging torque period, results in relatively more sinusoidal back-emf waveform, Fig. 5.7 (b), and less harmonics, Fig. 5.8 (b), thus lower electromagnetic torque ripple, Fig. 5.9 (b). However, for 60 degree skew angle, which is the actual cogging torque period on load, the back-emf waveform is significantly improved, Fig. 5.7 (c) and Fig. 5.8 (c), consequently this leads to a significant reduction in the electromagnetic torque ripple, Fig. 5.9 (c).

It is well known that the electromagnetic torque of the PM machine is the multiplication of the PM flux linkage and q-axis current. Therefore, by equivalence, the electromagnetic torque ripple can be also represented by the multiplication of the PM flux linkage variations and q-axis current. The influence of electric loading and rotor skew on the PM flux linkage is illustrated in Fig. 5.10. It shows that the actual PM flux linkage variations, i.e. with full magnetic saturation, are relatively larger comparing with their open-circuit counterpart, as shown in Fig. 5.10 (a) and Fig. 5.10 (b). These variations are reduced to nearly half when the machine is skewed by 30 electrical degrees, as illustrated in Fig. 5.10 (c) and Fig. 5.10 (d), but it is significantly minimized when the skew angle is 60 electrical degrees, Fig. 5.10 (e) and Fig. 5.10 (f). This further illustrates the influence of skew angle on the electromagnetic torque ripple reduction. It is worth mentioning that the skew technique can result in a slight performance reduction. In addition, a larger skew angle leads to a larger reduction. In the

analyzed prototype machine, the 30 degree skew angle causes around 2% reduction in the back-emf waveform (PM flux linkage), but the 60 degree angle increases the reduction to about 4 %, as illustrated in Fig. 5.11. However, this skew is still desirable, since it eliminates the actual cogging torque and reduces the actual electromagnetic torque ripple by more than 75%. Consequently, the torque ripple will be significantly minimized.

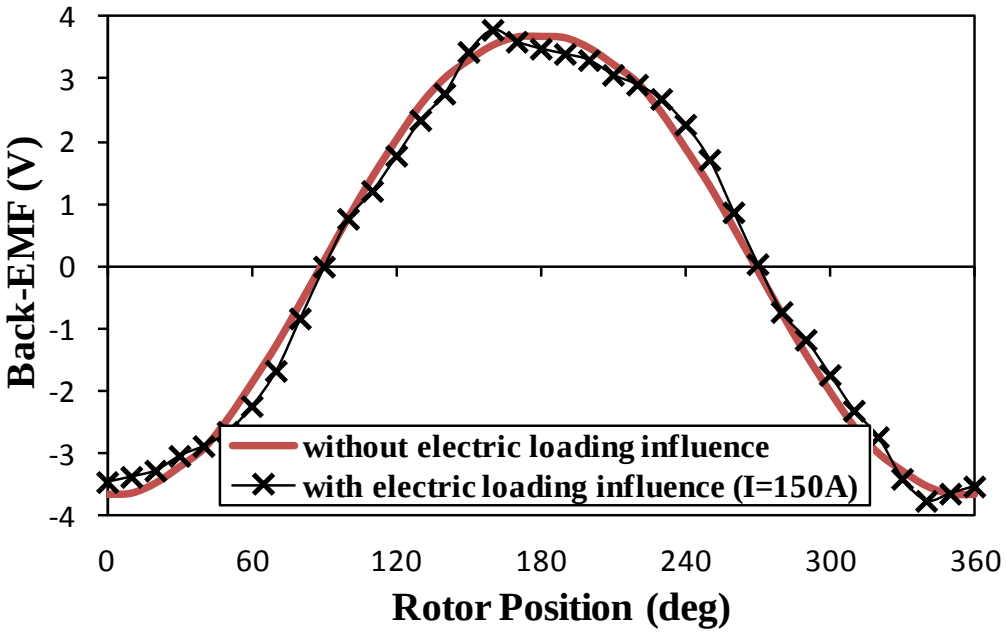

(a) Without rotor step skew

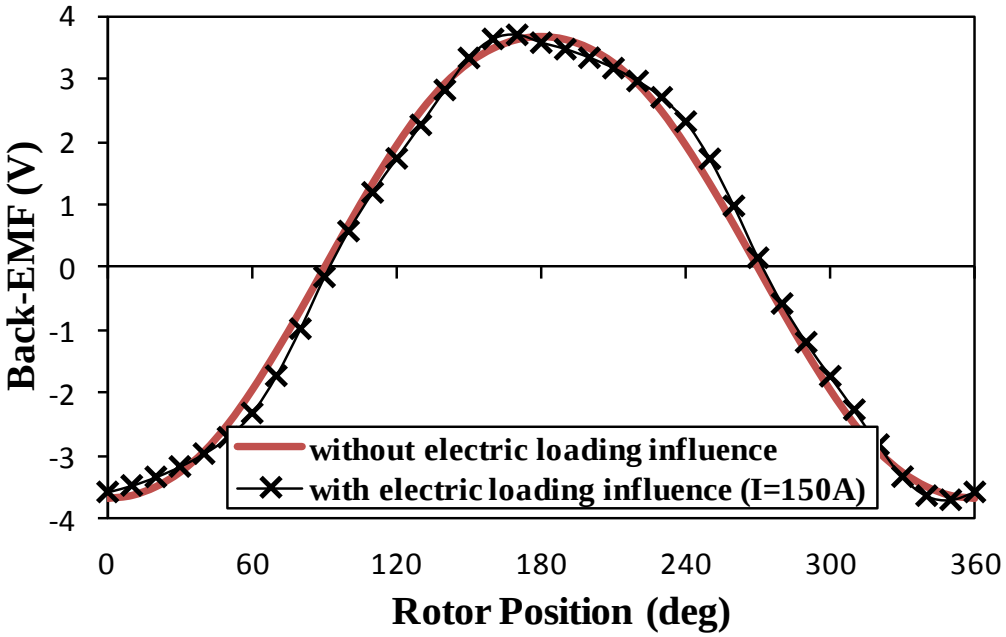

(b) With 30 electrical degree rotor step skew angle

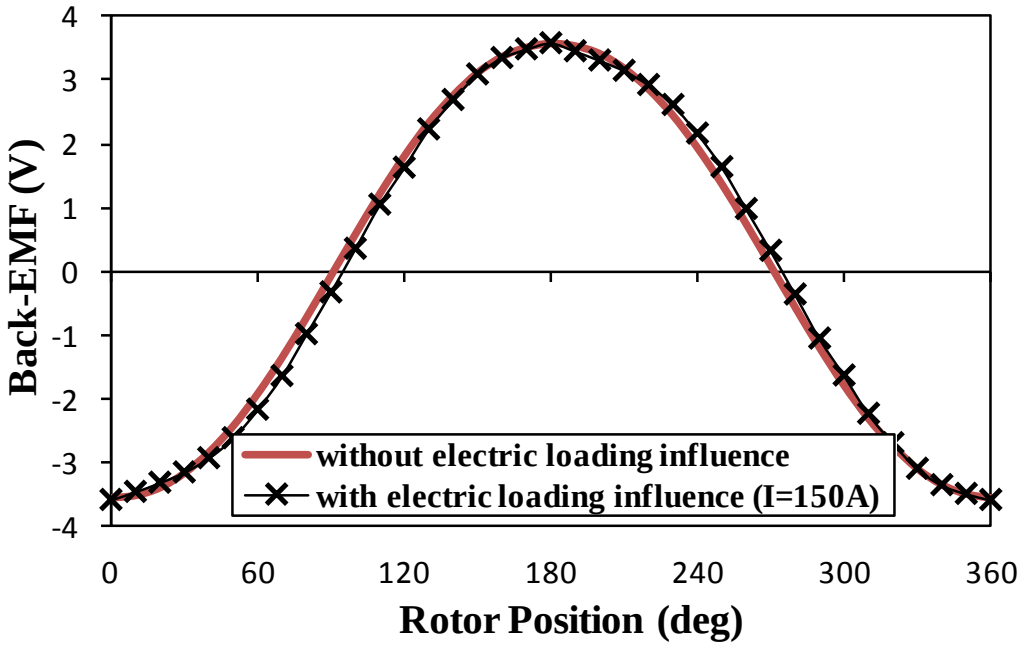

(c) With 60 electrical degree rotor step skew angle

Fig. 5.7 Comparison of back-emf wavforms of machines having un-skewed and step skewed rotors without/with electric loading influence, at 150 A_{peak} phase current.

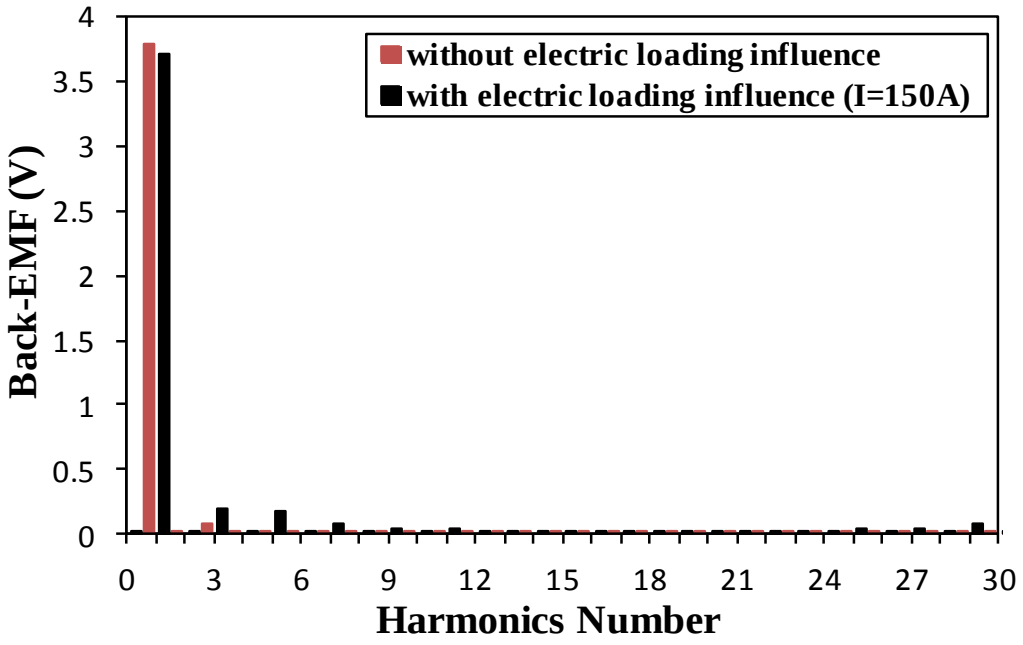

(a) Without rotor step skew

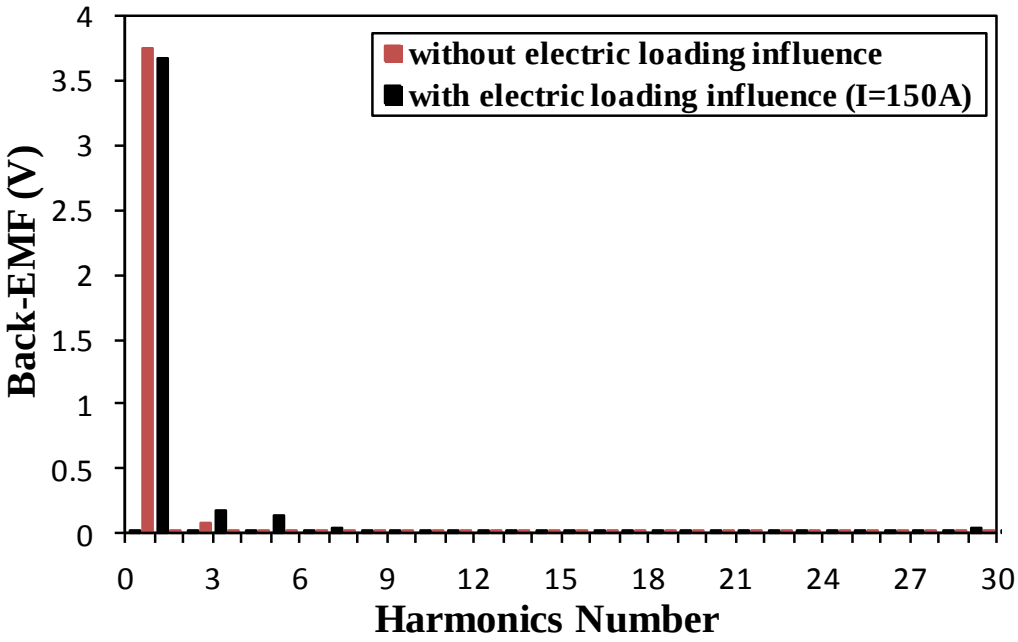

(b) With 30 electrical degree rotor step skew angle

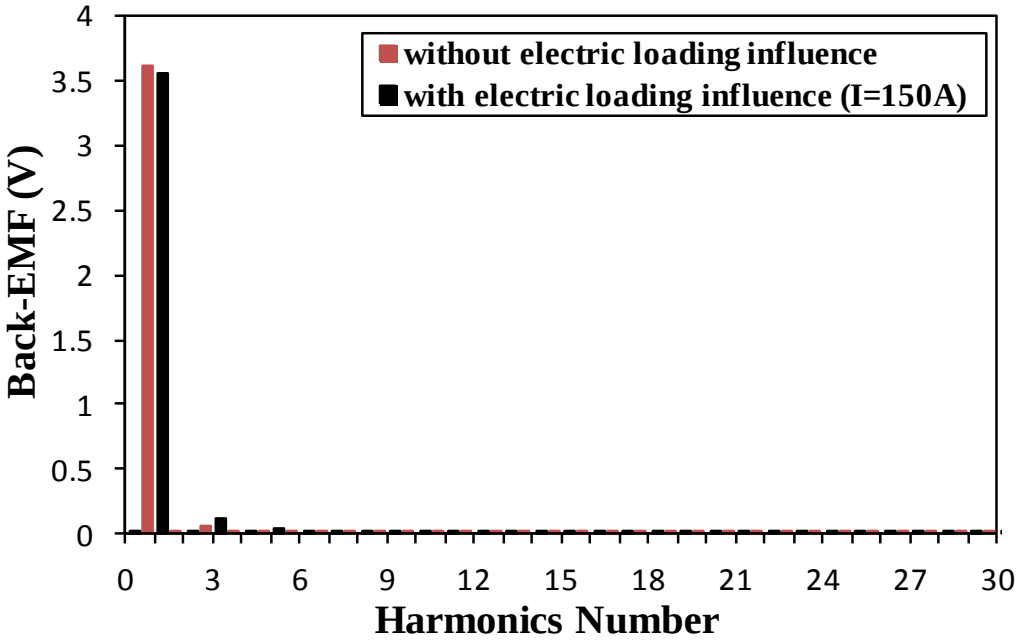

(c) With 60 electrical degree rotor step skew angle

Fig. 5.8 Comparison of back-emf harmonics of machines having un-skewed and step skewed rotors without/with electric loading influence, at 150 A_{peak} phase current.

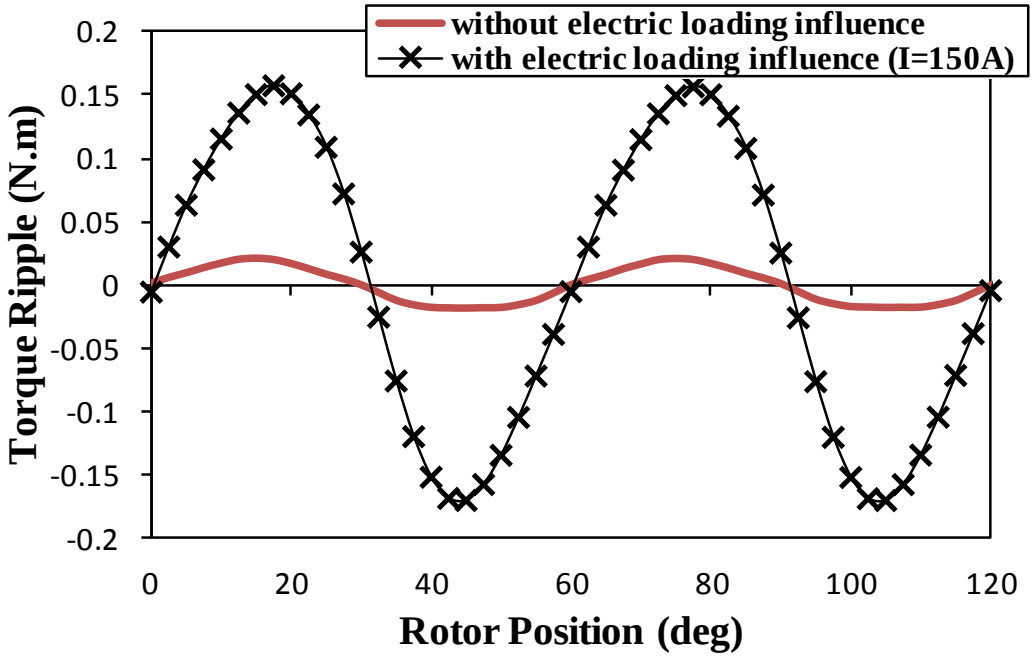

(a) Without rotor step skew

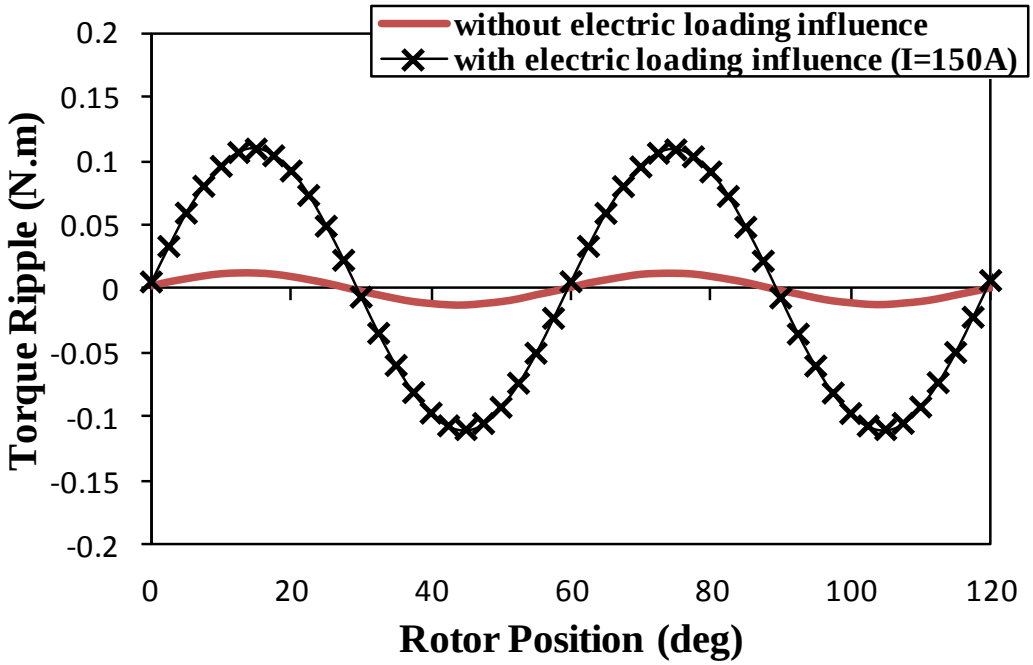

(b) With 30 electrical degree rotor step skew angle

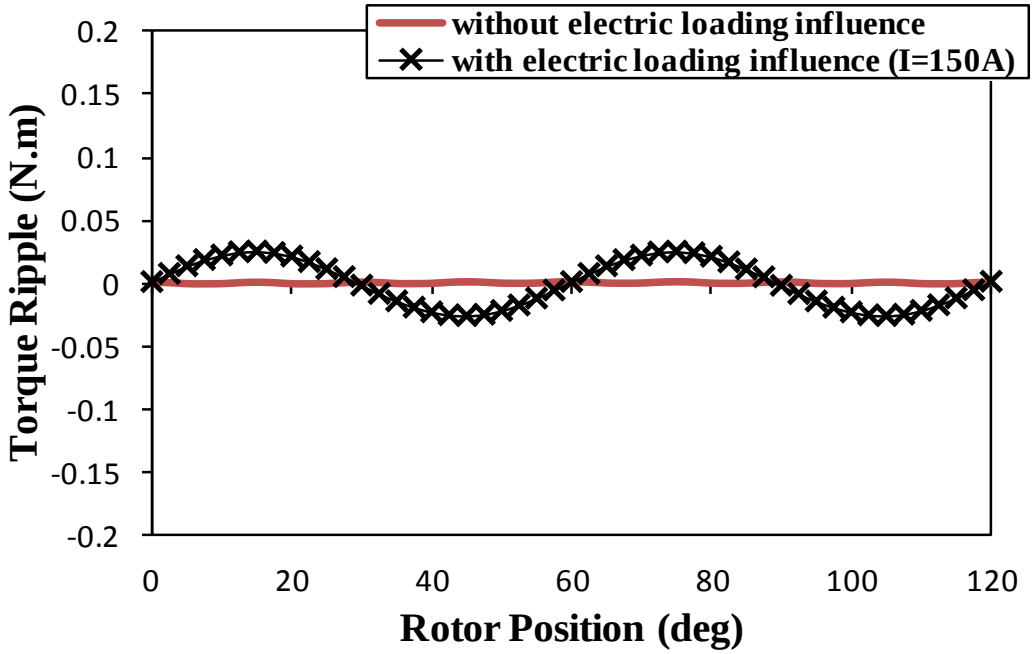

(c) With 60 electrical degree rotor step skew angle

Fig. 5.9 Comparison of electromagnitic torque ripples of machines having unskewed and step skewed rotors without/with electric loading influence, at 150 A_{peak} phase current.

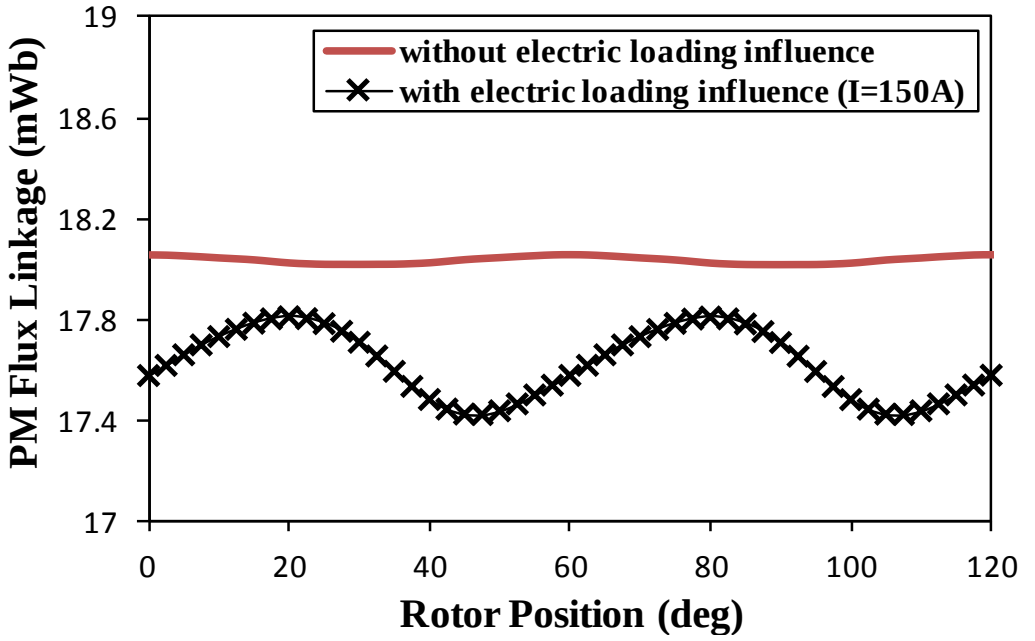

(a) Waveforms, without rotor step skew

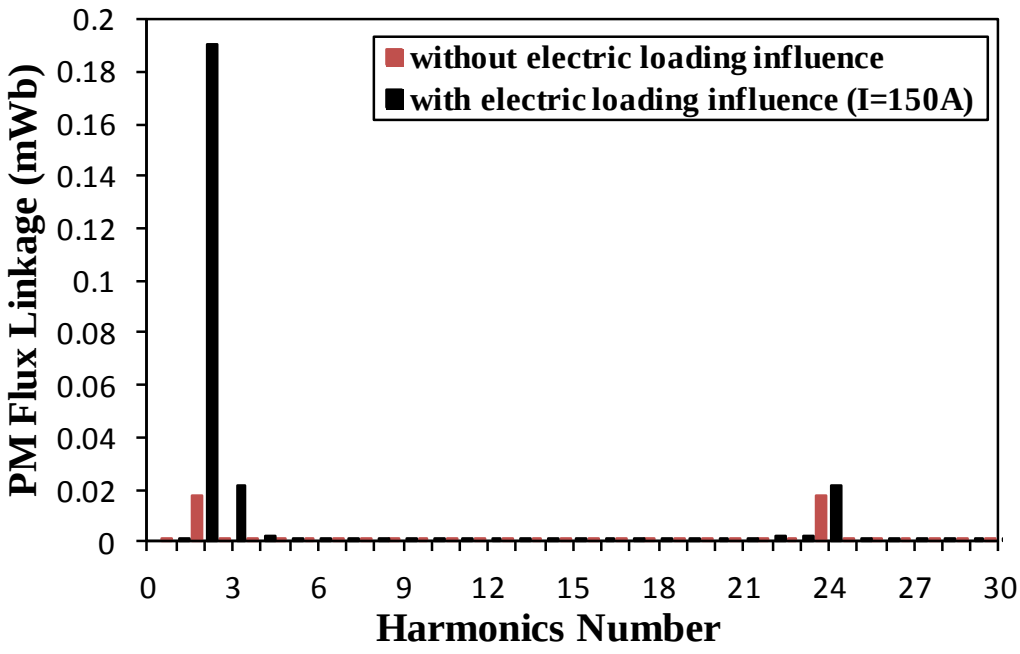

(b) Harmonics, without rotor step skew

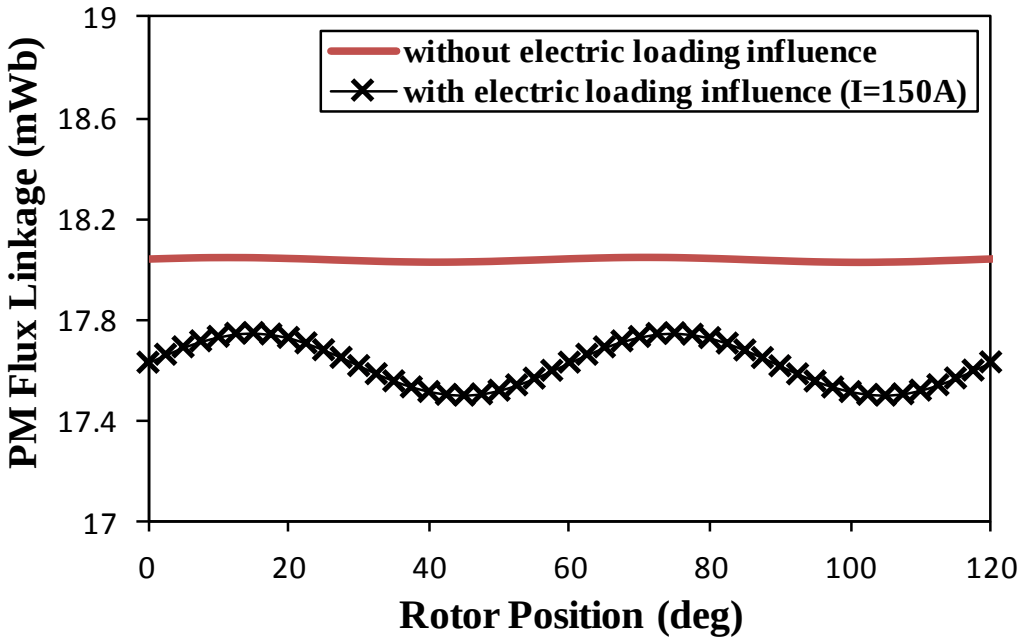

(c) Waveforms, with 30 electrical degree rotor step skew angle

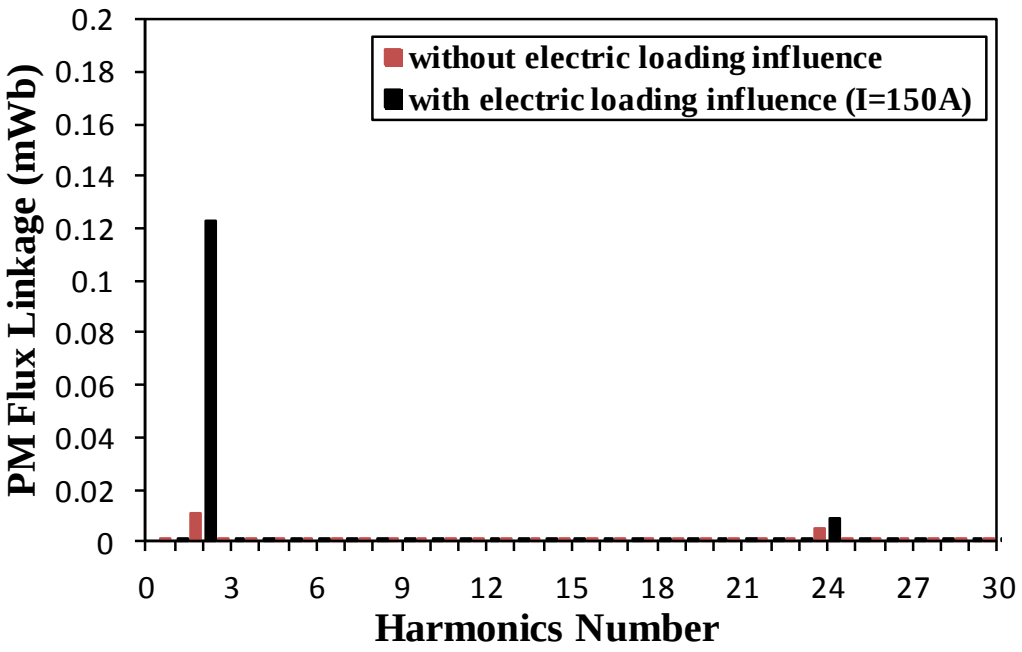

(d) Harmonics, with 30 electrical degree rotor step skew angle

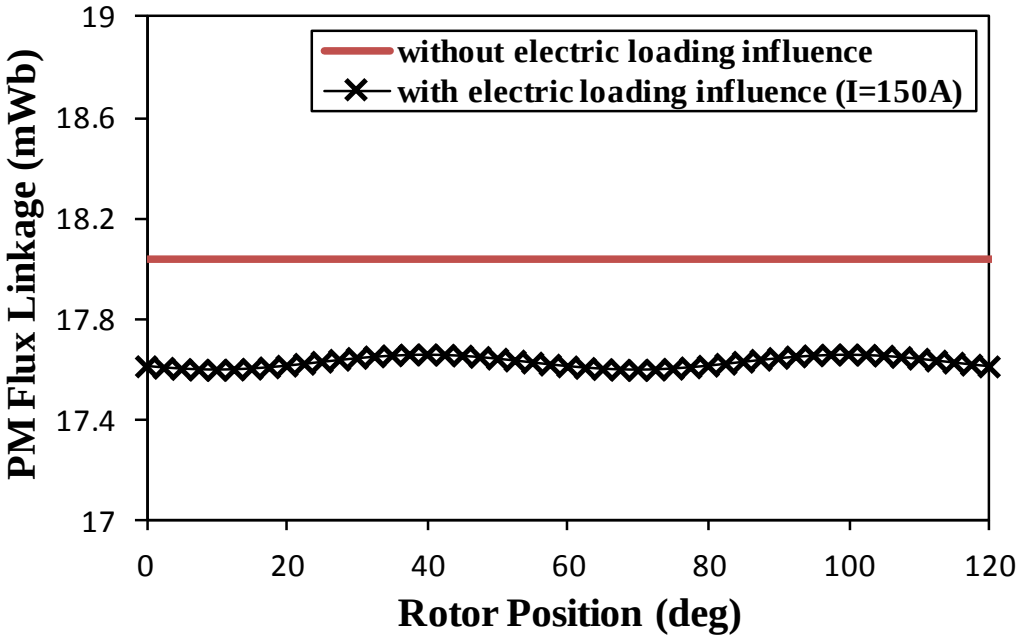

(e) Waveforms, with 60 electrical degree rotor step skew angle

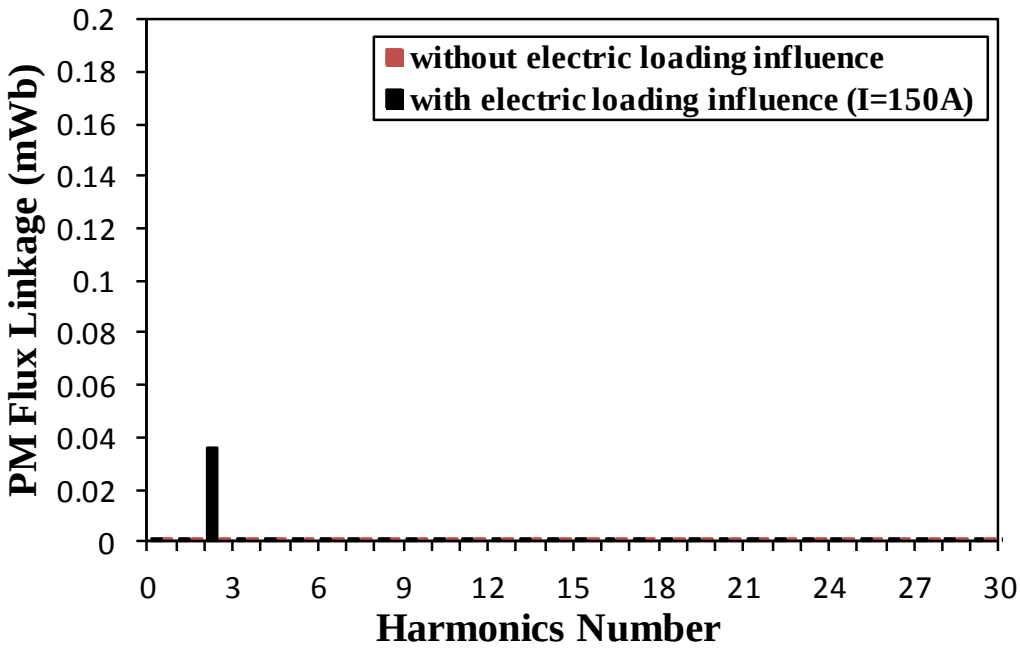

(f) Harmonics, with 60 electrical degree rotor step skew angle

Fig. 5.10 Comparison of d-axis PM flux linkage wavforms and their variation harmonics (fundemental harmonics not included) of machines having un-skewed and step skewed rotors without/with electric loading influence, at 150 A_{peak} phase current.

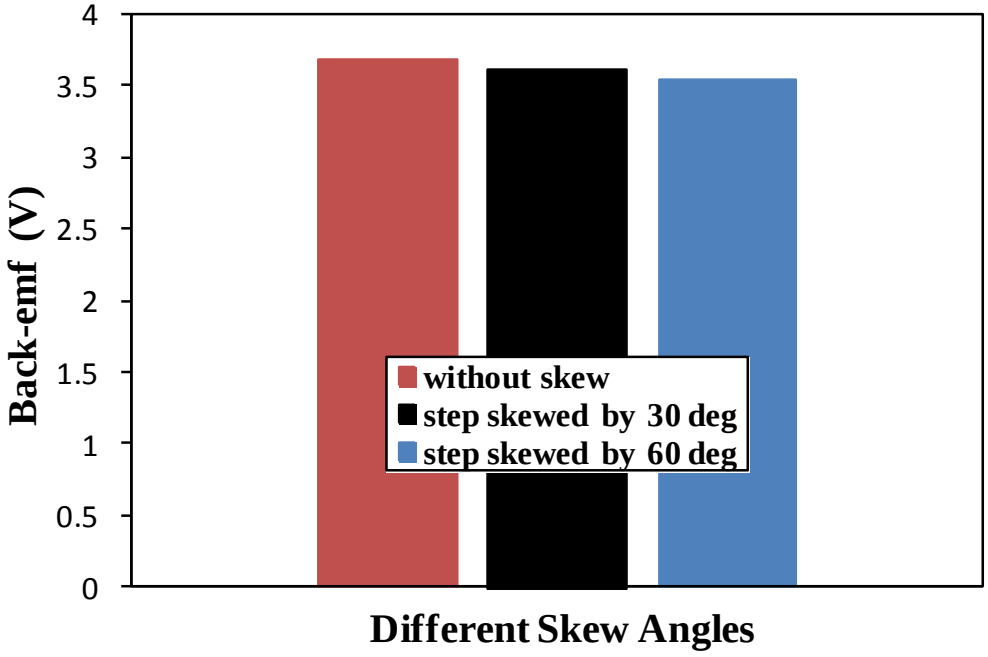

Fig. 5.11 Comparison of back-emf fundamental harmonics of machines having un-skewed and step skewed rotors, at 400 rpm.

5.4. Torque Ripple

The output torque of the PM machine can be defined by:

$$T = 1.5p[\psi_{md} I_q + (L_d - L_q) I_d I_q] \quad (5.1)$$

where I_d, I_q, ψ_{md}, L_d, L_q and p are dq-axis currents, d-axis PM flux linkage, dq-axis inductances and pole pair numbers, respectively.

Based on (5. 1), the output torque ripple waveform of the PM machine when the current is ideally sinusoidal can be given as follow:

$$T = 1.5p[\Delta\psi_{md}(\theta) I_q + \Delta L_{dq}(\theta) I_d I_q] + T_{cog}(\theta) \quad (5.2)$$

where $\Delta\psi_{md}(\theta)$, $\Delta L_{dq}(\theta)$ and $T_{cog}(\theta)$ are variation of the d-axis PM flux linkage, dq-axis inductance differentiation and cogging torque as function of rotor position, respectively. On the other hand, $1.5p\Delta\psi_{md}(\theta) I_q$ and $\Delta L_{dq}(\theta) I_d I_q$ are the electromagnetic and reluctance torque ripples, respectively.

In the prototype fractional-slot PM machines with concentrated winding, the saliency ratio is almost one, i.e. d- and q-axis inductances are nearly the same, as shown in Fig. 5.12. Therefore, such machines are normally operated at nearly zero current angle, i.e. $I_q \approx I_{phase}$ and $I_d \approx 0$. In addition, the variation of dq-axis inductances and their differentiation are significantly small, as illustrated in Fig. 5.12 and Fig. 5.13, respectively. Moreover, such differentiation is even smaller when the machine is skewed, it is reduced by more than 65% when the machine is skewed by 60 electrical degrees, Fig. 5.13. Consequently, the contribution of the reluctance torque ripple into the total output torque ripple is negligible in the prototype machine. It is worth mentioning that during the flux weakening the d-axis current is increased to control the machine voltage. Therefore, the contribution of the reluctance torque ripple could become more significant. However, this is not the subject of this chapter.

In order to prove this conclusion as well as the analyses and discussions in section 5.2 and 5.3, the cogging torque and electromagnetic torque ripple without and with electric loading influence are respectively added together and compared with the calculated FE load torque

ripple, e.g. Maxwell stress, of the prototype machine without and with 30 and 60 electrical degree step skewed rotors, Fig. 5.14. A good agreement exists between them when the full magnetic saturation, i.e. with electric loading influence, is considered. In addition, the 30 electrical degrees skew angle reduces the load torque ripple, as shown in Fig. 5.14(b). However, a significant minimization can be obtained when the rotor is skewed by 60 electrical degrees, Fig. 5.14(c). In conclusion, the 60 degrees skew angle can minimize the load torque ripple by more than 90%, but causes only around 4% reduction in the electromagnetic performance.

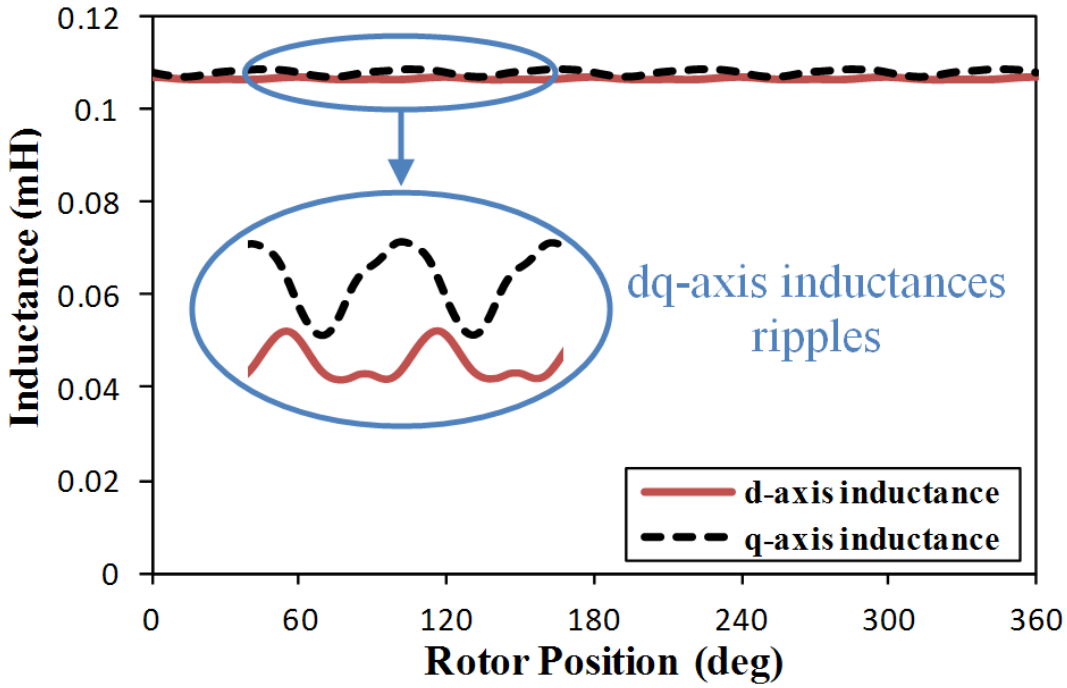

Fig. 5.12 Variation of dq-axis inductance against rotor position, at 150 A_{peak} load current.

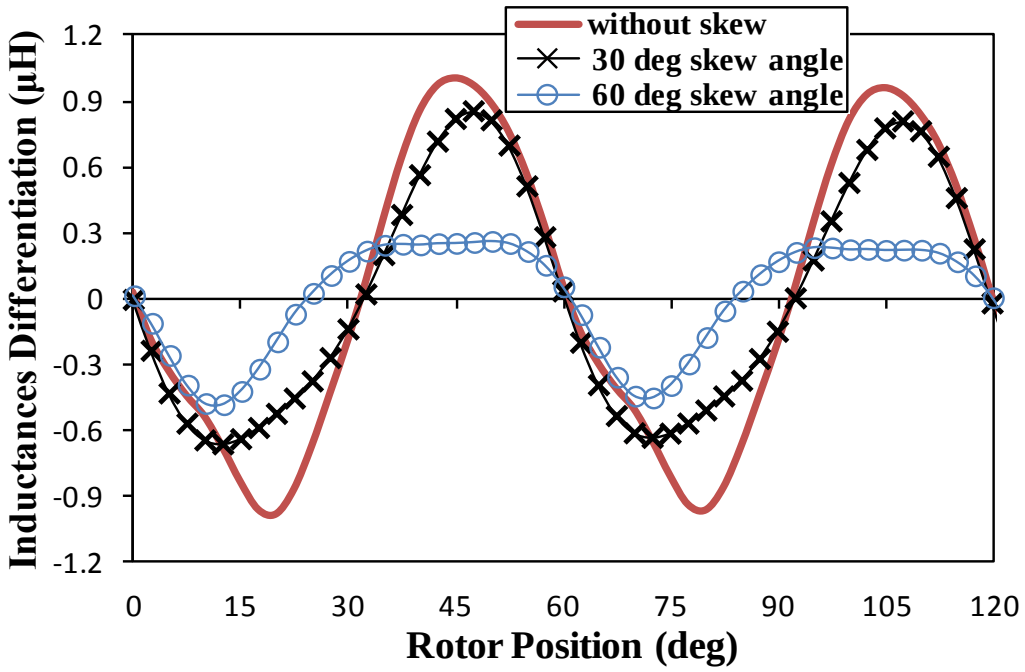

Fig. 5.13 Variation of dq-axis inductance differentiation against rotor position for different rotor skew angles.

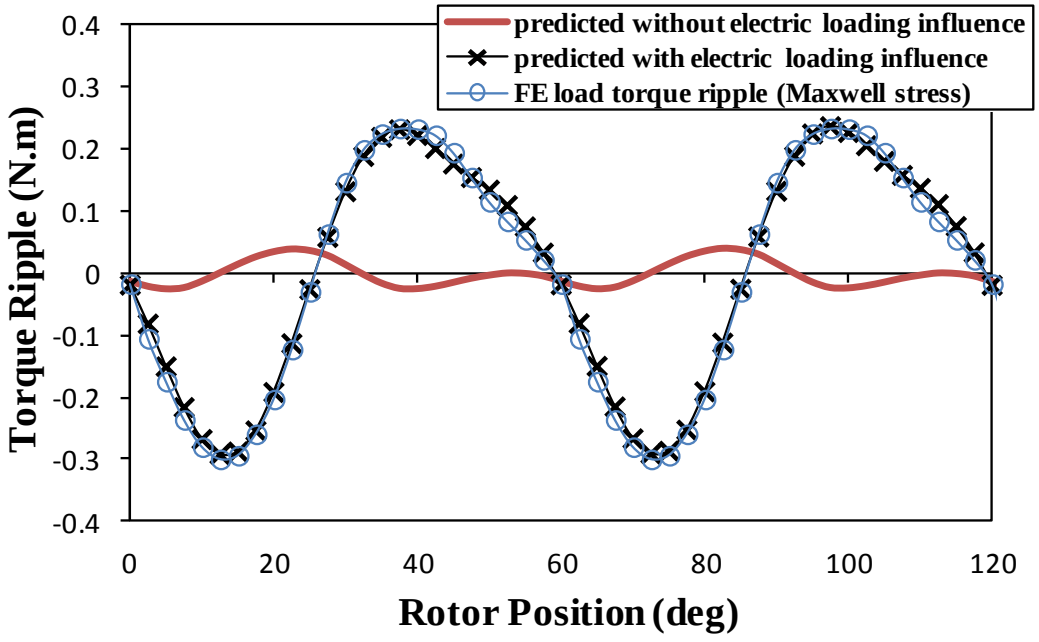

(a) Without rotor step skew

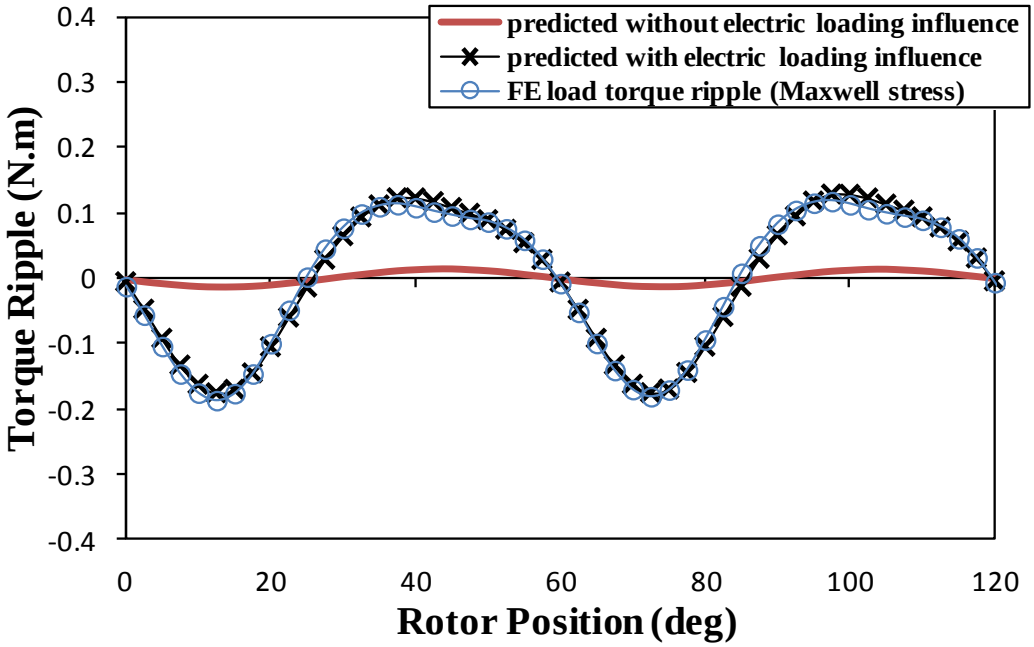

(b) With 30 electrical degree rotor step skew

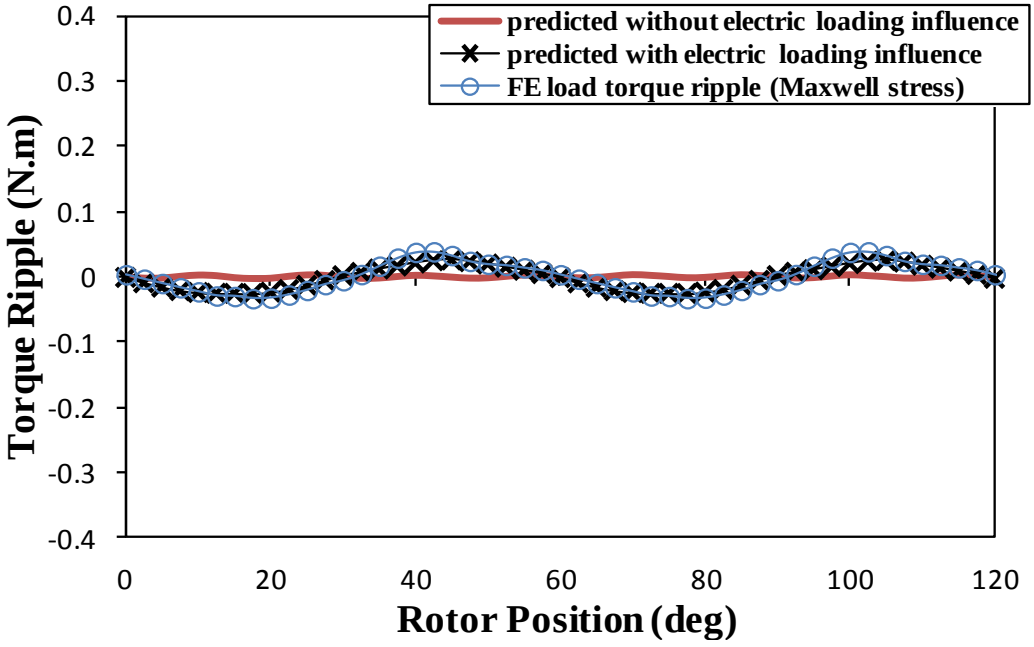

(c) With 60 electrical degree rotor step skew

Fig. 5.14 Comparison of predicted (cogging torque + electromagnetic torque ripple) and FE calculated load torque ripples of machines machines having un-skewed and step skewed rotors without/with electric loading influence, at 150 A_{peak} load current.

5.5. Number of Skew Steps

In order to achieve an effective torque ripple reduction, the rotors of the studied machines during the foregoing investigations, i.e. sections 5.2, 5.3 and 5.4, are skewed by 4 steps for both 30 and 60 electrical degree angles. However, in this section the possibility of utilizing lower skew steps, i.e. 3 or 2, are investigated. The reason behind such investigation is to examine the possibility of decrease the manufacturing cost and complexity of more skew steps, without influencing the load torque ripple minimizing. The open-circuit cogging torque can be, theoretically, eliminated if the machine is step skewed by 2 steps of 15 electrical degrees or 3 steps of 10 electrical degrees, as shown in Fig. 5.15. However, the effectiveness of such skews on the actual cogging torque is much lower, Fig. 5.16 (a). Alternatively, the actual cogging torque can be significantly minimized when the machine is step skewed by 3 steps of 20 electrical degrees, the same as the 4 steps of 15 electrical degrees, as illustrated in Fig. 5.16(b). In addition, when the machine is skewed by 2 steps of 30 electrical degrees the actual cogging torque is also relatively small, Fig. 5.16(b). In order to investigate the influence of the mentioned skew angle and step combinations on the smoothing of the output torque, the load torque ripple of machines having these different skew combinations are calculated and compared together with their counterpart of machine has un-skewed rotor in Fig. 5.17. When the machine is skewed according to open-circuit cogging torque period, the load torque ripple reduction is nearly the same for any skew angle and step combination, this reduction is about 40%, Fig. 5.17(a). However, as mentioned before, the torque ripple reduction is more significant when the machine is skewed according to the actual cogging torque period, no matter whatever the number of skew steps, Fig. 5.17(b). On the other hand, larger skew angle and more skew steps result in a larger electromagnetic performance reduction, as shown Fig. 5.18. This figure compares the output torque reduction due to different skew angle and step combinations as a percentage of the average output torque of the un-skewed machine. For example, skewing the machine according to the actual cogging torque angle significantly suppresses the load torque ripple, but it also causes about 3-4% reduction in the electromagnetic performance. Moreover, the machine with 2 skew steps of 30 electrical degree skew angle and generates nearly the same load torque ripple as its counterpart with 4 steps of 15 electrical degree skew angle, Fig. 5.17(b), but it has lower electromagnetic performance reduction, as shown in Fig. 5.18. However, it should be mentioned that the skew causes an extra flux leakage on the z-axis direction. This could cause an adverse effect on the bearing life time, due to the induced voltages.

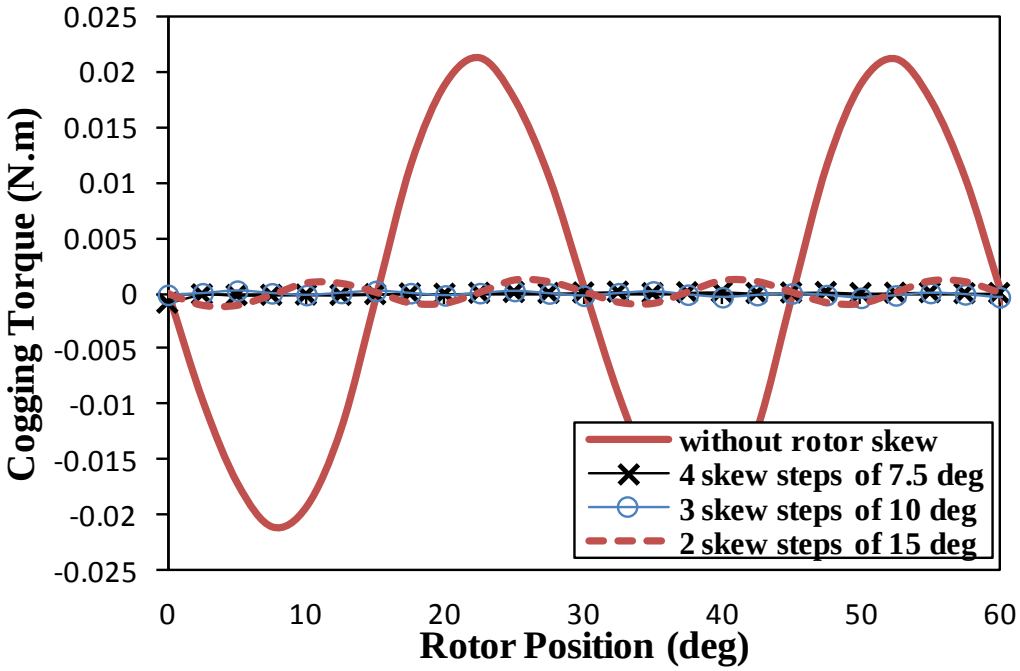

Fig. 5.15 Comparison of open-circuit cogging torque of machines having different skew step and angle combiations.

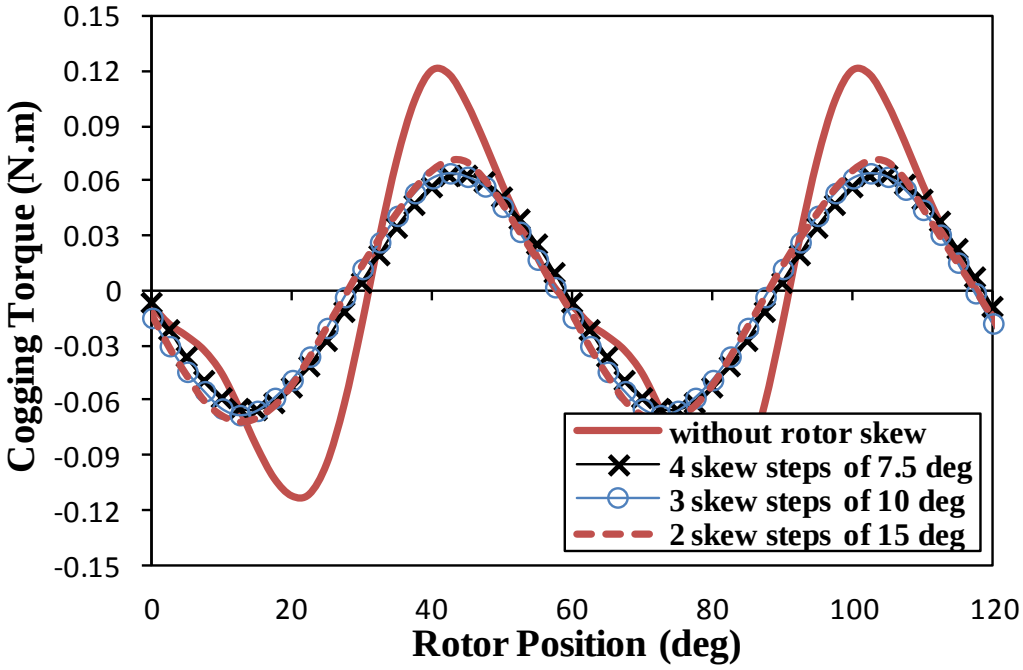

(a) Skew according to open-circuit cogging torque period

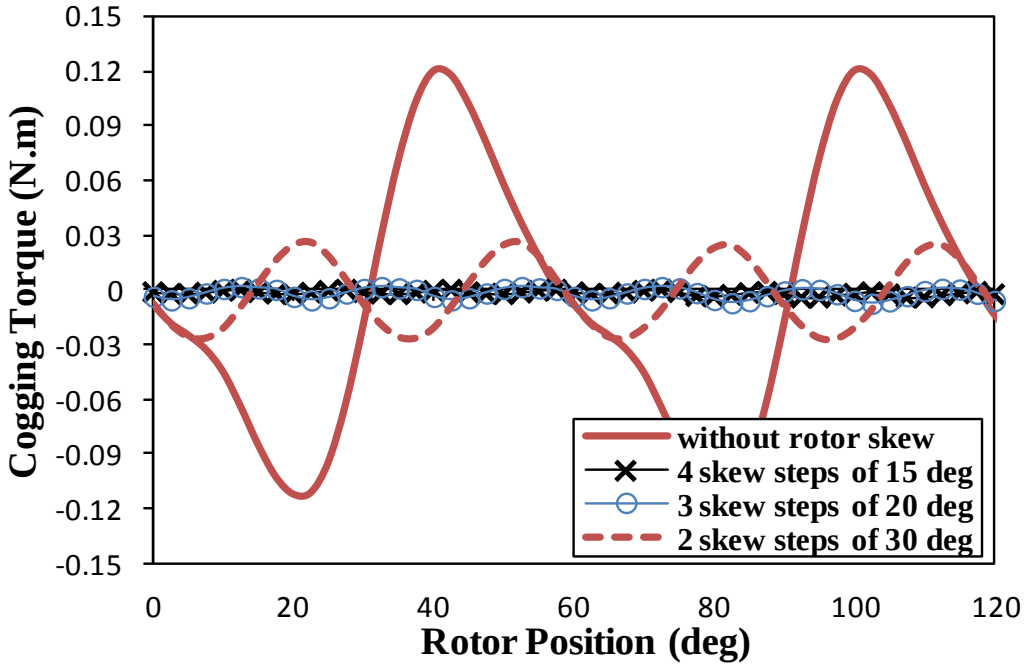

(b) Skew according to actual cogging torque period

Fig. 5.16 Comparison of actual cogging torque of machines having different skew step and angle combiations, at 150 A_{peak} load current.

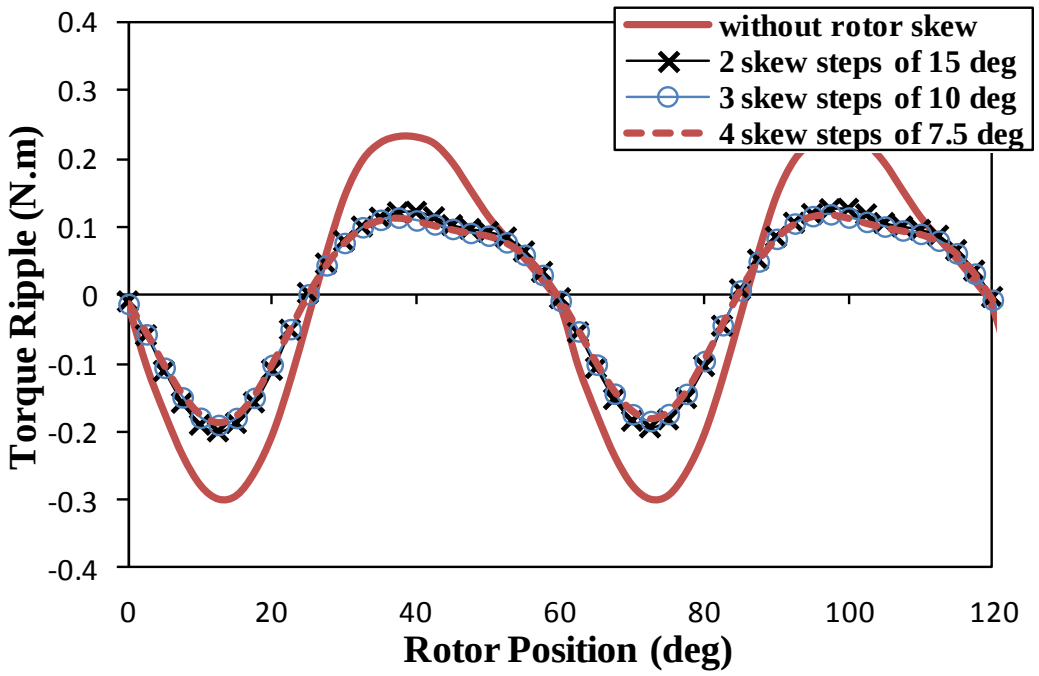

(a) Skew according to open-circuit cogging torque period

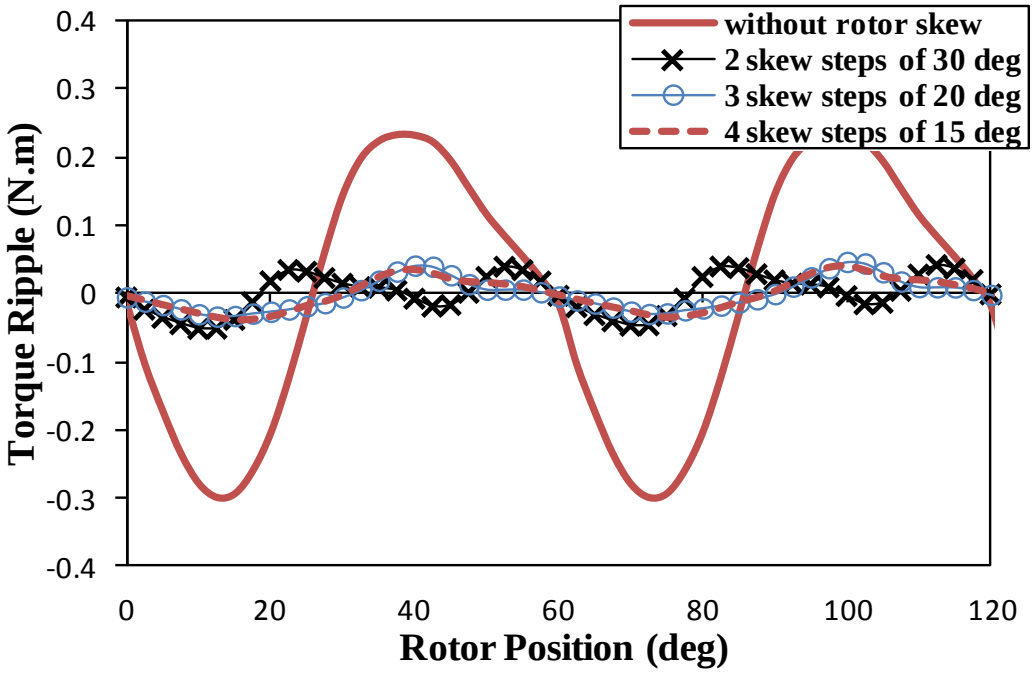

(b) Skew according to actual cogging torque period

Fig. 5.17 Comparison of load torque ripple of machines having different skew step and angle combiations, at 150 A_{peak} load current.

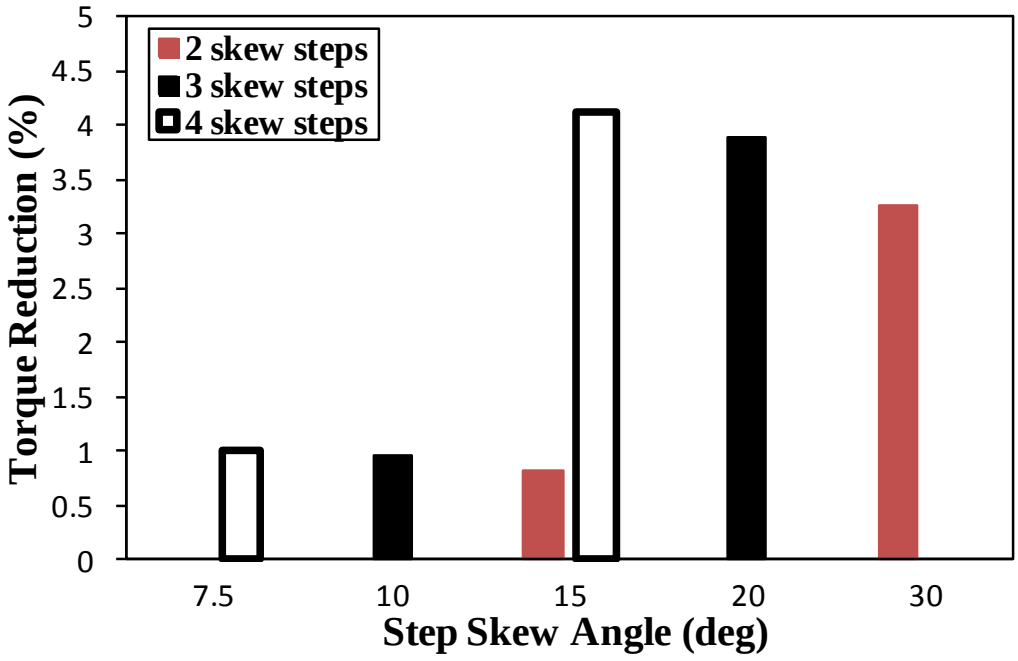

Fig. 5.18 Comparison of average output torque reduction due to skew of machines having different skew step and angle combiations, at 150 A_{peak} load current.

5.6. Experimental Validation

It is extremely difficult to measure the cogging torque or back-emf accounting for the load conditions. However, alternatively all these results can be confirmed by measuring and comparing the torque ripples. The measured load torque ripple of the prototype machine, which has 30 electrical degrees and 4 steps skewed rotor, is compared with its predicted counterpart, i.e. cogging torque + electromagnetic torque ripple, with/without accounting for the influence of the electric loading in Fig. 5.19. It shows a good agreement between the measured (via in-line torque transducer) and the predicted torque ripples when the magnet saturation influence is fully accounted for, while the predicted torque ripple is significantly lower if the electric loading influence is not considered. This validates and proves the analysis method and results. It is worth noting that the contribution of the reluctance torque ripple in the prototype machine is relatively small, as discussed in section 5.4, and has been neglected in the predicted results.

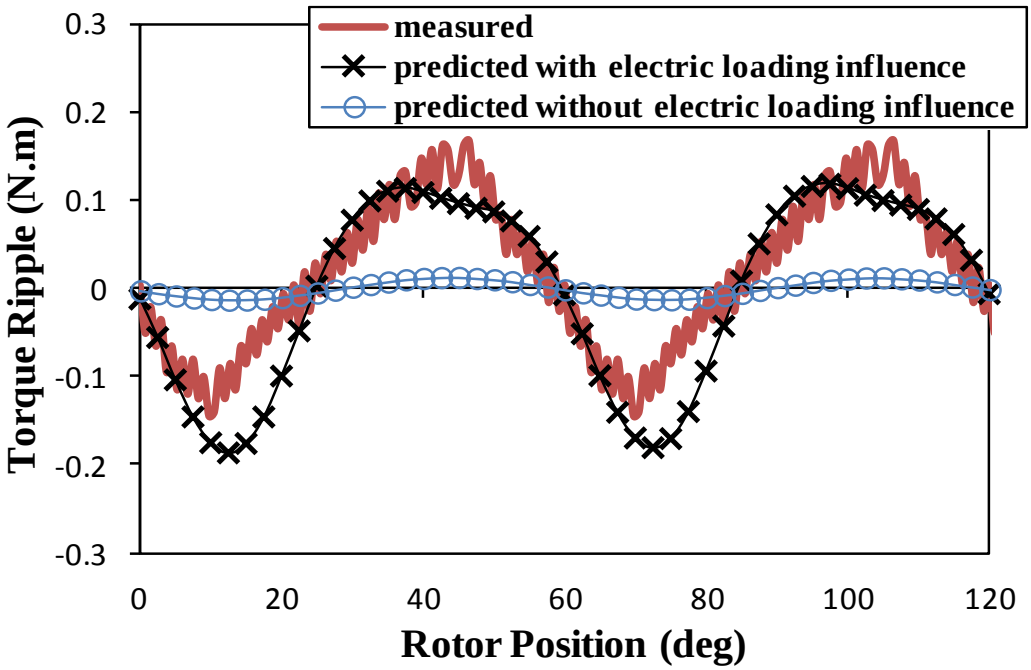

Fig. 5.19 Comparison of measured and predicted (cogging torque + electromagnetic torque ripple) torque ripples of prototype machine, at 150 A_{peak} load current.

5.7. Conclusions

The cogging torque, back-emf and associated torque ripples in PM machines having un-skewed and step skewed rotors have been investigated taking into account the influence of load conditions by employing a FP FE technique. The magnitude of the actual cogging torque, i.e. with electric load influence, is significantly larger than its open-circuit counterpart. This is due to the extra flux leakage through tooth tips and in turn higher saturation level in the stator teeth in the prototype machine. For the same reason, the actual back-emf waveform is also distorted, thus it contains larger harmonics and results in larger electromagnetic torque ripple. Furthermore, the increase of actual cogging torque depends on the magnetic saturation level, which is determined by the electric loading value. In addition, due to the electric loading influence, the actual cogging torque periodicity also varies to become the same as the total load torque ripple periodicity. Therefore, the skew technique, which is based on the open-circuit cogging torque period, becomes less effective. However, it has been shown that the actual cogging torque can be effectively eliminated if the machine is skewed by one actual cogging period on load. In addition, such skew can also significantly minimize the electromagnetic torque ripple. A comparison of load torque ripple and electromagnet performance reduction has been carried out for different skew angle and step combinations. The analysis results are partially confirmed by experiment.

Chapter 6: Electromagnetic Performance Analysis of Synchronous Reluctance Machines Having Non-overlapping Concentrated Windings and AC Sinusoidal Bipolar Excitation

6.1. Introduction

The switched reluctance (SR) machines are an attractive solution for many applications, which are operated at high speeds and in harsh environments, e.g. high temperature and pressure, since they have a robust rotor structure without PMs or coils, [108, 151]. Furthermore, such machines are equipped with concentrated windings, thus the shorter end-winding and low copper loss are also advantages for such machines. In addition, due to the significant increase of the PM material price, the SR machines are becoming more desirable to employ in the electric/hybrid electric vehicles [106, 152-154]. Therefore, they have been significantly investigated to minimize or even to overcome their disadvantage, such as high torque ripple, noise and vibrations [155, 156]. The main cause behind the larger torque ripple is the sudden extinguish of the phase currents when the rotor moves from the unaligned to the aligned positions [157]. This issue can be diminished if the phases are continuously excited, i.e. using the AC sinusoidal bipolar excitation [121]. Under such excitation the SR machine becomes a salient-pole synchronous reluctance (SynR) machine with concentrated winding [158]. Thus, it can be operated using the ordinary 3-phase inverter [120], which is shown in Fig. 6.1. This chapter presents a comparative study for the electromagnetic performance of three 6 stator/4 rotor poles SynR machines having different non-overlapping concentrated winding connections, which are further illustrated in section 6.2. In general, the output torque of the SynR machines is due to the variations of the self and mutual inductances when the relative position between the stator and rotor teeth varies from the unaligned to aligned. Therefore, such inductances will be particularly highlighted. In addition, the machine line voltage, torque- and power-speed characteristics and efficiency are also analyzed, to examine the ability of utilizing such machines in the electric/hybrid electric vehicles. Moreover, the electromagnetic performance of 12 stator/4 rotor poles SynR machine, which has overlapping concentrated winding, is also analyzed and compared with its counterparts of the 6 stator/4 rotor SynR machines.

The major dimensions and parameters of the analyzed 6 stator/4 rotor and 12 stator/4 rotor poles machines, which have been optimized for the maximum average output torque under the same current density, are given in Table 6.1. The optimization result of the 6 stator/4 rotor poles machine are illustrated in Fig. 6.2. On the other hand, the optimization results of 12 stator/4 rotor poles machine will be shown in section 6.7. Furthermore, in order to validate the analyses the 6 stator/4 rotor poles machine is prototyped and tested.

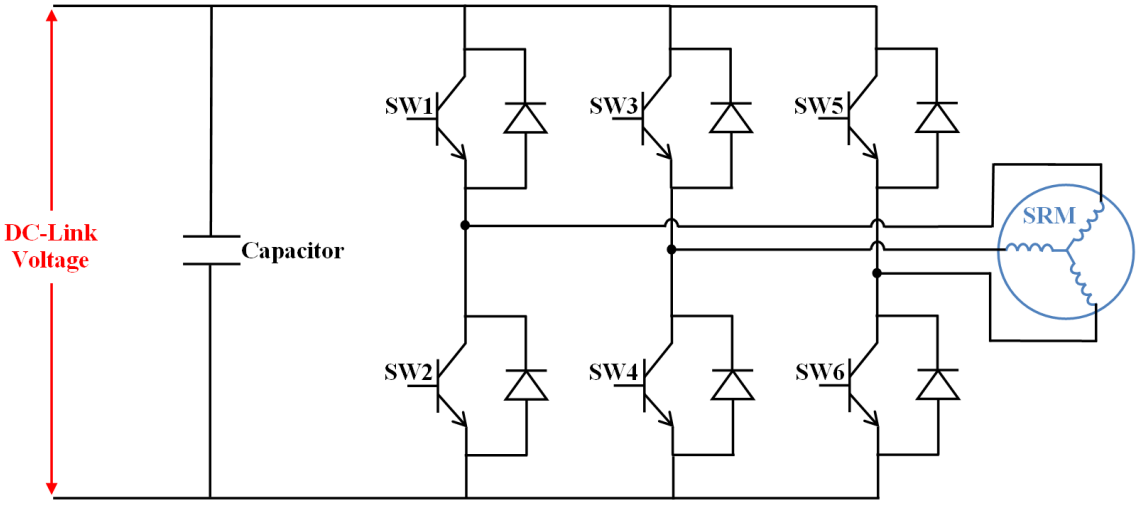

Fig. 6.1 Standard bipolar driver inverter for SR machines under AC bipolar excitation, i.e. salient-pole SynR machine.

Table 6.1 Major Dimensions and Parameters.

Parameters	***6 Stator/4 Rotor poles***	***12 Stator/4 Rotor poles***
Stator Outer Diameter	110 mm	
Stator Inner Diameter	58 mm	59.8 mm
Rotor Outer Diameter	57.2 mm	59 mm
Rotor Yoke Thickness	10.1	10.7
Shaft Diameter	20 mm	
Axial Length	175 mm	
Stator Pole Width	15.5 mm	8.5 mm
Stator Yoke Thickness	8.25 mm	8.5 mm
Rotor Pole Width	17.5 mm	14.5 mm
Air Gap Length	0.4 mm	
Maximum Current Density	34 A_{rms}/mm^2	
Packing Factor	52 %	
Number of coils per Phase	2 coils	4 coils
Number of turns per coil	21 turns	10 turns

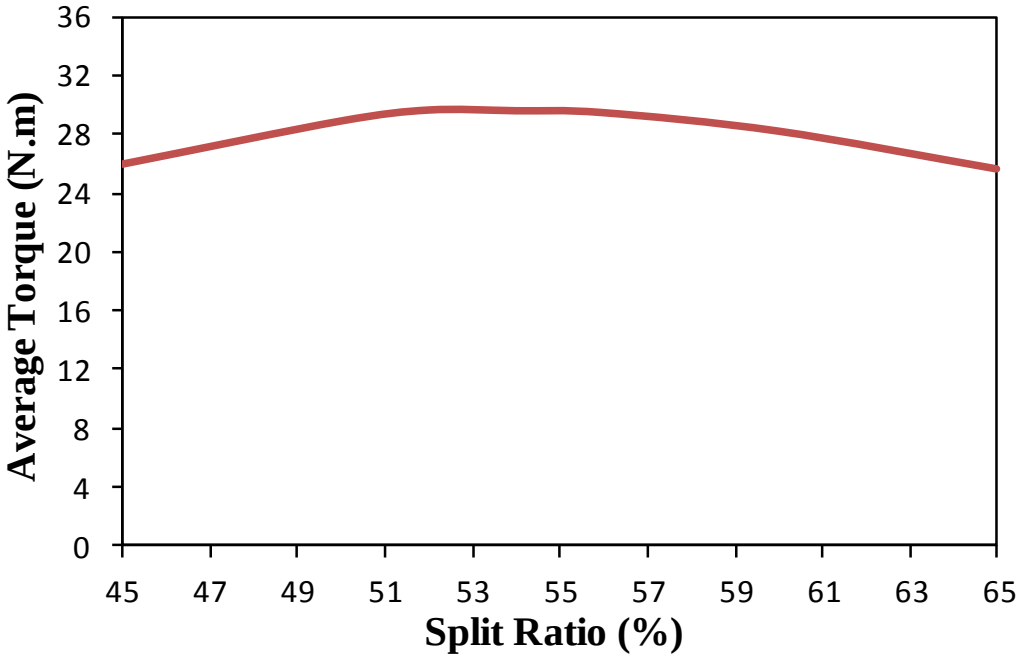

(a) Split ratio

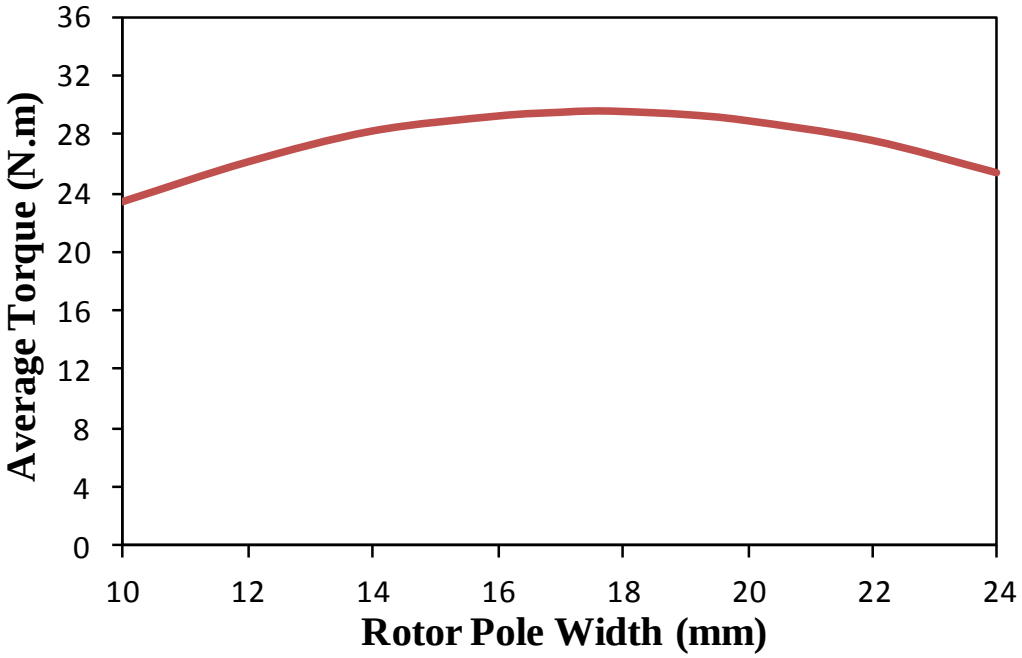

(b) Rotor pole width

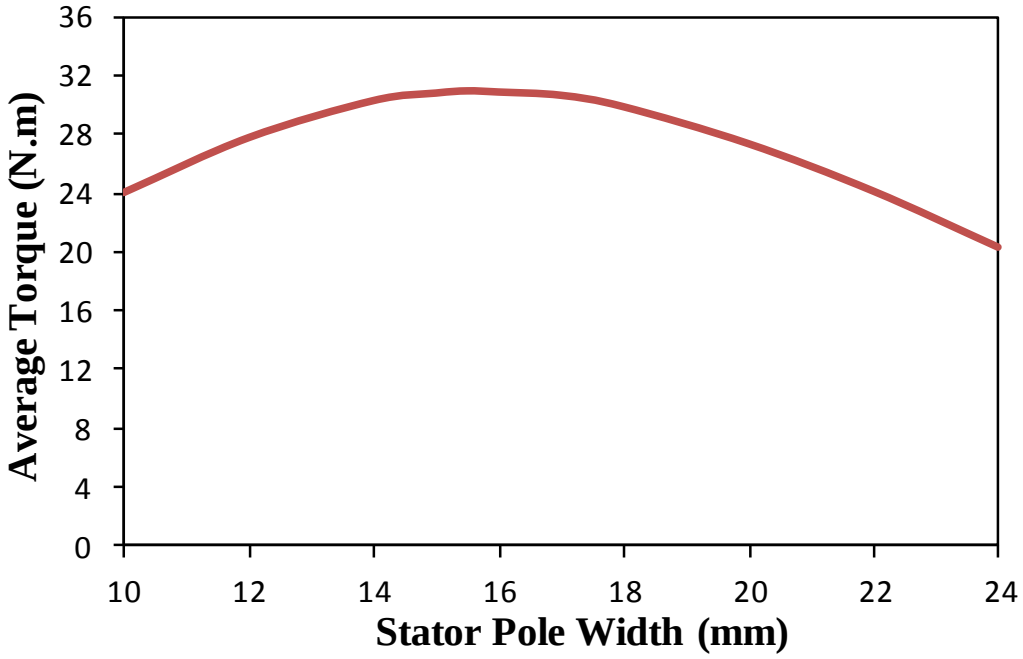

(c) Stator pole width

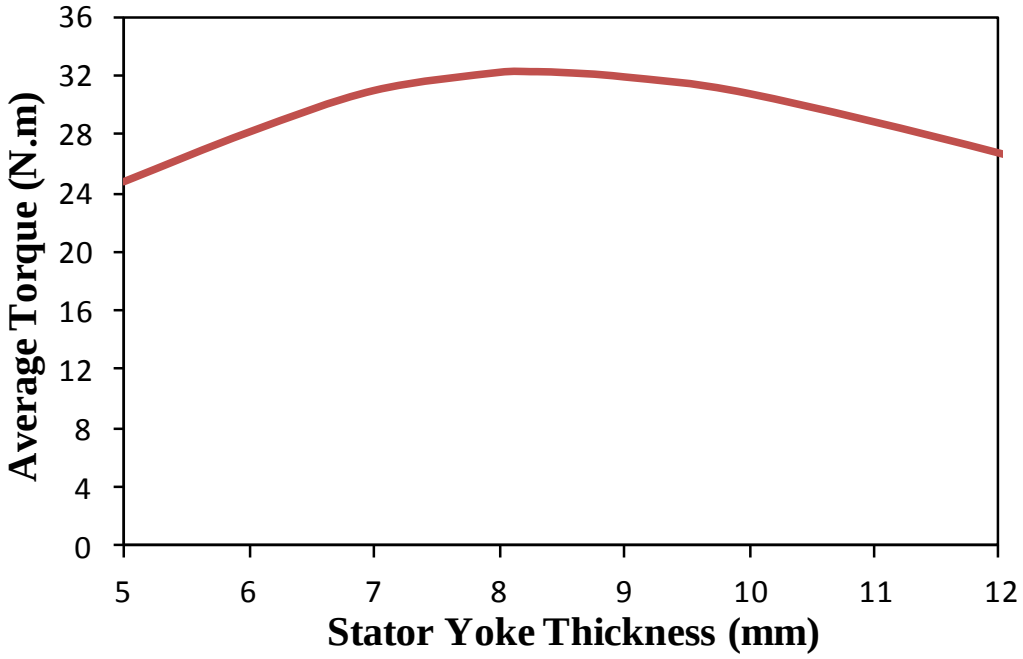

(a) Stator yoke thickness

Fig. 6.2 Variation of average output torque of 6 stator/4 rotor poles machine against split ratio, rotor and stator pole widths and stator yoke thickness, at 34 A_{rms}/mm^2 current density.

6.2. Different Winding Connections

All studied 6 stator/4 rotor poles machines are equipped with concentrated windings, consisting of two coils per phase and 3 phases are star connected. According to the connecting way of each phase coils, i.e. the coil polarity, thus the flux direction, there are three possible winding connections, which in this chapter are classified into [113, 124]:

a) asymmetric connection: has uneven coil polarity in the stator slots, thus asymmetric flux directions, as shown in Fig. 6.3(a);

b) symmetric connection: has symmetric flux directions since its phase coil polarities are the same in each stator slot, as illustrated in Fig. 6.3(b);

c) hybrid connection: has the same coil polarity and flux direction for all coils, as shown in Fig. 6.3(c). In this connection the winding polarity is similar to the full pitch wound machine, which will be investigated in section 6.7.

In the first two connections, i.e. asymmetric and symmetric, the torque is mainly produced by the variations of the phase self inductances, since their mutual inductances are negligibly small, as will be shown later. However, in the hybrid winding connection there are more interaction between phase fluxes, thus the variations of the mutual inductances become more significant, as will be demonstrated in the next section. Consequently, in the last connection, the output torque becomes due to the variations of both the self and mutual inductances, this is the reason behind such connection name. Further discussions, analyses and comparison will be carried out to further illustrate the output torque generation as well as to highlight the benefits and drawbacks of each connection.

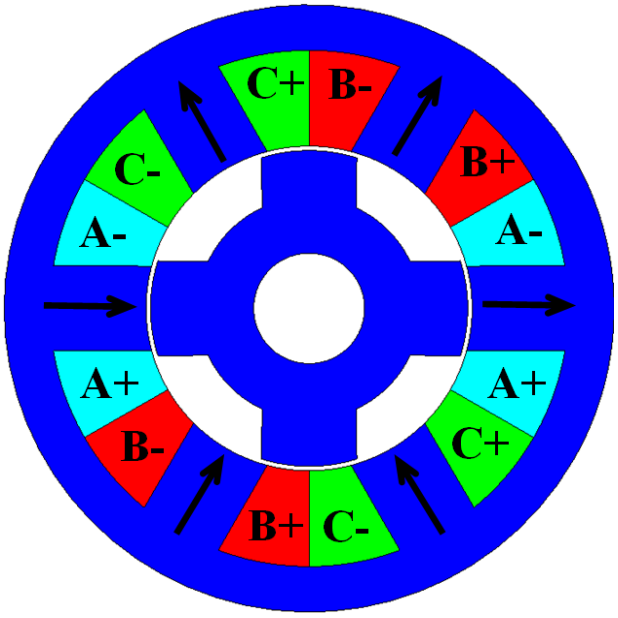

(a) Asymmetric winding

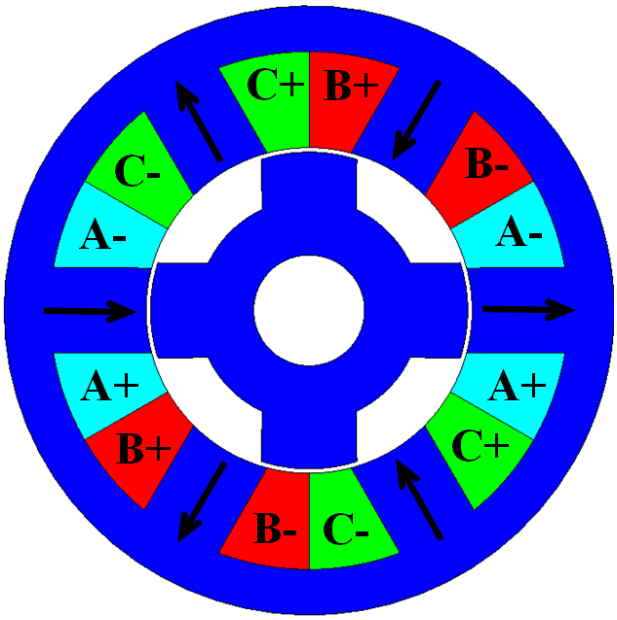

(b) Symmetric winding

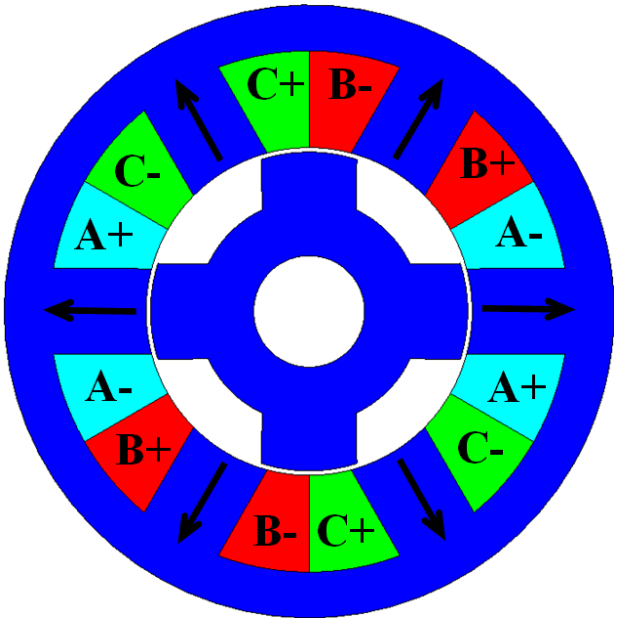

(c) Hybrid winding

Fig. 6.3 Comparison of three different concentrated winding connections of 6 stator/4 rotor poles machine.

6.3. Electromagnetic Performance

It is well known that the SynR machines are normally operated at large current density, thus high torque/power density can be achieved [113, 159]. In this chapter, the investigations are carried out for a maximum current density of 34 A_{rms}/mm^2. However, the machines are also examined for different lower current density values. The excitation phase current waveforms against the rotor position are shown in Fig. 6.4. It is worth mentioning that in this chapter the rotor position will be defined by the mechanical degree, i.e. mech. deg.

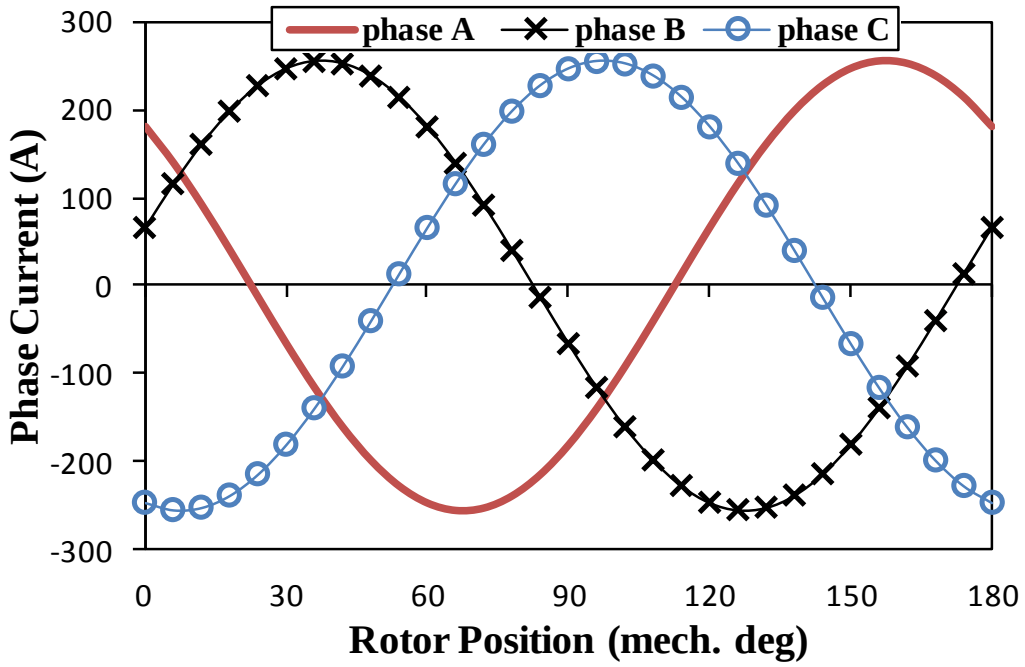

Fig. 6.4 Excitation phase current waveforms, at 34 A_{rms}/mm^2 current density.

6.3.1. Flux linkages

The phase flux linkage of the 6 stator/4 rotor poles SynR machines having different winding connections are compared in Fig. 6.5. The phase flux linkage waveforms are asymmetric when the phase coils are unevenly distributed, Fig. 6.5 (a). Such asymmetry becomes more significant at larger current density, i.e. high magnetic saturation, Fig. 6.5 (b). As will be shown later, this phenomenon increases the required DC-link voltage to drive the machine. On the other hand, even at significantly large current density, i.e. 34 A/mm^2, the phase flux linkage of the symmetric and hybrid winding connections are uniform as shown in Fig. 6.5 (c) and Fig. 6.5 (d), respectively. Moreover, the flux density magnitudes of three connections are nearly the same, since they have the same electric loadings and turn numbers. However,

they exhibit totally different waveform shapes. In its turn, this will result in different inductance variations, thus different output torques. These characteristics will be investigated in sequence in the following sections.

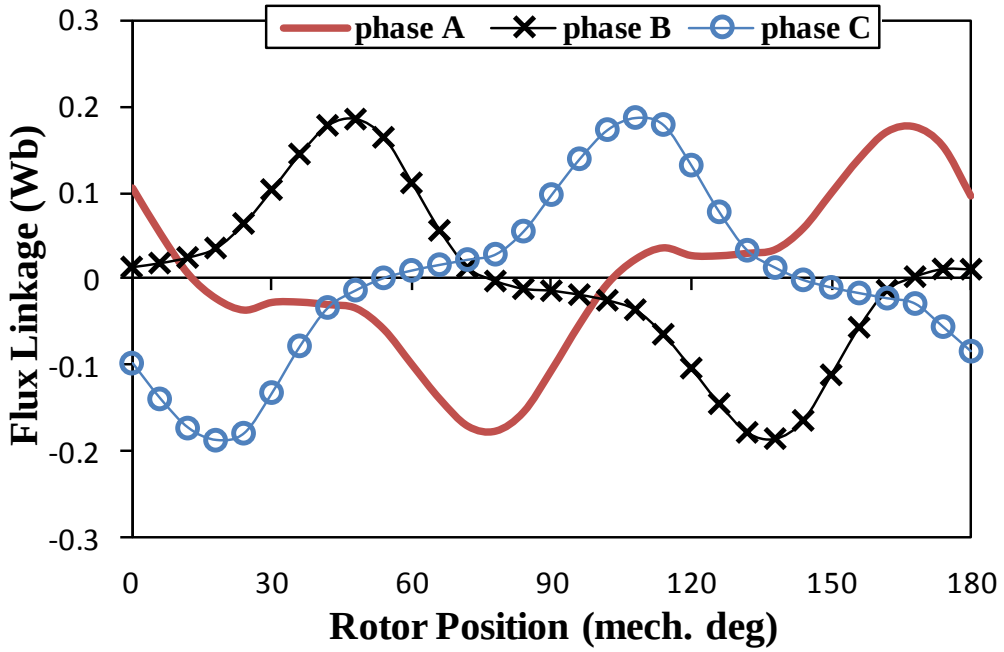

(a) Asymmetric connection at $6A_{rms}/mm^2$ current density

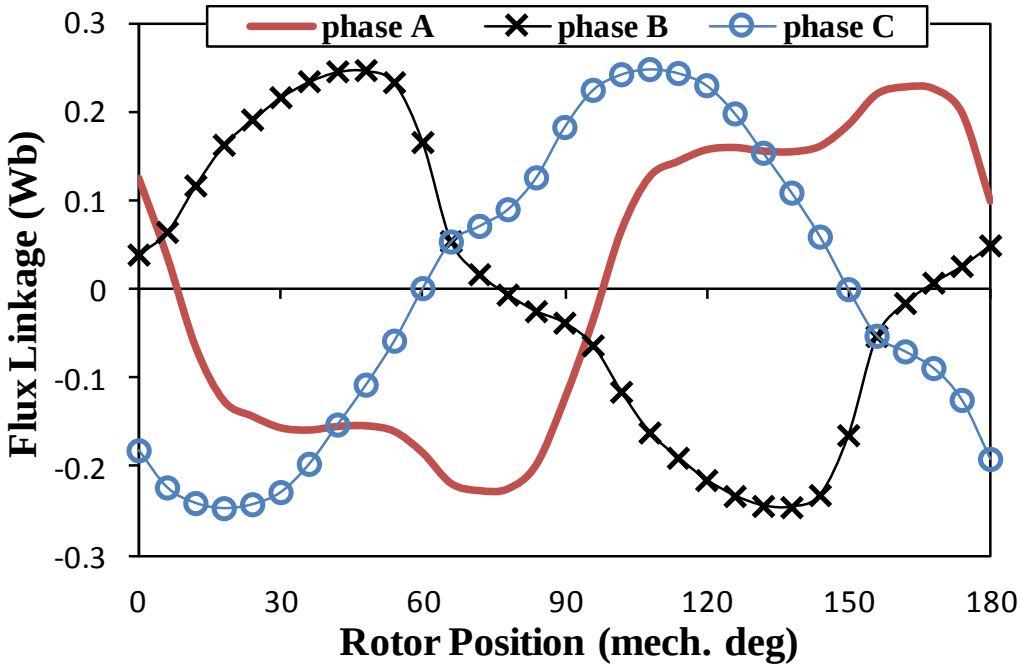

(b) Asymmetric connection at $34A_{rms}/mm^2$ current density

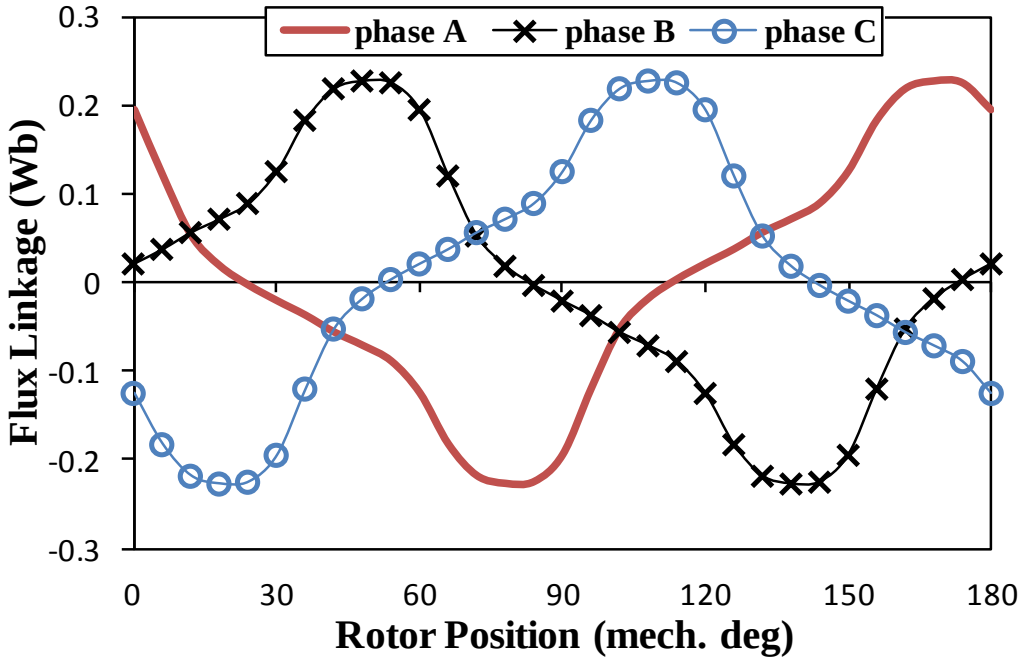

(c) Symmetric connection at $34A_{rms}/mm^2$ current density

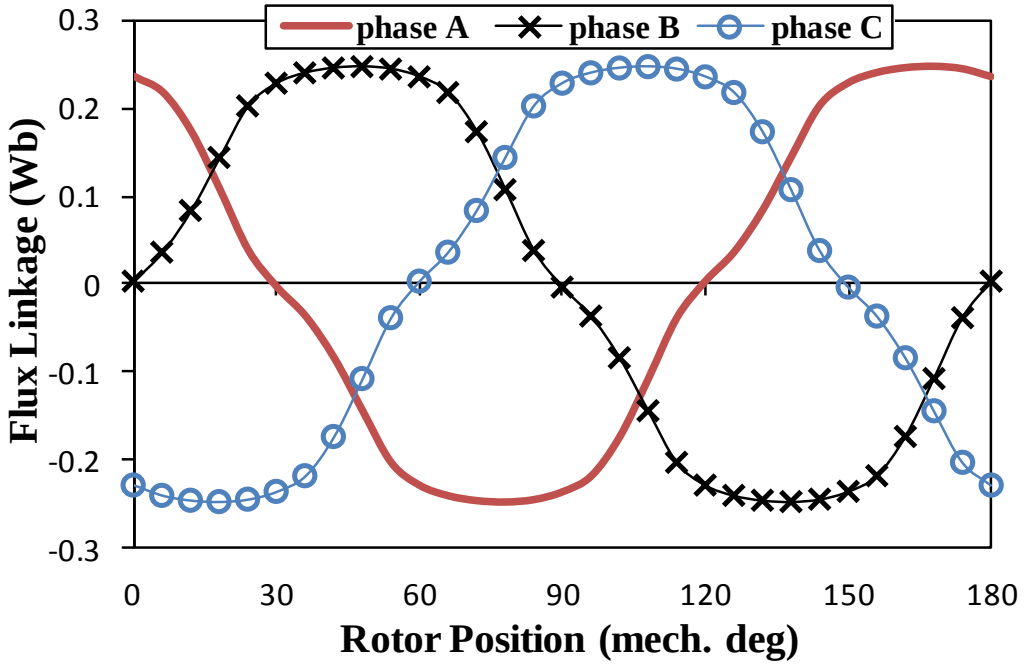

(d) Hybrid connection at $34A_{rms}/mm^2$ current density

Fig. 6.5 Variation of flux linkage waveforms of 6 stator/4 rotor poles machines having different winding connections at 45 deg current angle.

6.3.2. Phase Self Inductances

The self inductances of the analyzed 6 stator/4 rotor poles SynR machines having different winding connections are calculated for different current densities and compared in Fig. 6.6. Different current densities result in different magnetic saturation levels. The comparison clearly shows that the sensitivity of the SynR machine self inductance to magnetic saturation very much depends on the way of winding connection. Such sensitivity is relatively significant in the asymmetric and symmetric connections, Fig. 6.6 (a) and Fig. 6.6 (b), respectively. However, on the other hand, it is comparatively lower when the hybrid winding connection is utilized, Fig. 6.6 (c). This is due to different flux distributions and paths of each winding connection, i.e. the machine with hybrid winding has relatively shorter flux paths, as clearly noticed in Fig. 6.7. Furthermore, the phase self inductances of machines having different winding connections at 34 A_{rms}/mm^2 current density are compared together in Fig. 6.8. The SR machines with asymmetric and symmetric connections exhibit nearly the same self inductance variations, which are much larger than their counterparts of the machine with hybrid connection. Therefore, the first two machines are expected to exhibit the same output torque, which from the self inductance variation point of view only should be larger than its counterpart of the machine with hybrid connection.

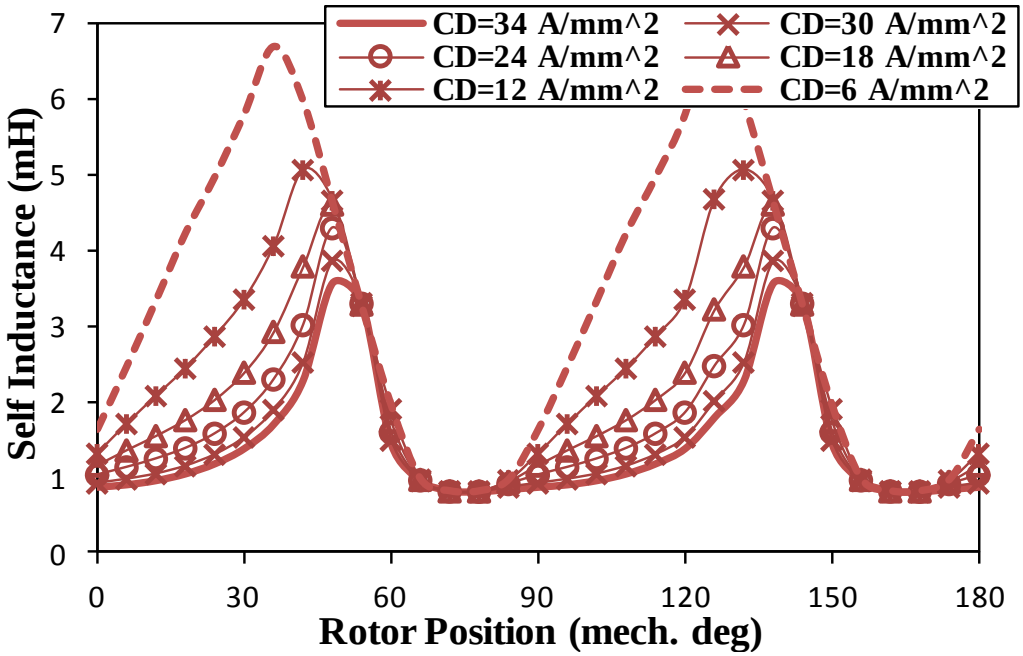

(a) Asymmetric winding connection

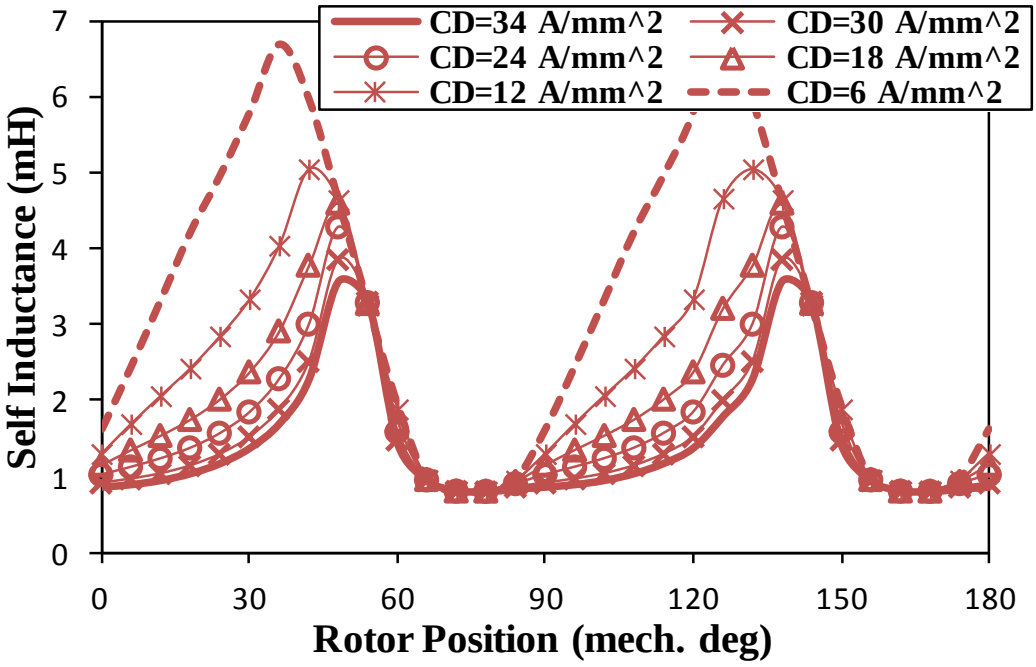

(b) Symmetric winding connection

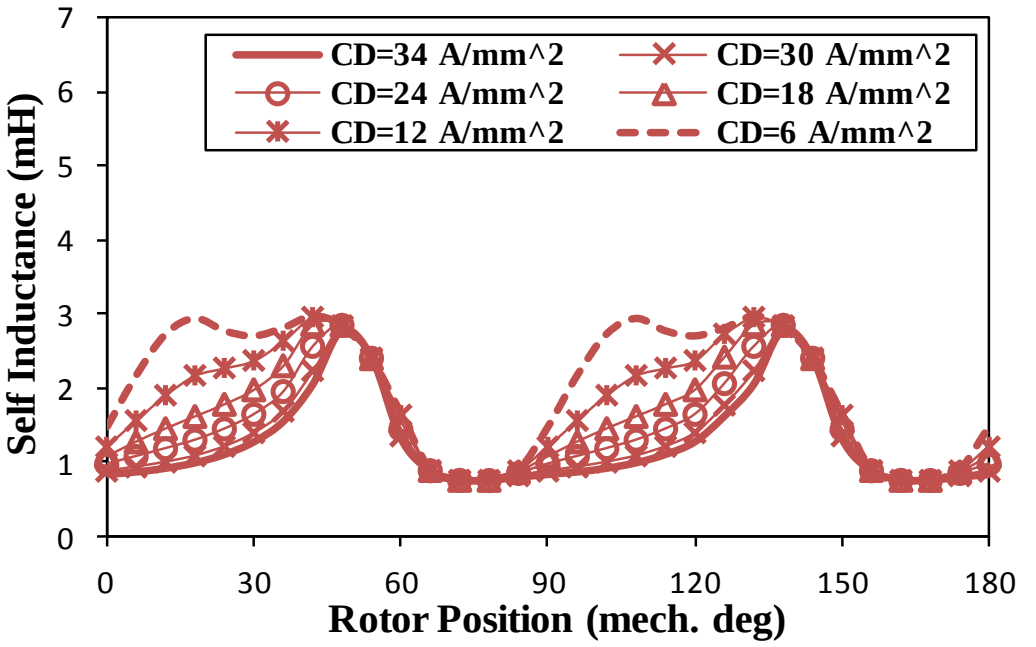

(c) Hybrid winding connection

Fig. 6.6 Comparison of phase self inductances of 6 stator/4 rotor poles machines having different winding connections for different current densities.

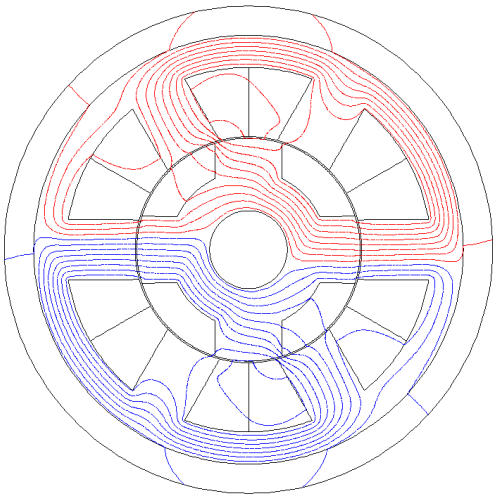

(a) Asymmetric winding connection

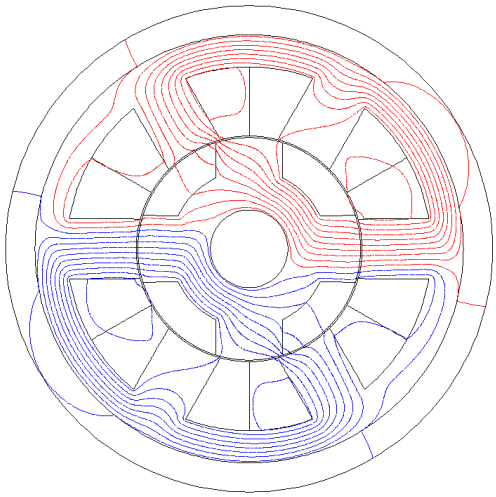

(b) Symmetric winding connection

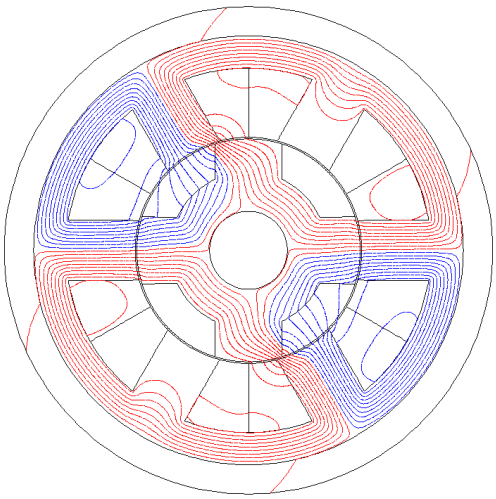

(c) Hybrid winding connection

Fig. 6.7 Comparsion of load flux distributions of 6 stator/4 rotor poles machines having different winding connections, at 34 A_{rms}/mm^2 current density.

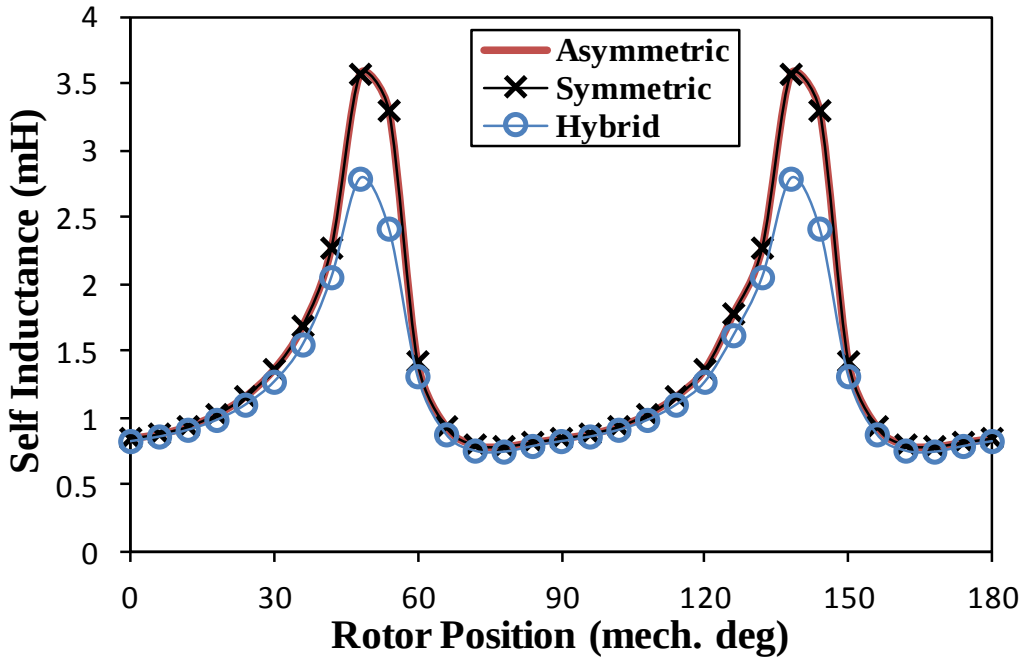

Fig. 6.8 Comparsion of variations of phase self inductances of 6 stator/4 rotor poles machine for different winding connections, at 34 A_{rms}/mm^2 current density.

6.3.3. Mutual Inductances

The electromagnetic interaction between the phase fluxes is significantly small in the machines having asymmetric and symmetric winding connections, Fig. 6.7. Thus, the mutual inductances of such machines are also relatively small, as shown in Fig. 6.9(a) and Fig. 6.9(b), respectively. On the other hand, the machine with the hybrid winding connection exhibits relatively large mutual inductance variations, Fig. 6.9(c). Consequently, the contribution of the mutual torque, i.e. due to mutual inductance variation, to the total output torque of such machine is relatively significant. This confirms that the output torque of the machine with hybrid connection is due to the variations of both the self and mutual inductances. Therefore, the machine with hybrid winding connection is expected to deliver larger output torque comparing with the asymmetric and symmetric connections. Further analyses and illustration are presented in section 6.3.5.

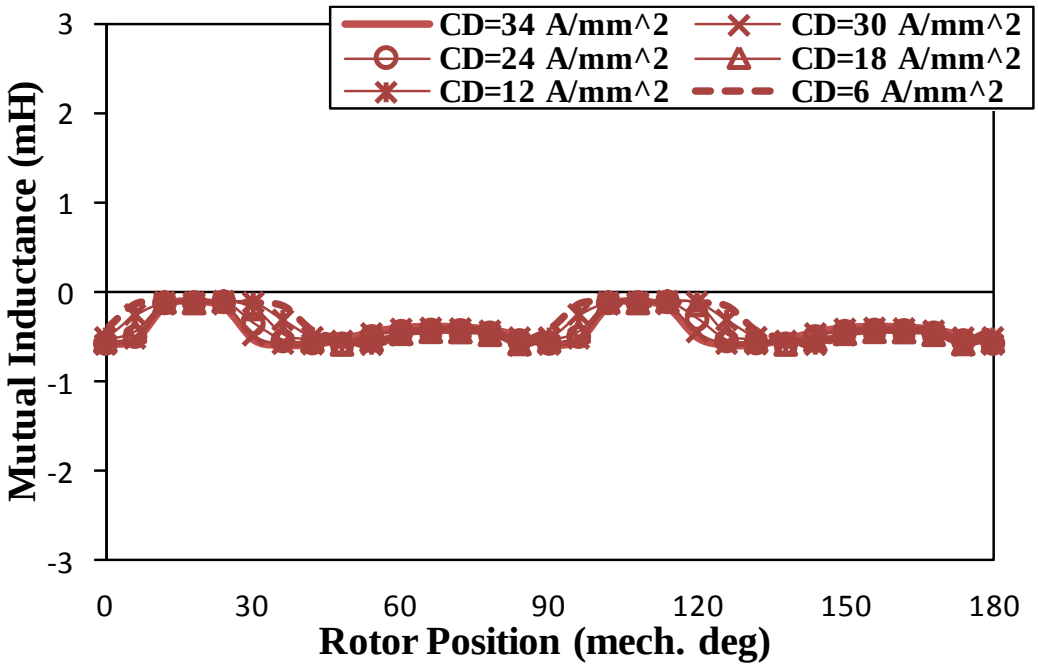

(a) Asymmetric winding connection

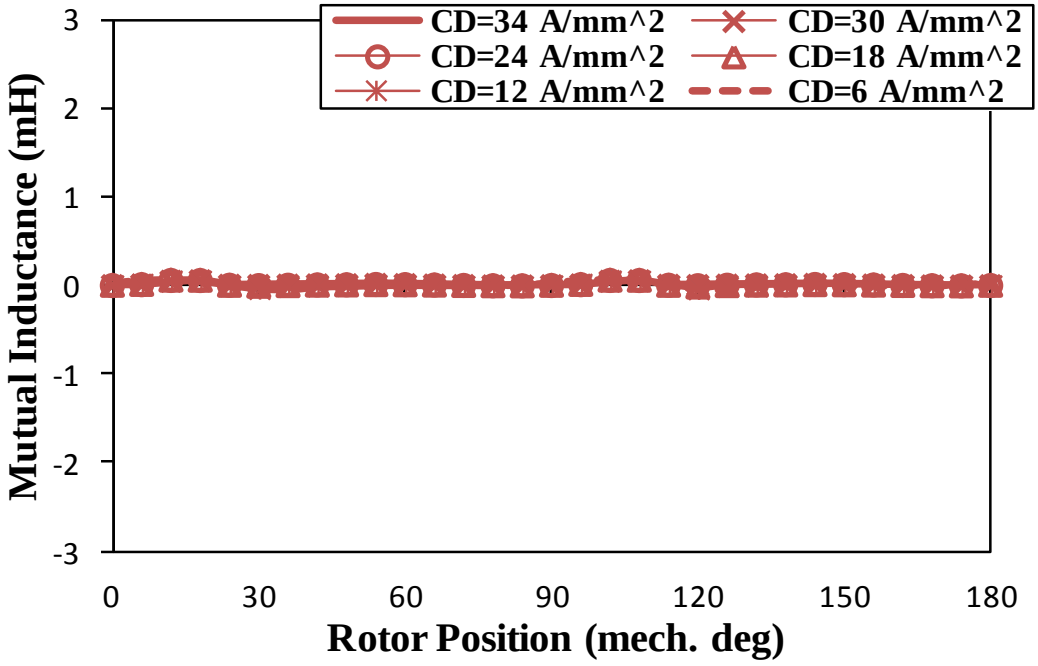

(b) Symmetric winding connection

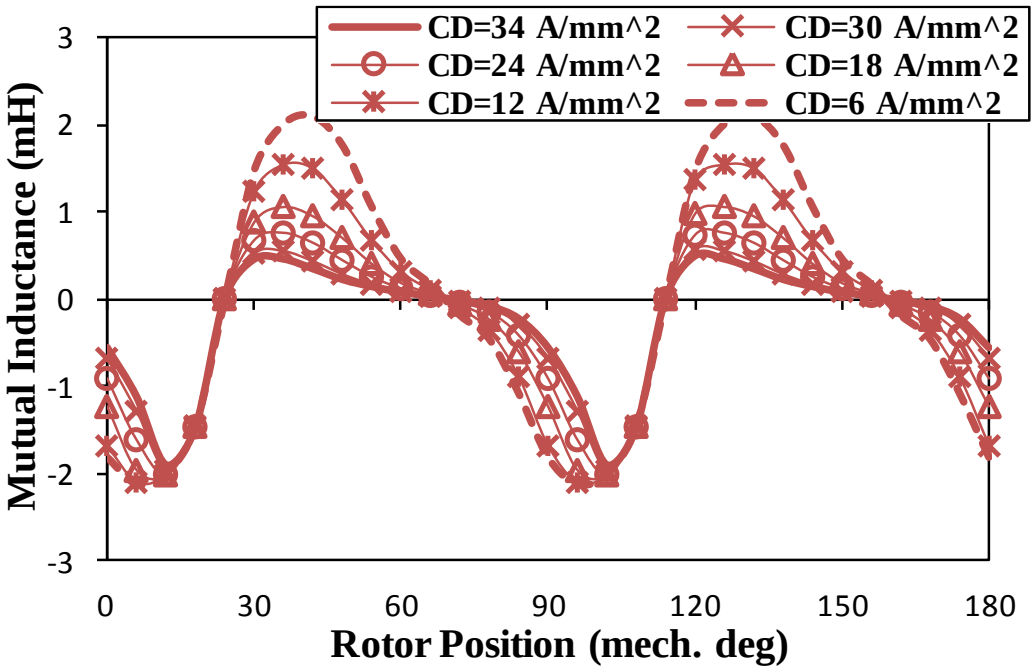

(c) Hybrid winding connection

Fig. 6.9 Comparison of mutual inductances of 6 stator/4 rotor poles machines having different winding connections for different current densities.

6.3.4. Phase Voltage

Using the phase current I_{ph}, resistance R_{ph} and flux linkage ψ_{ph} the phase and line voltages of the SynR machines can be calculated by (6.1) and (6.2), respectively, [160].

$$V_{ph} = I_{ph}R_{ph} + \frac{d\psi_{ph}}{dt} = I_{ph}R_{ph} + \frac{\Delta\psi_{ph}}{\Delta t} \tag{6.1}$$

$$V_{line} = V_{phA} - V_{phB} \tag{6.2}$$

where Δt is the time step of phase flux linkage variations.

Equation (6.1) is utilized to predict the three phase voltage waveforms of the three 6 stator/ 4 rotor poles SynR machines under investigation, Fig. 6.10. Due to non-symmetrical flux linkage waveforms of the machine with asymmetric winding connection, Fig. 6.5(b), its phase voltage waveforms are also non-uniform and they have sharp spikes, Fig. 6.10 (a). In turn, these spikes enlarge the required DC-link voltage to operate the machine since the DC link voltage should be higher than the maximum values, i.e. spikes, of the machine line

voltage, this issue will be further discussed in section 6.5. On the other hand, the machines having symmetric and hybrid winding connections have uniform phase voltage waveforms, Fig. 6.10(b) and Fig. 6.10(c), since their flux linkage waveforms are symmetric, Fig. 6.5 (c) and Fig. 6.5 (d).

Furthermore, the machine line voltages under the three winding connections are compared in Fig. 6.11. It shows that the peak line voltage of the machine with the asymmetric winding connection is nearly double of its counterpart of the machine with symmetric winding connection. This is due to the non-uniform phase voltage waveforms, Fig. 6.10(a). Furthermore, the phase voltage waveforms of machine with hybrid winding connection are uniform, Fig. 6.10(c). However, the line voltage of such machine is also relatively larger, Fig. 6.11. This means the utilization of symmetric winding connection should reduce the DC link voltage requirements. Furthermore, in order to examine the influence of the magnetic saturation on the line voltage behavior of the three considered winding connections. The variations of the machine peak line voltage with such connections are calculated and compared in Fig. 6.12. At low current density, i.e. low magnetic saturation level, the asymmetric and symmetric winding connections result in nearly the same peak line voltage since the asymmetry of the flux linkage waveform of the machine with asymmetric winding connection is relatively low, Fig. 6.5(a). Thus, the line voltage distortions and peaks are relatively small. However, at higher magnetic saturation level, i.e. larger current density, the asymmetric winding connection leads to much larger peak line voltage. On the other hand, the line voltage of the machine with hybrid winding connection is the largest at low current density. But it becomes lower than its counterpart of the machine with asymmetric winding connection when the current density is relatively large. This is because at high magnetic saturation the non-uniformity of the flux density waveforms of such machine becomes more significant, Fig. 6.5(a) and Fig. 6.5(b). Thus, the phase and line voltage distortions and peaks become larger.

It should be mentioned that in the following calculations, investigations and comparisons the maximum, i.e. peak line voltage, will be considered as a reference. However, more analyses are required to determine the required DC-link voltage.

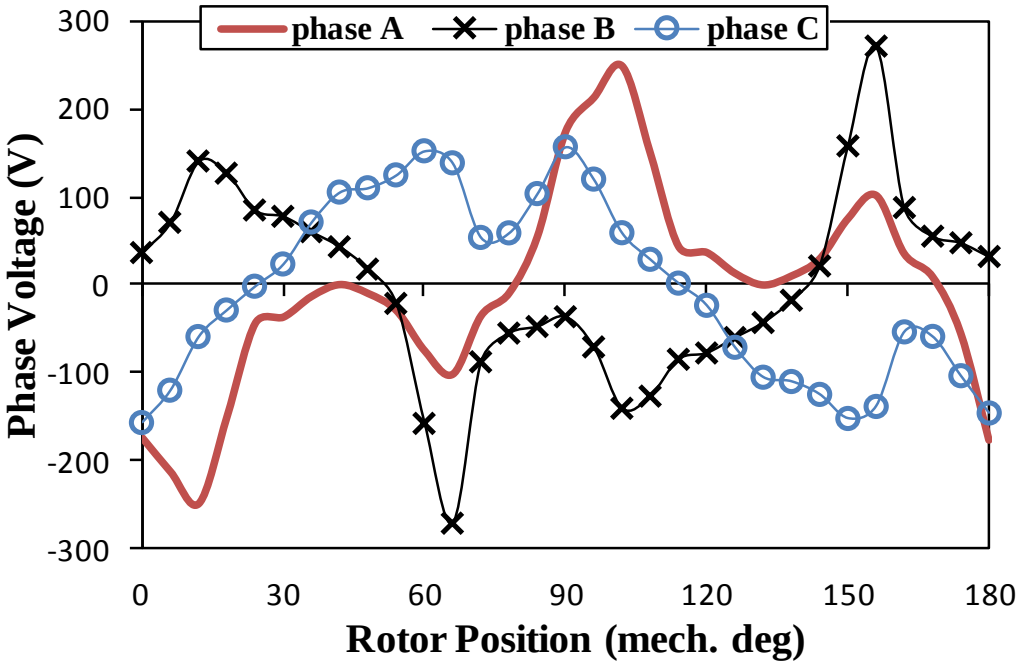

(a) Asymmetric winding connection

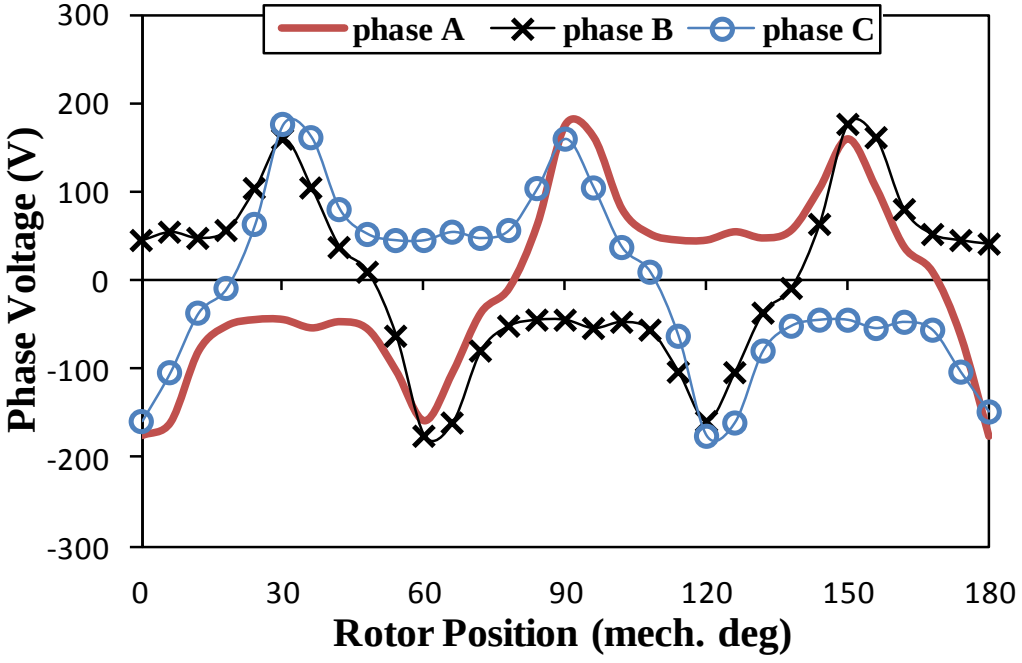

(b) Symmetric winding connection

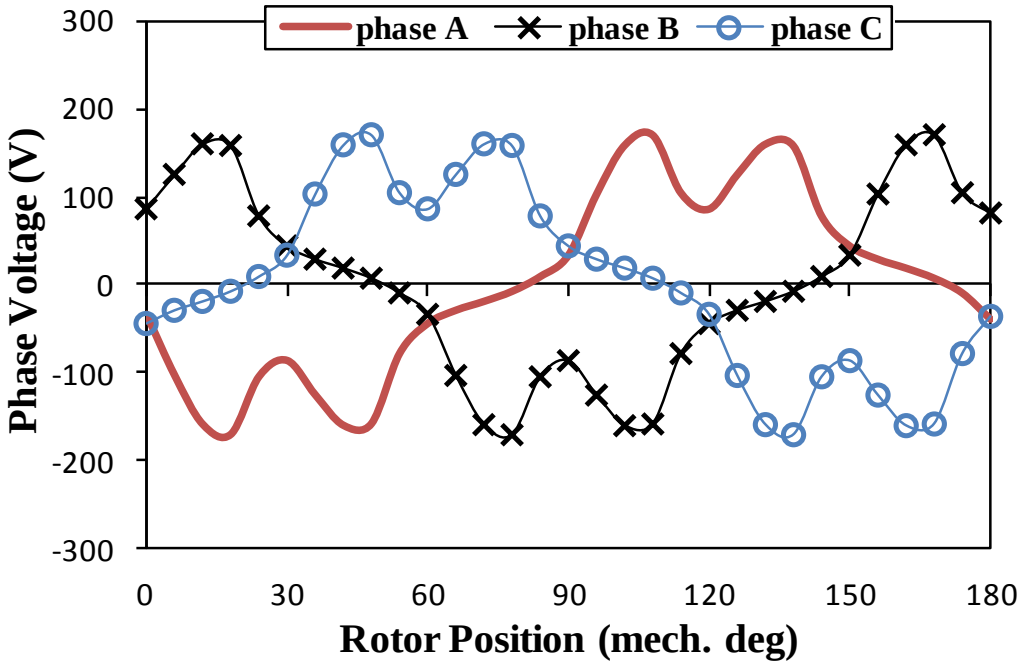

(c) Hybrid winding connection

Fig. 6.10 Comparison of phase voltage waveforms of 6 stator/4 rotor poles machines having different winding connections, at 34 A_{rms}/mm^2 current density and 2500 rpm.

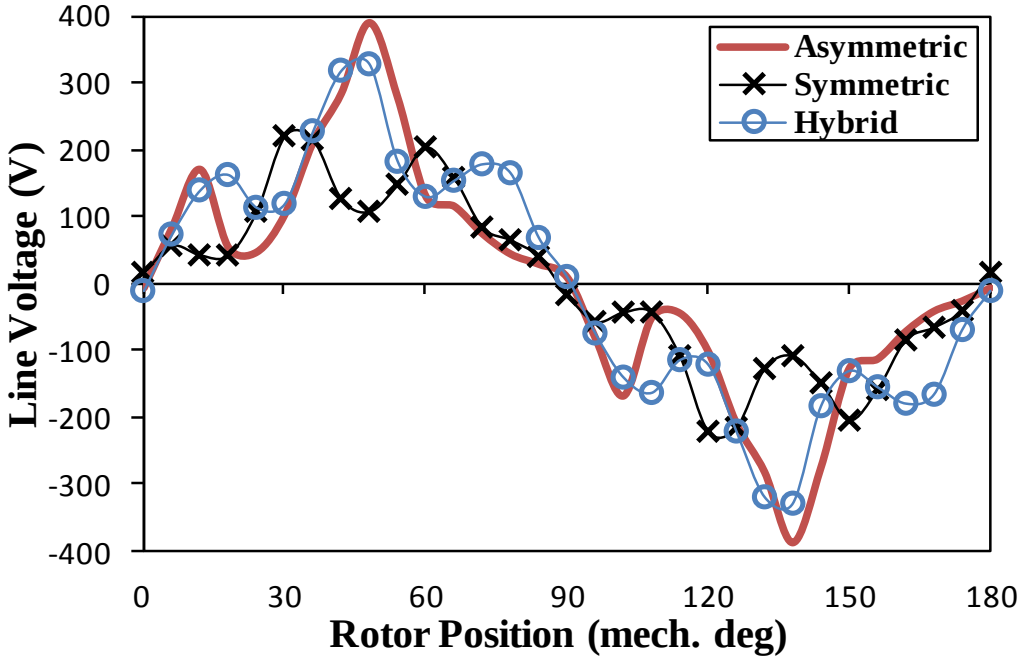

Fig. 6.11 Comparison of line voltage waveforms of 6 stator/4 rotor poles machines having different winding connections, at 34 A_{rms}/mm^2 current density and 2500 rpm.

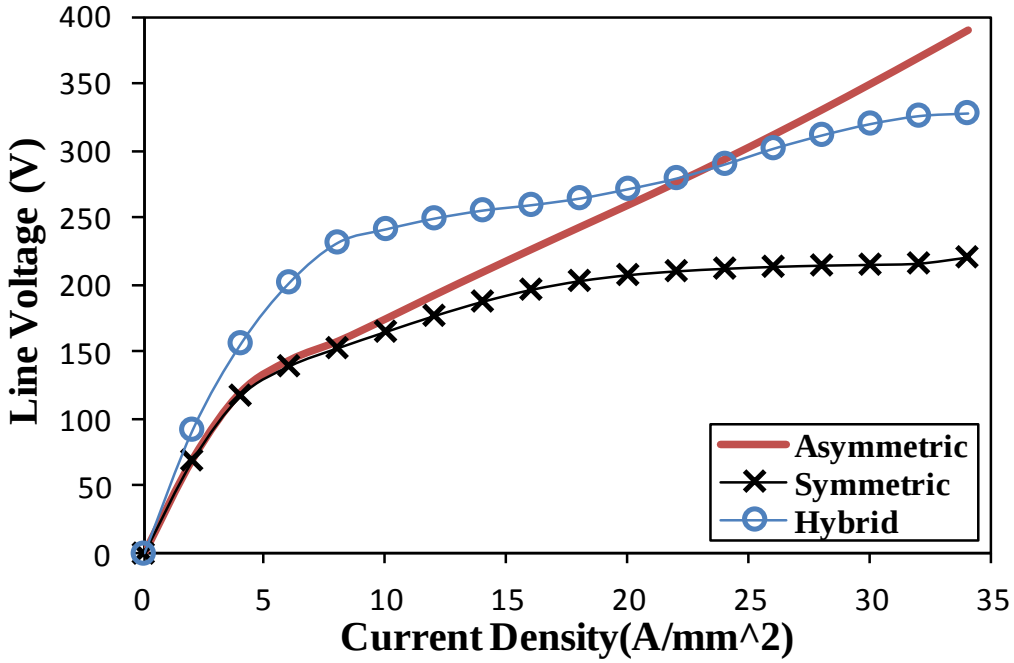

Fig. 6.12 Comparison of peak line voltage against current density of 6 stator/4 rotor poles machines having different winding connections at 2500 rpm.

6.3.5. Output Torque

The output torque waveforms of the analyzed 6 stator/4 rotor pole SynR machine are predicted for the three different winding connections and compared in Fig. 6.13. The output torque of the machine with the hybrid winding connection is much larger comparing with its counterparts of the machines with asymmetric and symmetric connections. As mentioned before, this is due to the relatively larger mutual inductance variations of such connection. On the other hand, the analyzed machine exhibits similar output torque when its windings are asymmetrically or symmetrically connected. But the symmetric winding connection results in lower torque ripple, as clearly shown in Fig. 6.14, since its flux linkage waveforms are relatively less distorted, Fig. 6.5. It can be also noticed that the torque ripple period due to asymmetric winding connection is 90 mechanical degree, while it 30 mechanical degree for both the symmetric and hybrid counterparts. This is due to non-uniformity of the phase flux linkage waveforms of the asymmetric winding connection, Fig. 6.5(b), since the torque ripple period is the phase flux linkage waveforms repetition period divided by the pole pair number, i.e. while they are uniform for the other two connections, i.e. for asymmetric connection: 180/2=90 mechanical degree while for other two connections: 60/2=30 mechanical degree. In order to illustrate the influence of the magnetic saturation, the variations of the average output torque against the current density of the analyzed machine

with three considered winding connections are calculated and compared in Fig. 6.15. It demonstrates that at relatively low current densities, i.e. relatively low saturation level, all connections results in nearly the same average output torque. For the asymmetric and symmetric winding connections, this phenomenon is always the same for any current density value. However, the average output torque of the machine with the hybrid winding connection becomes significantly larger when the current density increases. This is due to the influence of the magnetic saturation in such connection is relatively small comparing with other two connections as discussed before. Furthermore, in order to evaluate the quality of the output torque, the torque ripple as a percentage of the average torque against the current density of the three winding connections is compared in Fig. 6.16. At relatively low current density, both asymmetric and symmetric connections results in nearly the same torque ripple percentage, which is significantly lower than its counterpart of the machine with hybrid connection. The torque ripple percentage due to such connection sharply decreases when the current density increases since the average output torque becomes larger. Comparing with the asymmetric connection, both the symmetric and hybrid winding connections result in lower torque ripple percentage when the current density is significant. Thus, it can be concluded that the symmetric winding connection results in the most excellent output torque quality. In addition, at high current density the hybrid connection becomes more desirable since it has nearly the same torque percentage as the symmetric winding connection, but its average output torque is significantly larger.

In the previous calculations, the current has been injected at current angle of 45 electrical degrees, thus the d- and q-axis currents are equal since, in theory, such angle should leads to the maximum output torque. However, due to the magnetic saturation, the maximum possible output torque of the motor could be at different angle. Therefore, the motor output torque against the current angle of the analysed 6 stator/4 rotor poles machines with three considered winding connections are calculated for different current densities in the range of 0 to 90 electrical degrees. As shown in Fig. 6.17, the maximum output torque for all winding connections can be achieved at the current angle of 50 electrical degrees. Therefore, in order to operate such machines at their maximum torque per ampere capability, such angle should be employed.

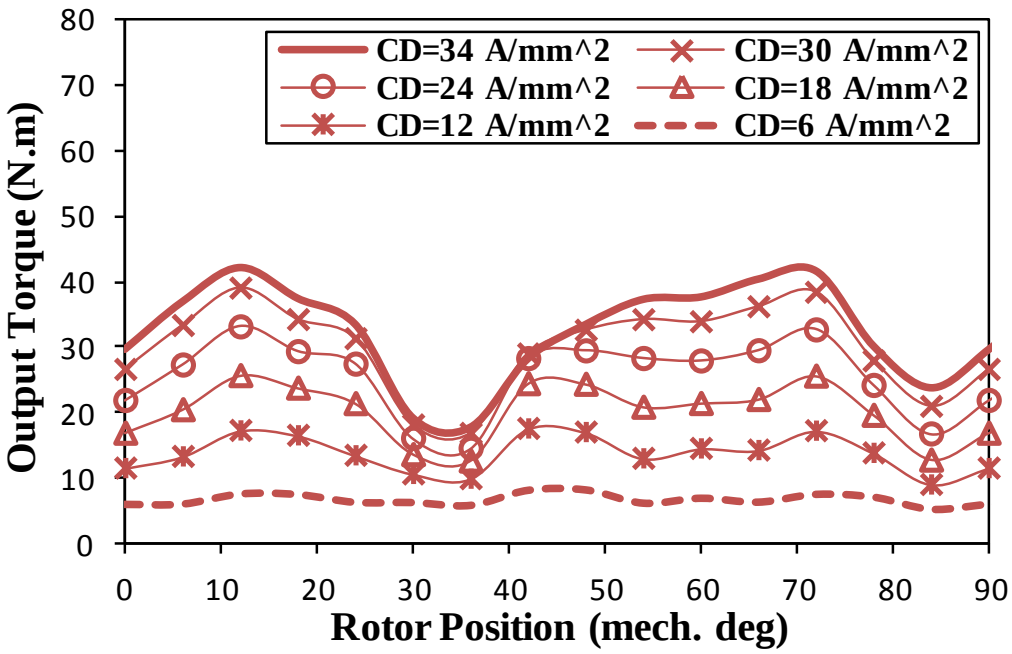

(a) Asymmetric winding connection

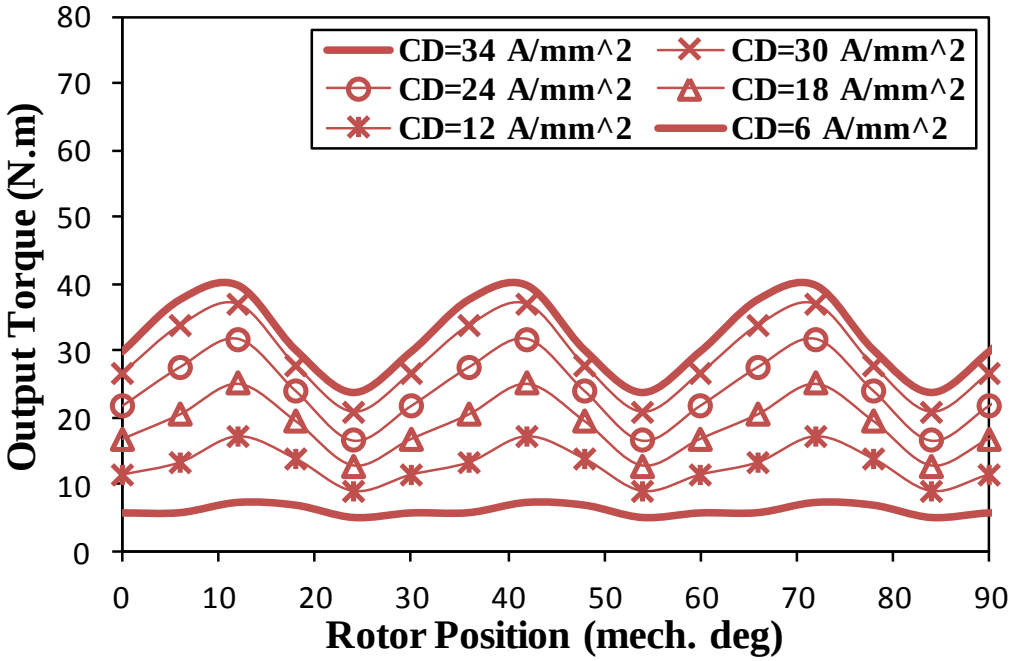

(b) Symmetric winding connection

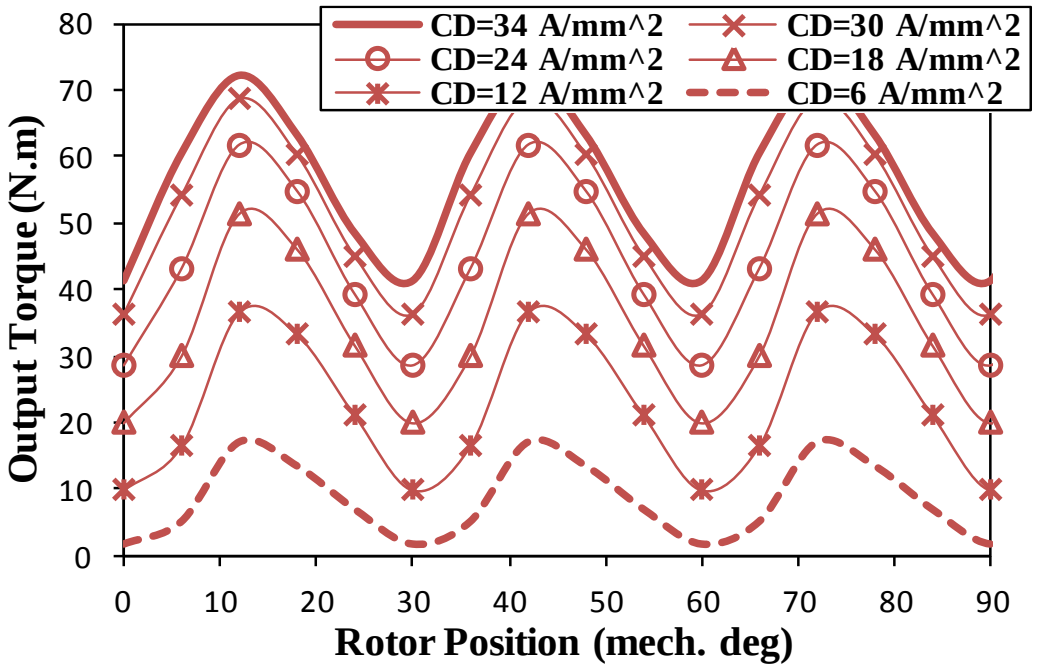

(c) Hybrid winding connection

Fig. 6.13 Variation of output torque waveforms of 6 stator/4 rotor poles machines having different winding connections at different current density.

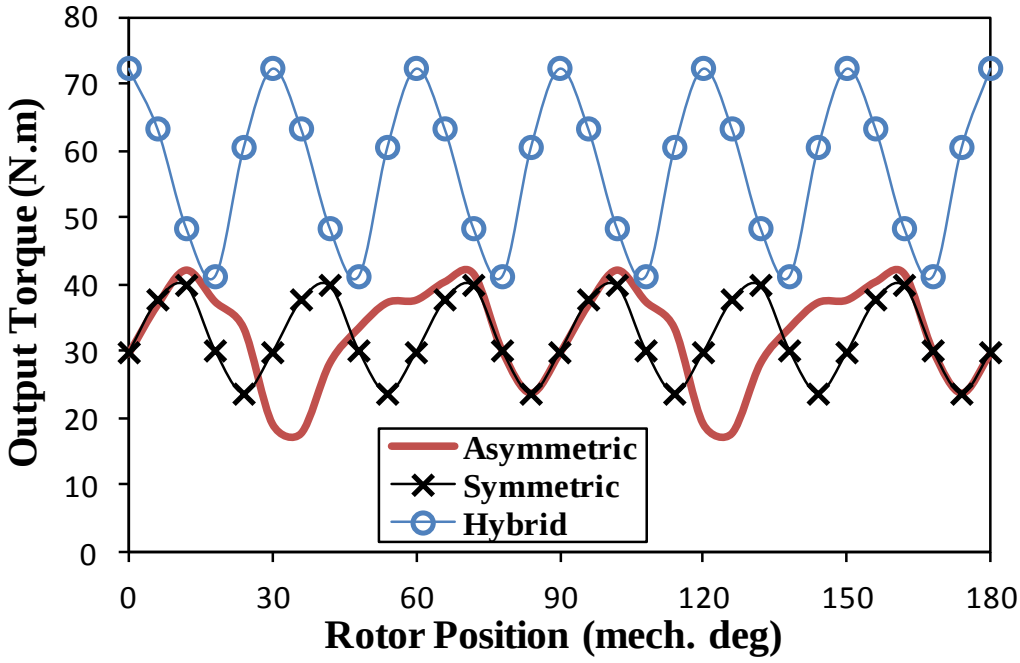

Fig. 6.14 Comparison of output torque waveforms of 6 stator/4 rotor poles machines having different winding connections at 34 A_{rms}/mm^2 current density.

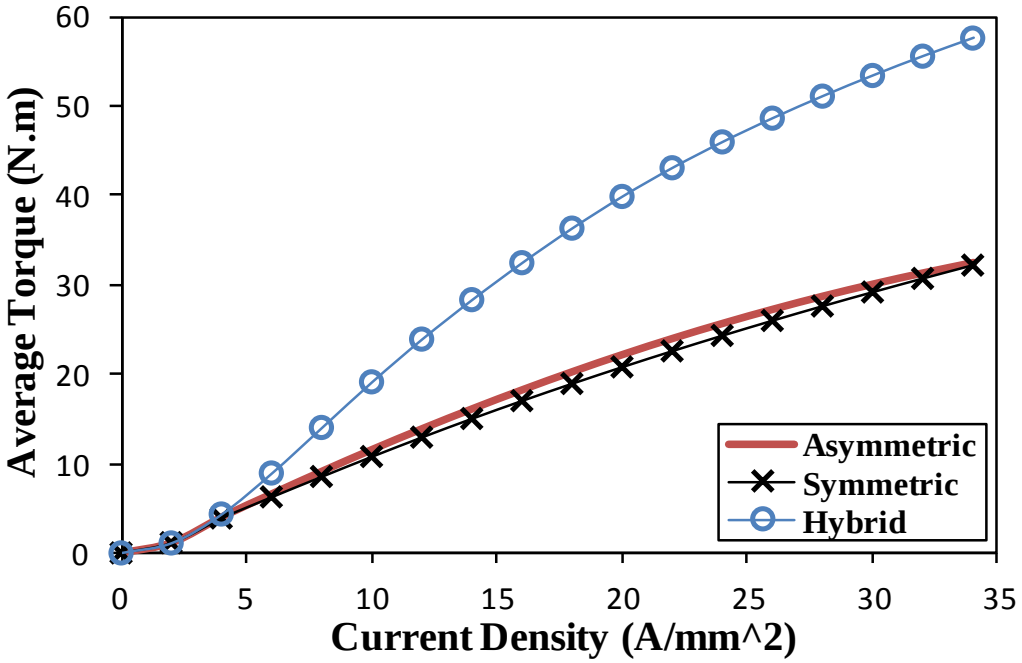

Fig. 6.15 Comparison of average output torque of 6 stator/4 rotor poles machines having different winding connections at different current densities.

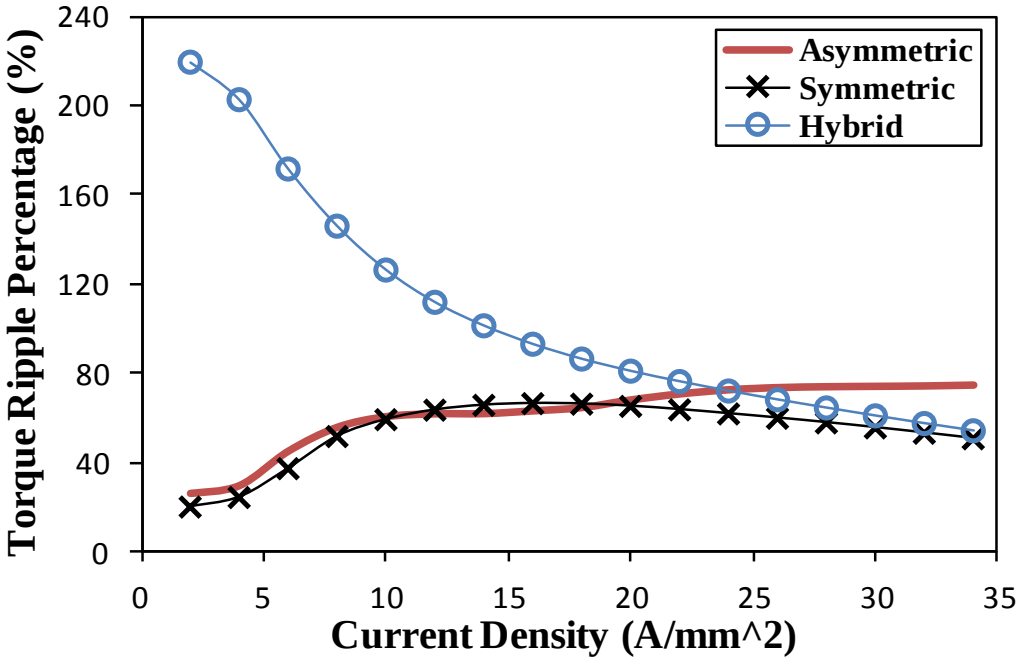

Fig. 6.16 Comparison of torque ripples of 6 stator/4 rotor poles machines having different winding connections at different current densities.

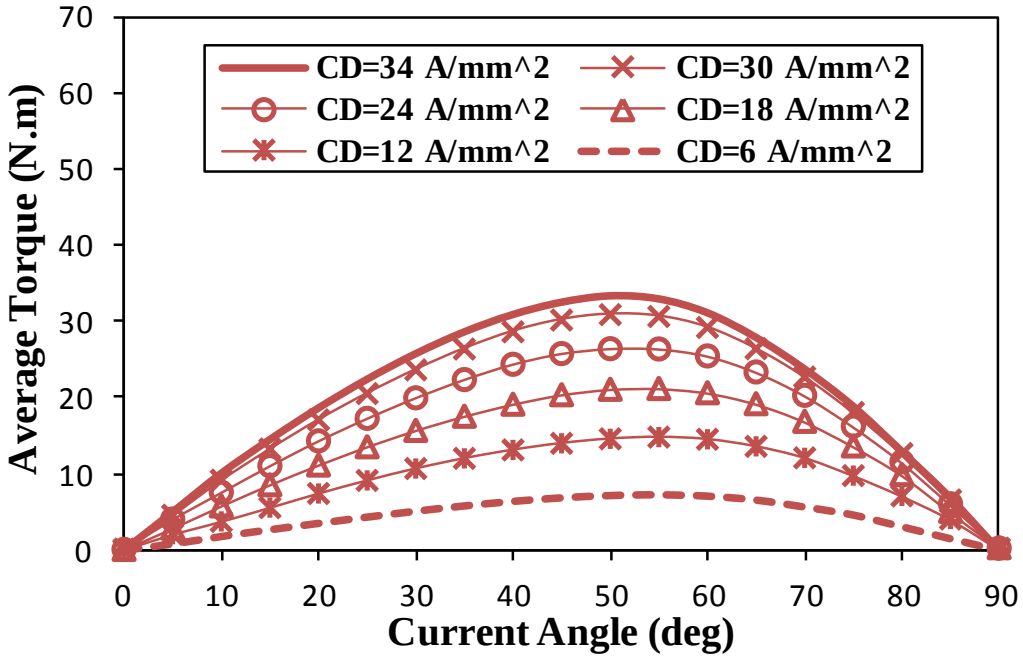

(a) Asymmetric winding connection

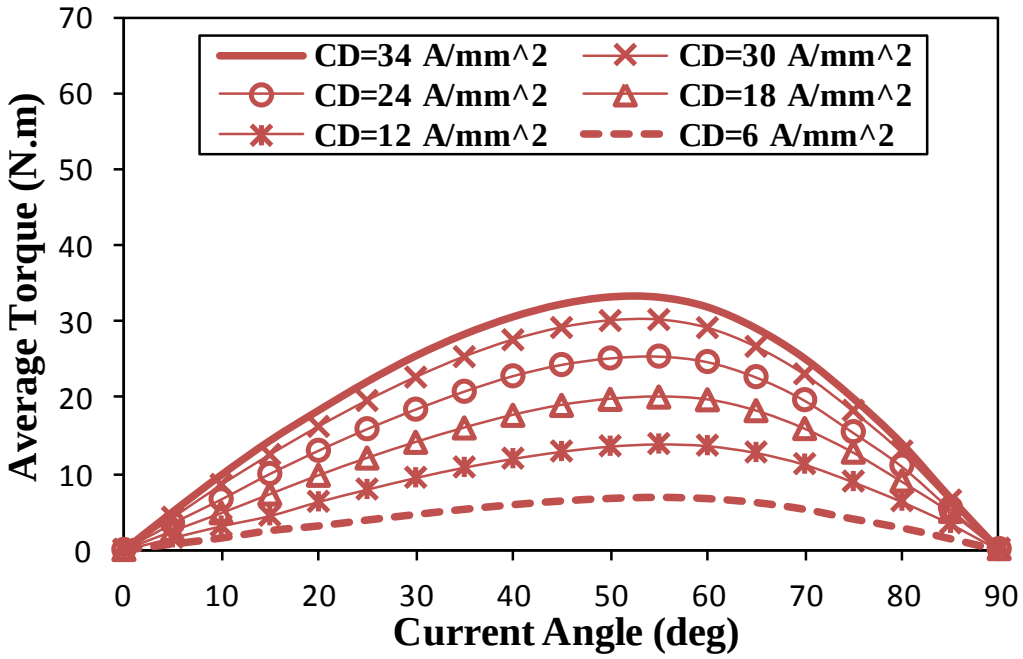

(b) Symmetric winding connection

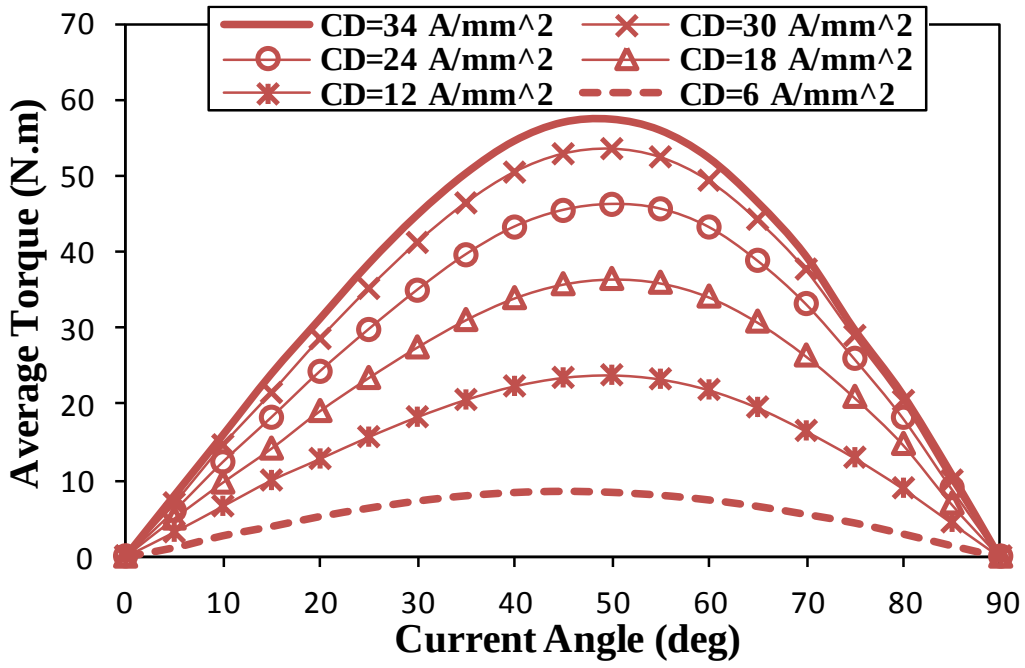

(c) Hybrid winding connection

Fig. 6.17 Variaiton of average output torque against current angle of 6 stator/4 rotor poles machines having different winding connections at different current density.

6.4. Torque-Speed Characteristics

In order to investigate the influence of the current angle on the line voltages of the studied 6 stator/4 rotor poles machines, thus to examine the possibility of utilising such angle to satisfy the voltage limitation during the flux weakening operation. The peak line voltage against the current angle is calculated for the three different winding connections. During machine operation, the voltage limitation, i.e. DC-link voltage (U_{DC}), should be ideally higher than the peak value of the machine line voltage. Therefore, in the following calculation, e.g. torque-speed characteristics prediction, the peak value of the line voltage will be considered, as shown in Fig. 6.18. It shows that for all winding connections, the influence of the current angle on the line voltage is negligible at low current density. However, at relatively high current densities the line voltage gradually increases against the current angle, i.e. such increase becomes shaper when the current angle is larger than 60 electrical degrees. Therefore, in the calculation of the torque-speed characteristics the current angle will be fixed at optimal current angle while it also results in nearly in the same line voltage as the 45 degree current angle, Fig. 6.18. However, the reason for such voltage behaviour is thoroughly investigated in section 6.5.

In order to predict the torque-speed curve of the analyzed machines, the variations of their peak line voltage against the current density are calculated for different rotation speeds, as shown in Fig. 6.19. These results together with the variations of output torque against the current density, Fig. 6.15, are utilized to predict the torque-speed curve for voltage limitation of 600V. It should be mentioned that the voltage drop on the inverter drive switches is ignored during these analyses. In order to clearly illustrate such procedure, the determination of the optimal output torque at 6000 rpm is explained in details for the machine with the asymmetric winding connection. At such speed, the voltage limit can be satisfied at current density of 19 A/mm^2, as shown in Fig. 6.19(a). The corresponding output torque of this current density is 21.5 Nm, as illustrated in Fig. 6.20. This process needs to be carried out over whole speed range, thus the whole torque-speed characteristics are obtained. The predicted torque- and power-speed characteristics of the studied 6 stator/4 rotor poles SynR machines having different winding connections are compared in Fig. 6.21, while the corresponding peak phase currents and line voltages are given in Fig. 6.22 and Fig. 6.23, respectively. Although the machine with hybrid winding connection gives a significantly larger maximum output torque comparing with other two winding connections, e.g. it is about 70% larger when the current density is 34A/mm^2, such winding connection exhibits

the lowest flux weakening operation performance for all the current densities since during the flux weakening operation, the machines are operated at relatively low current densities, i.e. low phase currents, as shown in Fig. 6.22. However, comparing with the other two winding connections, the hybrid winding connection produces a larger line voltage at relatively low current density, as shown in Fig. 6.12. The behaviour of the line voltage of the studied machines will be investigated in more details in the next section. In addition, in terms of maximum output power, the difference between the symmetric and hybrid winding connections becomes relatively small, i.e. it is about 10% at 34A/mm^2 current density as illustrated in Fig. 6.21(b) since the machine with the symmetric winding connection exhibits wider constant torque region, Fig. 6.21(a), thus larger output power at higher speed. Such difference becomes even smaller when the maximum current density is lower, Fig. 6.21(f).

Furthermore, at relatively larger current density, e.g. 34 A/mm^2, the constant-torque region of the machine with the symmetric winding connection is wider than its counterpart of the machine with the asymmetric winding connection, Fig. 6.21 (a). However, the utilizing of the asymmetric winding connection results in slightly larger output torque at lower current densities, Fig. 6.21(b), and Fig. 6.21(c), since the benefit of the symmetric winding connection over its asymmetric counterpart in terms of line voltage reduction is significant at relatively large current densities. However, it is nearly diminished at low current density, low magnetic saturation level, as illustrated in Fig. 6.12 as well as Fig. 6.18. In conclusion, the benefits and disadvantages, thus the suitability of such winding connections is determined according to application requirement as well as voltage and current limitations. In order to present a more comprehensive comparison, the losses and efficiency of the studied machines are also analysed and compared in section 6.6.

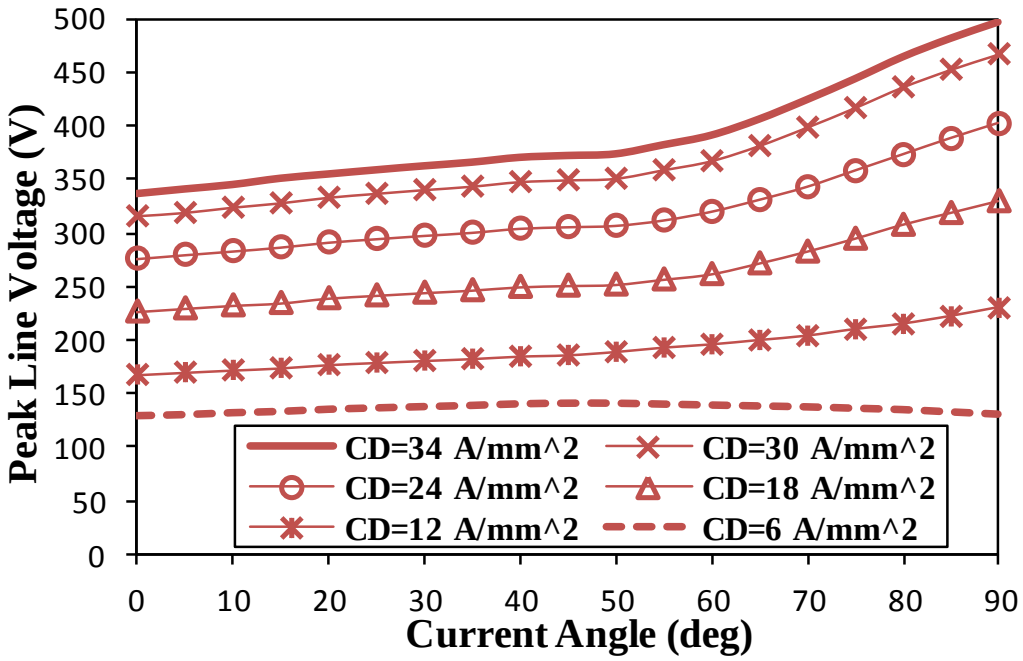

(a) Asymmetric winding connection

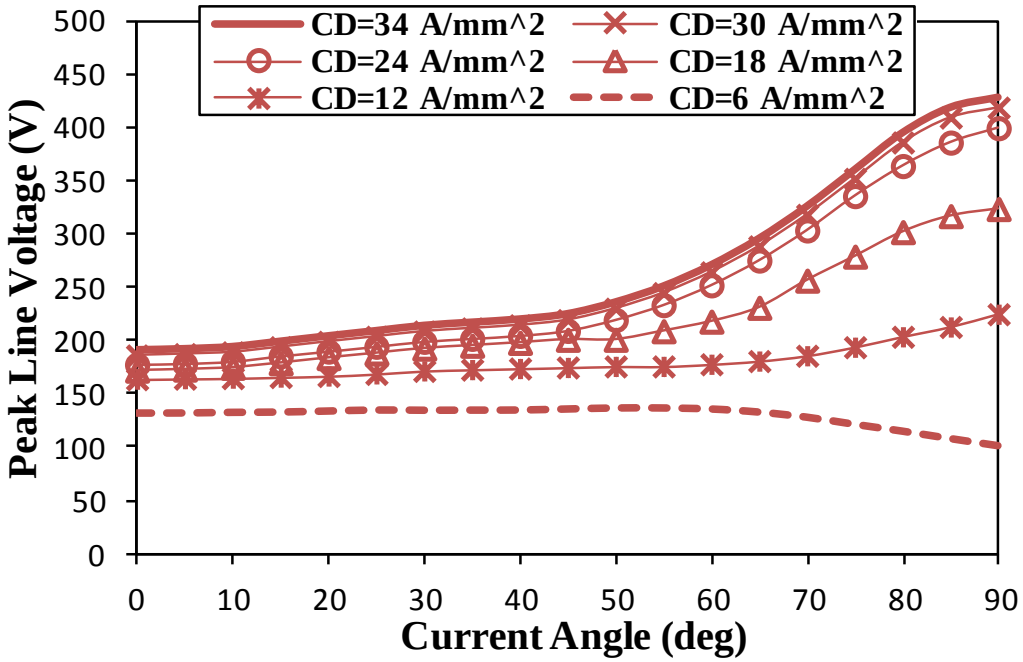

(b) Symmetric winding connection

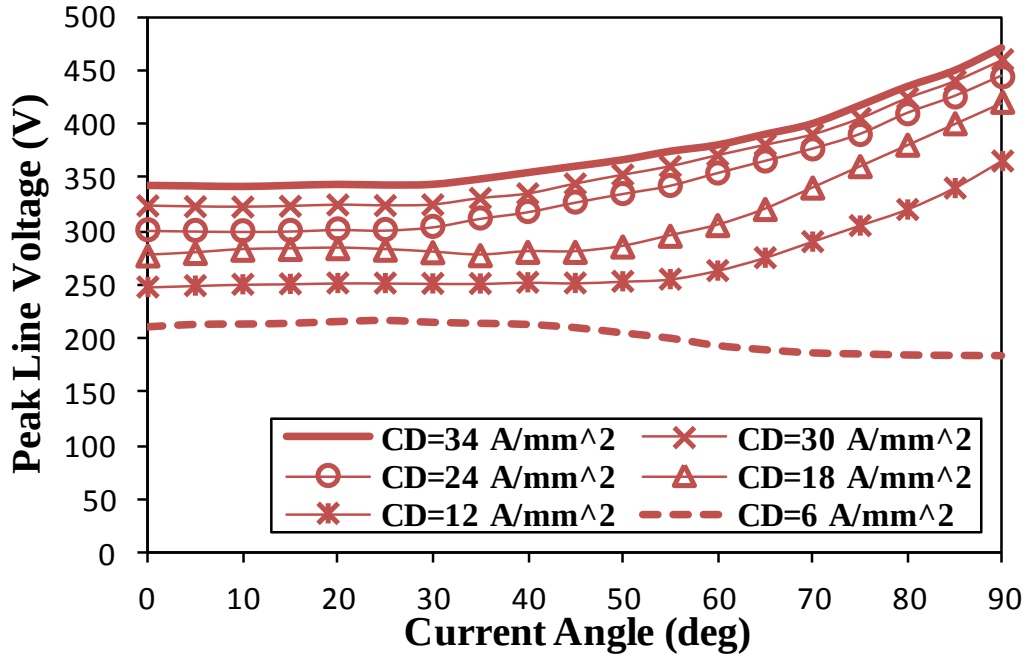

(c) Hybrid winding connection

Fig. 6.18 Comparison of variaitons of peak line voltage against current angle of 6 stator/4 rotor poles machines having different winding connections at different current densities

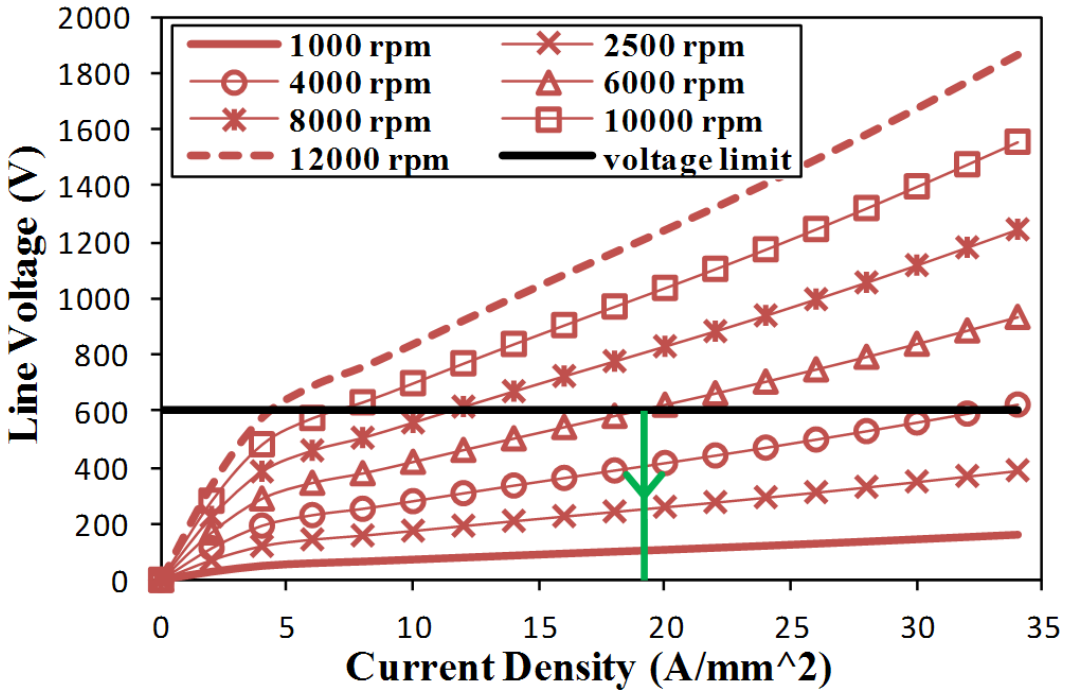

(a) Asymmetric winding connection

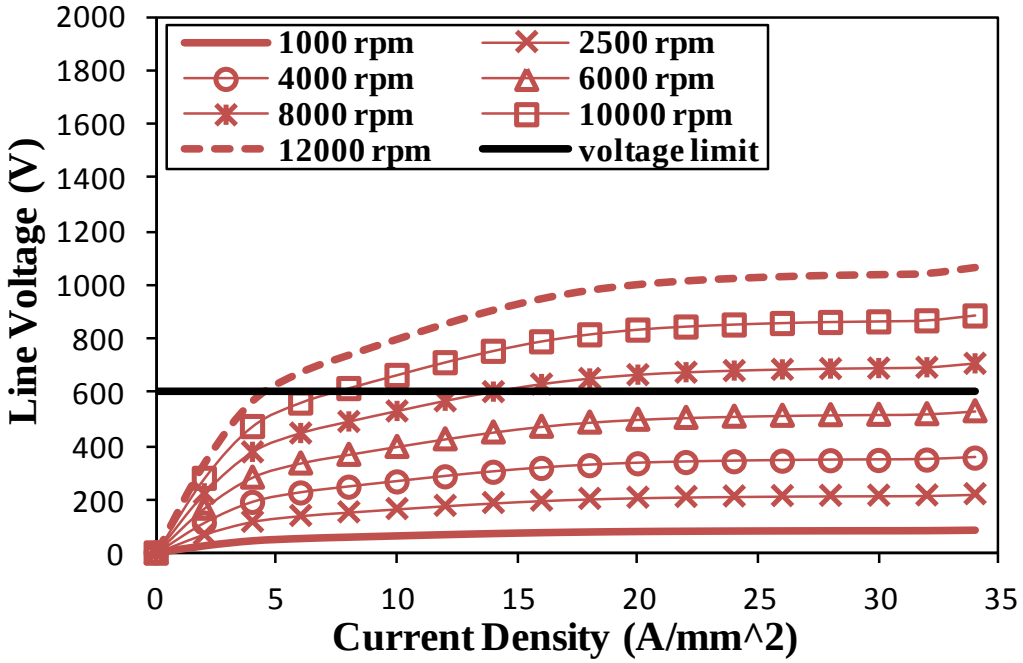

(b) Symmetric winding connection

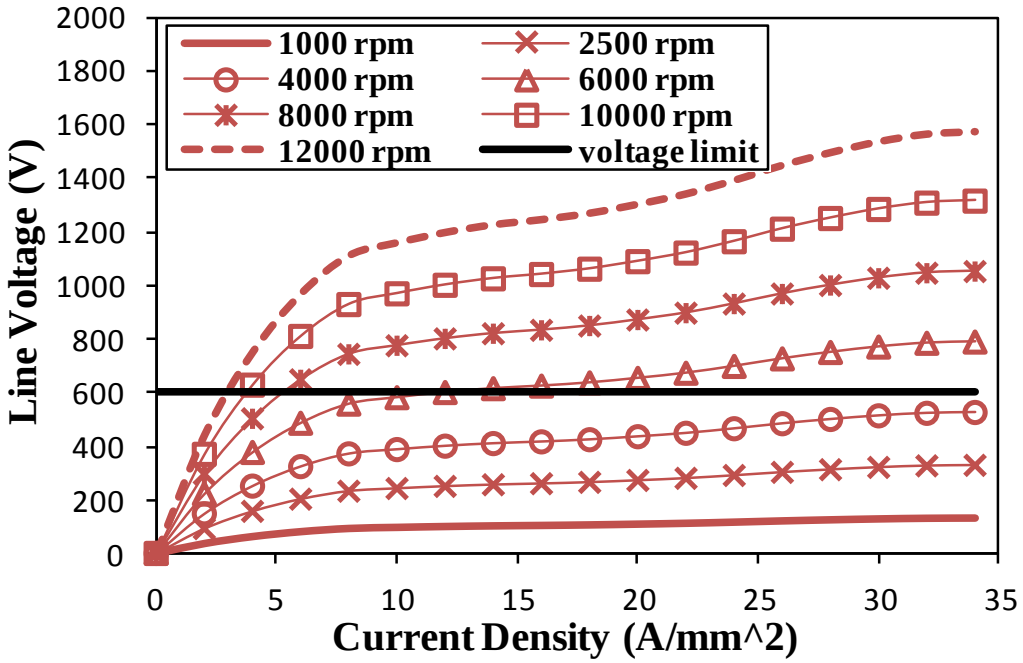

(c) Hybrid winding connection

Fig. 6.19 Comparison of variaitons of peak line voltage against current density of 6 stator/4 rotor poles machines having different winding connections at different rotating speeds.

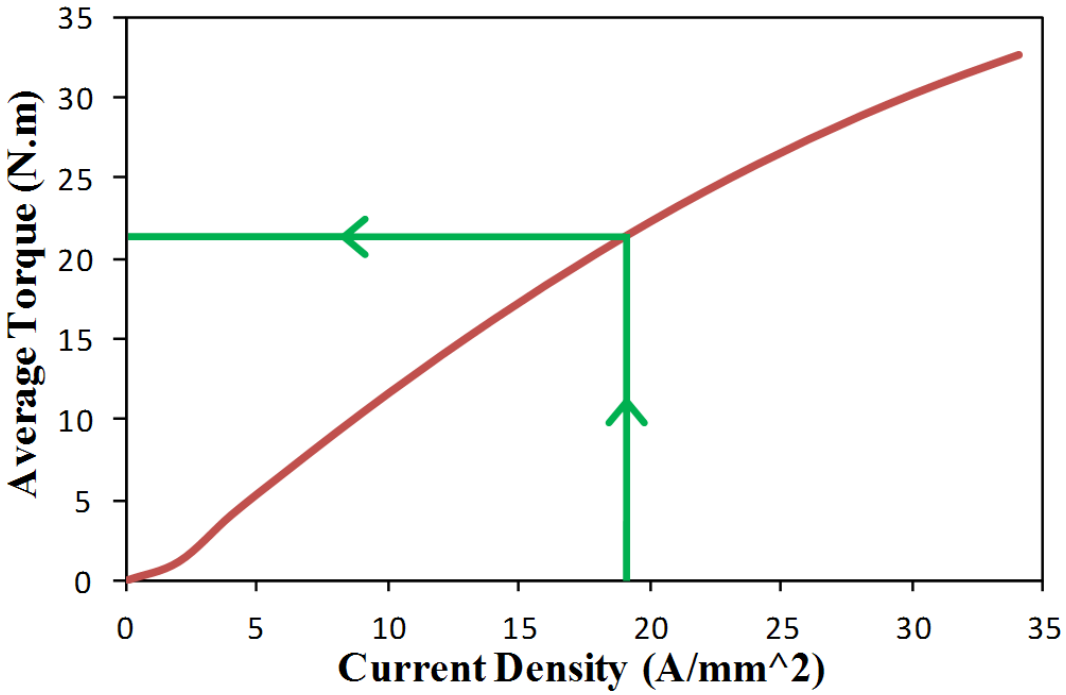

Fig. 6.20 Variation of average output torque of 6 stator/4 rotor poles machine with asymmetric winding connection at different current densities.

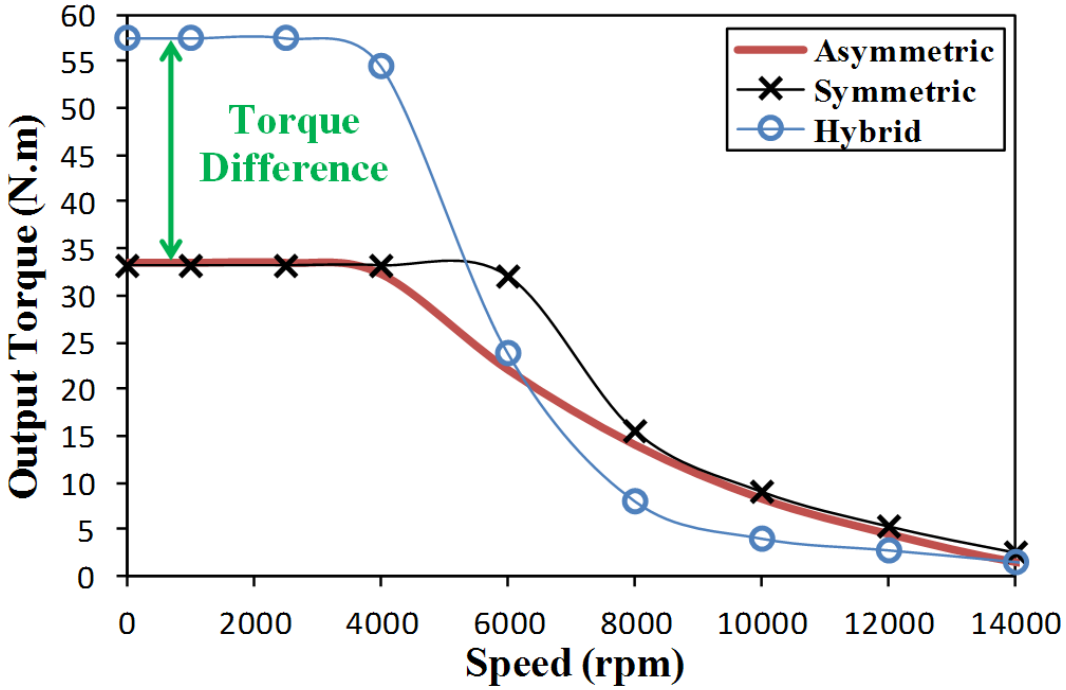

(a) Torque-speed curves at 34 A_{rms}/mm^2 maximum current density

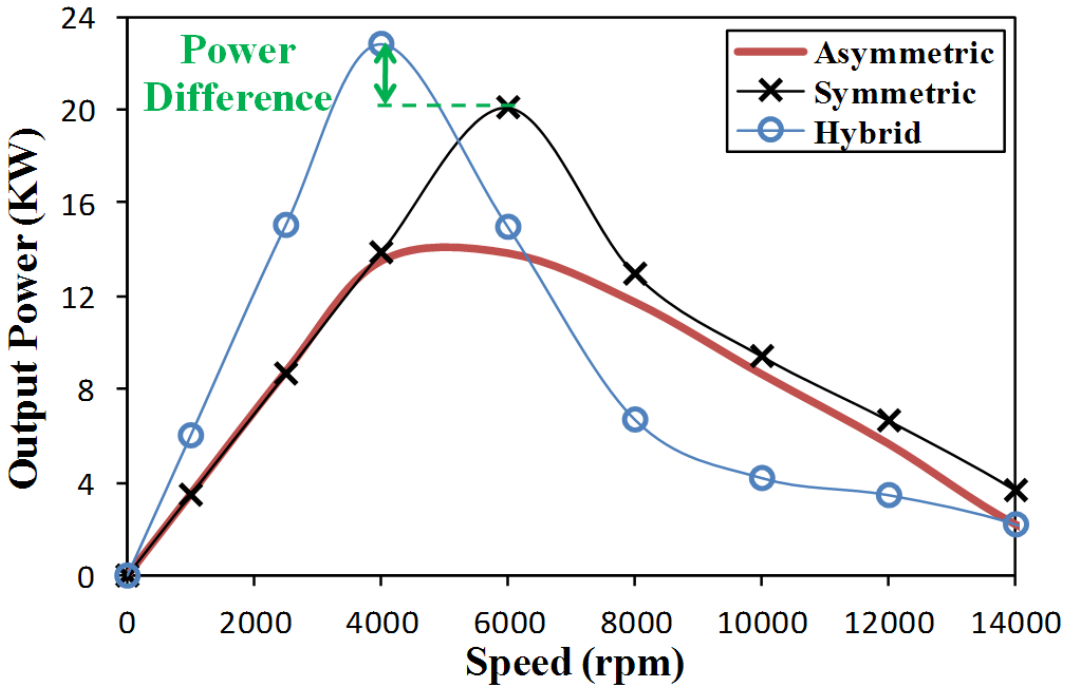

(b) Power-speed curves at 34 A_{rms}/mm^2 maximum current density

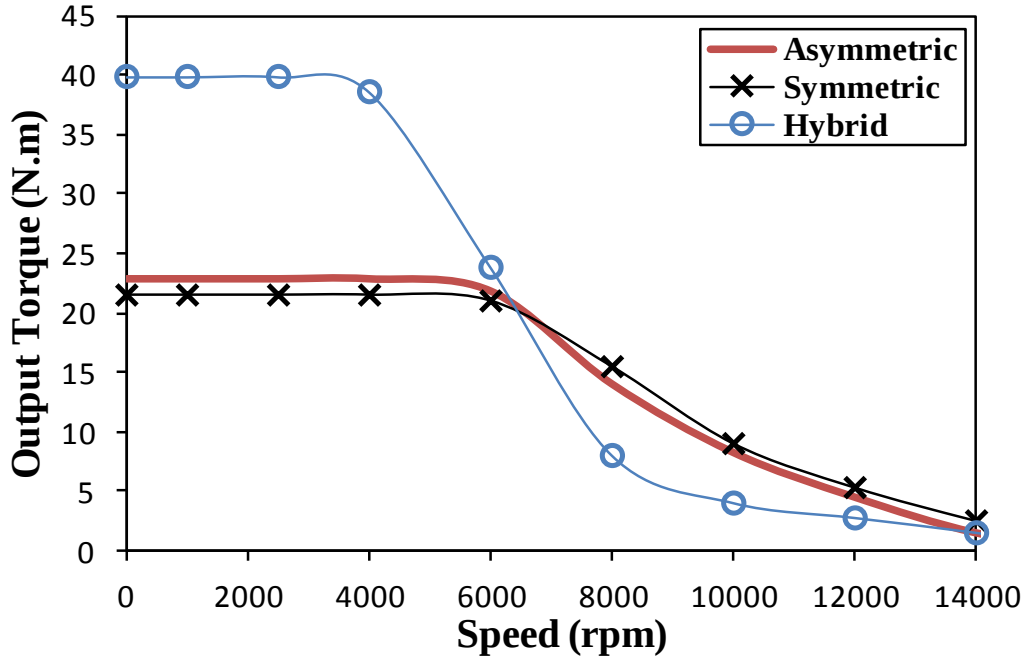

(c) Torque-speed curves at 20 A_{rms}/mm^2 maximum current density

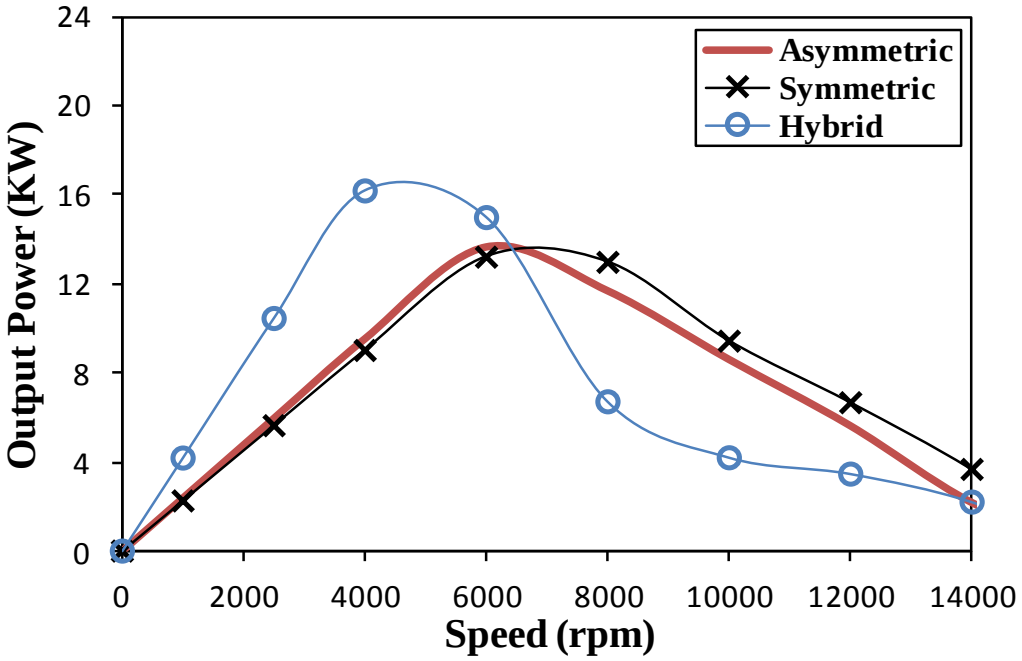

(d) Power-speed curves at 20 A_{rms}/mm^2 maximum current density

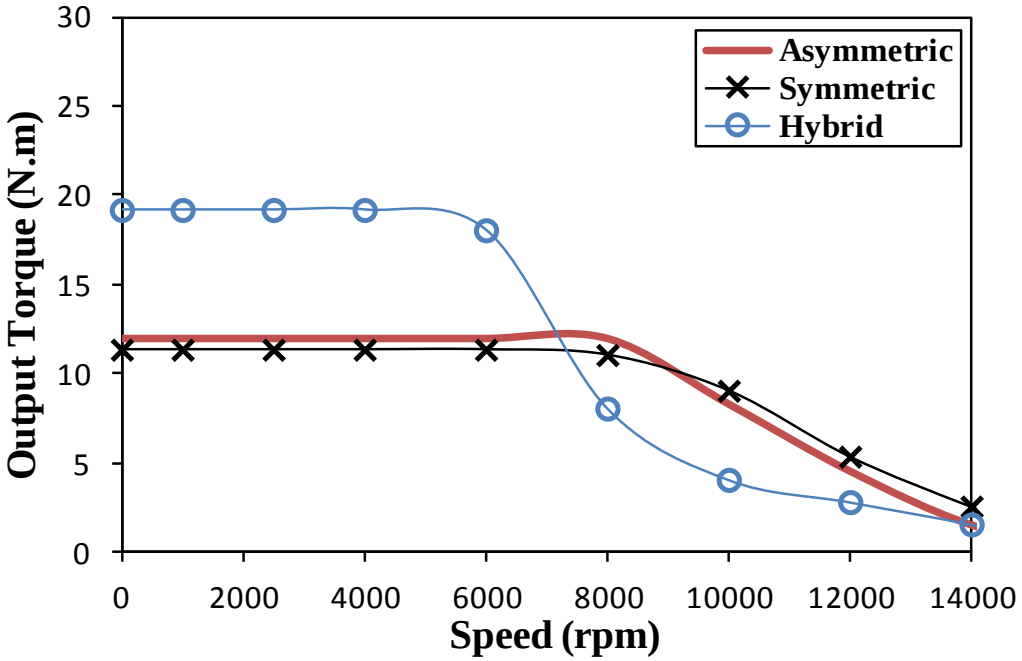

(e) Torque-speed curves at 10 A_{rms}/mm^2 maximum current density

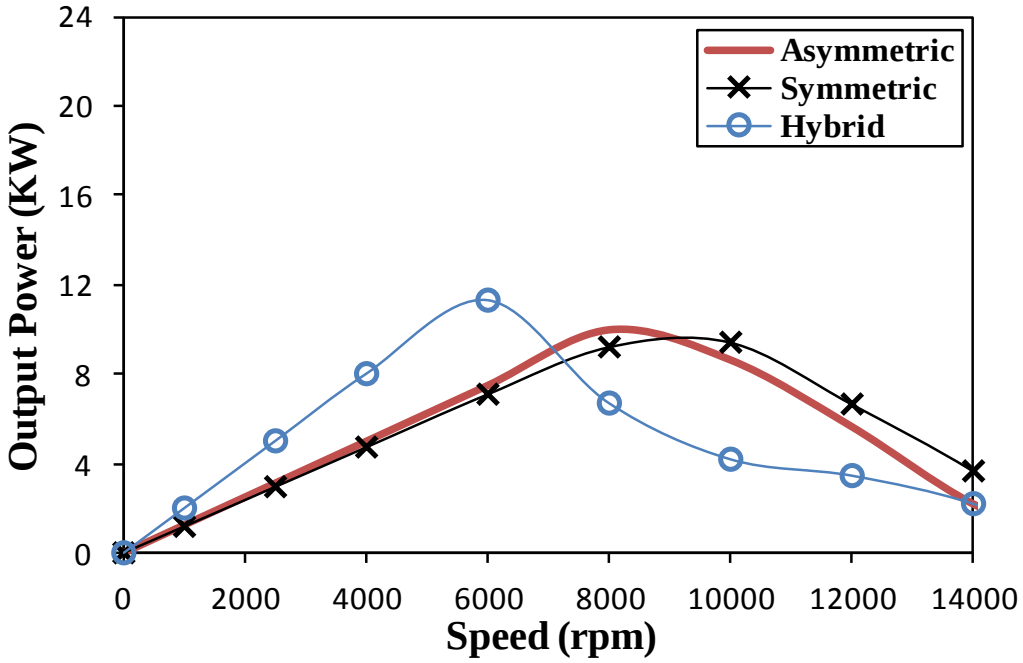

(f) Power-speed curves at 10 A_{rms}/mm^2 maximum current density

Fig. 6.21 Comparison of torque- and power-speed characterstics of 6 stator/4 rotor poles machines having different winding connections at different current densities.

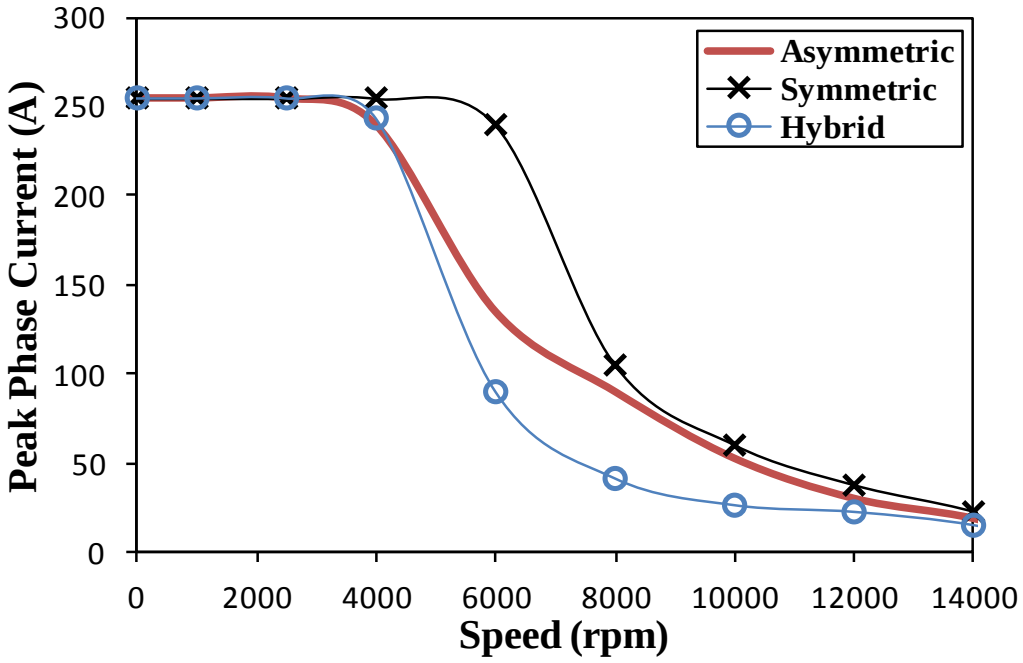

(a) Maximum current density is 34 A_{rms}/mm^2

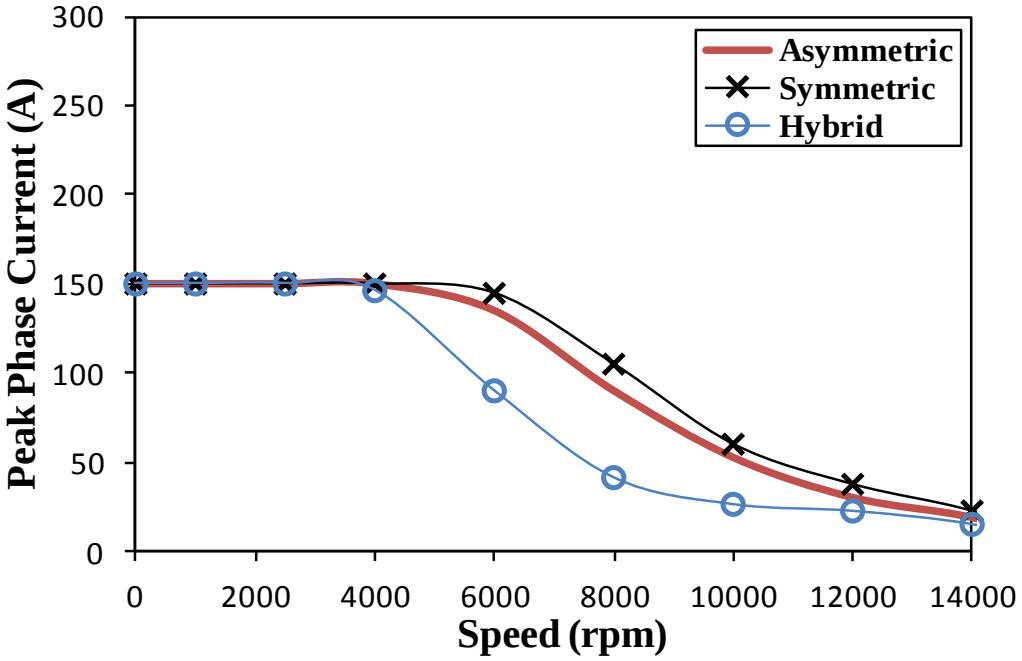

(b) Maximum current density is 20 A_{rms}/mm^2

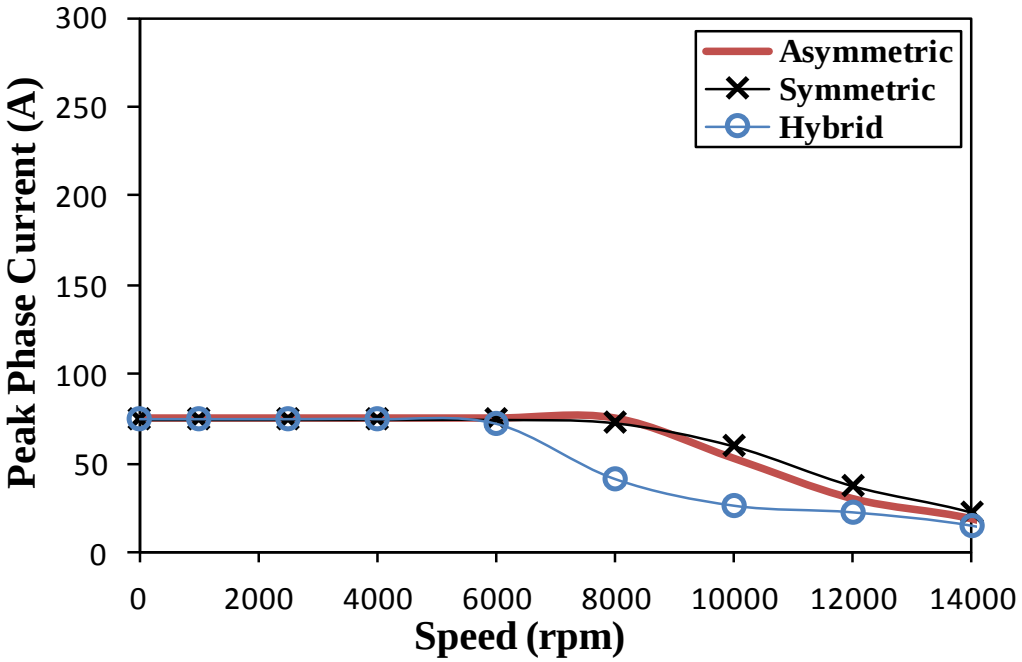

(c) Maximum current density is 10 A_{rms}/mm^2

Fig. 6.22 Variation of corresponding peak phase current of 6 stator/4 rotor poles machines having different winding connections at different current densities.

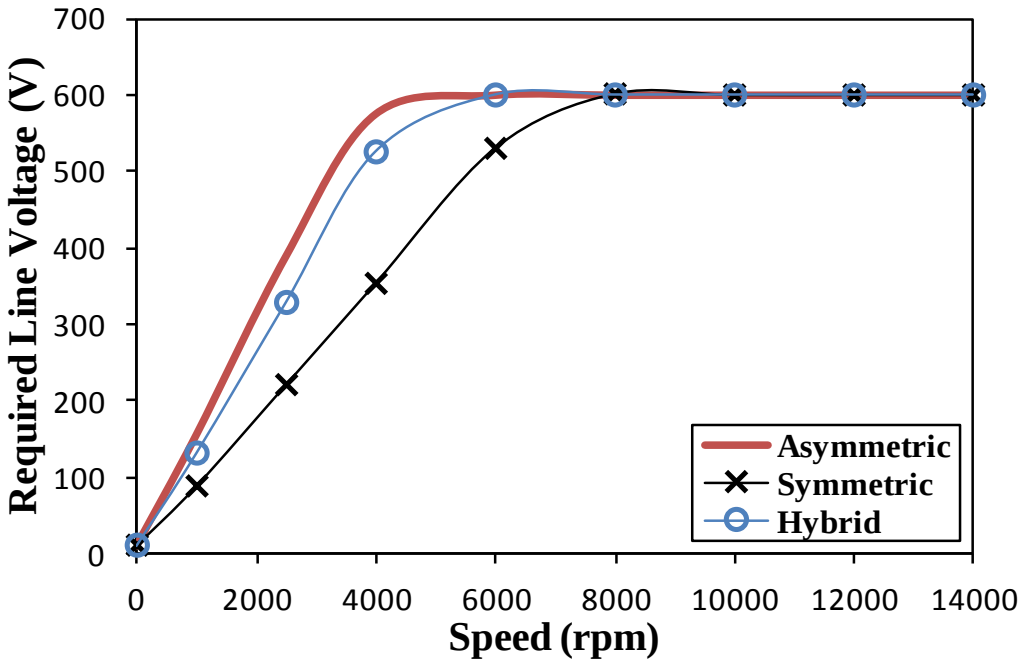

(a) Maximum current density is 34 A_{rms}/mm^2

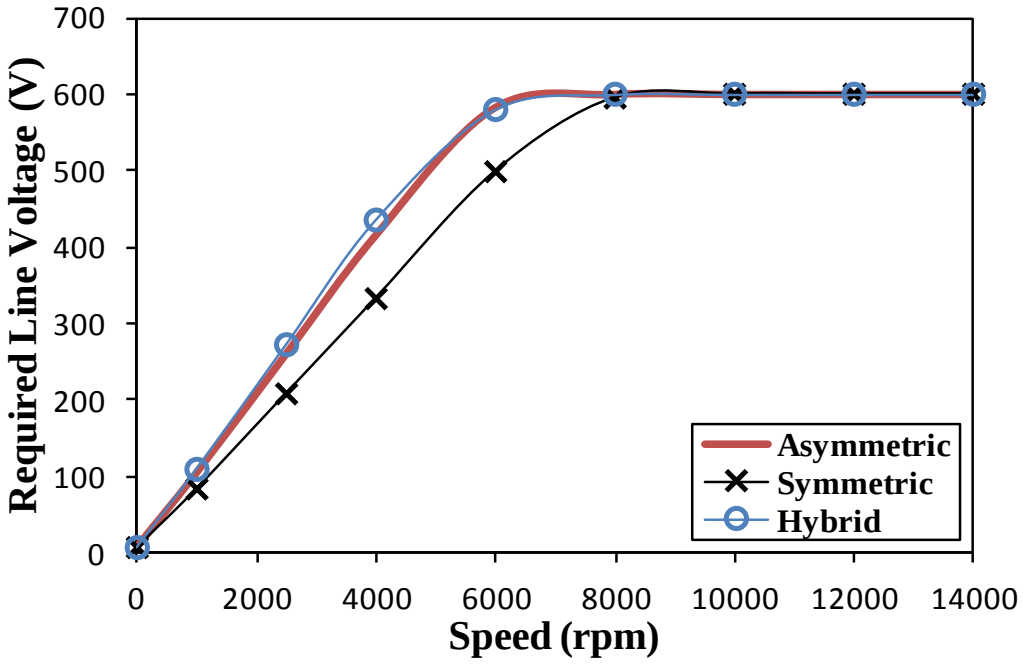

(b) Maximum current density is 20 A_{rms}/mm^2

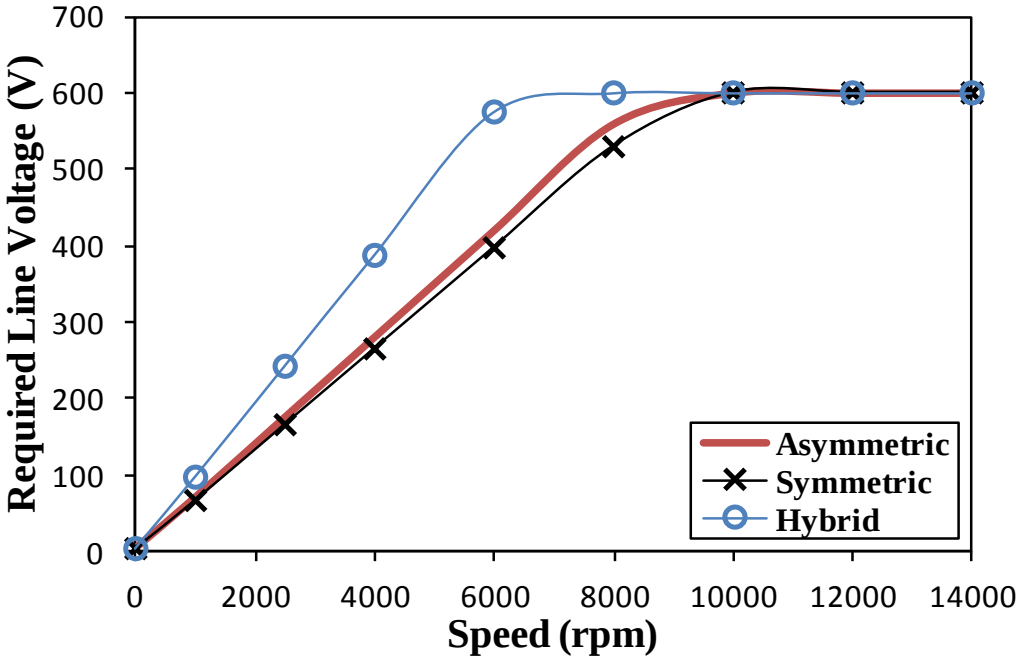

(c) Maximum current density is 10 A_{rms}/mm^2

Fig. 6.23 Variation of required peak line voltage of 6 stator/4 rotor poles machines having different winding connections at different current densities.

6.5. Investigation of Machine Line Voltage

In order to further illustrate the unexpected asymmetric and spike behaviours of the line voltage, it is thoroughly investigated, analysed and discussed in this section. As shown before, the flux linkage waveforms of the machine with asymmetric winding connection are non-uniform, Fig. 6.5(a), since its coils are asymmetrically located in the stator. However, at larger current density, i.e. higher magnetic saturation, the non-uniformity of such waveforms is more significant, Fig. 6.5(b). In addition, the flux linkage waveforms under the other two winding connections are uniform, as respectively shown in Fig. 6.5(c) and Fig. 6.5(d). However, at relatively large current density, their line voltage behaviour against the current angle is very much similar to their counterpart of the asymmetric winding connection, Fig. 6.18. Thus, the most likely reason for the experienced line voltage performance is due to the magnetic saturation, which will be confirmed in the following analyses and discussions.

The flux linkage waveforms of 6 stator/4 rotor poles SynR machines having different winding connections at 34 A/mm^2 current density and 90 degree current angle are shown in Fig. 6.24. Comparing with their counterparts under current angle of 45 degree, Fig. 6.5, the non-uniformity of the flux linkage waveform of the machine with the asymmetric connection still exists. In addition, for all winding connections, the flux linkage magnitude is lower when the current angle is 90 degree, but the reduction is more signifcant for the machine with the symmetric connection. However, the peak line voltage is still larger when the current angle is larger as shwon in Fig. 6.18. For further illustration, the variations of the maximum flux linkages and line voltage under the three winding connections against the current angle at 34 A_{rms}/mm^2 current density are calculated and compared in Fig. 6.25 and Fig. 6.26, respectively. For all winding connections, the flux linkage reduces when the current angle is larger, as shown in Fig. 6.25. This is due to the larger magnetic reluctance since larger current angle means that the phase currents are injected when the rotor and stator teeth are less aligned. Conversely, the line voltages increase when the current angle is larger, as illustrated in Fig. 6.26 since at such current density, the magnetic circuit of the machine is heavily saturated regardless the current angle, as can be clearly noticed in Fig. 6.27(a), Fig. 6.28(a) and Fig. 6.29(a). Under high magnetic saturation, larger current angles will increase the distortion of the line voltages, i.e. they start to exhibit even larger voltage spikes, as confirmed in Fig. 6.30. More investigations will be carried out to confirm such discussion. The flux linkage waveforms of the analysed machines with the three winding connections are calculated again at 6 A/mm^2 current density and 45 and 90 electrical degree current

angles, Fig. 6.31 and Fig. 6.32, respectively. The flux linkage waveforms of the machine with the asymmetric winding connection at 6 A/mm^2 and 45 degree current, Fig. 6.31(a), are nearly identical and they become lower and more uniform when the current angle becomes 90 degree, since the magnetic saturation is significantly lower at 6 A/mm^2 current density and becomes even lower when the current angle is 90 degree, as can be clearly noticed in Fig. 6.27. Furthermore, for all winding connections, comparing with the flux linkage reduction due to larger current angle at 34 A/mm^2 current density, Fig. 6.24, such reduction is more significant when the current density is 6 A/mm^2. This is again due to lower magnetic saturation, as confirmed in Fig. 6.27, Fig. 6.28 and Fig. 6.29. Moreover, these figures show that at low current density, i.e. 6A/mm^2, the magnetic saturation level becomes even lower when the current angle is larger, i.e. 90 degree. As a result, the line voltage at 6 A/mm^2 and 90 degree has no spike and is lower than its counterpart at 45 deg current angle, Fig. 6.33. This further proves the previous discussions and conclusions that the unexpected voltage behaviour is due to the high magnetic saturation. However, such influence is more significant when the asymmetric winding connection is employed. Therefore, the symmetric winding connection could be more suitable, especially at relatively high speed operation.

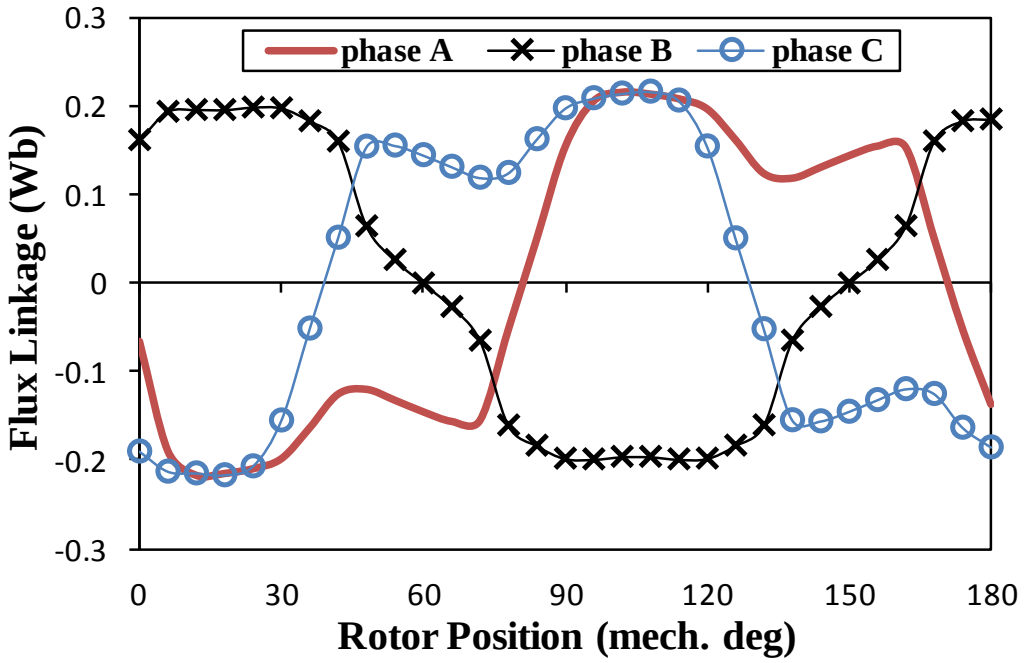

(a) Asymmetric connection

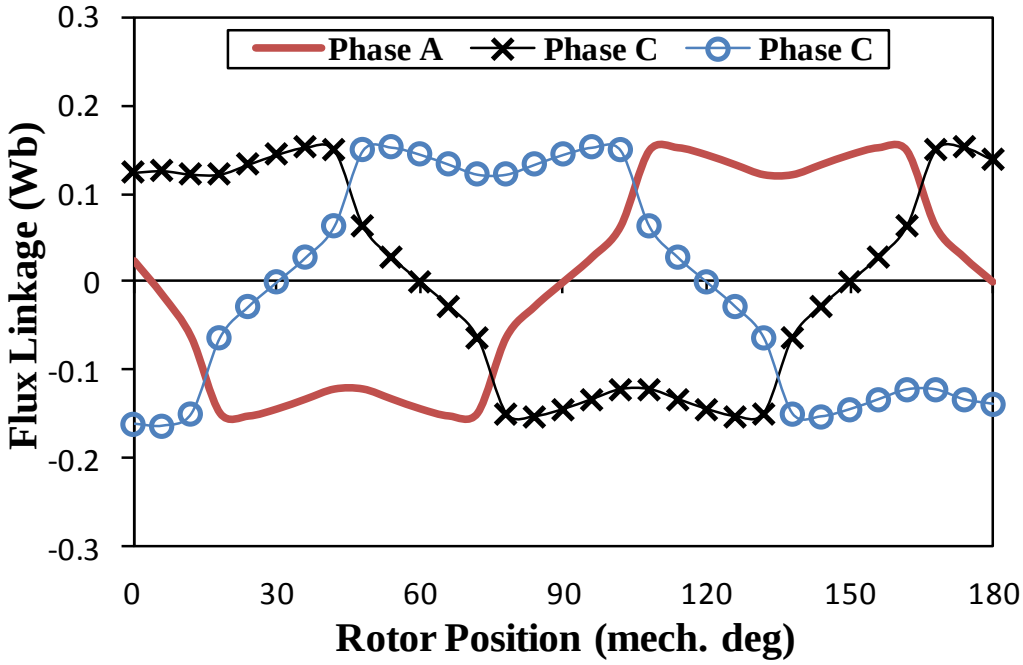

(b) Symmetric connection

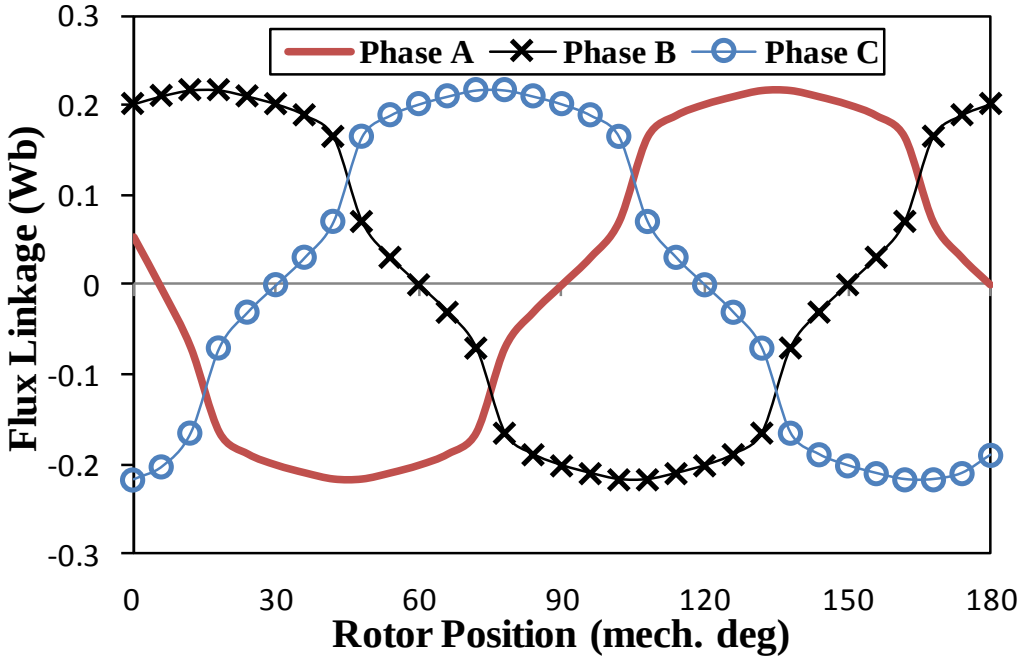

(c) Hybrid connection

Fig. 6.24 Variation of flux linkage waveforms of 6 stator/4 rotor poles machines having different winding connections at 34 A/mm^2 current density and 90 deg current angle.

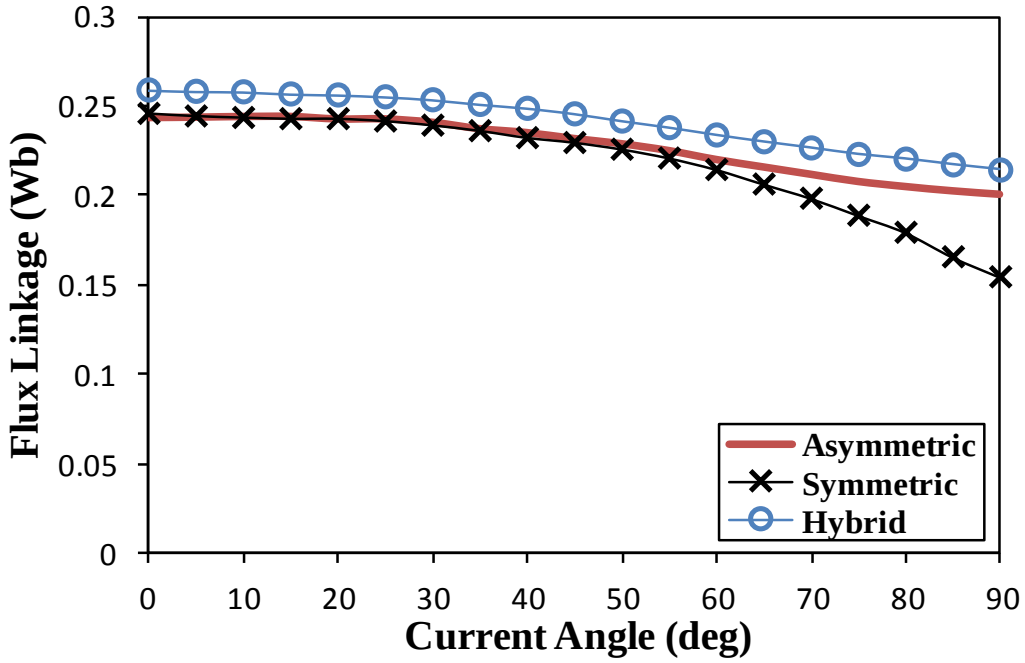

Fig. 6.25 Variation of maximum flux linkage against current angle of 6 stator/4 rotor poles machines having different winding connections at 34 A_{rms}/mm^2 current density.

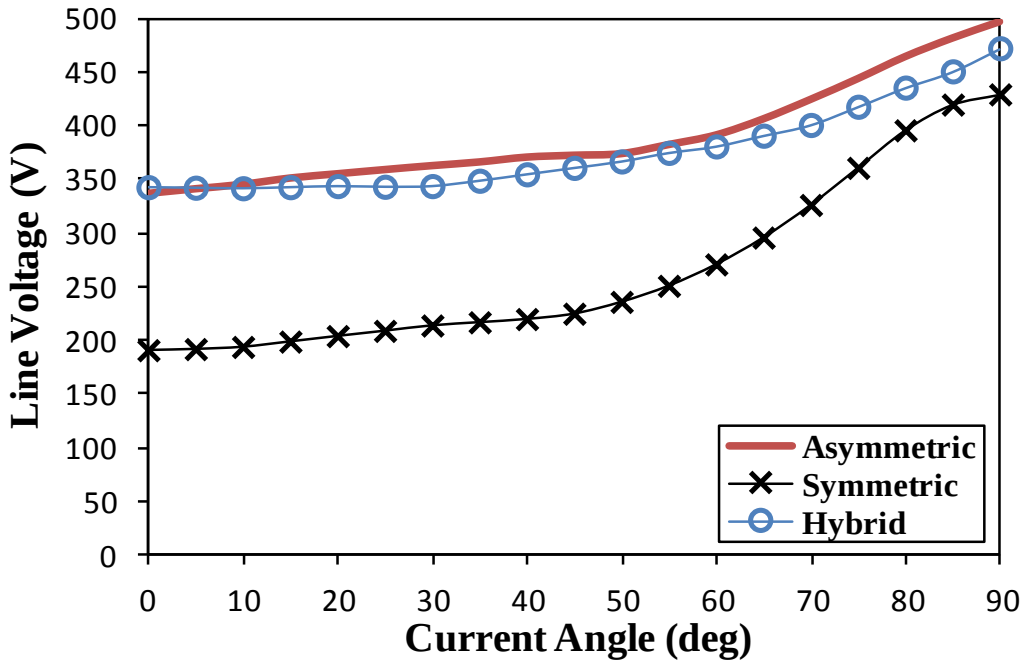

Fig. 6.26 Variation of maximum line voltage against current angle of 6 stator/4 rotor poles machines having different winding connections at 34 A/mm^2 current density.

(I) Current angle is 45 deg (II) Current angle is 90 deg

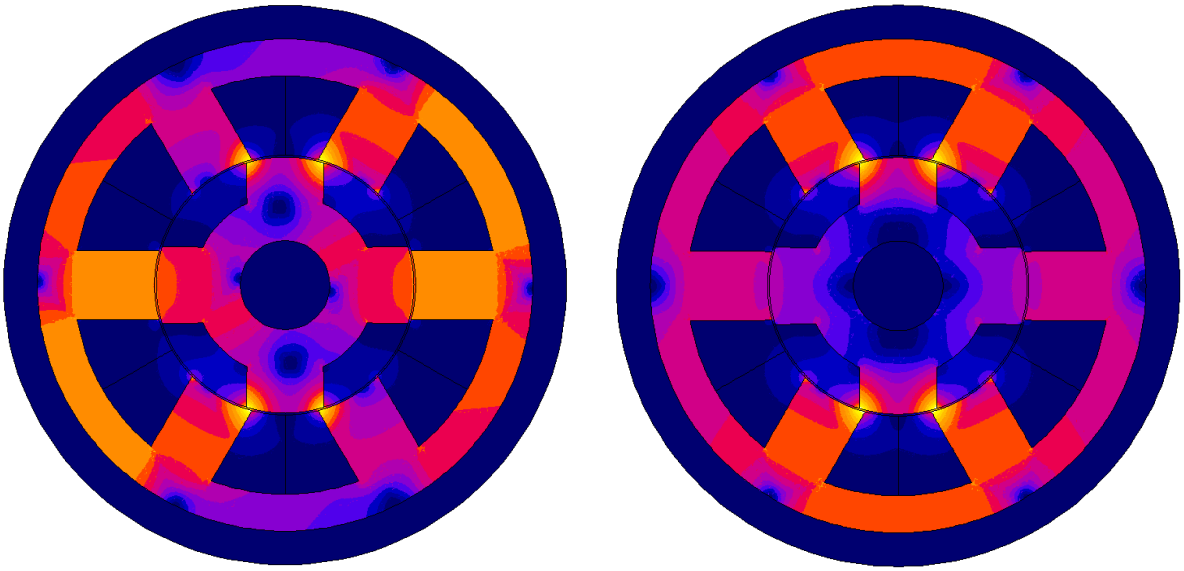

(a) Maximum current density is 34 A/mm^2 (100%)

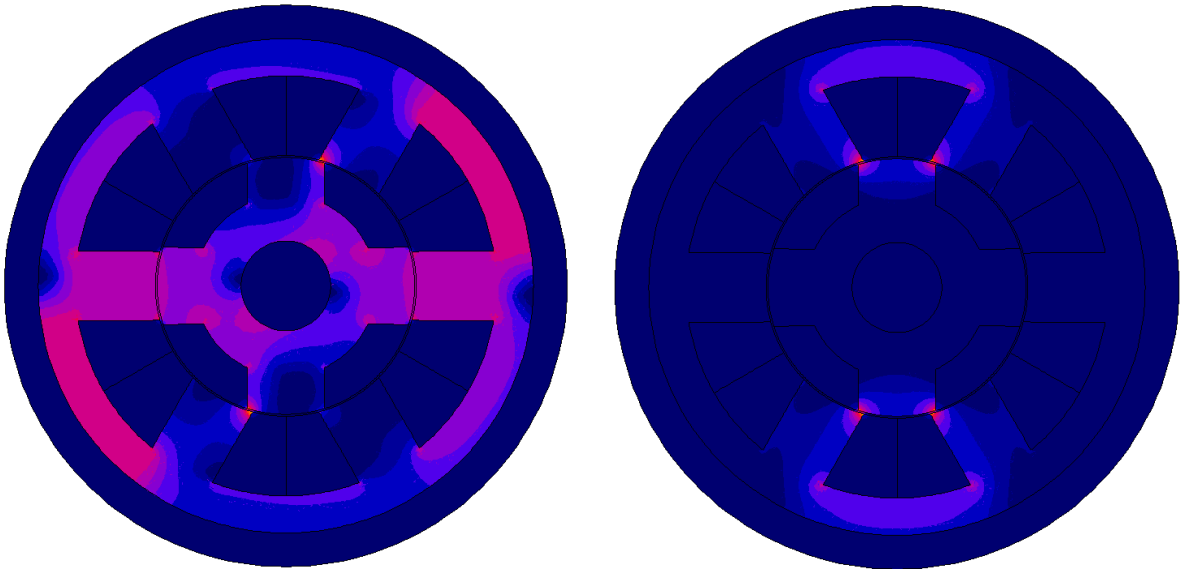

(b) Current density is 6 A/mm^2 (17.5%)

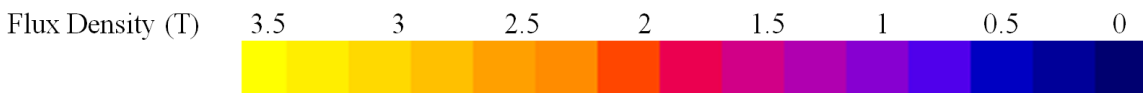

(c) Flux density scale (T)

Fig. 6.27 Flux density distribution of machines having asymmetric winding connection for different current densities and different current angles.

(I) Current angle is 45 deg (II) Current angle is 90 deg

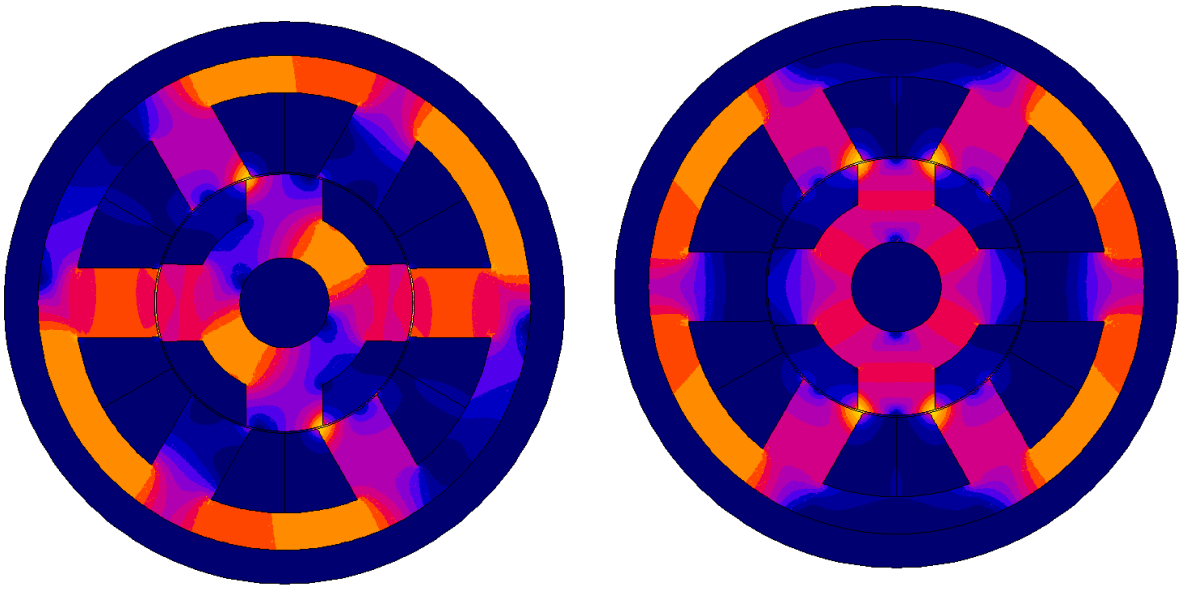

(a) Maximum current density is 34 A/mm^2

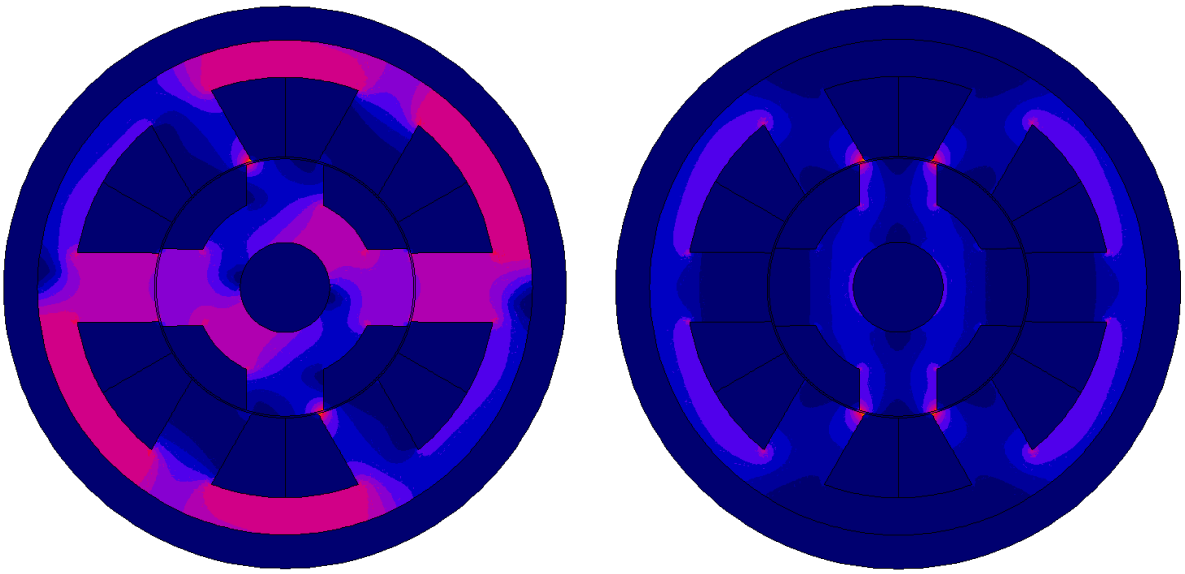

(b) Current density is 6 A/mm^2

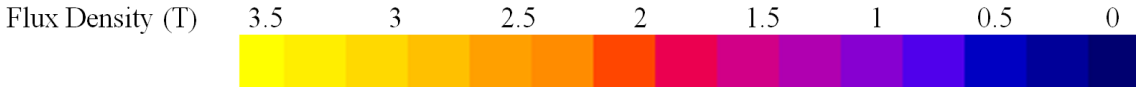

(c) Flux density scale (T)

Fig. 6.28 Flux density distribution of machines having symmetric winding connection for different current densities and different current angles.

(I) Current angle is 45 deg (II) Current angle is 90 deg

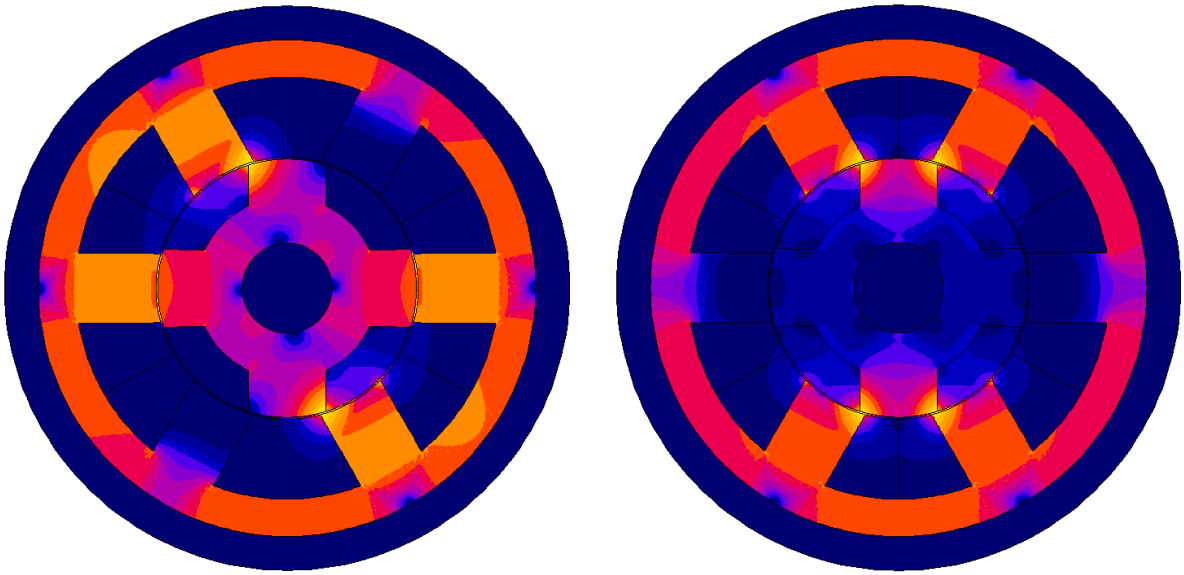

(a) Maximum current density is 34 A/mm^2

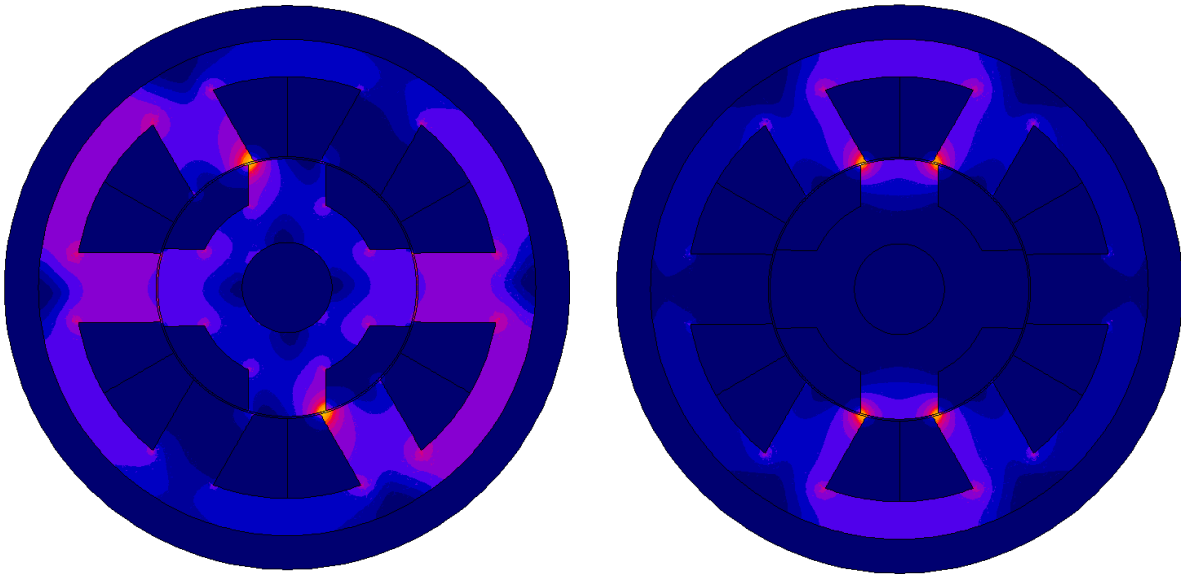

(b) Current density is 6 A/mm^2

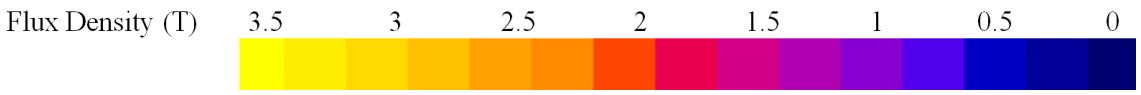

(c) Flux density scale (T)

Fig. 6.29 Flux density distribution of machines having hybrid winding connection for different current densities and different current angles.

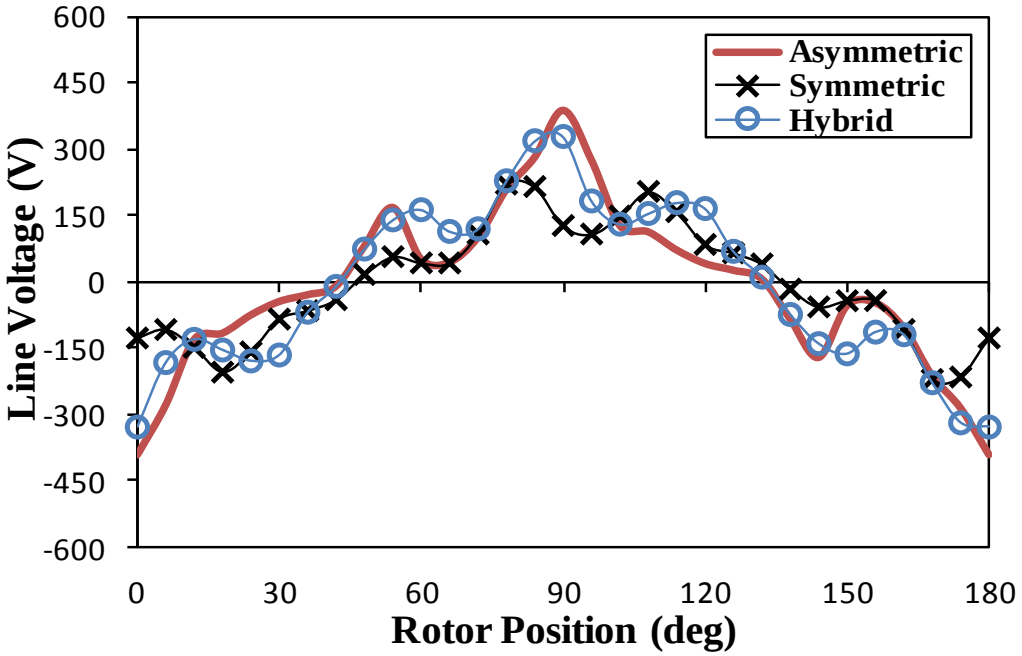

(a) Current angle is 45 degree

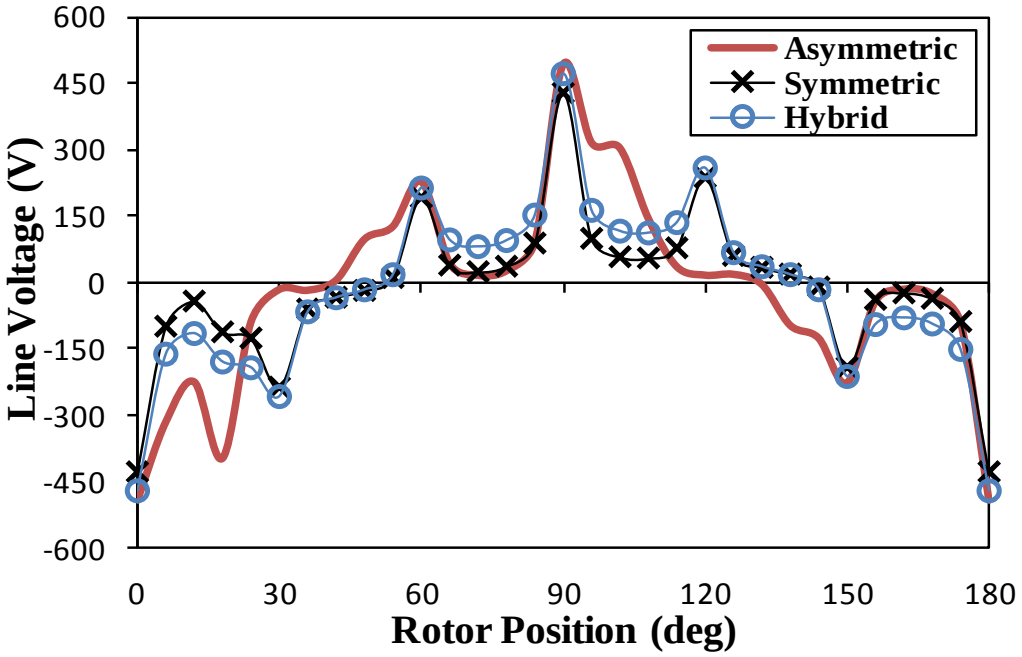

(b) Current angle is 90 degree

Fig. 6.30 Variations of line voltage waveform of 6 stator/4 rotor poles machines having different winding connections, at 34 A/mm^2 current density and different current angles.

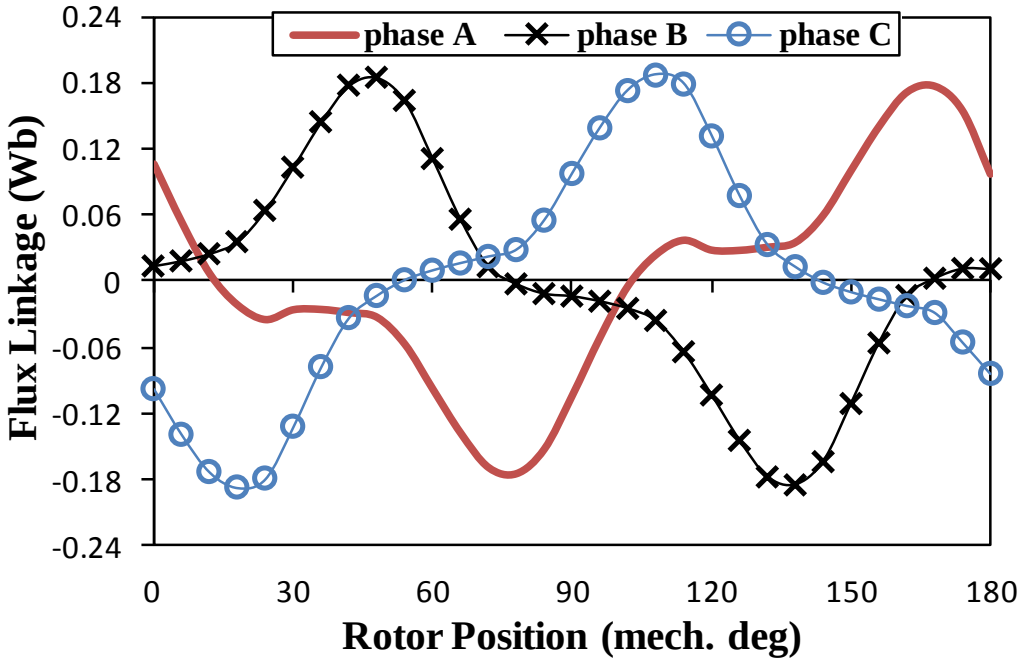

(a) Asymmetric winding connection

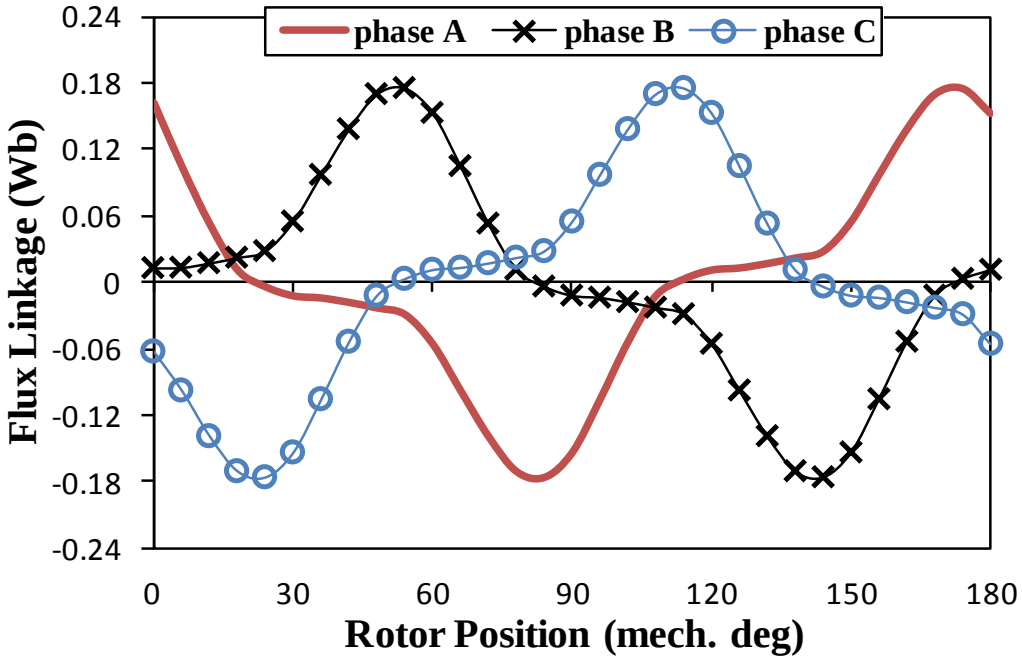

(b) Symmetric winding connection

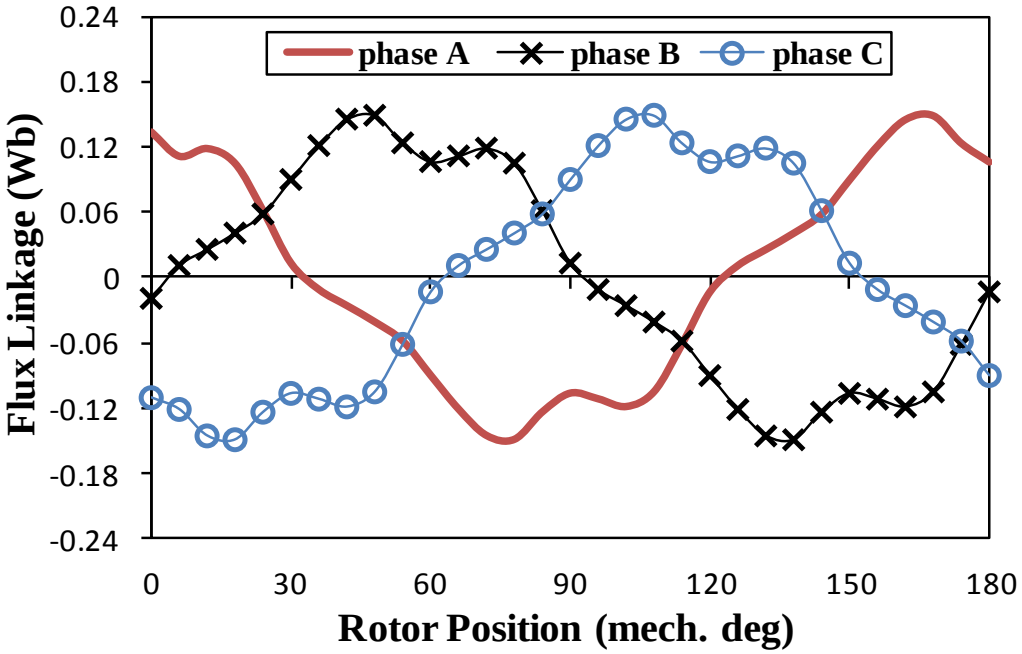

(c) Hybrid winding connection

Fig. 6.31 Variations of flux linkage waveforms of 6 stator/4 rotor poles machines having different winding connections at 6 A/mm^2 current density and 45 deg current angle.

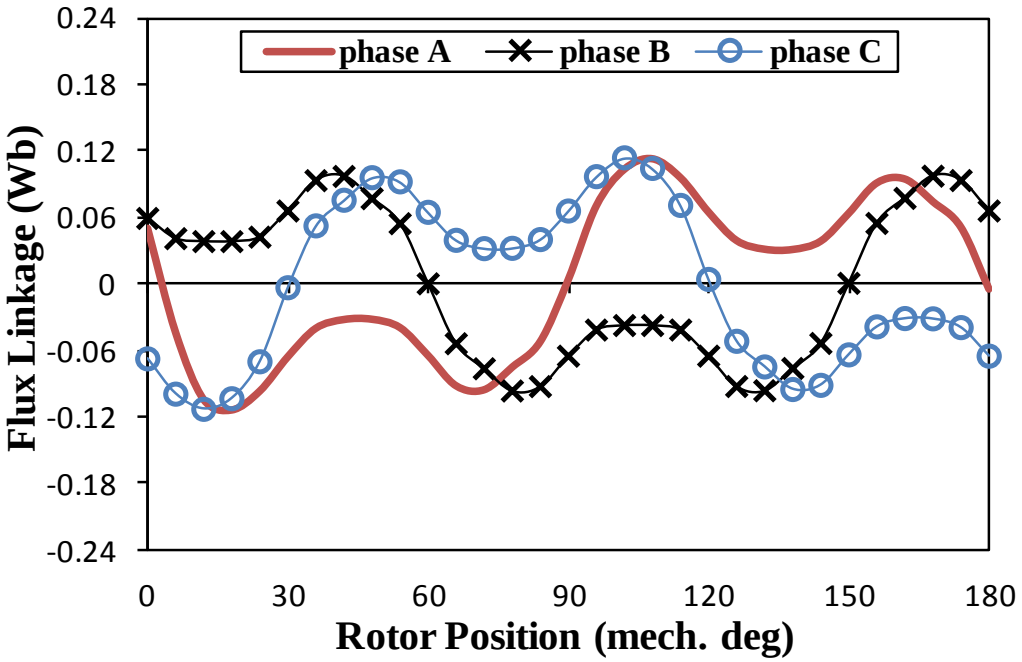

(a) Asymmetric winding connection

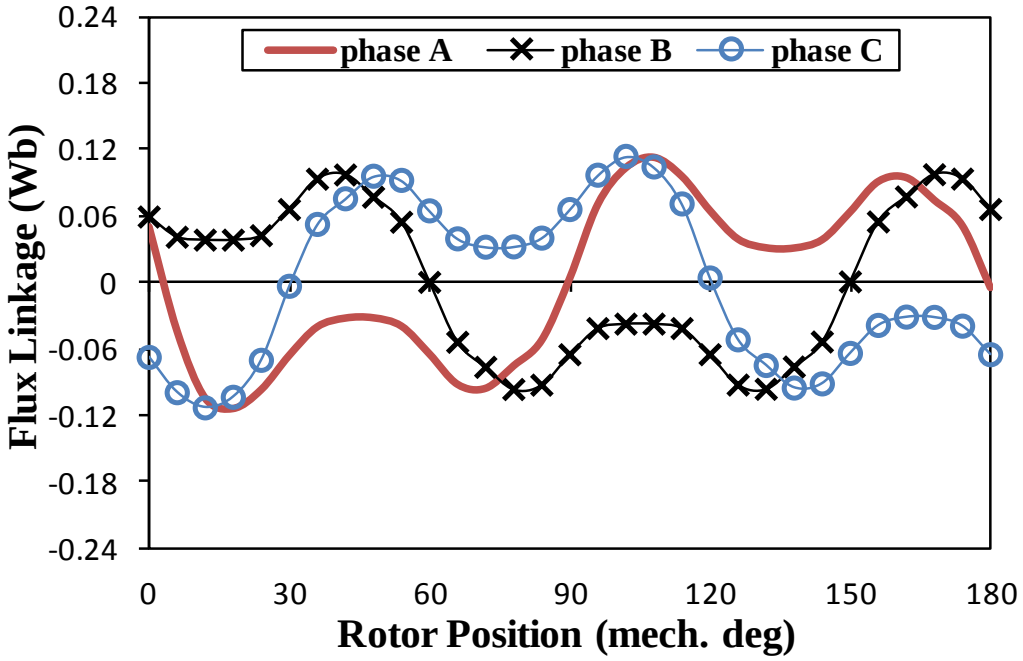

(b) Symmetric winding connection

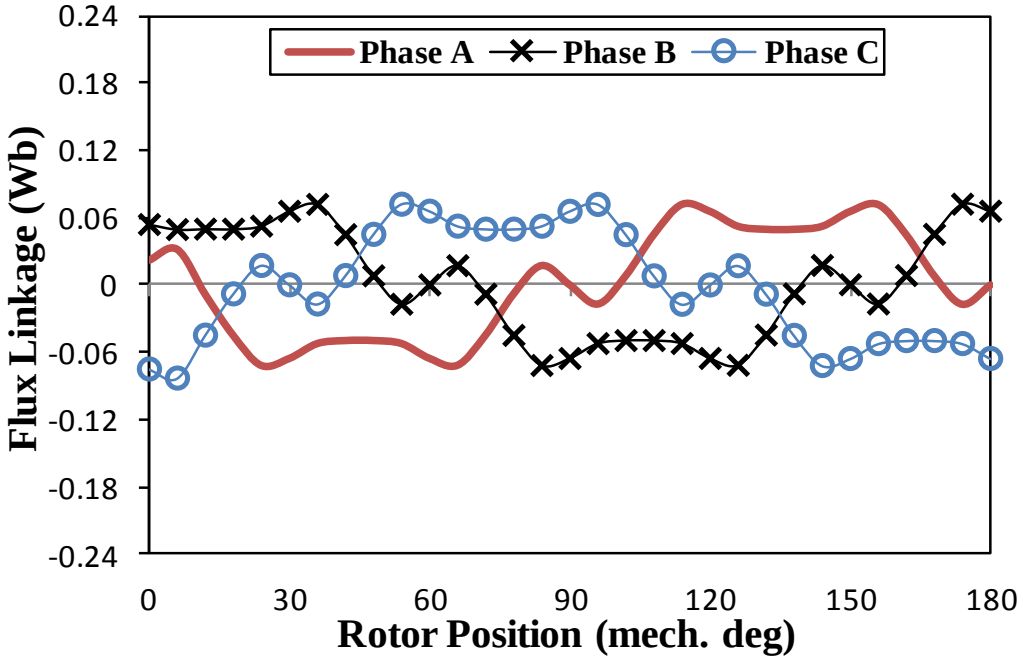

(c) Hybrid winding connection

Fig. 6.32 Variations of flux linkage waveforms of 6 stator/4 rotor poles machines having different winding connections at 6 A/mm^2 current density and 90 deg current angle.

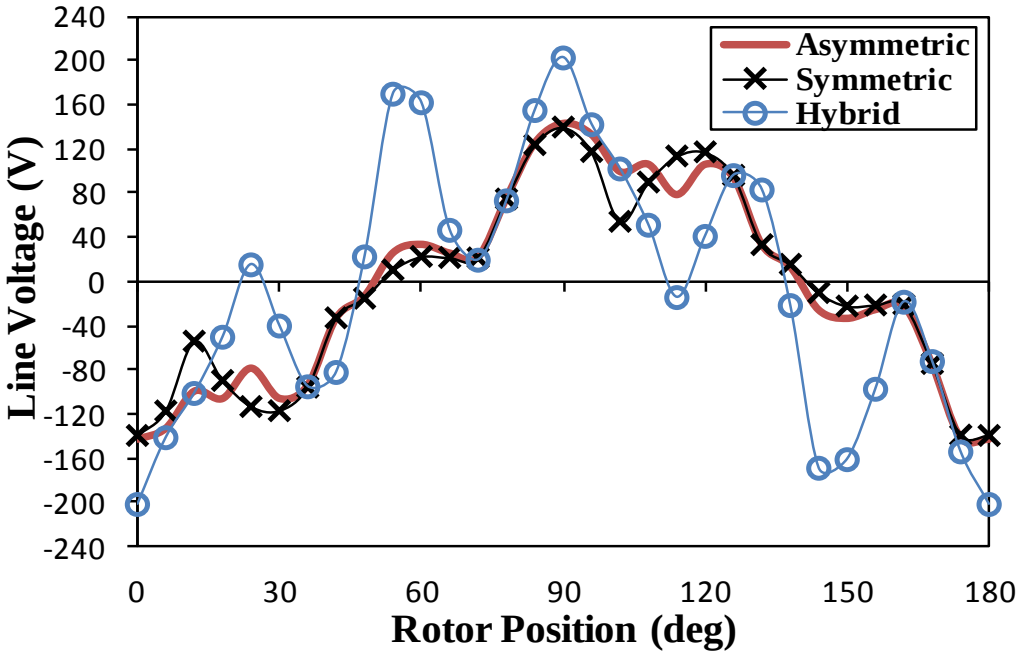

(a) Current angle is 45 degree

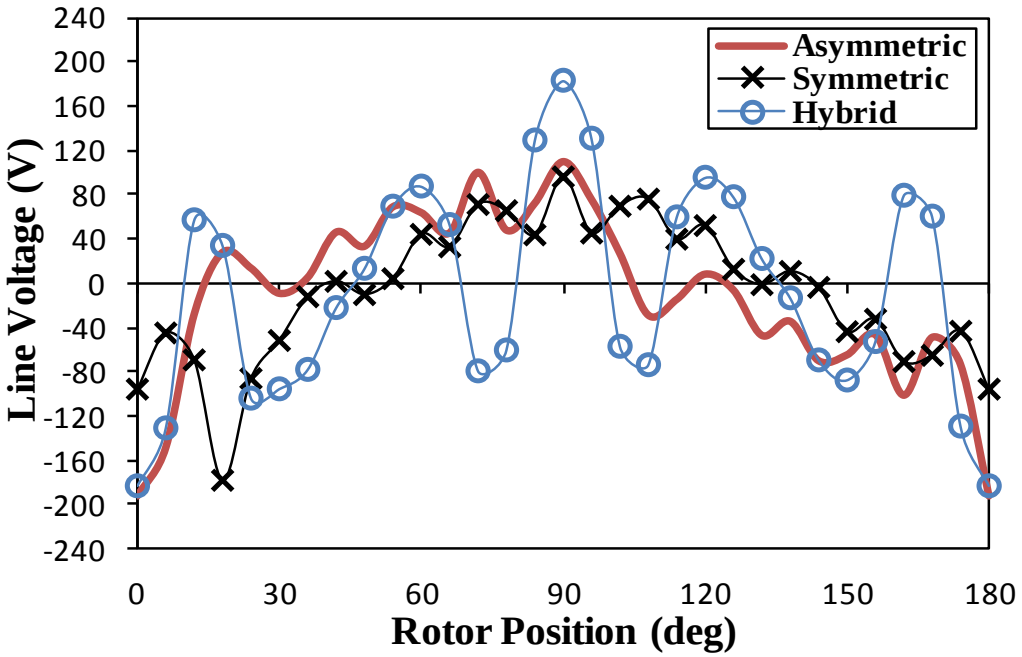

(b) Current angle is 90 degree

Fig. 6.33 Variations of line voltage waveforms of 6 stator/4 rotor poles machines having different winding connections at 6 A/mm^2 current density and different current angles.

6.6. Efficiency

In order to present a comprehensive comparison, the machine efficiency under the three winding connections is calculated and compared in this section. In general, the SR machine efficiency can be calculated by:

$$\eta = \frac{P_{output}}{P_{input}} = \frac{P_{em} - P_{Iron}}{P_{em} + P_{copper}} \times 100 \tag{6.3}$$

where P_{em}, P_{iron} and P_{copper} are the electromagnetic power, iron and copper losses, respectively.

In order to calculate the iron losses, the flux density distributions in the machine iron is obtained by the time stepped FE and then the losses including hysteresis loss (P_{hys}), eddy current (P_{eddy}), and excess (P_{exc}) losses are analytically calculated using (6.4) and experimentally determined iron loss coefficients, which are given in Table 6.2. The calculation method has been well illustrated and implemented in [161-163]. In addition, the copper loss can be estimated by (6.5).

$$\left.\begin{aligned} P_{hys} &= K_h f_{B_m} B_m^{a+bBm} K_{B_m} \\ P_{eddy} &= \frac{\sigma_{iron} d^2}{12 T_{cyc}} \int_{T_{cyc}} B(t)^2 dt \\ P_{exc} &= \frac{K_{exc}}{T_{cyc}} \int_{T_{cyc}} \left|B(t)\right|^{1.5} dt \end{aligned}\right\} \tag{6.4}$$

$$P_{copper} = 3 I_{rms}^2 R_{ph} = 3 \left(\frac{I_{peak}}{\sqrt{2}} \right)^2 R_{ph} \tag{6.5}$$

where B_m, f_{B_m}, T_{cyc}, K_{B_m}, I_{rms} and I_{peak} are flux density amplitude, frequency and cycle time, minor loop coefficient and phase current rms and peak values, respectively.

The variations of iron and copper losses, which correspond to the torque-speed characteristics at 34A/mm^2 maximum current density, Fig. 6.21(a), are predicted and compared for the three winding connections, Fig. 6.34 and Fig. 6.35, respectively. It can be noticed that for all the winding connections the main iron loss is generated in the stators

since comparing with the rotor, the stator flux path is longer, Fig. 6.7, the material volume is larger and the magnetic saturation level is higher, Fig. 6.29. Furthermore, at relatively high speeds, i.e. larger than 4000 rpm, the iron loss of the machine with the hybrid winding connection becomes lower comparing with the other two winding connection. This is because the phase current of such machine is also lower, as shown in Fig. 6.22(a), which is decreased in order to satisfy the voltage limitation, as already explained in section 6.4. On the other hand, the asymmetric and symmetric winding connections result in nearly the same level of iron loss, since they have similar flux paths, Fig. 6.7. Furthermore, the iron loss is proportional to the speed, while the higher the flux density which is a function of electric loading, the higher the iron loss. Therefore, the iron losses of all machines increase sharply with the speed up to ~ 8000 rpm. However, they gradually decrease for higher speeds. This is due to the significant decreasing of the phase current, i.e. the electric loading, at higher speeds, as illustrated in Fig. 6.22(a). The variations of the copper loss are exactly the same as their counterparts of the phase current, Fig. 6.22(a), they are large at relatively low speeds and sharply decrease at relatively high speeds. The obtained losses are utilised to calculate the efficiency-speed characteristics, which is given Fig. 6.36. It shows that at low speed the efficiencies of all machines are relatively low, since their output powers are still relatively low while their copper losses are relatively large. However, these efficiencies gradually increase to achieve a relatively larger value for such type of machine, i.e. the maximum is about 93%. Furthermore, the machine with the hybrid winding connection exhibits the highest efficiency all over the speed range, since its output power is the largest and its iron loss is significantly low. However, at relatively high speeds, all winding connections results in nearly the same efficiency.

Table 6.2 Iron Loss Coefficients for Prototype Machine.

Parameter	***Value***
Lamination Thickness (d)	0.35 mm
Material Density	7850 Kg/m^3
Material Conductivity (σ_{iron})	2220000 $\Omega^{-1}.m^{-1}$
Excess Loss Constant (K_{exc})	0.0002
Hysteresis Loss Constant (K_h)	0.0179
a	0.841
b	1.023

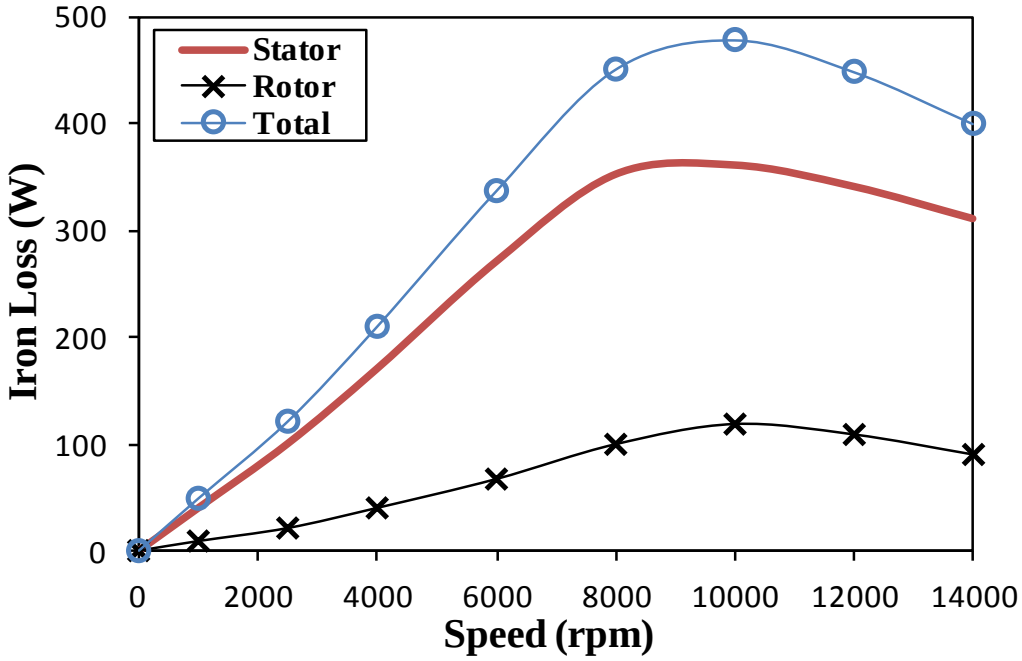

(a) Asymmetric winding connection

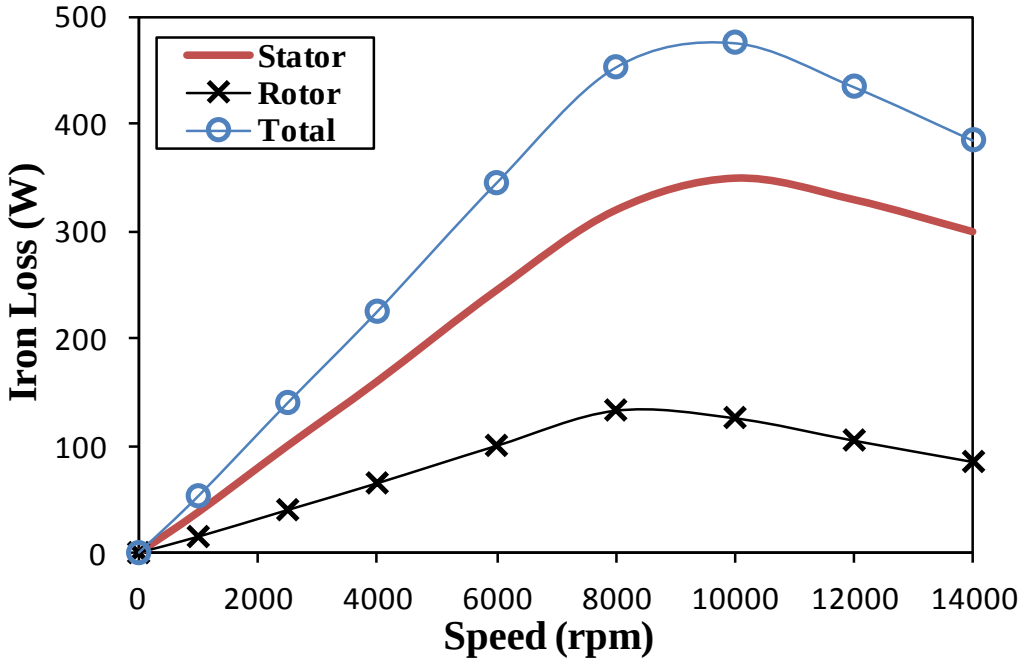

(b) Symmetric winding connection

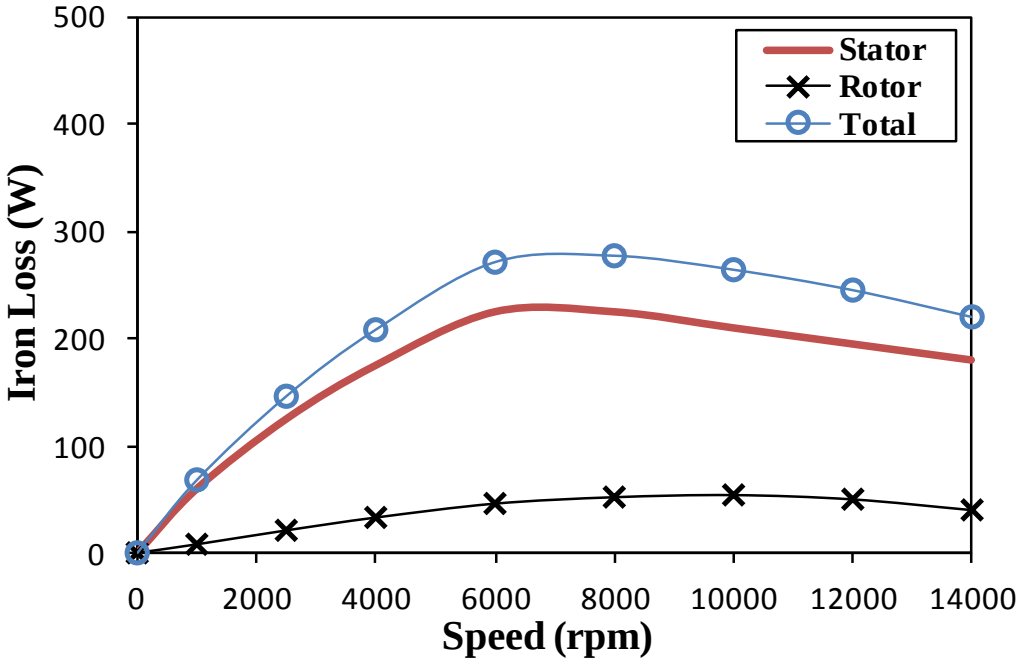

(c) Hybrid winding connection

Fig. 6.34 Comparison of iron loss variations of 6 stator/4 rotor poles machines having different winding connections, at 34 A/mm^2 maximum current density.

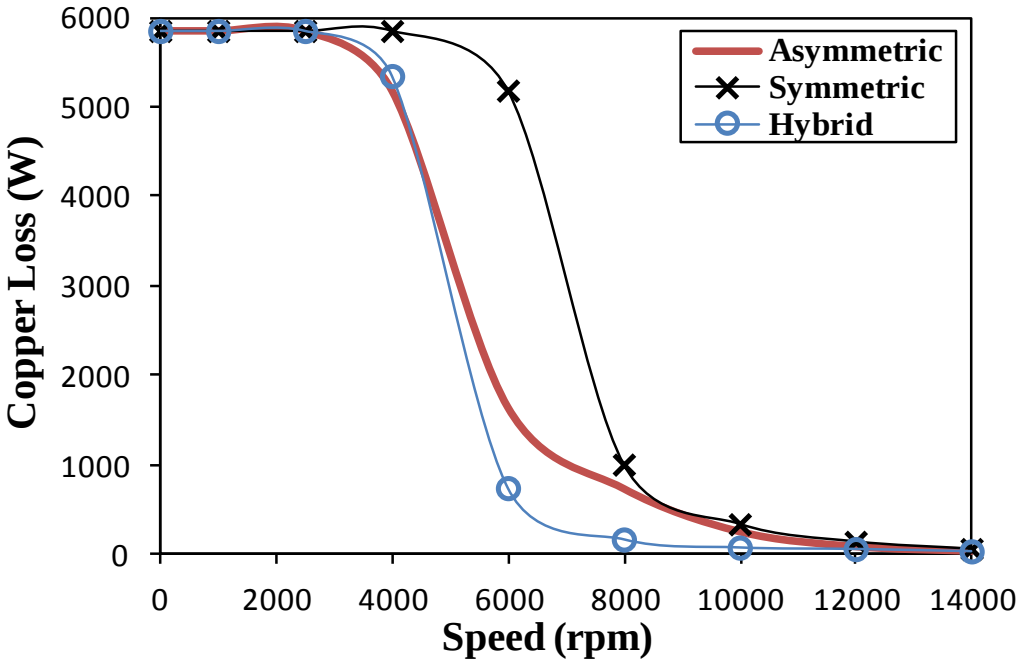

Fig. 6.35 Comparison of copper loss variations of 6 stator/4 rotor poles machines having different winding connections, at 34 A/mm^2 maximum current density.

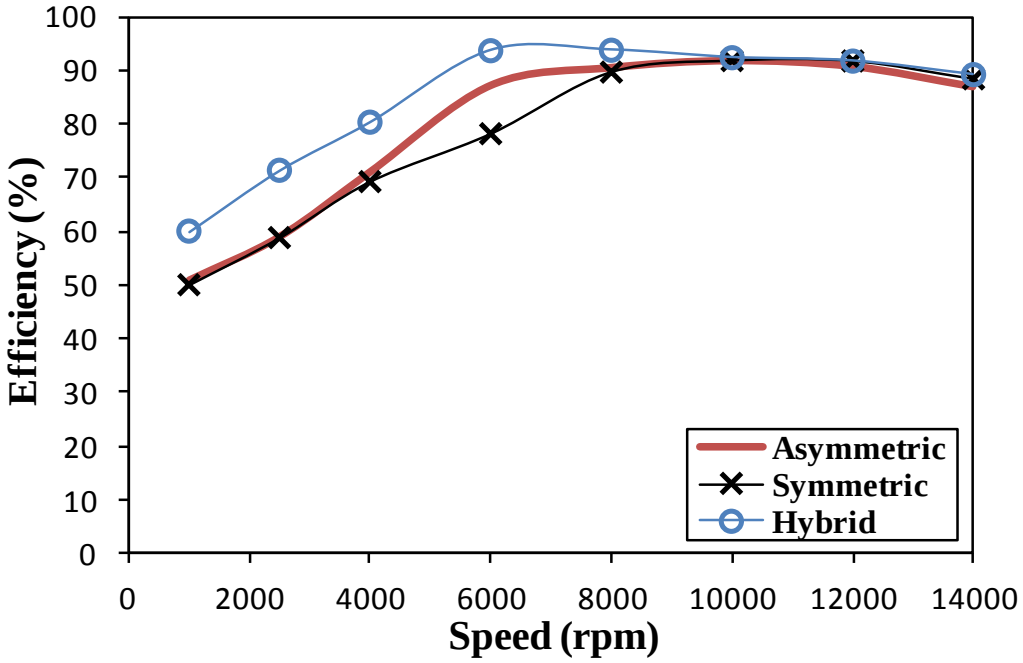

Fig. 6.36 Comparison of efficiency of 6 stator/4 rotor poles machines having different winding connections, at 34 A/mm^2 maximum current density.

6.7. Comparison of Non-overlapping and Overlapping Concentrated Windings

The preceding investigations are based on the SynR machines having non-overlapping concentrated winding. However, in order to further extend the analyses carried out in this chapter, the electromagnetic performance of SynR machine having overlapping concentrated winding will be also investigated and compared with its counterpart of the non-overlapping concentrated winding. The investigations will be carried out on a 12 stator/4 rotor poles SynR machine, whose air gap length and external dimensions, i.e. stator outer diameter and axial length, are exactly the same as their counterparts of the investigated 6 stator/4 rotor poles machine. On the other hand, the 12 stator/4 rotor poles machine has been optimised to determine the optimal split ratio, rotor and stator pole widths and stator back iron thickness, as shown in Fig. 6.37. The optimization has been performed to achieve the maximum average output torque at same current density, i.e. 34 A_{rms}/mm^2. The optimal dimensions of the machine are shown in Table 6.1.

The comparison will be performed between the overlapping winding SynR machine and their non-overlapping symmetric and hybrid winding connection counterparts since the non-overlapping concentrated symmetric winding connection exhibits the better torque quality, i.e. the lower torque ripple, generates the lower line voltage, the wider torque-speed characteristics and has nearly the same output torque as the non-overlapping concentrated asymmetric winding connection. On the other hand, the non-overlapping concentrated hybrid winding connection leads to the largest average output torque and efficiency.

The cross-section lamination and phase winding layout of the SR machine with overlapping winding are given in Fig. 6.38. It is worth mentioning that the number of turns per phase of the compared machines is nearly the same, i.e. it is differed by two. Thus, to carry out the comparison under the same peak current density, i.e. 34 A_{rms}/mm^2, the maximum phase current of the overlapping winding machine is decreased from 180 A_{rms} to 170 A_{rms}.

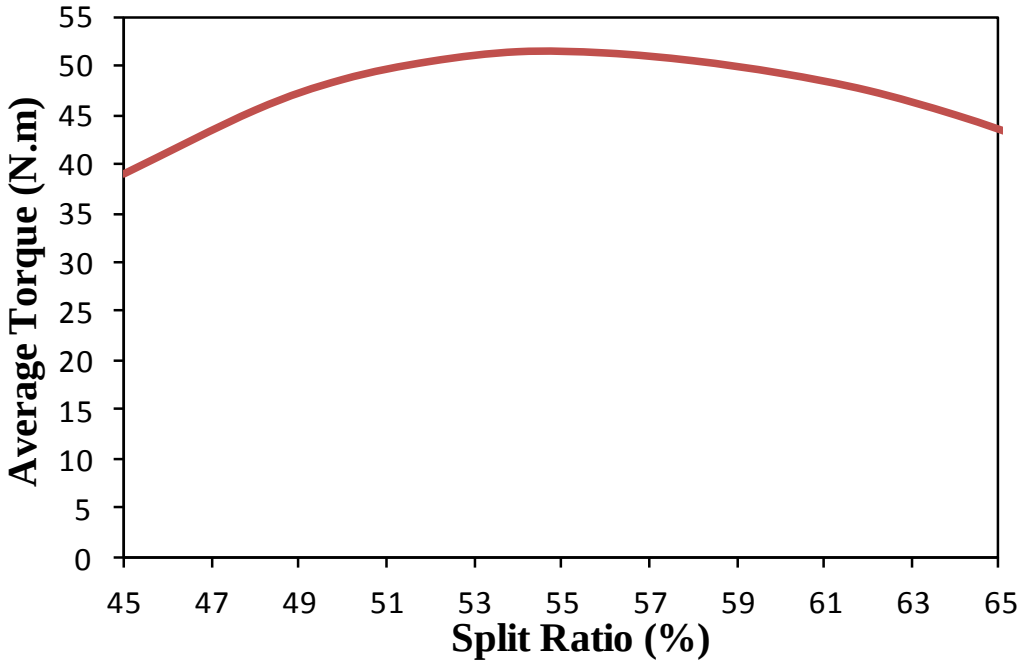

(a) Split ratio

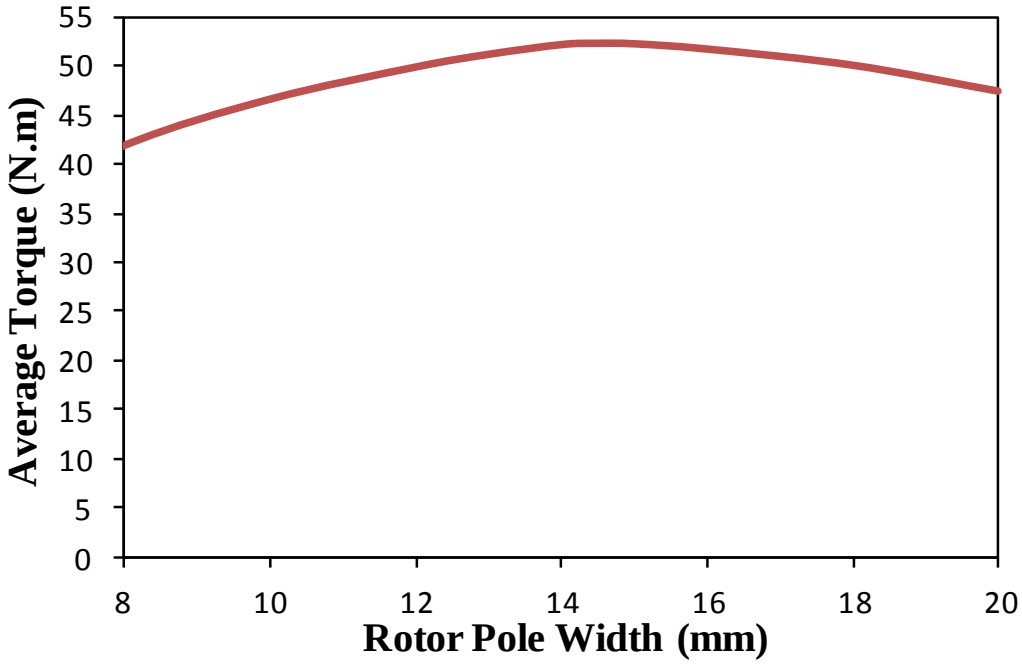

(b) Rotor pole width

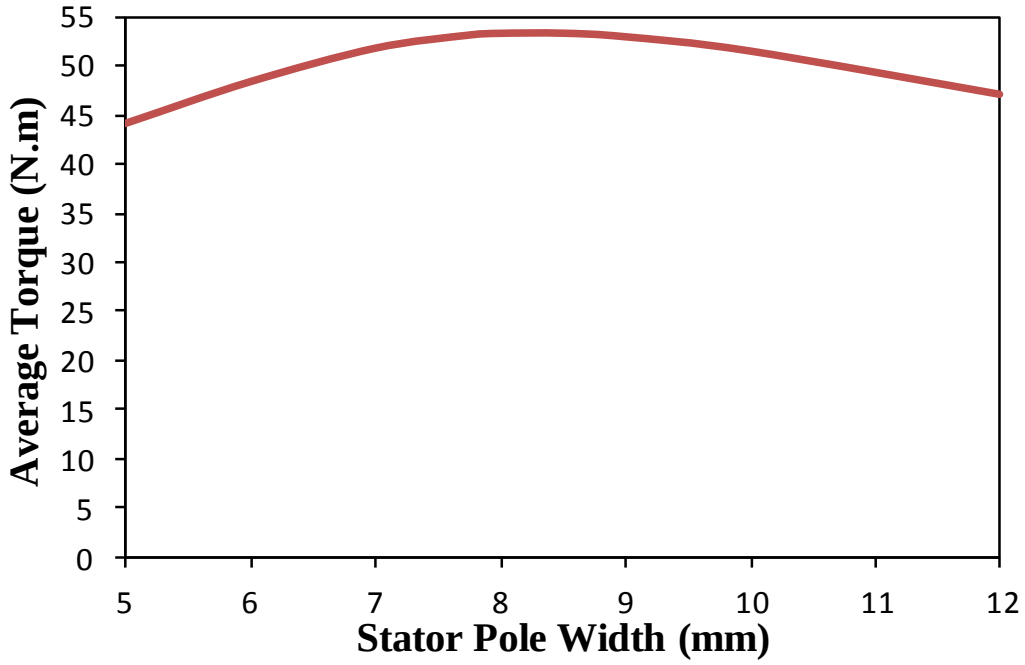

(b) Stator pole width

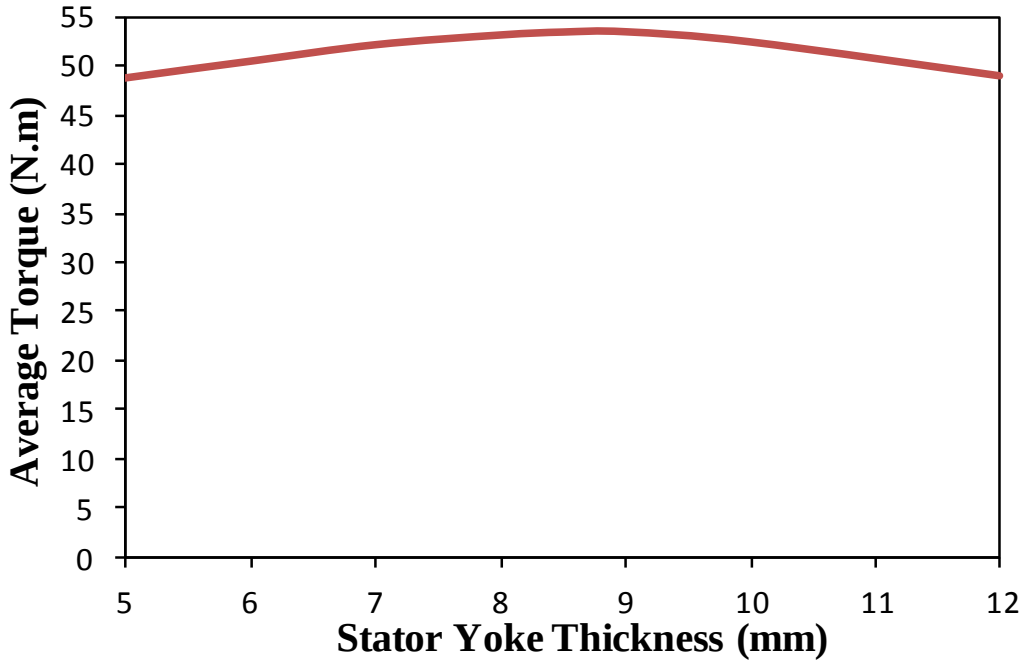

(c) Stator yoke thickness

Fig. 6.37 Variation of average output torque against split ratio, rotor and stator pole widths and stator yoke thickness, at 34 A_{rms}/mm^2 current density.

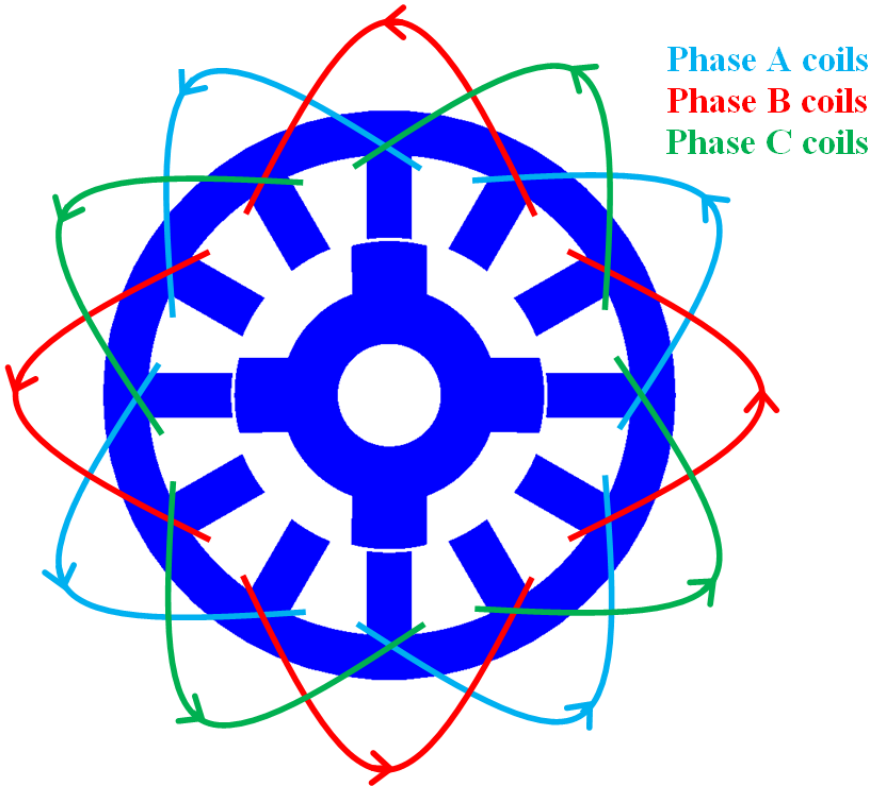

Fig. 6.38 Cross-section lamination and winding layout of 12 stator/4 rotor poles SynR machine.

6.7.1. Electromagnetic Performance

In this section, the electromagnetic performance, i.e. the flux linkage, self and mutual inductances and output torque, of the 12 stator/4 rotor poles SynR machine is predicted using the FE tool and compared with its counterpart of the 6 stator/4 rotor poles SynR machine with different winding connections, i.e. symmetric and hybrid. The variation of three phase flux linkage waveforms of the overlapping winding machine at 34 A_{rms}/mm^2 current density is shown in Fig. 6.39. Due to the symmetry of the phase winding distribution, Fig. 6.38, the flux linkage waveforms are identical for 3 phases, but comparing with the non-overlapping concentrated hybrid winding connection the waveform is slightly distorted, as shown in Fig. 6.40. Thus, the overlapping winding connection is expected to result in larger torque ripple. Furthermore, in terms of flux linkage magnitude both the overlapping winding and non-overlapping hybrid winding connections have nearly the same magnitude, which is slightly larger than its counterpart of non-overlapping symmetric winding connection, Fig. 6.40. Moreover, the first two connections have similar self inductance variations, which are smaller than their counterpart of the non-overlapping symmetric winding connection, as illustrated in Fig. 6.41. The mutual inductance variations of the analysed machines are

compared in Fig. 6.42. Although the 12 stator/4 rotor poles SynR overlapping winding machine has relatively larger mutual inductance variation, it is much smaller than its counterpart of the 6 stator/4 rotor poles non-overlapping winding machine with hybrid winding connection, which has more interlink between phase fluxes, as can be clearly noticed in Fig. 6.7 (c) and Fig. 6.43. In order to examine the influence of the magnetic saturation on the self and mutual inductances of the overlapping winding machine, the variation of such inductances against the current density is calculated and shown in Fig. 6.44 and Fig. 6.45, respectively. Due to the flux distribution that is exhibited by the 12 stator/4 rotor machine, Fig. 6.43, the influence of the magnetic saturation on the inductances is relatively significant.

Furthermore, the phase and line voltage waveforms of the SynR machine with overlapping winding are compared with their counterparts of the non-overlapping symmetric and hybrid winding connections in Fig. 6.46 and Fig. 6.47, respectively. The voltage waveforms of the machine with overlapping winding are more distorted and contain larger voltage spikes, which in turn enlarge DC link voltage requirement. Therefore, for the same voltage limitation, the 12 stator/ 4 rotor poles machine will exhibit lower flux weakening capability, as will be shown in section 6.7.2. Furthermore, the variation of the maximum line voltage against the current density of the three machines are compared in Fig. 6.48. It shows that at relatively low current density, i.e. low magnetic saturation, both overlapping winding and the non-overlapping hybrid winding machines generate the same maximum line voltage, which is larger than their counterpart of the non-overlapping symmetric winding machine. However, the overlapping winding machine generates much larger peak line voltage when the current density is relatively large. This means the influence of the magnetic saturation on the line voltage distortion, voltage spike, is more significant in such machine, as also confirmed in Fig. 6.47.

The output torque waveforms of the three investigated machines are compared in Fig. 6.49. Comparing the 6 stator/4 rotor poles machine with non-overlapping symmetric winding connection, its 12 stator/4 rotor poles counterpart generates much larger output torque, since the torque in 12 stator/4 rotor poles machine is produced by the variations of both self and mutual inductances, Fig. 6.44 and Fig. 6.42, respectively. On the other hand, such machine exhibits slightly lower output torque than the 6 stator/4 rotor poles counterpart with hybrid winding connection since its self inductance variation is also slightly smaller, as shown in Fig. 6.41. Furthermore, the machine with overlapping winding exhibit the largest torque

ripple, since the influence of the magnetic saturation is more significant in such machine. The variation of the average output torque against the current density of the three machines are calculated and compared in Fig. 6.50. A similar average output torque exhibits at relatively low current density, but the difference starts to increase when the current density becomes larger. It also shows that the 6 stator/ 4 rotor poles machine with hybrid winding connection exhibits the best performance in terms of average output torque. In order to study the output torque quality, the torque ripple, i.e. percentage of the torque ripple to the average output torque, against the current density of the three machines are calculated and plotted in Fig. 6.51. The 12 stator/4 rotor poles machine exhibits relatively larger torque ripple.

In the previous calculations, the phase current is injected at 45 electrical angle, i.e. the d- and q-axis currents are equal. However, due to the magnetic saturation the optimal current angle could be different. Therefore, the variation of the average output torque against the current angle of the 12 stator/4 rotor poles machine is calculated for different current densities and shown in Fig. 6.52. It shows that the optimal current is 50 degree at low current density. However, it becomes 55 degree when the current density thus the magnetic saturation is high. Consequently, to operate such machine at its maximum output torque the current should be injected at current angle of 55 electrical degrees.

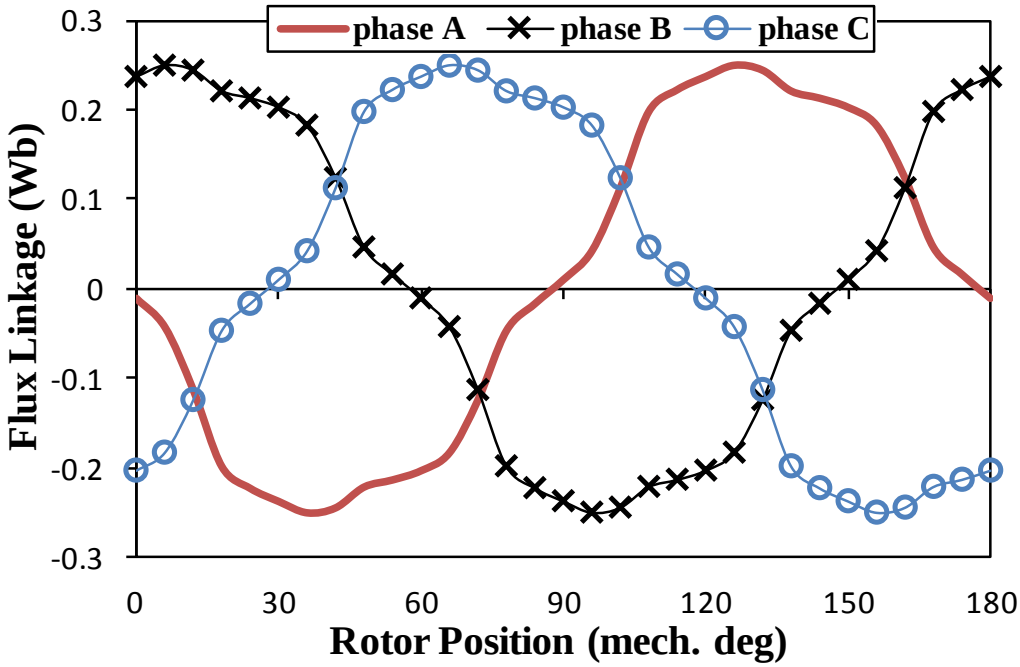

Fig. 6.39 Variation of flux linkage waveforms of 12 stator/4 rotor poles machine, at 34 A_{rms}/mm^2 current density.

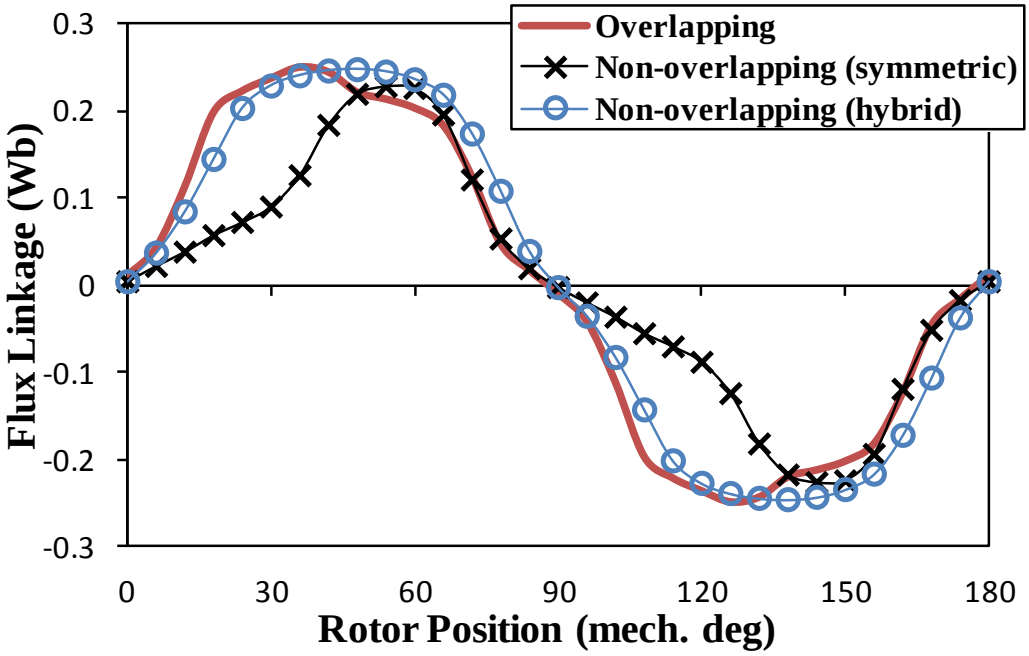

Fig. 6.40 Comparison of flux linkage waveforms of 12 stator/4 rotor poles and 6 stator/4 rotor poles machines having different winding connections, at 34 A_{rms}/mm^2 current density.

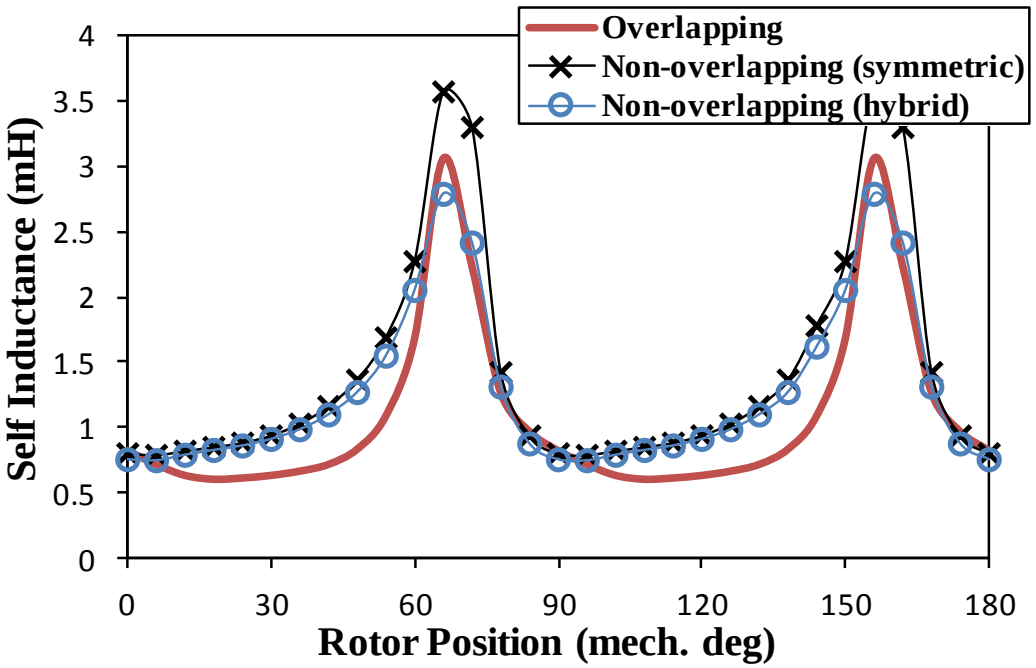

Fig. 6.41 Comparison of self inductance variations of 12 stator/4 rotor poles and 6 stator/4 rotor poles machines having different winding connections, at 34 A/mm^2 current density.

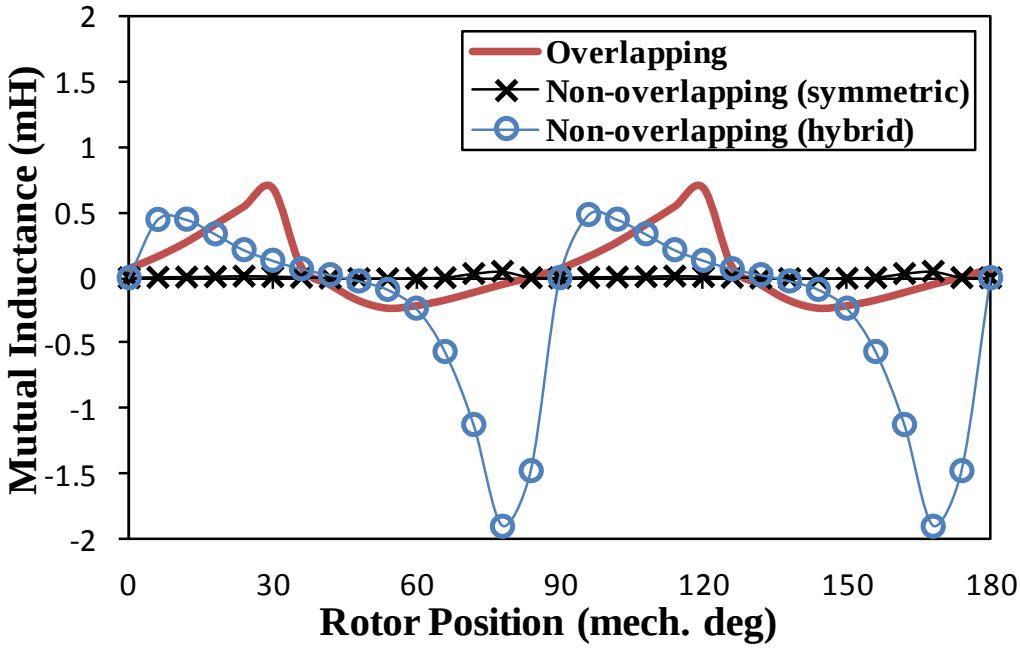

Fig. 6.42 Comparison of mutual inductance of 12 stator/4 rotor poles and 6 stator/4 rotor poles machines having different winding connections, at 34 A_{rms}/mm^2 current density.

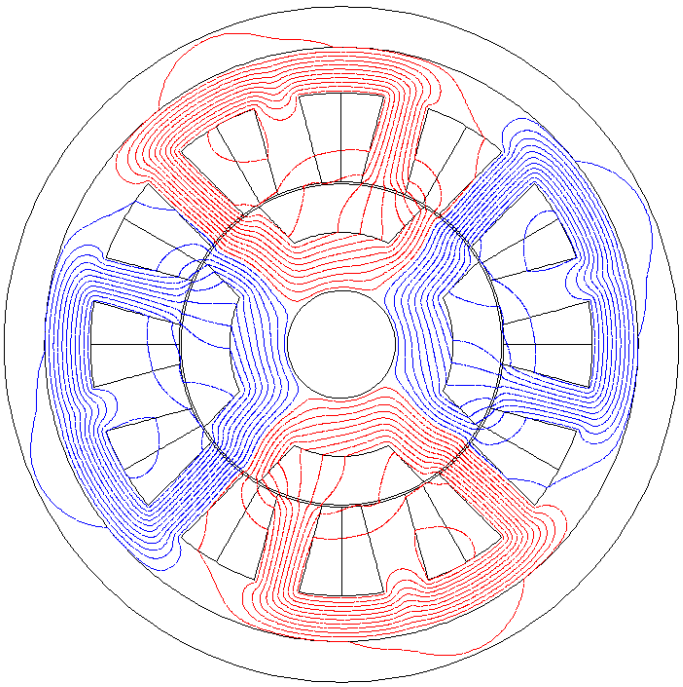

Fig. 6.43 Equal potential distributions of 12 stator/4 rotor poles machine, at 34 A_{rms}/mm^2 current density.

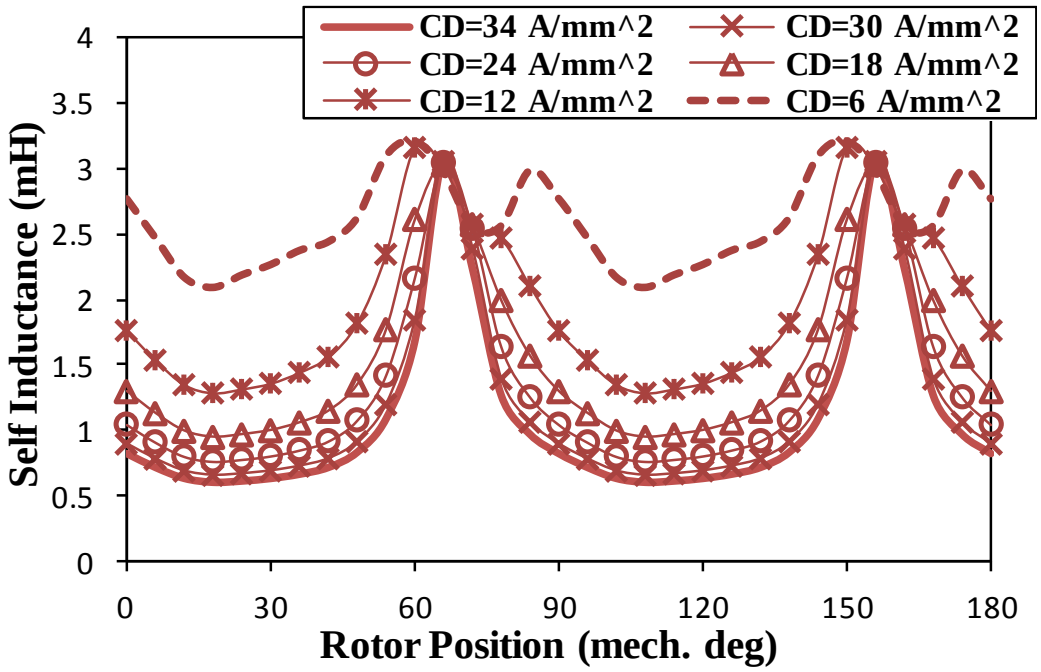

Fig. 6.44 Variation of self inductances of 12 stator/4 rotor poles machine for different current densities.

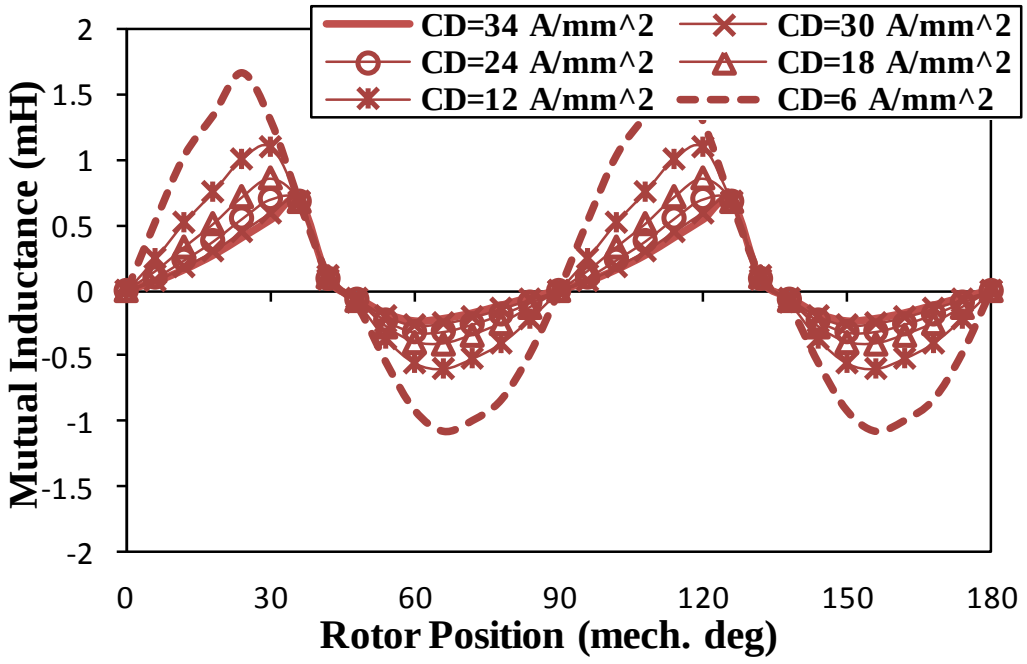

Fig. 6.45 Variation of mutual inductances of 12 stator/4 rotor poles machine for different current densities.

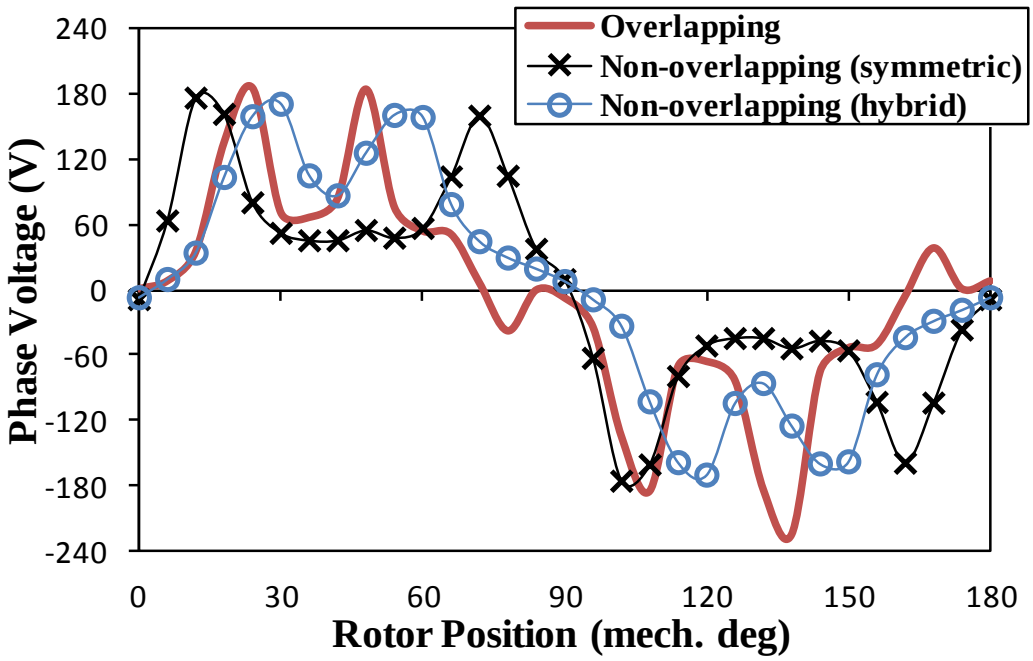

Fig. 6.46 Comparison of phase voltage waveforms of 12 stator/4 rotor poles and 6 stator/4 rotor poles machines having different winding connections, at 34 A_{rms}/mm^2 current density.

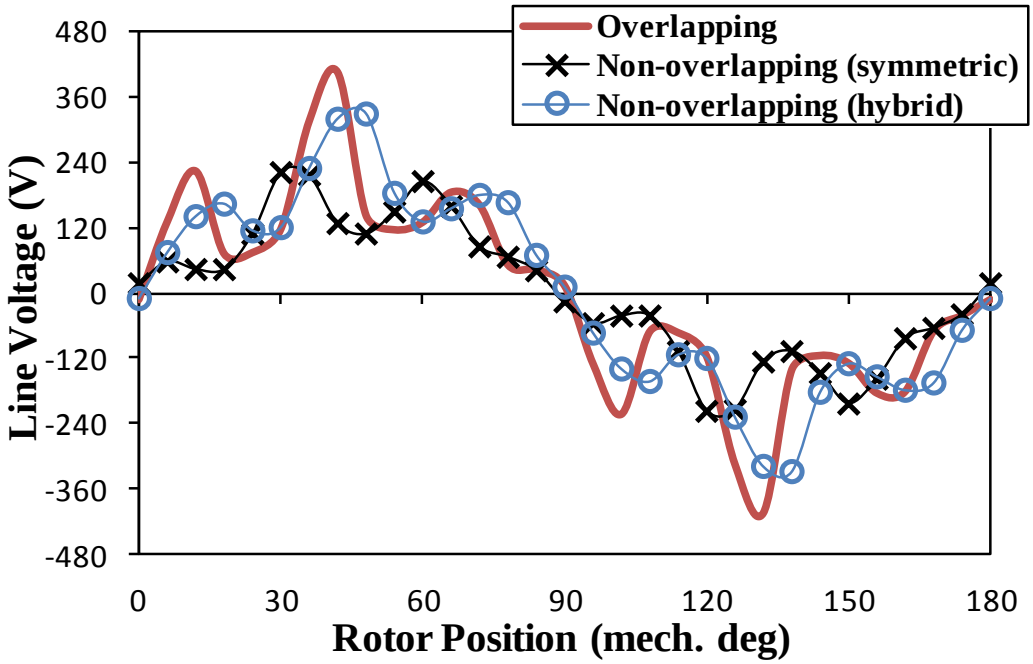

Fig. 6.47 Comparison of line voltage waveforms of 12 stator/4 rotor poles and 6 stator/4 rotor poles machines having different winding connections, at 34 A_{rms}/mm^2 current density.

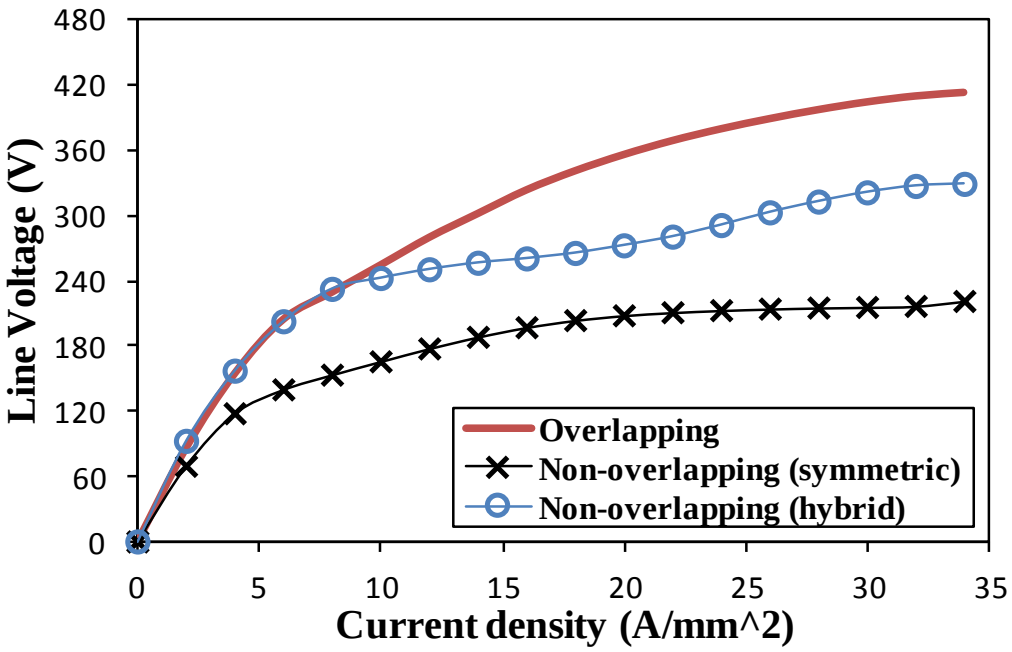

Fig. 6.48 Comparison of maximum line voltage against current density of 12 stator/4 rotor poles and 6 stator/4 rotor poles machines having different winding connections, at 34 A_{rms}/mm^2 current density.

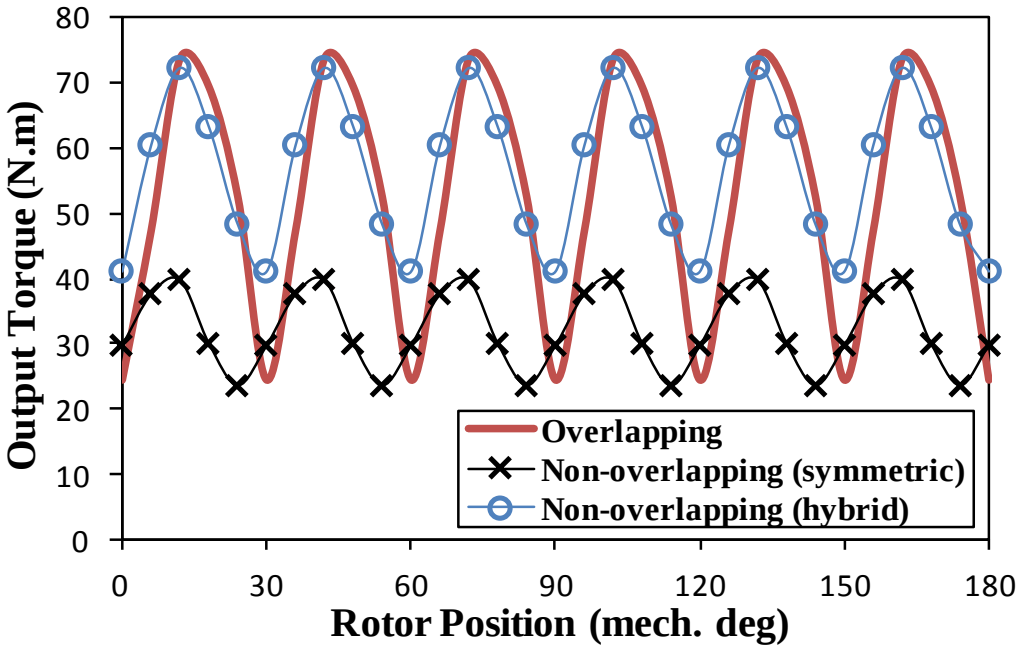

Fig. 6.49 Comparison of output torque waveforms of 12 stator/4 rotor poles and 6 stator/4 rotor poles machines having different winding connections, at 34 A_{rms}/mm^2 current density.

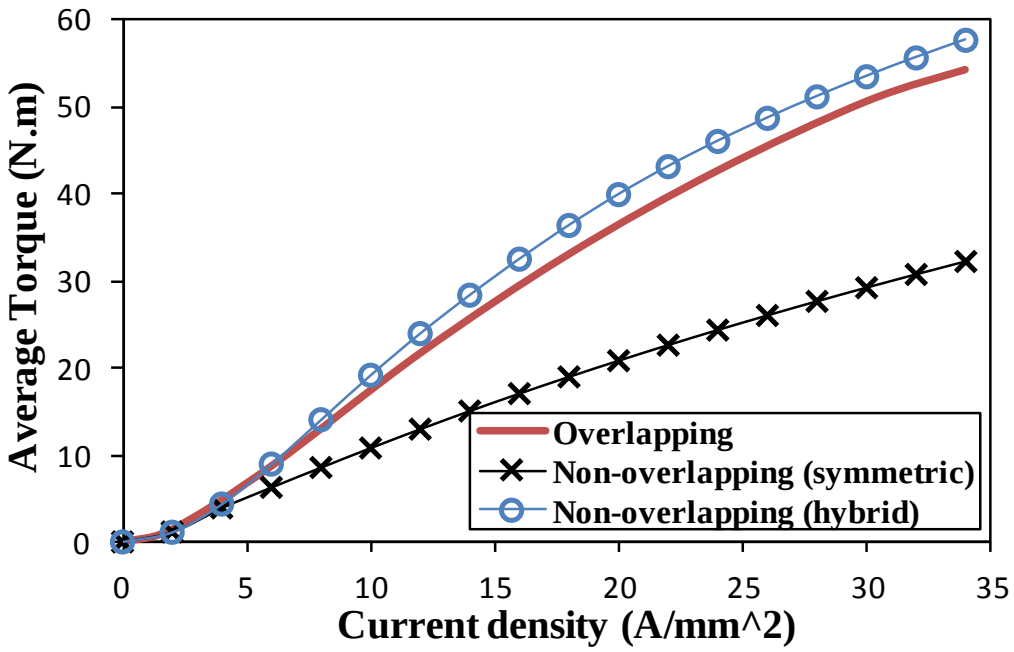

Fig. 6.50 Comparison of average output torque against current density of 12 stator/4 rotor poles and 6 stator/4 rotor poles machines having different winding connections.

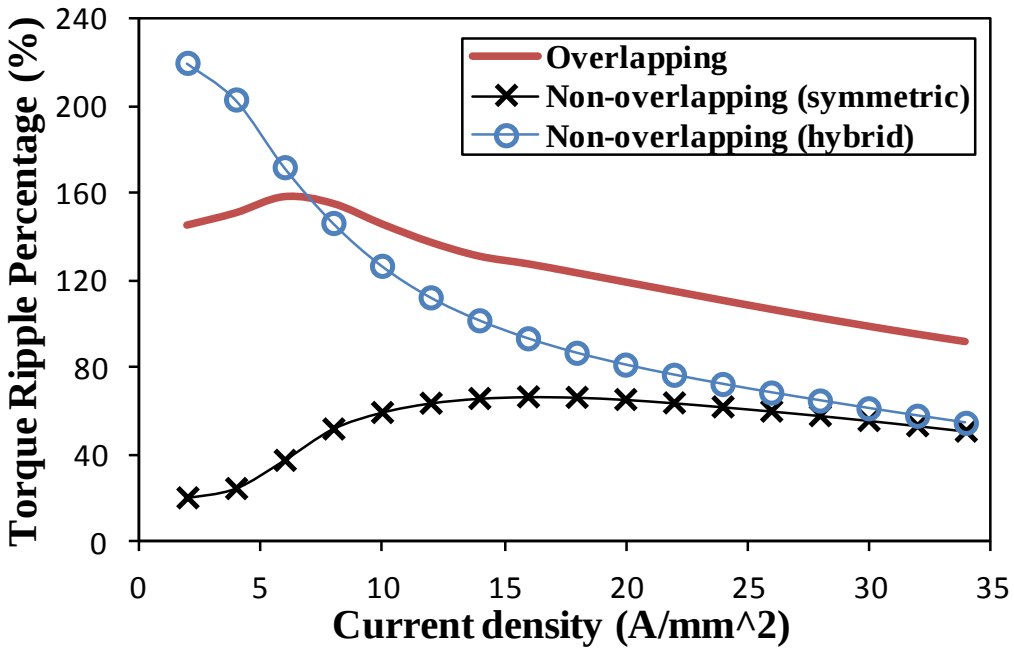

Fig. 6.51 Comparison of torque ripple percentage against current density of 12 stator/4 rotor poles and 6 stator/4 rotor poles machines having different winding connections.

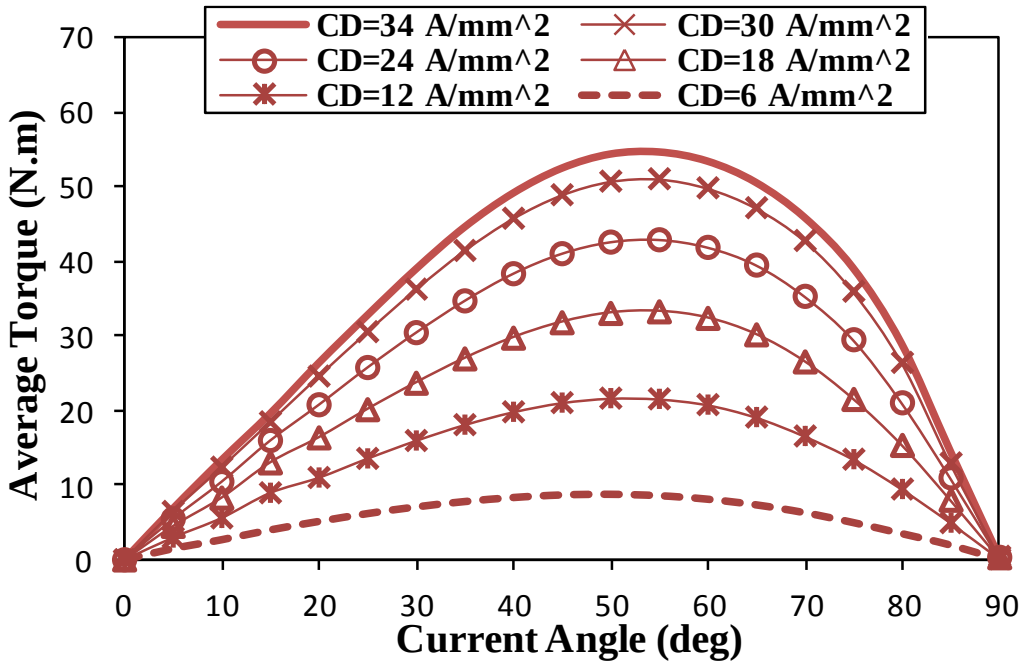

Fig. 6.52 Variaiton of average output torque against current angle of 12 stator/4 rotor poles machine for different current densities.

6.7.2. Torque and Power Speed Characteristics

Similar to the 6 stator/4 rotor poles machine, the 12 stator/4 rotor poles machine line voltage increases when the current angle increases, as shown in Fig. 6.53. Therefore, the torque-speed characteristics will be predicted at fixed current angle, i.e. 55 electrical degrees, while the flux weakening operation will be achieved by decreasing the current density. For this purpose, the variation of the maximum line voltage and average output torque against current density of 12 stator/4 rotor poles machine are calculated, as shown in Fig. 6.54 and Fig. 6.55, respectively. Then, they are considered together, in the same way as explained in section 6.4, to predict the torque- and power-speed characteristics of such machine at different maximum current densities. These characteristics are compared with their counterparts of the 6 stator/4 rotor poles machine with symmetric and hybrid connections in Fig. 6.56. The corresponding peak phase current and require line voltage are compared in Fig. 6.57 and Fig. 6.58, respectively. The 12 stator/4 rotor poles machine exhibits the narrowest flux weakening operation region. This is due to its larger line voltage requirements, Fig. 6.58, which in turn is due to larger voltage spike in the line voltage waveform, Fig. 6.47. Furthermore, although the output torque of such machine is larger than its counterpart of the 6 stator/4 rotor pole

machine with symmetric winding connection, its maximum output power is lower, Fig. 6.56 (b). Furthermore, at relatively high speed, the 12 stator/4 rotor poles machine and its 6 stator/4 rotor poles counterpart with the hybrid winding connection show a similar performance since at relatively low current density, such two machines generate nearly the same average output torque, Fig. 6.50, and line voltage, Fig. 6.48.

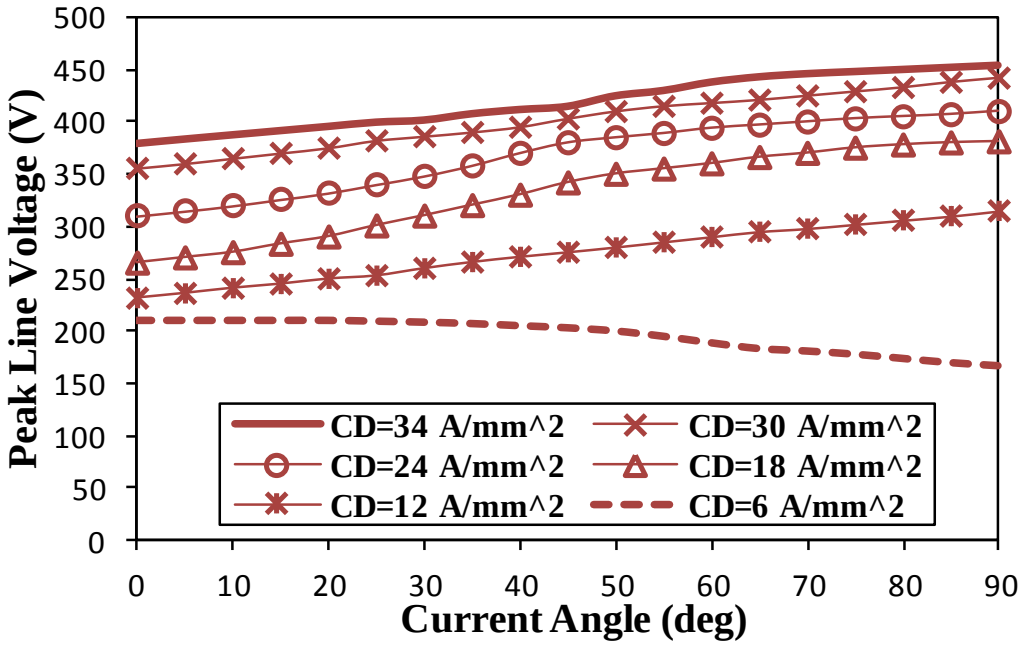

Fig. 6.53 Variation of peak line voltage against current angle of 12 stator/4 rotor poles machine for different current densities, at 2500 rpm.

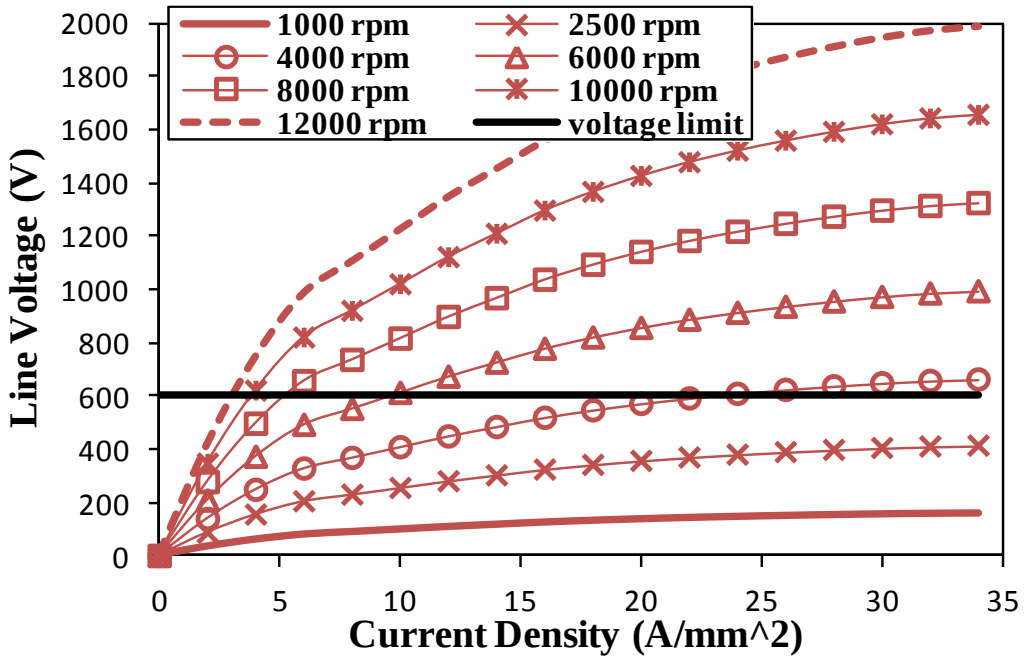

Fig. 6.54 Variaitons of line voltage against current density of 12 stator/4 rotor poles machine for different rotating speeds.

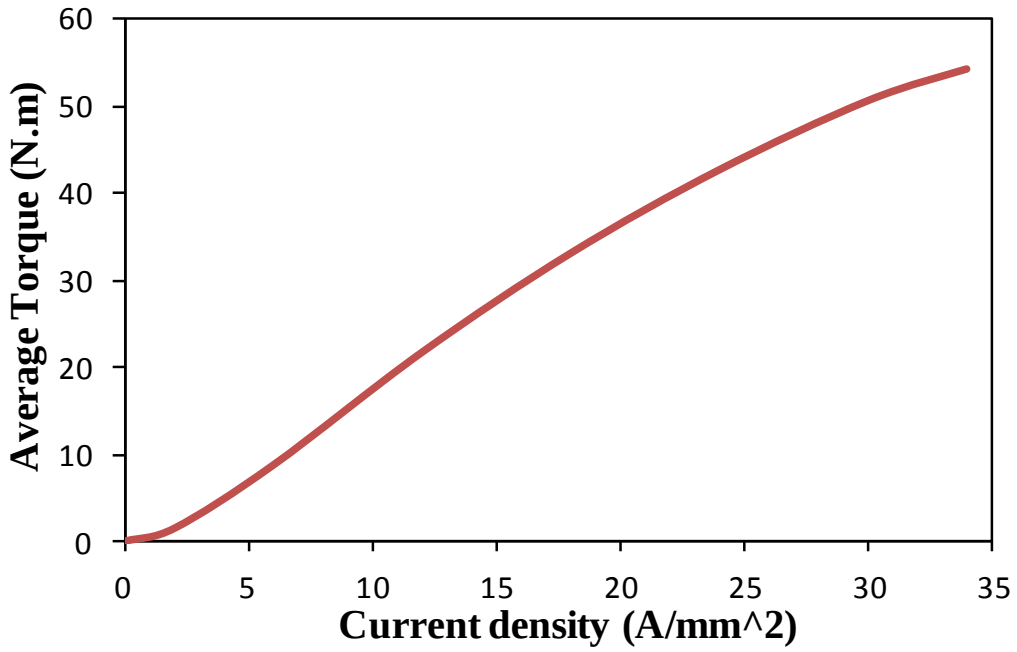

Fig. 6.55 Variation of average output torque against current density of 12 stator/4 rotor poles machine.

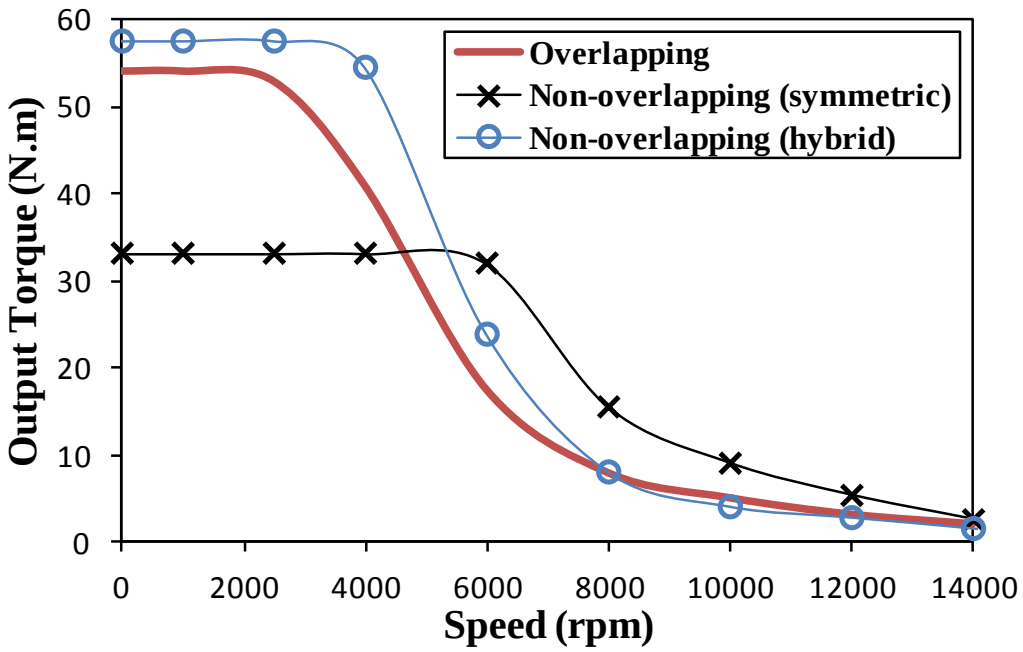

(a) Torque-speed curves at 34 A/mm^2 maximum current density

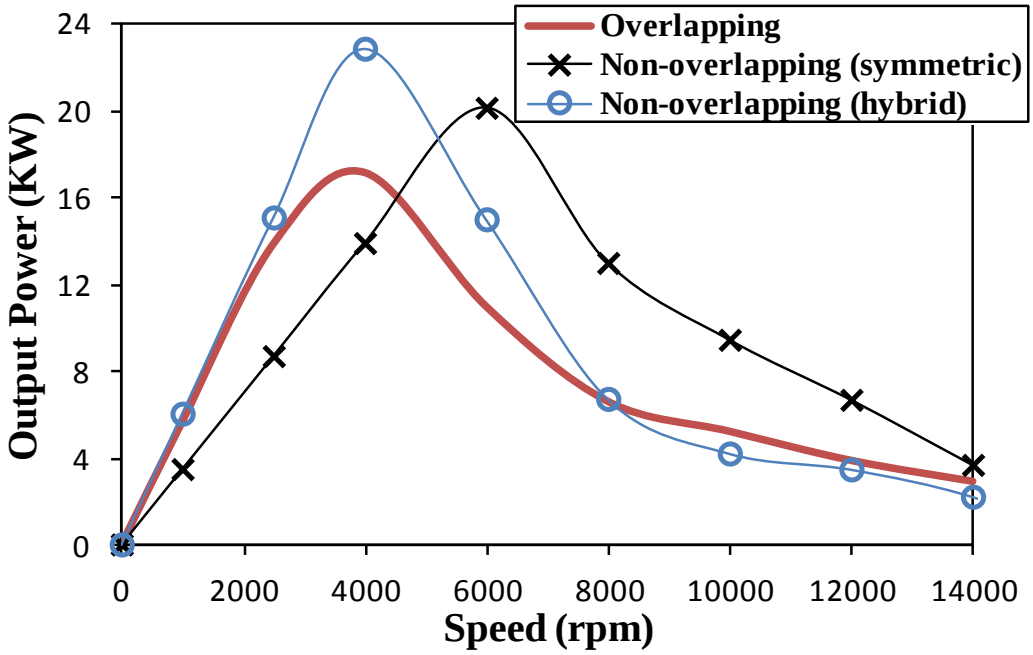

(b) Power-speed curves at 34 A/mm^2 maximum current density

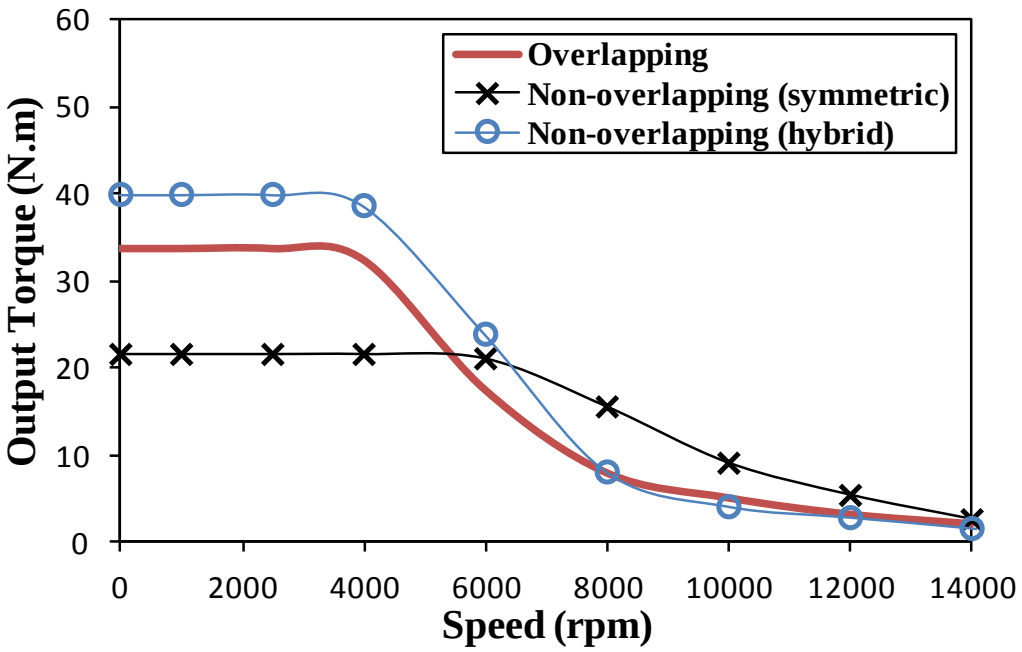

(c) Torque-speed curves at 20 A/mm^2 maximum current density

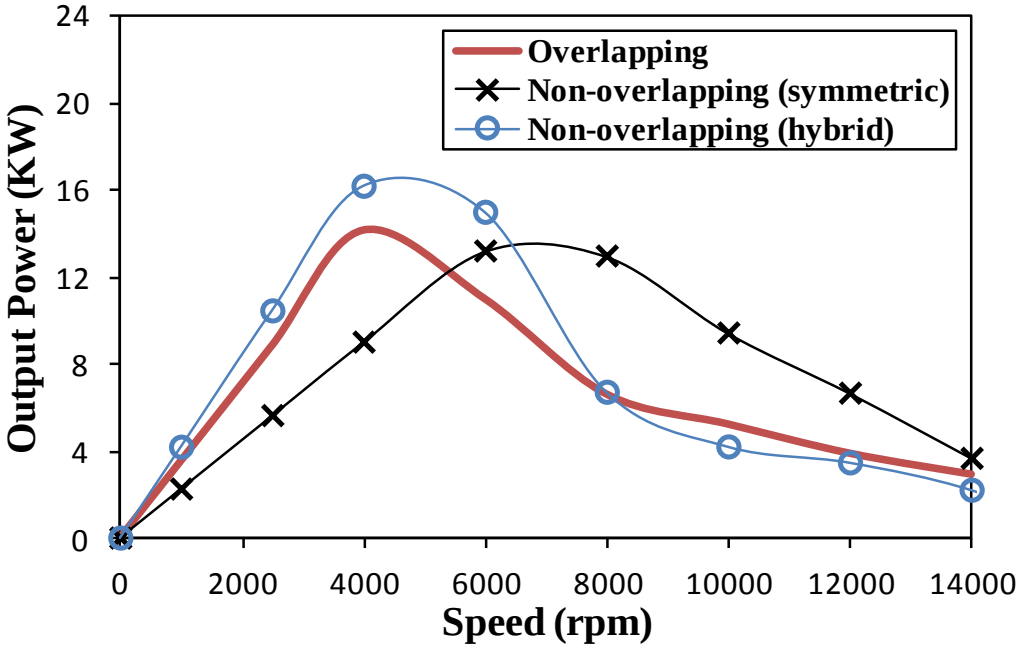

(d) Power-speed curves at 20 A/mm^2 maximum current density

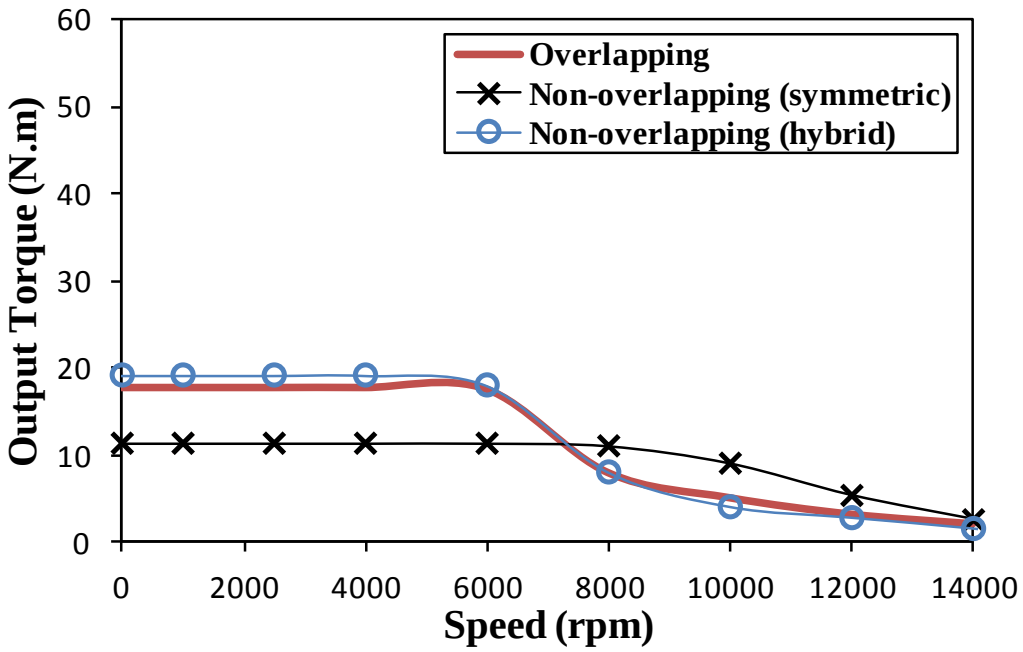

(e) Torque-speed curves at 10 A/mm^2 maximum current density

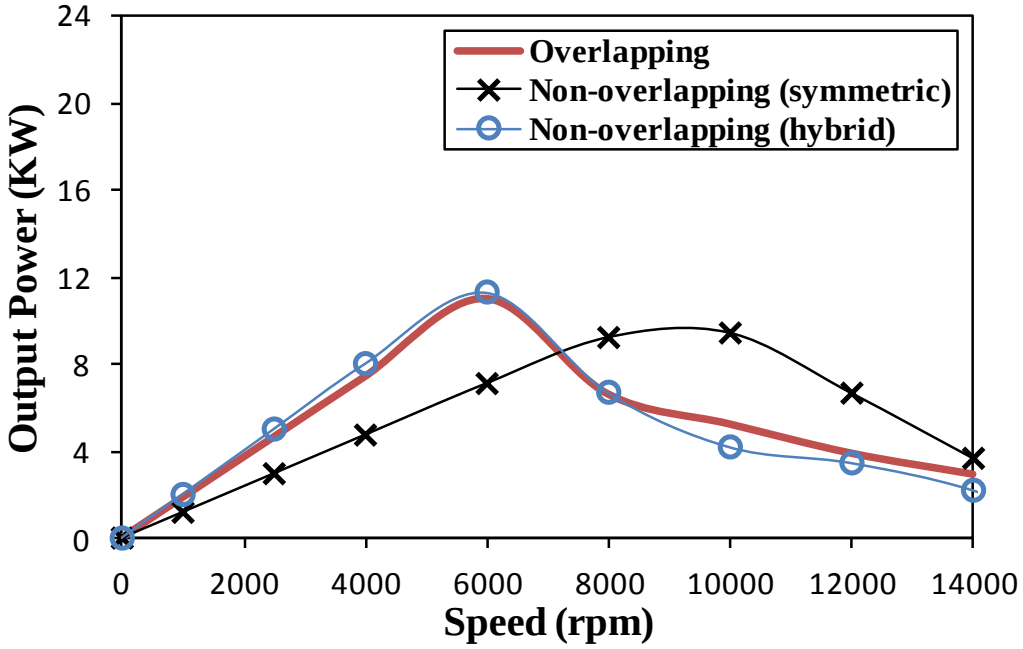

(f) Power-speed curves at 10 A/mm^2 maximum current density

Fig. 6.56 Comparison of torque and power-speed characterstics of 12 stator/4 rotor poles and 6 stator/4 rotor poles machines having different winding connections.

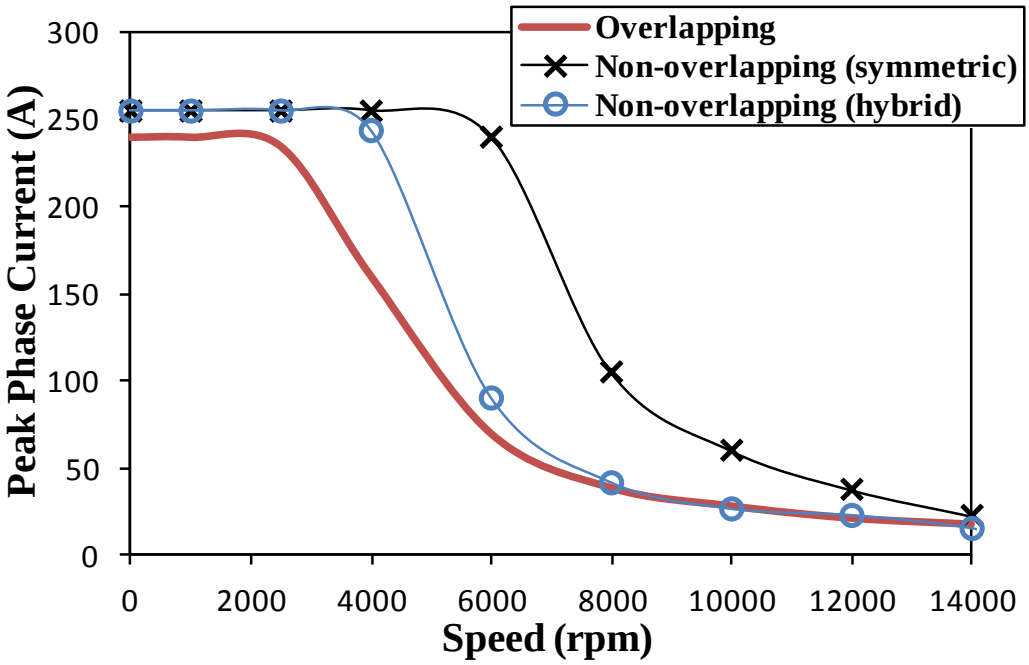

(a) Maximum current density is 34 A_{rms}/mm^2

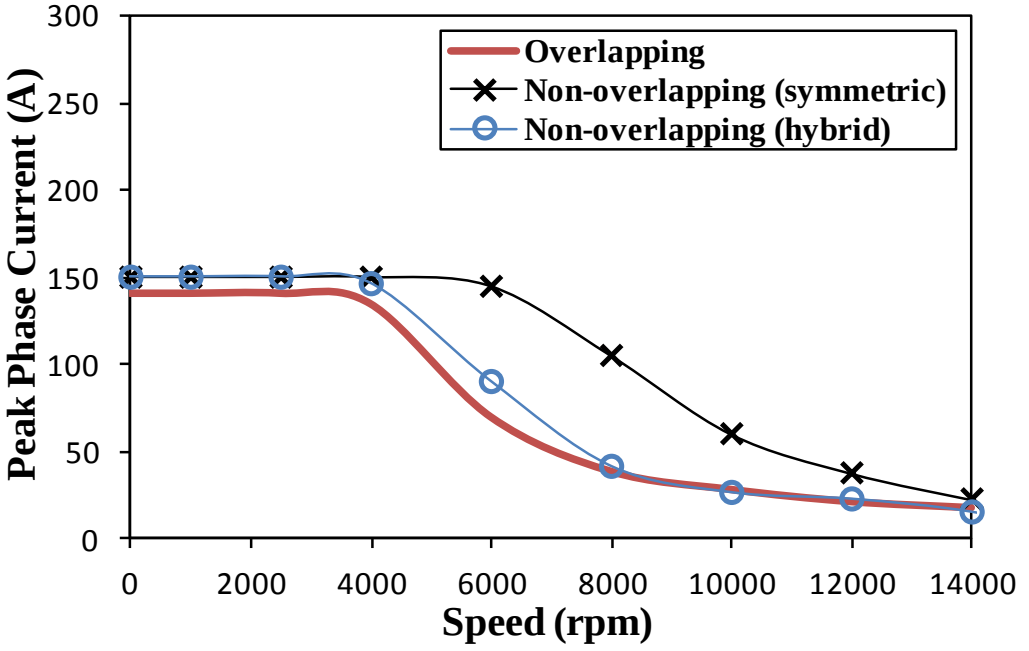

(b) Maximum current density is 20 A_{rms}/mm^2

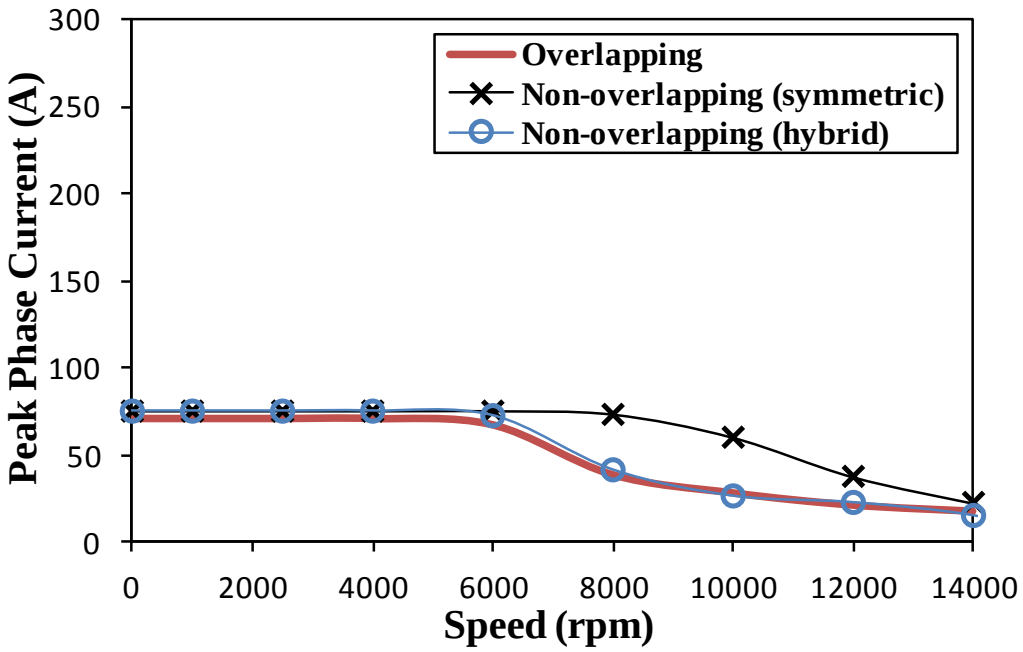

(c) Maximum current density is 10 A_{rms}/mm^2

Fig. 6.57 Variation of peak phase current of 12 stator/4 rotor poles and 6 stator/4 rotor poles machines having different winding connections for different current densities.

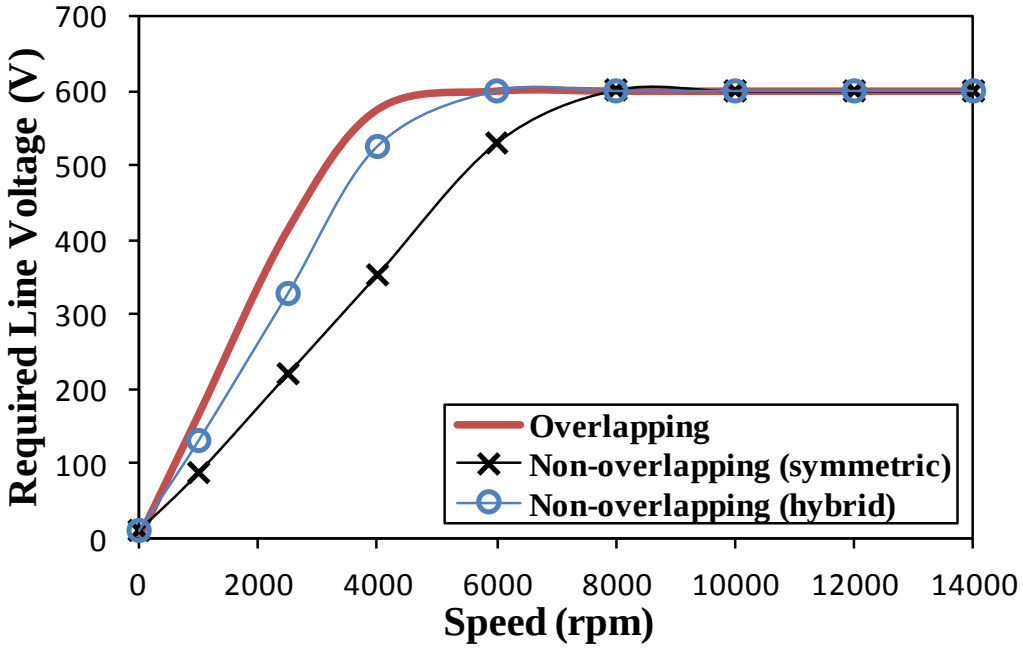

(a) Maximum current density is 34 A/mm^2

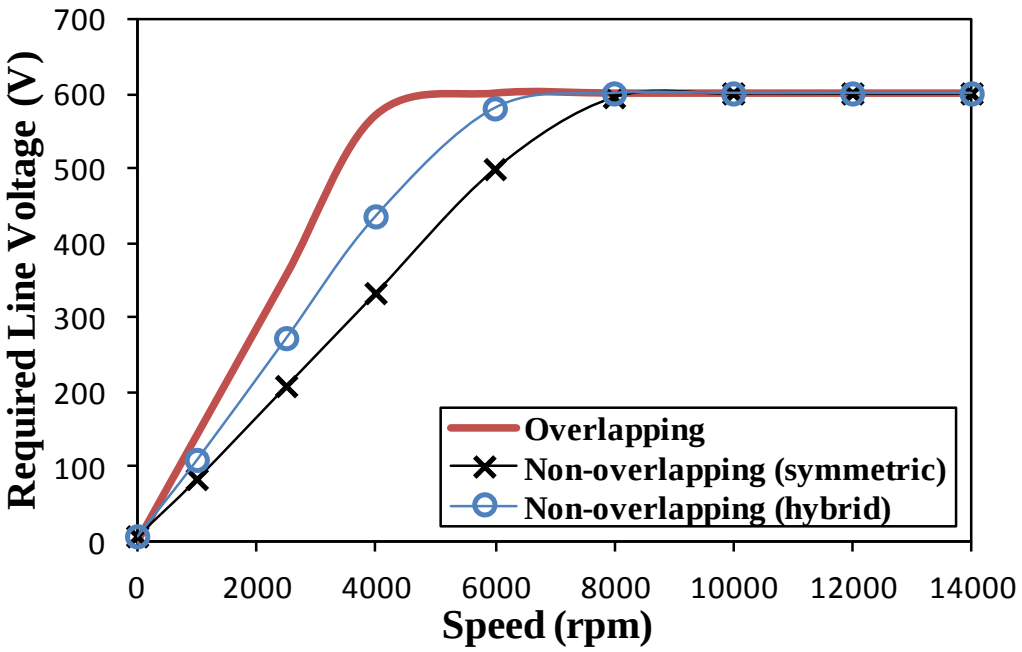

(b) Maximum current density is 20 A/mm^2

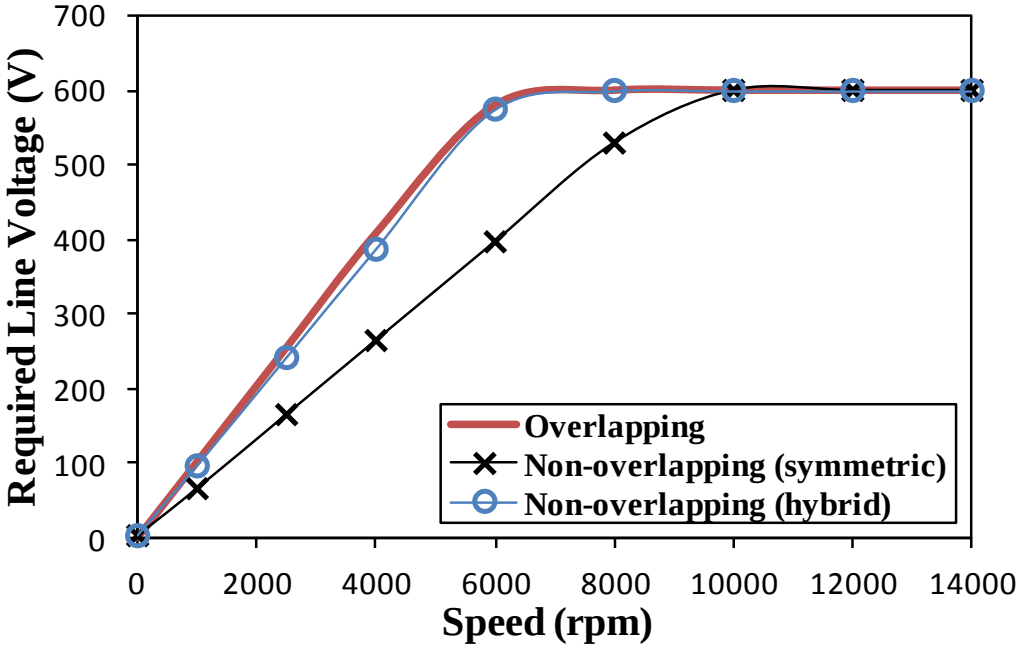

(c) Maximum current density is 10 A/mm^2

Fig. 6.58 Variation of peak line voltage of 12 stator/4 rotor poles and 6 stator/4 rotor poles machines having different winding connections for different current densities.

6.7.3. Efficiency

In order to present a comprehensive comparison, the efficiencies of the three considered machines will be compared in this section. For this purpose, the corresponding iron and copper losses associated with the torque-speed characteristics at 34 A/mm^2 maximum current density of the 12 stator/4 rotor poles machine are calculated and shown in Fig. 6.59 and Fig. 6.60, respectively. Comparing with their counterparts of the 6 stator/4 rotor poles machine with symmetric and hybrid winding connection, Fig. 6.34 and Fig. 6.35, the iron loss of the 12 stator/4 rotor poles machine is lower at relatively low speeds since the phase current of this machine is also lower, as shown in Fig. 6.57(a). However, at relatively high speeds both machines with overlapping and non-overlapping hybrid winding connections generate nearly the same iron loss, which is lower than its counterpart of the machine with the non-overlapping symmetric winding connection. This is because the first two machines have lower phase current, Fig. 6.57(a).

Moreover, the copper loss of the 12 stator/4 rotor poles machine is the largest in constant torque region since it has larger phase resistance, i.e. due to longer end-winding. This loss becomes relatively low in the flux wakening operation region, due to the reduction of the phase current variation, Fig. 6.57(a). The efficiency of the three machines is compared in Fig. 6.61. It shows that at low speeds the 12 stator/4 rotor poles machine and its 6 stator/4 rotor poles counterpart with hybrid winding connection exhibit nearly the same efficiency, which is much larger than their counterpart of the 6 stator/4 rotor poles machine with symmetric winding connection. On other hand, at high speeds, all machines exhibit nearly the same efficiency, which is relatively large, i.e. maximum of 93%. Therefore, the SR machines in general demonstrate better performance when operated at high speeds.

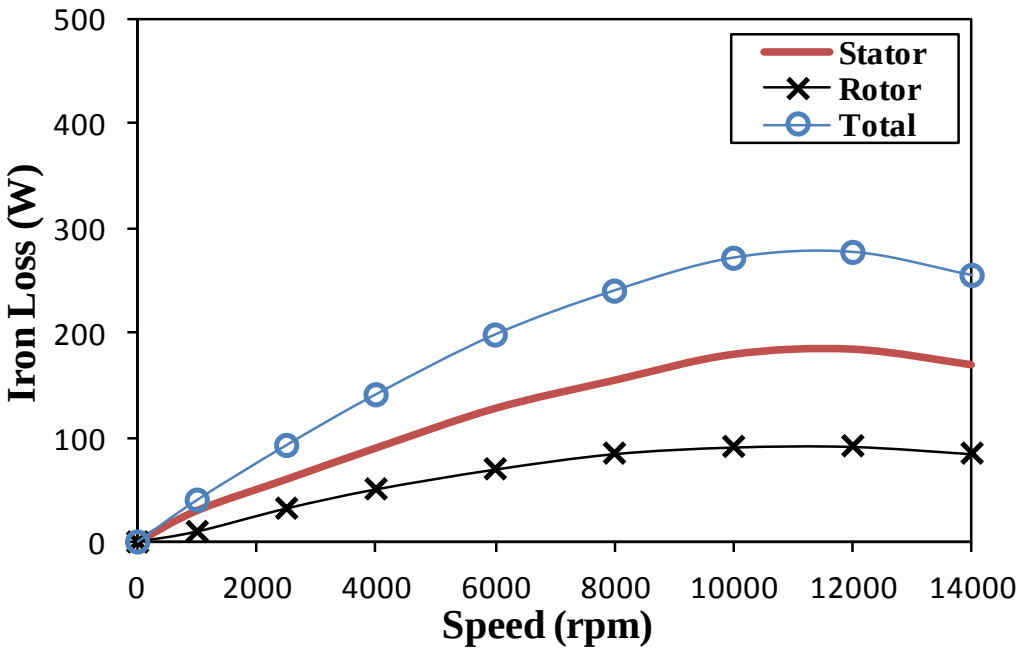

Fig. 6.59 Variation of iron loss of 12 stator/4 rotor poles machine, at 34 A/mm^2 maximum current density.

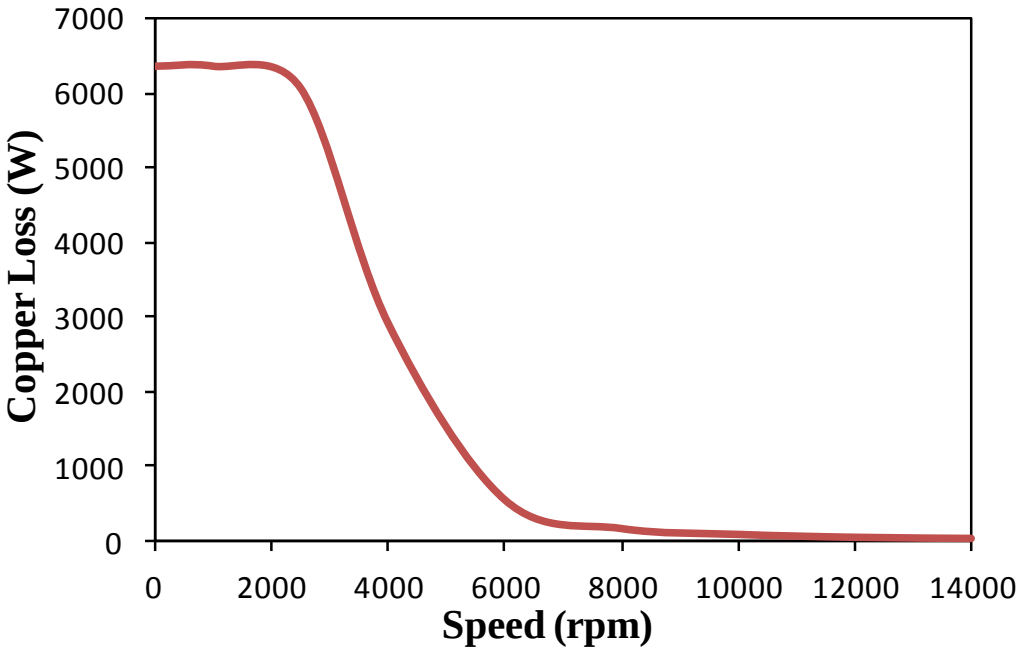

Fig. 6.60 Variation of copper loss of 12 stator/4 rotor poles machine, at 34 A/mm^2 maximum current density.

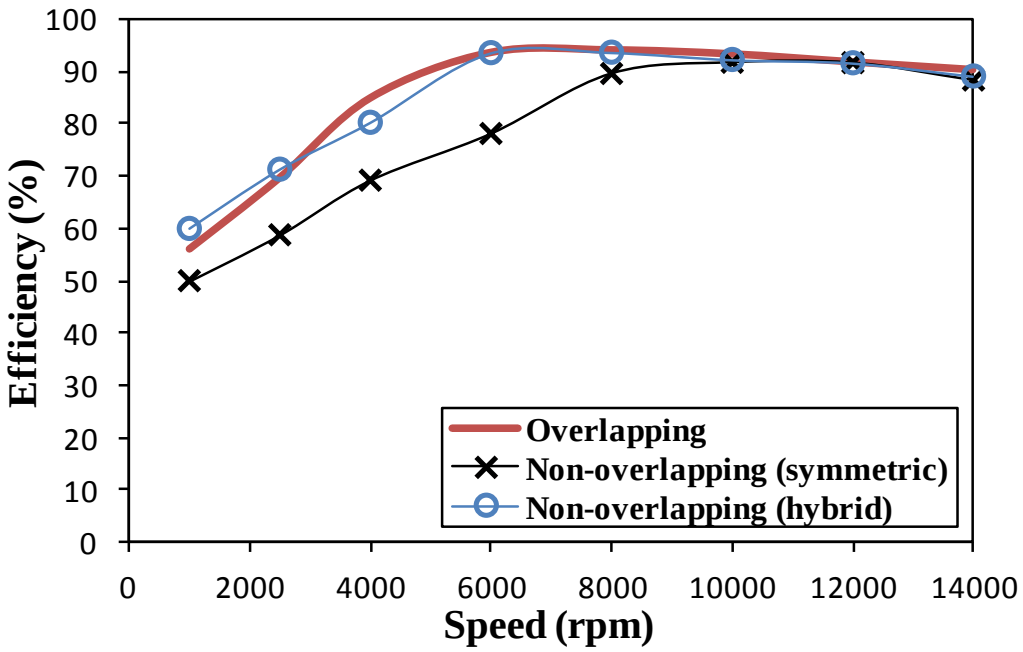

Fig. 6.61 Comparison of efficiency of 12 stator/4 rotor poles and 6 stator/4 rotor poles machines having different winding connections for 34 A/mm^2 maximum current density.

Table 6.3 Comparison of characteristics of 12 stator/4 rotor poles and 6 stator/4 rotor poles machines having different winding connections, at 34 A/mm^2 current density and 2500 rpm.

Characteristics	***Overlapping***	***Non-overlapping***	
		Symmetric	***Hybrid***
Average torque (N.m)	53.9	32	56
Torque ripple (N.m)	49.3	16	31
Torque ripple Percentage (%)	91.4	50	55
Output Power (KW)	14.1	8	15
Iron loss (W)	94	140	143
Copper loss (W)	6347	5843	5843
Efficiency (%)	69.6	59	71

6.8. Experimental Measurements

In order to validate the analyses and investigations of this chapter, the 6 stator 4 rotor SynR machine has been prototyped, Fig. 6.62. In the next chapter, i.e. Chapter 7, the same prototype machine will be investigated again under the AC sinusoidal bipolar with DC bias excitation, which requires two coils on each stator tooth, i.e. one for the AC sinusoidal excitation while the other for the DC bias. Therefore, in order to experimentally validate both excitations using the same prototype machine, each stator tooth has been wound with two coils, the first is 8 turns while the another is 13 turns. The four ends of each coil have been taken outside the motor, as illustrated in Fig. 6.62 (b). Under the AC excitation, these two coils are connected together in series to form a 21 turns coil per stator tooth, the six coils are linked together to create the three phase winding, as shown in Fig. 6.63. On the other hand, under the AC+DC excitation, the 13 turn coils will be excited by three phase AC sinusoidal currents, while the 8 turns coils will be connected to a DC excitation source, as will be further illustrated in Chapter 7. It should be mentioned that the packing factor of the prototype machine is 0.4.

The measurements include the variation of the output torque against the current angle and maximum output torque against phase current, i.e. current density. The test rig including the prototype machine is illustrated in Fig. 6.64. The measured and predicted variations of the output torque against the current angle of the three studied winding connections under 10 and 15 A/mm^2 current densities are compared in Fig. 6.65. On the other hand, the measured and predicted maximum output torque against the current density under these connections is compared in Fig. 6.66. The good agreement strongly confirms and the analyses and conclusions of this chapter.

(a) Stator and rotor

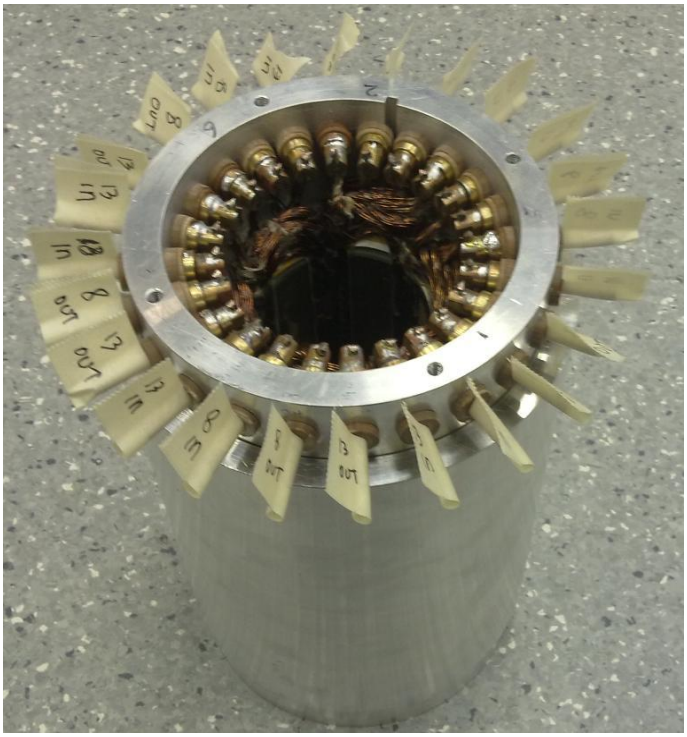

(b) Stator with coil connection

Fig. 6.62 6 stator/4 rotor prototype machine.

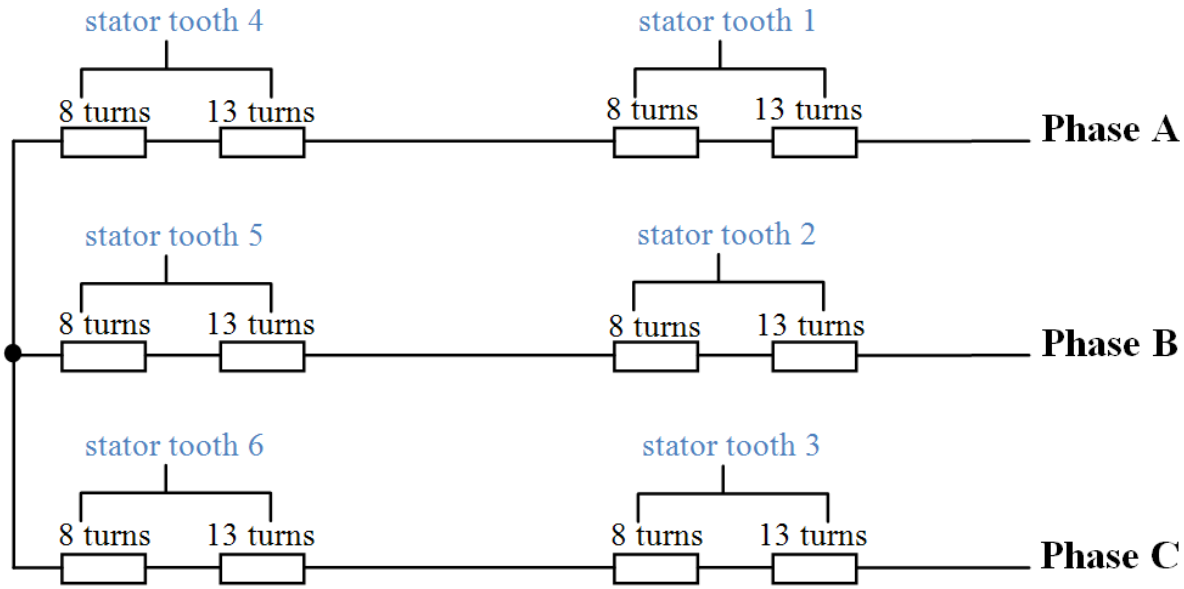

Fig. 6.63 Winding connection of 6 stator/4 rotor prototype machine under AC excitation.

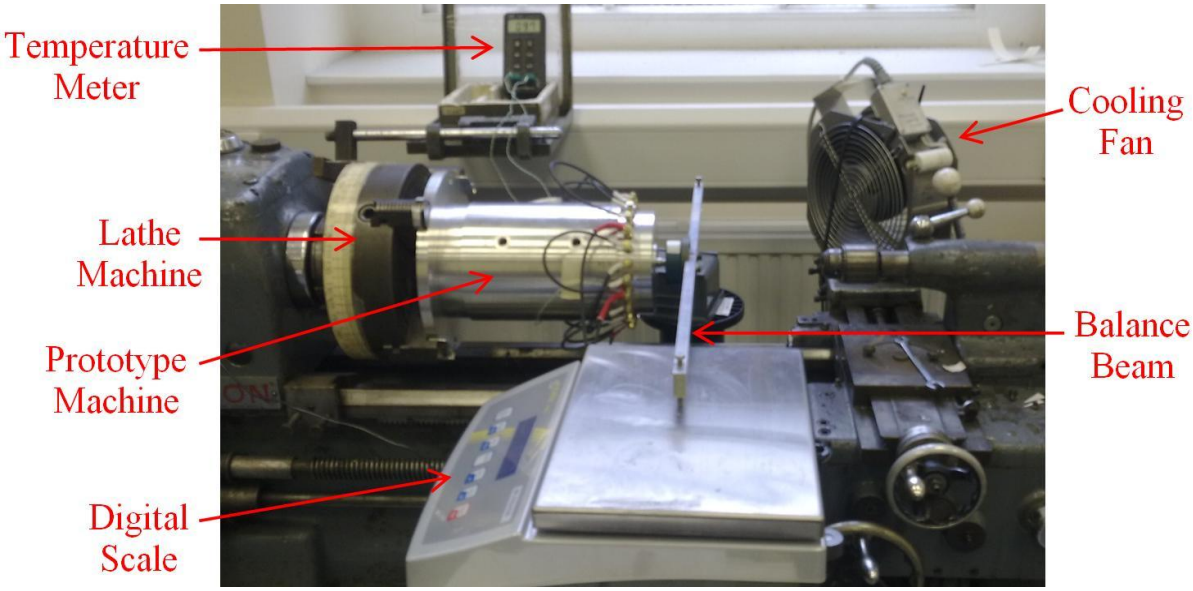

Fig. 6.64 Test rig for measuring torque-phase current angle and magnitude characteristics.

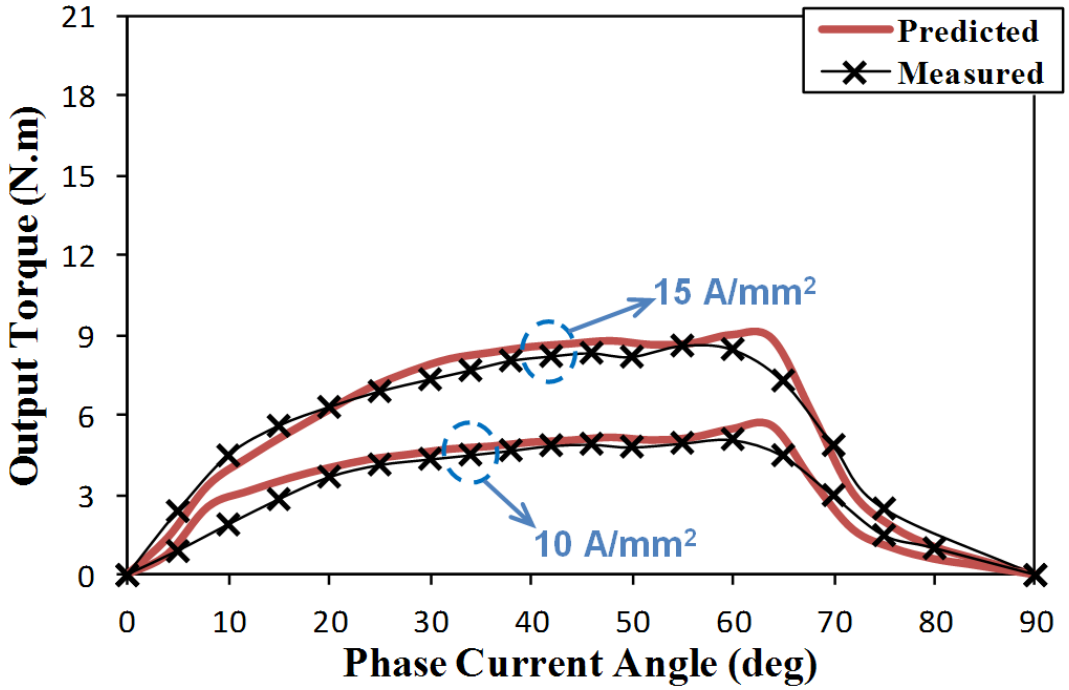

(a) Asymmetric winding connection

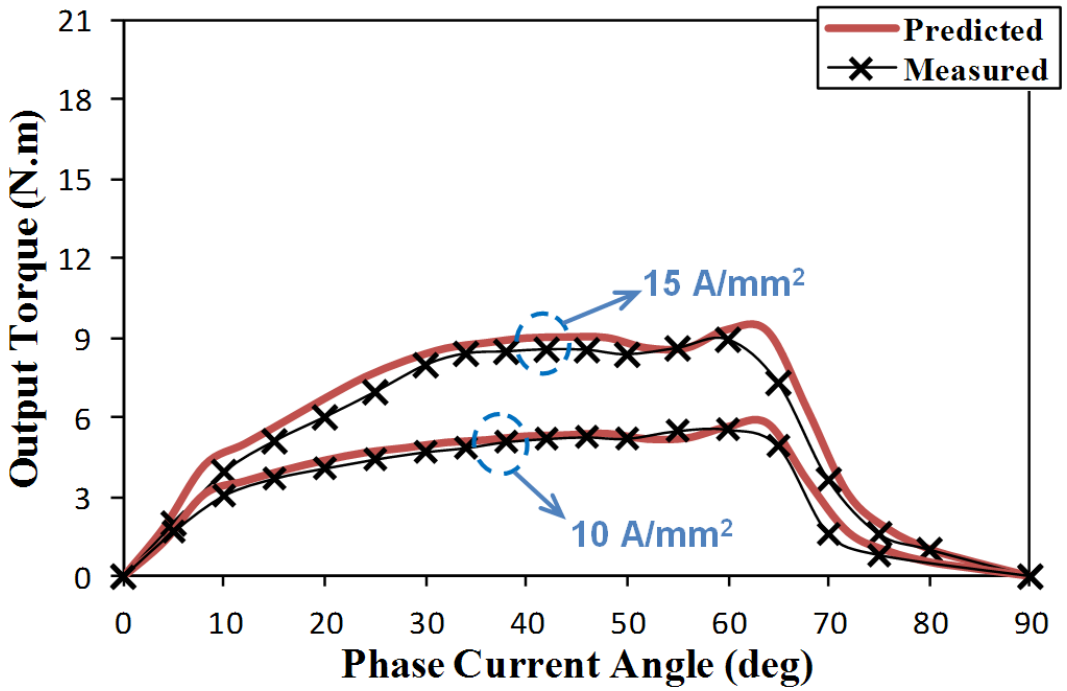

(b) Symmetric winding connection

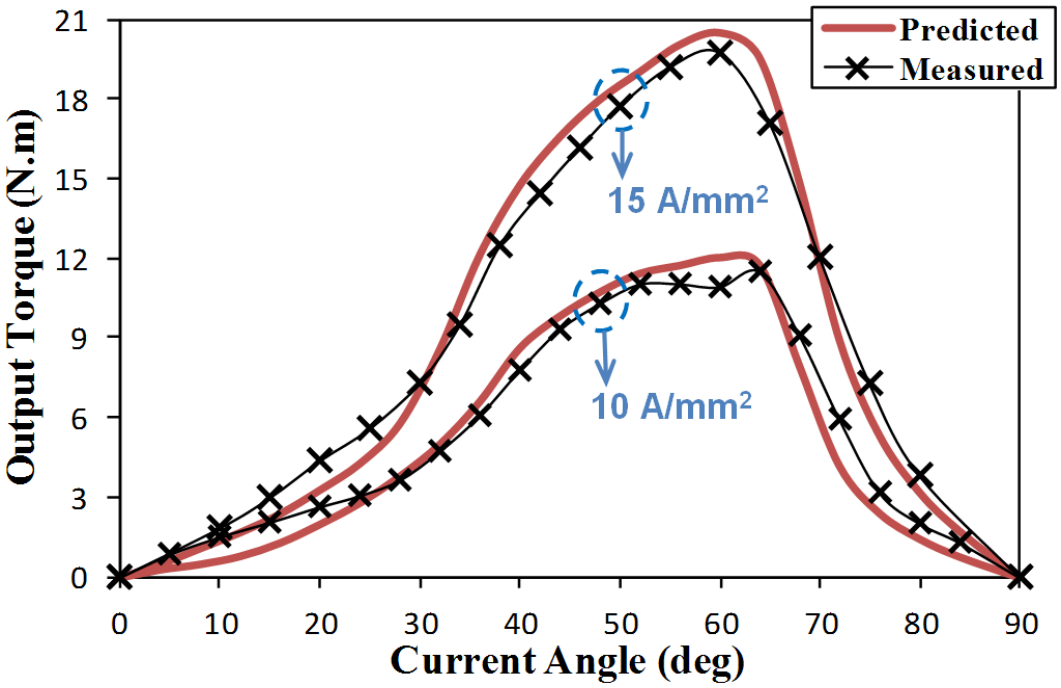

(c) Hybrid winding connection

Fig. 6.65 Comparison of measured and predicted output torque variations against current angle of 6 stator/ 4 rotor poles prototype machine for different winding connections, at 10 and 15 A/mm^2 current densities.

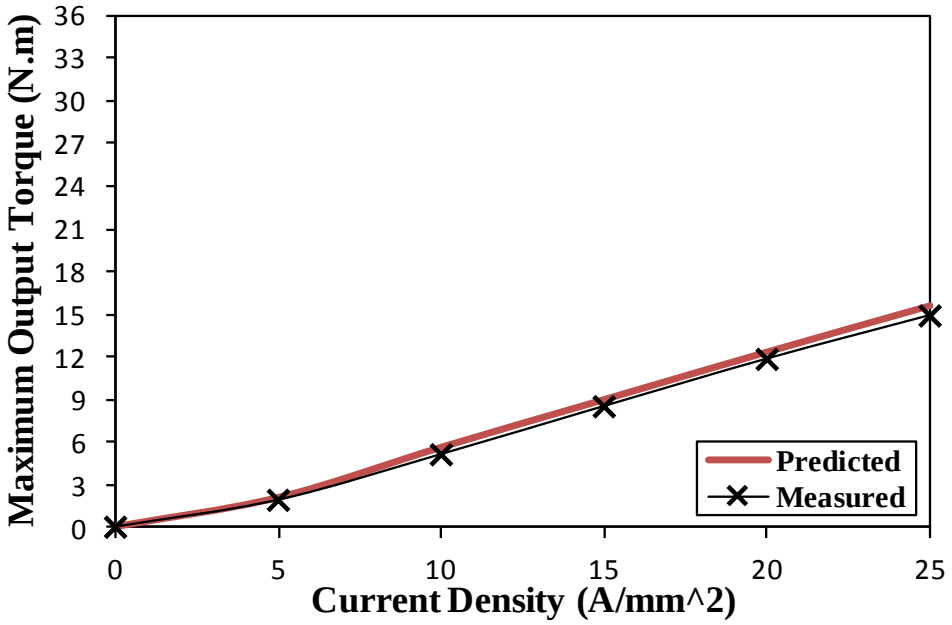

(a) Asymmetric winding connection

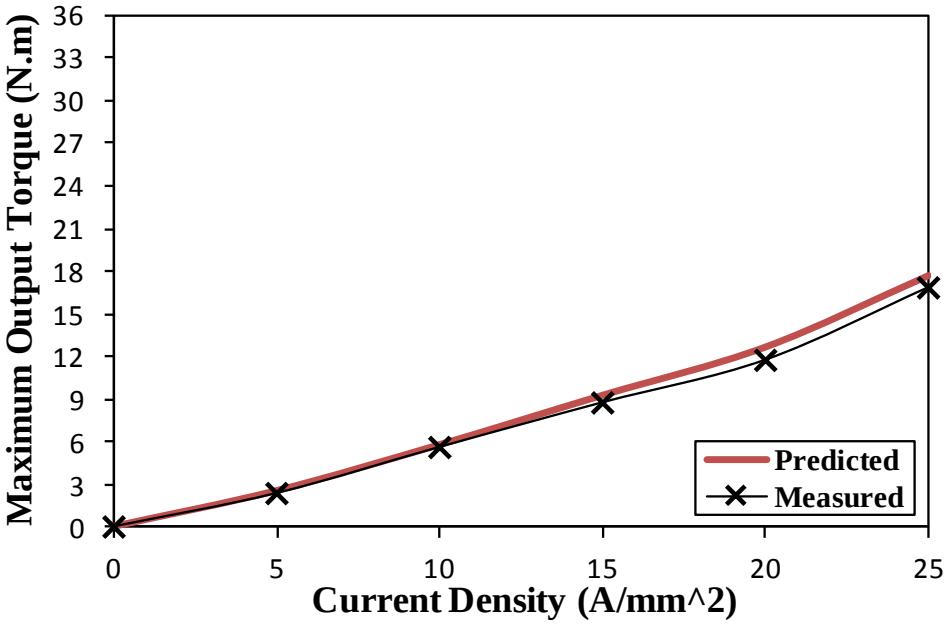

(b) Asymmetric winding connection

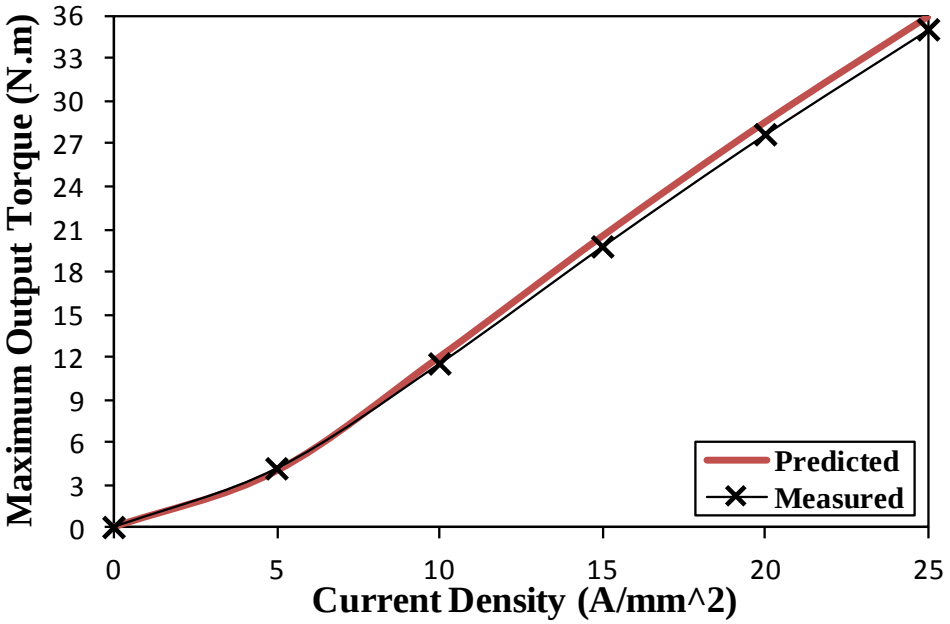

(c) Hybrid winding connection

Fig. 6.66 Comparison of measured and predicted maximum output torque variations against phase current magnitude of 6 stator/ 4 rotor poles prototype machine for different winding connections.

6.9. Conclusions

The electromagnetic performance of 6 stator/4 rotor poles SynR machines having different non-overlapping concentrated winding connections, i.e. asymmetric, symmetric and hybrid, and AC sinusoidal bipolar excitation have been investigated, analysed and compared in this chapter. It is found that, in addition to the self inductance variations, the machine with hybrid winding connection has relatively larger mutual inductance variations and shorter phase flux paths. Thus, such machine exhibits relatively larger average output torque and efficiency and lower iron loss comparing with the other two winding connections. Comparing with the machine having symmetric winding connection, its counterpart that employs asymmetric winding connection generates slightly larger average output torque, but much larger torque ripple. In addition, due to the non-uniform 3-phase flux linkage waveforms of the asymmetric winding connection machine, its 3-phase voltage waveforms are also not uniform. Thus, the required DC-link voltage to operate such machine is larger than other two counterparts. In term of output torque ripple, the symmetric winding connection leads to the best performance. In addition, such connection results in the widest flux weakening operation region as well as relatively higher efficiency at high speeds. On the other hand, at significantly large current densities, i.e. high magnetic saturation level, the hybrid connection can be also an attractive choice, since it combines the significantly large output torque and relatively low torque ripple with the relatively high efficiency.

Furthermore, the 6 stator/4 rotor poles machines having non-overlapping symmetric and hybrid winding connections have been compared with their 12 stator/4 rotor poles counterpart with overlapping winding in terms of output torque, torque ripple, torque-speed characteristics and efficiency. It can be concluded that comparing with the 6 stator/4 rotor machine has non-overlapping symmetric winding connection, the 12 stator/4 rotor poles machine exhibits relatively larger mutual inductance variation, thus produces significantly larger average output torque. However, this torque is lower than its counterpart of the 6 stator/4 rotor machine with non-overlapping hybrid winding connection, which has larger mutual inductance variation. The 12 stator/4 rotor poles machine generates the largest torque ripple. In addition, the line voltage of such machine is relatively large, thus it exhibits the narrowest flux weakening operation region. In general, the SynR machines under AC sinusoidal bipolar excitation could be a good choice for the electric/hybrid electric vehicles since they exhibit relatively large output torque, power and efficiency. However, the torque ripple, DC-link voltage, noise and vibration issues should be first further investigated.

Chapter 7: Electromagnetic Performance Analysis of Synchronous Reluctance Machines Having Non-overlapping Concentrated Windings and AC Sinusoidal Bipolar with DC Bias Excitation

7.1. Introduction

It is well known that the PM machines, which have two excitation sources, i.e. PMs and phase currents, exhibits larger torque density comparing with the other type of machines. However, due to the limitation of resources and significant increase in price of the PM materials, the magnetless machine topologies become more and more desirable as an alternative. The magnets in the PM machines are equivalent to constant DC excitation sources. Therefore, the AC sinusoidal bipolar excited SynR machines, which are investigated in Chapter 6, have the potential to exhibit larger torque density if two excitation sources are employed. The first one is the DC bias which is equivalent to the PMs excitation, while the second one is the standard AC sinusoidal excitation. Such machines will be designed as a SynR machine having AC sinusoidal bipolar with DC bias excitation. The operation principle and electromagnetic performance of the machines under such excitation are thoroughly investigated in this chapter using FE analysis tool. In addition, its electromagnetic performance is compared with its counterpart without DC bias excitation and conventional unipolar SR machine. Finally, experimental results are provided to support the investigation.

7.2. Operation Principles

The investigations are carried out on the 6 stator/4 rotor poles machine, whose major dimensions are given in Table 6.1. In order to operate the SynR machine under AC sinusoidal bipolar with DC bias excitation, each stator tooth is wound with two coils, the first belongs to the AC sinusoidal excitation, while the other is connected to the DC current source. The AC current coils are linked together to form the standard three phase winding connection, which is connected to a standard 3-phase inverter. On the other hand, the DC current coils are connected together in series, with polarity consideration, to a separate DC source. An example of the coil connections is illustrated in Fig. 7.1. The operation principles of such excitation can be simply summarized as follows: under DC excitation only, i.e. AC

coils are not excited (open-circuit), the DC flux, which is equivalent to magnet flux in PM machines, interlinks with the AC coils of each phase and induces phase voltages, which equivalently will be called the back-emf. Consequently, similar to PM machines, an output torque will be generated if the AC coils are excited by AC sinusoidal currents. Furthermore, due to the interaction between the DC flux and stator slotting, an open-circuit torque ripple or cogging torque will be generated. Further illustrations and investigations are given in the following sections.

Moreover, similar to the AC sinusoidal bipolar excitation, the coils under AC sinusoidal bipolar with DC bias excitation have the possibility to be connected either asymmetrically, Fig. 7.2(a), or symmetrically, Fig. 7.2(b). However, it should be illustrated that in the case of asymmetric winding connection only 4 DC coils become required, i.e. no need for DC coils on phase B teeth (no DC coils on teeth 2 and 5 in Fig. 7.1). This is because such coils do not contribute to the output torque, but they only generate an extra copper loss. The machine electromagnetic performance under such two winding connections will be investigated and compared in this chapter. It is also worth mentioning that the hybrid winding connection, which is investigated in Chapter 6, is not suitable when the machine is excited by AC sinusoidal currents with DC bias since it exhibits a significantly small open-circuit flux linkage waveform, as illustrated in Fig. 7.3. Consequently, such connection results in an extremely small output torque, thus is not considered in this chapter. Furthermore, under such excitation the current frequency is determined by the rotor pole number, i.e. similar to the switched flux PM (SFPM) machines. In other words, the current frequency should be doubled comparing with the AC sinusoidal bipolar excitation since one electric cycle is completed when the rotor mechanically rotates one rotor pole pitch, as shown in Fig. 7.3.

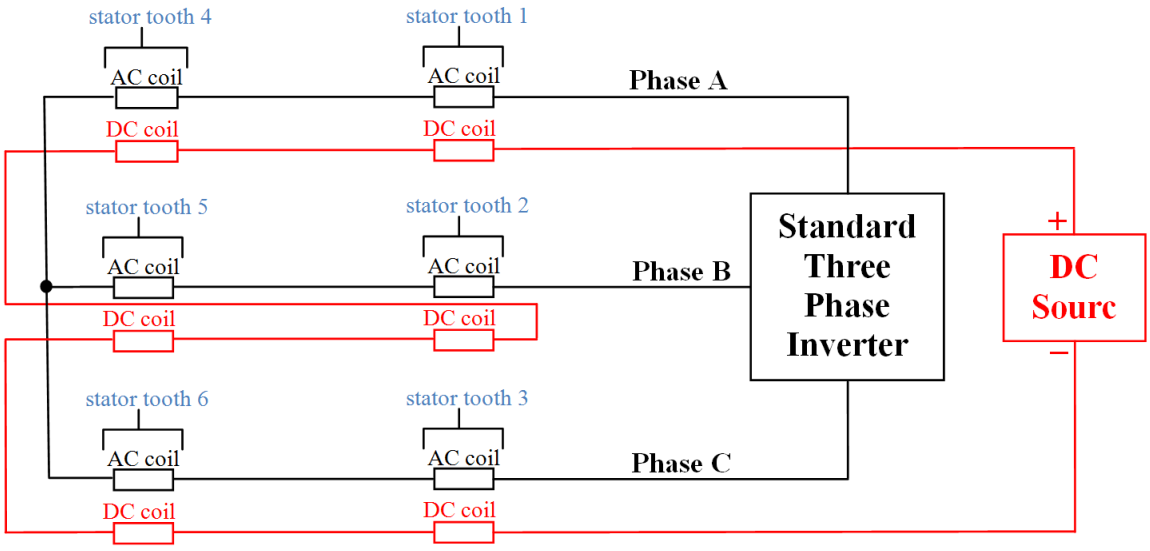

Fig. 7.1 Winding connection under AC sinusoidal bipolar with DC bias excitation.

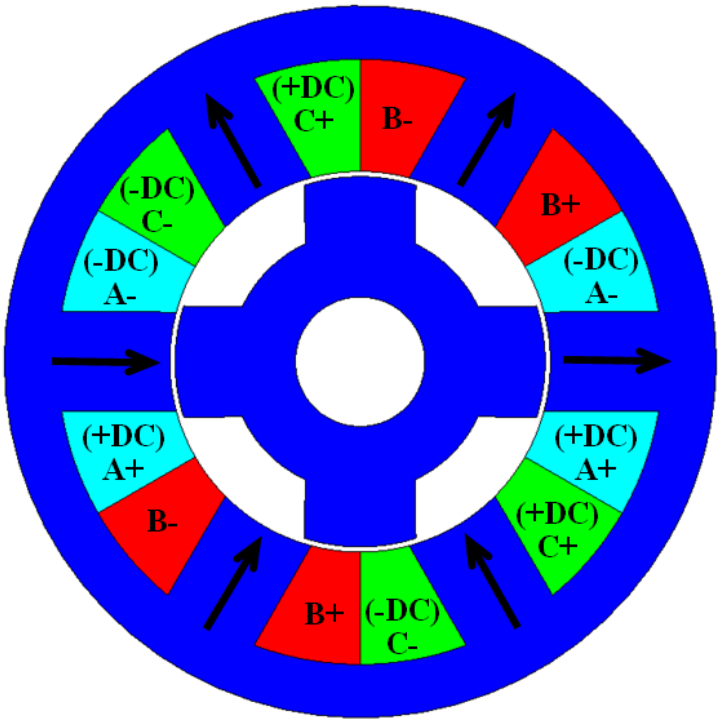

(a) Asymmetric winding connection

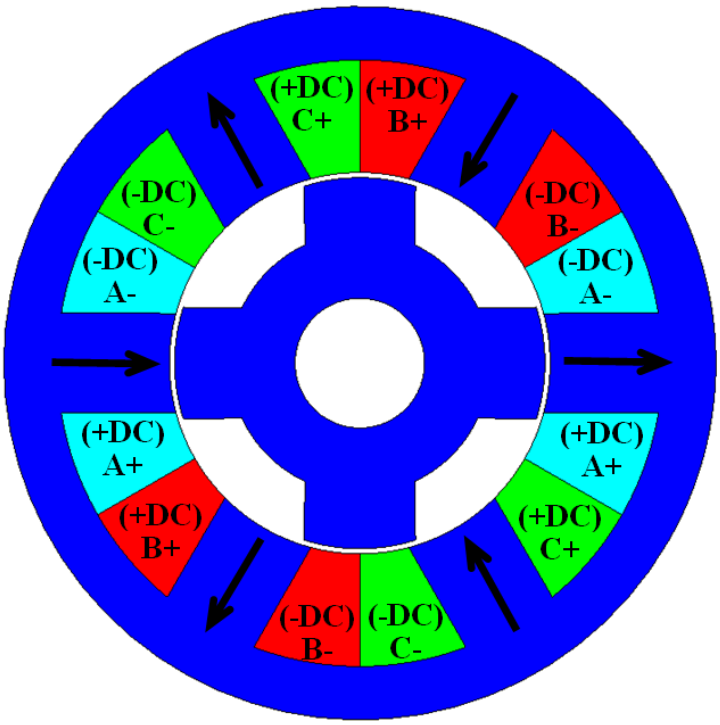

(b) Symmetric winding connection

Fig. 7.2 Comparison of asymmetric and symmetric winding connections of 6 stator/4 rotor poles machine under AC sinusoidal bipolar with DC bias excitation, (+DC) and (-DC) refer to positive and negative polarity of DC excitation.

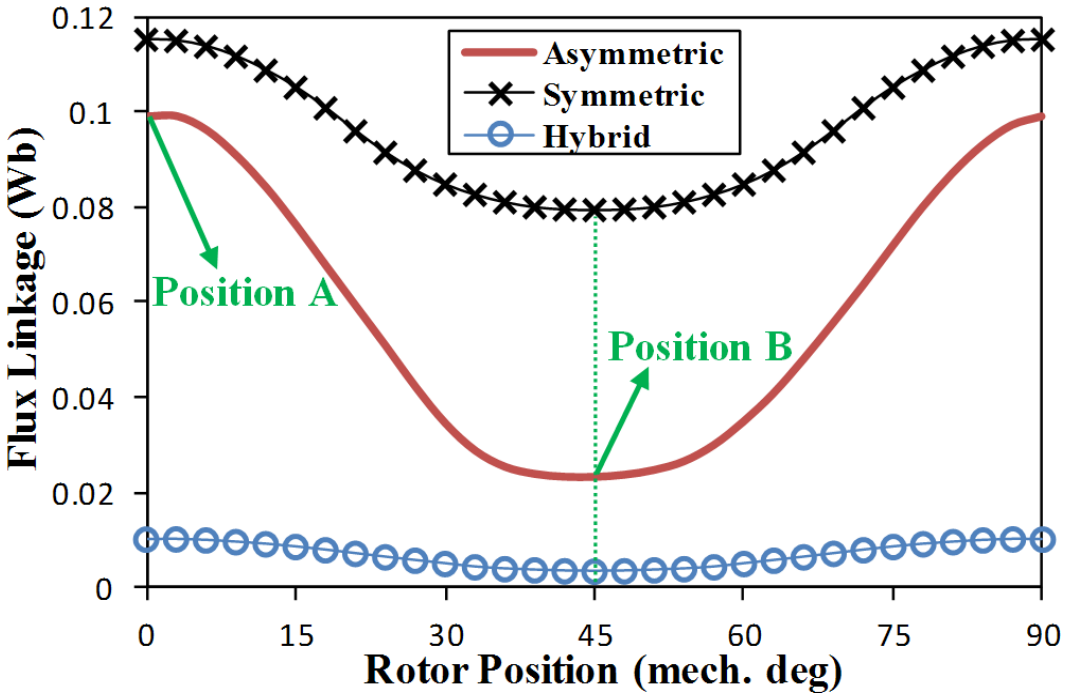

Fig. 7.3 Comparison of open-circuit flux linkage variations of 6 stator/4 rotor poles machines having different winding connections under DC bias excitation only, at 34 A/mm^2 current density.

7.3. Electromagnetic performance

As mentioned earlier, the operation principle of the AC sinusoidal bipolar with DC bias excitation is similar to its counterpart of the PM magnet machines, i.e. both have two excitations. Thus, this section firstly analyses the open-circuit characteristics, e.g. with DC excitation only, then it investigates the load performance, e.g. under both AC and DC excitations. It should be also mentioned that the maximum considered current density during the investigations is limited to 34 A/mm^2. However, both the open-circuit and load characteristics are examined and compared for different DC and AC current densities.

7.3.1. Open-Circuit

In order to carry out such investigations, the three phase AC coils are open-circuited while the DC coils are connected to the DC source according to Fig. 7.1. Both the normal and tangential open-circuit air gap flux density components at 34 A/mm^2 are given in Fig. 7.4. Comparing with the asymmetric winding connection, its symmetric counterpart results in a larger normal open-circuit air gap flux density, which is identical every 180 mechanical degree, while the asymmetric winding connection waveform repeats once over the 360

mechanical degree, as shown in Fig. 7.4(a). This is due to the different flux distribution in each connection, as can be clearly seen in Fig. 7.5. For the same reason, the tangential components of both connections exhibit the same behaviour, Fig. 7.4(b). The open-circuit torque, i.e. cogging torque, of the two connections are predicted at 34 A/mm^2 DC current density and compared in Fig. 7.6(a). Under the asymmetric winding connection, the DC stator polarity repeats twice, as can be clearly seen in Fig. 7.2(a). This is equivalent to two stator slots from the cogging torque producing point of view. Thus, the cogging torque is produced by the interaction of the 4 rotor poles with these two slots. This means the cogging torque waveform will be repeated once every 90 mechanical degree, as confirmed in Fig. 7.6(a). On the other hand, the DC stator polarity under the symmetric winding connection repeats once every 60 mechanical degree, as can be clearly seen in Fig. 7.2(a), Thus, the cogging torque period of the symmetric winding connection is 30 mechanical degree, since the least common multiple between the rotor poles and equivalent stator slots is 12, thus the cogging torque period is 360÷12=30. In order to examine the influence of the magnetic saturation, the cogging torque is predicted for different current densities and the peak values due to the two winding connections are compared in Fig. 7.6(b). It shows that the influence of the magnetic saturation is different according to the winding connection. Under the asymmetric winding connection, the flux density distribution is not affected by the current density, i.e. the magnetic saturation level, as can be noticed by comparing Fig. 7.5(a) and (b) with Fig. 7.7(a) and (b), respectively. Therefore, the cogging torque of such connection is directly proportional to the current density. On the other hand, the cogging torque of the symmetric winding connection sharply increases for relatively small current densities, then it gradually decreases when the current density becomes more significant since the flux density distribution under such connection varies according to the current density value, i.e. the magnetic saturation level, as can be clearly noticed by comparing Fig. 7.5(c) and (d) with Fig. 7.7(c) and (d), respectively. The comparison illustrates that for significantly large current densities, Fig. 7.5(c) and (d), the flux density distribution becomes relatively more balanced, thus the change of cogging torque with rotor position is relatively small. However, at relatively low current density, Fig. 7.7(c) and (d), such distribution becomes less balanced, thus the cogging torque becomes relatively large.

Furthermore, the three phase open-circuit flux linkages, which are seen by the AC coils, are calculated for 34A/mm^2 current density and compared for the two winding connections in Fig. 7.8. It shows that the flux linkage waveforms of the asymmetric winding connection are non-uniform, Fig. 7.8(a), since the winding distribution of such connection are also non-

uniform, Fig. 7.2(a). On the other hand, the symmetric winding connection results in uniform flux linkage waveforms, which are larger than their counterparts of the asymmetric connection, since such connection has larger air gap flux density, Fig. 7.4. However, the maximum to minimum variation of such waveforms is smaller since for the symmetric winding connection, the difference between the flux distribution at the maximum flux linkage position of phase A, i.e. when the rotor poles are full aligned with the phase A stator poles, Fig. 7.5(c), and its minimum flux linkage position, i.e. the rotor pole and the phase A stator poles are un-aligned, Fig. 7.5(d), is relatively small comparing with the counterpart of the asymmetric winding connection, Fig. 7.5(a) and Fig. 7.5(b), respectively. Consequently, the induced open-circuit phase voltage waveforms, i.e. the back-emf waveforms, of the asymmetric winding connection is non-uniform and larger comparing with the counterparts of the symmetric winding connection, as shown in Fig. 7.9. Moreover, in order to investigate the influence of the magnetic saturation on such characteristics, the variations of phase A flux linkage and back-emf waveforms for different current densities are compared in Fig. 7.10 and Fig. 7.11, respectively. For the asymmetric winding connection, larger DC current densities increase the flux linkage waveforms and their variation, Fig. 7.10(a). As a result, the back-emf waveforms also increase, but such increasing becomes significantly small at relatively large DC current density, as illustrated in Fig. 7.11(a). This is an expected and normal behaviour since the magnetic circuit becomes more saturated. However, on the other hand, the magnetic saturation influence is more significant when the machine is equipped with the symmetric winding connection since, the variations of flux linkage waveforms are larger when the DC current density is relatively larger, but they become gradually less when such current densities are significantly large, as illustrated in Fig. 7.10(b). Consequently, the back-emf waveforms of the symmetric winding connection are larger when the current density is relativity large and they are much smaller when the current density is significantly large, as shown in Fig. 7.11(b). Comparing with the asymmetric winding connection, the back-emf waveform of the symmetric winding connection is larger at relatively larger current density, i.e. 12 A/mm^2. Therefore, for such current density the studied machine is expected to produce larger output torque if it is equipped by symmetric winding connection. On the other hand, for significantly large current densities, the larger output torque is expected to be obtained from the machine with asymmetric winding connection. Further analyses and discussions regarding the output torque generation will be provided in the next section.

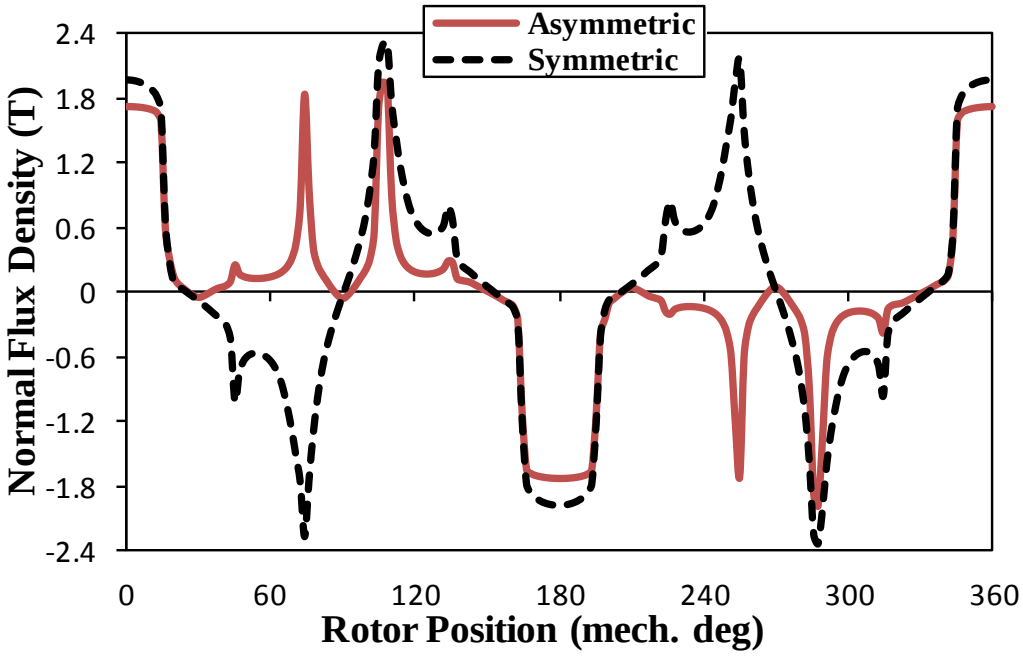

(a) Normal

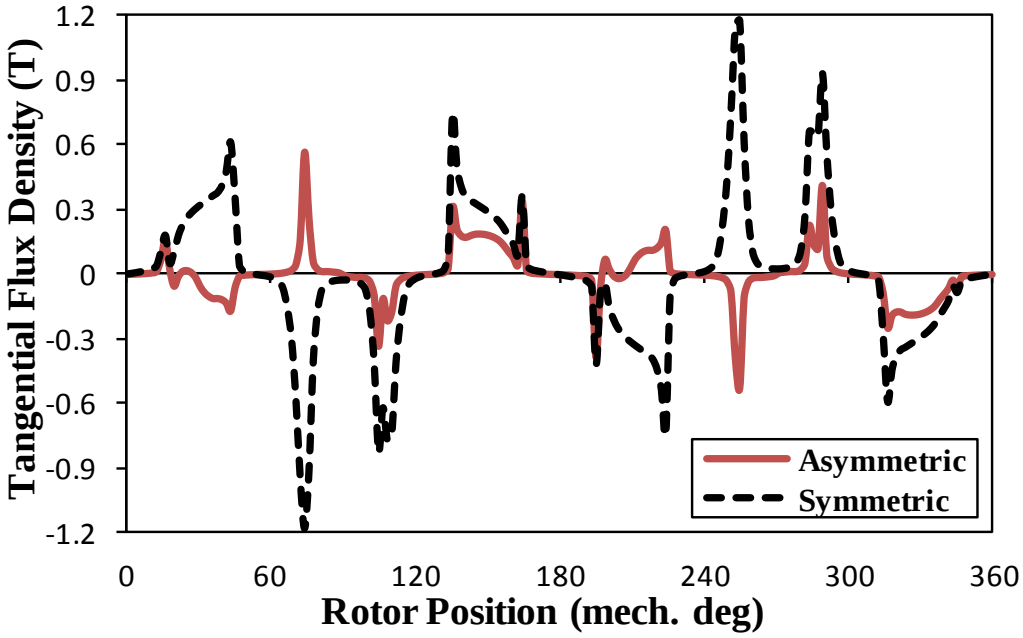

(b) Tangential

Fig. 7.4 Comparison of normal and tangential open-circuit air gap flux density distributions of 6 stator/4 rotor poles machines having different winding connections under DC bias excitation only, at 34 A/mm^2 DC current density.

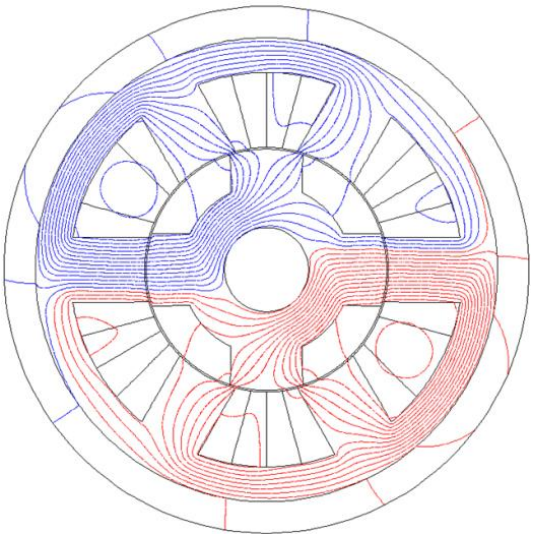

(a) Asymmetric winding connection at maximum flux linkage position for phase A

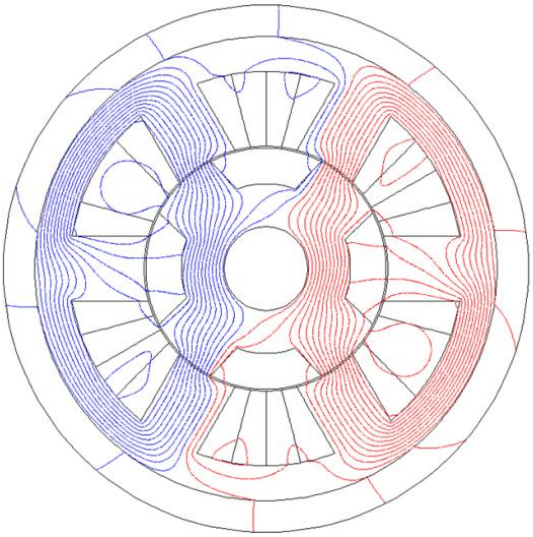

(b) Asymmetric winding connection at minimum flux linkage position for phase A

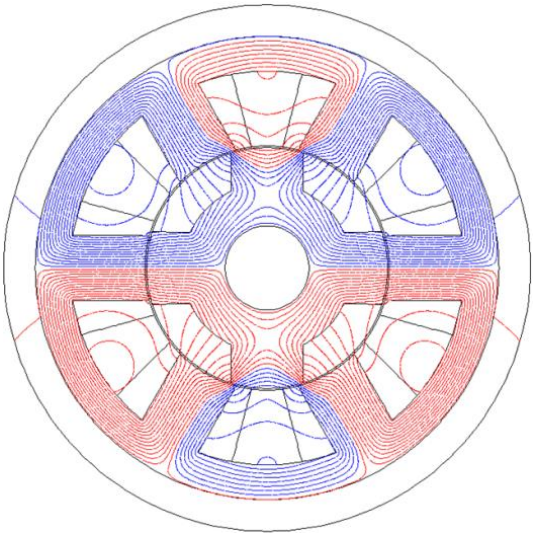

(c) Symmetric winding connection at maximum flux linkage position for phase A

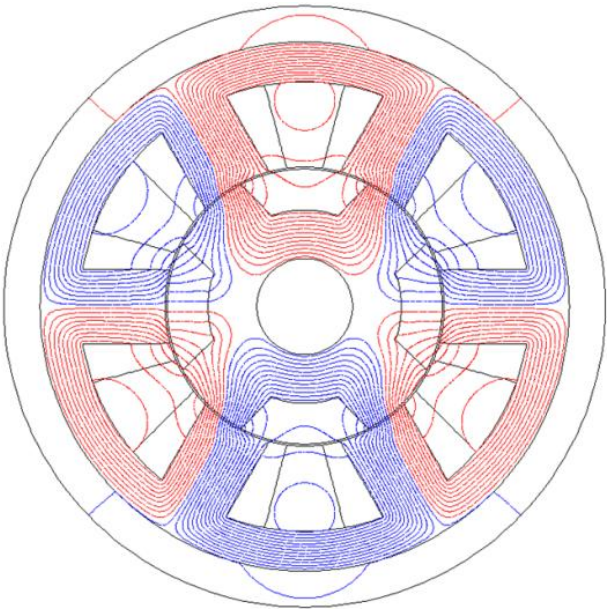

(d) Symmetric winding connection at minimum flux linkage position for phase A

Fig. 7.5 Equal potential distributions of 6 stator/4 rotor poles machines having different winding connections and different rotor positions, at 34 A/mm^2 DC current density.

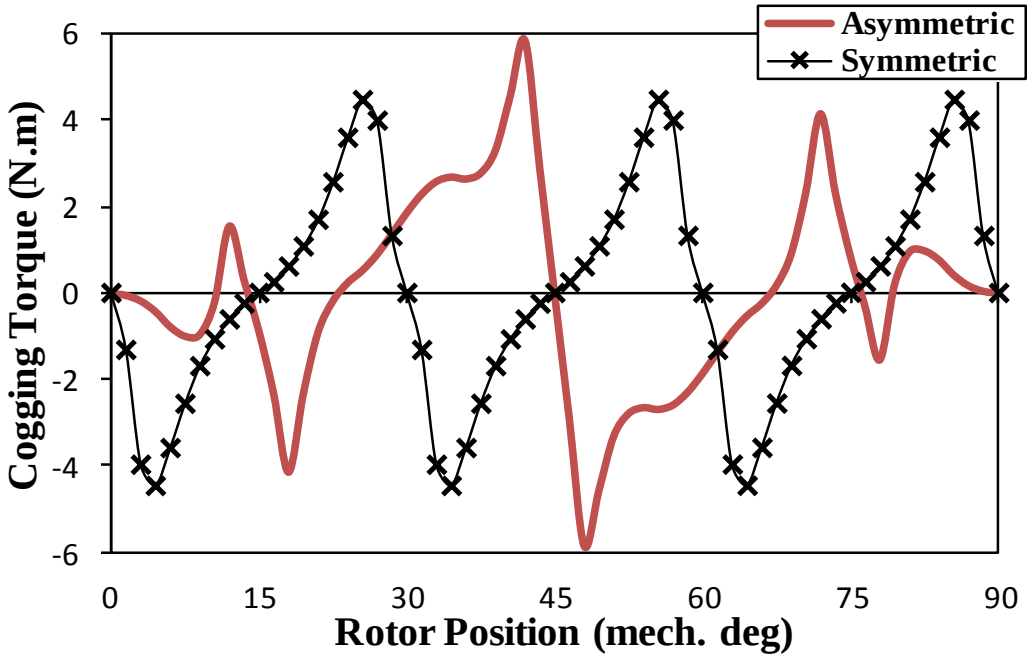

(a) Waveforms, at 34 A/mm^2 DC current density

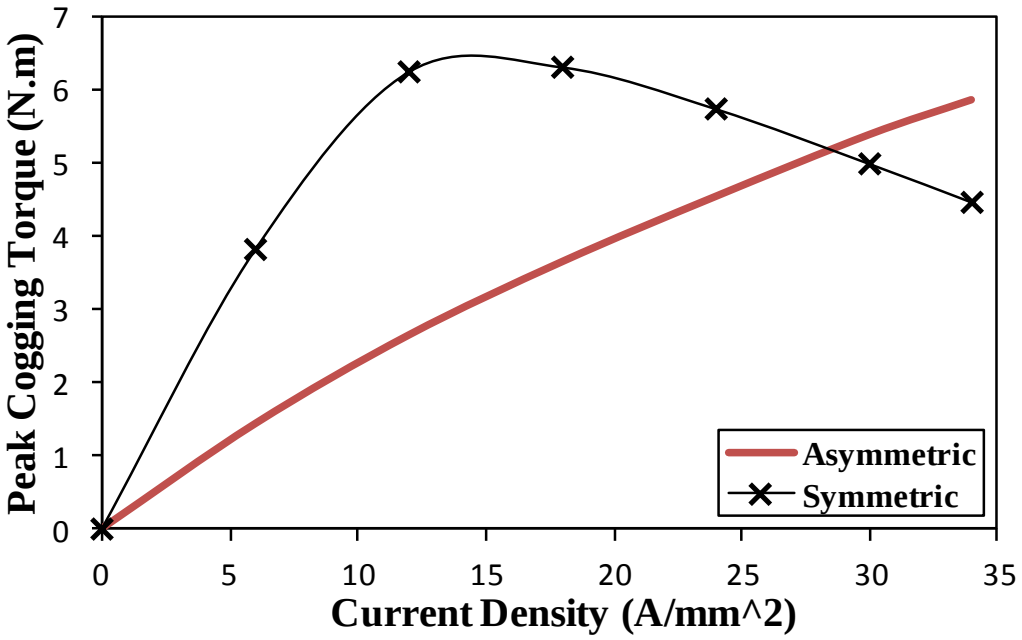

(b) Peak values at different DC current densities

Fig. 7.6 Comparison of cogging torque of 6 stator/4 rotor poles machines having different winding connections under DC bias excitation only.

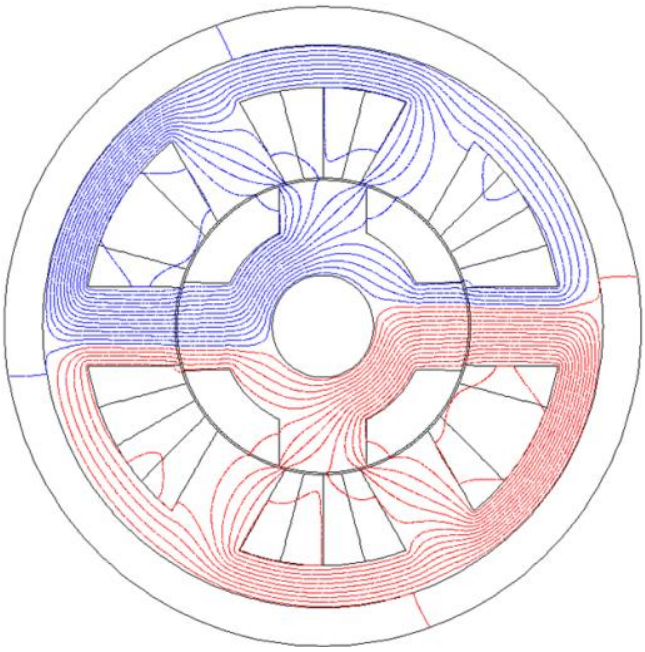

(a) Asymmetric winding connection at maximum flux linkage position for phase A

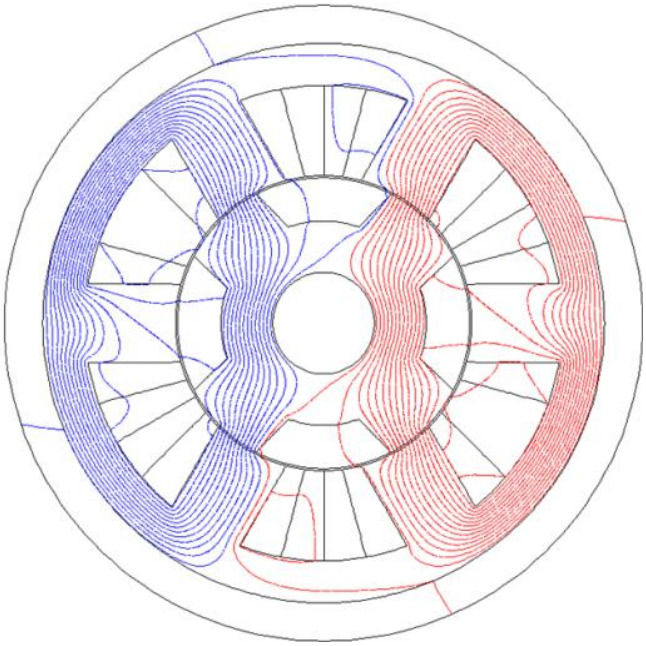

(b) Asymmetric winding connection at minimum flux linkage position for phase A

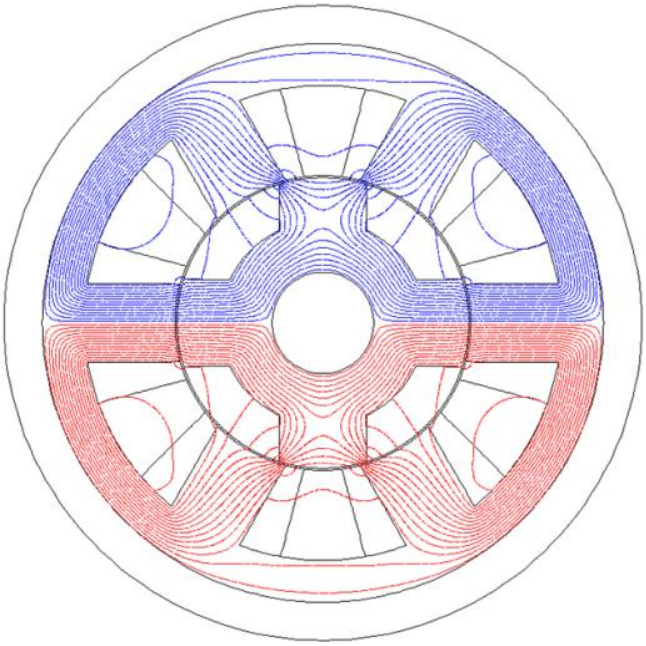

(c) Symmetric winding connection at maximum flux linkage position for phase A

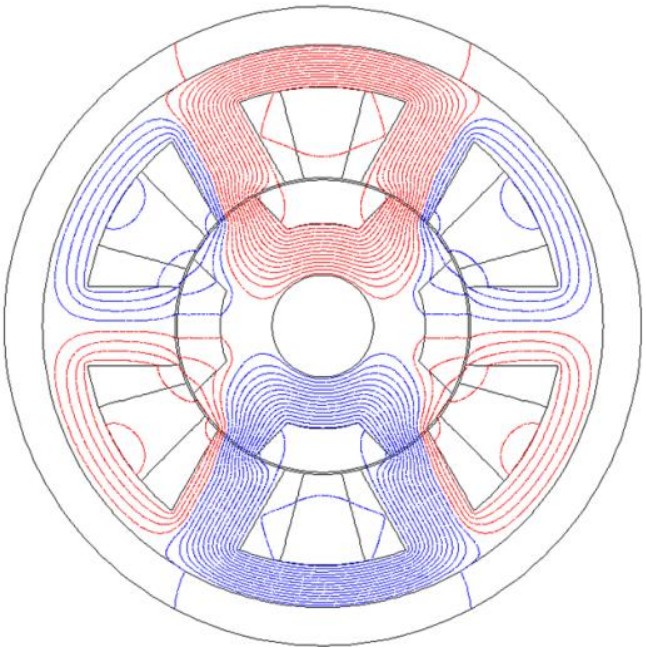

(d) Symmetric winding connection at minimum flux linkage position for phase

Fig. 7.7 Equal potential distributions of 6 stator/4 rotor poles machines having different winding connections and different rotor positions, at 12 A/mm^2 DC current density.

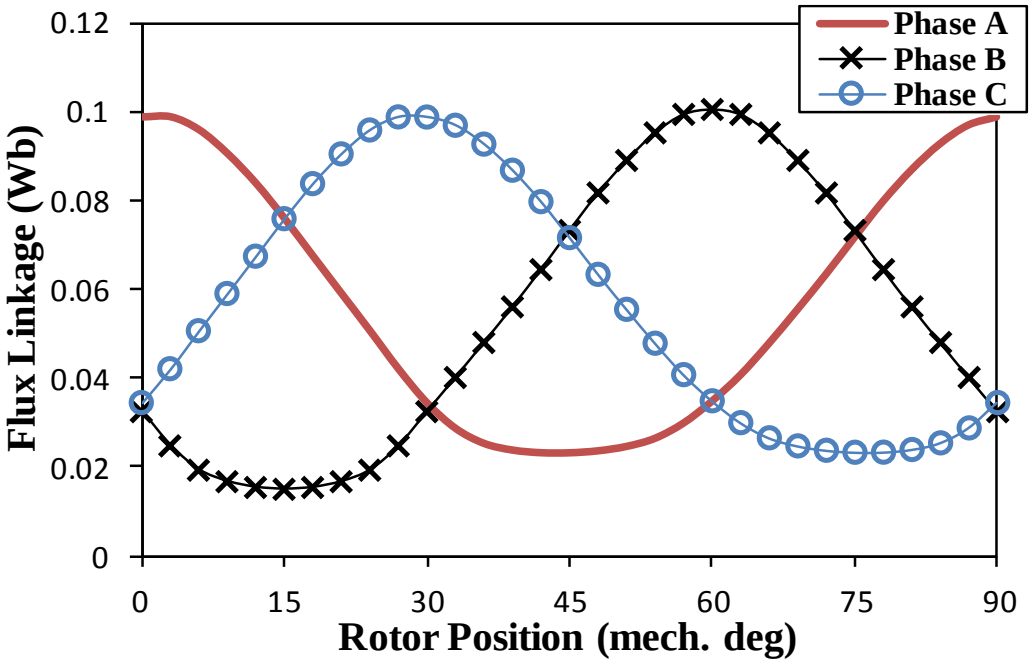

(a) Asymmetric winding connection

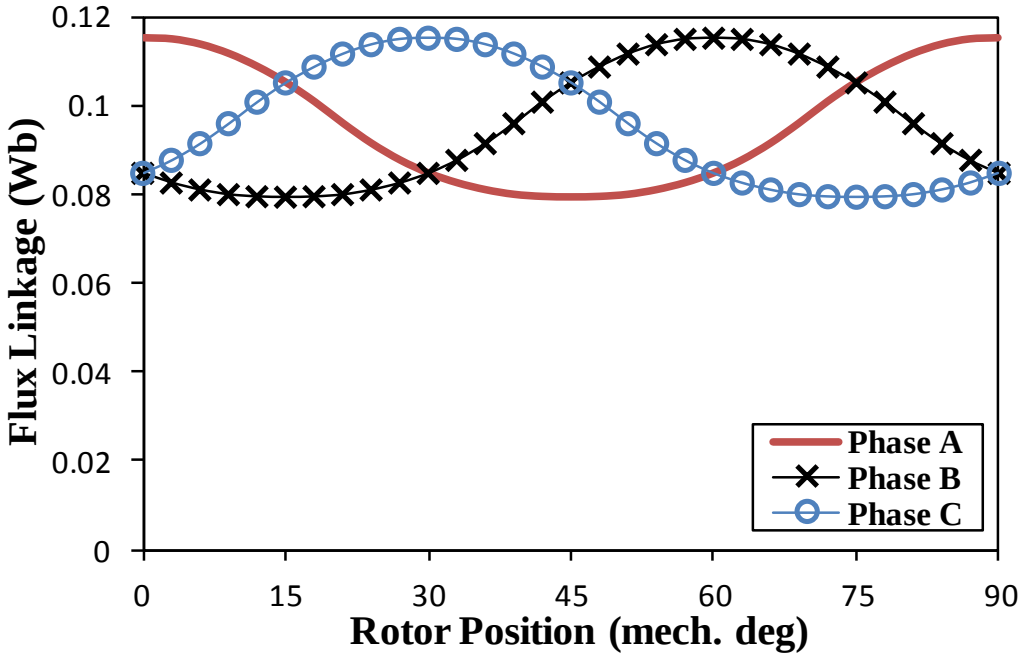

(b) Symmetric winding connection

Fig. 7.8 Comparison of three phase open-circuit flux linkage waveforms of 6 stator/4 rotor poles machines having different winding connections, at 34 A/mm^2 DC current density.

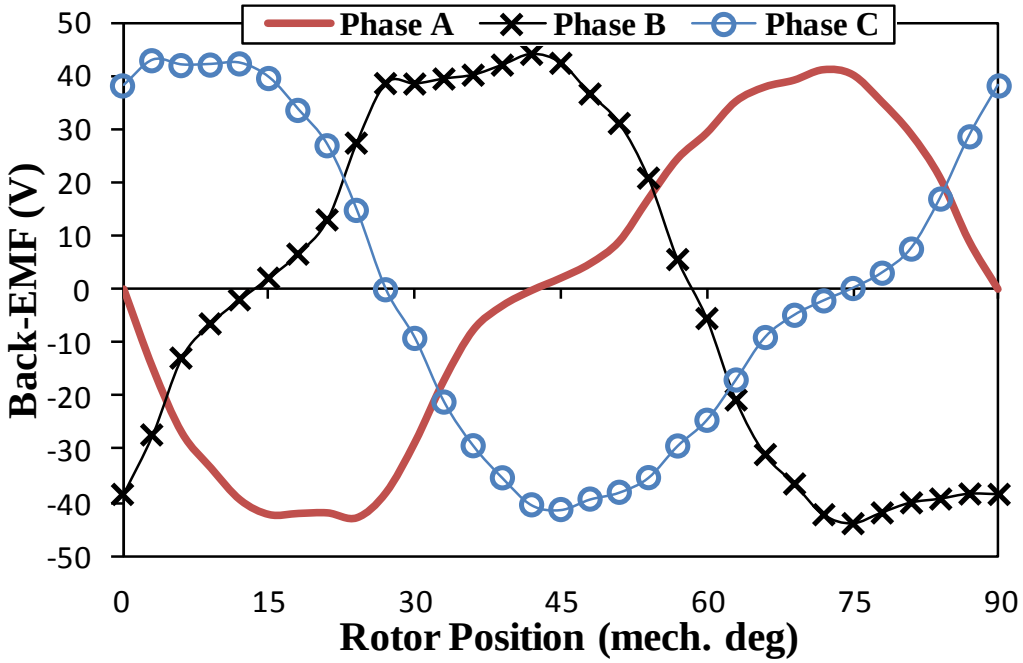

(a) Asymmetric winding connection

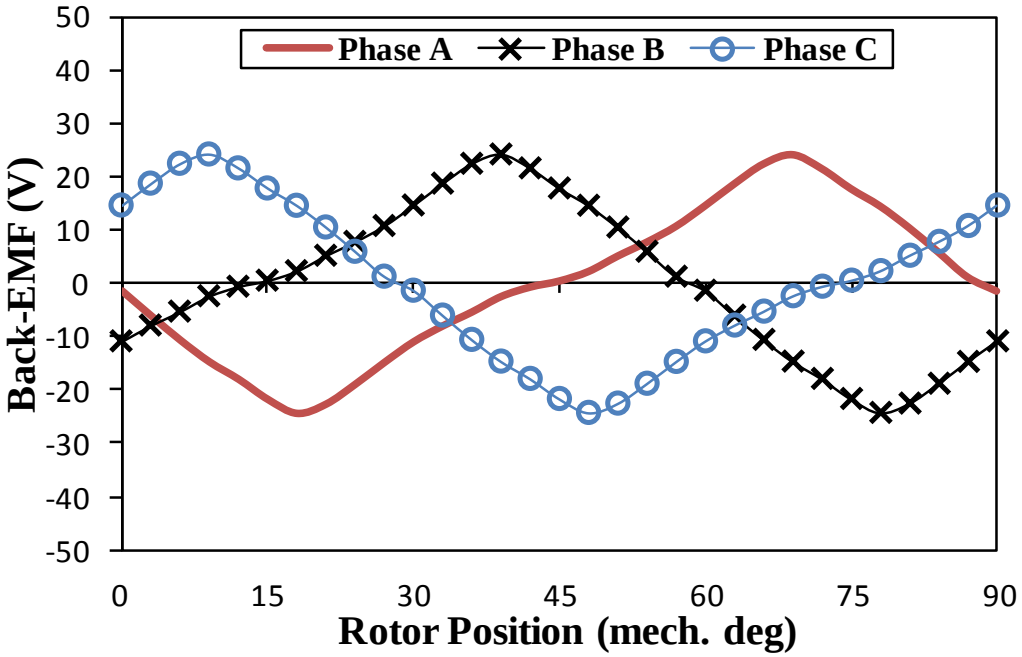

(b) Symmetric winding connection

Fig. 7.9 Comparison of three phase back-emf waveforms of 6 stator/4 rotor poles machines having different winding connections, at 34 A/mm^2 DC current density and 2500 rpm speed.

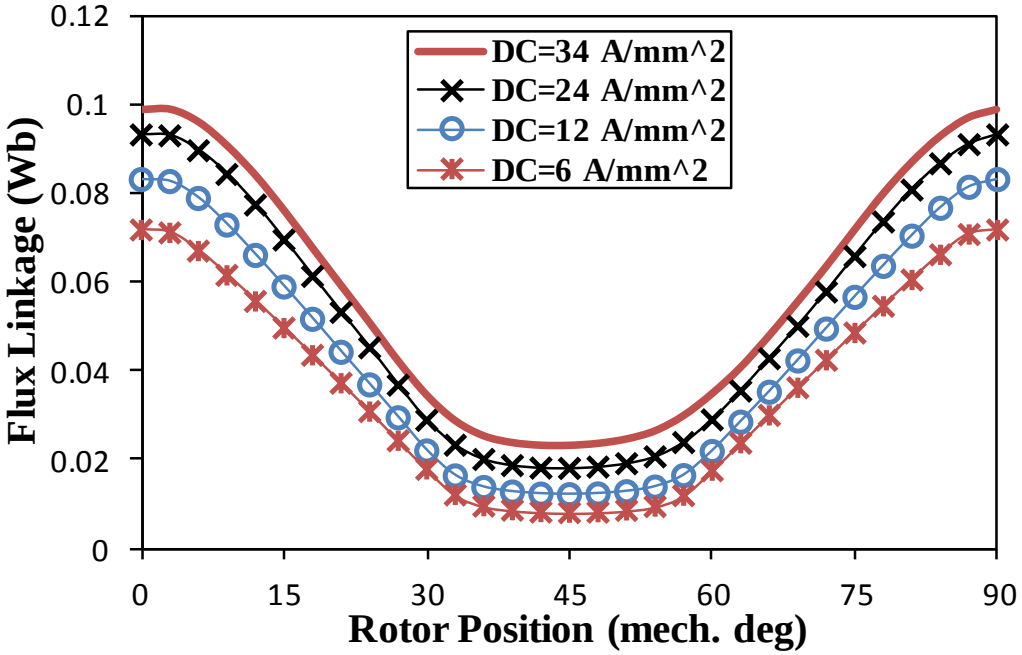

(a) Asymmetric winding connection

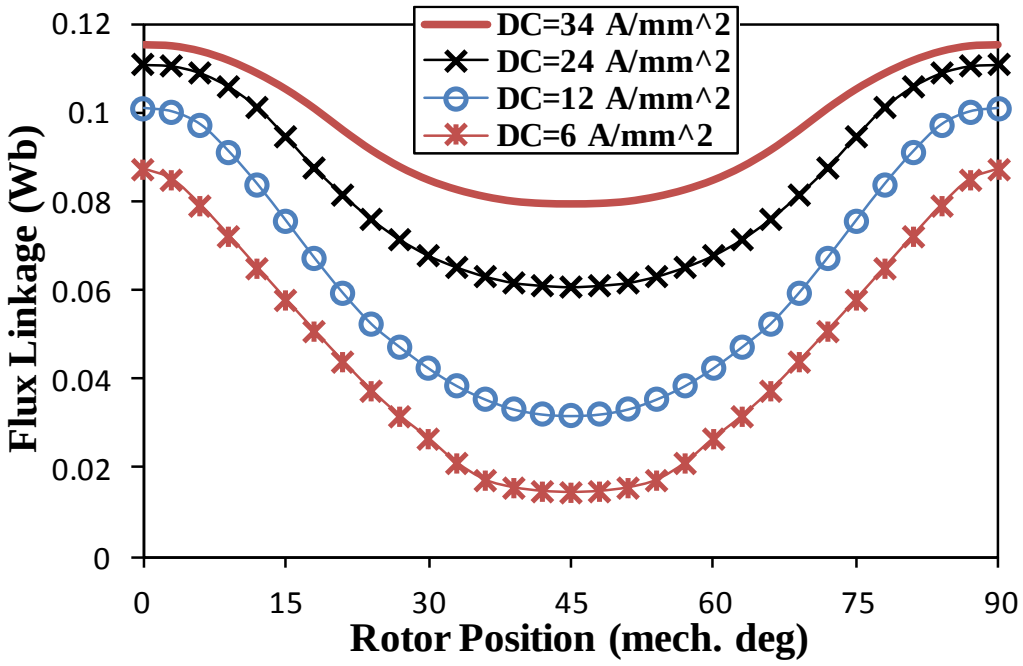

(b) Symmetric winding connection

Fig. 7.10 Comparison of open-circuit flux linkage waveforms of 6 stator/4 rotor poles machines having different winding connections for different DC current densities.

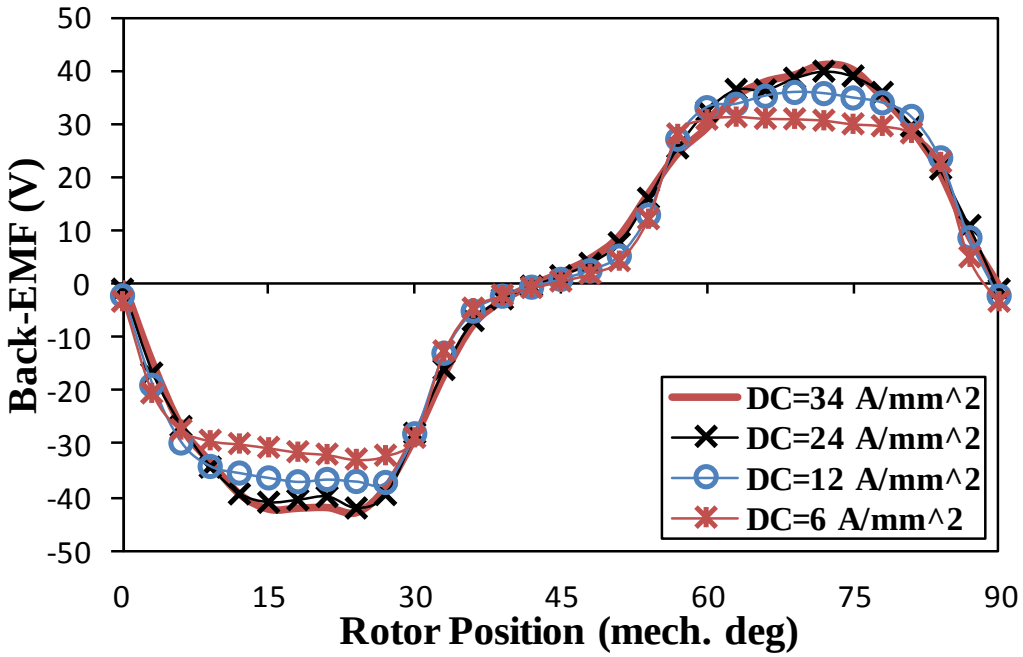

(a) Asymmetric winding connection

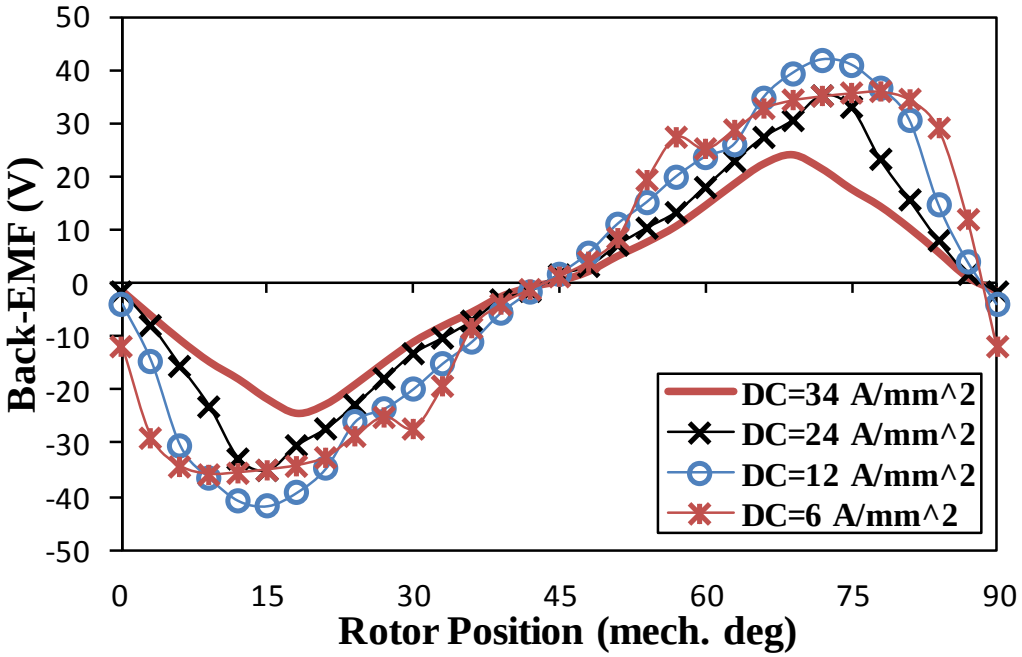

(b) Symmetric winding connection

Fig. 7.11 Comparison of back-emf waveforms of 6 stator/4 rotor poles machines having different winding connections under different DC current densities and 2500 rpm speed.

7.3.2. Load

7.3.2.1. Output Torque

As already illustrated, due to the DC excitation, voltages are induced in the AC coils, i.e. back-emfs. Therefore, the studied machine should generate output torque if the three phase windings are excited by three phase AC sinusoidal currents. In theory, similar to the switched flux PM machines, the maximum output torque should be achieved if these currents are injected in phase with the back-emf waveforms, i.e. $I_q=I_{Phase}$, $I_d=0$. In addition, initially both the AC and DC coils are assumed to have the same current density, i.e. $J_{DC}=J_{AC\ rms}$ However, the optimal injected current angle as well as the optimal ratio of AC to DC current densities will be further investigated. The AC coils of the studied machine are energized by the AC currents at 34 A_{rms}/mm^2 total current density. The obtained output torque waveforms for the both winding connections are compared in Fig. 7.12. It proves the ability of producing output torque when the machine is excited by AC sinusoidal bipolar with DC bias. In order to examine the machine torque capability under such excitation, its electromagnetic performance is to be compared with its counterparts of the conventional unipolar and AC

sinusoidal bipolar excitations in section 7.6. Comparing with the symmetric winding connection and under the same AC and DC current densities and zero AC current angle, the asymmetric winding connection results in a larger output torque, since its back-emf waveforms are larger, Fig. 7.9. However, the symmetric winding connection leads to lower torque ripple, because it has lower cogging torque and more uniform back-emf waveforms. Furthermore, in order to investigate the influence of magnetic circuit on the output torque capability and torque ripple of each winding connection, the output torque of the machine with both winding connections is calculated for different current densities. The average output torque and maximum torque ripple, i.e. peak to peak value, are compared in Fig. 7.13. Up to 12 A/mm^2 current density, the symmetric winding connection leads to relatively larger average output torque output. However, for larger current densities, the output torque increase of such winding connection starts to be saturated. Thus, the asymmetric winding connection exhibits larger average torque, Fig. 7.13(a). Such performance has been expected, since it is exactly the same as the back-emf behaviour of the two winding connections, as shown in Fig. 7.11. Furthermore, the symmetric winding connection results in significantly lower torque ripple at relatively larger current densities since the cogging torque becomes lower, Fig. 7.6, and back-emf is less distorted, Fig. 7.11.

Moreover, in order to determine the optimal current angle, the output torque of the analysed machine is calculated for different current angles, i.e. between -90 to +90 electrical degrees, and for different current densities. The average output torque against the current angle of the machines having two winding connections is given in Fig. 7.14. It shows that for all current densities the machine with the symmetric winding connection delivers its maximum output torque at 15 electrical degrees current angle. On the other hand, the optimal current angle is 0 degree when the machine has symmetric winding connection. In addition, Fig. 7.14 again shows that the influence of the magnetic saturation with asymmetric winding connection is relatively low comparing with the symmetric counterpart. As mentioned before, during the earlier investigations the AC and DC current densities are assumed to be equal, i.e. the AC/DC current density ratio is one. However, in the upcoming analyses the optimal ratio, which results in the maximum average output torque, will be determined for each winding connection. For this purpose, the average output torque against the AC/DC current density ratio is calculated for both connections at 34 A/mm^2 average current density and the results are compared in Fig. 7.15(a). It shows that the optimal ratio is one when the machine has the asymmetric winding connection. However, such ratio is two for the symmetric winding connection, which results in a larger maximum average output torque comparing with the

asymmetric winding connection. On the other hand, comparing with the asymmetric winding connection the symmetric winding connection results in significantly lower torque ripple, especially when the ratio is lower than two. However, it becomes the same when the ratio is larger, as illustrated in Fig. 7.15(b). The exhibited behavior of the output torque is due to the variations of the back-emf under different winding connections and different current densities. The asymmetric winding connection results in a larger back-emf when the DC current density is larger, but the increasing is saturated when the current density is larger than 24 A/mm^2, as shown in Fig. 7.11(a). Thus, when the AC/DC ratio is smaller than one, i.e. DC current density is larger than 34 A/mm^2, the back-emf slightly increases. However, in this case the AC current density is lower, thus the output torque will be also lower. On the other hand, when the ratio is larger than one, the back-emf becomes lower. Although the AC current density is larger, but the average output torque actually becomes smaller. In addition, the increase of the AC current density contributes more to the torque ripple, as shown in Fig. 7.16(a). However, the back-emf of the machine has symmetric winding connection is larger when the DC current density is relativity large and it is much smaller when such current density is significantly large, as shown in Fig. 7.11(b). Therefore, when the AC/DC current density ratio is relatively small, e.g. 0.6, the DC current density is significantly larger, thus the back-emf is small and in addition the AC current density is also small. Therefore, the output torque is very small, as shown in Fig. 7.16(b). When the AC/DC current density ratio gradually increases, the back-emf becomes larger since the DC current density becomes relatively large. In addition, the AC current density becomes larger, thus both the average torque and torque ripple become larger, as shown in Fig. 7.16(b). Furthermore, when the ratio is relatively larger, e.g. larger than two, the back-emf starts decreasing since the DC current density is relatively low. Consequently, the average torque becomes lower, while the torque ripple becomes significantly large since the AC current density is also very large, as shown in Fig. 7.15 and Fig. 7.16(b). Further analyses, including the machine line voltage, will be carried out in the next section and then the most appropriate winding connection can be determined in terms of the torque- and power-speed characteristics.

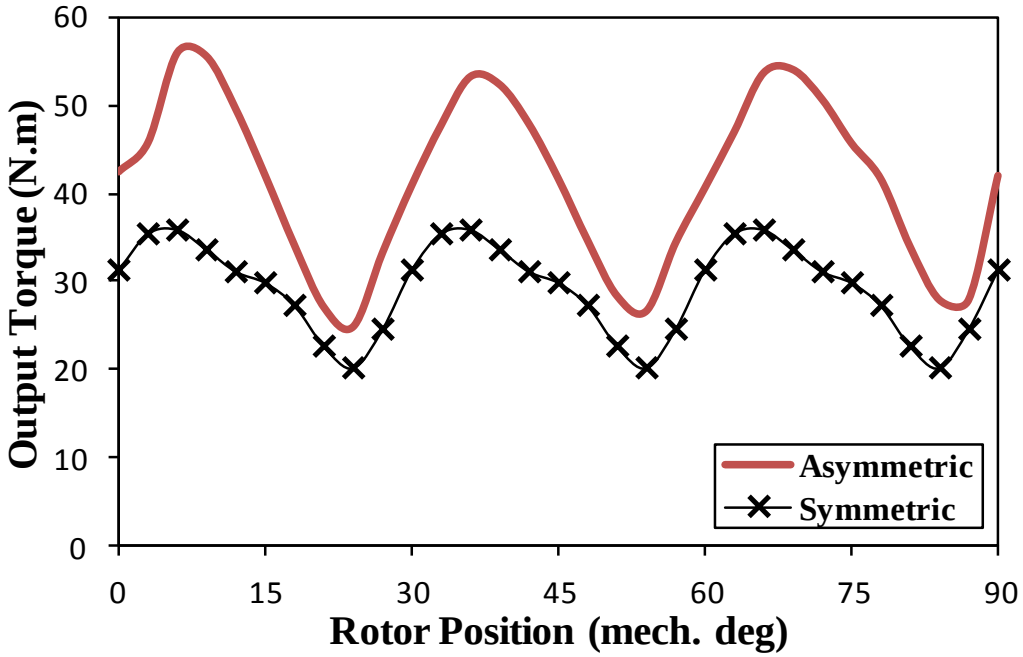

Fig. 7.12 Comparison of output torque waveforms of 6 stator/4 rotor poles machines having different winding connections, at 34 A/mm^2 average current density and J_{DC}=J_{AC} rms.

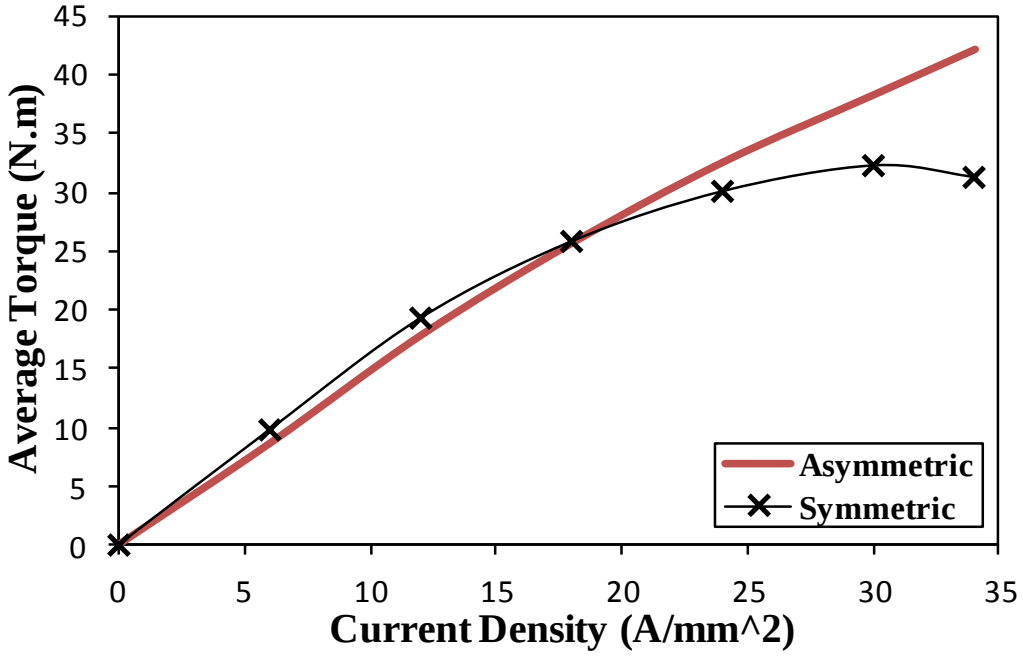

(a) Average output torque

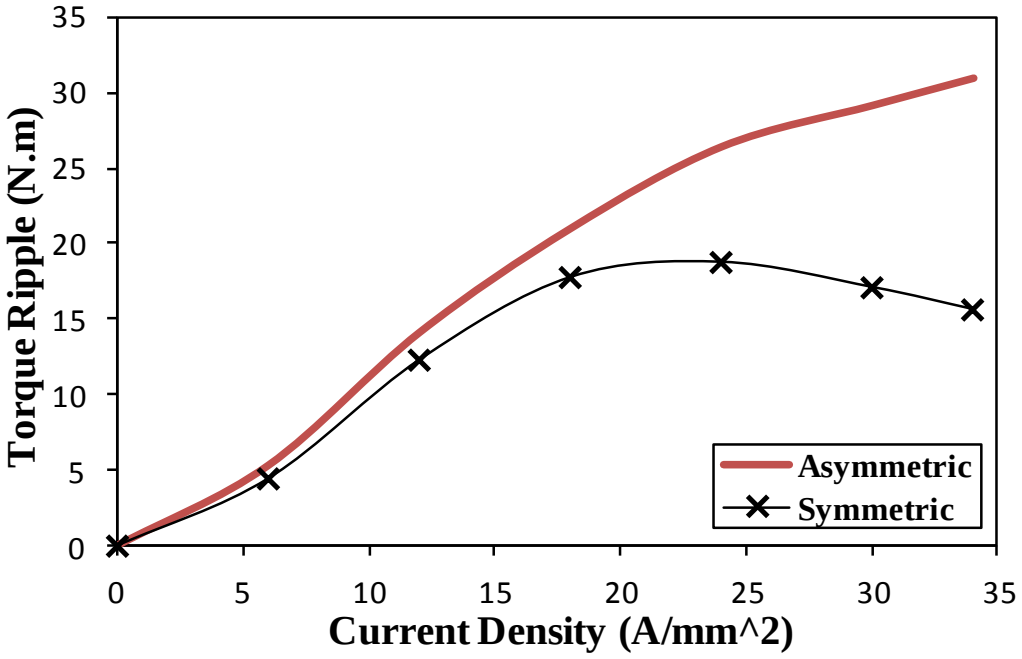

(b) Maximum torque ripple

Fig. 7.13 Comparison of average output torque and torque ripple of 6 stator/4 rotor poles machines having different winding connections for different current densities, J_{DC}=J_{AC} rms.

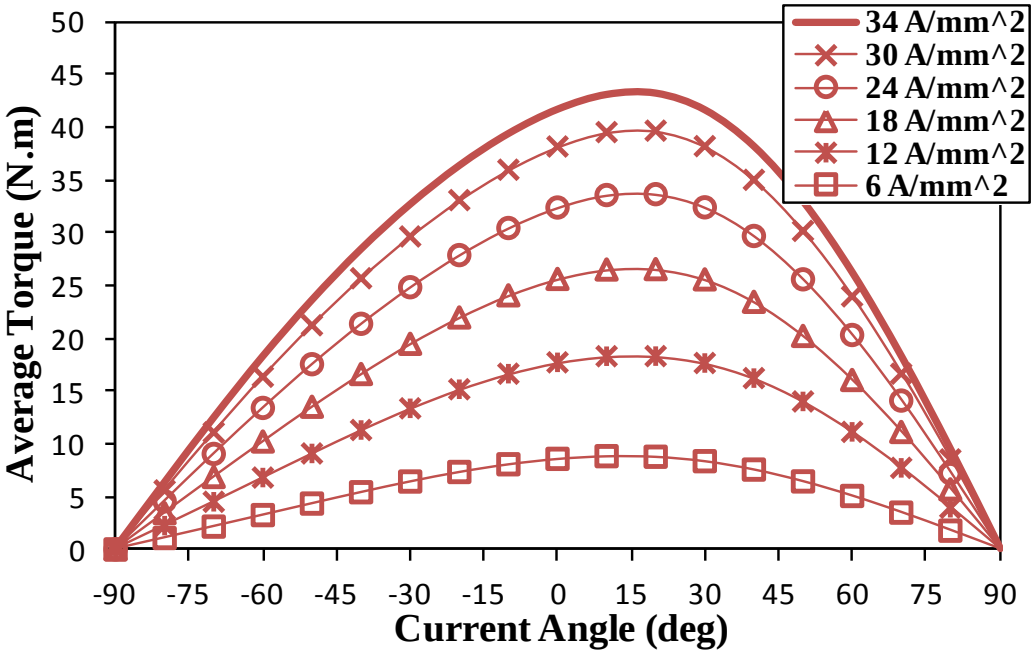

(a) Asymmetric winding connection

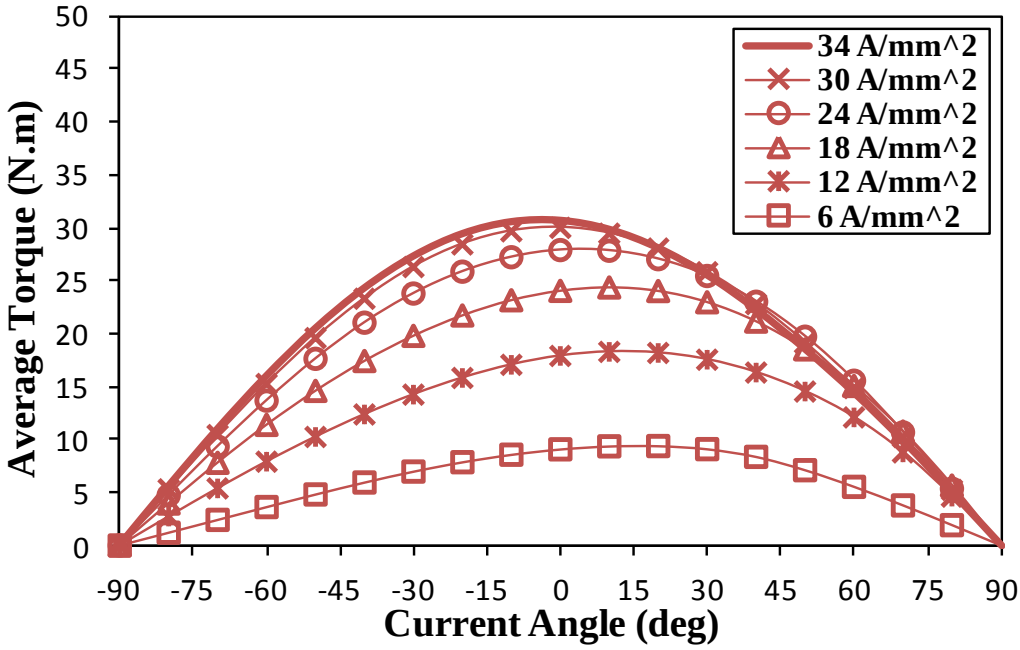

(b) Symmetric winding connection

Fig. 7.14 Comparison of average output torque against current angle of 6 stator/4 rotor poles machines having different connections for different current densities, at $J_{DC}=J_{AC}$ rms.

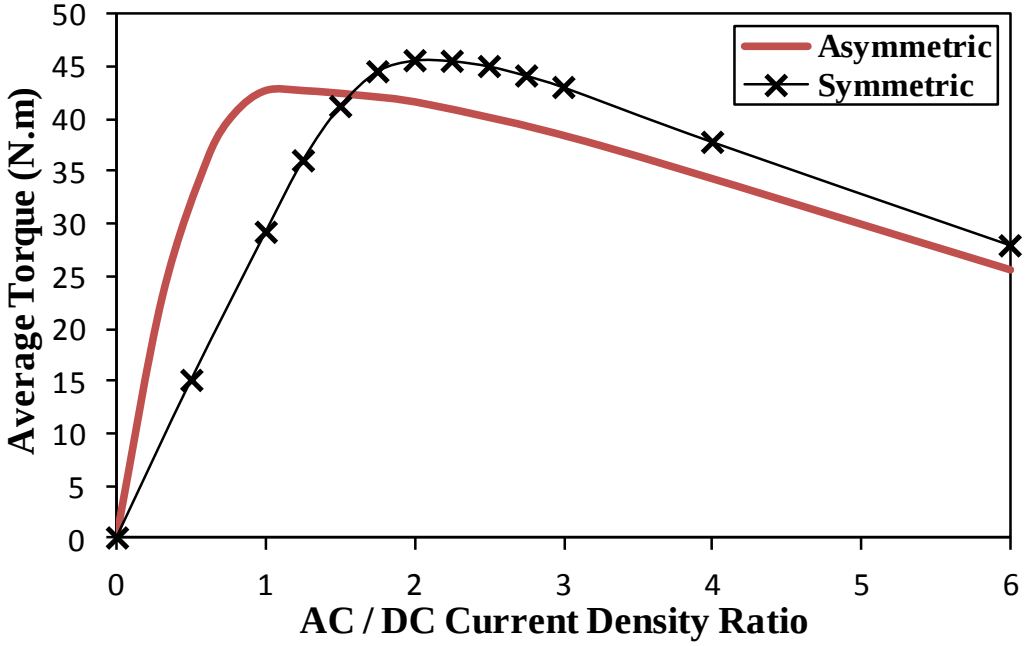

(a) Average output torque

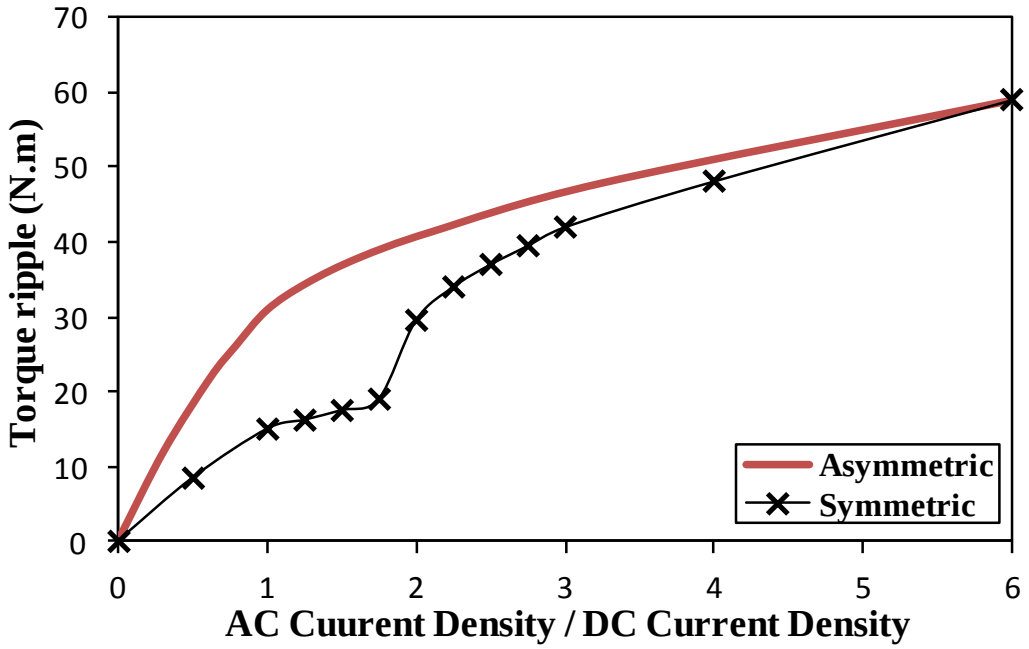

(b) Torque ripple

Fig. 7.15 Comparison of average output torque and torque ripple against AC/DC current density ratio of 6 stator/4 rotor poles machines having different winding connections, at 34 A/mm^2 average current density.

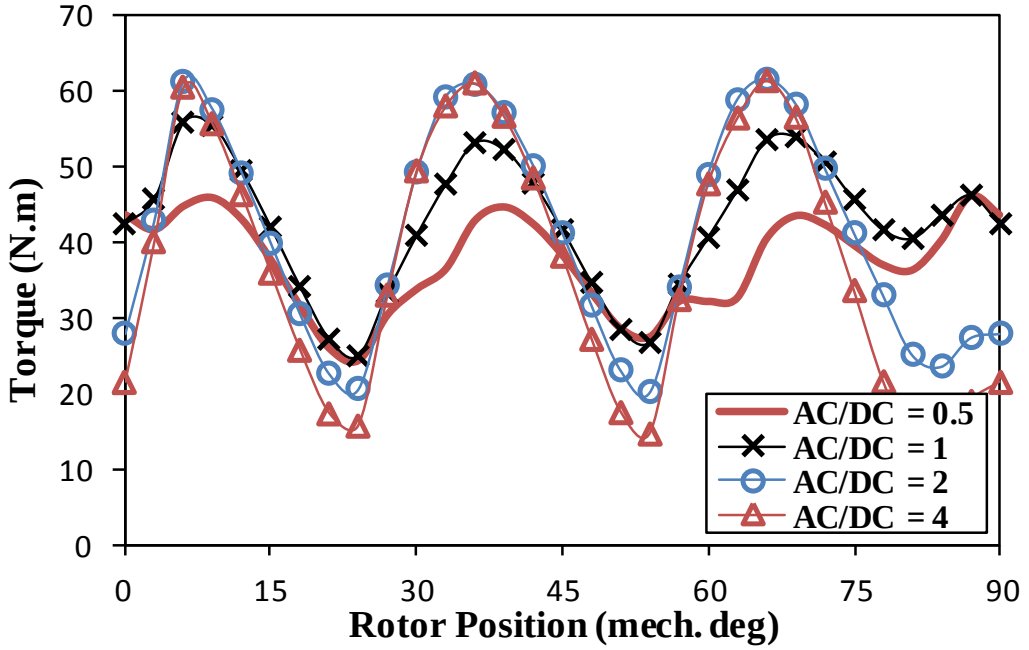

(a) Asymmetric winding connection

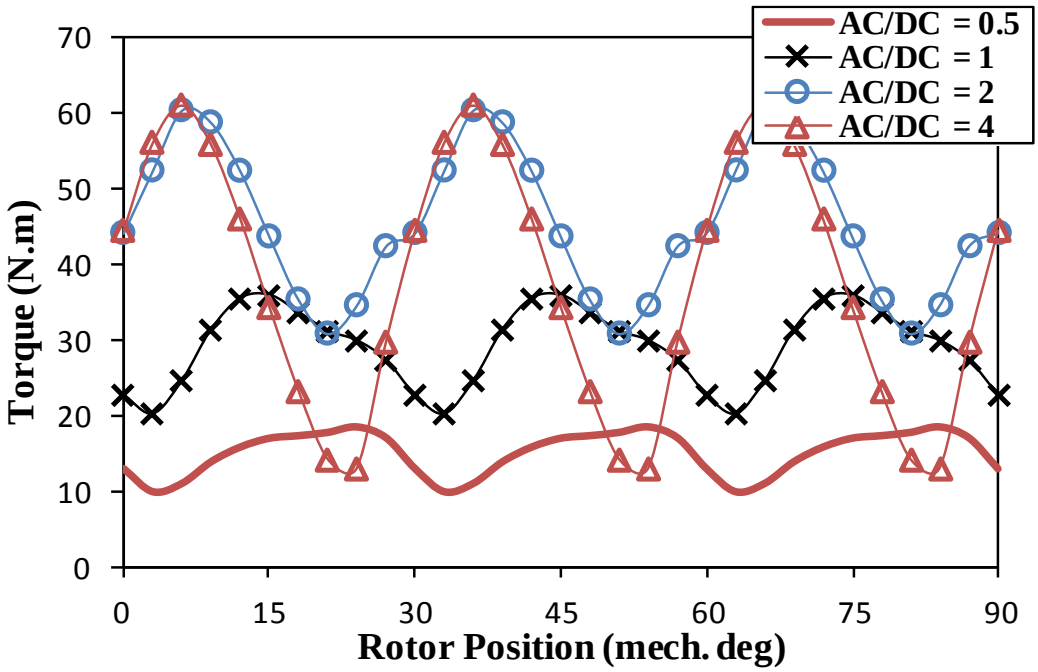

(b) Symmetric winding connection

Fig. 7.16 Comparison of output torque waveforms of 6 stator/4 rotor poles machines having different winding connections for different AC/DC current density ratios, at 34 A/mm^2 average current density.

7.3.2.2. Line Voltage

During the dynamic analyses of the machine performance, e.g. torque- and power-speed characteristics, the line voltage of the machine is an important issue since the maximum possible base speed, i.e. the constant torque region, as well as the flux weakening capability are directly determined according to such voltage. In this section, the line voltage are compared for the two winding connections to determine the most suitable winding connection for subsequent use in the prediction of the torque- and power-speed characteristics, which will be carried out in section 7.4.

The line voltage can be calculated according to (6.1) and (6.2). Initially, the investigations will be carried out for the same DC and AC current densities, but further analyses will be performed when the AC/DC ratio is not unity. The variation of the maximum line voltage against current angle under both winding connections are calculated for different total current densities while the DC and AC current densities are equal, the results are presented in Fig. 7.17. It should be mentioned that the current angle is varied in the range between 0

and 90 electrical degrees since in this range the d-axis current becomes negative, thus it is the flux weakening operation region. In general, larger AC current angle should weaken the machine line voltage. However, the influence of such angle on the line voltage of the machine with the asymmetric winding connection is relatively small when the current density is relatively larger, as shown in Fig. 7.17(a). This is because the magnetic saturation due to such connection is significantly larger even when the current angle is 90 degree, as illustrated in Fig. 7.18(a) and (b). In turn, this leads to larger non-uniformity and distortion in the phase voltage waveform, as shown in Fig. 7.19(a) and (b). This results in larger voltage spike in the line voltage waveform, as illustrated in Fig. 7.21(a). In order to match the voltage requirement of the machine the voltage limitation should be larger than the maximum line voltage value, Fig. 7.21. On the other hand, larger current angle leads to a relatively larger reduction in the line voltage when the symmetric winding connection is employed, Fig. 7.17(a) and Fig. 7.21(c). This is because the symmetrical distribution of phase windings results in uniform phase voltage waveforms, as shown in Fig. 7.20, thus they have no voltage spikes at larger current angle. Consequently, the line voltage of the machine with symmetric winding connection is relatively more uniform and lower when the current angle increases. Therefore, it can be concluded that the weak influence of the AC current angle on the line voltage of the machine with asymmetric winding connection at relatively larger current densities is due to the asymmetry distribution of phase windings and high magnetic saturation.

In order to further clarify this phenomenon, the phase and line voltage waveforms of the machine with asymmetric winding connection are calculated at 6 A/mm^2 current density and 0 and 90 electrical degree AC current angle, the results are given in Fig. 7.19(c), Fig. 7.19(d), and Fig. 7.21(b), respectively. The phase voltage waveforms, Fig. 7.19(c), are relatively more uniform and less distorted, since the magnetic saturation level is relatively small, as shown in Fig. 7.18(c). Furthermore, when the AC current angle increases, i.e. 90 degree, the magnetic saturation becomes even lower, Fig. 7.18(d). Consequently, the phase voltage waveforms are more similar, Fig. 7.19(d). Thus, the line voltage waveform at larger current angle is lower than its counterpart and 0 current angle, as confirmed in Fig. 7.21(b). Thus, the increase of the AC current angle will decrease the line voltage at relatively small current angle as expected. This confirms that the unexpected behavior at relatively larger current angle is due to the significant magnetic saturation as well as the non-uniformity of the phase winding connected since the line voltage of the machine with symmetric winding connection decreases when the current angle increases even at significant current densities,

as shown in Fig. 7.17(b). However, on the other hand, the line voltage of symmetric winding connection is larger when the current density is relatively larger, but it is lower when the current density is very large. This behavior is the same as the back-emf-current density variation, Fig. 7.11(b), which has been explained in section 7.3.1. Furthermore, according to Fig. 7.17, it can be concluded that comparing with the asymmetric winding connection, the machine line voltage due to the symmetric winding connection is significantly lower and influence of the AC current angle is larger.

In addition, as shown in the previous section, the machine with symmetric winding connection produces its maximum average output torque when the AC/DC current density ratio is 2. Such torque is about 7% larger than its counterpart of the machine with asymmetric winding connection, as illustrated in Fig. 7.14(a). However, at such ratio, the machine line voltage becomes larger than its counterpart due to the asymmetric winding connection, as shown in Fig. 7.22. This is because the larger AC current results in larger voltage distortion and spikes, as shown in Fig. 7.23. On the other hand, when the AC/DC ratio is 1.75, the machine with symmetric winding connection generates nearly the same maximum average output torque and significantly lower torque ripple, Fig. 7.24. In addition, the machine line voltage at such ratio is lower, as shown in Fig. 7.22 since the AC current becomes relativity lower, thus the voltage spike in the line voltage waveform is also lower, Fig. 7.23.

According to the previous discussions, it can be concluded that the symmetric winding connection is the more appropriate option to be employed when the SynR machines are operated under the AC sinusoidal bipolar with DC bias excitation, especially when wide flux weakening operation is required since the larger average output torque can be obtained while the torque ripple and line voltage are significantly lower. Therefore, such connection will be utilized during the investigation of the torque- and power-speed characteristics in section 7.4.

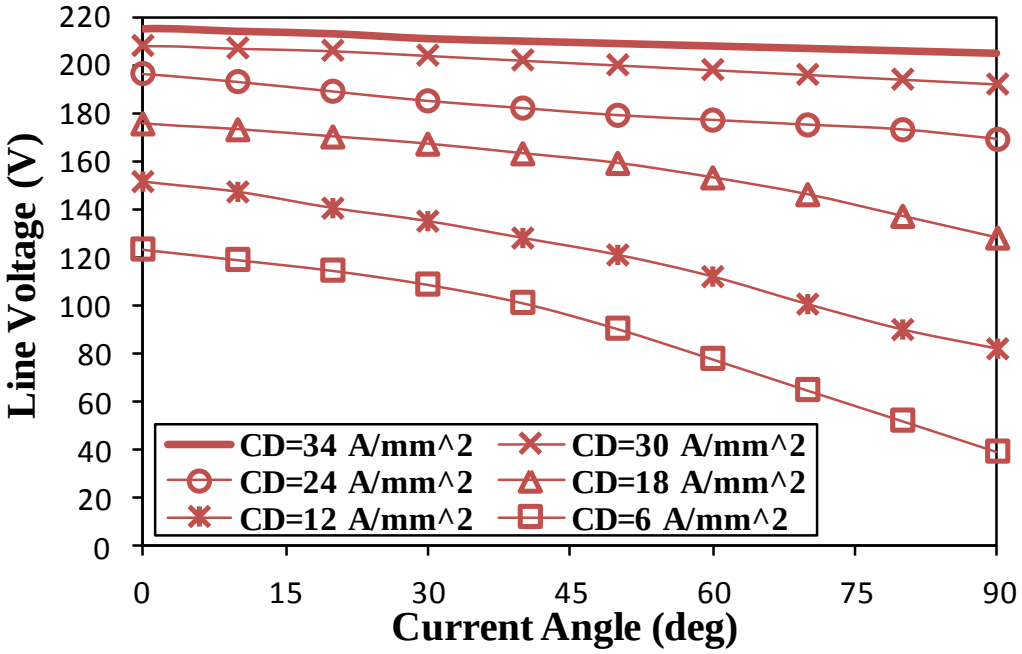

(a) Asymmetric winding connection

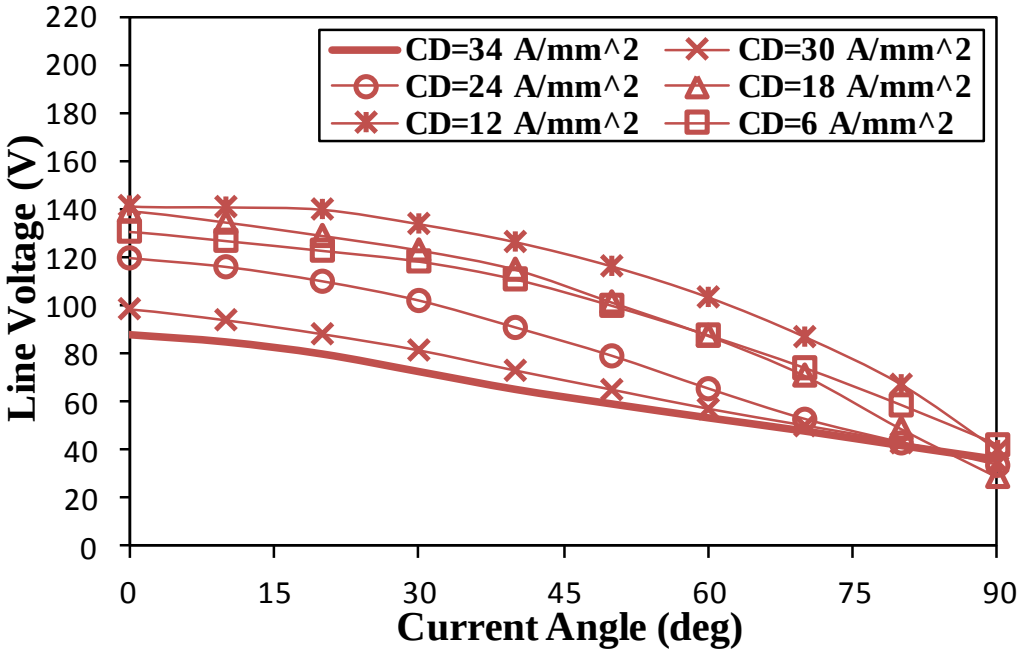

(b) Symmetric winding connection

Fig. 7.17 Comparison of maximum line voltage against current angle of 6 stator/4 rotor poles machines having different winding connections for different total current densities, at J_{DC}=J_{AC} rms and 2500 rpm speed.

(I) Asymmetric winding connection (II) Symmetric winding connection

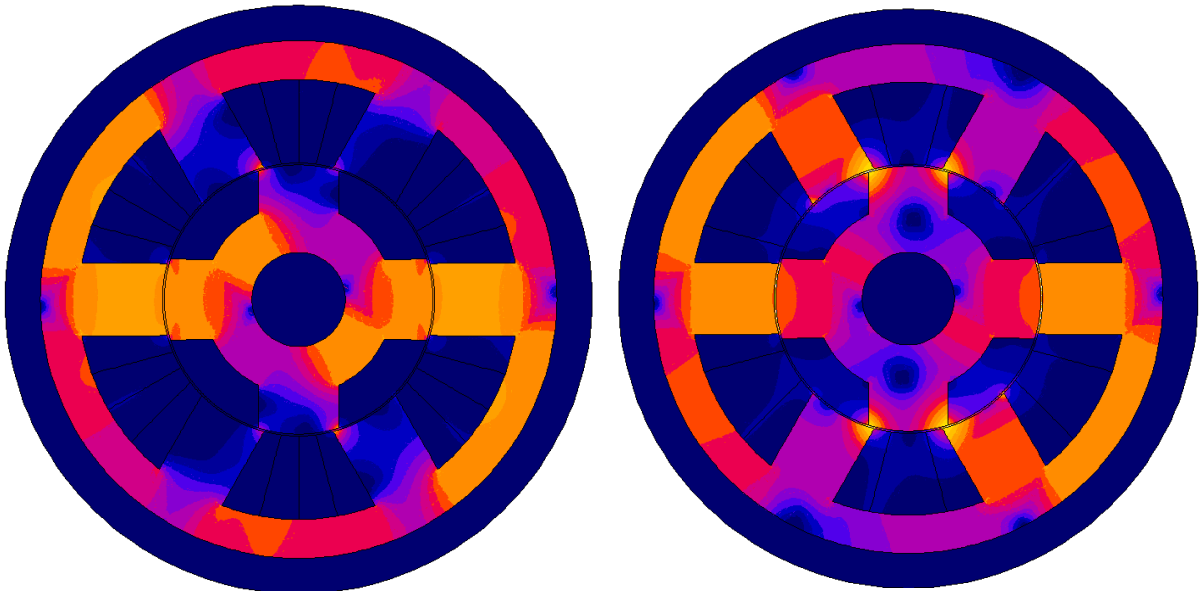

(a) 34 A/mm^2 average current density and 0 electrical degree AC current angle

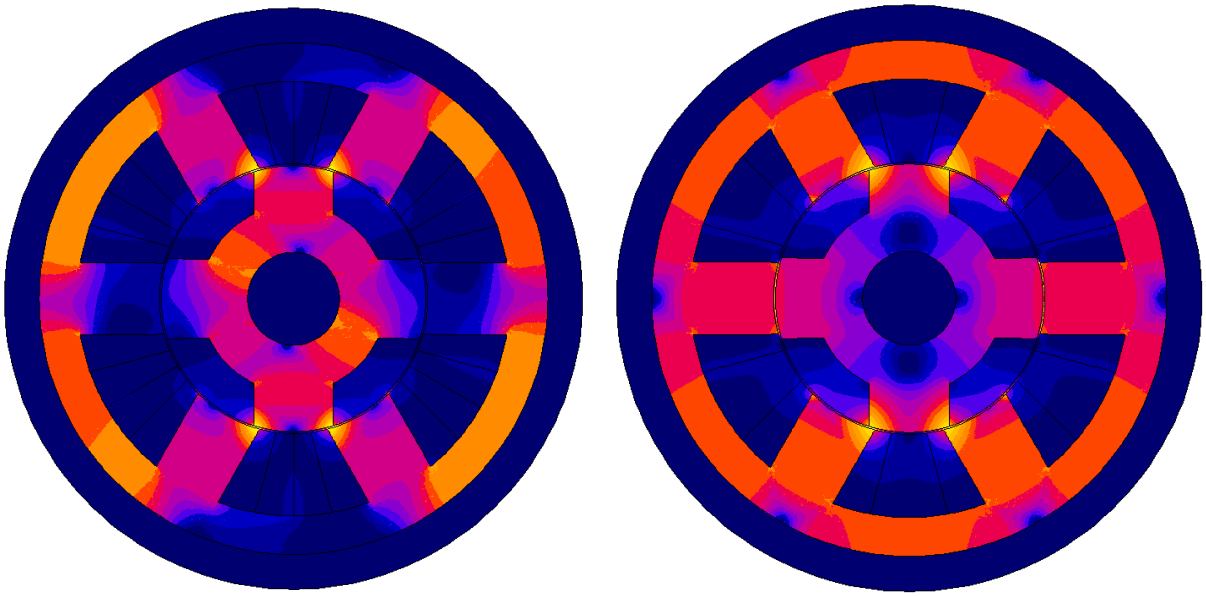

(b) 34 A/mm^2 average current density and 90 electrical degree AC current angle

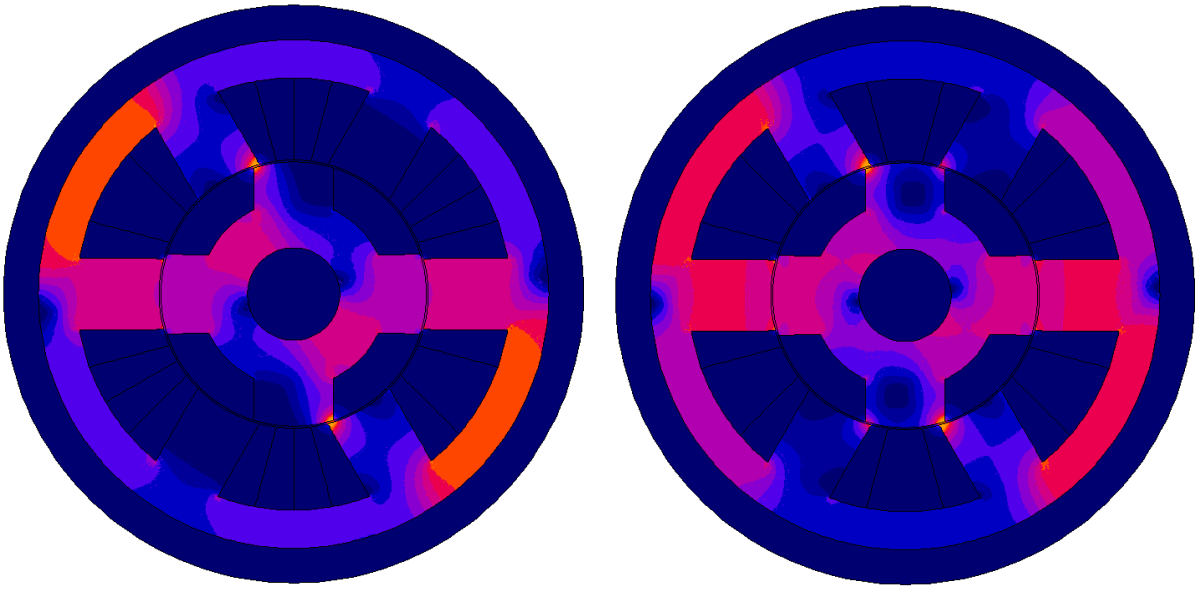

(c) 6 A/mm^2 average current density and 0 electrical degree AC current angle

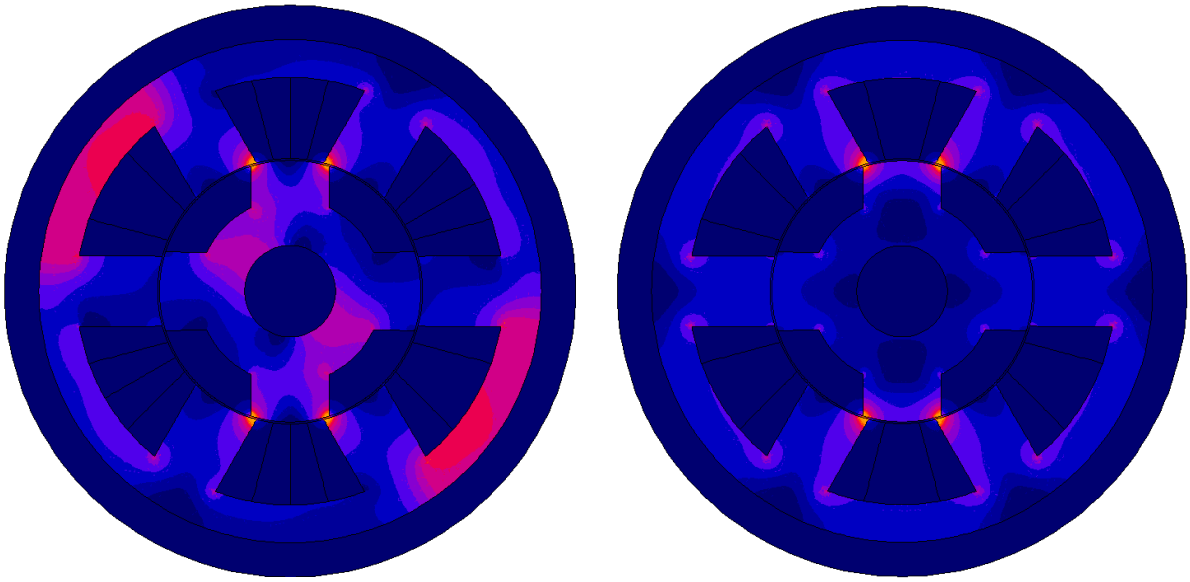

(d) 6 A/mm^2 average current density and 90 electrical degree AC current angle

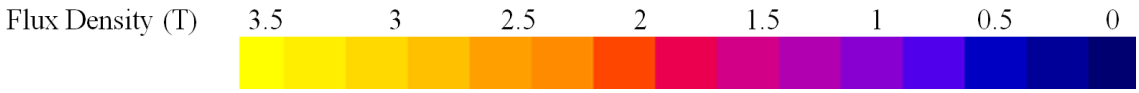

(e) Flux density scale (T)

Fig. 7.18 Flux density distributions of 6 stator/4 rotor poles machine having asymmetric and symmetric winding connections for different average current densities and current angles.

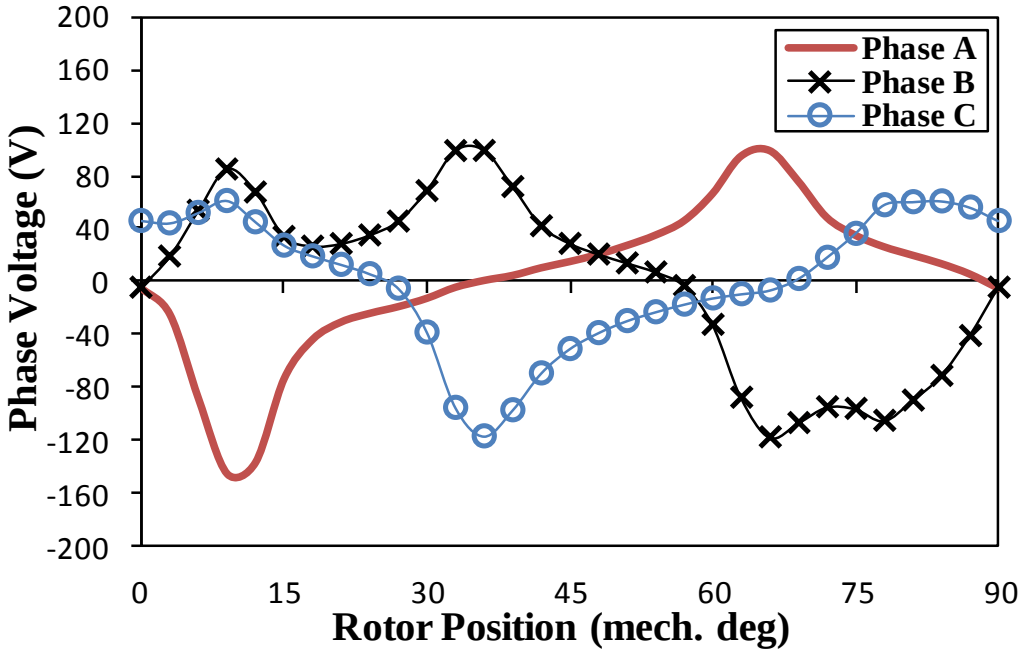

(a) 34 A/mm^2 average current density and 0 electrical degree AC current angle

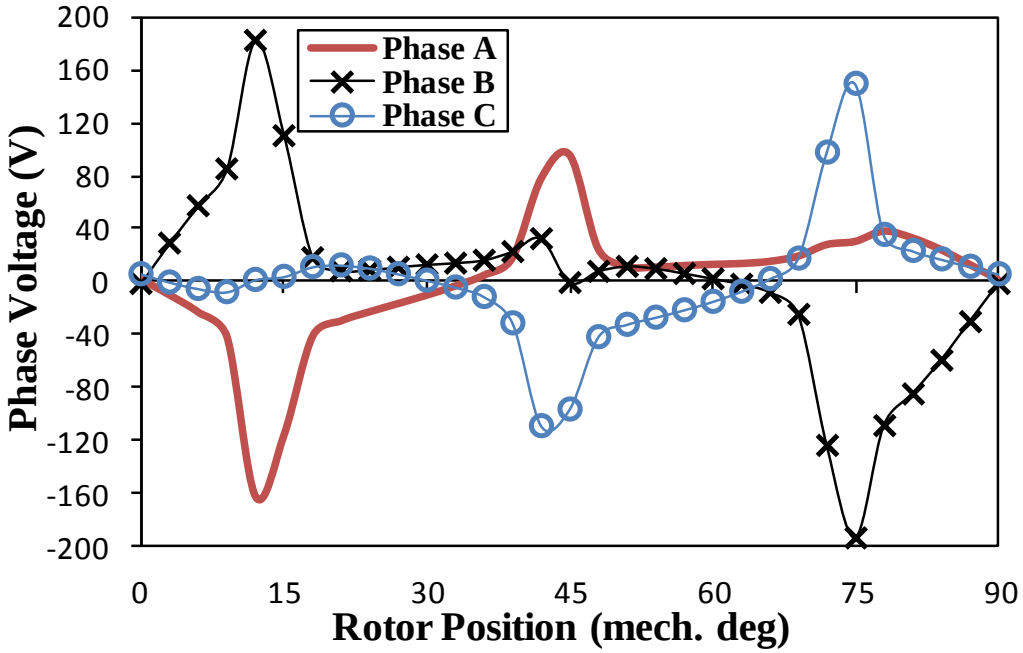

(b) 34 A/mm^2 average current density and 90 electrical degree AC current angle

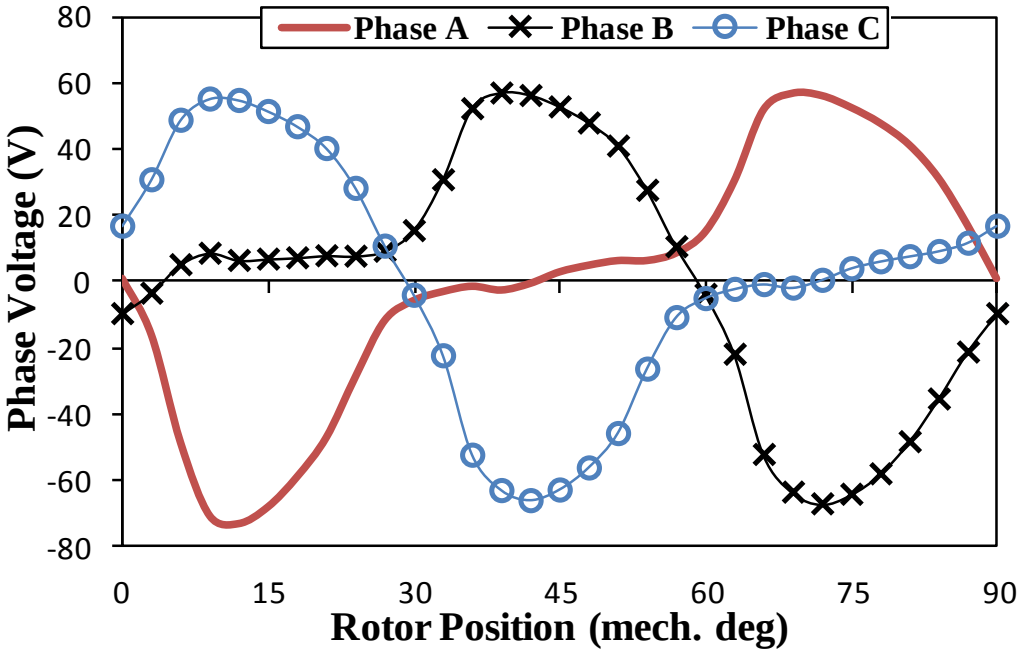

(c) 6 A/mm^2 average current density and 0 electrical degree AC current angle

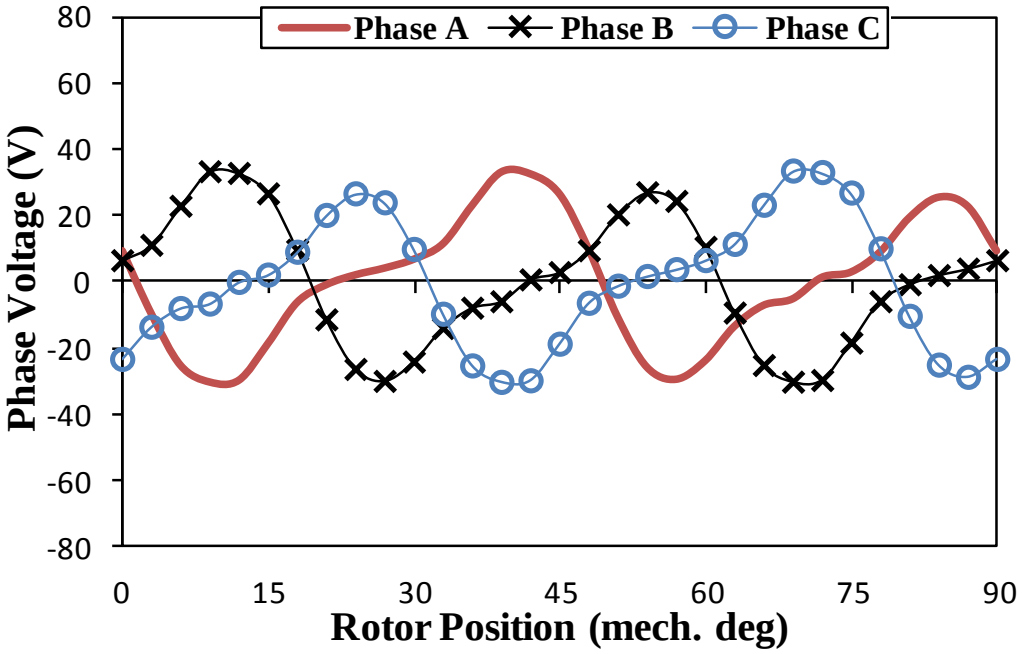

(d) 6 A/mm^2 average current density and 90 electrical degree AC current angle

Fig. 7.19 Comparison of phase voltage waveforms of 6 stator/4 rotor poles machine having asymmetric winding connection for different average current densities and current angles, at 2500 rpm.

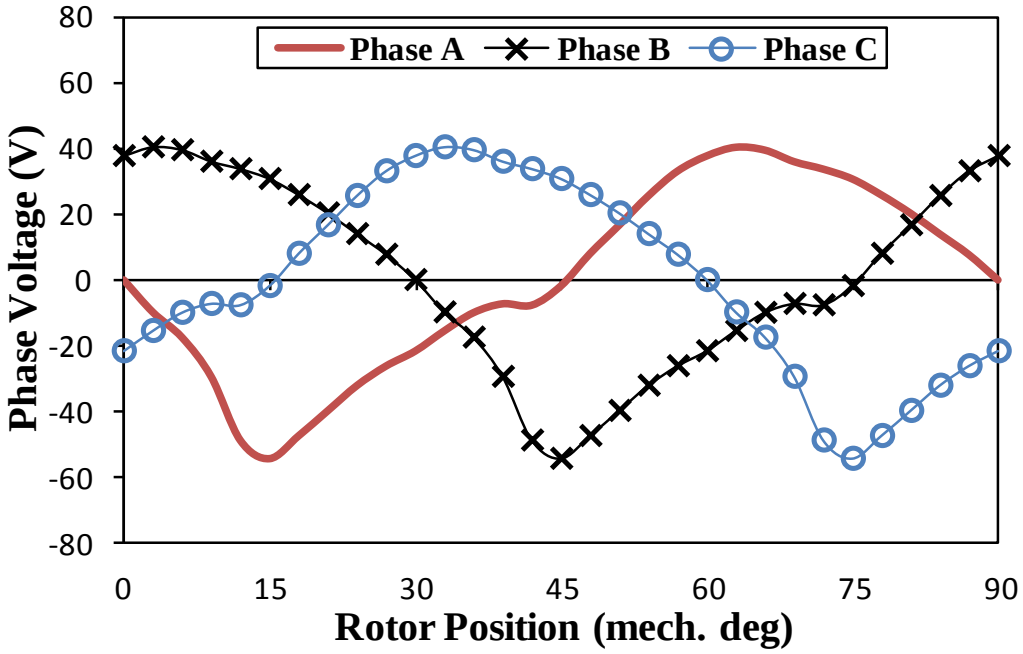

(a) 34 A/mm^2 average current density and 0 electrical degree AC current angle

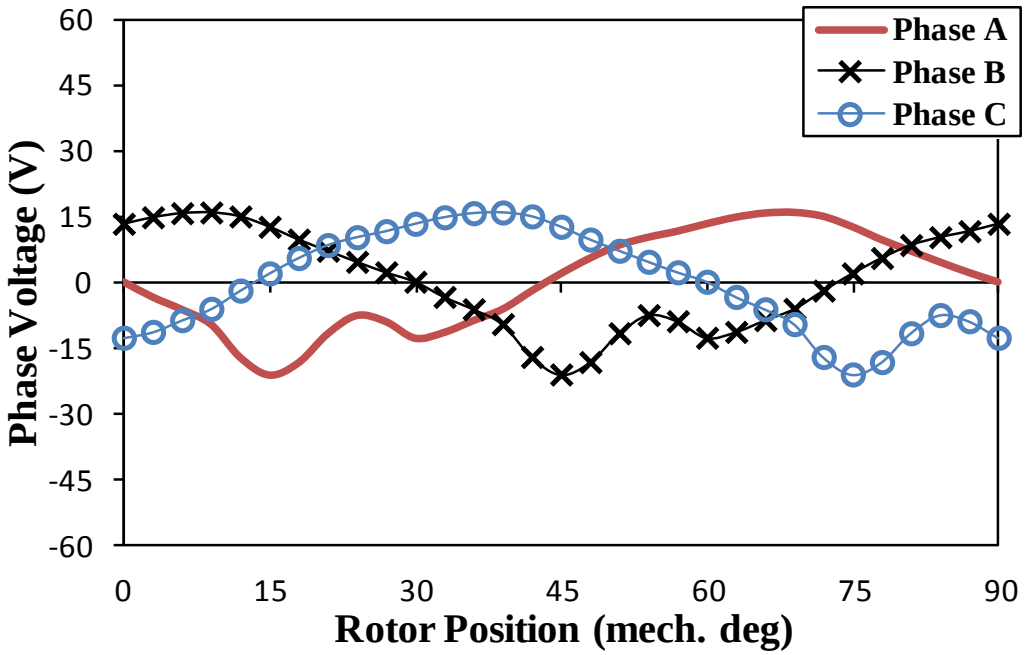

(b) 34 A/mm^2 average current density and 90 electrical degree AC current angle

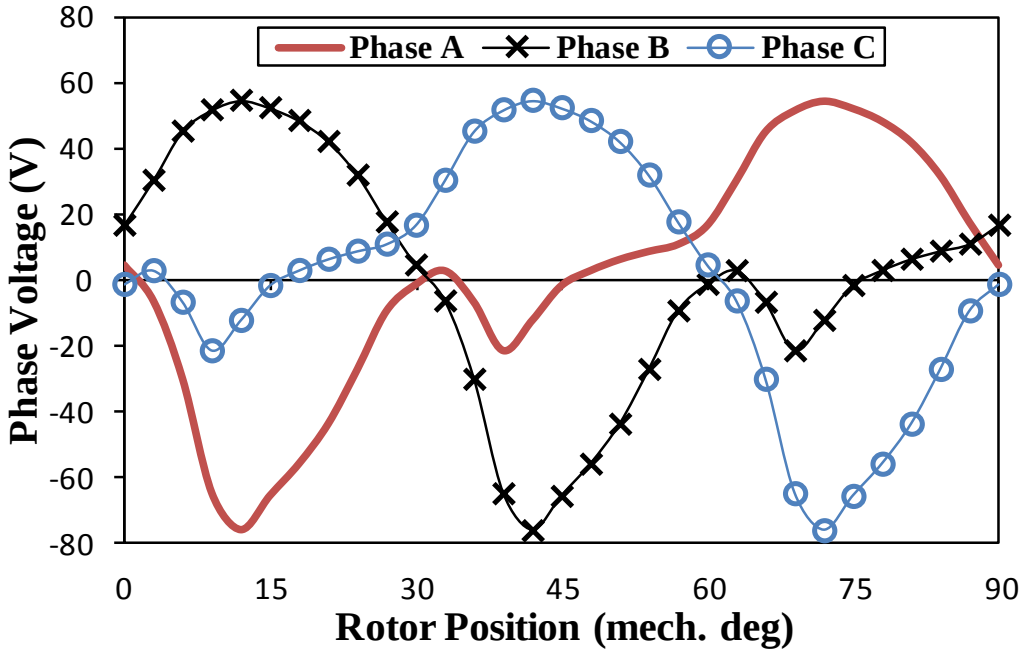

(c) 6 A/mm^2 average current density and 0 electrical degree AC current angle

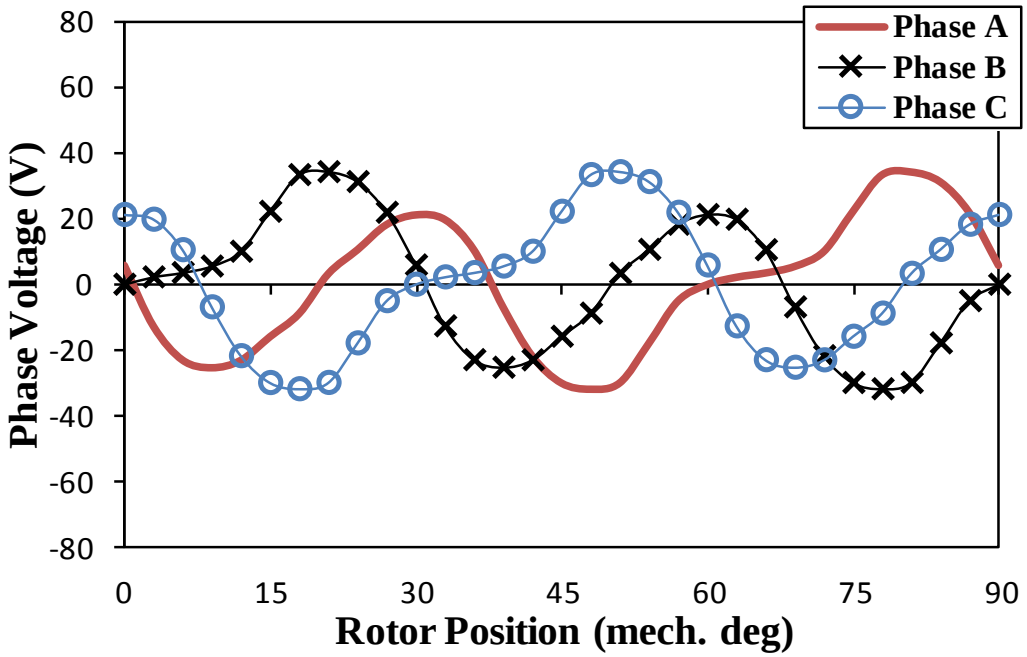

(d) 6 A/mm^2 average current density and 90 electrical degree AC current angle

Fig. 7.20 Comparison of phase voltage waveforms of 6 stator/4 rotor poles machine having symmetric winding connection for different average current densities and current angles, at 2500 rpm.

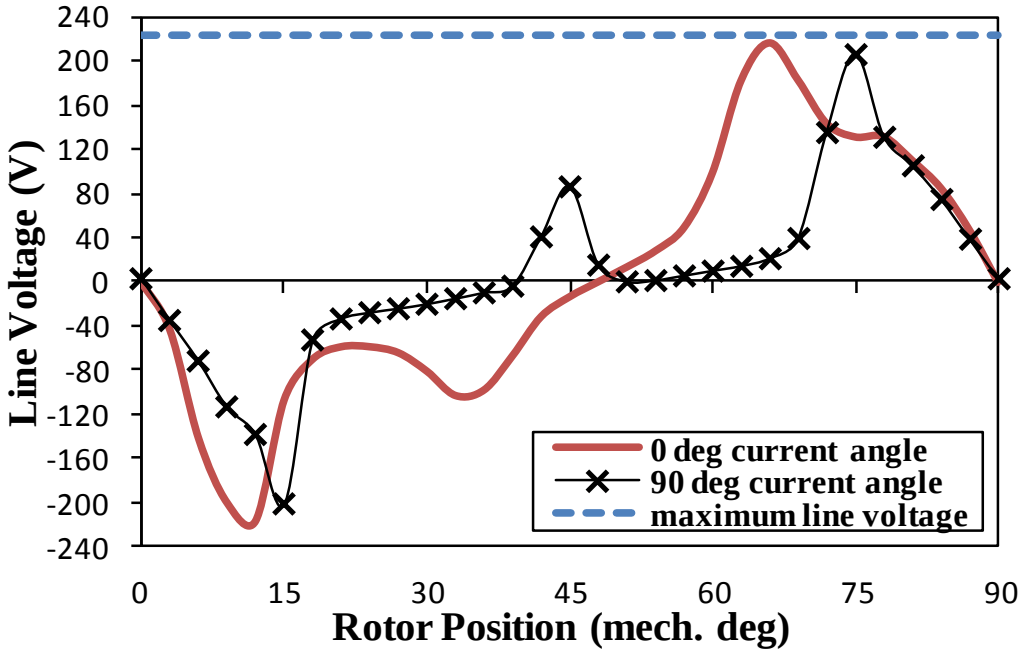

(a) Asymmetric, at 34 A/mm^2 average current density

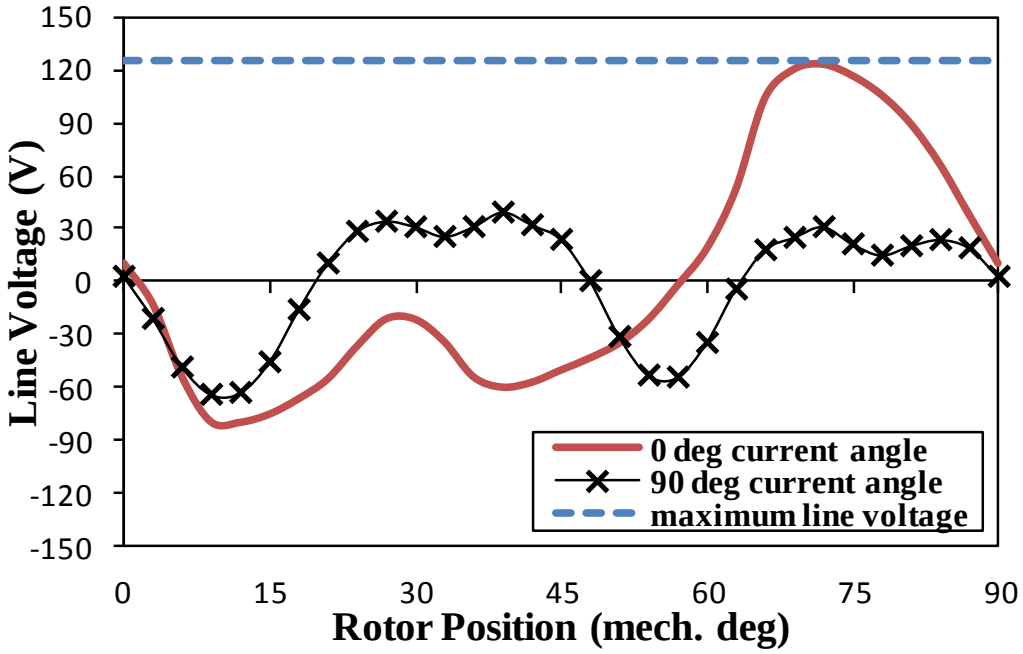

(b) Asymmetric, at 6 A/mm^2 average current density

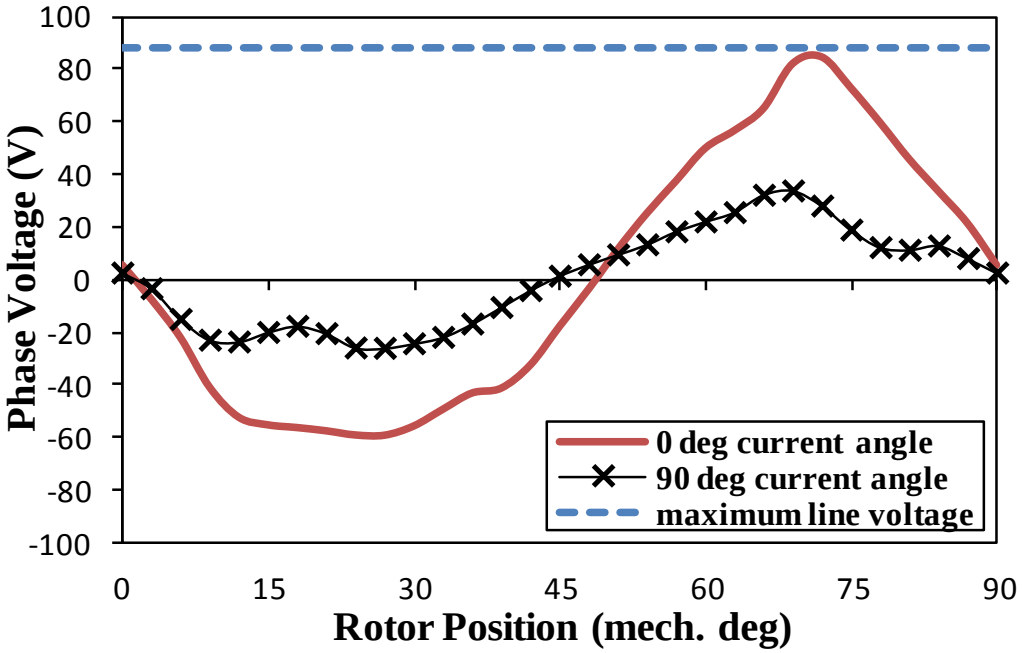

(c) Symmetric, at 34 A/mm^2 average current density

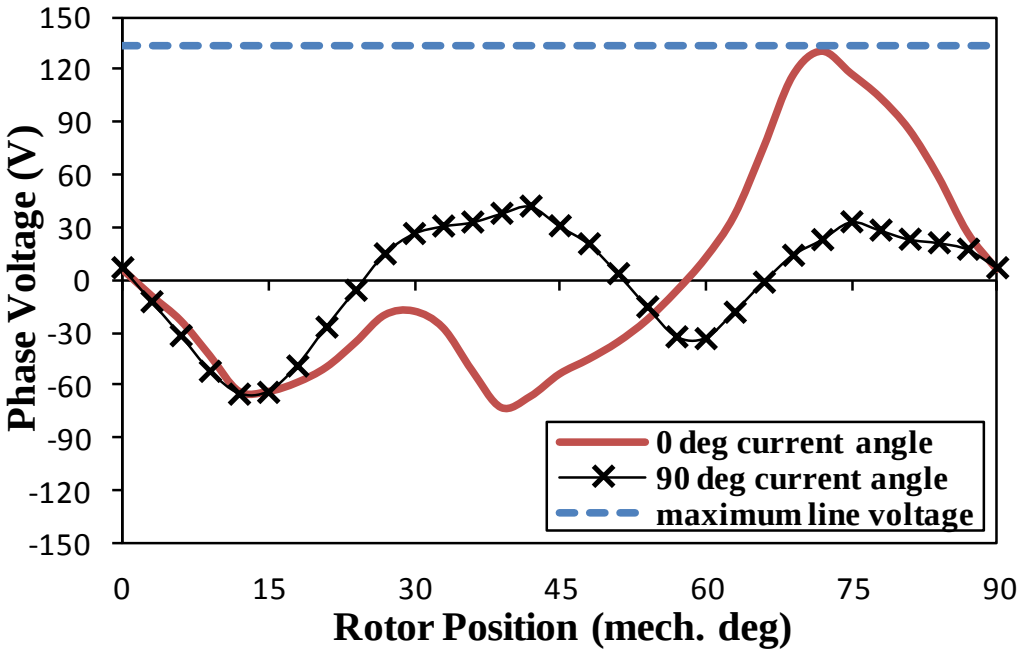

(d) Symmetric, at 6 A/mm^2 average current density

Fig. 7.21 Comparison of line voltage waveforms of 6 stator/4 rotor poles machines having asymmetric and symmetric winding connections for different average current densities and current angles, at 2500.

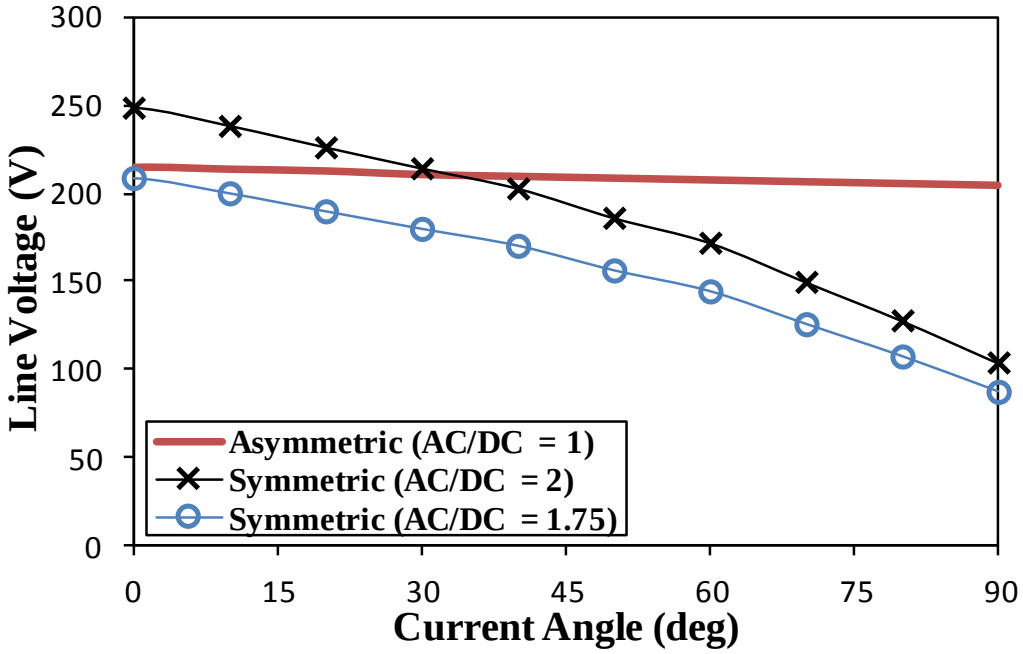

Fig. 7.22 Comparison of line voltage against current angle of 6 stator/4 rotor poles machines having different winding connections and AC/DC current density ratios, at 34 A/mm^2 average current density and 2500 rpm.

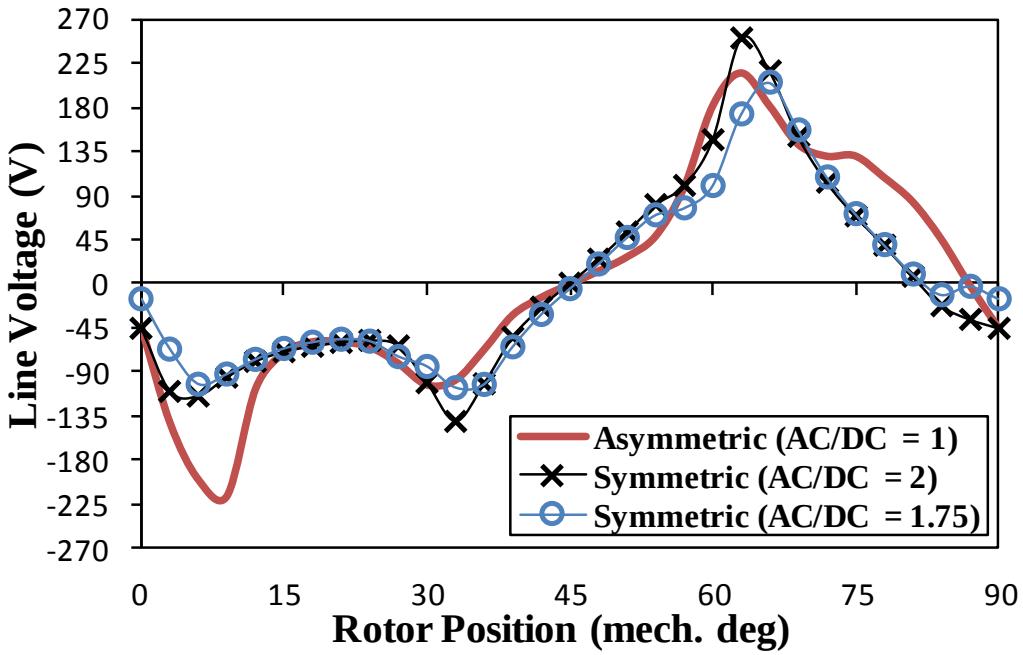

Fig. 7.23 Comparison of line voltage waveforms of 6 stator/4 rotor poles machines having different winding connections and AC/DC current density ratios, at 34 A/mm^2 average current density and 2500 rpm.

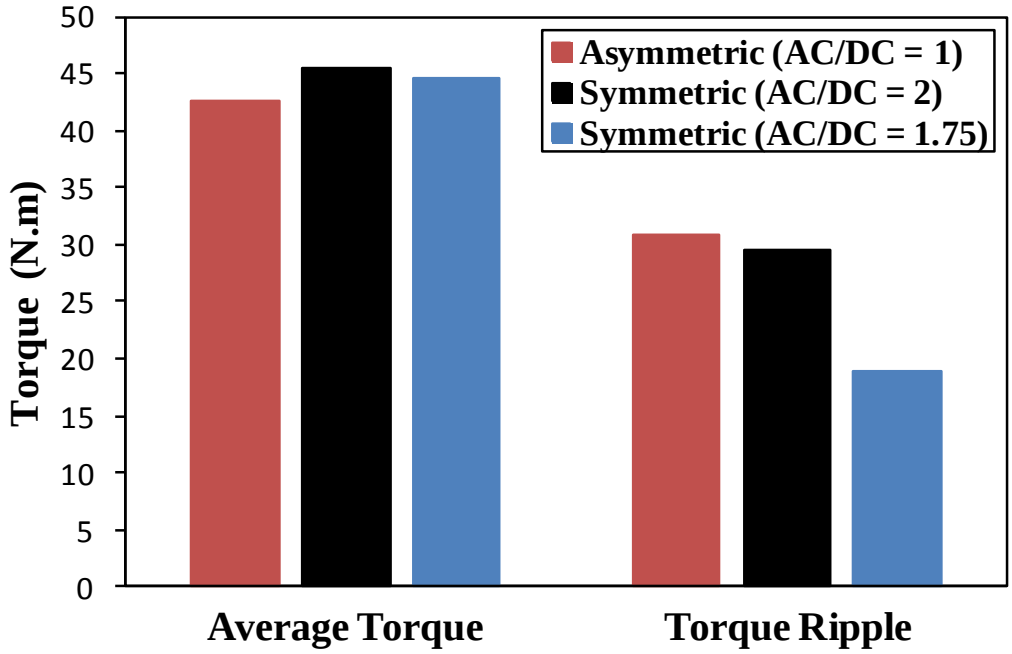

Fig. 7.24 Comparison of average output torque and torque ripple of 6 stator/4 rotor poles machines having different winding connections and AC/DC current density ratios, at 34 A/mm^2 total current density

7.4. Torque and Power Speed Characteristics

As mentioned before, the purpose of AC sinusoidal with DC bias excitation is to improve the electromagnetic performance of SynR machine, such as large average torque, low torque ripple, wide flux weakening region, low DC-link voltage requirement and high efficiency. In the previous sections, the torque capability and line voltage have been investigated and the symmetric winding connection has been chosen as the more appropriate winding connection. Therefore, in this section, the torque- and power-speed characteristics of the SynR machine under symmetric winding connection will be investigated. However, for reference, the torque-speed characteristics of the machine with the asymmetric winding connection are calculated and compared with their counterparts of the machine with symmetric winding connection in Appendix B.

As mentioned in the previous section, the machine is operated to deliver the maximum output torque at 2 AC/DC ratio. Therefore, the torque- and power-speed characteristics will be predicted by varying both the AC/DC ratio and the AC current angle. For this purpose, the output torque and the line voltage against AC current angle are calculated for different AC/DC ratio, as shown in Fig. 7.25 and Fig. 7.26, respectively. These data can be then

utilised to predict the torque- and power-speed characteristics for any specified conditions and voltage limitation, i.e. the 200V is given as an example in this section. It should be mentioned that the voltage drop on the power electronics drive is not considered in these investigations. In general, the larger the AC/DC ratio is the larger the line voltage since a larger AC/DC ratio means the AC current is larger, thus more voltage distortion and larger voltage spike, Fig. 7.23. In addition, the DC excitation is lower, thus the back-emf is larger, as shown in Fig. 7.11(a). For the same reasons, the larger the ratio the larger the output torque, but it should be mentioned that the torque ripple will also be larger. Therefore, in order to obtain the maximum possible torque-speed performance at the specified line voltage limitation, at each speed the optimal AC/DC ratio and AC current angle combination, which results in the maximum output torque within the voltage limitation, is utilised. The obtained torque- and power-speed characteristics are shown in Fig. 7.27, while Fig. 7.28 shows the variation of the corresponding AC and DC current densities. In general, the machine exhibits relatively larger output torque and wide flux weakening operation region. However, in order to make a more systematic judgment, such characteristics will be compared with their counterpart of the conventional unipolar and AC sinusoidal bipolar excitation in section 7.6. The torque- and power-speed characteristics are also predicted by employing an alternate technique, i.e. constant DC/varing AC. Then, the results of the two techniques are compared, thus the better performance can be detrmined. In the constant DC/varying AC technique, the DC current density is kept constant while both the AC current density and angle are varied to operate the machine at the best performance within the specified limits. In this case, the SynR machine becomes even more similer to PM machine. For this purpose, the variations of the output torque and machine line voltage against the AC current angle are calculated at 23 A/mm^2 DC current density and for different AC current density, as respectively shown in Fig. 7.29 and Fig. 7.30. In the constant-torque region, the AC/DC ratio and AC current angle are kept constant, i.e. at 2 and 0 degree, but in the flux weakening region both the AC current density and angle are adjusted to operate the machine at its maximum performance with the voltage limitation. The predicted torque- and power-speed characterstics by using such technique are compared with their counterparts of the varying AC/DC ratio technique in Fig. 7.27. In addition, the corresponding DC and AC current densities are compared with their counterparts of the other two techniques in Fig. 7.28. In general, both techiques result in the same performance in the constant-torque region. However, comparing with the varying AC/DC ratio technique, the constant DC/varying AC counterpart produces lower performance during the flux weakening.

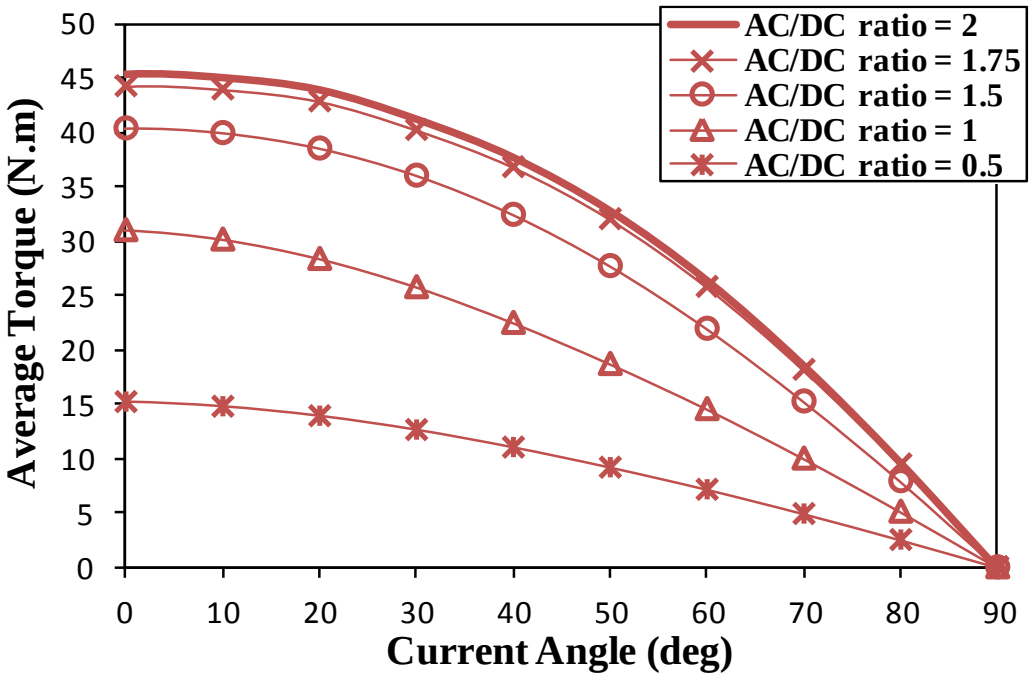

Fig. 7.25 Variation of average output torque against AC current angle of 6 stator/4 rotor poles machines having symmetric winding connection for different AC/DC current density ratios, at 34 A/mm^2 average current density.

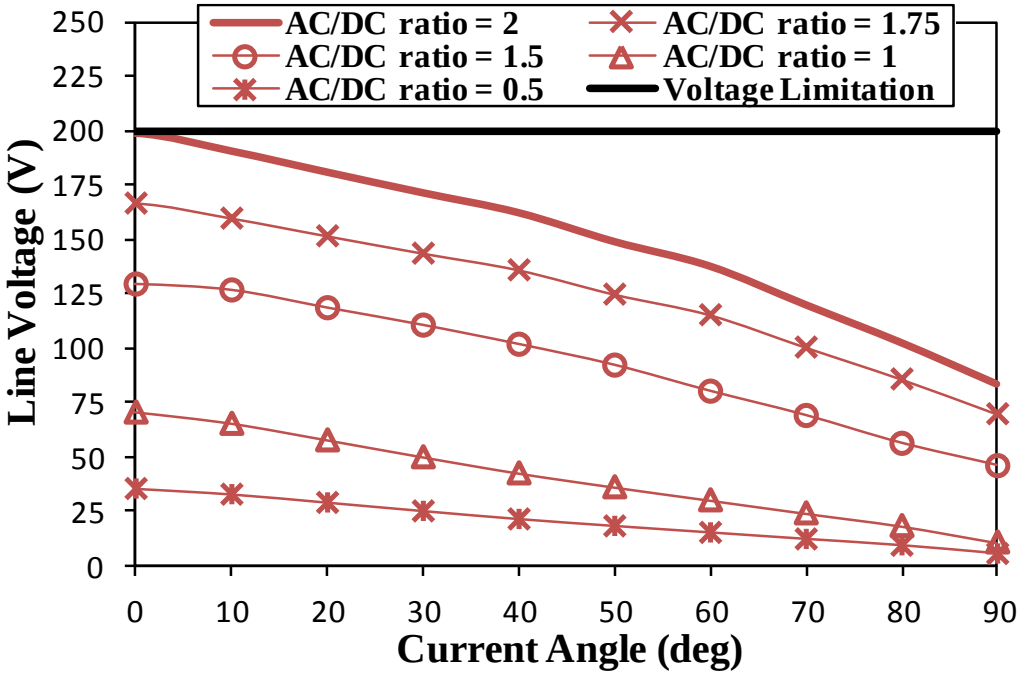

(a) 2000 rpm

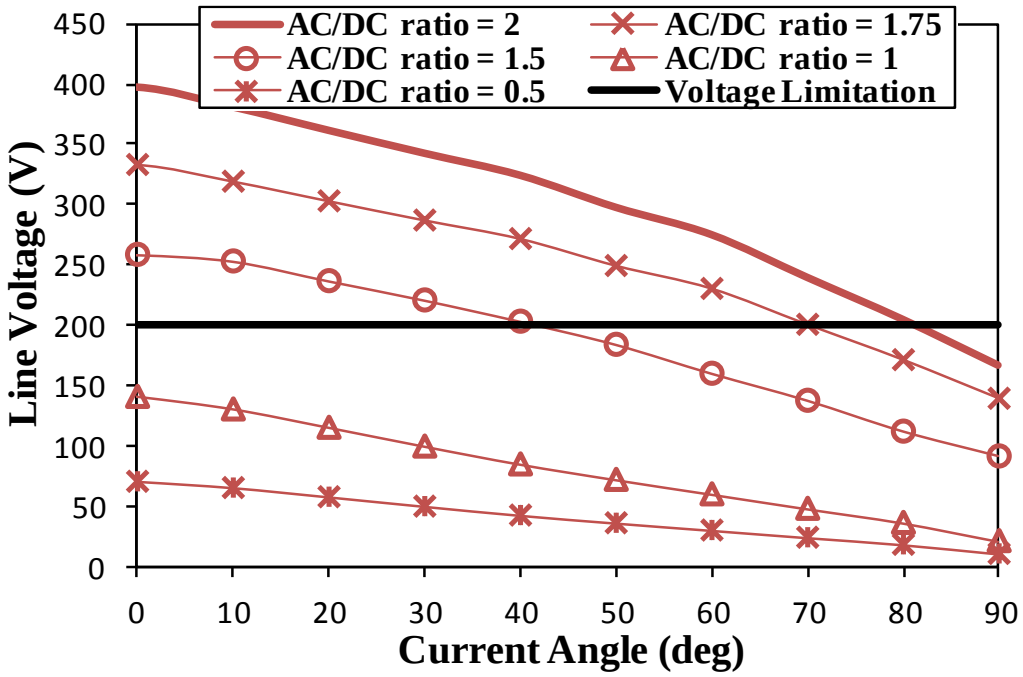

(b) 4000 rpm

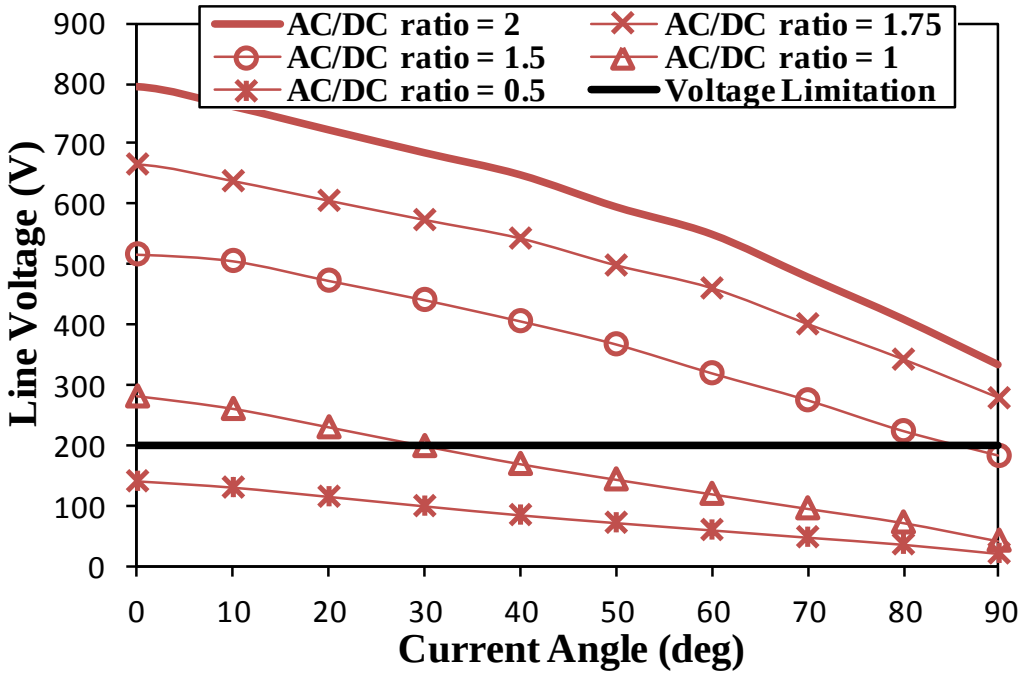

(c) 8000 rpm

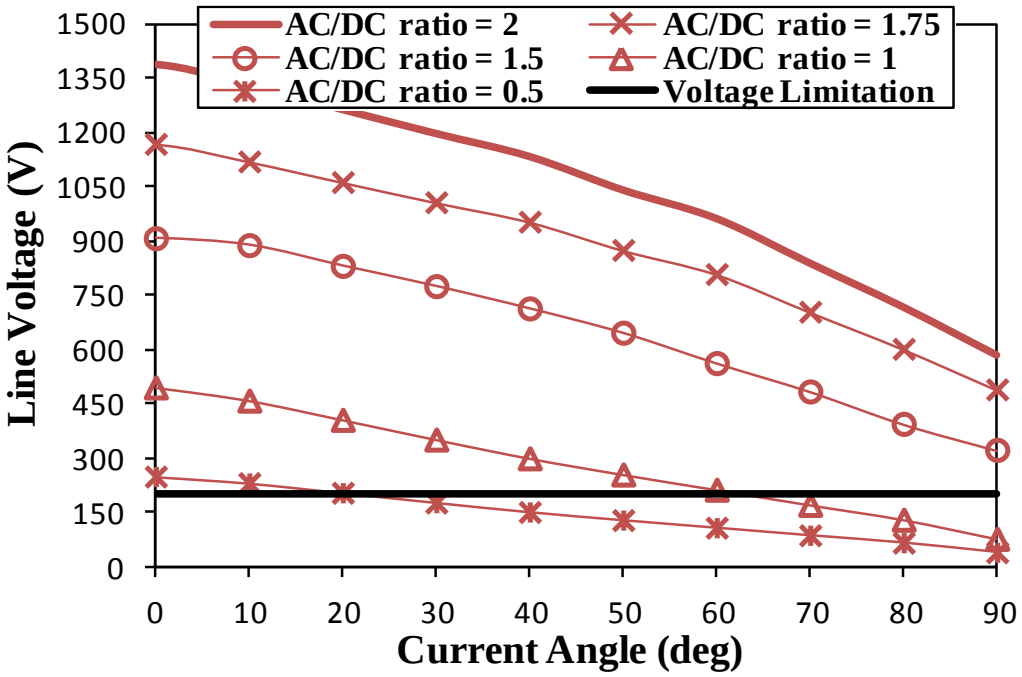

(d) 14000 rpm

Fig. 7.26 Variation of line voltage against AC current angle of 6 stator/4 rotor poles machines having symmetric winding connection for different AC/DC current density ratios and speeds, at 34 A/mm^2 average current density.

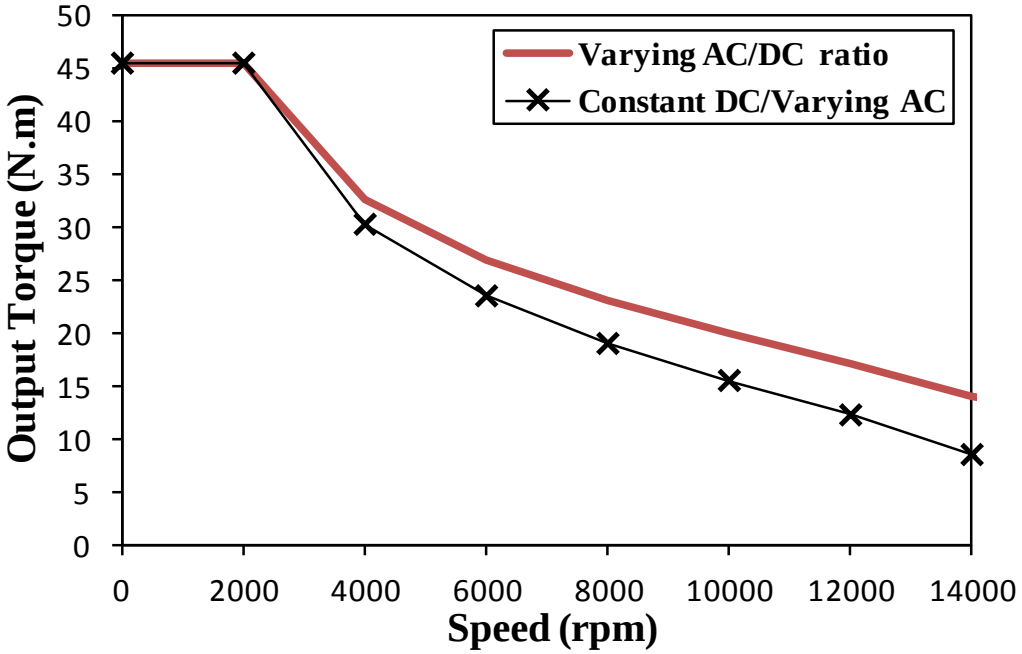

(a) Torque-speed characteristics

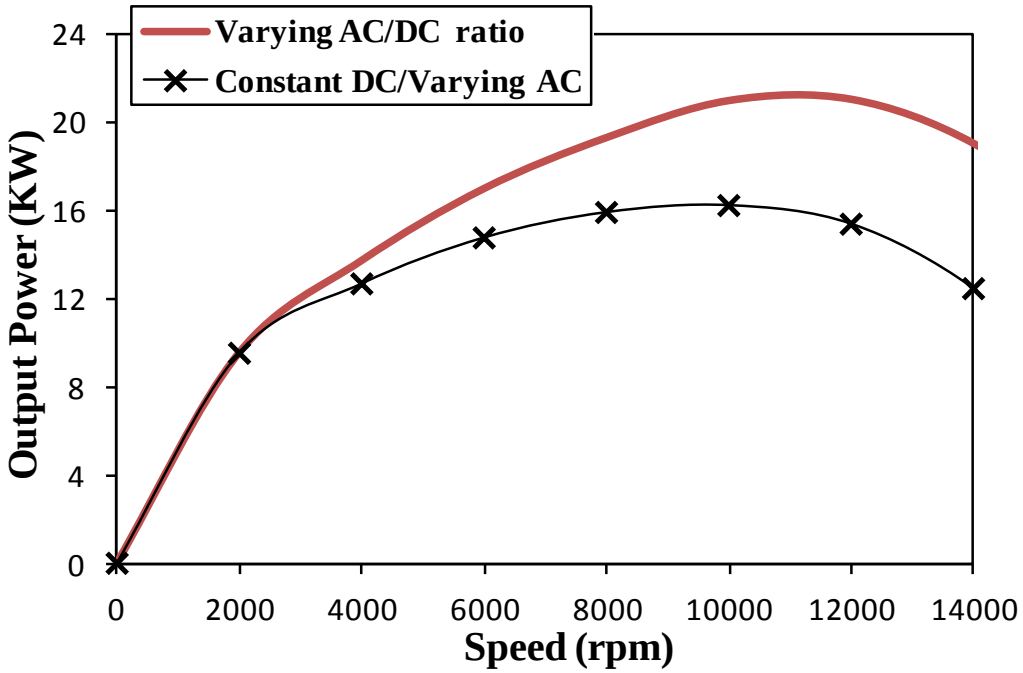

(b) Power-speed characteristics

Fig. 7.27 Variation of torque- and power-speed characteristics of 6 stator/4 rotor poles machines having symmetric winding connection due to different prediction techniques, at 34 A/mm^2 average current density and 200 V voltage limitation.

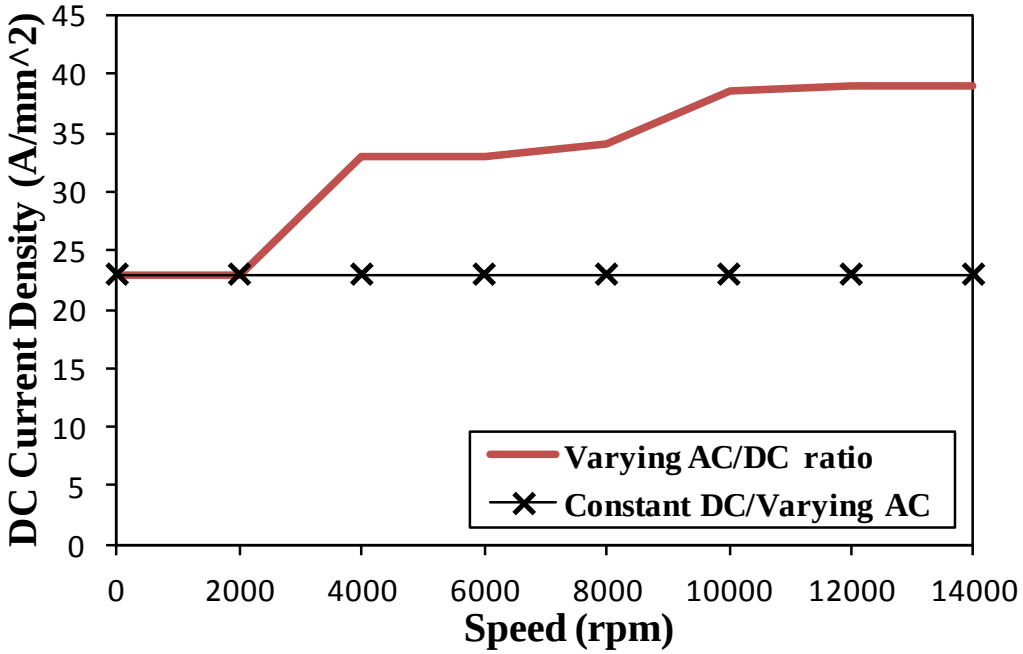

(a) DC current density

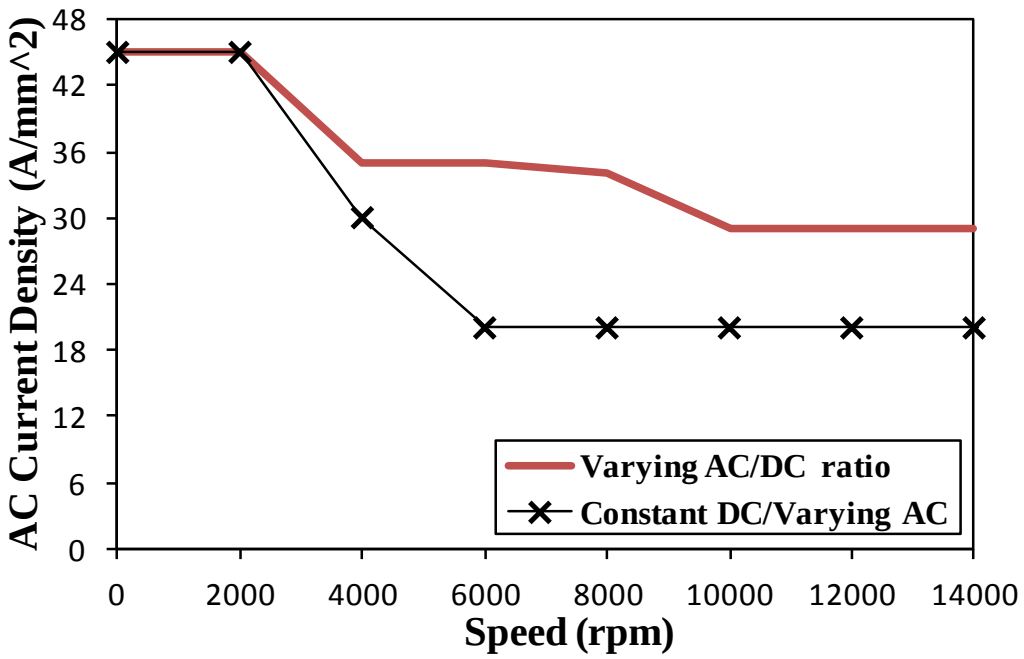

(b) AC current density

Fig. 7.28 Variation of AC and DC current densities and AC current of 6 stator/4 rotor poles machines having symmetric winding connection due to different prediction techniques, at 34 A/mm^2 average current density and 200 V voltage limitation.

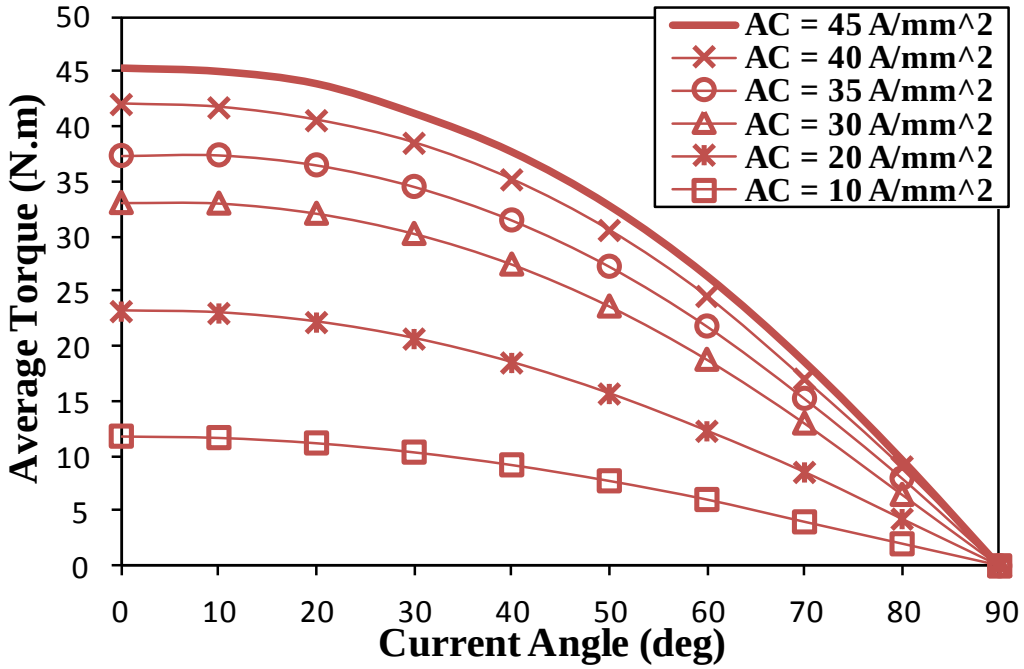

Fig. 7.29 Variation of average output torque against AC current angle of 6 stator/4 rotor poles machines having symmetric winding connection for different AC current densities, at 23 A/mm^2 constant DC current density.

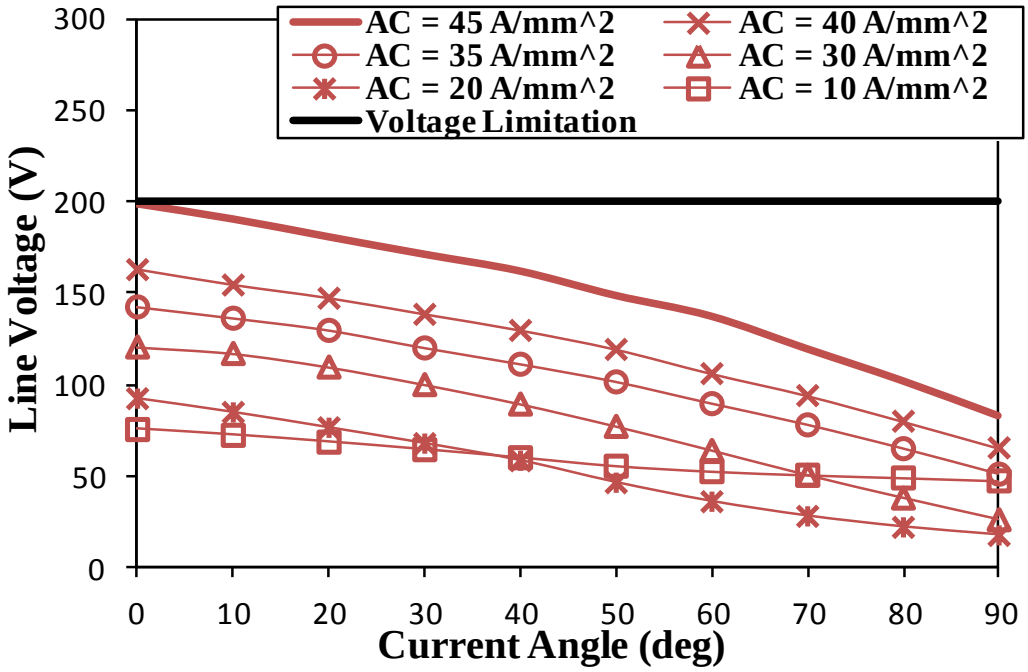

(a) 2000 rpm

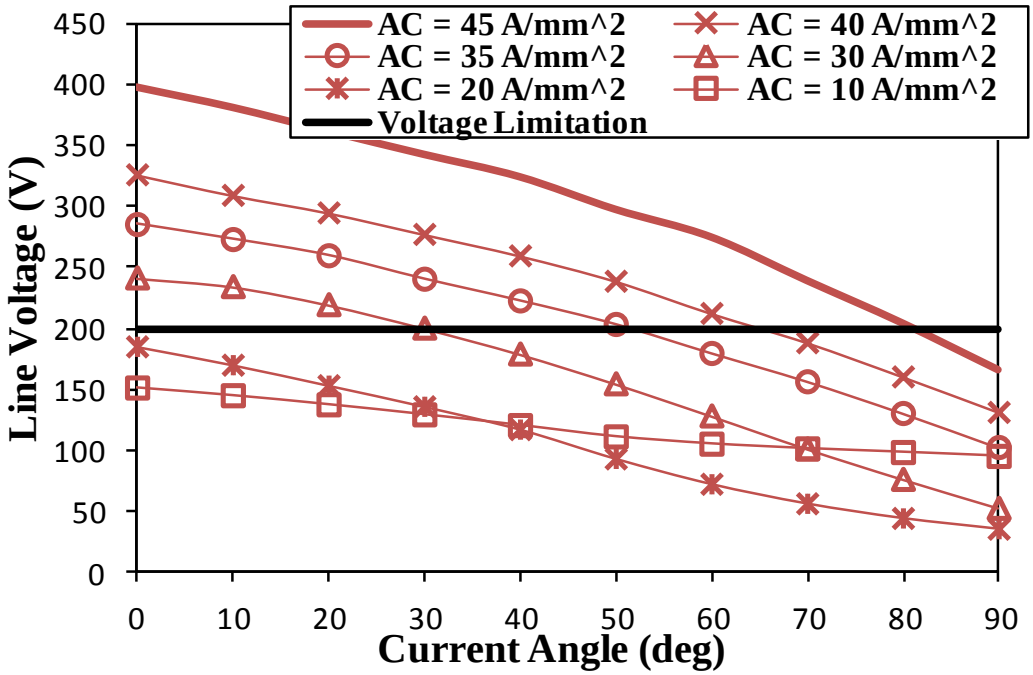

(b) 4000 rpm

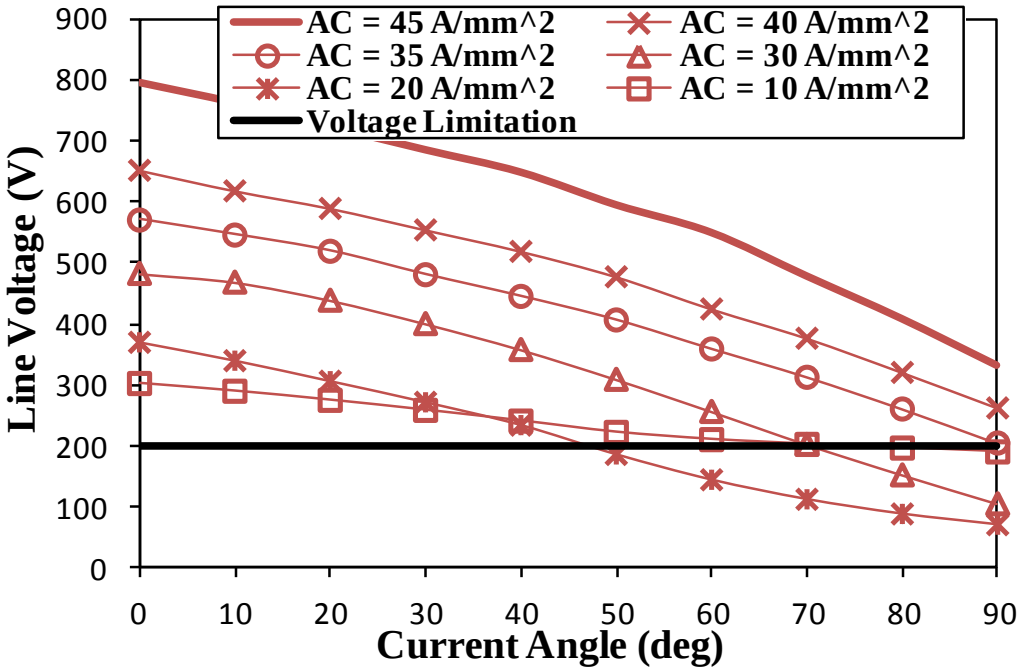

(c) 8000 rpm

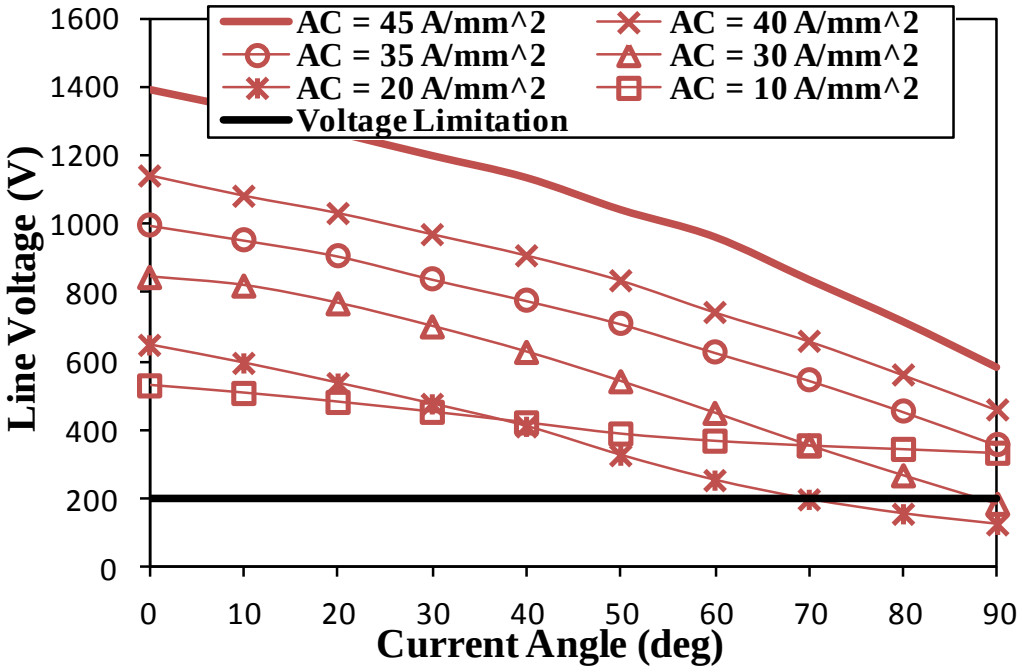

(d) 14000 rpm

Fig. 7.30 Variation of line voltage against AC current angle of 6 stator/4 rotor poles machines having symmetric winding connection for different AC current densities and rotating speeds, at 23 A/mm^2 constant DC current density.

7.5. Losses and Efficiency

Both the iron and copper losses as well as the machine efficiency will be predicted and calculated using the same method that is used in Section 6.6. The losses against speed are calculated according to the corresponding DC and AC current densities of the varying AC/DC ratio and constant DC/varying AC prediction techniques, Fig. 7.28(a) and Fig. 7.28(b), respectively. The iron and copper losses results are respectively shown in Fig. 7.31 and Fig. 7.32. The constant DC/varying AC technique results in significantly lower iron and copper losses comparing with the varying AC/DC counterpart. This is because the first technique utilizes lower AC current density during the flux weakening region, as can be noticed in Fig. 7.28. Therefore, although the varying AC/DC technique results in slightly larger output power, Fig. 7.27, but the efficiency is larger when the constant DC/varying AC technique is used, as illustrated in Fig. 7.33. Clearly, for the varying AC/DC ratio, there remains some optimization to be done regarding the optimal total current density in terms of maximum efficiency. However, due to time limit, this will be done in the future.

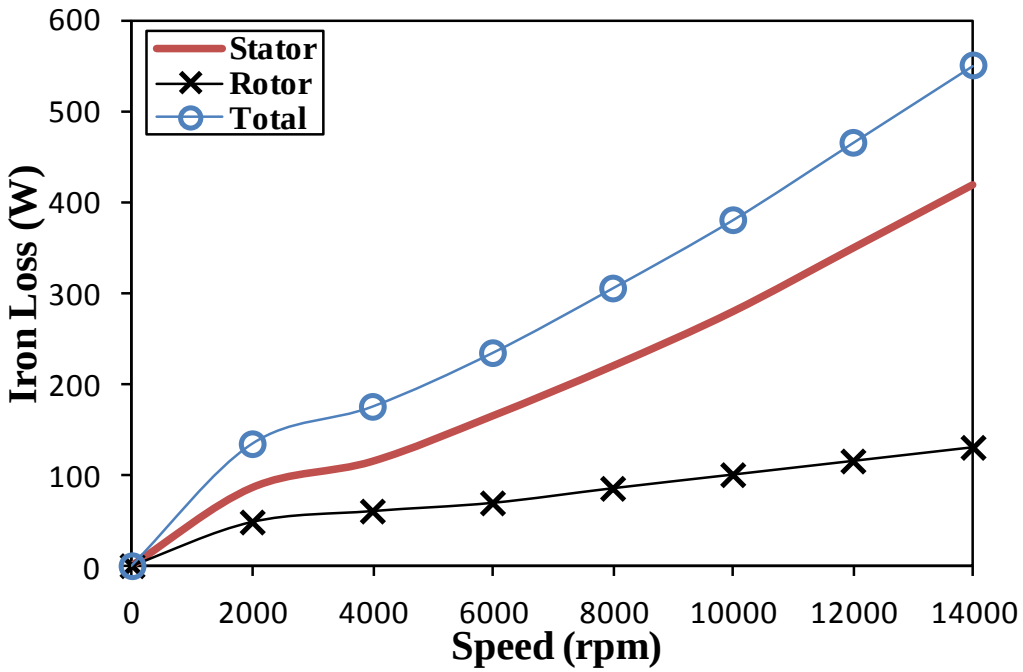

(a) Varying AC/DC ratio

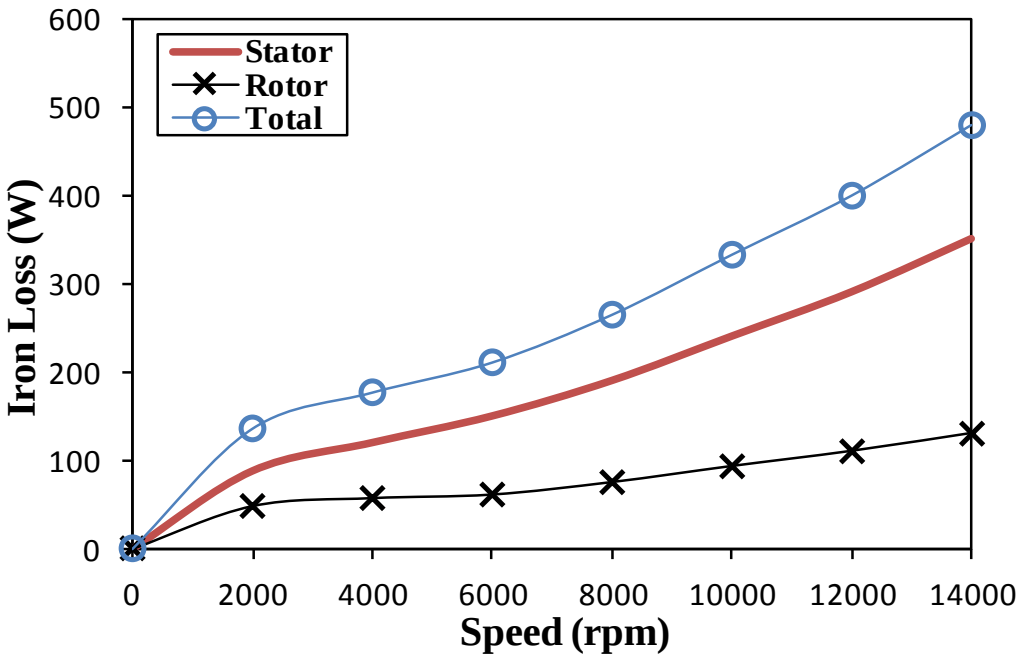

(b) Constant DC/varying AC

Fig. 7.31 Comparison of iron loss of 6 stator/4 rotor poles machines having symmetric winding connection.

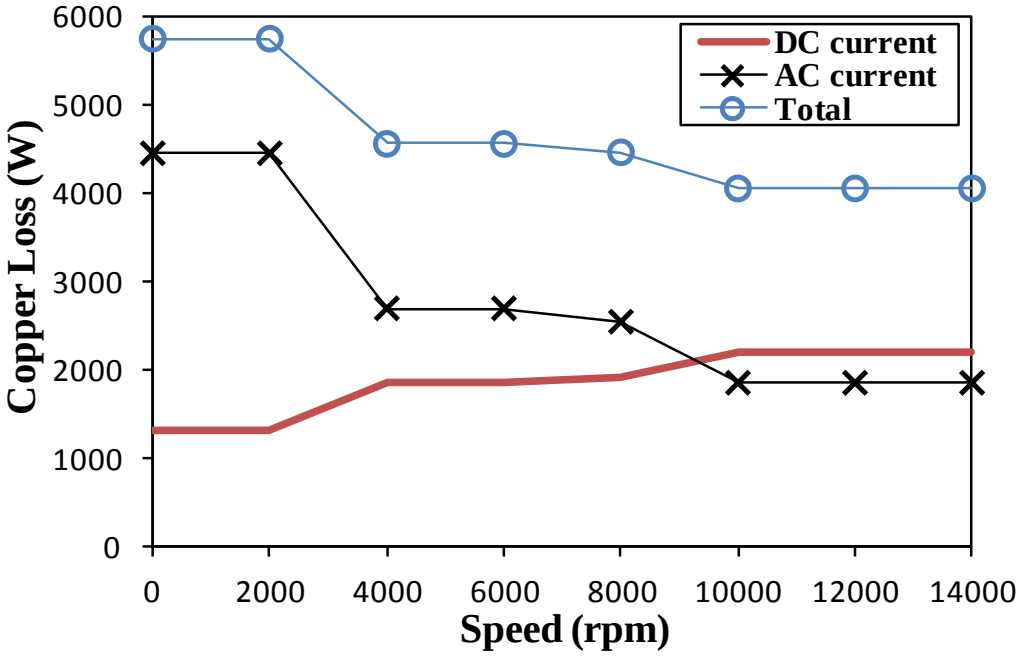

(a) Varying AC/DC ratio

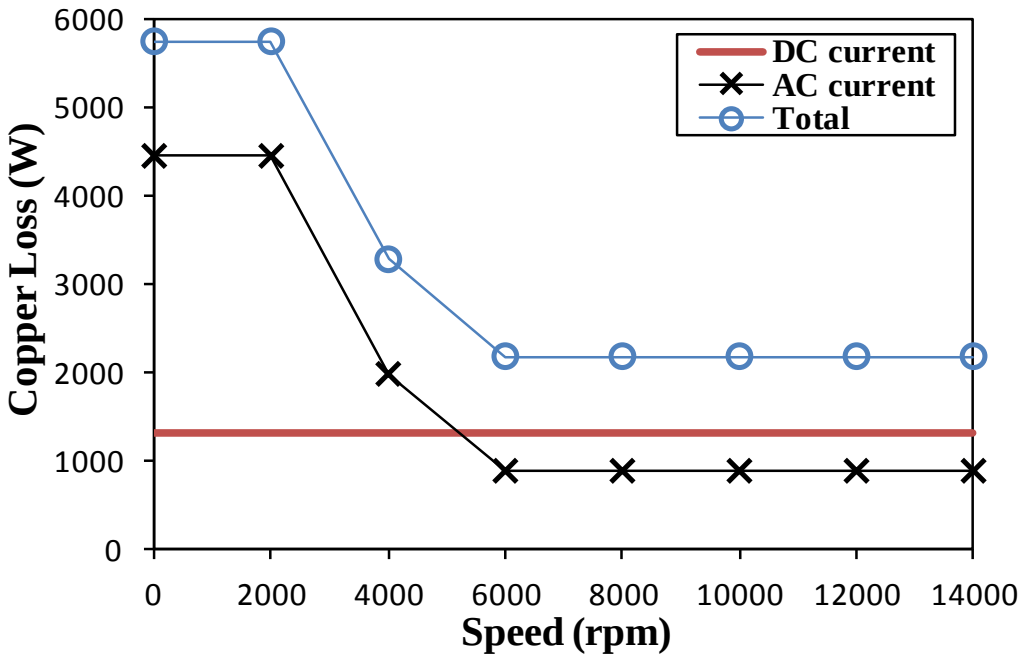

(b) Constant DC/varying AC

Fig. 7.32 Comparison of copper loss of 6 stator/4 rotor poles machines having symmetric winding connection.

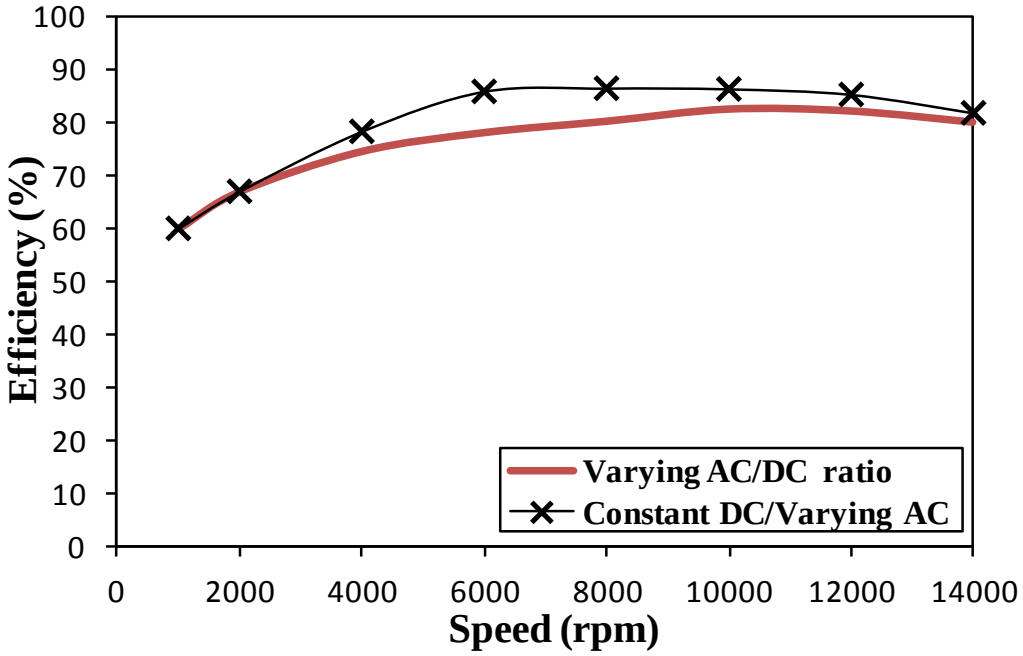

Fig. 7.33 Comparison of efficiency of 6 stator/4 rotor poles machines having symmetric winding connection.

7.6. Comparison of Alternate Excitation Techniques

The electromagnetic performance of the SynR machine under AC sinusoidal bipolar excitation has been thoroughly investigated in Chapter 6. In this Chapter, the DC bias has been added to the AC sinusoidal excitation. This section illustrates the benefits and disadvantages of these two excitation techniques over the conventional SR unipolar excitation counterpart, which is analyzed in Appendix C. The electromagnetic performance of the analyzed SynR machine under the foregoing three specified excitation techniques is compared in this section. The comparison includes the average output torque, torque ripple, losses and efficiency. Under the AC sinusoidal bipolar excitation, both the symmetric and hybrid winding connections are considered. It is also worth mentioning that the 1.75 AC/DC ratio is used for the AC sinusoidal bipolar with DC bias excitation since such ratio results in nearly the same average torque as the optimal counterpart, but the produced torque ripple is significantly lower, as illustrated in Fig. 7.24. The output torque waveforms under different excitations at 34 A/mm^2 are shown in Fig. 7.34, while the corresponding average output torques and torque ripples are compared in Fig. 7.35 and Fig. 7.36. Moreover, the variations of the average torque, torque ripple and torque ripple percentage of the machine against the current density are compared for the three different excitations in, Fig. 7.37. In order to further extend the comparison, the output power, iron and copper losses and efficiency of the motor under the three different excitations are calculated and compared in Fig. 7.38 and Fig. 7.39 and Fig. 7.40, respectively. For further illustration the characteristics of all machines are also presented in Table 7.1.

In summary, both AC bipolar excitations can significantly reduce the torque ripple of the SR machine. The AC bipolar with the DC bias excitation offers relatively large average output torque and low losses, thus higher efficiency. However, at relatively larger current densities, the AC bipolar with hybrid winding connection offers the largest average torque and relatively low torque ripple percentage and high efficiency.

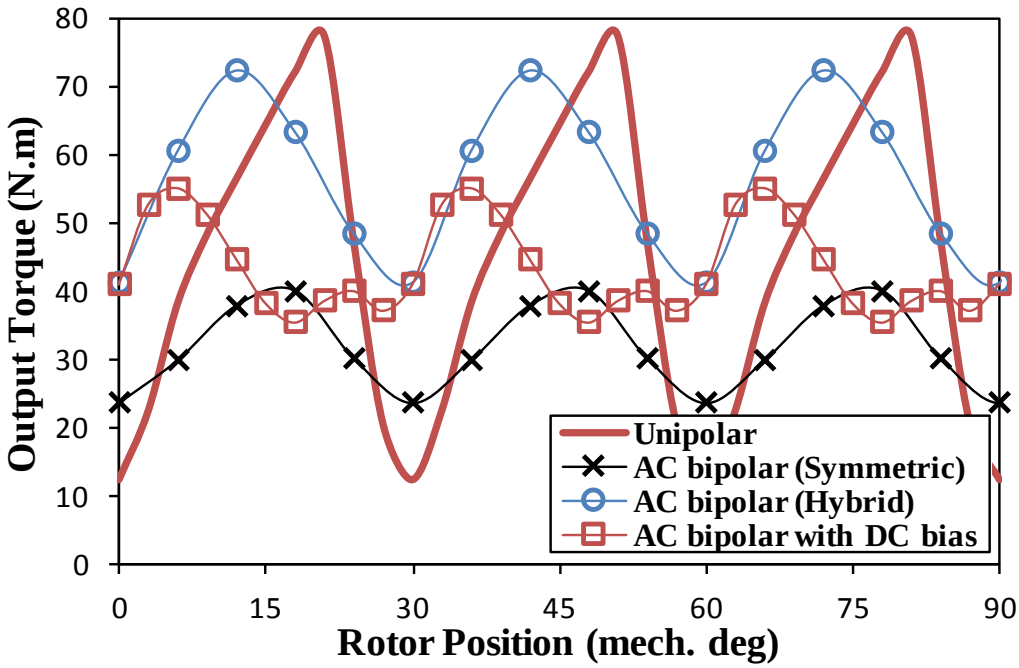

Fig. 7.34 Comparison of output torque waveforms of 6 stator/4 rotor poles machines under different excitation techniques, at 34 A/mm^2 current density.

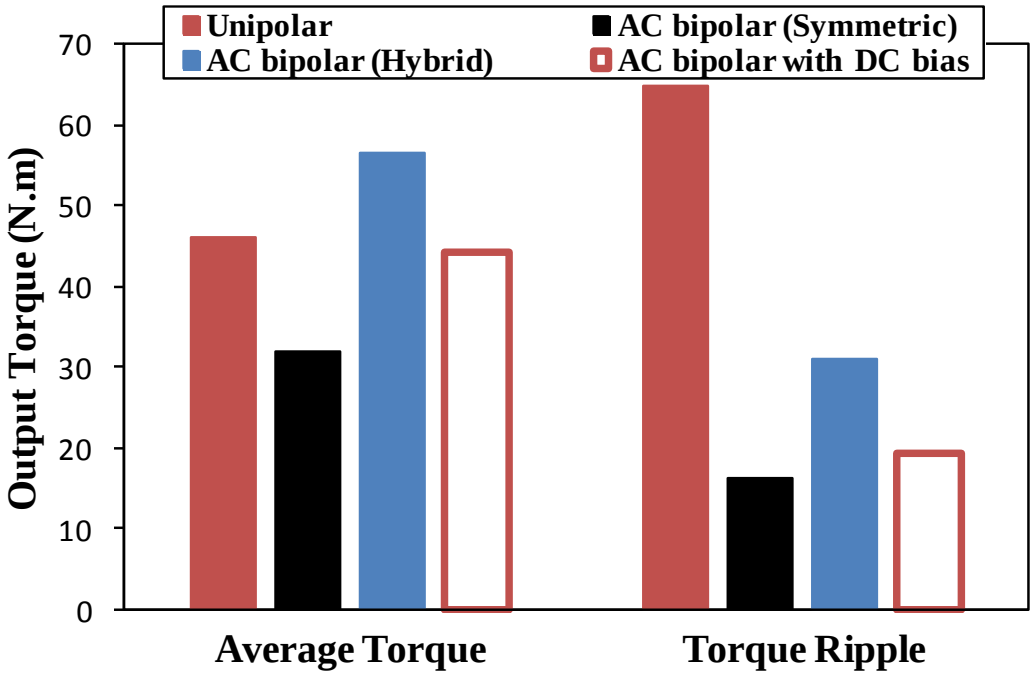

Fig. 7.35 Comparison of average torque and torque ripple of 6 stator/4 rotor poles machines under different excitation techniques, at 34 A/mm^2 current density.

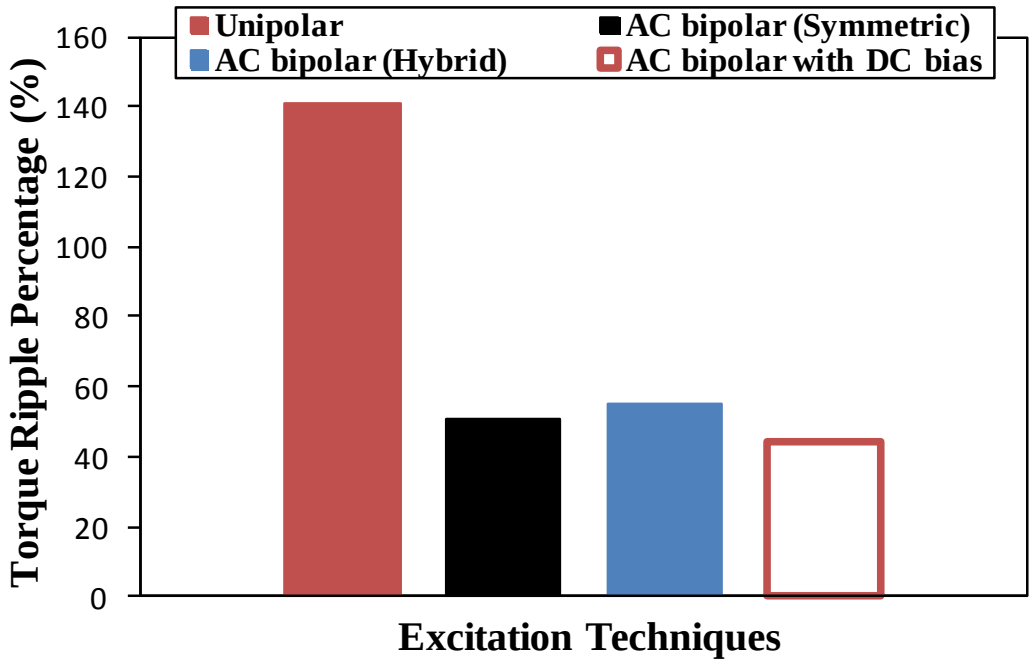

Fig. 7.36 Comparison of torque ripple percentage of 6 stator/4 rotor poles machines under different excitation techniques, at 34 A/mm^2 current density.

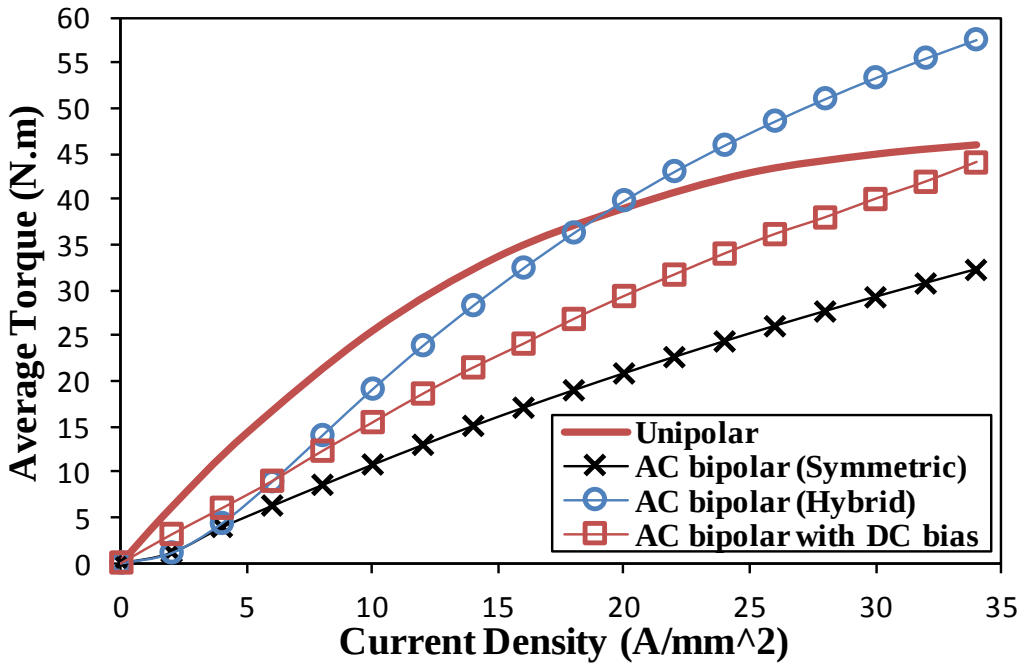

(a) Average output torque

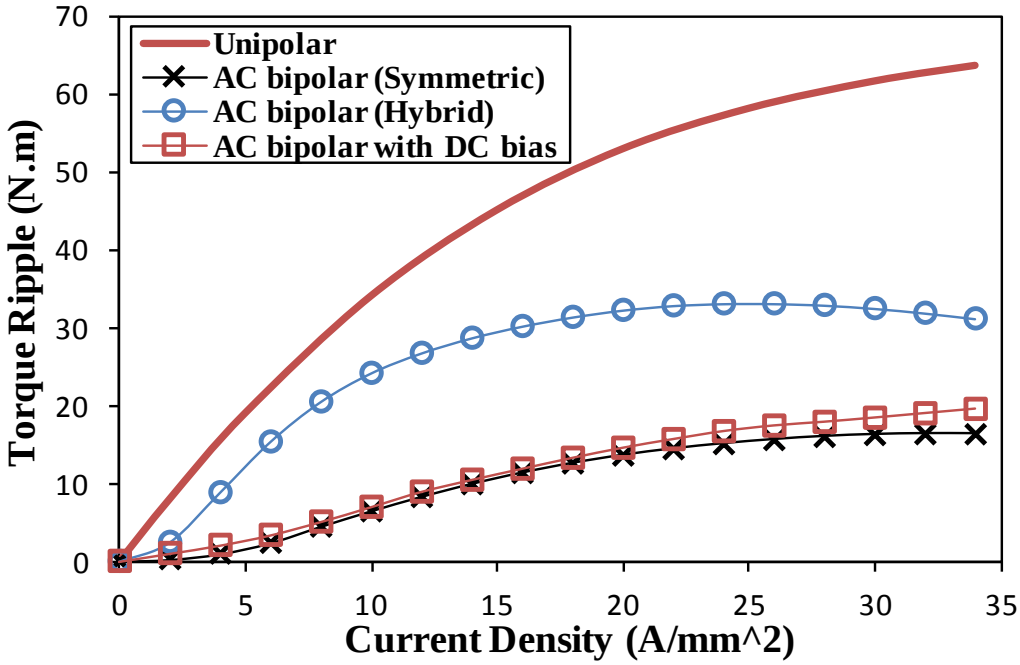

(b) Torque ripple

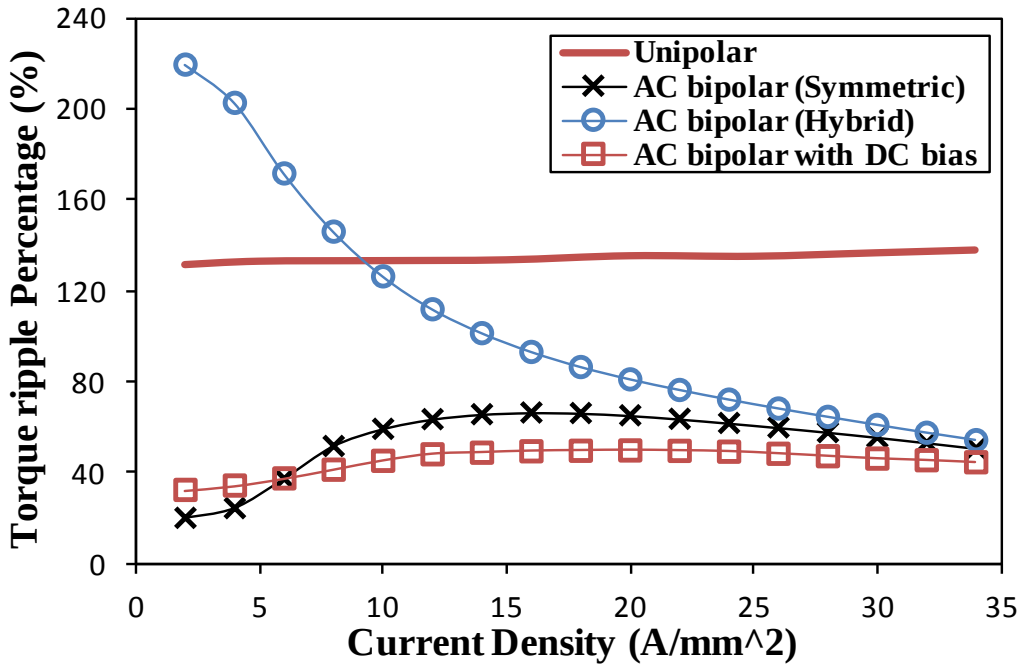

(c) Torque ripple percentage

Fig. 7.37 Comparison of average torque, torque ripple and torque ripple percentage against current density of 6 stator/4 rotor poles machine under different excitation techniques.

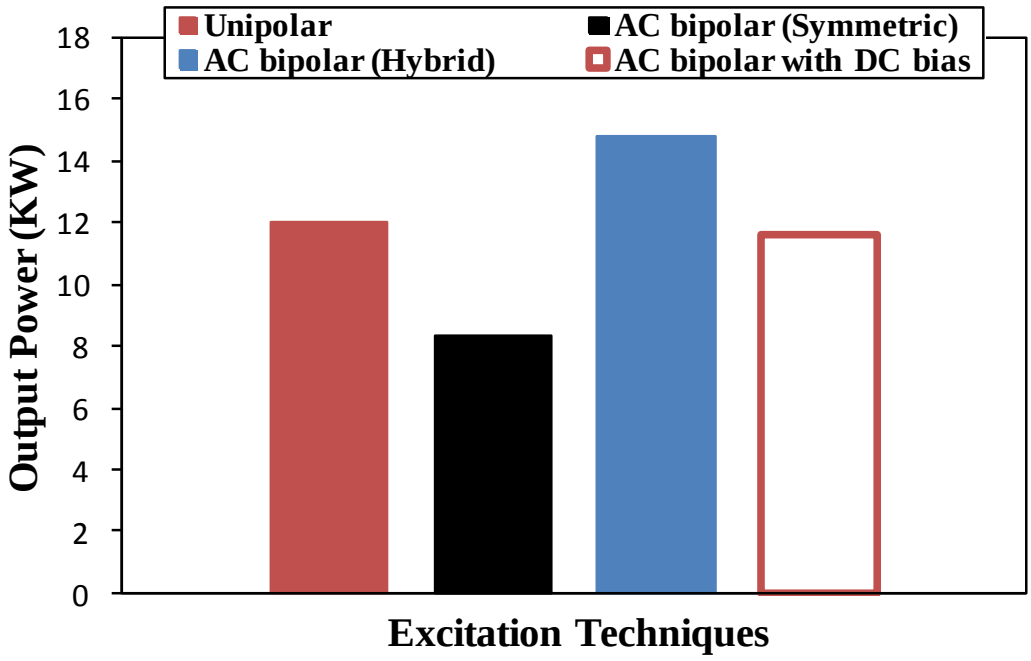

Fig. 7.38 Comparison of output power of 6 stator/4 rotor poles machines under different excitation techniques, at 34 A/mm^2 current density and 2500 rpm.

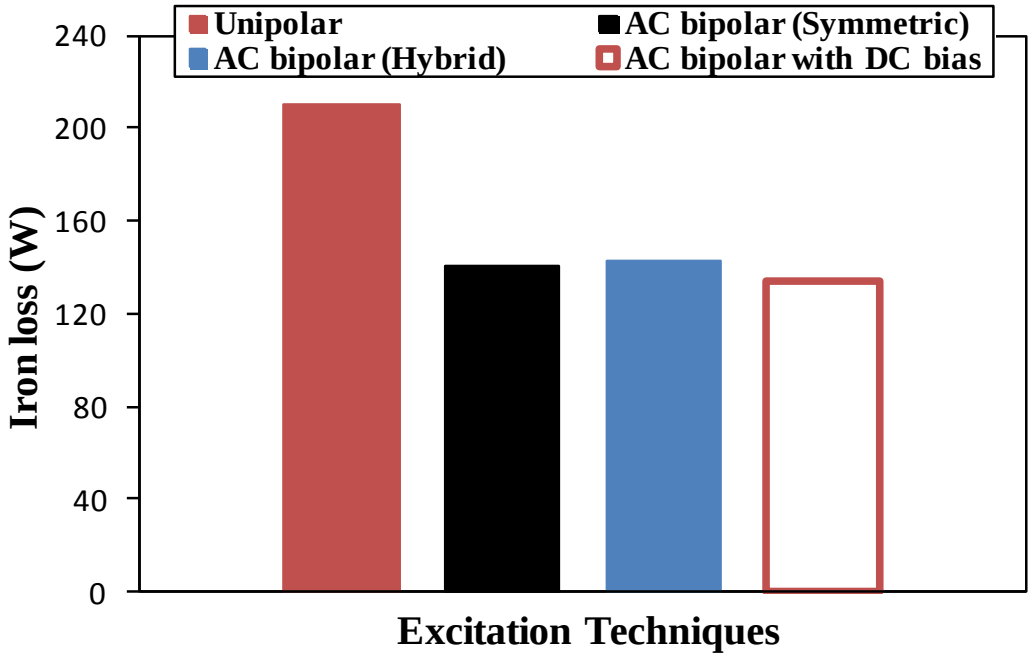

(a) Iron loss

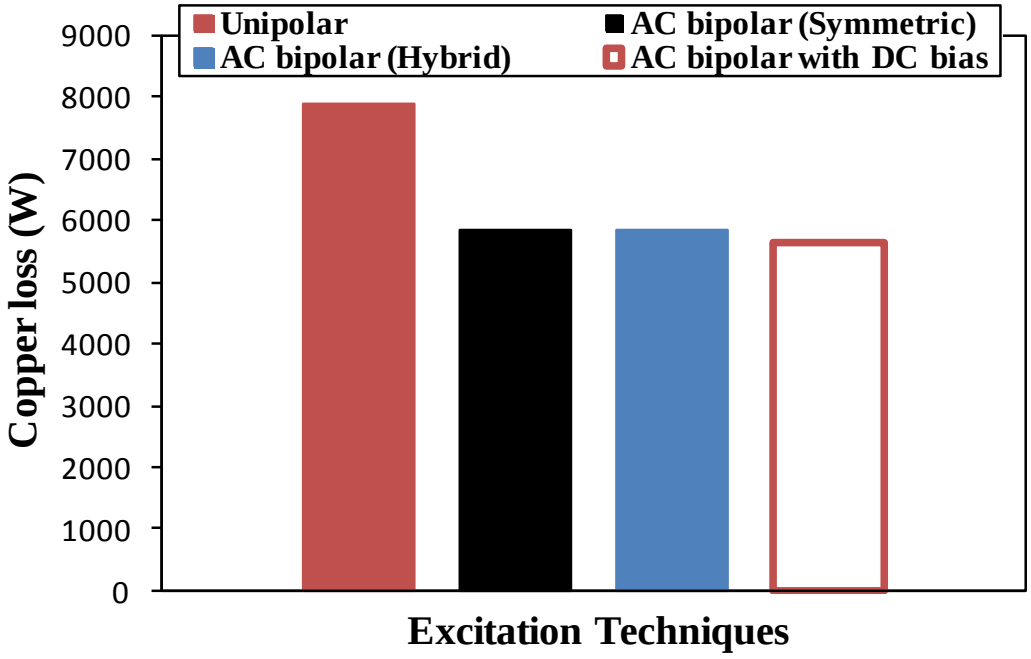

(b) Copper loss

Fig. 7.39 Comparison of iron and copper losses of 6 stator/4 rotor poles machines under different excitation techniques, at 34 A/mm^2 current density and 2500 rpm.

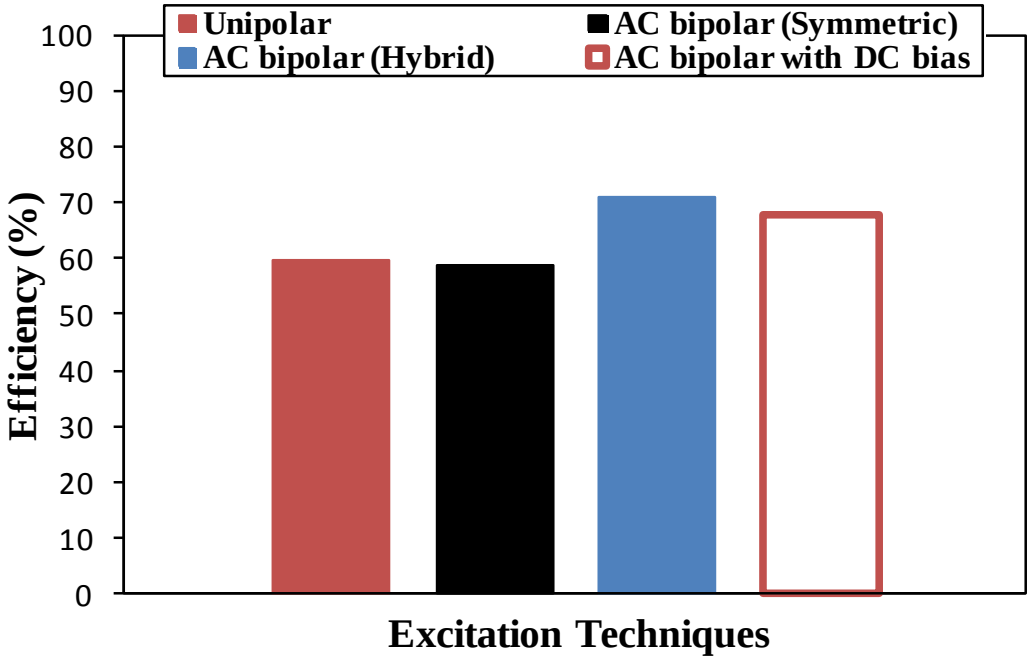

Fig. 7.40 Comparison of efficiency of 6 stator/4 rotor poles machines under different excitation techniques, at 34 A/mm^2 current density and 2500 rpm.

Table 7.1 Comparison of characteristics of 6 stator/4 rotor poles machines having different excitation techniques, at 34 A/mm^2 current density and 2500 rpm.

Characteristics	***Unipolar (conventional SR)***	***AC bipolar (Symmetric)***	***AC bipolar (Hybrid)***	***AC bipolar with DC bias***
Average torque (N.m)	46	32	56	44.5
Torque ripple (N.m)	65	16	31	19.5
Torque ripple Percentage (%)	141	50	55	44
Output Power (KW)	12	8	15	11.5
Iron loss (W)	210	140	143	134
Copper loss (W)	7888	5843	5843	5650
Efficiency (%)	59.5	59	71	68

7.7. Experimental Measurements

In order to validate the analyses of this chapter, the back-emf, cogging torque and output torque against AC phase current magnitude and angle, also the output torque against the AC/DC current density ratio are measured and compared with the predicted results for the same prototype machine, which have been used in Chapter 6. As mentioned in Chapter 6, each stator tooth of the 6 stator/4 rotor poles prototype machine is equipped with two coils. In order to operate such machine under the AC bipolar with DC bias excitation, the 13 turn coils are connected together to form the three phase winding, while the 8 turn coils are connected in series to the DC current source, as illustrated in Fig. 7.41. It is worth mentioning that the current polarity, i.e. in or out direction, is determined according to the connection to be employed, i.e. asymmetric or symmetric. In addition, as mentioned earlier, for the asymmetric winding connection only 4 DC coils have been connected, according to Fig. 7.2(a). The prototype machine is tested using the same test rig that is shown in Fig. 6.64. The measured and predicted back-emf waveforms of the prototype machine for different winding connections and current densities are compared in Fig. 7.42. It confirms the producing of the back-emf, which can be controlled by adjusting the DC bias value. It is worth mentioning that it is practically hard to measure the back-emf for relatively larger DC bias value since the cogging torque becomes relatively large, as confirmed in Fig. 7.43. For

both winding connections, there is a good agreement between the measured and predicted cogging torque periodicity. However, in terms of the magnitude, the disagreement is most likely due to the manufacturing tolerances and errors. The output torque against the AC phase current angle and magnitude and the AC/DC current density ratio are measured and compared with their predicted counterparts in Fig. 7.44, Fig. 7.45 and Fig. 7.46, respectively. The exhibited good agreement of these characteristics strongly confirms the discussions and conclusions of this chapter.

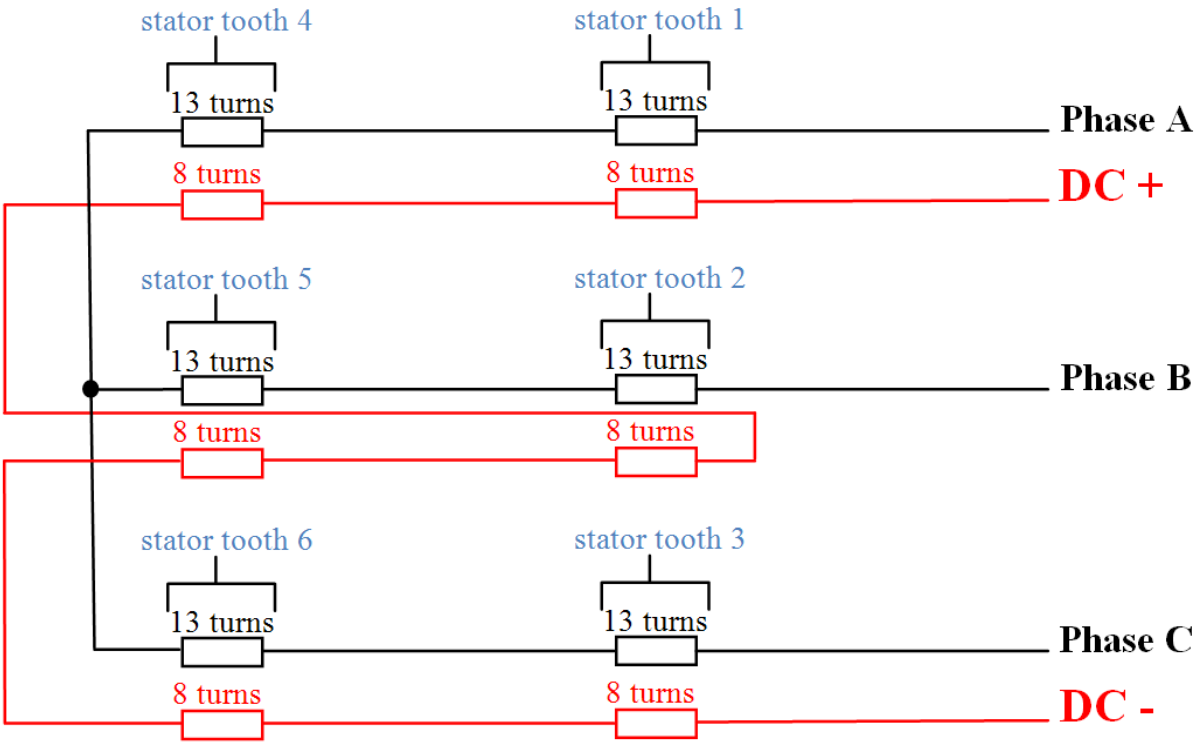

Fig. 7.41 Winding connection of 6 stator/4 rotor prototype machine under AC bipolar with DC bias excitation.

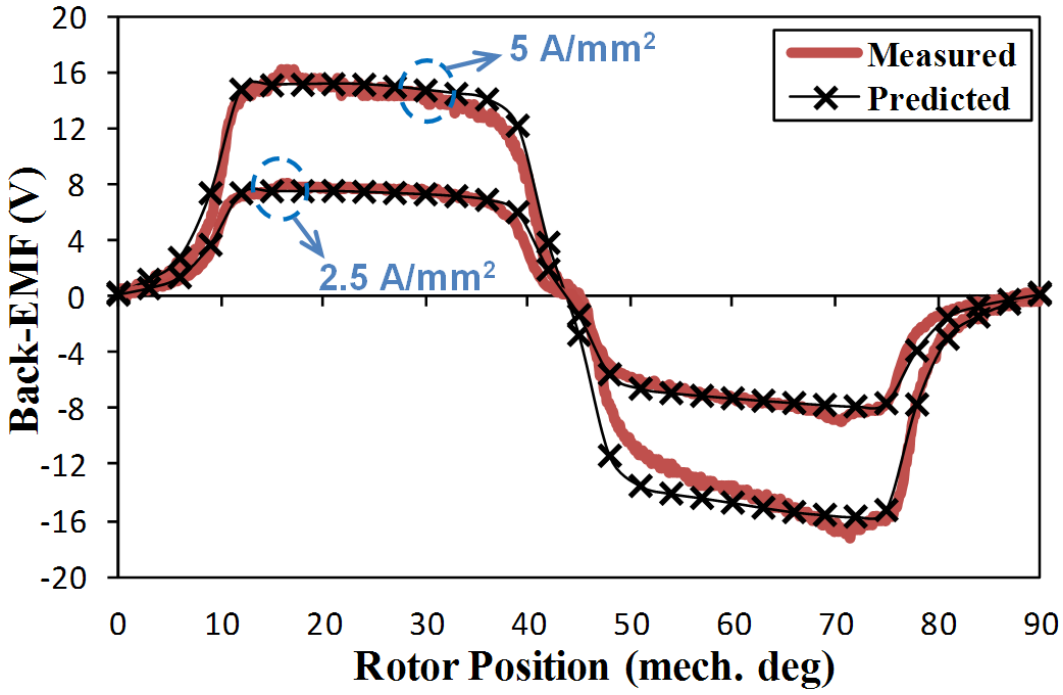

(a) Asymmetric winding connection

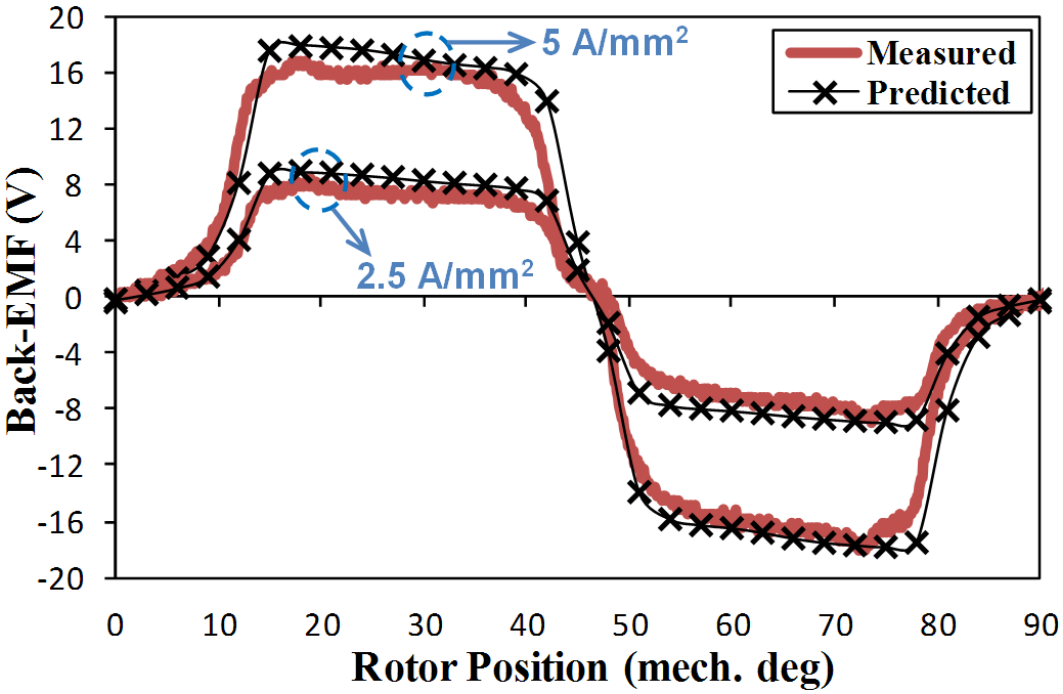

(b) Symmetric winding connection

Fig. 7.42 Comparison of measured and predicted back-emf waveforms of 6 stator/4 rotor prototype machine under different winding connections, at 2.5 and 5 A/mm^2 DC current densities and 2500 rpm.

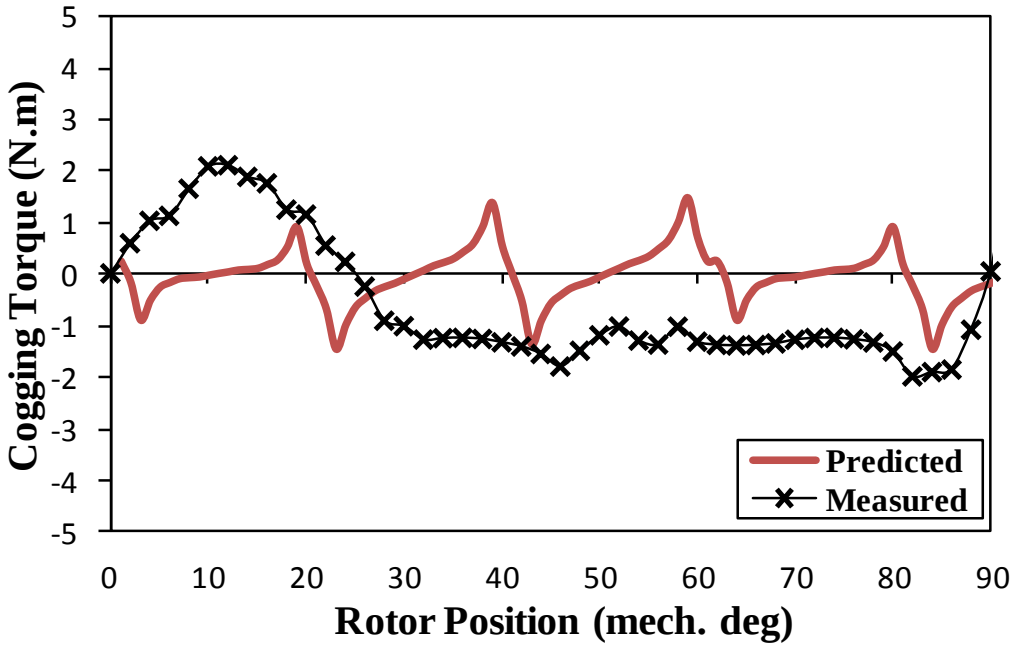

(a) Asymmetric winding connection, at 10 A/mm^2 current density

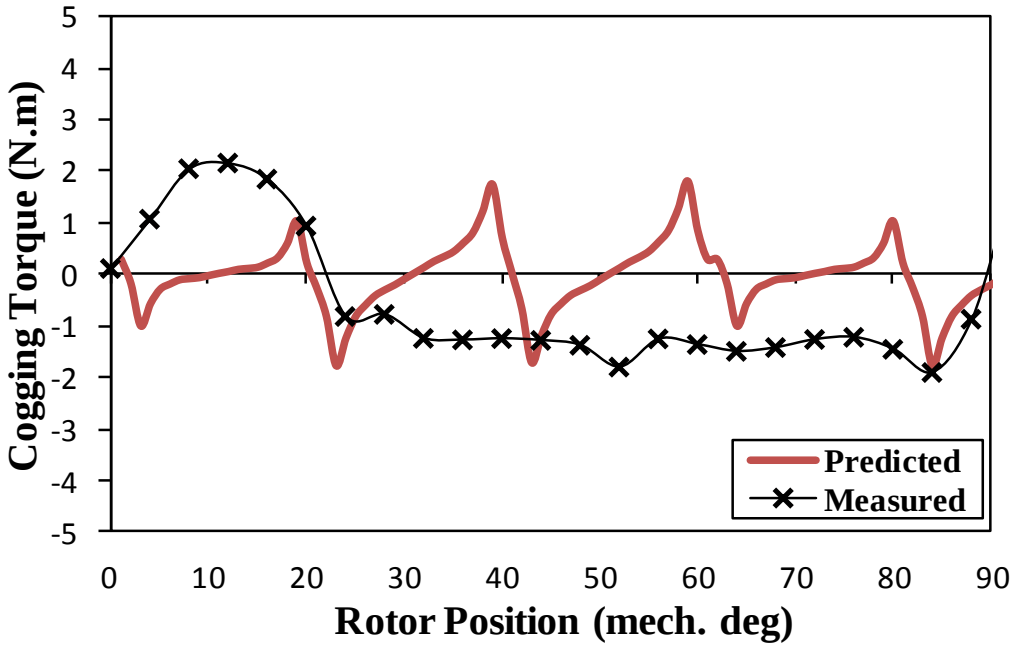

(b) Asymmetric winding connection, at 15 A/mm^2 current density

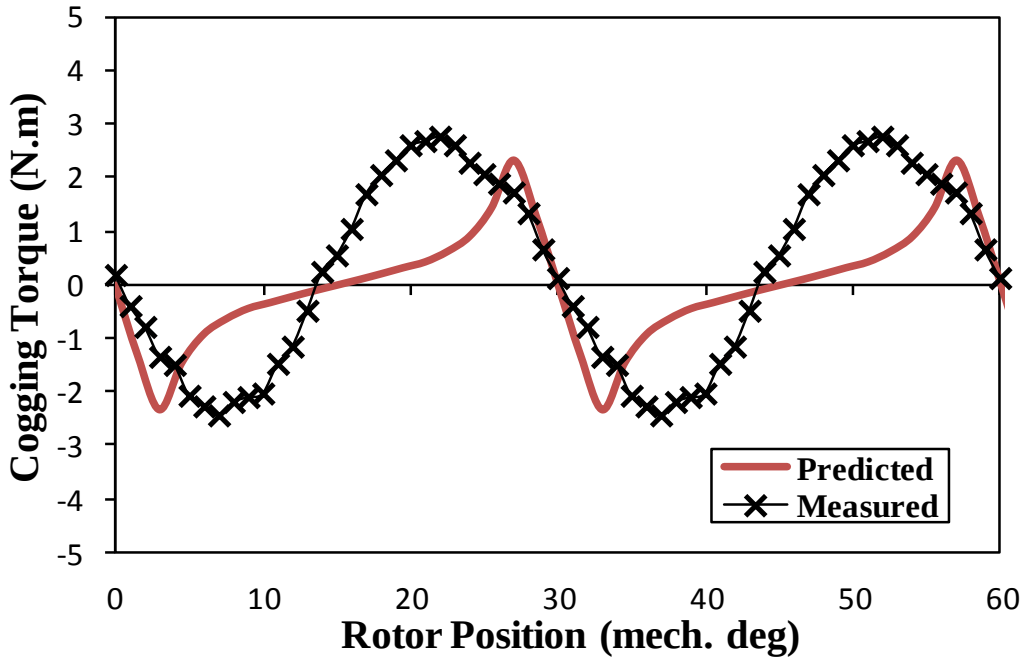

(c) Symmetric winding connection, at 10 A/mm^2 current density

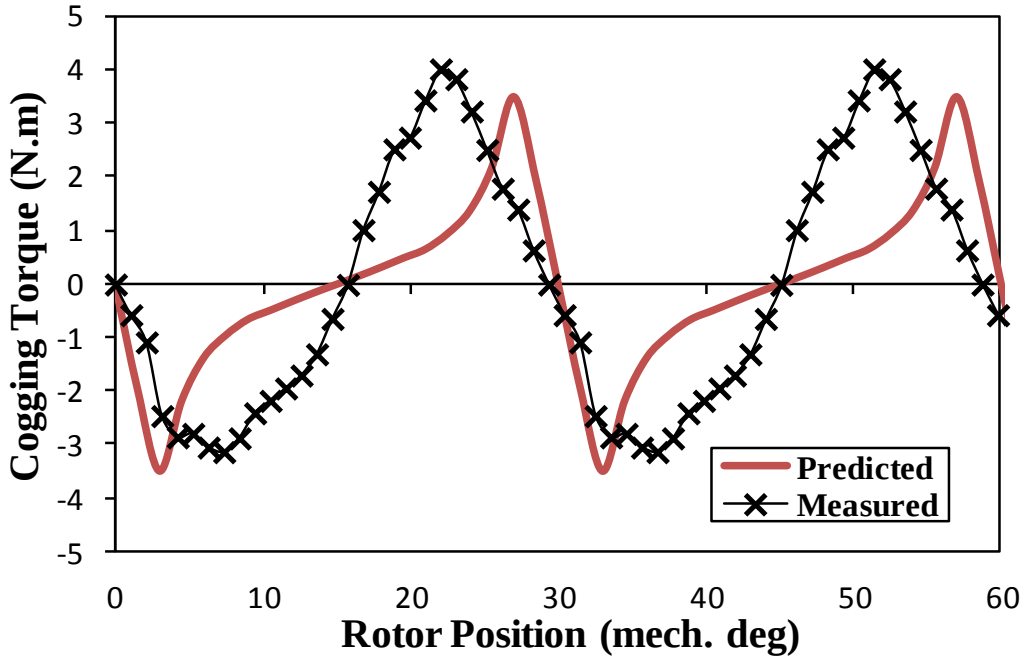

(d) Symmetric winding connection, at 15 A/mm^2 current density

Fig. 7.43 Comparison of measured and predicted cogging torque waveforms of 6 stator/4 rotor prototype machine under different winding connections and for different DC current densities.

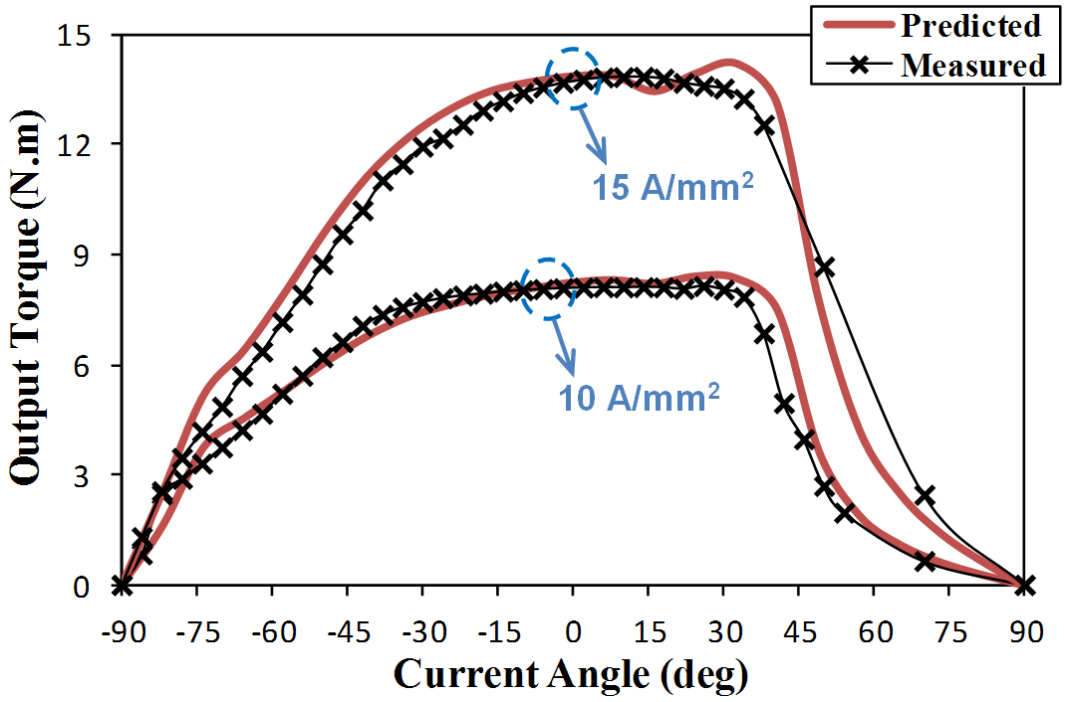

(a) Asymmetric winding connection

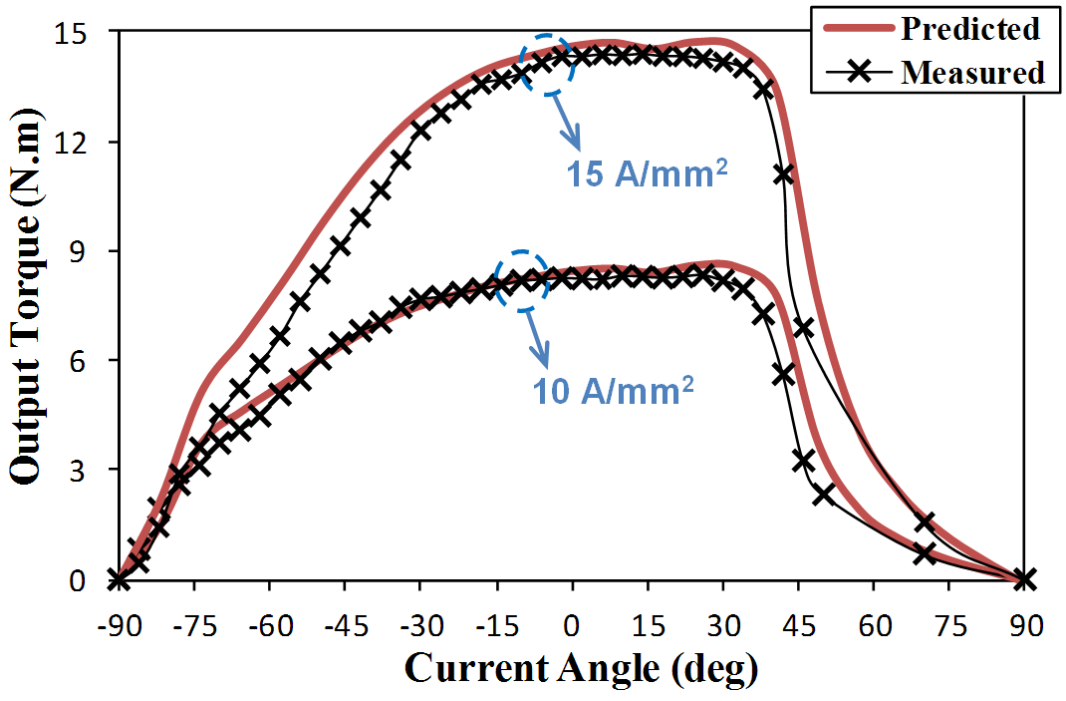

(b) Symmetric winding connection

Fig. 7.44 Comparison of measured and predicted output torque against AC phase current angle of 6 stator/4 rotor prototype machine under different winding connections, at 10 and 15 A/mm^2 total current densities and when AC and DC current densities are equal.

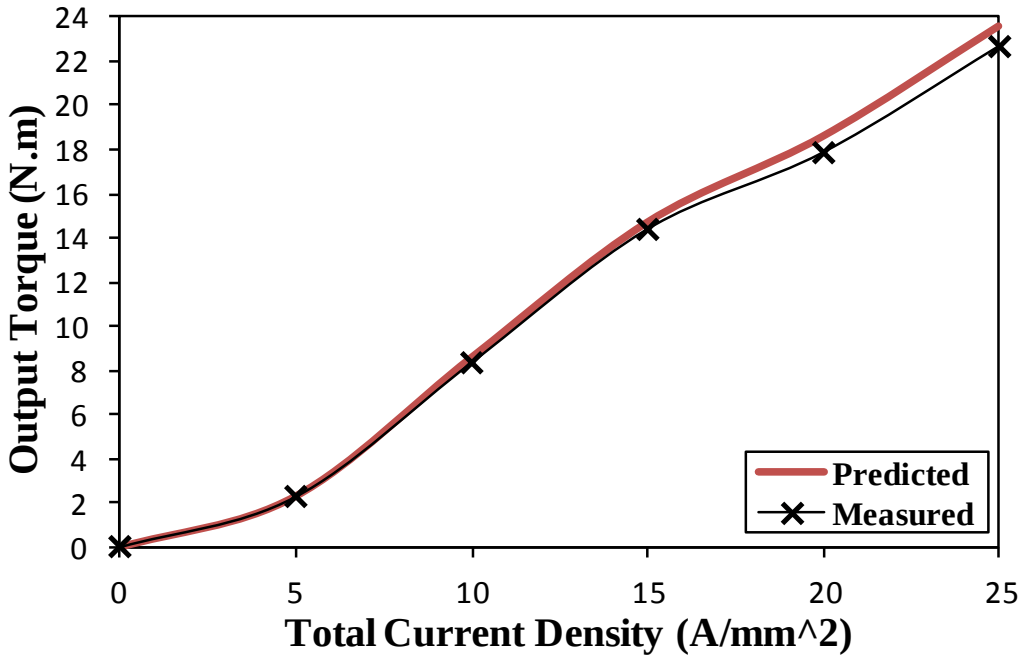

(a) Asymmetric winding connection

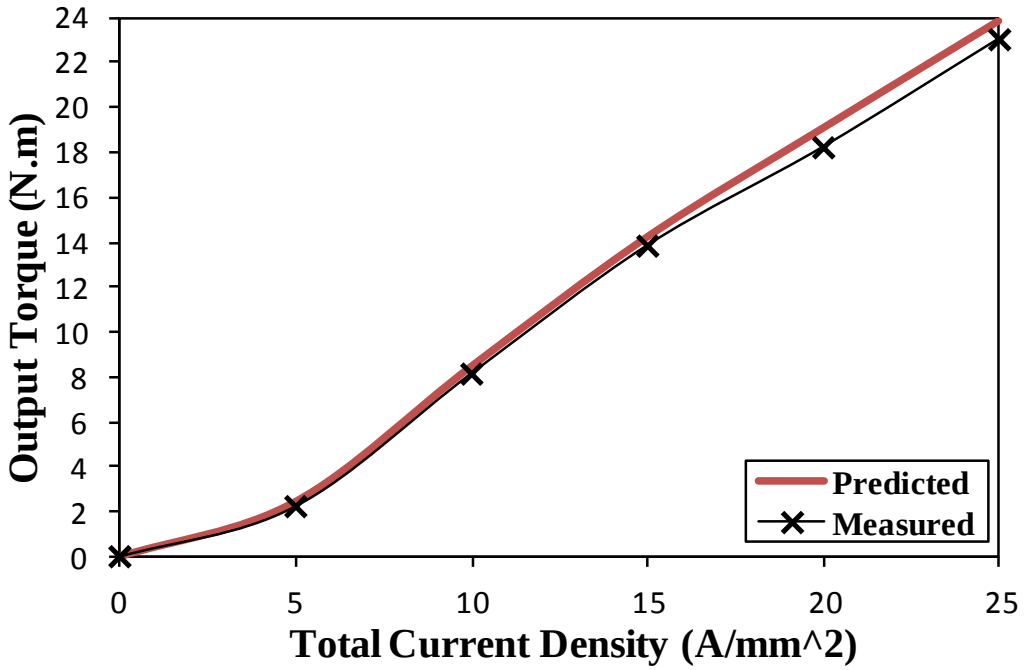

(b) Symmetric winding connection

Fig. 7.45 Comparison of measured and predicted output torque against current density of 6 stator/4 rotor prototype machine under different winding connections and for different current densities, when $I_q=I_{Phase}$, $I_d=0$ and AC and DC current densities are equal.

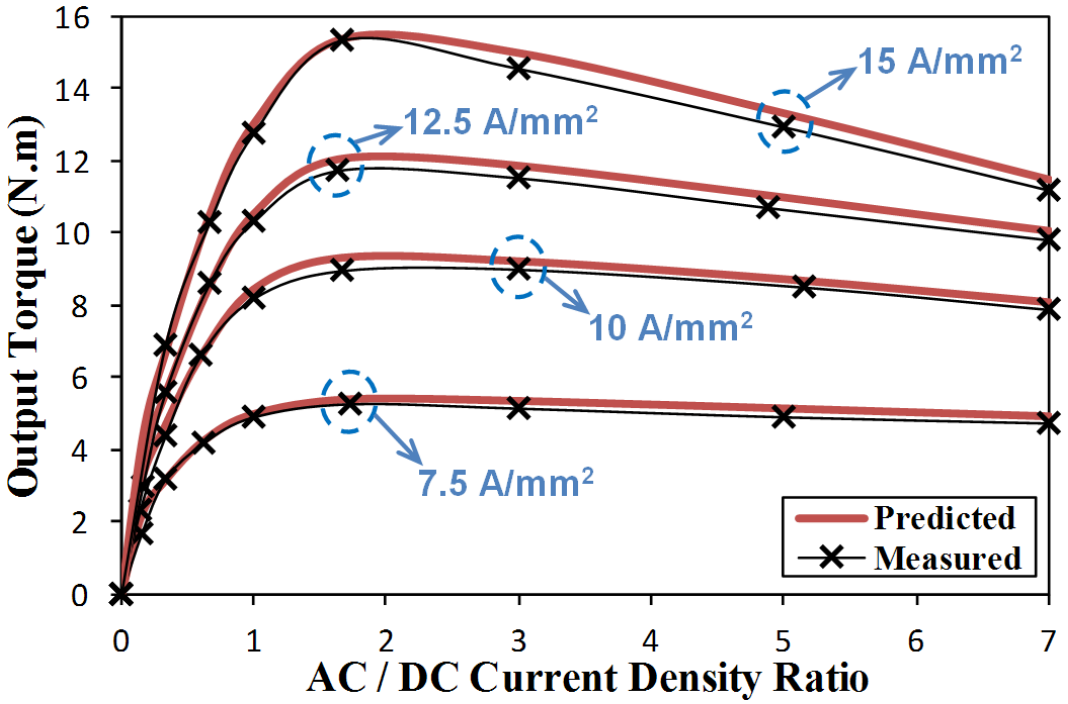

(a) Asymmetric winding connection

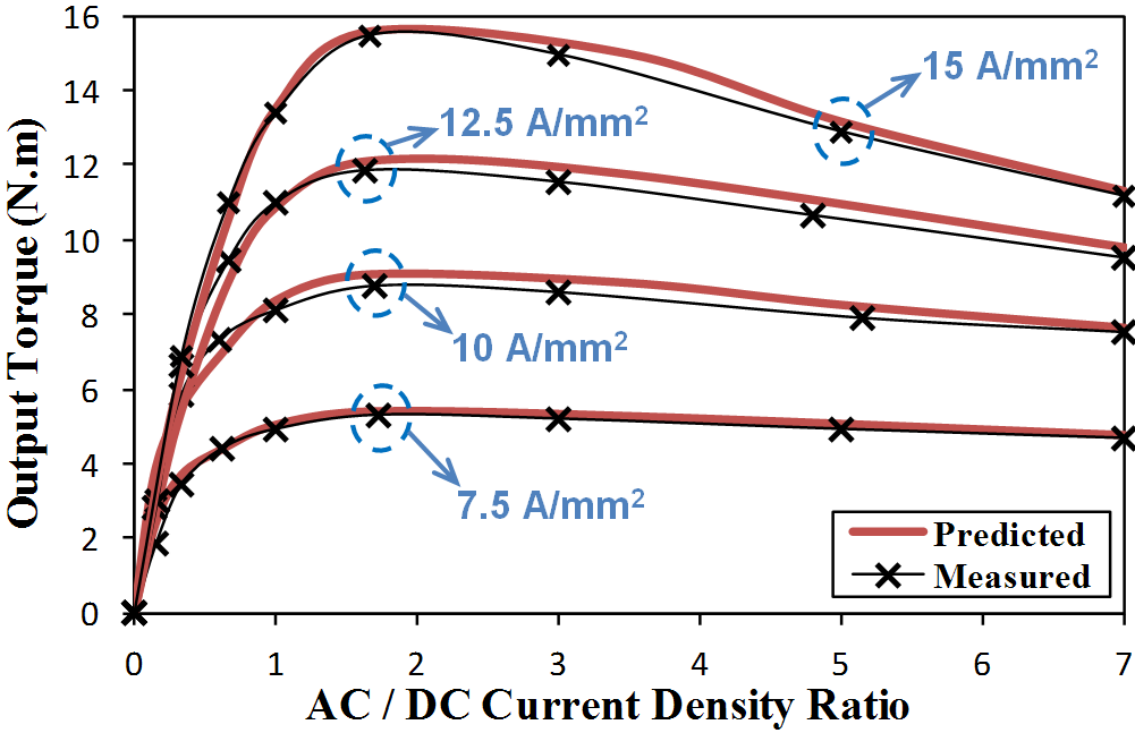

(b) Symmetric winding connection

Fig. 7.46 Comparison of measured and predicted output torque against AC/DC current density ratio of 6 stator/4 rotor prototype machine under different winding connections and for different total current densities.

7.8. Conclusions

The operation principles and electromagnetic performance of a 6 stator/4 rotor poles SynR machines having AC sinusoidal bipolar with DC bias excitation have been examined and analyzed. Both the asymmetric and symmetric winding connections have been taken into account during the investigations. Under such excitation, the machine becomes very similar to the PM counterparts. Thus, the DC bias, which is similar to the PM excitation, results in cogging torque and back-emf. In general, the cogging torque magnitude and period as well as back-emf waveforms strongly depend on the winding connection type. For example, at relatively large current densities the cogging torque magnitude due to asymmetric winding connection is much larger than its counterpart caused by the symmetric winding connection. However, this connection results in significantly larger cogging torque when the current density is relatively low. Furthermore, the asymmetric winding connection leads to larger back-emf when the DC bias is the larger. When the machine is occupied with symmetric winding connection such phenomenon is the same up to a specific DC bias value, i.e. 18 A/mm^2 in the studied machine. However, the back-emf starts gradually decreasing if the DC bias is further increased. This is due to different flux density distribution, thus different magnetic saturation sensitivity of each winding connection.

More importantly, the ability of the SynR machine to produce output torque under the proposed excitation has been proved. Furthermore, the generated output torque has been extensively investigated and the following conclusions have been obtained.

The optimal AC phase current angle depends on the winding connections, i.e. zero for the symmetric connection and 15 electrical degrees for its asymmetric counterpart. The symmetric winding connection results in much lower torque ripple. The maximum possible output torque can be delivered when the AC/DC ratio is 2 and the winding are symmetrically connected. However, a 1.75 AC/DC ratio could be more desirable, since it leads to nearly the same average torque as the optimal counterpart, i.e. 2, but significantly lower torque ripple and line voltage. Moreover, a relatively large torque-, power- and efficiency-speed characteristics can be obtained by operating the machine at 1.75 AC/DC ratio in the constant-torque region and at constant DC bias and adjusted AC current magnitude and angle in the flux weakening operation region.

The electromagnetic performance of the SR machine under AC bipolar with DC bias excitation has been compared with its counterparts under the conventional unipolar and AC

sinusoidal bipolar excitation. Comparing with the conventional unipolar excitation, the AC sinusoidal bipolar excitations, i.e. both without and with DC bias, result in significantly low torque ripple. The AC bipolar with DC bias excitation exhibits a relatively large average output torque and low losses, thus high efficiency. On the other hand, at relatively large current densities, the AC bipolar with hybrid winding connection offer the largest average torque and relatively low torque ripple percentage as well as high efficiency.

Chapter 8: General Conclusions

The electromagnetic performance of fractional-slot IPM machines having non-overlapping concentrated winding has been analysed and investigated in this thesis. The influence of the magnetic cross-coupling and saturation as well as manufacturing limitations and tolerances have been particularly examined.

Furthermore, the electromagnetic characteristics of the SR machine have been also analysed and compared under different excitations, i.e.

a). Conventional unipolar.
b). AC sinusoidal bipolar, i.e. salient-pole SynR machine.
c). AC sinusoidal bipolar with DC bias, i.e. salient-pole SynR machine with DC bias.

This chapter summarizes the conclusions obtained from the carried out research. In addition, it underlines the future works, which can be potentially undertaken to further expand the research area of this thesis.

8.1. PM Machines

8.1.1. Torque-Speed Characteristics

The FP method has been employed to separately examine the influence of the magnetic saturation and cross-coupling on the dq-axis parameters of the fractional-slot IPM machines having non-overlapping concentrated winding. The idea behind such investigation is to determine the level of the magnetic cross-coupling effect on each parameter and to find the simple yet accurate model to predict the torque-speed characteristics of such machines. The investigations have shown that the partial cross-coupling model, which considers that the PM flux is a function of q-axis current and the d- and q-axis inductances are each as a function of its corresponding current only, is a relatively simple yet accurate technique for predicting the torque-speed characteristics of such PM machines. This technique is compared with the direct finite element (FE) and dq-axis flux linkages prediction methods and verified by the experimental results.

8.1.2. Influence of Additional Stator Air Gaps

The influence of the additional stator gaps between segmented stator teeth and yoke, which exist due to manufacturing limits, on the electromagnetic performance, particularly the cogging torque, of PM machines having modular stators has been analysed. Both uniform and non-uniform additional stator gaps are studied. It has been found that:

a). The uniform additional stator gaps increase the cogging torque amplitude but have no effect on its periodicity.

b). The non-uniform stator gaps significantly increase both the amplitude and periodicity of the cogging torque.

c). The skewing technique, which is usually very effective in reducing cogging torque, becomes ineffective when the non-uniform additional stator gaps exist.

d). As confirmed by measurements, the non-uniformity of the additional stator gaps has a negligible influence on the back-emf waveform and the torque-speed characteristics.

8.1.3. Influence of Alternate Slot Openings

The influence of alternate slot openings, i.e. open slot, closed slot and hybrid slot, on the electromagnetic performance, mainly the torque-speed characteristics and cogging torque, of the fractional-slot IPM machines are investigated accounting for the influence of such slot openings on the cross-coupling level and manufacturing limitation and tolerance. It is concluded that:

a). The machine with the closed slot design, which significantly decreases the cogging torque, exhibits the lowest electromagnetic performance and also has a significantly large cross-coupling level comparing with the other two types of slot openings.

b). The machine with hybrid slot openings generates nearly the same torque as the machine with open slot, while its cogging torque is significantly smaller and is very similar to the machine with closed slots.

c). The influence of the cross-coupling on the PM flux linkage and dq-axis inductances depends on the slot opening type. However, the consideration of cross-coupling is more important on the PM flux linkage rather than the dq-axis inductances.

d). The cogging torque sensitivity against the additional stator gaps is strongly determined by the slot opening materials.

e). For all machines, the non-uniformity of such gaps causes a significant increase in the cogging torque and also diminishes the effectiveness of rotor skewing. However, this influence is comparatively more significant in the closed slot and hybrid slot designs.

8.1.4. Influence of Electric Loading and Magnetic Saturation

The cogging torque, back-emf and torque ripple of PM machines have been examined taking into account the influence of load conditions. The following conclusions can be drawn from the investigations:

a). The magnitude of the actual cogging torque, i.e. with the influence of the load conditions, is significantly larger than its open-circuit counterpart. This is due to the extra flux leakage through tooth tips due to higher saturation level in the stator teeth.

b). For the same reason, the actual back-emf waveform is comparatively more distorted, thus it contains larger harmonics and results in larger electromagnetic torque ripple.

c). The increase of actual cogging torque depends on the magnetic saturation level, which is determined by the value of the electric loading.

d). Due to the influence of electric loading, the actual cogging torque periodicity also varies to become the same as the torque ripple. Therefore, the skew technique, which is based on the open-circuit cogging torque period, becomes less effective.

e). The actual cogging torque thus the torque ripple can be effectively eliminated if the machine is skewed by one actual cogging period.

Furthermore, a comparison between different skew angle and step combinations has been carried out from the load torque ripple and electromagnet performance reduction points of view. It has been shown that for the prototype machine when the machine is skewed by 30 electrical degree and 2 skew steps, the load torque ripple is significantly suppressed while the electromagnet torque reduction is relatively small.

8.2. SynR Machines

8.2.1. AC Sinusoidal Bipolar Excitation

The electromagnetic performance of 6 stator/4 rotor poles SR machines having AC sinusoidal bipolar excitation, i.e. salient-pole SynR machine, and different non-overlapping concentrated winding connections, i.e. asymmetric, symmetric and hybrid, have been investigated. The following conclusions can be made:

a). In addition to the self inductance variation, the machine with hybrid winding connection has relatively larger mutual inductance variation. Thus, such machine exhibits relatively larger average output torque, low iron loss and high efficiency and comparing with the symmetric and asymmetric winding connections.

b). Comparing with the symmetric winding connection, its asymmetric winding counterpart has nearly the same average torque, but significantly larger torque ripple.

c). Due to the non-uniform flux linkage waveforms of machine which has an asymmetric winding connection, the phase voltage waveforms are also not uniform. Thus, the required DC-link voltage is much larger than the symmetric and hybrid winding connections.

d). The symmetric winding connection exhibits the lowest torque ripple and the widest flux weakening operation region as well as relatively larger efficiency at high speeds.

e). On the other hand, at significantly large current densities, i.e. high magnetic saturation level, the hybrid connection can also be an attractive choice, since it combines the significantly large output torque and relatively low torque ripple percentage with the relatively high efficiency.

Furthermore, the performances of the 6 stator/4 rotor poles machines having non-overlapping concentrated symmetric and hybrid winding connections have been compared with their 12 stator/4 rotor poles counterpart that has overlapping concentrated winding. It can be concluded that:

a). Comparing with the 6 stator/4 rotor poles machine, which has non-overlapping symmetric winding connection, the 12 stator/4 rotor poles machine produces significantly larger average output torque. However, this torque is lower than the

counterpart of the 6 stator/4 rotor machine with non-overlapping hybrid winding connection.

b). The 12 stator/4 rotor poles machine generates the largest output torque ripple since its flux linkage waveforms are comparatively more distorted.

c). For the same reason, the line voltage of the 12 stator/4 rotor poles machine is relatively large, thus it exhibits relatively narrow flux weakening operation region.

8.2.2. AC Sinusoidal Bipolar with DC Bias Excitation

The operation principle and electromagnetic performance of a 6 stator/4 rotor poles SR machines having AC sinusoidal bipolar excitation with DC bias excitation, i.e. SynR machines with DC bias excitation, have been analyzed. Both the asymmetric and symmetric winding connections have been taken into account during the investigations. Under such excitation:

a). The SynR machine becomes very similar to the PM counterparts. Thus, the DC bias, which is similar to the PMs excitation, results in cogging torque and back-emf, which strongly depend on the winding connection type.

b). At relatively large current densities, the machine cogging torque magnitude under the asymmetric winding connection is much larger than that with the symmetric winding connection, vice versa when the current density is relatively low.

c). The asymmetric winding connection leads to larger back-emf when the DC bias is the larger. When the machine is equipped with symmetric winding connection such phenomenon is the same up to a specific DC bias value, i.e. 18 A/mm^2 in the studied machine. However, the back-emf starts gradually decreasing if the DC bias is further increased. This is due to different magnetic saturation sensitivity for each winding connection.

More importantly, the ability of the SR machine to produce output torque under the proposed excitation has been proved. Furthermore, the generated output torque has been extensively investigated and the following conclusions have been obtained:

a). The optimal AC phase current angle depends on the winding connections, i.e. zero for the symmetric connection and 15 electrical degree for its asymmetric counterpart.

b). The maximum possible output torque of the machine can be delivered when the AC/DC ratio is 2 and the winding are symmetrically connected.

c). Comparing with the asymmetric wind connection, its symmetric counterpart results in much lower torque ripple. Therefore, such connection is more suitable to be utilized when the SR machine is excited by the AC sinusoidal bipolar with DC bias excitation.

d). The 1.75 AC/DC ratio is more desirable, since it leads to nearly the same average torque as its optimal counterpart, i.e. 2, but significantly lower torque ripple and line voltages.

e). A relatively large torque-, power- and efficiency-speed characteristics can be obtained by operating the machine at 1.75 AC/DC ratio.

8.2.3. Comparison of Different Excitation Techniques

The electromagnetic performance of the 6 stator/4 rotor poles SR machine has been compared under three different excitation techniques, i.e. conventional unipolar, AC sinusoidal bipolar, i.e. salient-pole SynR machines, without and with DC bias excitation. The following conclusions can be drawn out of this evaluation:

a). Comparing with the conventional unipolar excitation, the AC sinusoidal bipolar excitations, i.e. both without and with DC bias, result in significantly low torque ripple.

b). The machine, which is excited by the AC bipolar with the DC bias, exhibits a relatively large average output torque and power, and low losses, thus large efficiency.

c). At relatively large current densities, the AC sinusoidal bipolar excitation together with the hybrid winding connection offer the largest average torque and relatively low torque ripple percentage as well as a relatively large efficiency.

8.3. Future Work

The followings are some examples of the future possible work areas:

I. The influence of magnetic saturation and cross-coupling can be similarly investigated in the integral-slot IPM and other PM machine topologies.

II. The influence of the additional stator gaps in the PM machine having individual stator tooth/back-iron segments can be investigated and compared with those having the separated stator tooth and back-iron segments.

III. The influence of the non-uniform additional stator gaps together with the rotor eccentricity on the cogging torque and unbalanced magnetic forces can be examined.

IV. More investigations can be carried out to reduce the torque ripple of the SynR machine without and with DC bias excitation

V. The line voltage of the SR machine under the AC sinusoidal bipolar excitation can be further investigated toward reducing the required DC-link voltage, i.e. reducing the sharp voltage spike.

VI. Further investigations can be carried out to examine the ability of applying the dq-axis theory on the salient-pole SynR machine without and with DC bias excitation.

VII. The dynamic control performance of machine under alternate excitations.

The foregoing items IV to VII are currently being investigated by other PhD students in the Electrical Machines and Drives Research Group at The University of Sheffield.

References

[1] B. Fahimi, A. Emadi, and R. B. Sepe, "A switched reluctance machine-based starter/alternator for more electric cars," *Energy Conversion, IEEE Transactions on,* vol. 19, pp. 116-124, 2004.

[2] K. M. Rahman and S. E. Schulz, "Design of high-efficiency and high-torque-density switched reluctance motor for vehicle propulsion," *Industry Applications, IEEE Transactions on,* vol. 38, pp. 1500-1507, 2002.

[3] J. Chen, C. V. Nayar, and L. Xu, "Design and finite-element analysis of an outer-rotor permanent-magnet generator for directly coupled wind turbines," *Magnetics, IEEE Transactions on,* vol. 36, pp. 3802-3809, 2000.

[4] H. Li and Z. Chen, "Overview of different wind generator systems and their comparisons," *Renewable Power Generation, IET,* vol. 2, pp. 123-138, 2008.

[5] R. M. Saunders and R. H. Weakley, "Design of permanent-magnet alternators," *American Institute of Electrical Engineers, Transactions of the,* vol. 70, pp. 1578-1581, 1951.

[6] J. J. Germishuizen and M. J. Kamper, "IPM traction machine with single layer non-overlapping concentrated windings," *Industry Applications, IEEE Transactions on,* vol. 45, pp. 1387-1394, 2009.

[7] V. B. Honsinger, "Performance of polyphase permanent magnet machines," *Power Apparatus and Systems, IEEE Transactions on,* vol. PAS-99, pp. 1510-1518, 1980.

[8] E. C. Lovelace, T. Keim, J. H. Lang, D. D. Wentzloff, T. M. Jahns, J. Wai, and P. J. McCleer, "Design and experimental verification of a direct-drive interior PM synchronous machine using a saturable lumped-parameter model," in *Industry Applications Conference, 2002. 37th IAS Annual Meeting. Conference Record of the,* 2002, pp. 2486-2492 vol.4.

[9] F. W. Merrill, "Permanent-magnet excited synchronous motors," *Power Apparatus and Systems, Part III. Transactions of the American Institute of Electrical Engineers,* vol. 73, pp. 1754-1760, 1954.

[10] M. Rahman, T. Little, and G. Slemon, "Analytical models for interior-type permanent magnet synchronous motors," *Magnetics, IEEE Transactions on,* vol. 21, pp. 1741-1743, 1985.

[11] M. A. Rahman and T. A. Little, "Dynamic performance analysis of permanent magnet synchronous motors," *Power Engineering Review, IEEE,* vol. PER-4, pp. 40-40, 1984.

[12] S. Vaez, V. I. John, and M. A. Rahman, "An on-line loss minimization controller for interior permanent magnet motor drives," *Energy Conversion, IEEE Transactions on,* vol. 14, pp. 1435-1440, 1999.

[13] P. Zhou, M. A. Rahman, and M. A. Jabbar, "Field circuit analysis of permanent magnet synchronous motors," *Magnetics, IEEE Transactions on,* vol. 30, pp. 1350-1359, 1994.

[14] Z. Q. Zhu, Y. S. Chen, and D. Howe, "Maximising the flux-weakening capability of permanent magnet brushless AC machines and drives," in *Power Electronics and*

Motion Control Conference, 2000. Proceedings. IPEMC 2000. The Third International, 2000, pp. 552-557 vol.2.

[15] T. M. Jahns, "Torque production in permanent-magnet synchronous motor drives with rectangular current excitation," *Industry Applications, IEEE Transactions on*, vol. IA-20, pp. 803-813, 1984.

[16] Y. F. Shi, Z. Q. Zhu, and D. Howe, "Torque-speed characteristics of interior-magnet machines in brushless AC and DC modes, with particular reference to their flux-weakening performance," in *Power Electronics and Motion Control Conference, 2006. IPEMC 2006. CES/IEEE 5th International*, 2006, pp. 1-5.

[17] Z. Q. Zhu, J. X. Shen, and D. Howe, "Flux-weakening characteristics of trapezoidal back-EMF machines in brushless DC and AC modes," in *Power Electronics and Motion Control Conference, 2006. IPEMC 2006. CES/IEEE 5th International*, 2006, pp. 1-5.

[18] P. Pillay and R. Krishnan, "Application characteristics of permanent magnet synchronous and brushless DC motors for servo drives," *Industry Applications, IEEE Transactions on*, vol. 27, pp. 986-996, 1991.

[19] C. Anyuan, R. Nilssen, and A. Nysveen, "Performance comparisons among radial-flux, multistage axial-flux, and three-phase transverse-flux PM machines for downhole applications," *Industry Applications, IEEE Transactions on*, vol. 46, pp. 779-789, 2010.

[20] S. Y. Kwak, J. K. Kim, and H. K. Jung, "Characteristic analysis of multilayer-buried magnet synchronous motor using fixed permeability method," *Energy Conversion, IEEE Transactions on*, vol. 20, pp. 549-555, 2005.

[21] C. Ming, K. T. Chau, and C. C. Chan, "Static characteristics of a new doubly salient permanent magnet motor," *Energy Conversion, IEEE Transactions on*, vol. 16, pp. 20-25, 2001.

[22] L. Yuefeng, L. Feng, and T. A. Lipo, "A novel permanent magnet motor with doubly salient structure," *Industry Applications, IEEE Transactions on*, vol. 31, pp. 1069-1078, 1995.

[23] Z. Q. Zhu and J. T. Chen, "Advanced flux-switching permanent magnet brushless machines," *Magnetics, IEEE Transactions on*, vol. 46, pp. 1447-1453, 2010.

[24] Z. Q. Zhu, J. T. Chen, Y. Pang, D. Howe, S. Iwasaki, and R. Deodhar, "Analysis of a novel multi-tooth flux-switching PM brushless AC machine for high torque direct-drive applications," *Magnetics, IEEE Transactions on*, vol. 44, pp. 4313-4316, 2008.

[25] F. Profumo, Z. Zheng, and A. Tenconi, "Axial flux machines drives: a new viable solution for electric cars," *Industrial Electronics, IEEE Transactions on*, vol. 44, pp. 39-45, 1997.

[26] Z. Q. Zhu and C. C. Chan, "Electrical machine topologies and technologies for electric, hybrid, and fuel cell vehicles," in *Vehicle Power and Propulsion Conference, 2008. VPPC '08. IEEE*, 2008, pp. 1-6.

[27] K. Boughrara, R. Ibtiouen, x, D. arko, O. Touhami, and A. Rezzoug, "Magnetic field analysis of external rotor permanent-magnet synchronous motors using conformal mapping," *Magnetics, IEEE Transactions on*, vol. 46, pp. 3684-3693, 2010.

[28] S. Yang and Z. Q. Zhu, "Analytical prediction of optimal split ratio for fractional-slot external rotor PM brushless machines," *Magnetics, IEEE Transactions on,* vol. 47, pp. 4187-4190, 2011.

[29] A. M. E.-. Refaie and T. M. Jahns, "Comparison of synchronous PM machine types for wide constant-power speed operation: converter performance," *Electric Power Applications, IET,* vol. 1, pp. 217-222, 2007.

[30] K. Inagaki, A. Chiba, M. A. Rahman, and T. Fukao, "Performance characteristics of inset-type permanent magnet bearingless motor drives," in *Power Engineering Society Winter Meeting, 2000. IEEE*, 2000, pp. 202-207 vol.1.

[31] A. R. Munoz, F. Liang, and M. W. Degner, "Evaluation of interior PM and surface PM synchronous machines with distributed and concentrated windings," in *Industrial Electronics, 2008. IECON 2008. 34th Annual Conference of IEEE*, 2008, pp. 1189-1193.

[32] N. Bianchi and S. Bolognani, "Interior PM synchronous motor for high performance applications," in *Power Conversion Conference, 2002. PCC Osaka 2002. Proceedings of the*, 2002, pp. 148-153 vol.1.

[33] W. L. Soong, D. A. Staton, and T. J. E. Miller, "Design of a new axially-laminated interior permanent magnet motor," *Industry Applications, IEEE Transactions on,* vol. 31, pp. 358-367, 1995.

[34] W. L. Soong and N. Ertugrul, "Field-weakening performance of interior permanent-magnet motors," *Industry Applications, IEEE Transactions on,* vol. 38, pp. 1251-1258, 2002.

[35] Z. Q. Zhu and D. Howe, "Influence of design parameters on cogging torque in permanent magnet machines," *Energy Conversion, IEEE Transactions on,* vol. 15, pp. 407-412, 2000.

[36] Z. Li, S. Z. Jiang, Z. Q. Zhu, and C. C. Chan, "Analytical methods for minimizing cogging torque in permanent-magnet machines," *Magnetics, IEEE Transactions on,* vol. 45, pp. 2023-2031, 2009.

[37] K. Dong-Hun, P. Il-Han, L. Joon-Ho, and K. Chang-Eob, "Optimal shape design of iron core to reduce cogging torque of IPM motor," *Magnetics, IEEE Transactions on,* vol. 39, pp. 1456-1459, 2003.

[38] Z. Q. Zhu, S. Ruangsinchaiwanich, N. Schofield, and D. Howe, "Reduction of cogging torque in interior-magnet brushless machines," *Magnetics, IEEE Transactions on,* vol. 39, pp. 3238-3240, 2003.

[39] K. Gyu-Hong and H. Jin, "Analytical prediction and reduction of the cogging torque in interior permanent magnet motor," in *Electric Machines and Drives, 2005 IEEE International Conference on*, 2005, pp. 1620-1624.

[40] T. M. Jahns and W. L. Soong, "Pulsating torque minimization techniques for permanent magnet AC motor drives-a review," *Industrial Electronics, IEEE Transactions on,* vol. 43, pp. 321-330, 1996.

[41] N. Bianchi and S. Bolognani, "Design techniques for reducing the cogging torque in surface-mounted PM motors," *Industry Applications, IEEE Transactions on,* vol. 38, pp. 1259-1265, 2002.

[42] Z. Q. Zhu, A. S. Thomas, J. T. Chen, and G. W. Jewell, "Cogging torque in flux-switching permanent magnet machines," *Magnetics, IEEE Transactions on,* vol. 45, pp. 4708-4711, 2009.

[43] Z. Q. Zhu, J. T. Chen, L. J. Wu, and D. Howe, "Influence of stator asymmetry on cogging torque of permanent magnet brushless machines," *Magnetics, IEEE Transactions on,* vol. 44, pp. 3851-3854, 2008.

[44] L. Gasparin, A. Cernigoj, S. Markic, and R. Fiser, "Additional cogging torque components in permanent-magnet motors due to manufacturing imperfections," *Magnetics, IEEE Transactions on,* vol. 45, pp. 1210-1213, 2009.

[45] J. Zou, J. Hu, and W. Liang, "Quantitatively evaluation on the cogging torque of permanent magnet motor caused by stator and rotor defect," in *Power Electronics and Drive Systems, 2003. PEDS 2003. The Fifth International Conference on,* 2003, pp. 682-685 Vol.1.

[46] L. Gasparin and R. Fiser, "Intensity of the native and additional harmonic components in cogging torque due to design parameters of permanent-magnet motors," in *Power Electronics and Drive Systems, 2009. PEDS 2009. International Conference on,* 2009, pp. 1062-1067.

[47] M. S. Islam, S. Mir, and T. Sebastian, "Issues in reducing the cogging torque of mass-produced permanent-magnet brushless DC motor," *Industry Applications, IEEE Transactions on,* vol. 40, pp. 813-820, 2004.

[48] G. Ombach and J. Junak, "Design of PM brushless motor taking into account tolerances of mass production-six sigma design method," in *Industry Applications Conference, 2007. 42nd IAS Annual Meeting. Conference Record of the 2007 IEEE*, 2007, pp. 2139-2146.

[49] G. Qi, J. T. Chen, Z. Q. Zhu, D. Howe, L. B. Zhou, and C. L. Gu, "Influence of skew and cross-coupling on flux-weakening performance of permanent-magnet brushless AC machines," *Magnetics, IEEE Transactions on,* vol. 45, pp. 2110-2117, 2009.

[50] K. Gyu-Hong, H. Jung-Pyo, K. Gyu-Tak, and P. Jung-Woo, "Improved parameter modeling of interior permanent magnet synchronous motor based on finite element analysis," *Magnetics, IEEE Transactions on,* vol. 36, pp. 1867-1870, 2000.

[51] B. Stumberger, G. Stumberger, D. Dolinar, A. Hamler, and M. Trlep, "Evaluation of saturation and cross-magnetization effects in interior permanent-magnet synchronous motor," *Industry Applications, IEEE Transactions on,* vol. 39, pp. 1264-1271, 2003.

[52] A. M. El-Serafi and J. Wu, "Determination of the parameters representing the cross-magnetizing effect in saturated synchronous machines," *Energy Conversion, IEEE Transactions on,* vol. 8, pp. 333-342, 1993.

[53] P. Vas, J. E. Brown, and K. E. Hallenius, "Cross-saturation in smooth-air-gap electrical machines," *Power Engineering Review, IEEE*, vol. PER-6, pp. 37-37, 1986.

[54] J. Hu, J. Zou, and W. Liang, "Finite element calculation of the saturation DQ-axes inductance for a direct drive PM synchronous motor considering cross-magnetization," in *Power Electronics and Drive Systems, 2003. PEDS 2003. The Fifth International Conference on,* 2003, pp. 677-681 Vol.1.

[55] N. Bianchi and S. Bolognani, "Magnetic models of saturated interior permanent magnet motors based on finite element analysis," in *Industry Applications Conference, 1998. Thirty-Third IAS Annual Meeting. The 1998 IEEE*, 1998, pp. 27-34 vol.1.

[56] A. M. El-Serafi, A. S. Abdallah, M. K. El-Sherbiny, and E. H. Badawy, "Experimental study of the saturation and the cross-magnetizing phenomenon in saturated synchronous machines," *Energy Conversion, IEEE Transactions on,* vol. 3, pp. 815-823, 1988.

[57] E. Levi and V. A. Levi, "Impact of dynamic cross-saturation on accuracy of saturated synchronous machine models," *Energy Conversion, IEEE Transactions on,* vol. 15, pp. 224-230, 2000.

[58] D. M. Ionel, J. F. Eastham, T. J. E. Miller, and E. Demeter, "Design considerations for permanent magnet synchronous motors for flux weakening applications," *Electric Power Applications, IEE Proceedings -*, vol. 145, pp. 435-440, 1998.

[59] Z. Azar, L. J. Wu, D. Evans, and Z. Q. Zhu, "Influence of rotor configuration on iron and magnet losses of fractional-slot IPM machines," in *Power Electronics, Machines and Drives (PEMD 2010), 5th IET International Conference on*, 2010, pp. 1-6.

[60] R. F. Schiferl and T. A. Lipo, "Power capability of salient pole permanent magnet synchronous motors in variable speed drive applications," *Industry Applications, IEEE Transactions on,* vol. 26, pp. 115-123, 1990.

[61] S. Morimoto, M. Sanada, and Y. Takeda, "Wide-speed operation of interior permanent magnet synchronous motors with high-performance current regulator," *Industry Applications, IEEE Transactions on,* vol. 30, pp. 920-926, 1994.

[62] M. T. Abolhassani, "A novel multiphase fault tolerant high torque density permanent magnet motor drive for traction application," in *Electric Machines and Drives, 2005 IEEE International Conference on*, 2005, pp. 728-734.

[63] J. Sang-Yong, "Numerical identification of D and Q axis parameters for multi-layer buried PM synchronous motor considering cross-magnetization," in *Electrical Machines and Systems, 2007. ICEMS. International Conference on*, 2007, pp. 729-734.

[64] Y. S. Chen, Z. Q. Zhu, and D. Howe, "Calculation of d- and q-axis inductances of PM brushless ac machines accounting for skew," *Magnetics, IEEE Transactions on*, vol. 41, pp. 3940-3942, 2005.

[65] X. B. Bomela and M. J. Kamper, "Effect of stator chording and rotor skewing on performance of reluctance synchronous machine," *Industry Applications, IEEE Transactions on,* vol. 38, pp. 91-100, 2002.

[66] J. A. Walker, D. G. Dorrell, and C. Cossar, "Flux-linkage calculation in permanent-magnet motors using the frozen permeabilities method," *Magnetics, IEEE Transactions on,* vol. 41, pp. 3946-3948, 2005.

[67] J. K. Tangudu, T. M. Jahns, A. M. El-Refaie, and Z. Q. Zhu, "Segregation of torque components in fractional-slot concentrated-winding interior PM machines using frozen permeability," in *Energy Conversion Congress and Exposition, 2009. ECCE 2009. IEEE*, 2009, pp. 3814-3821.

[68] L. Chong and M. F. Rahman, "Comparison of d- and q-axis inductances in an IPM machine with integral-slot distributed and fractional-slot concentrated windings," in *Electrical Machines, 2008. ICEM 2008. 18th International Conference on*, 2008, pp. 1-5.

[69] M. M. Liwschitz, "Distribution factors and pitch factors of the harmonics of a fractional-slot winding," *American Institute of Electrical Engineers, Transactions of the*, vol. 62, pp. 664-666, 1943.

[70] T. D. Nguyen and K. J. Tseng, "Comparison of axial flux permanent magnet machines with fractional and integral slot per pole," in *Power and Energy Society General Meeting, 2011 IEEE*, 2011, pp. 1-5.

[71] N. Bianchi and M. Dai Pre, "Use of the star of slots in designing fractional-slot single-layer synchronous motors," *Electric Power Applications, IEE Proceedings -*, vol. 153, pp. 459-466, 2006.

[72] M. Barcaro and N. Bianchi, "Torque components in integral- and fractional-slot IPM machines," in *Electric Machines & Drives Conference (IEMDC), 2011 IEEE International*, 2011, pp. 1340-1345.

[73] G. H. Jang, J. W. Yoon, N. Y. Park, and S. M. Jang, "Torque and unbalanced magnetic force in a rotational unsymmetric brushless DC motors," *Magnetics, IEEE Transactions on*, vol. 32, pp. 5157-5159, 1996.

[74] Z. Q. Zhu, D. Ishak, D. Howe, and J. Chen, "Unbalanced magnetic forces in permanent-magnet brushless machines with diametrically asymmetric phase windings," *Industry Applications, IEEE Transactions on*, vol. 43, pp. 1544-1553, 2007.

[75] J. Germishuizen and M. Kamper, "Design and performance characteristics of IPM machines with single layer non-overlapping concentrated windings," in *Industry Applications Conference, 2007. 42nd IAS Annual Meeting. Conference Record of the 2007 IEEE*, 2007, pp. 141-147.

[76] A. M. El-Refaie and T. M. Jahns, "Optimal flux weakening in surface PM machines using fractional-slot concentrated windings," *Industry Applications, IEEE Transactions on*, vol. 41, pp. 790-800, 2005.

[77] J. K. Tangudu and T. M. Jahns, "Comparison of interior PM machines with concentrated and distributed stator windings for traction applications," in *Vehicle Power and Propulsion Conference (VPPC), 2011 IEEE*, 2011, pp. 1-8.

[78] M. Inoue, Y. Kuroda, S. Nishimura, and H. Akita, "An evaluation of concentrated and distributed windings in interior PM and claw pole motors," in *Power Electronics and ECCE Asia (ICPE & ECCE), 2011 IEEE 8th International Conference on*, 2011, pp. 176-183.

[79] Z. Deming, Q. Xin, Z. Nan, and Y. Yangguang, "A comparative study of winding factors between distributed windings and non-overlapping concentrated windings," in *Electric Utility Deregulation and Restructuring and Power Technologies, 2008. DRPT 2008. Third International Conference on*, 2008, pp. 2725-2729.

[80] F. Magnussen, P. Thelin, and C. Sadarangani, "Performance evaluation of permanent magnet synchronous machines with concentrated and distributed windings including

the effect of field-weakening," in *Power Electronics, Machines and Drives, 2004. (PEMD 2004). Second International Conference on (Conf. Publ. No. 498)*, 2004, pp. 679-685 Vol.2.

[81] F. Magnussen and H. Lendenmann, "Parasitic effects in PM machines with concentrated windings," *Industry Applications, IEEE Transactions on*, vol. 43, pp. 1223-1232, 2007.

[82] N. Bianchi, S. Bolognani, M. D. Pre, and G. Grezzani, "Design considerations for fractional-slot winding configurations of synchronous machines," *Industry Applications, IEEE Transactions on*, vol. 42, pp. 997-1006, 2006.

[83] D. Ishak, Z. Q. Zhu, and D. Howe, "Eddy-current loss in the rotor magnets of permanent-magnet brushless machines having a fractional number of slots per pole," *Magnetics, IEEE Transactions on*, vol. 41, pp. 2462-2469, 2005.

[84] P. Salminen, M. Niemela, J. Pyhonen, and J. Mantere, "Performance analysis of fractional slot wound PM-motors for low speed applications," in *Industry Applications Conference, 2004. 39th IAS Annual Meeting. Conference Record of the 2004 IEEE*, 2004, pp. 1032-1037 vol.2.

[85] J. Wang, K. Atallah, Z. Q. Zhu, and D. Howe, "Modular 3-phase permanent magnet brushless machines for in-wheel applications," in *Vehicle Power and Propulsion Conference, 2006. VPPC '06. IEEE*, 2006, pp. 1-6.

[86] O. K. Soon, K. Sung-Il, Z. Peng, and H. Jung-Pyo, "Performance comparison of IPMSM with distributed and concentrated windings," in *Industry Applications Conference, 2006. 41st IAS Annual Meeting. Conference Record of the 2006 IEEE*, 2006, pp. 1984-1988.

[87] P. Salminen, M. Niemela, J. Pyrhonen, and J. Mantere, "High-torque low-torque-ripple fractional-slot PM-motors," in *Electric Machines and Drives, 2005 IEEE International Conference on*, 2005, pp. 144-148.

[88] A. M. El-Refaie and T. M. Jahns, "Comparison of synchronous PM machine types for wide constant-power speed range operation," in *Industry Applications Conference, 2005. Fourtieth IAS Annual Meeting. Conference Record of the 2005*, 2005, pp. 1015-1022 Vol. 2.

[89] A. M. El-Refaie, "Fractional-slot concentrated-windings synchronous permanent magnet machines: opportunities and challenges," *Industrial Electronics, IEEE Transactions on*, vol. 57, pp. 107-121, 2010.

[90] Z. Q. Zhu, K. Ng, N. Schofield, and D. Howe, "Improved analytical modelling of rotor eddy current loss in brushless machines equipped with surface-mounted permanent magnets," *Electric Power Applications, IEE Proceedings -*, vol. 151, pp. 641-650, 2004.

[91] K. Atallah, D. Howe, P. H. Mellor, and D. A. Stone, "Rotor loss in permanent-magnet brushless AC machines," *Industry Applications, IEEE Transactions on*, vol. 36, pp. 1612-1618, 2000.

[92] H. Wan-Ying, A. Bettayeb, R. Kaczmarek, and J. C. Vannier, "Optimization of magnet segmentation for reduction of eddy-current losses in permanent magnet

synchronous machine," *Energy Conversion, IEEE Transactions on,* vol. 25, pp. 381-387, 2010.

[93] A. M. El-Refaie and T. M. Jahns, "Impact of winding layer number and magnet type on synchronous surface PM machines designed for wide constant-power speed range operation," *Energy Conversion, IEEE Transactions on,* vol. 23, pp. 53-60, 2008.

[94] A. Emadi, L. Young Joo, and K. Rajashekara, "Power electronics and motor drives in electric, hybrid electric, and plug-in hybrid electric vehicles," *Industrial Electronics, IEEE Transactions on,* vol. 55, pp. 2237-2245, 2008.

[95] C. C. Chan and K. T. Chau, "An overview of power electronics in electric vehicles," *Industrial Electronics, IEEE Transactions on,* vol. 44, pp. 3-13, 1997.

[96] K. Vijayakumar, R. Karthikeyan, S. Paramasivam, R. Arumugam, and K. N. Srinivas, "Switched reluctance motor modeling, design, simulation, and analysis: a comprehensive review," *Magnetics, IEEE Transactions on,* vol. 44, pp. 4605-4617, 2008.

[97] G. W. Buckley, "Switched reluctance motors," in *Electrical Electronics Insulation Conference, 1995, and Electrical Manufacturing & Coil Winding Conference. Proceedings*, 1995, pp. 341-344.

[98] K. M. Rahman, B. Fahimi, G. Suresh, A. V. Rajarathnam, and M. Ehsani, "Advantages of switched reluctance motor applications to EV and HEV: design and control issues," *Industry Applications, IEEE Transactions on,* vol. 36, pp. 111-121, 2000.

[99] N. Schofield and S. Long, "Generator operation of a switched reluctance starter/generator at extended speeds," *Vehicular Technology, IEEE Transactions on,* vol. 58, pp. 48-56, 2009.

[100] G. J. Li, J. Ojeda, E. Hoang, M. Lecrivain, and M. Gabsi, "Comparative studies between classical and mutually coupled switched reluctance motors using thermal-electromagnetic analysis for driving cycles," *Magnetics, IEEE Transactions on,* vol. 47, pp. 839-847, 2011.

[101] J. A. Haylock, B. C. Mecrow, A. G. Jack, and D. J. Atkinson, "Operation of fault tolerant machines with winding failures," *Energy Conversion, IEEE Transactions on,* vol. 14, pp. 1490-1495, 1999.

[102] V. P. Vujicic, "Modeling of a switched reluctance machine based on the invertible torque function," *Magnetics, IEEE Transactions on,* vol. 44, pp. 2186-2194, 2008.

[103] R. S. Colby, F. M. Mottier, and T. J. E. Miller, "Vibration modes and acoustic noise in a four-phase switched reluctance motor," *Industry Applications, IEEE Transactions on,* vol. 32, pp. 1357-1364, 1996.

[104] S. A. Long, Z. Q. Zhu, and D. Howe, "Influence of load on noise and vibration of voltage and current controlled switched reluctance machines," in *Power Electronics, Machines and Drives, 2002. International Conference on (Conf. Publ. No. 487)*, 2002, pp. 534-539.

[105] N. T. Shaked and R. Rabinovici, "New procedures for minimizing the torque ripple in switched reluctance motors by optimizing the phase-current profile," *Magnetics, IEEE Transactions on,* vol. 41, pp. 1184-1192, 2005.

[106] M. Krishnamurthy, C. S. Edrington, A. Emadi, P. Asadi, M. Ehsani, and B. Fahimi, "Making the case for applications of switched reluctance motor technology in automotive products," *Power Electronics, IEEE Transactions on,* vol. 21, pp. 659-675, 2006.

[107] W. F. Ray, P. J. Lawrenson, R. M. Davis, J. M. Stephenson, N. N. Fulton, and R. J. Blake, "High-performance switched reluctance brushless drives," *Industry Applications, IEEE Transactions on,* vol. IA-22, pp. 722-730, 1986.

[108] C. Pollock and A. Michaelides, "Switched reluctance drives: a comparative evaluation," *Power Engineering Journal,* vol. 9, pp. 257-266, 1995.

[109] B. C. Mecrow, "New winding configurations for doubly salient reluctance machines," *Industry Applications, IEEE Transactions on,* vol. 32, pp. 1348-1356, 1996.

[110] L. Feng, L. Yuefeng, and T. A. Lipo, "A new variable reluctance motor utilizing an auxiliary commutation winding," *Industry Applications, IEEE Transactions on,* vol. 30, pp. 423-432, 1994.

[111] B. C. Mecrow, "Fully pitched-winding switched-reluctance and stepping-motor arrangements," *Electric Power Applications, IEE Proceedings B,* vol. 140, pp. 61-70, 1993.

[112] J. M. Kokernak and D. A. Torrey, "Magnetic circuit model for the mutually coupled switched-reluctance machine," *Magnetics, IEEE Transactions on,* vol. 36, pp. 500-507, 2000.

[113] G. J. Li, X. Ojeda, S. Hlioui, E. Hoang, M. Gabsi, and C. Balpe, "Comparative study of switched reluctance motors performances for two current distributions and excitation modes," in *Industrial Electronics, 2009. IECON '09. 35th Annual Conference of IEEE*, 2009, pp. 4047-4052.

[114] F. Sahin, H. B. Ertan, and K. Leblebicioglu, "Optimum geometry for torque ripple minimization of switched reluctance motors," *Energy Conversion, IEEE Transactions on,* vol. 15, pp. 30-39, 2000.

[115] J. W. Ahn, H. G. Kim, and T. H. Kim, "Comparisons of excitation methods for EV-SR drive," in *Electrical Machines and Systems, 2005. ICEMS 2005. Proceedings of the Eighth International Conference on*, 2005, pp. 639-643 Vol. 1.

[116] R. T. Naayagi and V. Kamaraj, "Minimization of torque ripple in switched reluctance machine for direct drive applications," in *Emerging Technologies, 2005. Proceedings of the IEEE Symposium on*, 2005, pp. 388-392.

[117] C. Yong Kwon, Y. Hee Sung, and K. Chang Seop, "Pole-shape optimization of a switched-reluctance motor for torque ripple reduction," *Magnetics, IEEE Transactions on,* vol. 43, pp. 1797-1800, 2007.

[118] J. Hur, G. H. Kang, J. Y. Lee, J. P. Hong, and B. K. Lee, "Design and optimization of high torque, low ripple switched reluctance motor with flux barrier for direct drive," in *Industry Applications Conference, 2004. 39th IAS Annual Meeting. Conference Record of the 2004 IEEE*, 2004, p. 407 Vol.1.

[119] X. Chen, Z. Deng, J. Peng, and X. Li, "Comparison of two switched reluctance motors with bipolar excitation," in *Power Electronics, Machines and Drives (PEMD 2010), 5th IET International Conference on*, 2010, pp. 1-6.

[120] X. Liu, Z. Q. Zhu, M. Hasegawa, A. Pride, R. Deodhar, T. Maruyama, and Z. Chen, "Performance comparison between unipolar and bipolar excitations in switched reluctance machine with sinusoidal and rectangular waveforms," in *Energy Conversion Congress and Exposition (ECCE), 2011 IEEE*, 2011, pp. 1590-1595.

[121] X. Liu, Z. Q. Zhu, M. Hasegawa, A. Pride, R. Deodhar, T. Maruyama, and Z. Chen, "DC-link capacitance requirement and noise and vibration reduction in 6/4 switched reluctance machine with sinusoidal bipolar excitation," in *Energy Conversion Congress and Exposition (ECCE), 2011 IEEE*, 2011, pp. 1596-1603.

[122] X. Liu, Z. P. Pan, and Z. Q. Zhu, "Analysis of average torque in switched reluctance motor with unipolar and bipolar excitations based on an improved Fourier series model," in *Vehicle Power and Propulsion Conference (VPPC), 2010 IEEE*, 2010, pp. 1-6.

[123] X. Ojeda, X. Mininger, M. Gabsi, and M. Lecrivain, "Sinusoidal feeding for switched reluctance machine: application to vibration damping," in *Electrical Machines, 2008. ICEM 2008. 18th International Conference on*, 2008, pp. 1-4.

[124] P. Debiprasad and V. Ramanarayanan, "Mutual coupling and its effect on steady-state performance and position estimation of even and odd number phase switched reluctance motor drive," *Magnetics, IEEE Transactions on,* vol. 43, pp. 3445-3456, 2007.

[125] Z. Q. Zhu, "Fractional slot permanent magnet brushless machines and drives for electric and hybrid propulsion systems," *International Journal for Computation & Mathematics in Electrical & Electronic Engineering,* vol. 30, pp. 9-31, 2011.

[126] Y. S. Chen, Z. Q. Zhu, and D. Howe, "Influence of inaccuracies in machine parameters on field-weakening performance of PM brushless AC drives," in *Electric Machines and Drives, 1999. International Conference IEMD '99*, 1999, pp. 691-693.

[127] D. M. Ionel, M. J. Balchin, J. F. Eastham, and E. Demeter, "Finite element analysis of brushless DC motors for flux weakening operation," *Magnetics, IEEE Transactions on,* vol. 32, pp. 5040-5042, 1996.

[128] H. Nagura, Y. Iwaji, J. Nakatsugawa, and N. Iwasaki, "New vector controller for PM motors which modeled the cross-coupling magnetic flux saturation," in *Power Electronics Conference (IPEC), 2010 International*, 2010, pp. 1064-1070.

[129] Z. Q. Zhu and Z. Azar, "Influence of end-effect and cross-coupling on torque-speed characteristics of switched flux permanent magnet machines," in *Power Electronics and ECCE Asia (ICPE & ECCE), 2011 IEEE 8th International Conference on,* 2011, pp. 145-152.

[130] J. T. Chen, "High-torque direct-drive flux-switching permanent magnet brushless AC machines," *PhD Thesis, the Department of Electronic and Electrical Engineering, University of Sheffield,* 2009.

[131] Z. Q. Zhu and D. Howe, "Electrical machines and drives for electric, hybrid, and fuel cell vehicles," *Proceedings of the IEEE,* vol. 95, pp. 746-765, 2007.

[132] R. Islam, I. Husain, A. Fardoun, and K. McLaughlin, "Permanent-magnet synchronous motor magnet designs with skewing for torque ripple and cogging torque reduction," *Industry Applications, IEEE Transactions on,* vol. 45, pp. 152-160, 2009.

[133] Z. Q. Zhu, S. Ruangsinchaiwanich, D. Ishak, and D. Howe, "Analysis of cogging torque in brushless Machines having nonuniformly distributed stator slots and stepped rotor magnets," *Magnetics, IEEE Transactions on,* vol. 41, pp. 3910-3912, 2005.

[134] G. Heins, T. Brown, and M. Thiele, "Statistical analysis of the effect of magnet placement on cogging torque in fractional pitch permanent magnet motors," *Magnetics, IEEE Transactions on,* vol. 47, pp. 2142-2148, 2011.

[135] M. Thiele, G. Heins, and T. Brown, "Decoupling manufacturing sources of cogging torque in fractional pitch PMSM," in *Electric Machines & Drives Conference (IEMDC), 2011 IEEE International*, 2011, pp. 924-929.

[136] Z. Q. Zhu, L. J. Wu, and Z. P. Xia, "An accurate subdomain model for magnetic field computation in slotted surface-mounted permanent-magnet machines," *Magnetics, IEEE Transactions on,* vol. 46, pp. 1100-1115, 2010.

[137] Z. Q. Zhu, "A simple method for measuring cogging torque in permanent magnet machines," in *Power & Energy Society General Meeting, 2009. PES '09. IEEE*, 2009, pp. 1-4.

[138] E. Hoang, M. Gabsi, M. Lecrivain, and B. Multon, "Influence of magnetic losses on maximum power limits of synchronous permanent magnet drives in flux-weakening mode," in *Industry Applications Conference, 2000. Conference Record of the 2000 IEEE*, 2000, pp. 299-303 vol.1.

[139] P. Vas, K. E. Hallenius, and J. E. Brown, "Cross-saturation in smooth-air-gap electrical machines," *Energy Conversion, IEEE Transactions on,* vol. EC-1, pp. 103-112, 1986.

[140] H. De Gersem, K. Hameyer, and T. Weiland, "Skew interface conditions in 2-D finite-element machine models," *Magnetics, IEEE Transactions on,* vol. 39, pp. 1452-1455, 2003.

[141] M. S. Islam, S. Mir, T. Sebastian, and S. Underwood, "Design considerations of sinusoidally excited permanent-magnet machines for low-torque-ripple applications," *Industry Applications, IEEE Transactions on,* vol. 41, pp. 955-962, 2005.

[142] D. Min, A. Keyhani, and T. Sebastian, "Torque ripple analysis of a PM brushless DC motor using finite element method," *Energy Conversion, IEEE Transactions on,* vol. 19, pp. 40-45, 2004.

[143] L. Touzhu and G. Slemon, "Reduction of cogging torque in permanent magnet motors," *Magnetics, IEEE Transactions on,* vol. 24, pp. 2901-2903, 1988.

[144] K. Kwang-Heon, S. Dong-Joon, and W. Jong-Soo, "Analysis of skew effects on cogging torque and BEMF for BLDCM," in *Industry Applications Society Annual Meeting, 1991., Conference Record of the 1991 IEEE*, 1991, pp. 191-197 vol.1.

[145] D. C. Hanselman, "Effect of skew, pole count and slot count on brushless motor radial force, cogging torque and back EMF," *Electric Power Applications, IEE Proceedings* -, vol. 144, pp. 325-330, 1997.

[146] L. Dosiek and P. Pillay, "Cogging torque reduction in permanent magnet machines," *Industry Applications, IEEE Transactions on,* vol. 43, pp. 1565-1571, 2007.

[147] W. Fei and P. Luk, "A new technique of cogging torque suppression in direct-drive permanent-magnet brushless machines," *Industry Applications, IEEE Transactions on,* vol. 46, pp. 1332-1340, 2010.

[148] D. C. Hanselman, "Minimum torque ripple, maximum efficiency excitation of brushless permanent magnet motors," *Industrial Electronics, IEEE Transactions on,* vol. 41, pp. 292-300, 1994.

[149] S. K. Panda, X. Jian-Xin, and Q. Weizhe, "Review of torque ripple minimization in PM synchronous motor drives," in *Power and Energy Society General Meeting - Conversion and Delivery of Electrical Energy in the 21st Century, 2008 IEEE,* 2008, pp. 1-6.

[150] G. Ombach and J. Junak, "Comparative study of IPM motors with different air gap flux distribution," in *Power Electronics, Machines and Drives, 2008. PEMD 2008. 4th IET Conference on*, 2008, pp. 301-304.

[151] A. G. Hofmann, K. A. Kasper, and R. W. De Doncker, "High-speed switched reluctance drives: A promising alternative to power electric vehicles," in *Power Electronics and ECCE Asia (ICPE & ECCE), 2011 IEEE 8th International Conference on*, 2011, pp. 169-175.

[152] R. B. Inderka, M. Menne, and R. W. A. A. De Doncker, "Control of switched reluctance drives for electric vehicle applications," *Industrial Electronics, IEEE Transactions on,* vol. 49, pp. 48-53, 2002.

[153] X. D. Xue, J. K. Lin, Z. Zhang, T. W. Ng, K. F. Luk, K. Cheng, and N. C. Cheung, "Study of motoring operation of in-wheel switched reluctance motor drives for electric vehicles," in *Power Electronics Systems and Applications, 2009. PESA 2009. 3rd International Conference on*, 2009, pp. 1-6.

[154] K. Kiyota and A. Chiba, "Design of switched reluctance motor competitive to 60 kW IPMSM in third generation hybrid electric vehicle," in *Energy Conversion Congress and Exposition (ECCE), 2011 IEEE*, 2011, pp. 3562-3567.

[155] N. Vattikuti, V. Rallabandi, and B. G. Fernandes, "A novel high torque and low weight segmented switched reluctance motor," in *Power Electronics Specialists Conference, 2008. PESC 2008. IEEE*, 2008, pp. 1223-1228.

[156] P. P. de Paula, W. M. da Silva, J. R. Cardoso, and S. I. Nabeta, "Assessment of the influences of the mutual inductances on switched reluctance machines performance," in *Electric Machines and Drives Conference, 2003. IEMDC'03. IEEE International*, 2003, pp. 1732-1738 vol.3.

[157] N. Inanc, A. Derdiyok, and V. Ozbulur, "Torque ripple minimization of a switched reluctance motor including mutual inductances via sliding mode control technique," in *Industrial Electronics, 1997. ISIE '97., Proceedings of the IEEE International Symposium on*, 1997, pp. 1024-1028 vol.3.

[158] T. Lubin, T. Hamiti, H. Razik, and A. Rezzoug, "Comparison between finite-element analysis and winding function theory for inductances and torque calculation of a synchronous reluctance machine," *Magnetics, IEEE Transactions on,* vol. 43, pp. 3406-3410, 2007.

[159] W. Shuanghong, Z. Qionghua, M. Zhiyuan, and Z. Libing, "Implementation of a 50-kW four-phase switched reluctance motor drive system for hybrid electric vehicle," *Magnetics, IEEE Transactions on,* vol. 41, pp. 501-504, 2005.

[160] N. Schofield, S. A. Long, D. Howe, and M. McClelland, "Design of a switched reluctance machine for extended speed operation," *Industry Applications, IEEE Transactions on,* vol. 45, pp. 116-122, 2009.

[161] S. D. Calverley, G. W. Jewell, and R. J. Saunders, "Prediction and measurement of core losses in a high-speed switched-reluctance Machine," *Magnetics, IEEE Transactions on,* vol. 41, pp. 4288-4298, 2005.

[162] Y. Pang, Z. Q. Zhu, D. Howe, S. Iwasaki, R. Deodhar, and A. Pride, "Investigation of iron loss in flux-switching PM machines," in *Power Electronics, Machines and Drives, 2008. PEMD 2008. 4th IET Conference on,* 2008, pp. 460-464.

[163] K. Atallah, Z. Q. Zhu, and D. Howe, "An improved method for predicting iron losses in brushless permanent magnet DC drives," *Magnetics, IEEE Transactions on,* vol. 28, pp. 2997-2999, 1992.

Appendixes

Appendix A: Influence of End-Effect and Cross-Coupling on Torque-Speed Characteristics of Switched Flux Permanent Magnet Machines

A.1. Introduction

Permanent magnet (PM) brushless machines become more and more attractive for commercial and industrial applications, due to their inherent high torque density and high efficiency. In conventional PM machines the PMs are located on the rotor. However, in switched flux permanent magnet (SFPM) machines, the magnets, together with the windings, are placed on the stator, while the salient pole rotor is very simple without any windings or magnets, thus such machines are strong candidates for high speed applications [A.1, A.2]. This structure allows for higher electric loading, which is limited by the PM temperature rise and irreversible demagnetisation, since cooling magnets is more efficient when they are located in the stator. Therefore, such machines can exhibit relatively large torque density [A.3, A.4].

The SFPM machines were firstly proposed and designed as a single-phase machine about 6 decades ago [A.5]. However, later they were developed to be three-phase and even multi-phase machines [A.6-A.8]. The fault tolerant SFPM machines were developed in [A.9]. Furthermore, external rotor SFPM machines are suitable for the wheel electric propulsion system, since they combine the benefits of both the conventional PM and SR machines [A.10]. Moreover, a new SFPM machine topology, which utilizes both PM and field winding excitation, i.e. hybrid excited SFPM machine, was presented and investigated in [A.11-A.13]. Such topology allows for easier flux control [A.12], and can generate lower iron loss than the conventional SFPM machine [A.13].

The presence of magnets in the stator causes relatively large flux leakage at the stator end and outer surface [A.14], which can cause significant reduction in the electromagnetic performance of the machine. For example, it was reported in [A.3] that it can cause around 10% reduction in the back-emf waveform of a SFPM machine, which has 12 stator teeth and 10 rotor poles. An analytical technique to account for this effect in the SFPM machines was

proposed in [A.15]. However, it can also be accounted for by using 3D finite element (FE) analysis [A.16], which is also employed in this study.

The torque density of conventional SFPM machines can be similar to that of the fractional-slot PM machines. However, for the newly developed SFPM machine topologies, the torque capability can be further improved while the magnet volume can be reduced [A.1, A.2] and [A.17]. For example, the developed E-core and C-core and multi-tooth SFPM machines use almost half magnet volume compared with the conventional SFPM machines, while exhibit higher electromagnetic torque [A.18].

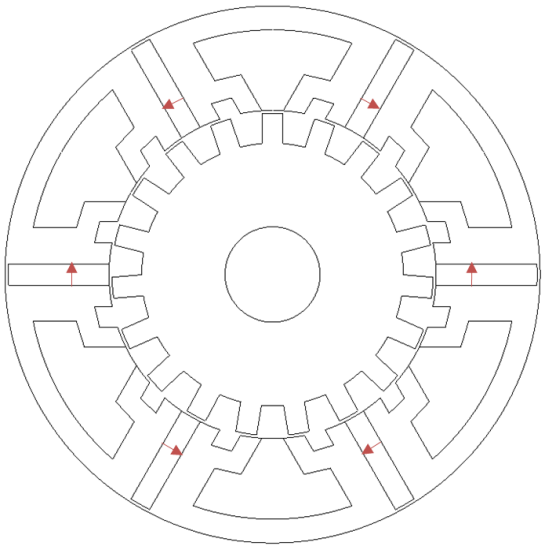

Fig.A.1. Cross-section of multi-tooth 6–4 stator pole/tooth, 19-rotor pole SFPM machine.

The electromagnetic performance of a multi-tooth 6–4 stator pole/tooth, 19-rotor pole SFPM machine, whose parameters are given in Table A.1 and the cross-section in Fig.A.1, has been investigated in [A.1] and [A.19]. However, the investigation has not considered the torque- and power-speed characteristics. Therefore, this study analyses these characteristics by using models accounting for different cross-coupling levels, viz. full cross-coupling on both PM flux linkage and dq-axis inductances, partial cross-coupling on the PM flux linkage only and without cross-coupling. In addition, the influence of the end-effect on the machine parameters and performance during both the constant-torque and flux weakening operation regions is also investigated. Both 2D and 3D FE models have been employed to carry out the investigation on the platform of Flux 2D/3D, and confirmed by the measurements. Fig. A.2 shows the open-circuit and load equal potential distributions of the prototype machine at the maximum PM flux position for phase A.

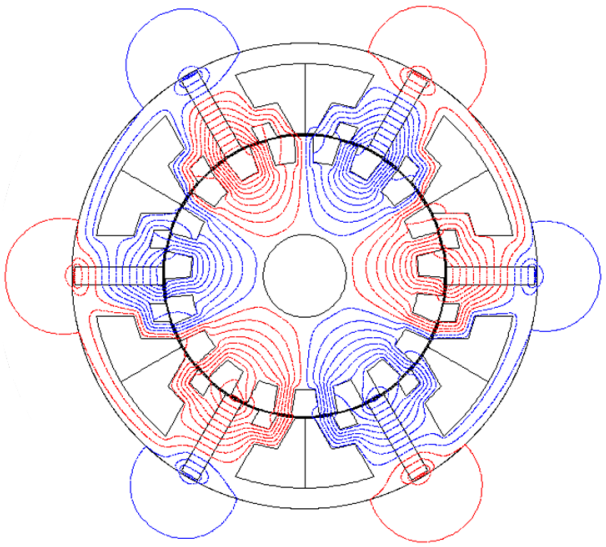

(a) Open-circuit

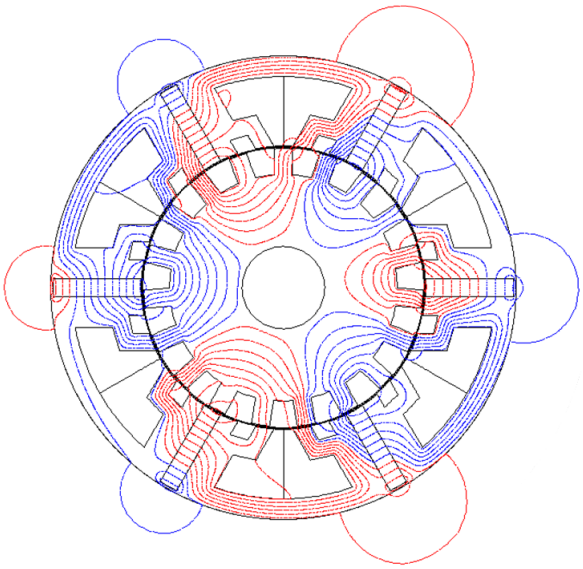

(b) Load

Fig. A.2. Equal potential distributions of multi-tooth 6–4 stator pole/tooth, 19-rotor pole SFPM machine.

Table A.1 Prototype Machine Parameters

Parameter	***Value***	***Parameter***	***Value***
Active axial length	25 mm	Magnet thickness	3.6 mm
Stator outer diameter	90 mm	Air gap length	0.5 mm
Stator inner diameter	55 mm	Rotor tooth width	3.6 mm
Stator tooth width	6.25 mm	Magnetic remanence	1.2 T
Stator yoke thickness	4 mm	Phase number of turn	72
Stator small slot depth	3 mm	Peak rated current	15 A

A.2. Prediction of Torque Speed Characteristics

The output torque of the SFPM machines can be calculated by [A.19]:

$$T = \frac{3}{2} N_R [\psi_d I_q - \psi_q I_d] = \frac{3}{2} N_R [\psi_{md} I_q + (L_d - L_q) I_d I_q] \quad \text{(A.1)}$$

where $N_R, \psi_{md}, \psi_d, \psi_q, L_d, L_q, I_d$ and I_q are the rotor pole number, PM flux linkage and dq-axis flux linkages, inductances and currents, respectively, $\psi_{md} I_q$ is the electromagnetic torque, and $(L_d - L_q) I_d I_q$ is the reluctance torque, which is due to the difference between d- and q-axis inductances.

Thus, the output torque can be directly calculated by the FE method (the virtual work in the software which is used) and checking the voltage limitation (direct FE method) or from (A.1) by using the FE predicted PM flux linkage and dq-axis inductances (indirect FE method).

A.2.1. Direct FE Method

Ideally, it is desirable to operate the machine at the maximum torque per ampere, thus the maximum capability of the machine is utilized. However, the phase voltage is proportional to the rotating speed, since it is given by:

$$V_{ph} = \sqrt{(R_a I_d - \omega \psi_q)^2 + (R_a I_q + \omega \psi_d)^2} \quad \text{(A.2)}$$

where R_a and ω are the phase resistance and electrical rotating speed.

For higher speeds above the base speed at which the phase voltage exceeds the limit, the current angle needs to be adjusted to weaken the PM flux in order to satisfy the voltage limitation, i.e. the flux weakening operation [A.20, A.21]. For some machines, including this prototype SFPM machine which has relatively large winding inductance, even the current magnitude needs to be reduced to satisfy the specified voltage limit. In the FE calculation, the output torque and phase voltage are calculated for different current magnitudes (from 0 till maximum phase current) and phases (between 0 and 90 deg.), as illustrated in Fig.A.3 and Fig.A.4, respectively. These data can be used to work out the machine torque-speed

characteristics. In order to clearly illustrate such procedure, the determination of the optimal output torque at 600 rpm rotating speed is explained in details. At such speed, the voltage limit can be satisfied by different combinations of current magnitude and phase, e.g. 15A / 51deg., 14A / 39 deg., 13A / 33deg. and 12A / 18deg., as shown in Fig. A.4(a)-(d), respectively. For each current magnitude and phase combination, the corresponding output torque can be obtained from Fig. A.3. The output torque values for the possible combinations of current magnitude and phase, which satisfy the voltage limitation at 600rpm, are shown in Fig. A.5. Hence, the optimal output torque and corresponding optimal current magnitude and phase combination for such speed can be obtained. This process needs to be carried out for different speed in order to predict the whole torque-speed characteristics, Fig. A.6(a) and the corresponding variation of the current magnitude and phase, Fig. A.6(b), over the range of three times the base speed.

In this FE method the torque is obtained directly. Thus, the cross-coupling and saturation are fully accounted for. Therefore, it is an accurate technique to analyze the highly saturated machines, such as the SFPM machines. However, this method is very time consuming.

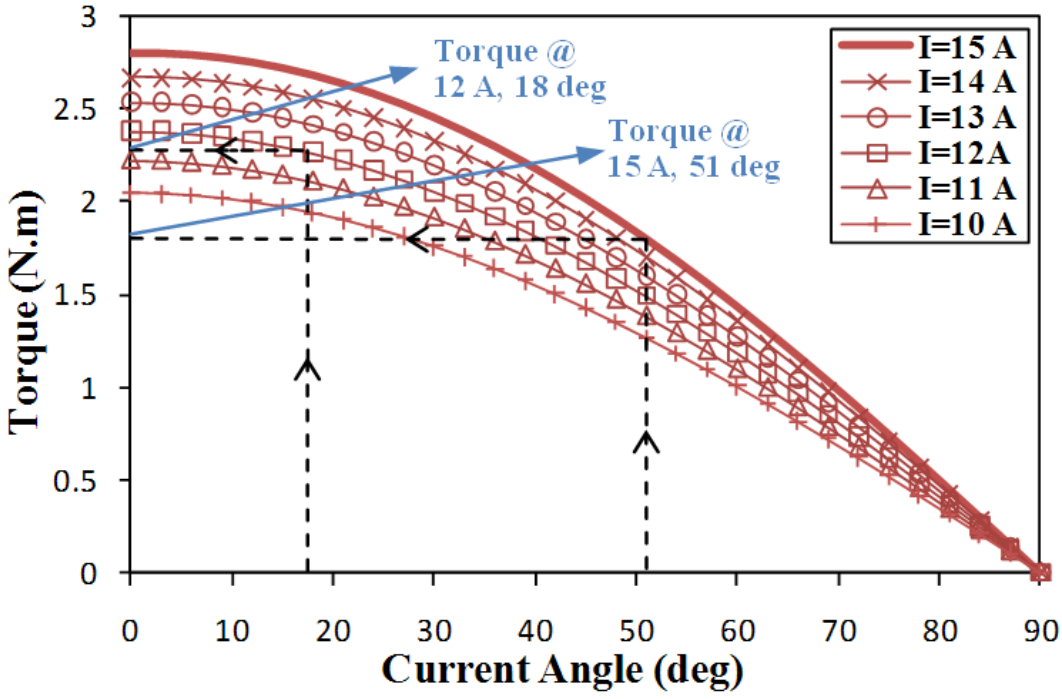

Fig. A.3. FE predicted variation of output torque with current angle for different phase current.

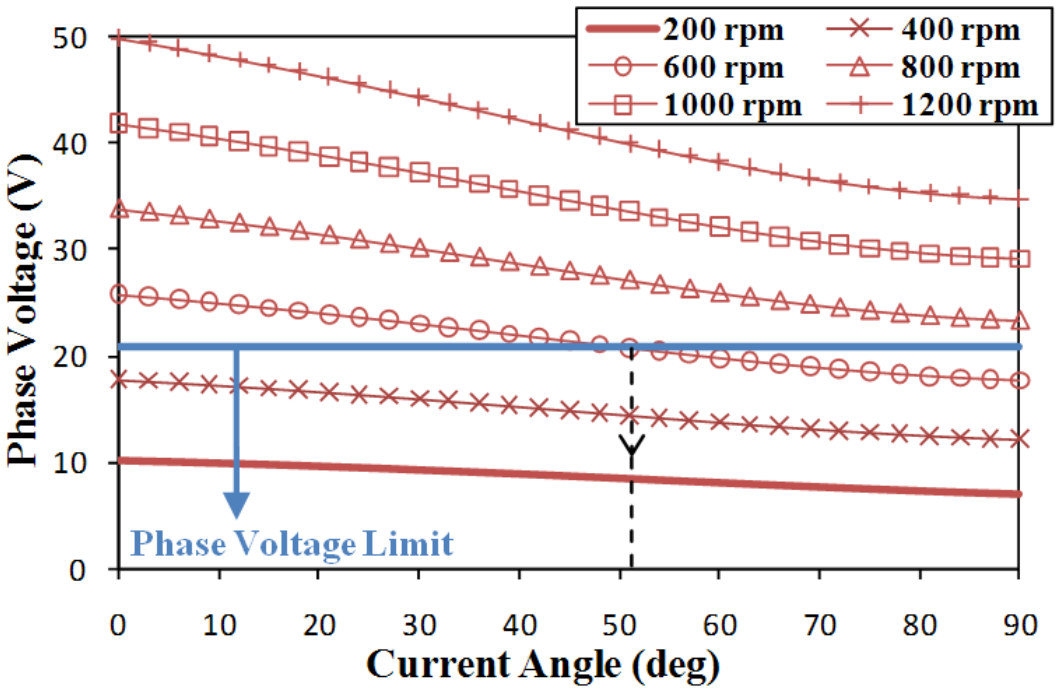

(a) Peak phase current is 15A

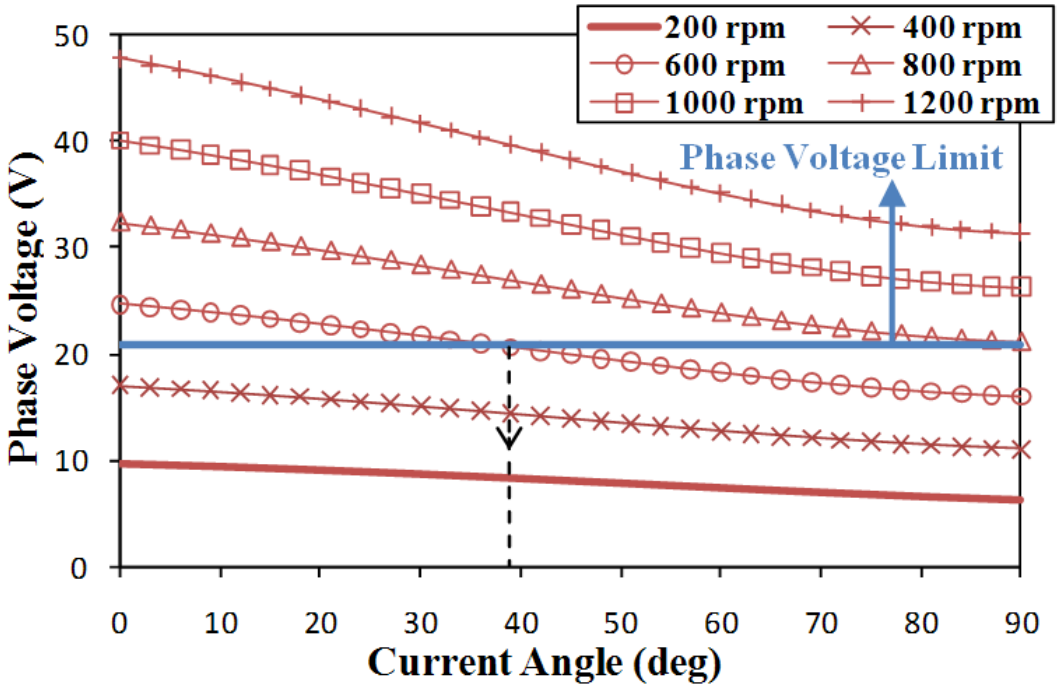

(b) Peak phase current is 14A

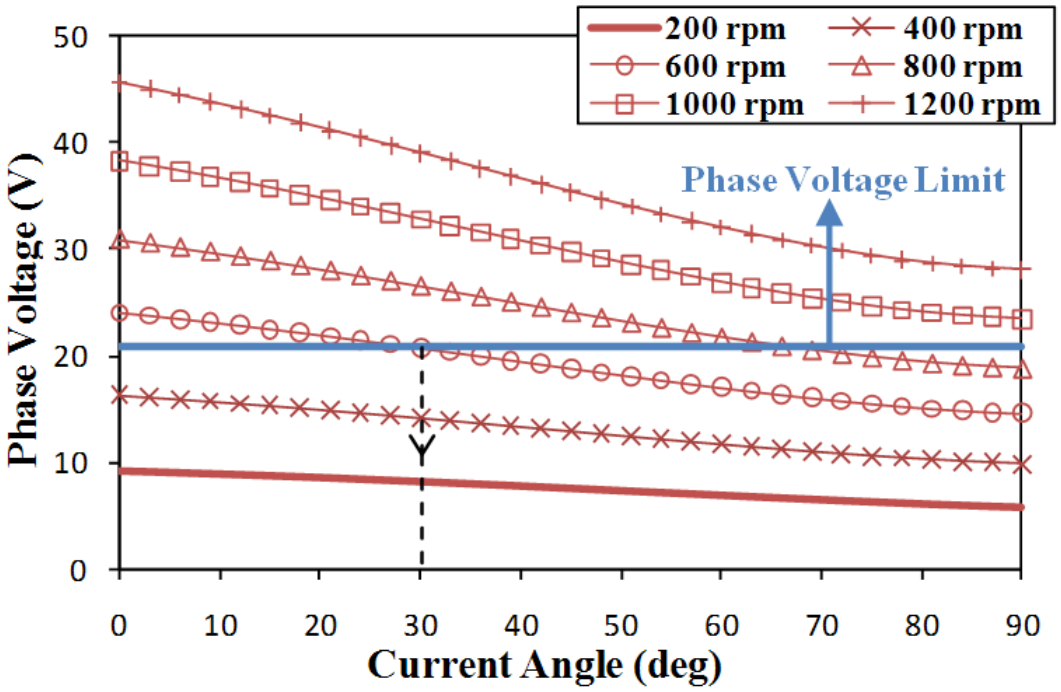

(c) Peak phase current is 13A

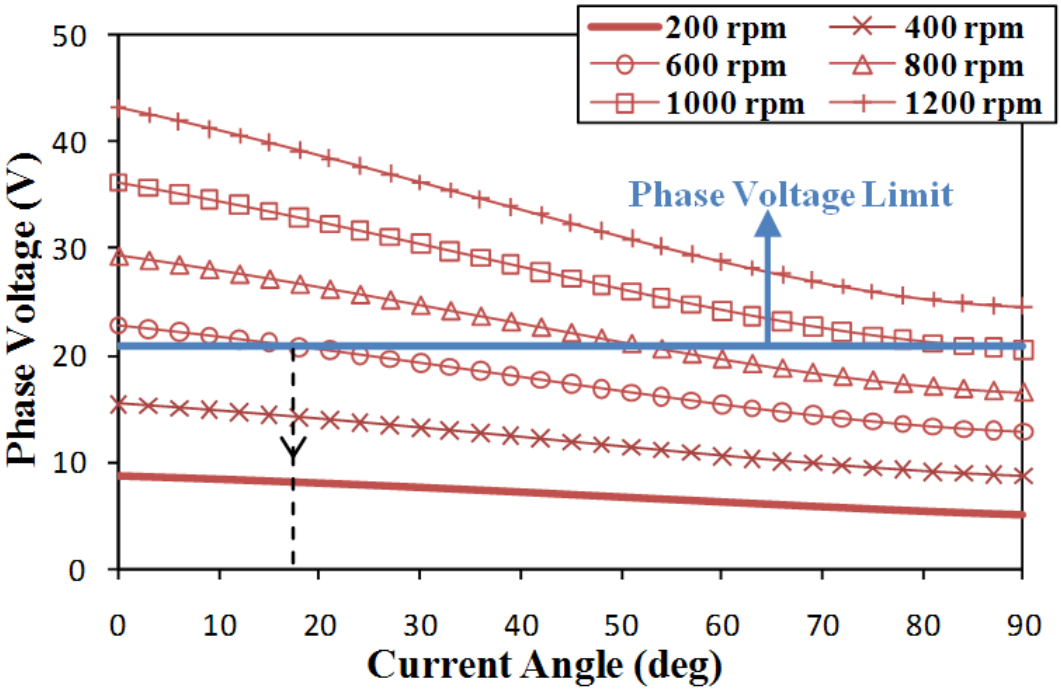

(d) Peak phase current is 12A

Fig. A.4. FE predicted variation of phase voltage with current angle for different rotating speed and different phase current.

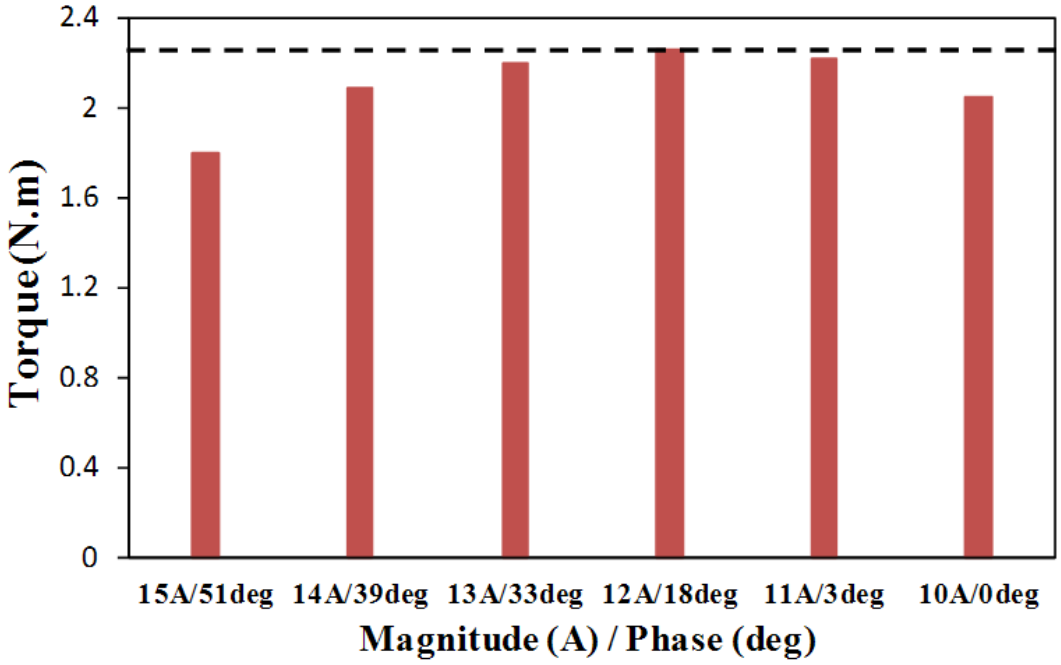

Fig. A.5 Output torque for different current magnitude and phase combinations, at 600 rpm.

A.2.2. Indirect FE Method

In this method, the PM flux linkage and dq-axis inductances, which are used to calculate the torque-speed characteristics, need to be pre-predicted in advance. The level of cross-coupling consideration during such calculation depends on the prediction method of the PM flux linkage and dq-axis inductances. To fully account for the cross-coupling and saturation, these parameters should be calculated as function of both d- and q-axis currents. For this purpose, the PM flux linkage of the prototype machine is calculated as function of q-axis current, Fig. A.7, while the dq-axis inductances, Fig. A.8, are calculated using (4. 7) and (4. 8). Basing on these results, the optimal constant torque and flux weakening performance of the prototype machine has been analytically calculated by using (A.1) and (A.2) and compared with results obtained by the direct FE method in Fig. A.6(a). In addition, the phase current magnitude and current angle of the two FE methods are compared in Fig. A.6(b). Both methods offer nearly the same accuracy, since there is a very good agreement between them. However, the indirect FE method takes much less time. It can be even faster when the cross-coupling is partially considered.

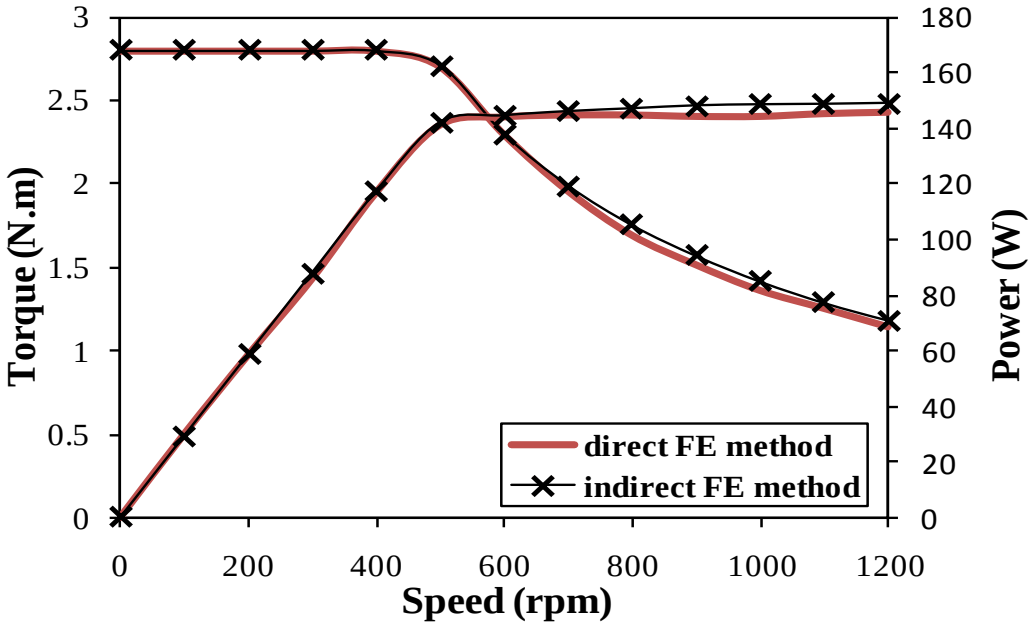

(a) Torque- and power-speed characteristics

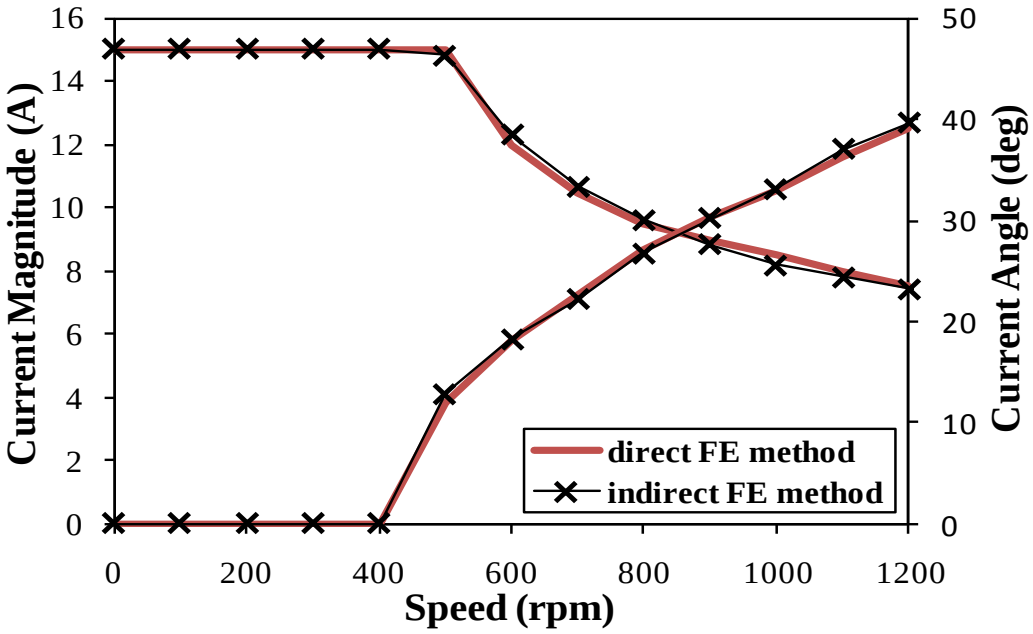

(b) Corresponding phase current magnitude and angle

Fig. A.6. Comparison of torque- and power-speed characteristics and corresponding phase current magnitude and angle of the multi-tooth machine using different prediction methods.

A.3. Influence of Cross-Coupling

In order to investigate the influence of cross-coupling on the performance of the multi-tooth FSPM machine, its torque-speed characteristics have been predicted again using the indirect FE method with partial cross-coupling consideration. In this case, the PM flux linkage is considered as a function of the q-axis current, Fig. A.7, while the dq-axis inductances are considered as functions of their corresponding current only, i.e. $L_d(I_d, I_q=0)$, Fig. A.8(a), and $L_q(I_d=0, I_q)$, Fig. A.8(b). The obtained results are shown in Fig. A.9. The full and partial cross-coupling models produce almost the same torque-speed curves. This indicates that the influence of cross-coupling on the dq-axis inductances is relativity small, as can also be noticed from Fig. A.8, but it is more significant on the PM flux linkage, Fig. A.7. In order to further demonstrate the relative large influence of cross-coupling on the PM flux linkage, the torque-speed characteristics are calculated for two cases without cross-coupling consideration. In both cases, each of the dq-axis inductances is a function of its corresponding current only, i.e. $L_d(I_d, I_q=0)$, Fig. A.8(a), and $L_q(I_d=0, I_q)$, Fig. A.8(b). However, the PM flux linkage is considered as a constant value, at either I_d=0A, I_q=0A (point A in Fig. A.7) or I_d=0A, I_q=15A (point B in Fig. A.7). The calculated results are also plotted in Fig. A.9. Comparing with the full cross-coupling model, both no cross-coupling models predict significantly different torque-speed characteristics. Therefore, the partial cross-coupling model, which is much easier and faster to calculate compared with the full cross-coupling model, can be utilized to accurately calculate the torque-speed characteristics of the multi-tooth SFPM machines.

Fig. A.10 compares the current magnitudes and phases of the four cross-coupling models. It shows that the phase current amplitudes are almost the same for all models. In addition, the current angles are zero for all models in the constant-torque region since the reluctance torque in such machine is negligible, as its dq-axis inductances are nearly the same, Fig. A.8. On the other hand, the current angles are different in the flux weakening region, the current magnitude and angle are adjusted to satisfy the phase voltage limit, which depends on the machine parameters.

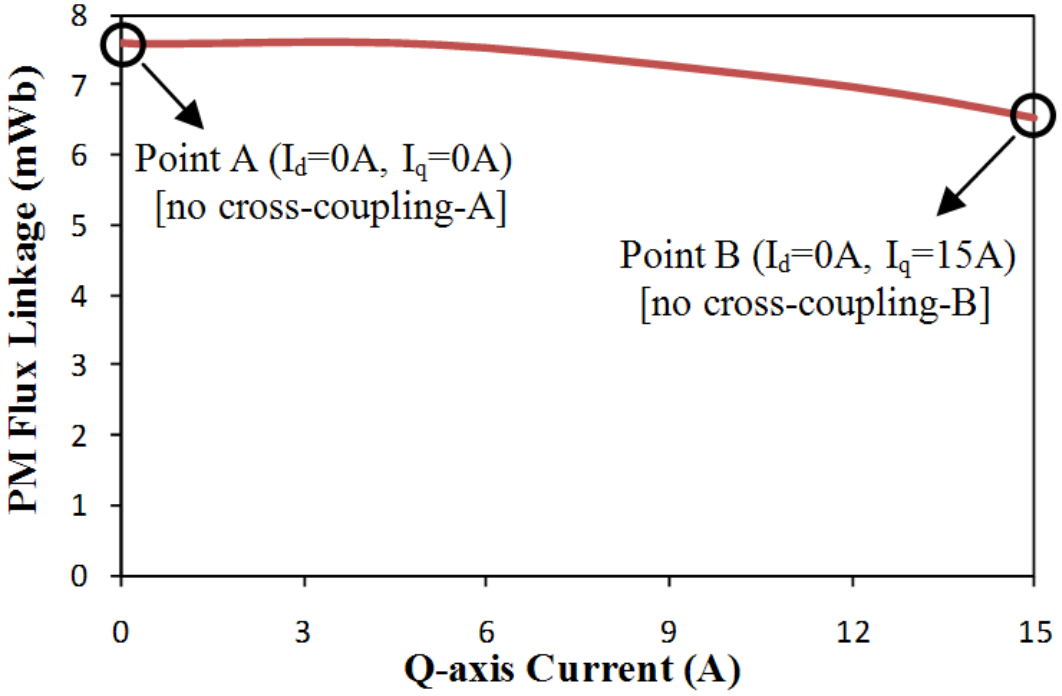

Fig. A.7 FE predicted variation of PM flux linkage against q-axis current.

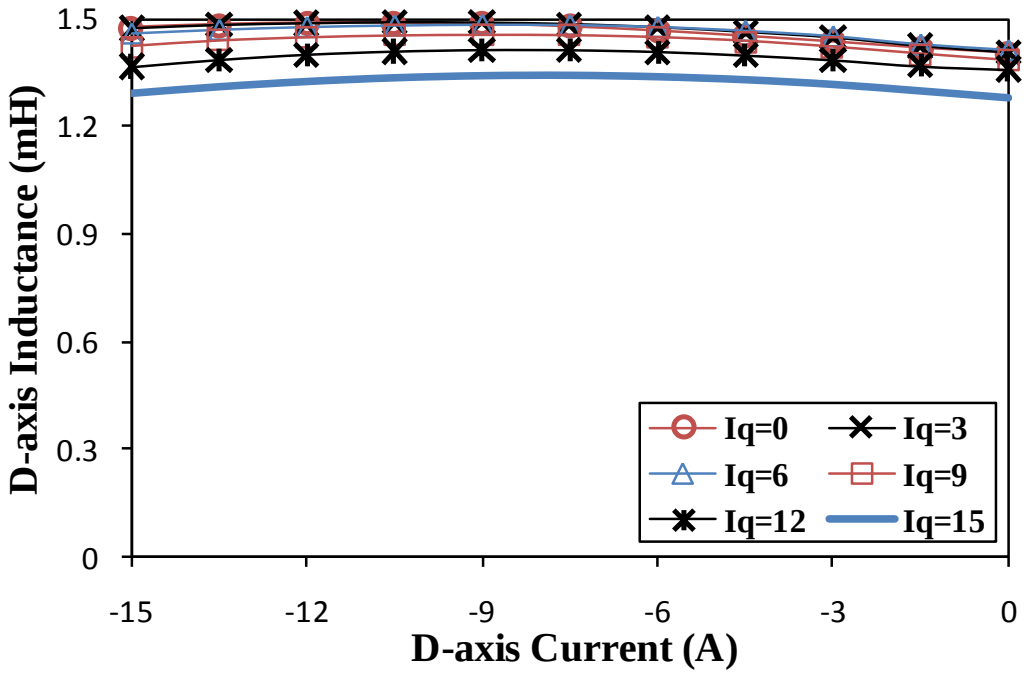

(a) d-axis inductance

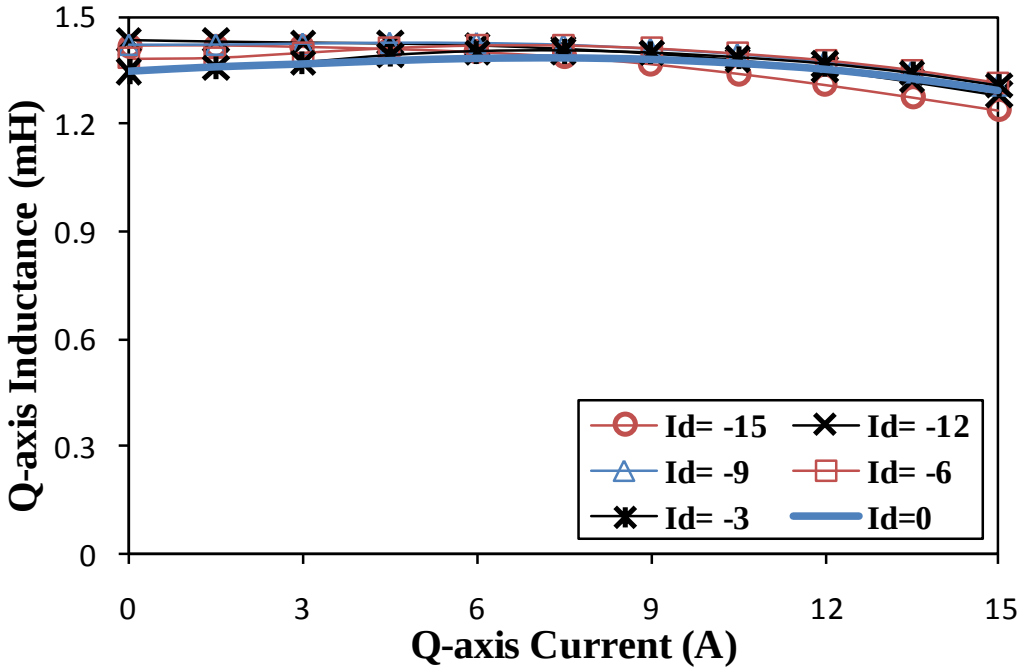

(b) q-axis inductance

Fig. A.8 FE predicted variation of dq-axis inductances as function with dq-axis currents.

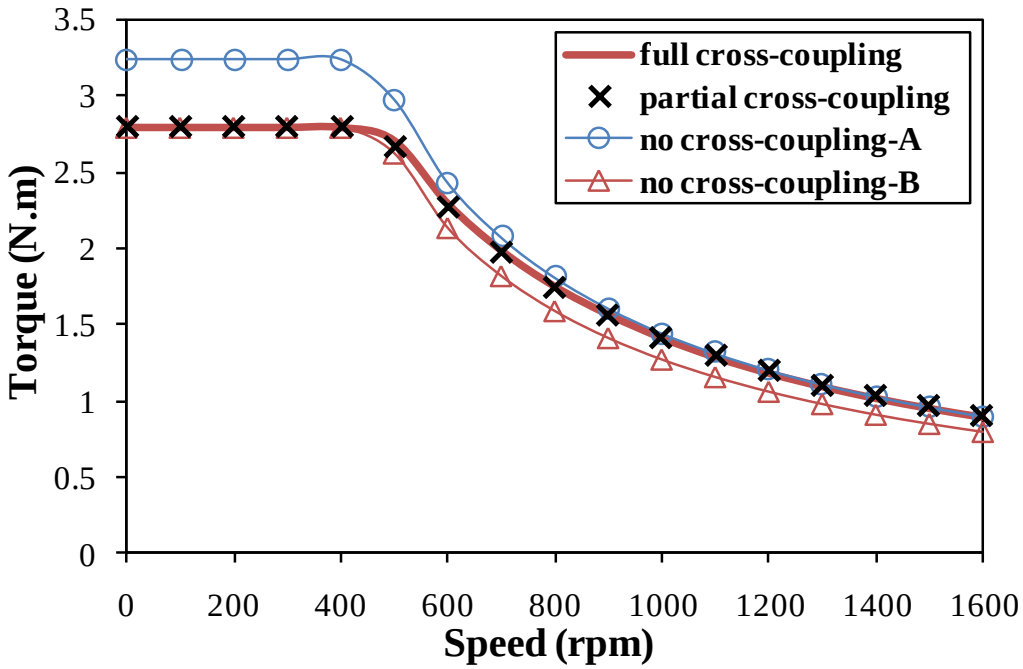

(a) Torque-speed characteristics

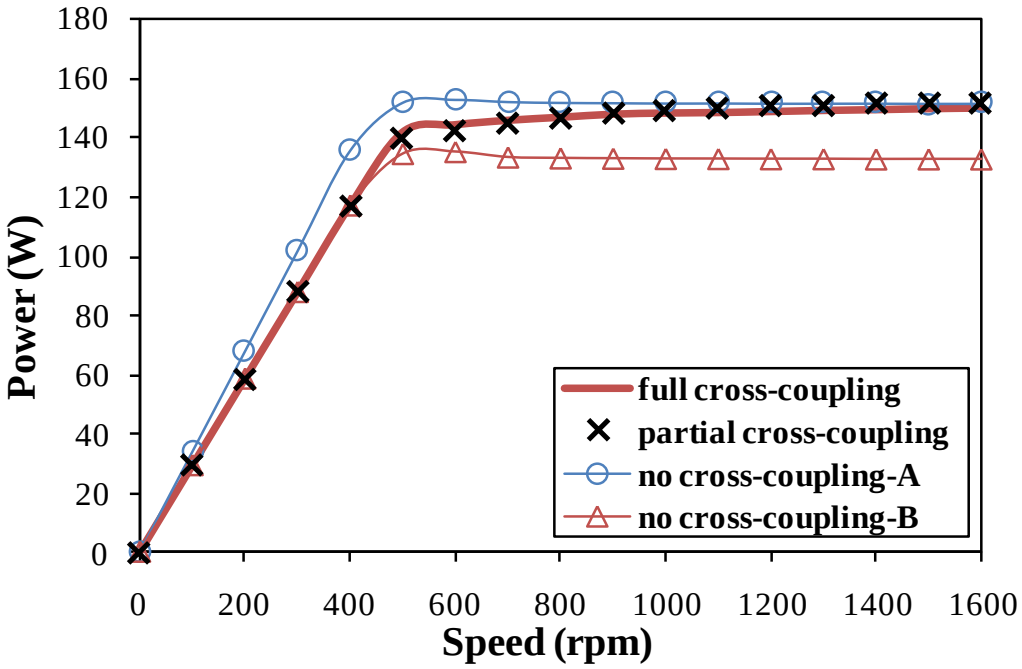

(b) Power-speed characteristics

Fig. A.9 Comparison of torque- and power-speed characteristics predicted by different cross-coupling accounting for models.

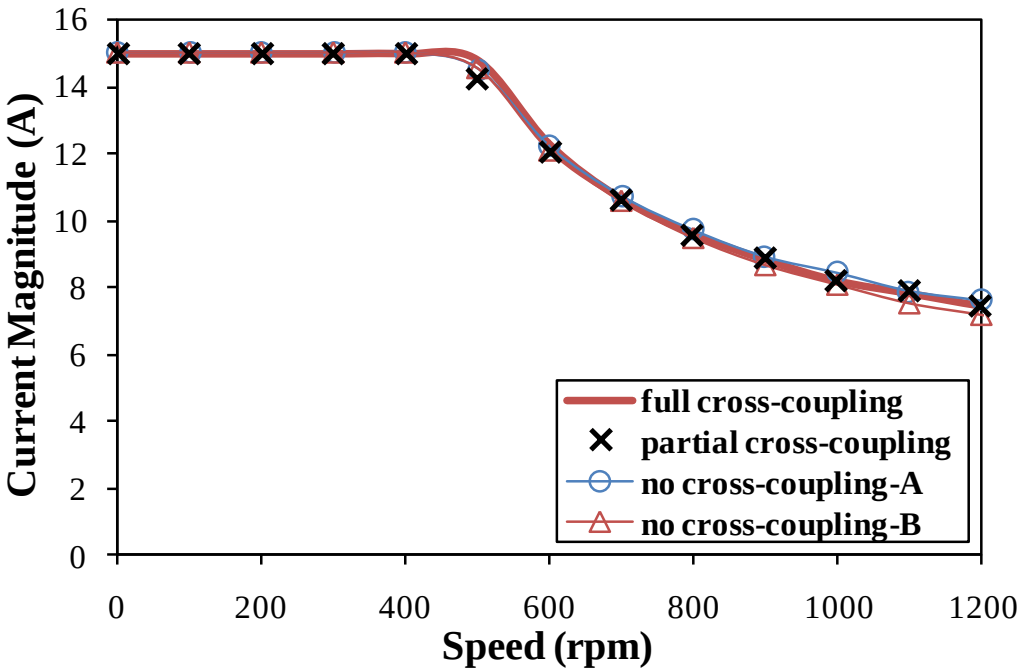

(a) Phase current

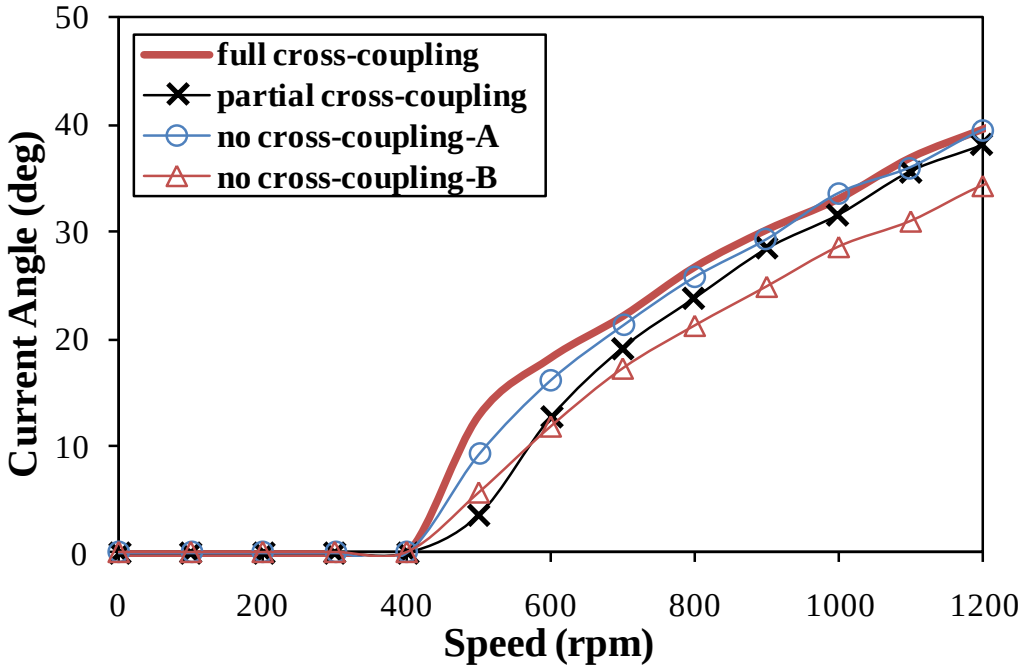

(b) Current angle

Fig. A.10 Comparison of corresponding current magnitudes and angles for different cross-coupling accounting for models.

A.4. Influence of End-Effect

Due to the presence of PMs in the stator, the end-effect in FSPM machines is relatively large [A.3]. The influence of the end-effect on the electromagnetic performance of the multi-tooth FSPM machine was highlighted in [A.19]. However, this paper investigates its influence on the dq-axis inductances and torque-speed characteristics, especially in the flux weakening region since it has not been considered before. In order to account for the end-effect, a 3D FE analysis has been employed. Fig. A.11 shows the 3D model of the prototype multi-tooth FSPM machine. The indirect FE method with partial cross-coupling consideration is employed to calculate the torque-speed characteristics, since, as illustrated earlier, it takes less time and gives similar accuracy as the full cross-coupling model.

The 3D FE predicted PM flux linkage as function of q-axis current is calculated and compared with that predicted by 2D FE in Fig. A.12. It shows that the 3D FE analysis predicts significantly lower PM flux linkage than the 2D FE analysis. This is due to the stator end effect, which cannot be accounted in the 2D model. It also shows that the larger the current is, the larger the influence of end-effect. The reduction is about 9% at zero current but becomes about 17% at the maximum current because larger currents cause higher saturation in the stator iron, leading to larger stator end flux leakage. On the other hand, the 3D FE analysis predicts larger dq-axis inductances than the 2D FE analysis, as shown in Fig. A.13. This is due to the stator end leakage inductance, which can be only accounted in the 3D model. For the same reason, the 3D FE predicted dq-axis flux linkages exhibit the same phenomenon, as illustrated in Fig. A.14. The 3D FE predicted PM flux linkage, Fig. A.12, and dq-axis inductances, Fig. A.13, are utilized to analytically calculate the torque- and power-speed characteristics, which are plotted in Fig. A.15. Comparing with the 2D model predicted results, the 3D model predicted characteristics are about 17% lower in the constant-torque region. However, this difference increases to more than 30% in the flux weakening region, as can be also noticed in Fig. A.16. This is due to the fact that in the constant-torque region the machine is operated at the maximum current magnitude and zero current angle, since the phase voltage is below the limitation and there is nearly no reluctance torque. Therefore, according to (A.1) the torque difference in this region is due to the difference in PM flux linkage, which is also 17%. However, in the flux weakening operation region, the current magnitude and phase need to be adjusted to match the voltage limitation. The 3D model predicted dq-axis flux linkages are larger, Fig. A.14, thus according to (A.2) they lead to larger phase voltage. This means the reduction of the current

magnitude need to be larger in the 3D model, as shown in Fig. A.17. Therefore, the larger torque difference in the flux wakening operation region is due to the decreasing in both the PM flux linkage, Fig. A.12, and phase current magnitude, Fig. A.17.

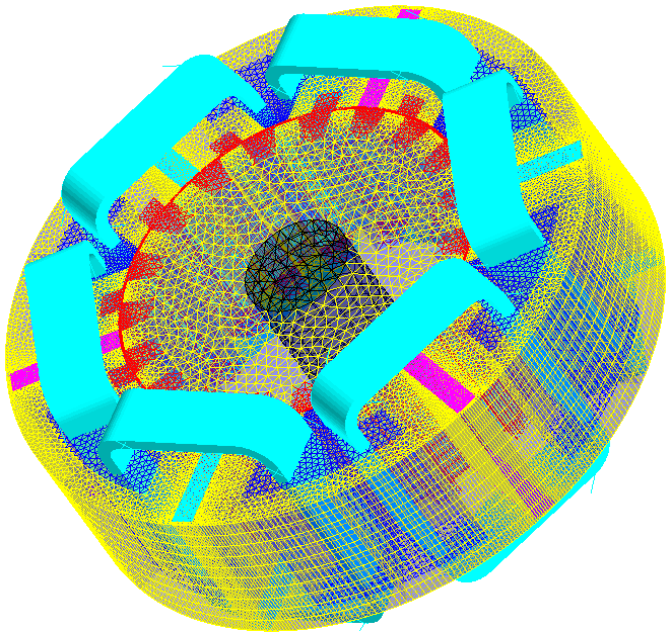

Fig. A.11. 3D meshed model of multi-tooth 6–4 stator pole/tooth, 19-rotor pole SFPM machine.

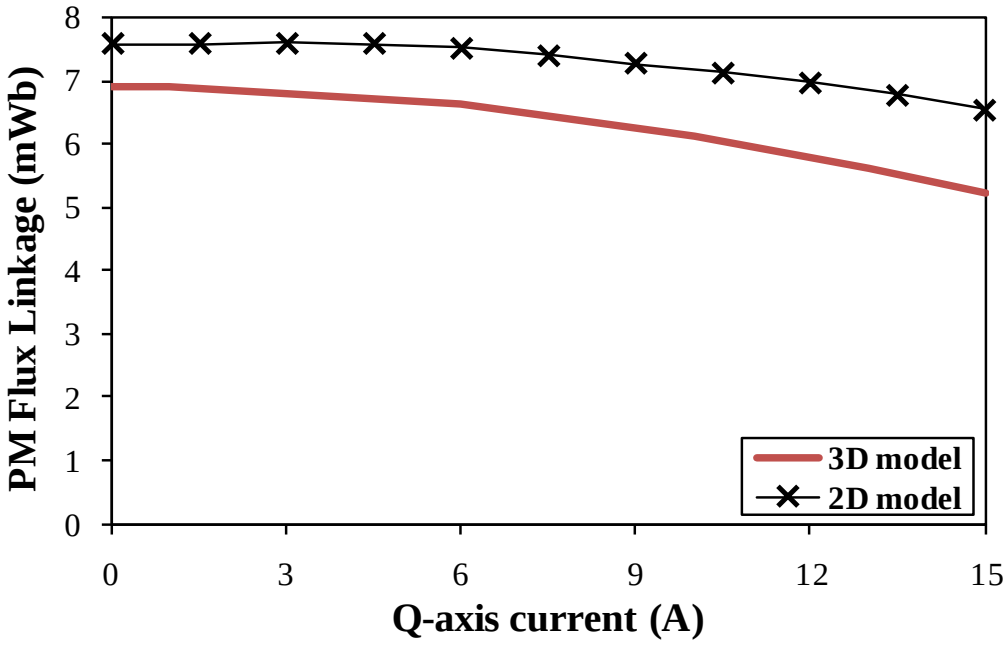

Fig. A.12 Comparison of 3D and 2D FE predicted variation of PM flux linkage with q-axis current.

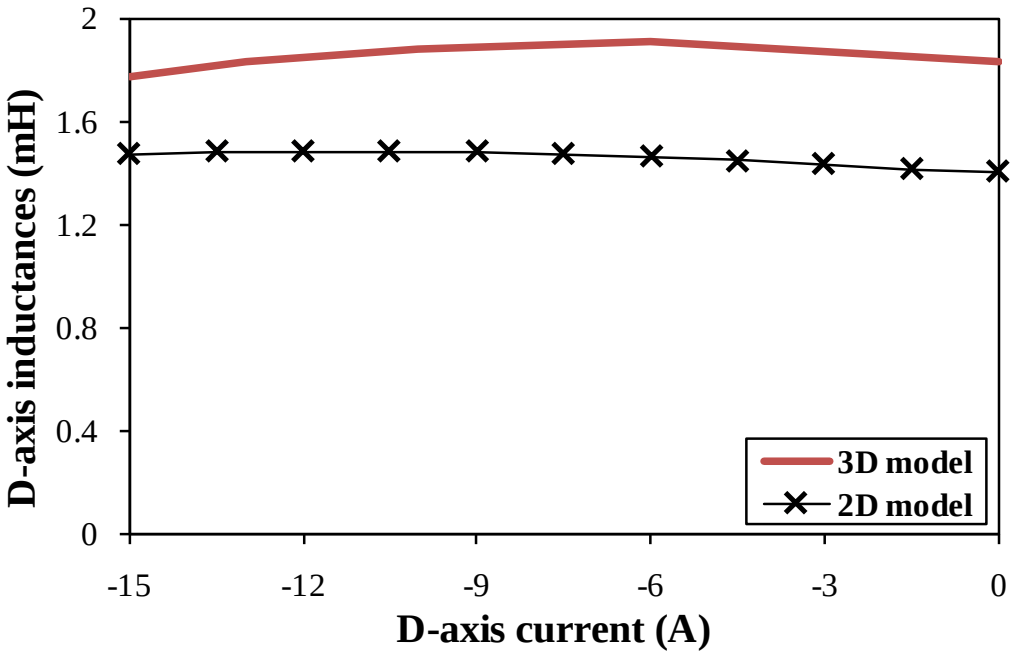

(a) d-axis inductance

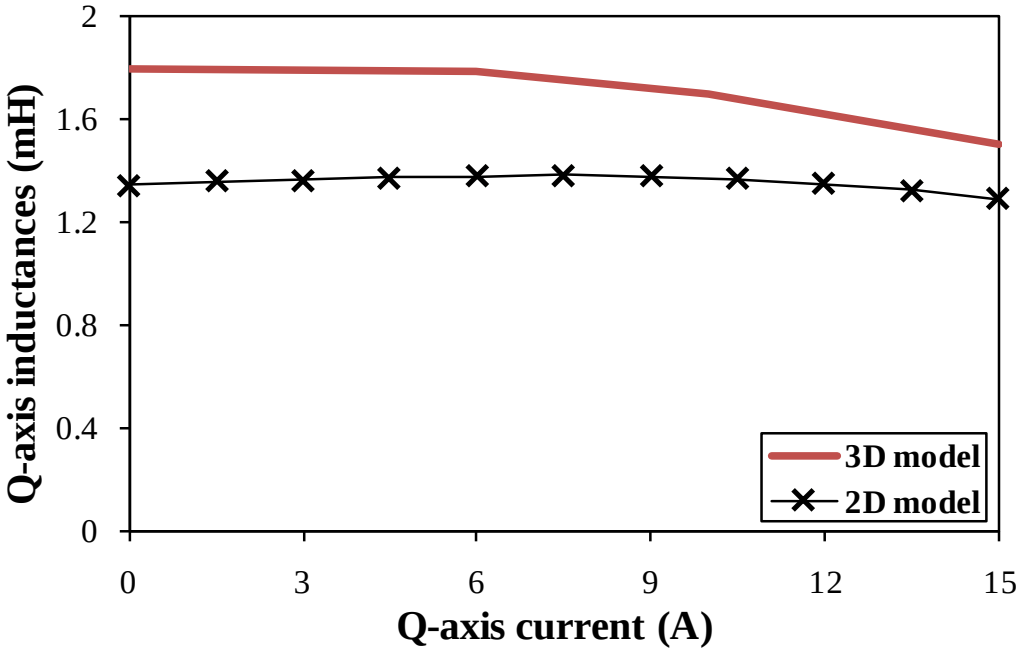

(b) q-axis inductance

Fig. A.13 Comparison of 3D and 2D FE predicted variation of dq-axis inductances against dq-axis currents.

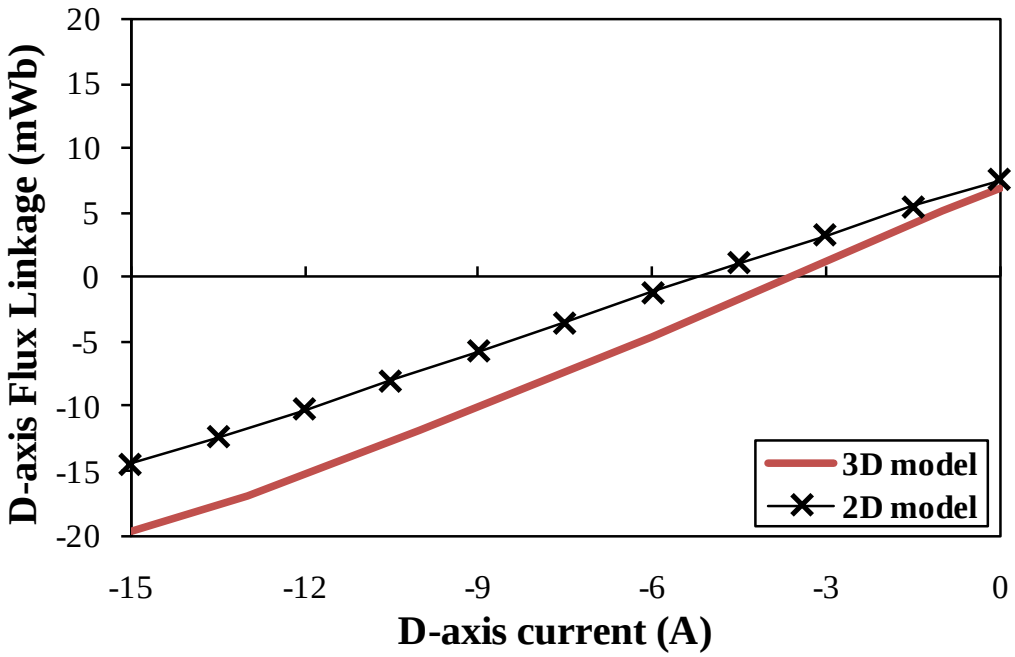

(a) d-axis flux linkage

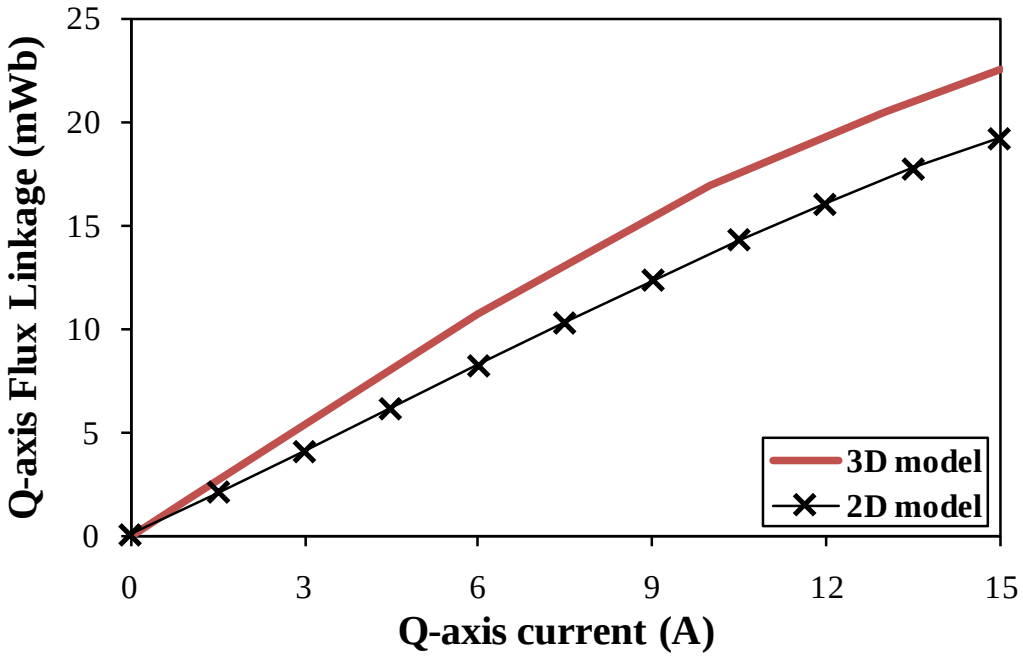

(b) q-axis flux linkage

Fig. A.14 Comparison of 3D and 2D model predicted variation of dq-axis flux linkages with dq-axis currents.

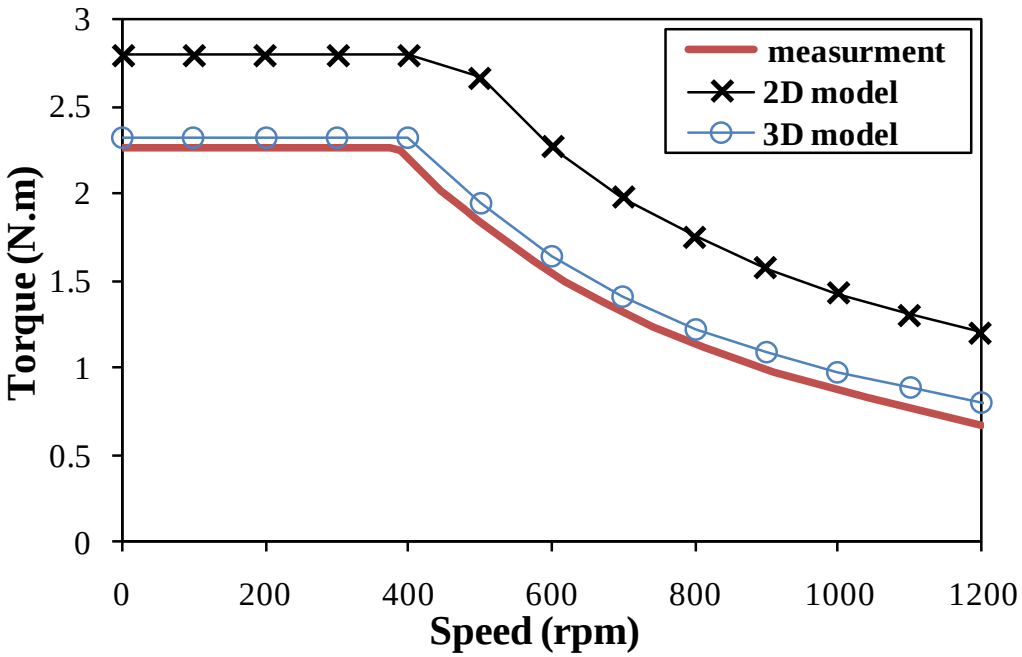

(a) Torque-speed Characteristics

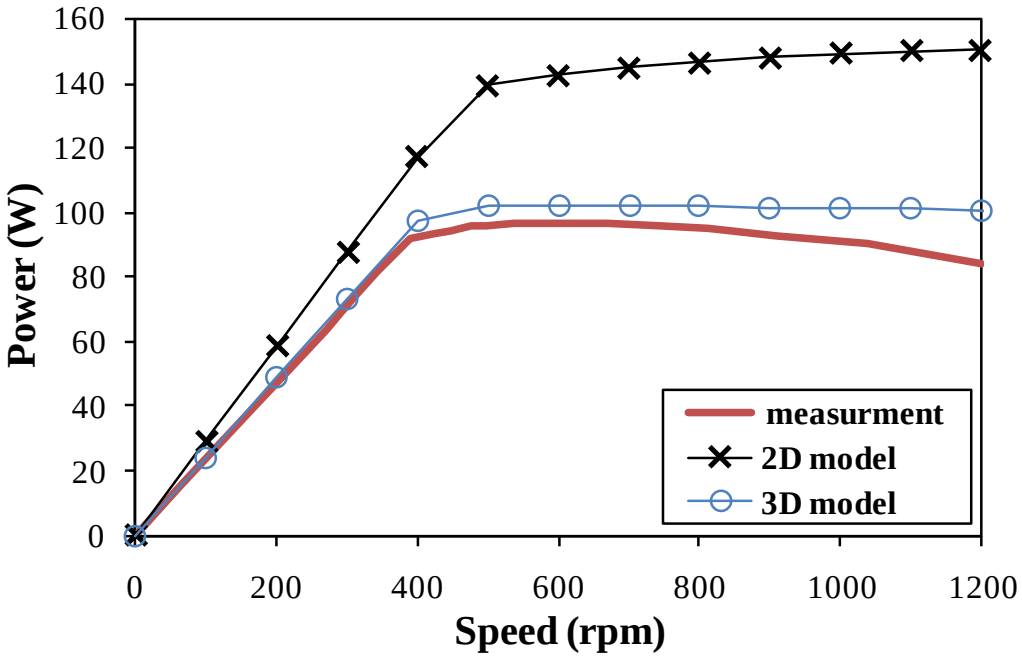

(b) Power-speed characteristics

Fig. A.15 Comparison of measured and 2D and 3D predicted torque- and power-speed characteristics.

A.5. Experimental Validation

In order to validate the FE calculations and findings, the prototype multi-tooth SFPM machine is built and its torque- and power-speed characteristics is measured and compared with their 2D and 3D FE predicted curves in Fig. A.15. During the measurement, the phase resistance, cable resistance, voltage drop and dead time on the inverter are compensated in the control algorithm. It shows that there is a significant difference between the 2D predicted and measured performances in both the constant-torque and flux weakening operation regions. This is due to the end-effect, since the agreement between the measured and 3D FE predicted results is good throughout the whole operation range. In addition, the measured phase current magnitudes are also plotted and compared with 2D and 3D model predicted current amplitudes in Fig. A.17. It shows that in the constant-torque region all current magnitudes are the same. However, in flux weakening region the measured and 3D model predicted phase current magnitudes become lower than the 2D model predicted due to the stator end leakage inductance, which cannot be considered in the 2D model. Therefore, smaller phase current is required to satisfy the voltage limitation. This clearly illustrates the significant reduction in the 3D model predicted and measured torque -speed characteristics, Fig. A.15.

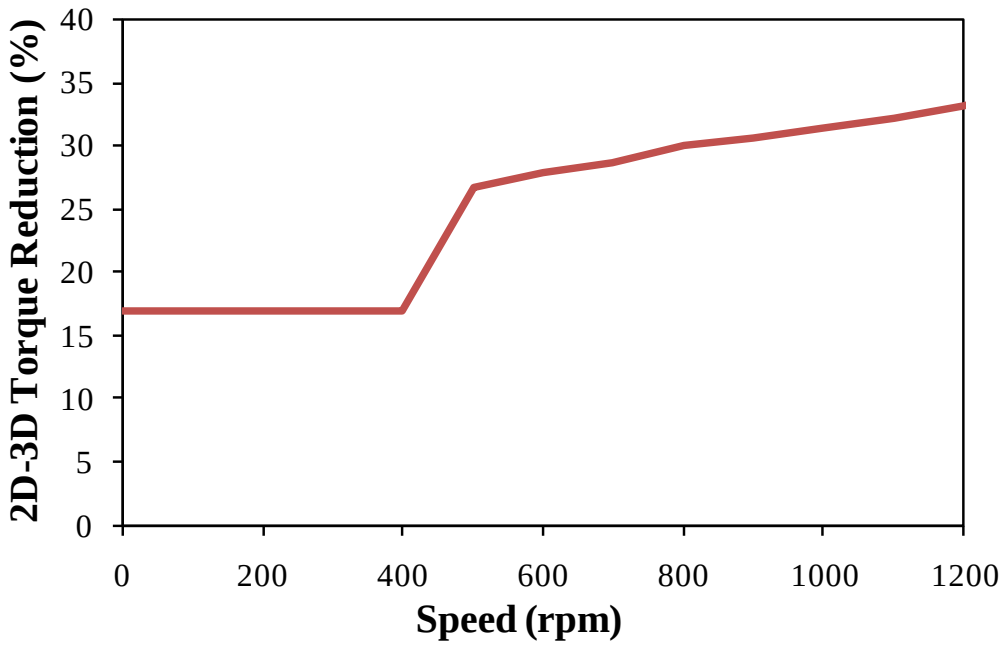

Fig. A.16 Torque reduction percentage between 2D and 3D FE predicted torque.

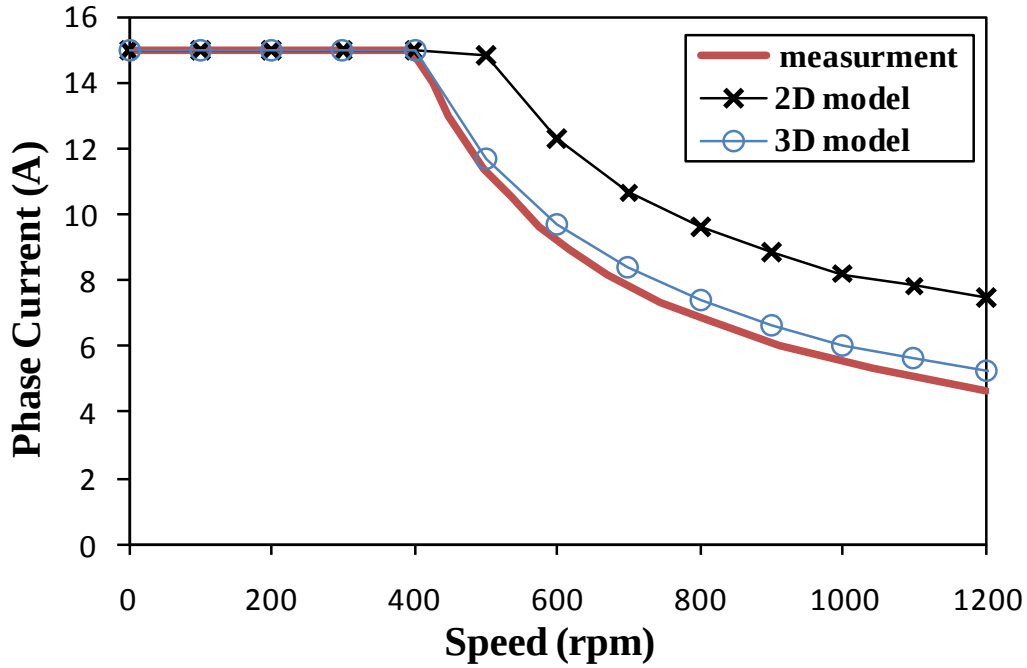

Fig. A.17 Comparison of measured and 2D and 3D FE predicted phase current magnitudes.

A.6. Conclusions

The torque- and power-speed characteristics of a multi-tooth (6-4 stator pole/tooth, 19-rotor pole) SFPM machine have been investigated by different prediction methods, accounting for different cross-coupling levels, vis. full, partial and without cross-coupling consideration. The influence of the cross-coupling on dq-axis inductances of the studied machine is relatively small. However, it is more significant on the PM flux linkage. Therefore, the partial cross-coupling model, which gives almost the same accuracy as the full cross-coupling model, is likely preferable to be employed in the analysis of the multi-tooth SFPM machine, since it is less complicated and less time consuming.

The influence of the end effect on the parameters and performance of the machine has also been studied. Similar to the electromagnetic performance, the end-effect causes a large reduction in torque-speed characteristics. However, such reduction is more significant in the flux weakening operation region due to the stator end leakage, which enlarges the dq-axis inductances and reduces the PM flux linkage. The discussions and analyses presented in this paper are applicable to the analysis of E-core and C-core SFPM machines [A.18].

References

[A.1] Z. Q. Zhu, J. T. Chen, Y. Pang, D. Howe, S. Iwasaki, and R. Deodhar, "Analysis of a novel multi-tooth flux-switching PM brushless ac machine for high torque direct-drive applications," *IEEE Trans. Magnetics*, vol. 44, no. 11, pp. 4313-4316, Nov 2008.

[A.2] Z. Q. Zhu and J. T. Chen, "Advanced flux-switching permanent magnet brushless machines," *IEEE Trans. Magnetics*, vol. 46, no. 6, pp. 1447-1453, Jun 2010.

[A.3] Z. Q. Zhu, Y. Pang, D. Howe, S. Iwasaki, R. Deodhar, and A. Pride, "Analysis of electromagnetic performance of flux-switching permanent-magnet machines by nonlinear adaptive lumped parameter magnetic circuit model," *IEEE Trans. Magnetics*, vol.41, no.11, pp.4277-4287 Nov 2005.

[A.4] J. T. Chen and Z. Q. Zhu, "Winding configurations and optimal stator and rotor pole combination of flux-switching PM brushless AC machines," *IEEE Trans. Energy Conversion*, vol. 25, no. 2, pp. 293-302, Jun. 2010.

[A.5] S. E. Rauch and L. J. Johnson, "Design principles of flux-switching alternators," *AIEE Trans.*, vol. 74III, pp. 1261-1268, 1955.

[A.6] Y. Amara, E. Hoang, M. Gabsi, M. Lecrivain, and S. Allano, "Design and comparison of different flux-switch synchronous machines for an aircraft oil breather application," *in Proc. 2nd IEEE Inter. Signals, System, Decision and Information Technology*, Mar 2003.

[A.7] E. Hoang, A. H. Ben-Ahmed, and J. Lucidarme, "Switching flux permanent magnet polyphases synchronous machines," *European Confer. Power Electronics and Applications*, vol. 3, 1997 pp. 903-908.

[A.8] A. S. Thomas, Z.Q. Zhu, R.L. Owen, G.W. Jewell, and D. Howe, "Multi-phase flux-switching permanent magnet brushless machine for aerospace application," *IEEE Trans. Industry Applications*, vol. 45, no. 6, pp. 1971-1981, Nov/Dec 2009.

[A.9] R. L. Owen, Z. Q. Zhu, A. S. Thomas, G. W. Jewell, and D. Howe, "Fault-tolerant flux switching permanent magnet brushless AC machines," *IEEE Industry Application Society Annual Meeting*, Oct. 2008.

[A.10] W. Fei, P.C.K. Luk, J. X. Shen, and Y. Wang, "A novel outer-rotor permanent magnet flux-switching machine for urban electric vehicle propulsion," *Inter. Confer. Power Electronics Systems and Applications*, May 2009.

[A.11] E. Hoang, M. Lecrivain, and M. Gabsi, "A new structure of a switching flux synchronous polyphased machine with hybrid excitation," in *Proc. Eur. Conf. Power Electronics and Applications*, Sep 2007, pp. 1-8.

[A.12] W. Hua, M. Cheng, and G. Zhang, "A novel hybrid excitation flux switching motor for hybrid vehicles," *IEEE Trans. Magnetics*, vol.45, no.10, pp.4728-4731, Dec 2009.

[A.13] R. L. Owen, Z. Q. Zhu, and G. W. Jewell, "Hybrid excited flux-switching PM machines," in *Proc. Eur. Conf. Power Electronics and Applications*, Sep 2009, pp. 1-10.

[A.14] Z.Q. Zhu, Y. Pang, W. Hua, M. Cheng, and D. Howe, "Investigation of end-effect in PM brushless machines having magnets in the stator," *J. Applied Physics*, vol. pp, no. 8, 08R319, 1-3, 2006.

[A.15] Z. Q. Zhu, J. T. Chen, Y. Pang, S. Iwasaki, and R. Deodhar, "Modeling of end-effect in flux-switching permanent magnet machines," *ICEM XIX Inter. Confer. on Electrical Machines and Systems*, Oct 2010, pp. 943-948.

[A.16] X. Zhu, M. Cheng, W. Hua, and J. Zhang, "Investigation of end effect and experimental validation for hybrid excited doubly salient machine," *IEEE Confer. electromagnetic Field Calculation*, Jun. 2006.

[A.17] J. T. Chen "High-torque direct-drive flux-switching permanent magnet brushless AC machines," *Ph.D. Thesis, the Department of Electronic and Electrical Engineering, University of Sheffield*, Oct 2009.

[A.18] J. T. Chen, Z. Q. Zhu, S. Iwasaki, and R. Deodhar, "Comparison of losses and efficiency in alternate flux-switching permanent magnet machines," *ICEM XIX Inter. Confer. on Electrical Machines*, Sept 2010, pp. 1-6.

[A.19] J. T. Chen, Z. Q. Zhu, and D. Howe, "Stator and rotor pole combinations for multi-tooth flux-switching PM brushless ac machines," *IEEE Trans. Magnetics*, vol. 44, no. 12, pp. 4659-4667, 2008.

[A.20] S. Morimoto, M. Sanada, and Y. Takeda, "Wide-speed operation of interior permanent magnet synchronous motors with high-performance current regulator," *IEEE Trans. Industrial Applications*, vol. 30, no. 4, pp. 920-926, Jul/Aug 1994.

[A.21] E. Hoang, M. Gabsi, M. Lecrivain and B. Multon, "Influence of magnetic losses on maximum power limits of synchronous permanent magnet drives in flux-weakening mode," *Proc. IEEE Industry Applications Society Annual Conference.* Vol.1, pp.299-303, 2000.

[A.22] G. Qi, J.T. Chen, Z.Q. Zhu, D. Howe, L.B. Zhou, and C.L. Gu, "Influence of skew and cross-coupling on d- and q- axis inductances and flux-weakening performance of PM brushless AC machine" *IEEE Trans. Magnetics*, vol. 45, no. 5, pp. 2854-2859, MAY 2009.

Appendix B: Torque Speed Characteristics of Synchronous Reluctance Machines Having AC Sinusoidal with DC Bias Excitation and Asymmetric winding Connection

The output torque and line voltage of the SynR 6 stator/4 rotor poles machines having different winding connections, i.e. asymmetric and symmetric, and AC sinusoidal with DC bias excitation have been investigated in section 7.3. As an outcome of these investigations, the symmetric winding connection has been determined to be used during the torque-speed characteristics prediction and analysis, section 7.4. However, for reference, the torque-speed characteristics of the 6 stator/4 rotor poles machine having AC sinusoidal with DC bias excitation and asymmetric winding connection are also predicted and compared with their counterparts of the machine with symmetric winding connection in this appendix. For this purpose, the average output torque and the maximum line voltage against AC current angle of such machine are calculated for different total current densities, as shown in Fig. B.1 and Fig. B.2, respectively. It is worth mentioning that both the AC and DC coils have the same current density since with the asymmetric winding connection the machine exhibits the maximum output torque at a unity AC/DC ratio, Fig. 7.15(a). These data have been then utilised to predict the torque- and power-speed characteristics at 200V voltage limitation. In order to obtain the maximum possible torque-speed performance at the specified voltage limitation, at each speed the optimal total current density and AC current angle combination, which results in the maximum output torque within the voltage limitation, is utilised. The obtained torque- and power-speed characteristics are plotted in Fig. B.3, i.e. asymmetric (varying total current density). For more comparison, the torque- and power-speed characteristics under asymmetric winding connetion have been also predicted using the constant DC/varing AC technique. For this purpose, the variations of the average output torque and machine maximum line voltage against the AC current angle are calculated at 34 A/mm^2 DC current density and for different AC current density, as respectively shown in Fig. B.4 and Fig. B.5. In the constant-torque region, the AC/DC ratio and AC current angle are kept constant, i.e. at 1 and 10 degree, but in the flux weakening operation region both the AC current density and angle are adjused to operate the machine at its maximum performance within the voltage limitation. The prediction results of the two techniques are compared with their counterparts of the symmetric winding connection in Fig. B.3. In general, the machine with symmetric winding connetion exhibits larger performance all over

the speed range. However, in the flux weakening operation region the differene becomes relatively larger. This is because the machine with the symmetric winding connetion exhibits larger average output torque as illusteated in Fig. 7.15(a). In addition, the machine with asymmetric winding connetion generates larger line voltage, as discussed in section 7.3.2.2. Furthermore, the machine with asymmetric winding connection produces beter performance when the constant DC/varing AC technique is used. This is because this technique results in larger output torque, as can be noted by comparing Fig. B.1 and Fig. B.4, since the DC current density is kept constant.

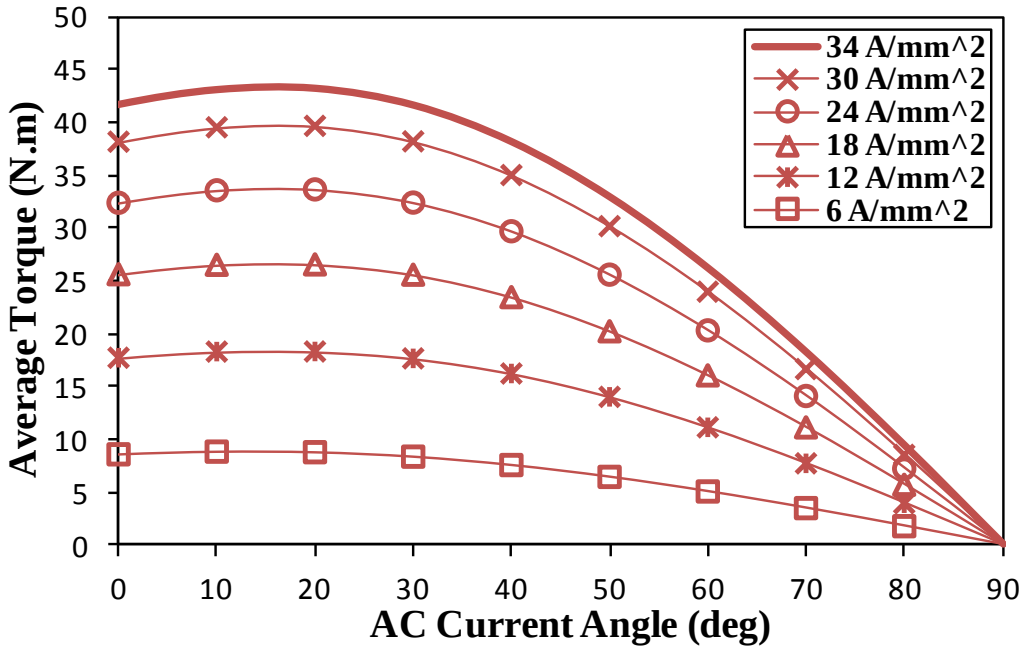

Fig. B.1 Variation of average output torque against AC current angle of 6 stator/4 rotor poles machine having asymmetric winding connection for different total current densities, at $J_{DC}=J_{AC\ rms}$.

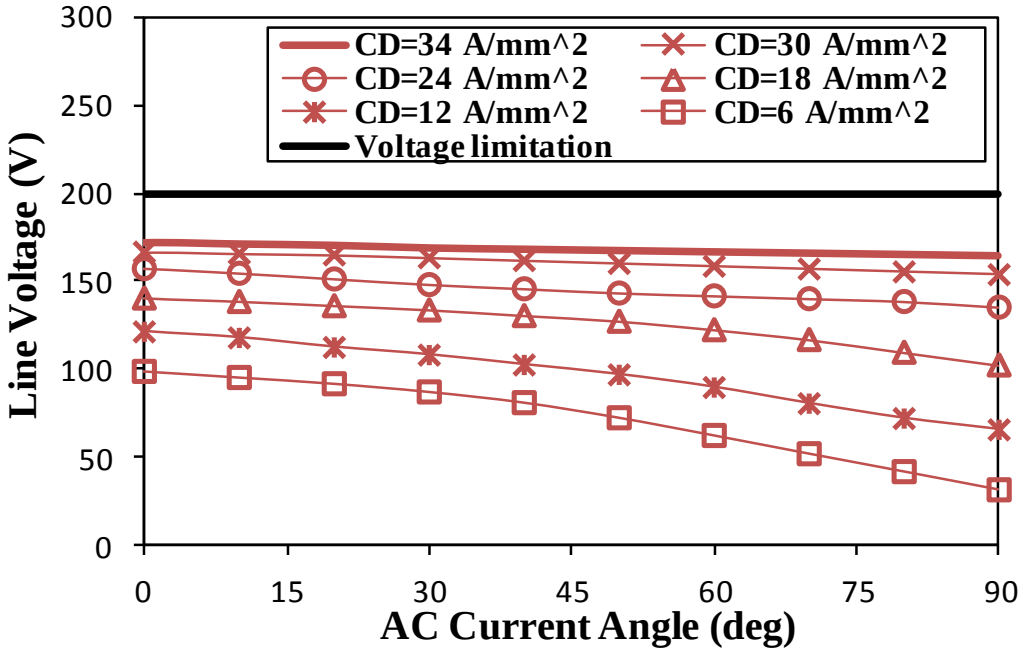

(a) 2000 rpm

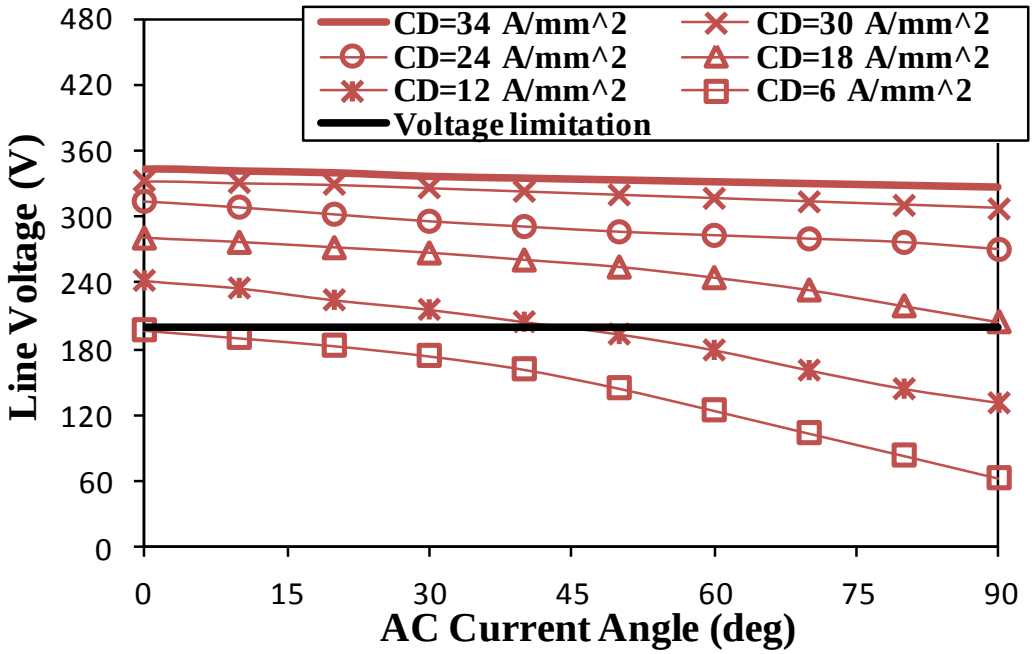

(b) 4000 rpm

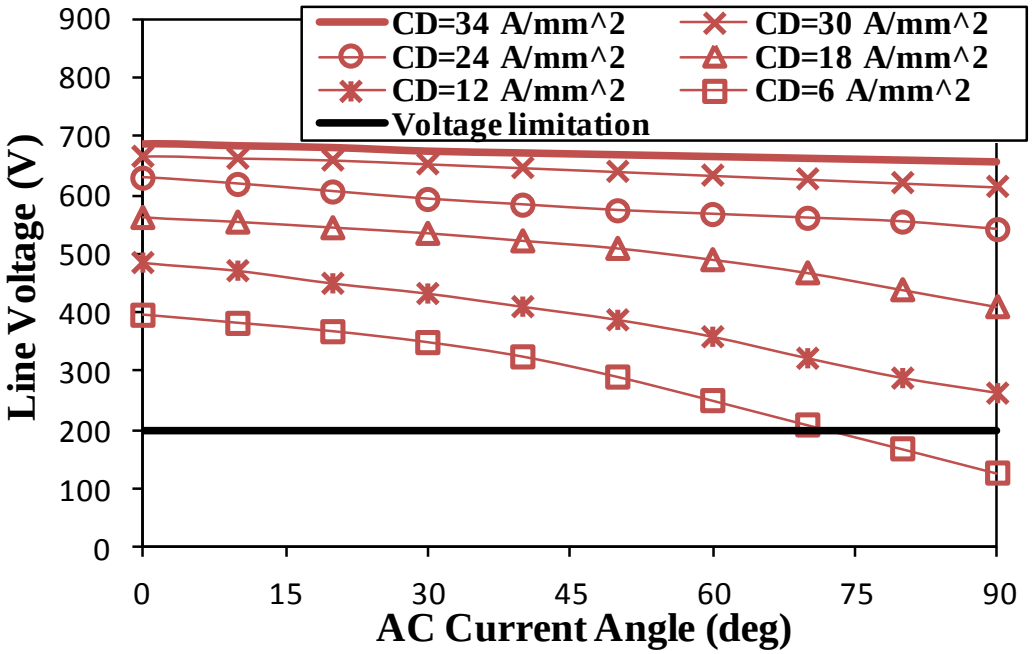

(c) 8000 rpm

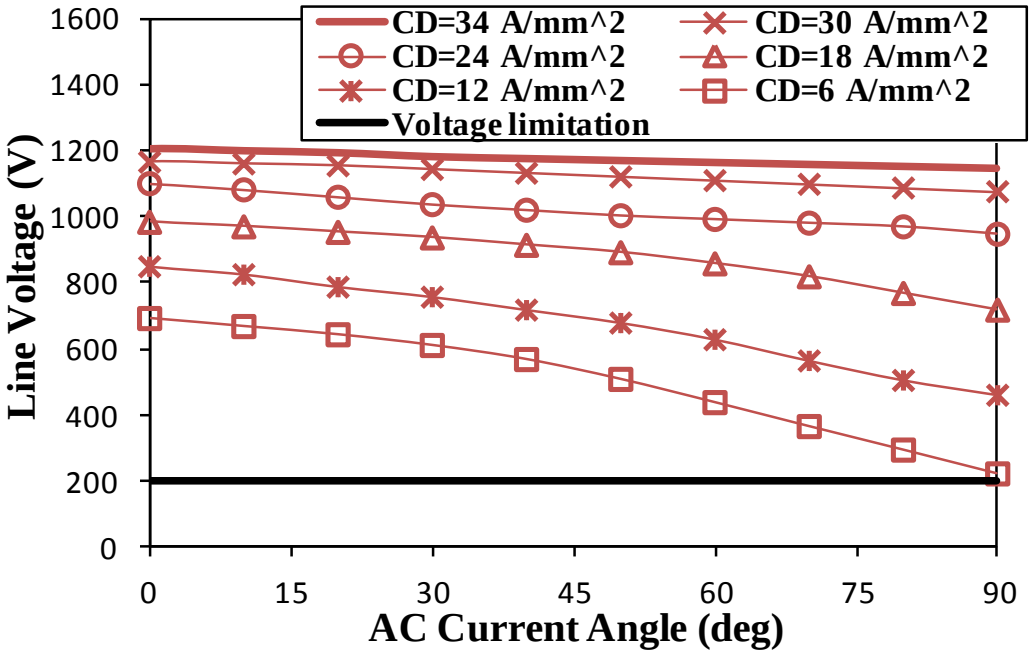

(d) 14000 rpm

Fig. B.2 Variation of maximum line voltage against AC current angle of 6 stator/4 rotor poles machines having asymmetric winding connection for different total current densities and speeds, at $J_{DC}=J_{AC\ rms}$.

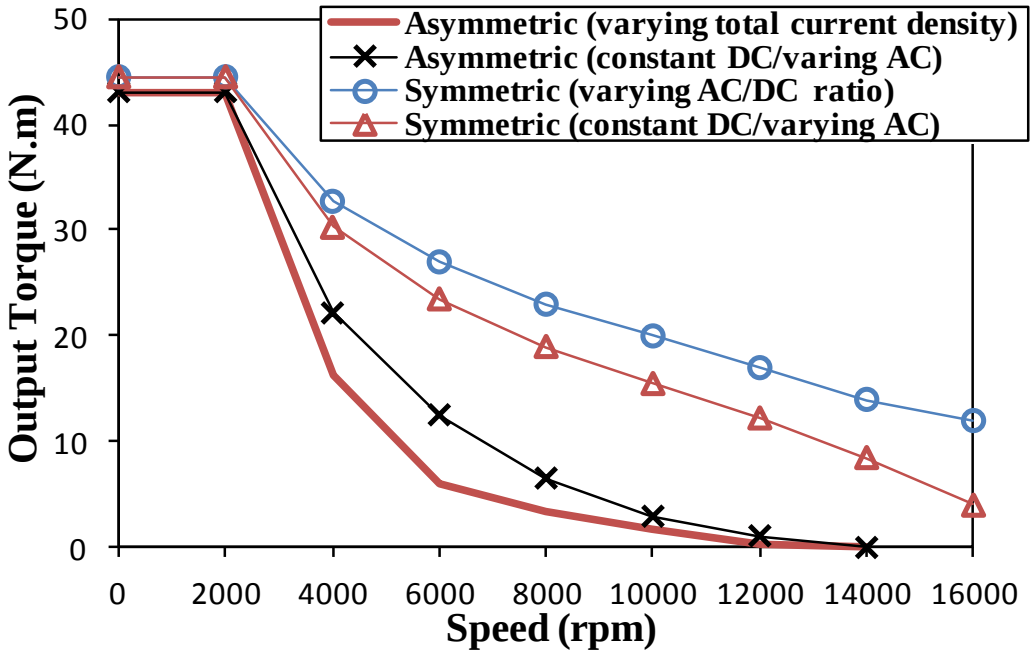

(a) Torque-speed characteristics

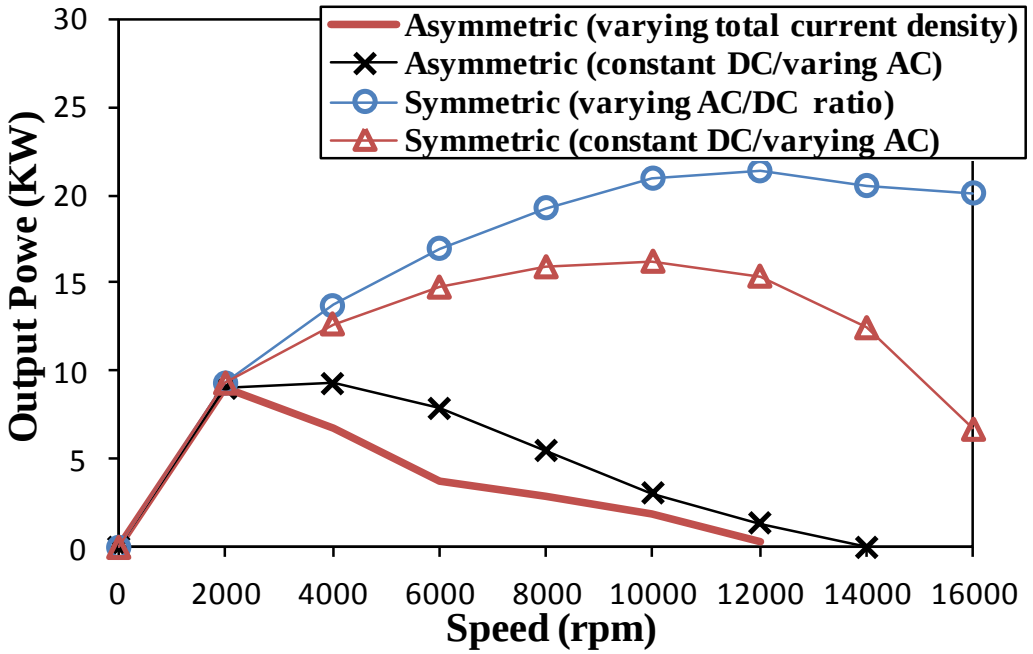

(b) Power-speed characteristics

Fig. B.3 Comparison of torque- and power-speed characteristics of 6 stator/4 rotor poles machines having asymmetric and symmetric winding connections under different prediction techniques, at 34 A_{rms}/mm^2 average current density and 200 V voltage limitation.

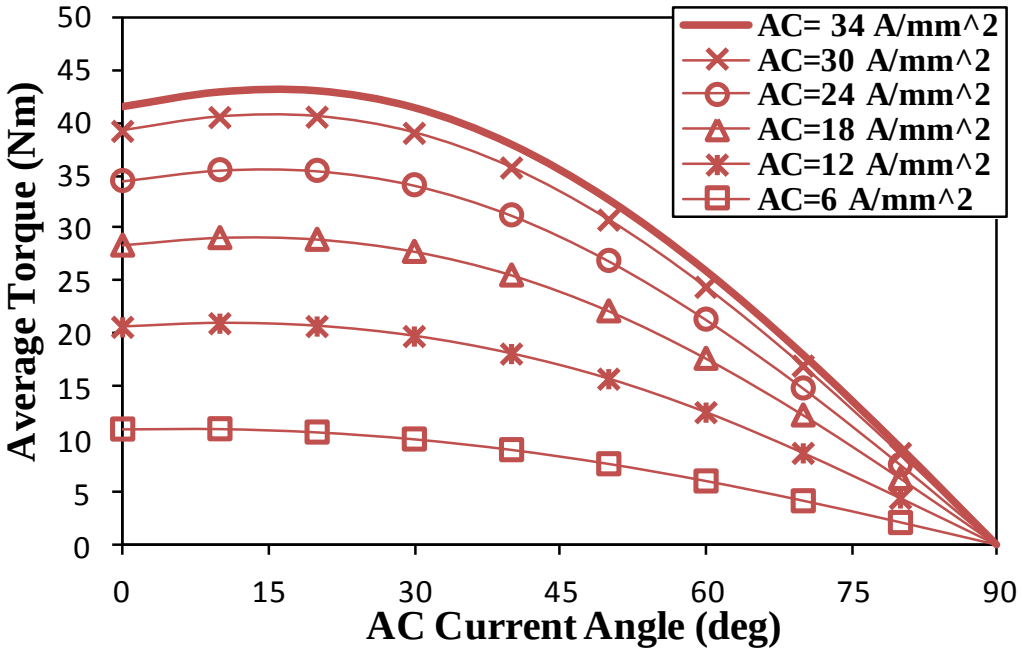

Fig. B.4 Variation of average output torque against AC current angle of 6 stator/4 rotor poles machines having asymmetric winding connection for different AC current densities, at 34 A/mm^2 DC constant current density.

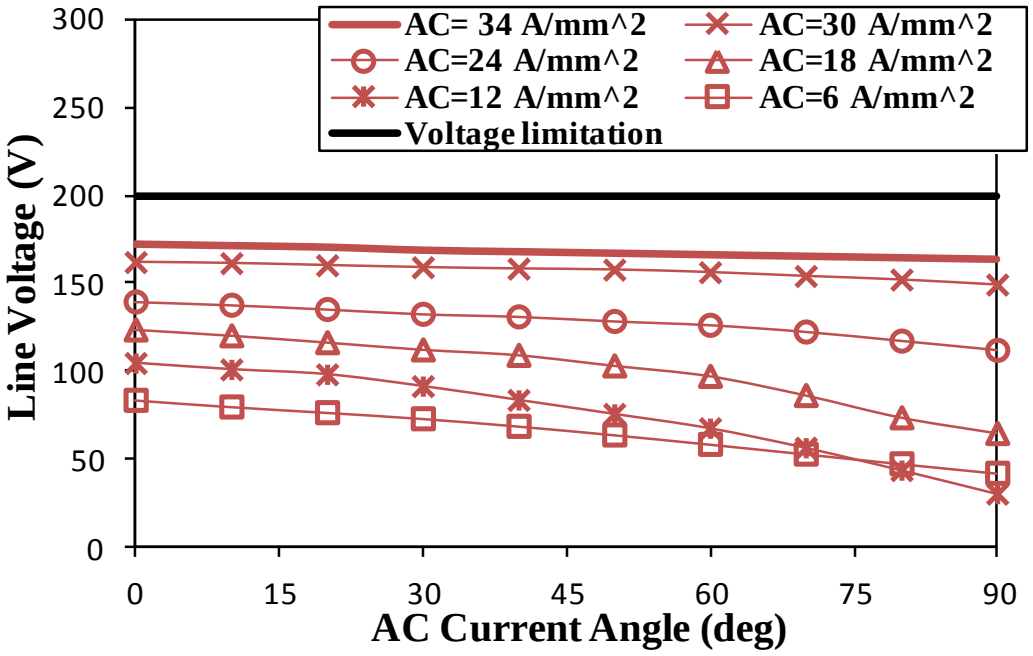

(a) 2000 rpm

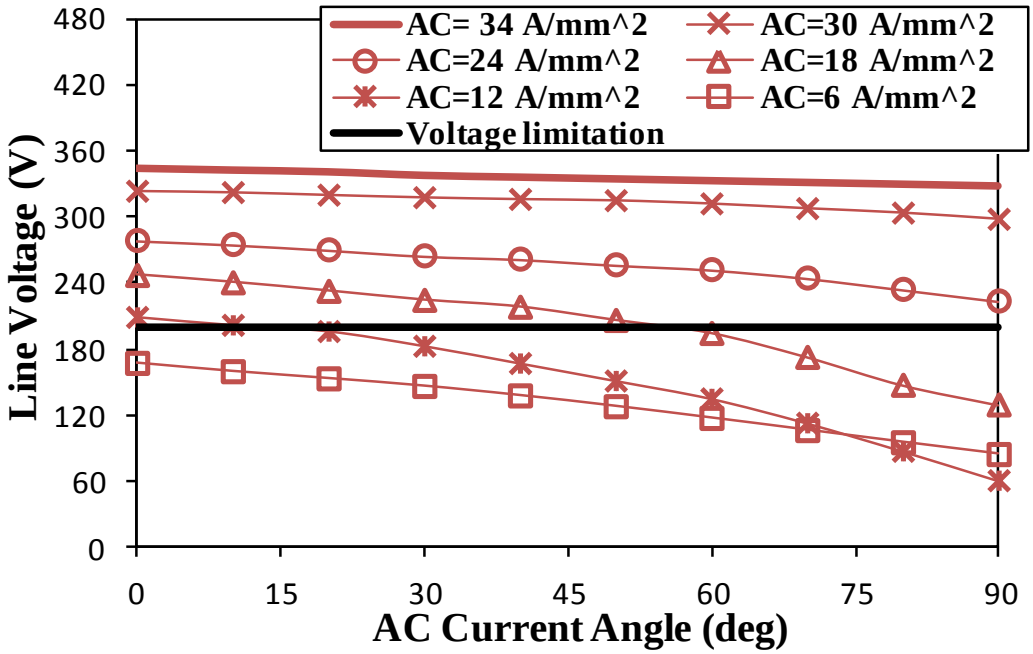

(b) 4000 rpm

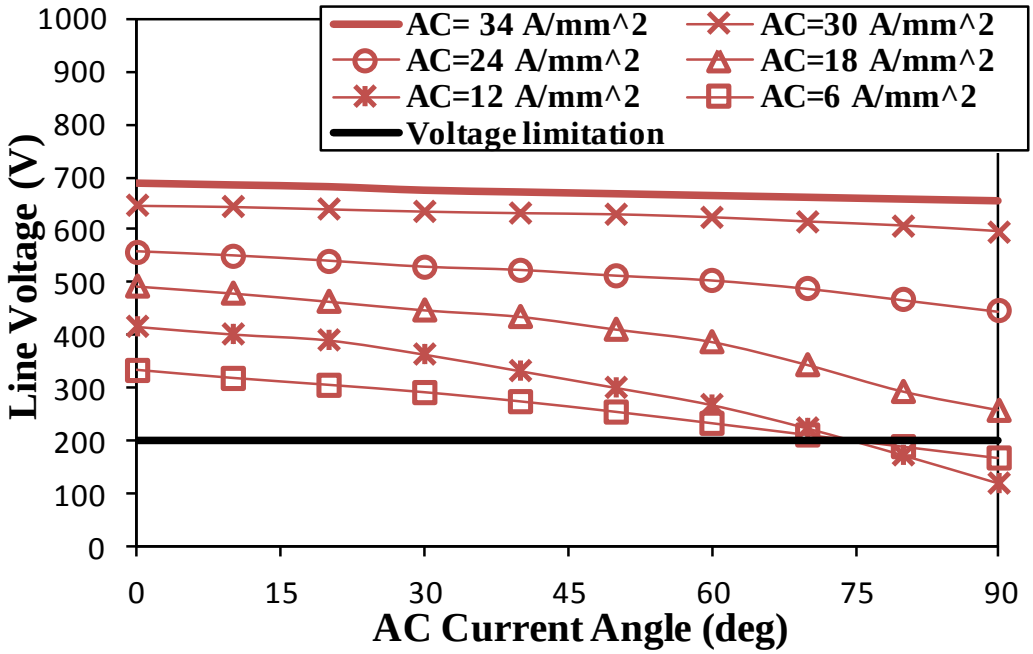

(c) 8000 rpm

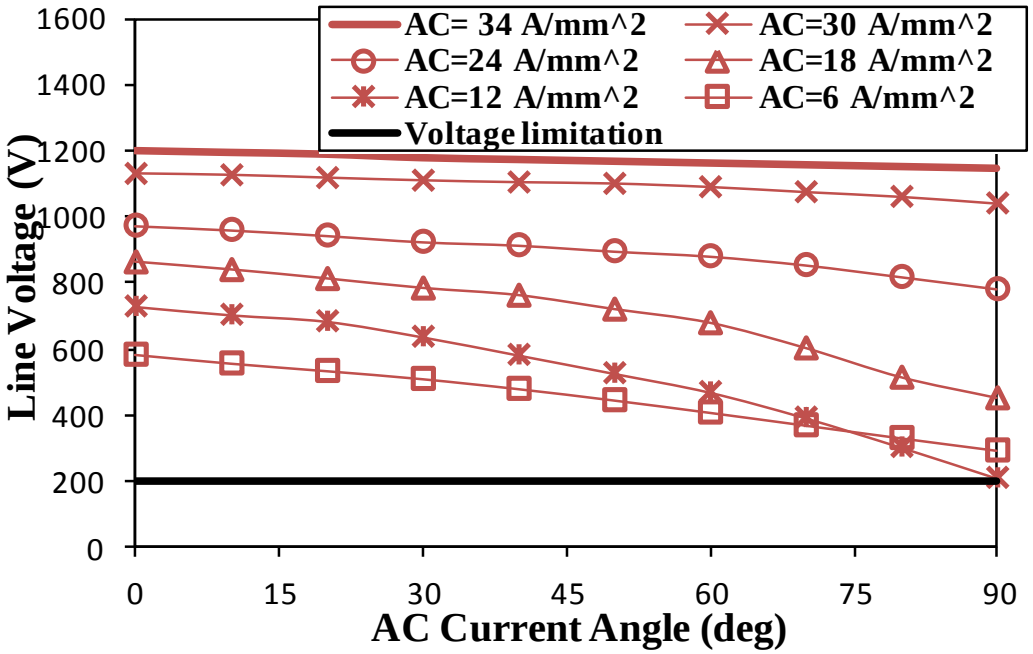

(d) 14000 rpm

Fig. B.5 Variation of line voltage against AC current angle of 6 stator/4 rotor poles machines having asymmetric winding connection for different AC current densities and speeds, at 34 A/mm^2 constant DC current density

Appendix C: Performance Analysis of SR Machine Under Unipolar Excitation-Conventional Operation

For the purpose of examining the capability of the SR machine under the bipolar excitation. The electromagnetic performance of such machine under the conventional unipolar excitation is predicted in this appendix and compared with its bipolar counterparts in Chapter 7. The analyses are carried out on exactly the same 6 stator/4 rotor pole machine, which is illustrated in Chapter 6 and Chapter 7, using the asymmetric half H-bridge converters, Fig. C.1, and under 100 V DC link voltage and 34 A/mm^2 maximum current density. The current density against the number of turns per coil at 2500 rpm is given in Fig. C.2. Such calculations are carried out for 30 mechanical degree commutation angle (conduction angle), which is the normal stroke angular displacement for the 3 phase 6 stator/4 rotor poles SR machine [C.1]. The normal on and off angle positions, i.e. the normal stork angle, are illustrated in Fig. C3 However, the commutation angle will be further optimized during the torque-speed characteristics prediction.

$$\text{Normal stroke angle} = \frac{360}{m.N_r} \tag{C. 1}$$

where m and N_r are the number of phases and rotor poles, respectively.

Fig. C.2 shows that lower number of turns results in larger average torque due to the larger current density, since the phase resistance and voltage become lower thus more current can flow in the phase coil. The maximum current density is satisfied when the number of turns per coil is 14, as shown in Fig. C.2. Thus, such number will be utilised in the following analyses. At 34 A/mm^2 current density, the machine can deliver 46 Nm average output torque. The output torque waveform is given in Fig. C.4. However, for further illustrations, the variation of average output torque and torque ripple against current density is shown in Fig. C.5.

The torque- and power-speed characteristics of the analysed machine under such excitation can be simply predicted by varying the rotating speed and calculate their corresponding output torques and powers. However, in order to obtain the maximum possible characteristics. The optimal on and off angles at each speed should be determined [C.1]. For this purpose, at each speed the commutation angle, i.e. the period between the on and off

angles, is varied between zero and 90 mechanical degree. In other words, the off angle is kept always 0 when the rotor is at the end of normal stroke position, Fig. C.3(b). However, the on angle is scanned between 0 and -90 mechanical degree with respect to the end of normal stroke position. At each angle the corresponding average torque and current density are calculated. The obtained results are illustrated in Fig. C.6. It shows that at any speed the torque gradually increases when the commutation angle increases, since a larger current can flows in the phase windings. Therefore, at relatively low speeds, e.g. 2000 rpm or lower, the commutation angle is even smaller than the normal stroke, thus the current density does not exceed the maximum allowed value, as shown in Fig. C.6 (a). On the other hand, further increasing in the commutation angle results in output torque reduction since a negative phase output torque is produced, as illustrated in Fig. C.7. When the negative phase part is relatively small, i.e. at relatively small commutation angle, the total average output torque of the motor is larger, in addition the torque ripple becomes smaller. However, at relatively larger commutation angle, the phase negative torque becomes larger, thus it will reduce the total average output torque of the machine. Such discussion is clearly illustrated in Fig. C.8. Furthermore, at relatively low speeds the maximum possible output torque is achieved at relatively small commutation angle. However, such angle becomes gradually larger when the speed increases since at low speeds the phase current rise is faster, since the commutation time for the same commutation angle is longer and the phase voltage is lower. The results of Fig. C.6 are utilised to predict the torque- and power-speed characteristics of the analysed machine which are plotted in Fig. C.9. In order to highlight the benefit of adjusting the commutation angle, such characteristics are calculated again for a fixed commutation angle, i.e. 30 mechanical degree. The obtained results are also plotted in Fig. C.9, while the corresponding variations of the current density and commutation angle are respectively compared in Fig. C.10(a) and Fig. C.10(b). Comparing with the fixed commutation angle method, the varying commutation angle counterpart results in much larger output torque and power, but at the same time larger current density is required. It should be also mentioned that even when the fixed commutation angle prediction method is utilised, the commutation angle is reduced at significantly low speeds, Fig. C.10(b) since if the normal stroke is maintained the current density will be significantly large. Furthermore, the variations of the related iron and copper losses against speed under the varying commutation angle prediction method are also estimated and given in Fig. C.11. Based on these data, the efficiency of the analysed machine under the conventional unipolar excitation is calculated and shown in Fig. C.12.

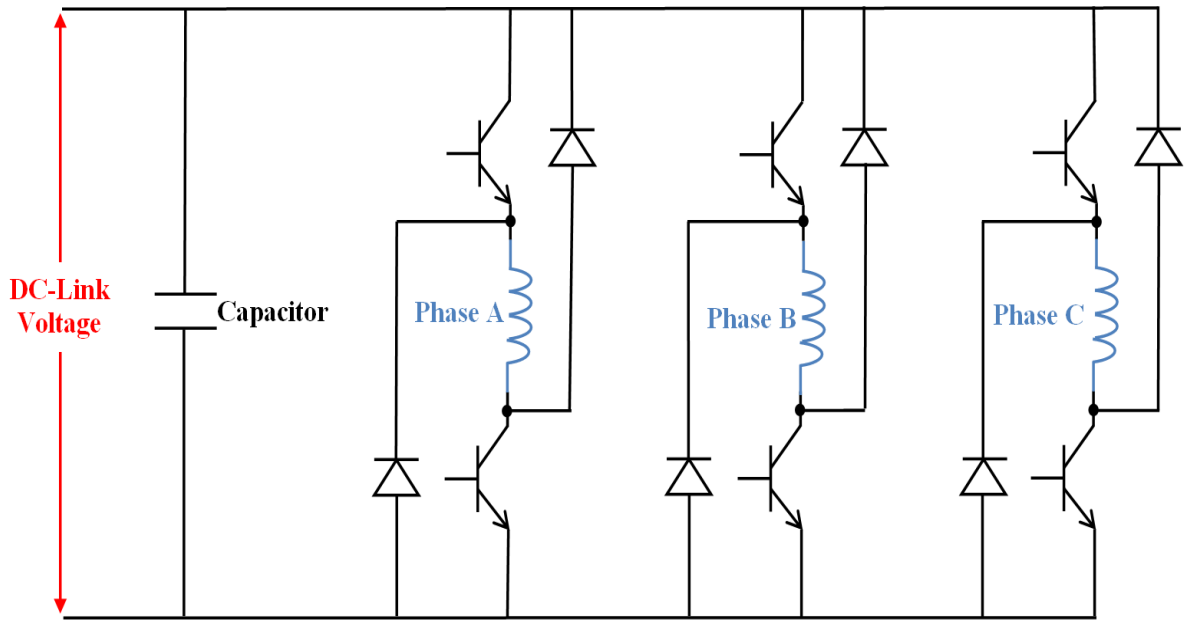

Fig. C.1 Asymmetric unipolar driver inverter for conventional SR machines.

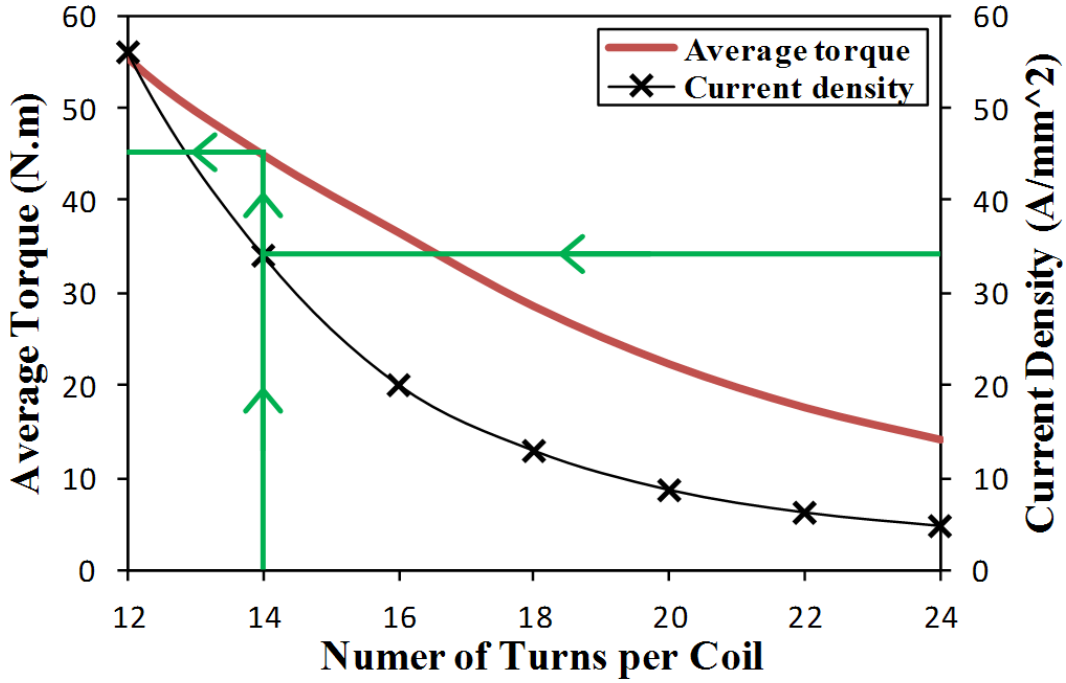

Fig. C.2 Variation of average output torque and current density against number of turns per coil of 6 stator/4 rotor poles SR motor, at 0 and 30 mechanical degree on and off angles and 2500 rpm

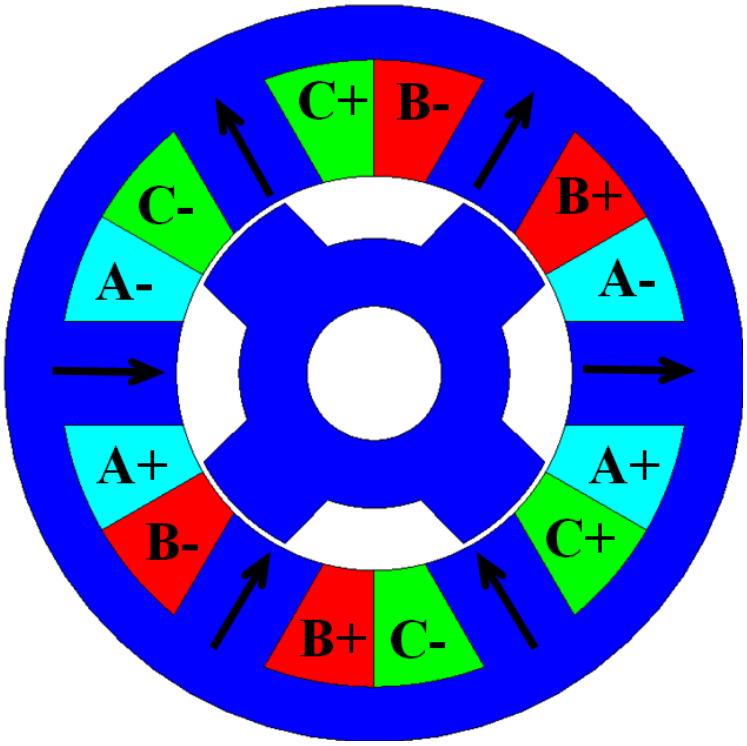

(a) Fully unaligned position with phase A, on angle

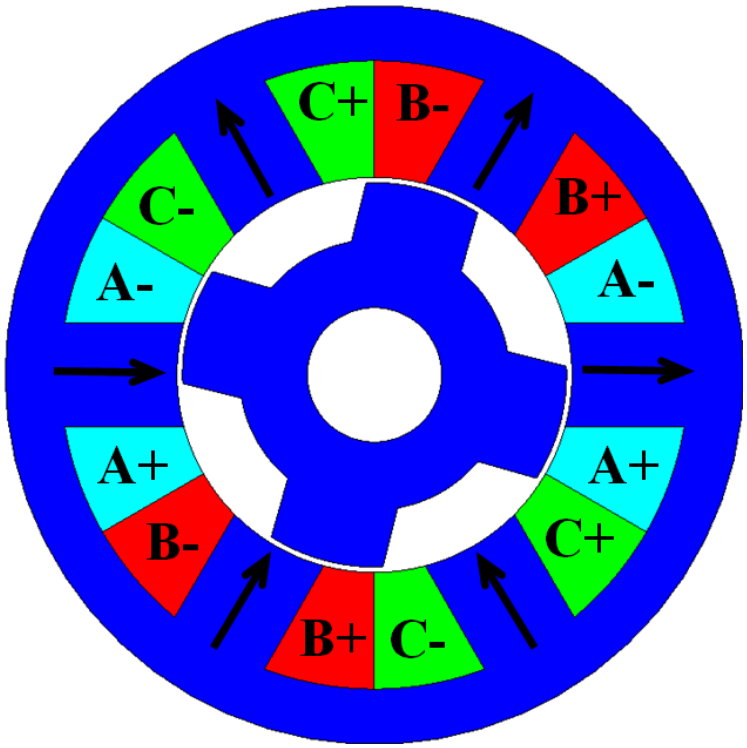

(b) End of normal stroke position, off angle

Fig. C.3 Different rotor positions of 6 stator/4 rotor poles machine, on and off angles for 30 mechanical degree normal stroke angular displacement.

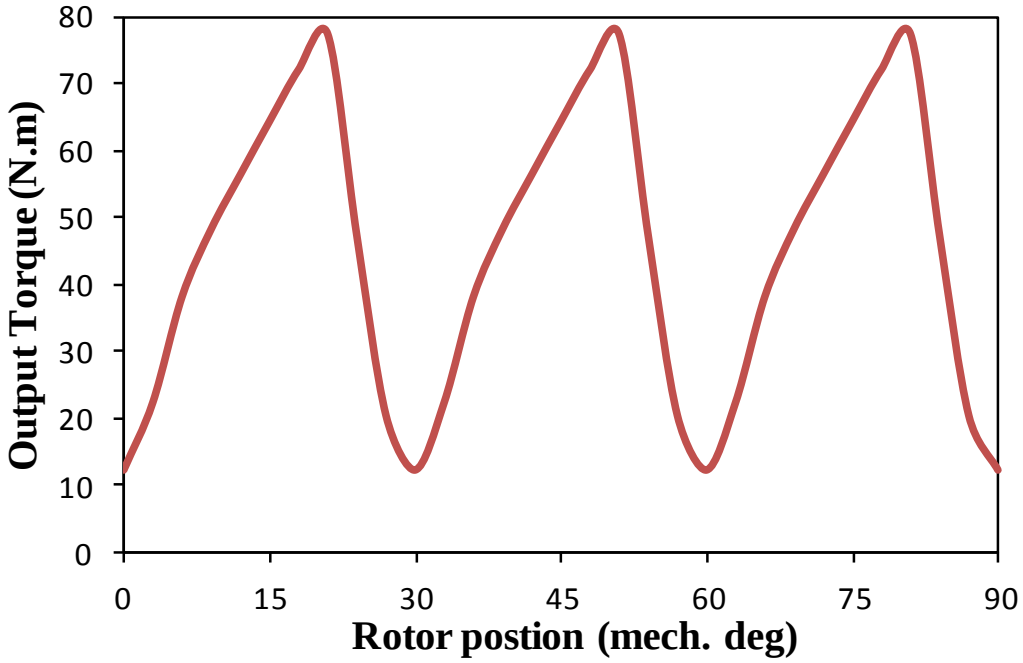

Fig. C.4 Output torque waveform of 6 stator/4 rotor poles SR machine, at 0 and 30 mechanical degree on and off angles, 34 A/mm^2 current density and 2500 rpm.

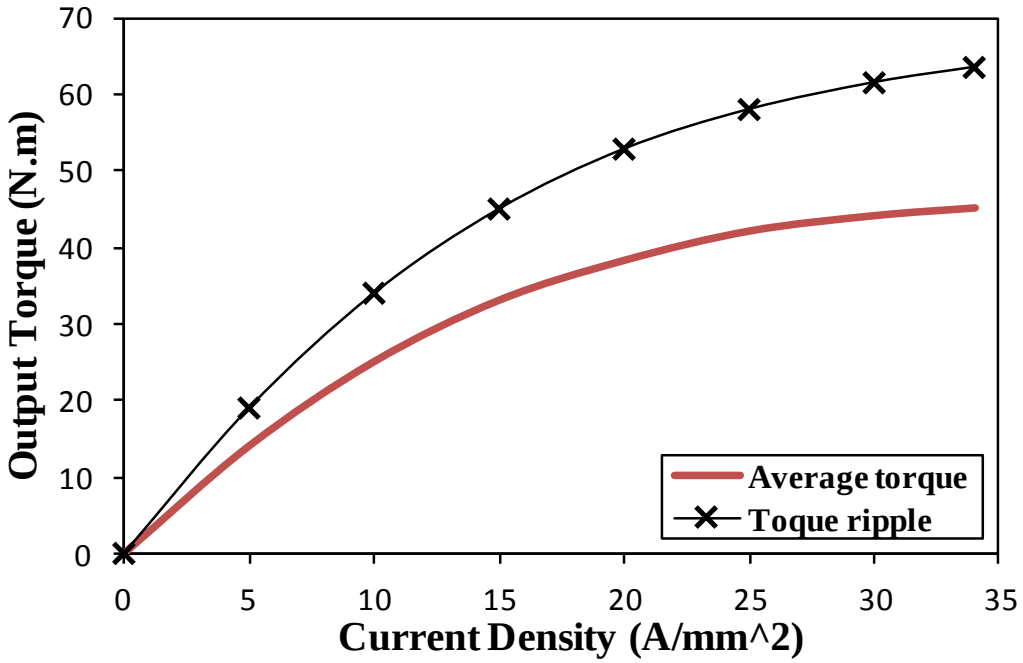

Fig. C.5 Variation of average torque and torque ripple against current density of 6 stator/4 rotor poles SR machine, at 0 and 30 mechanical degree on and off angles and 2500 rpm.

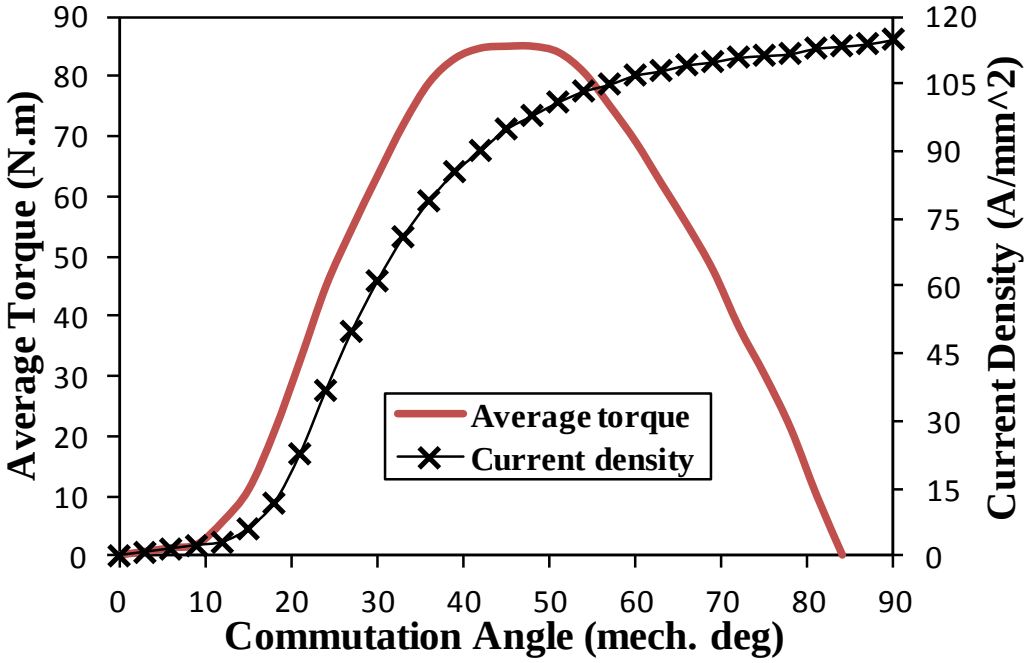

(a) 2000 rpm

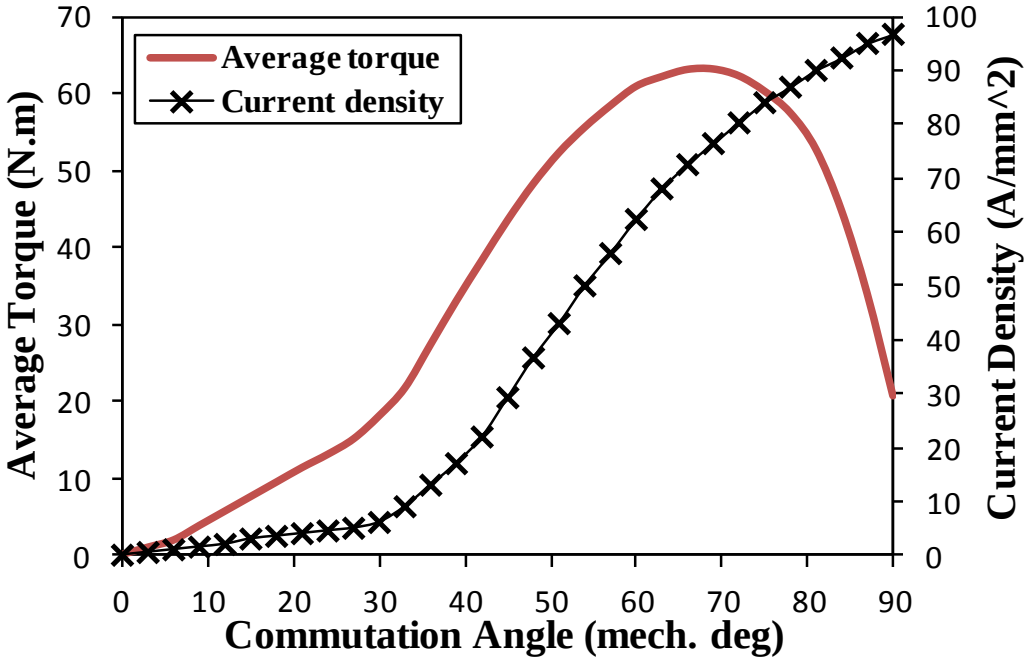

(b) 4000 rpm

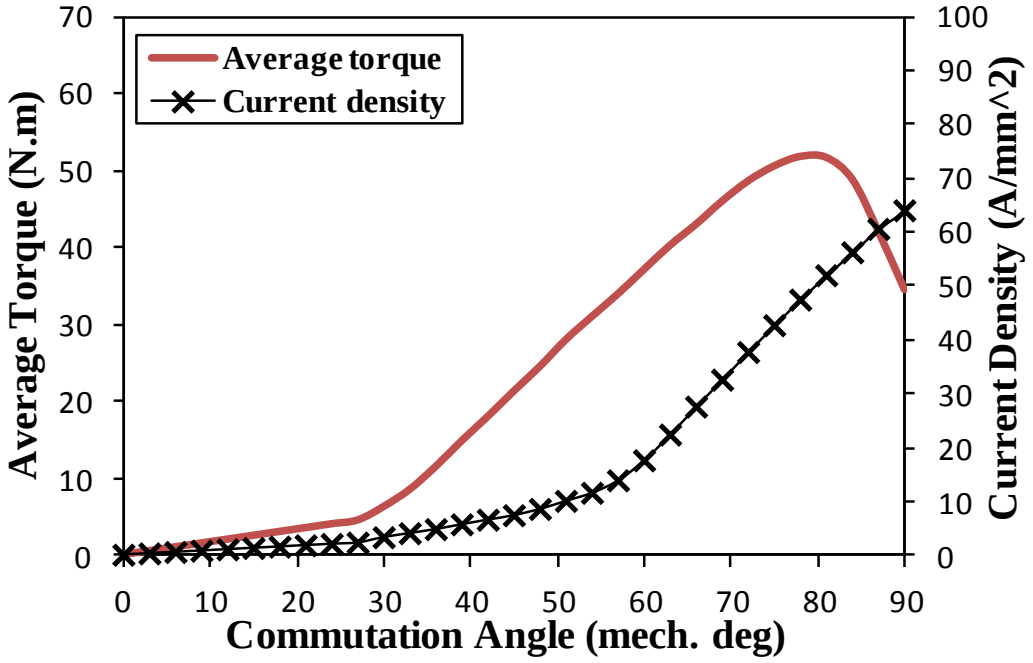

(c) 6000 rpm

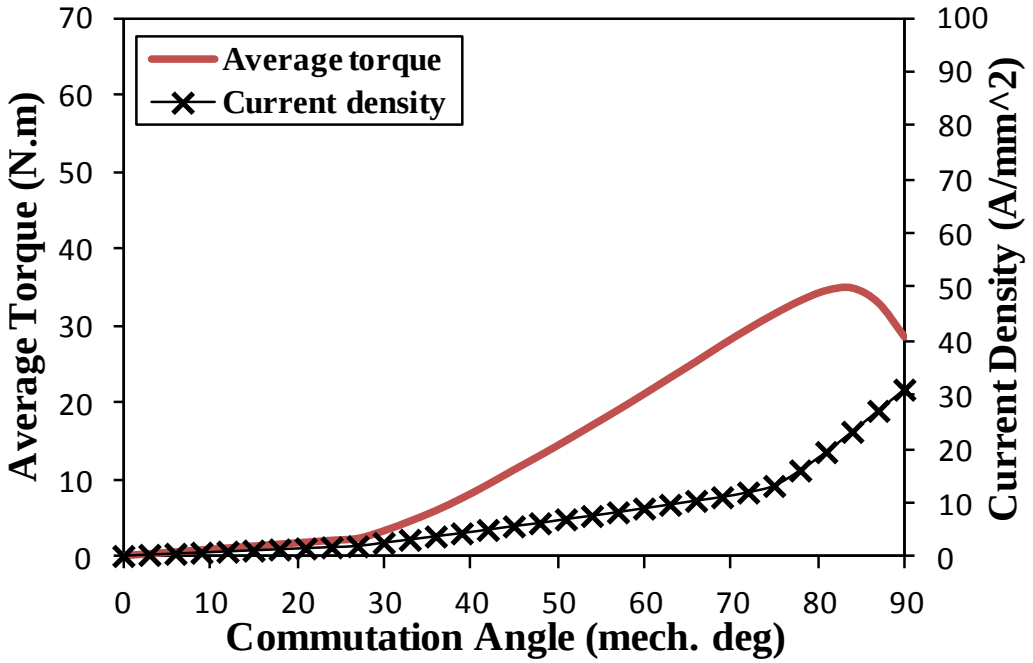

(d) Speed is 8000

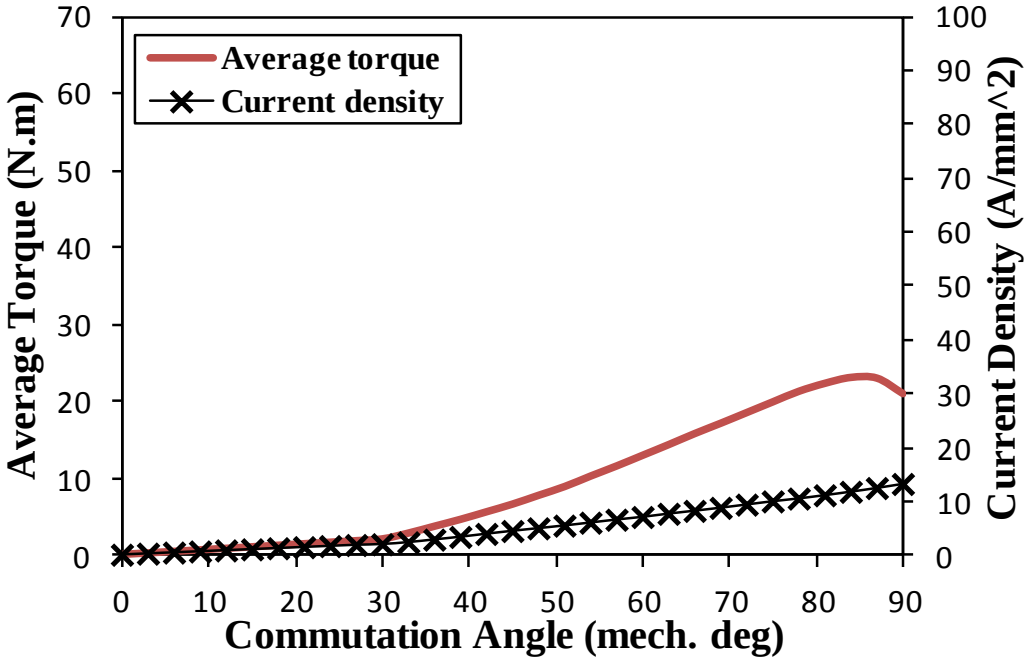

(e) 10000 rpm

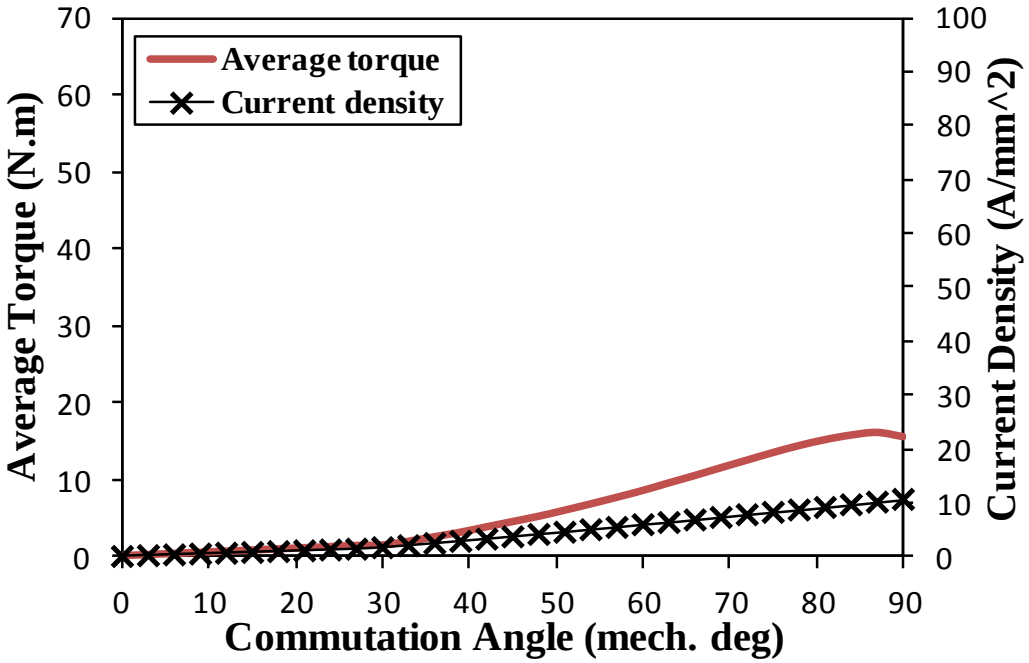

(f) 12000 rpm

Fig. C.6 Variation of average output torque and current density against commutation angle of 6 stator/4 rotor poles SR machine for different rotating speeds.

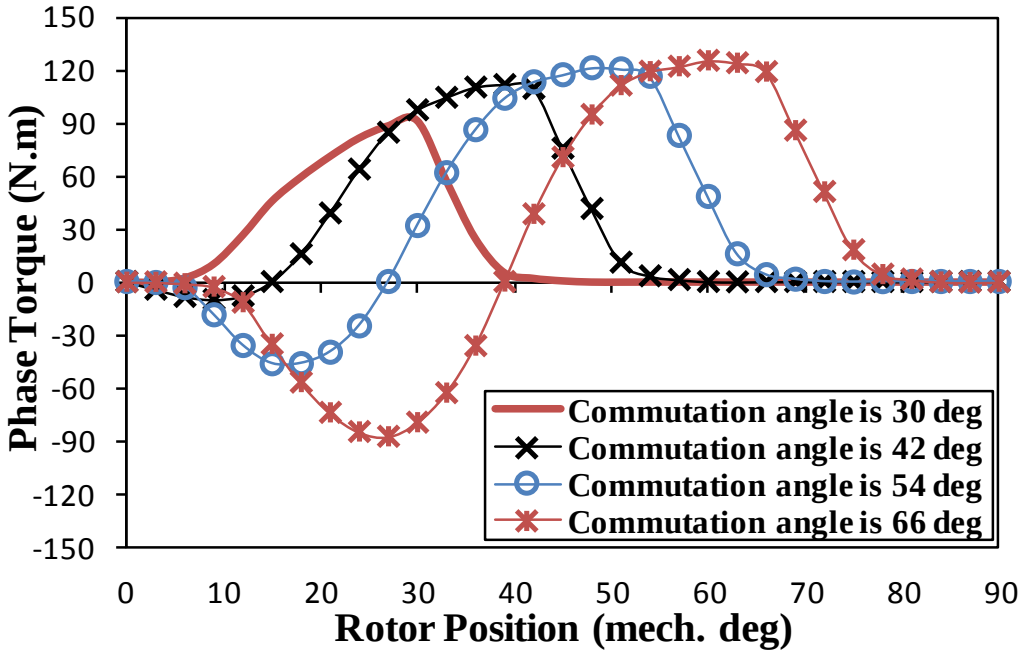

Fig. C.7 Variations of output torque of phase A of 6 stator/4 rotor poles SR machine for different commutation angles, at 2000 rpm.

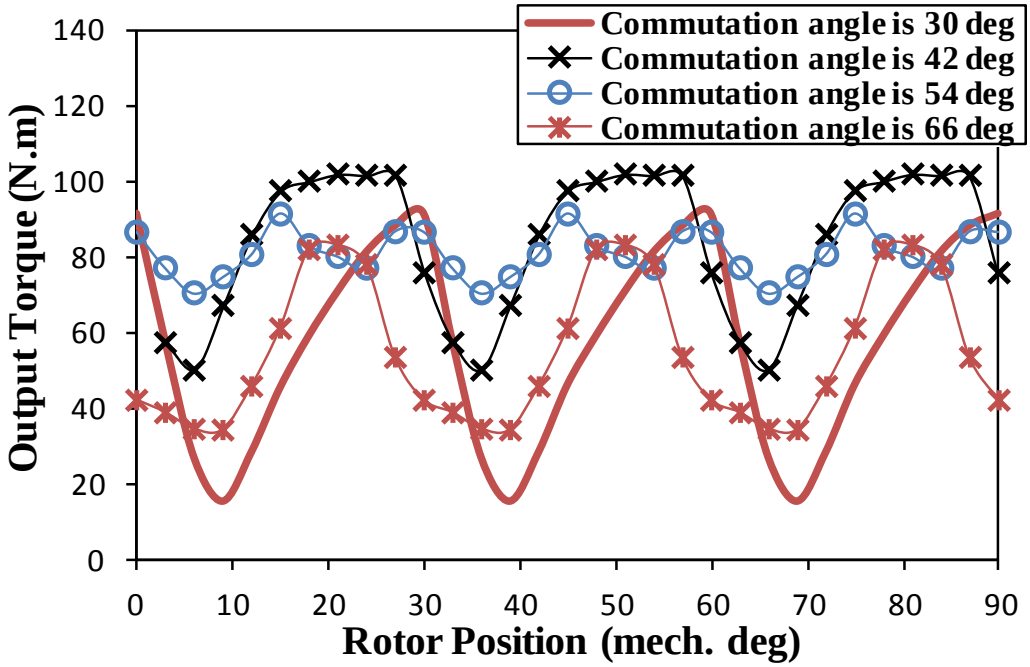

Fig. C.8 Variations of total output torque of 6 stator/4 rotor poles SR machine for different commutation angles, at 2000 rpm.

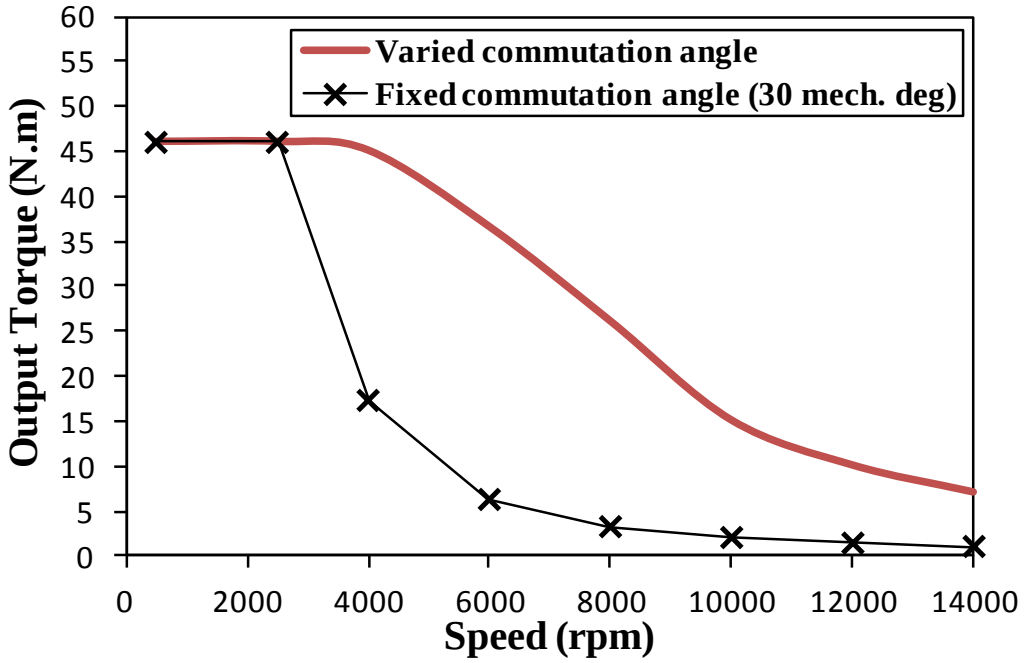

(a) Torque-speed characteristics

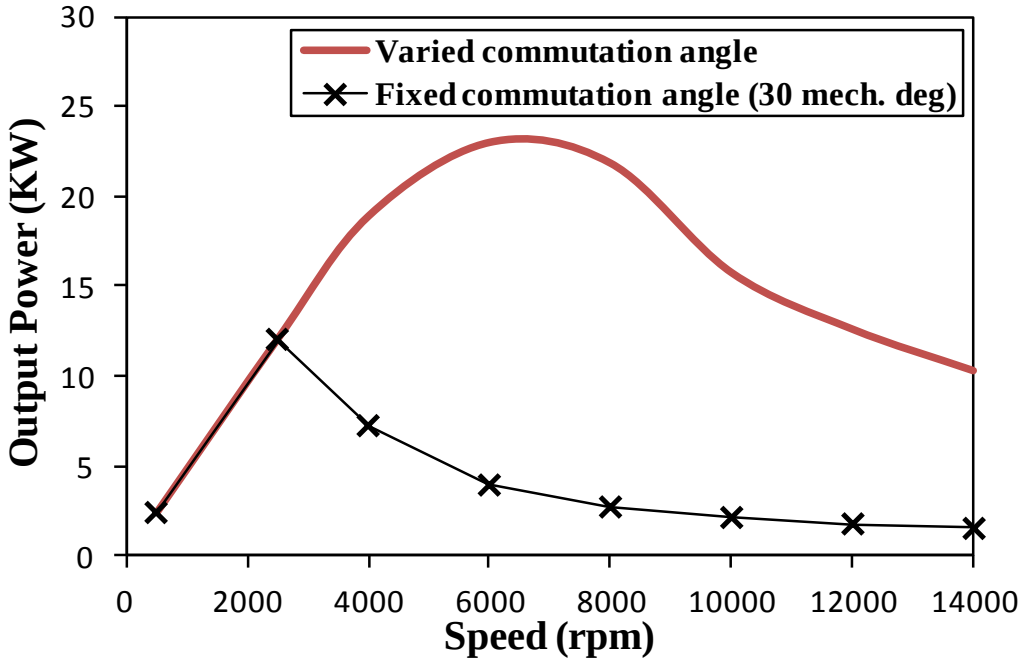

(b) Power-speed characteristics

Fig. C.9 Comparison of torque- and power-speed characteristics of 6 stator/4 rotor poles SR machine for different prediction methods.

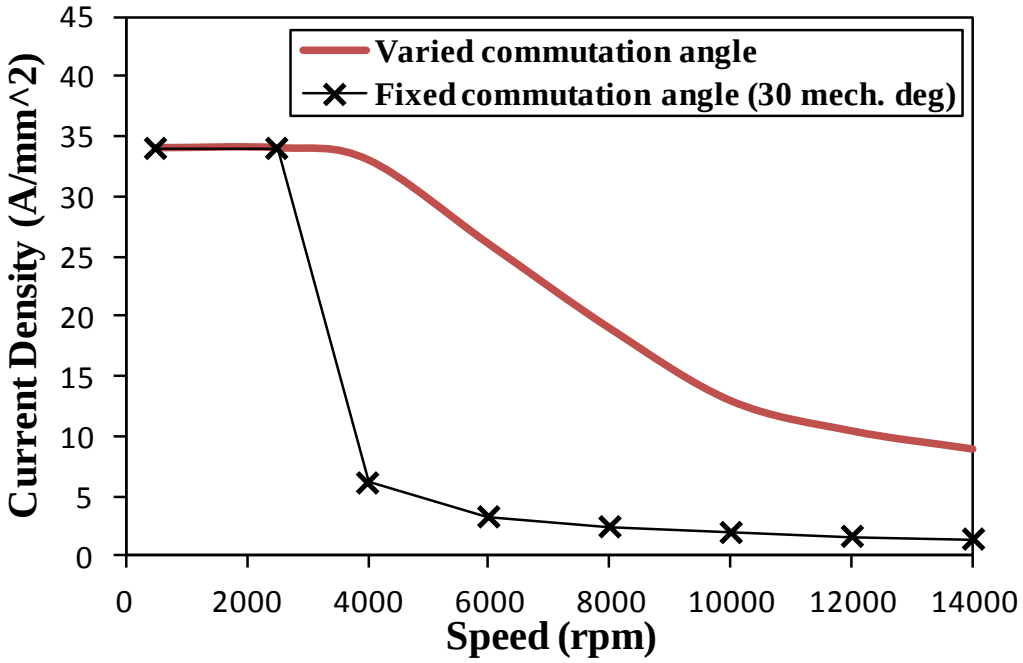

(a) Corresponding current density

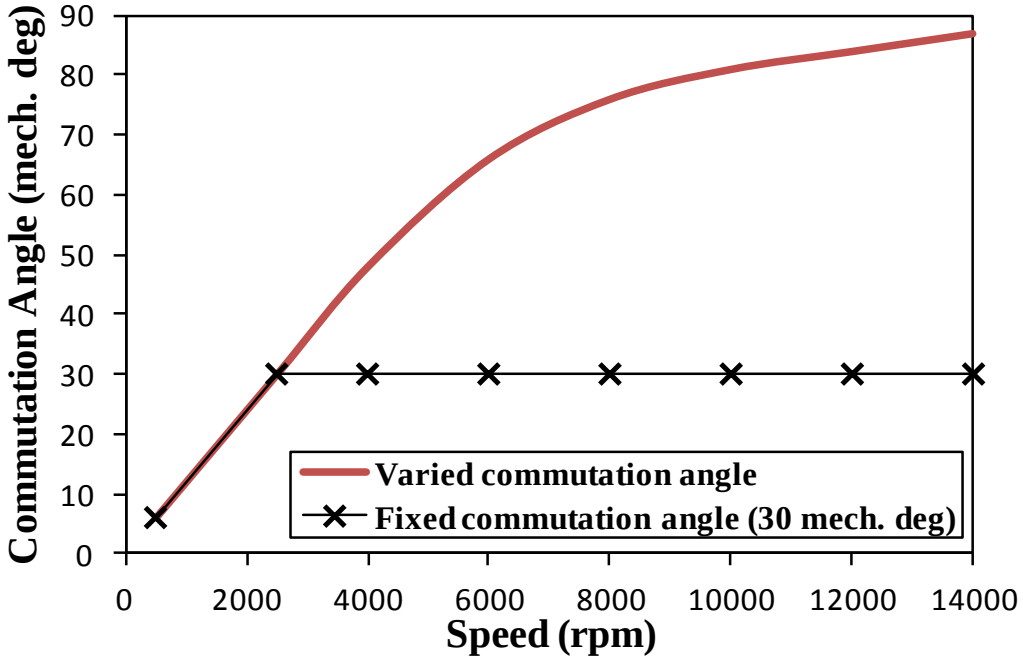

(b) Corresponding commutation angle

Fig. C.10 Comparison of corresponding variations of current density and commutation angles of 6 stator/4 rotor poles SR machine for different prediction methods.

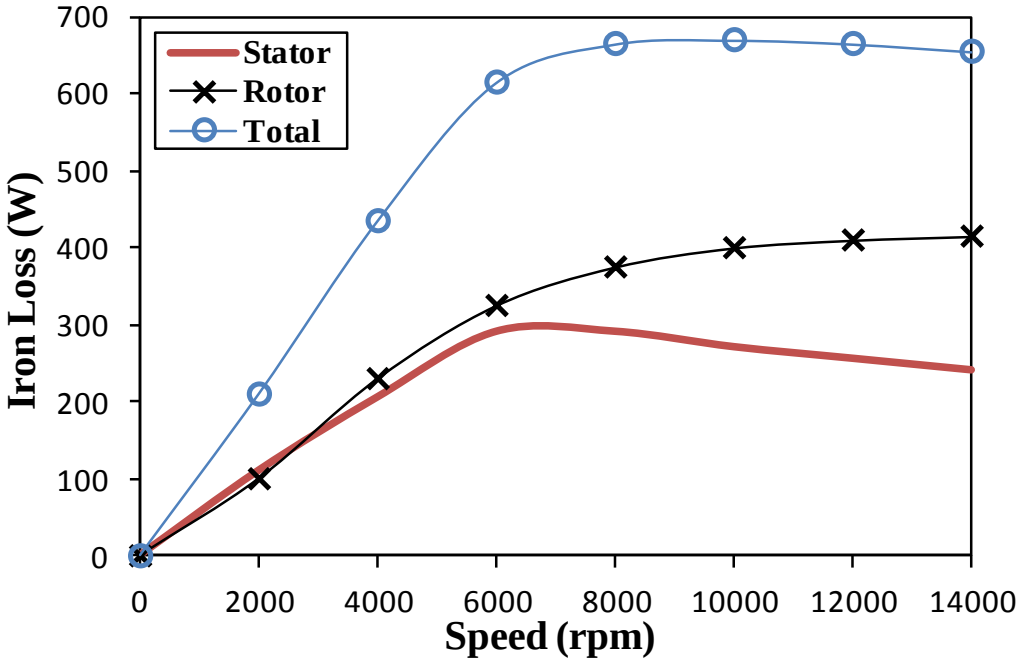

(a) Iron loss

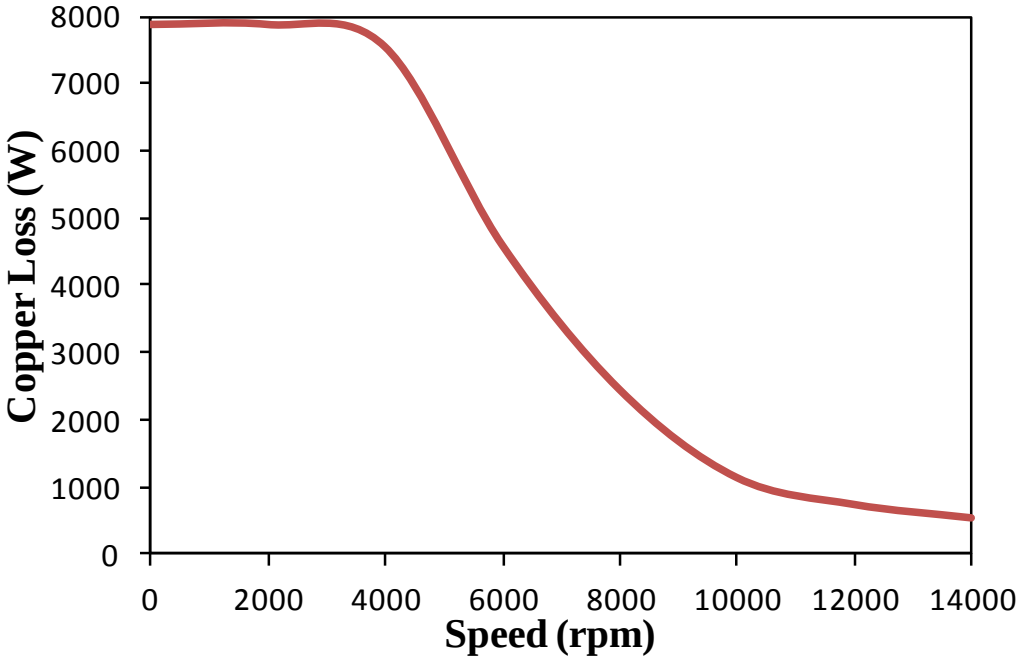

(b) Copper loss

Fig. C.11 Variations of corresponding iron and copper losses of 6 stator/4 rotor poles SR machine using varying commutation angle prediction method.

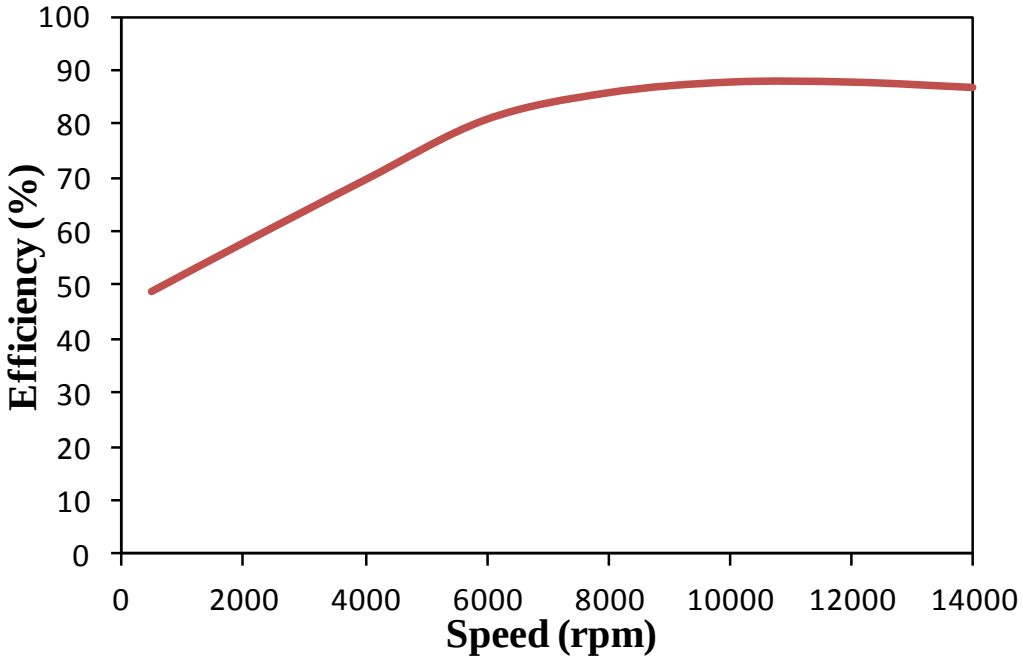

Fig. C.12 Corresponding efficiency of 6 stator/4 rotor poles SR motor using varying commutation angle prediction method.

References

[C.1.] T.J.E. Miller, "Switched reluctance motors and their controls" Monographs in Electrical and Electronics Engineering, no. 30, 1993.

Appendix D: Journal and Conference Publications During PhD Study

Journal Publication

1. Z. Azar, Z.Q. Zhu, and G. Ombach, "Influence of electric loading and magnetic saturation on cogging torque, back-EMF and torque ripple of PM machines," *IEEE Trans. Magnetics,* vol. 48, no. 10, pp. 2650-2658, Oct. 2012.

2. Z.Q. Zhu, Z. Azar, and G. Ombach, "Influence of additional air gaps between stator segments on cogging torque of permanent magnet machines having modular stators," *IEEE Trans. Magnetics,* vol. 48, no. 6, pp. 2049-2055, Jun. 2012.

3. Z. Azar, Z.Q. Zhu, and G. Ombach, "Investigation of torque-speed characteristics and cogging torque of fractional-slot IPM brushless AC machines having alternate slot openings,*" IEEE Trans. Industrial Applications,* vol. 48, no. 3, pp. 903-912, May/Jun. 2012.

4. Z.Q. Zhu and Z. Azar, "Torque-speed characteristics of switched flux permanent magnet machines," *Computation and Mathematics in Electrical and Electronics Engineering,* vol. 31, no.1, pp. 22-39, 2012.

Conference Publications

1. Z. Azar, Z.Q. Zhu, and G. Ombach, "Torque-speed performance analysis of fractional slot PM machines having concentrated winding using alternative method," *IET Int. Conf. Power Electronics, Machines and Drives (PEMD 2012),* Mar. 2012.

2. Z. Azar, Z.Q. Zhu, and G. Ombach, "Influence of alternate slot openings on torque-speed characteristics and cogging torque of fractional slot IPM brushless AC machines,*" IEEE Energy Conversion Congress and Exhibition*, Sep. 2011, pp. 2244-2251.

3. Z.Q. Zhu and Z. Azar, "Influence of end-effect and cross-coupling on torque-speed characteristics of switched flux permanent magnet machines," *IEEE 8th Inter. Conf. Power Electronics-ECCE Asia,* May/Jun. 2011, pp 145-152.

4. Z. Azar, L.J. Wu, D. Evans, and Z.Q. Zhu, "Influence of rotor configuration on iron and magnet losses of fractional-slot IPM machines," *IET Int. Conf. Power Electronics, Machines and Drives (PEMD 2010),* Apr. 2010.

5. D. Evans, Z. Azar, L.J. Wu, and Z.Q. Zhu, "Comparison of optimal design and performance of PM machines having non-overlapping windings and different rotor topologies," *IET Int. Conf. Power Electronics, Machines and Drives (PEMD 2010)***,** Apr. 2010.

Appendix E: Mechanical Drawings of Analysed Machines

Dimensions and drawings of the prototype machines are removed due to confidentiality.